TESIS DOCTORAL / DOKTOREGO TESIA

Mathematical models for glioma growth and migration inside the brain

Autora / Egilea:
Martina CONTE

Directores / Zuzendariak:
Prof. Luca GERARDO-GIORDA
Prof. Juan SOLER VIZCAÍNO

eman ta zabal zazu

Universidad del País Vasco
Euskal Herriko Unibertsitatea

Bilbao, 2021

DOCTORAL THESIS

Mathematical models for glioma growth and migration inside the brain

Author:
Martina CONTE

Supervisors:
Prof. Luca GERARDO-GIORDA
Prof. Juan SOLER VIZCAÍNO

Bilbao, 2021

This research was carried out at the Basque Center for Applied Mathematics (BCAM) within the Mathematical and Theoretical Biology (MTB) group. This research was supported by the Basque Government through the BERC 2014-2017 and BERC 2018-2021 programs, by the Ministry of Science, Innovation and Universities through the BCAM Severo Ochoa accreditations SEV-2013-0323 and SEV-2017-0718 and through the project RTI2018-093416-B-I00 funded by (AEI/FEDER, UE) and acronym "MULTIQUANT", by the European Union's Horizon 2020 research and innovation programme under the Marie Skłodowska-Curie grant agreement No. 713673 and by the fellowship from "la Caixa" Foundation (ID 100010434, the fellowship code is LCF/BQ/IN17/11620056).

"And once the storm is over, you won't remember how you made it through,
how you managed to survive. You won't even be sure, whether the storm is really over.
But one thing is certain. When you come out of the storm, you won't be the same person who walked in. That's what this storm's all about."

Haruki Murakami in *Kafka on the Shore* (2002)

Acknowledgements

Looking back at myself three-years ago, it is incredibly surprising to realize how many things have changed and how much I have changed. This thesis represents only the academic conclusion of my doctoral journey, but this Ph.D. has been about much more than that: it has been a truly life-changing experience. Despite all the little and big struggles, the falls and the achievements, the tears and the laughter, I could not be more grateful for the huge variety of experiences, emotions, and friendships that I have collected during these years. This doctoral journey would not have been possible without the support of the amazing people that I met along the way and I owe them my sincere gratitude.

First of all, I want to thank my supervisors Prof. Luca Gerardo-Giorda and Prof. Juan Soler for their support during this doctorate. Muchas gracias Juan por haber confiado en mí sin casi conocerme, por las oportunidades ofrecidas y por guiarme y aconsejarme cuando más lo necesitaba. E grazie mille Luca, per le possibilitá e la libertá datami nel scegliere la mia strada.

My sincere thanks goes to Prof. Christina Surulescu for hosting me at the TU Kaiserslautern, for sharing with me ideas and knowledge, and for the inspiring discussions.

Allo stesso modo vorrei ringraziare il Prof. Luigi Preziosi per avere accettato di ospitarmi al PoliTo e aver poi intrapreso virtualmente questa collaborazione quando l'emergenza COVID-19 ci ha costretti tutti a cambiare piani.

I would like to express my appreciation to the members of my committee, Prof. Virginia Muto, Prof. Miguel Ángel Herrero, and Prof. Andreas Deutsch, for accepting to participate in the defence of my thesis. In addition to that I want to thank the reviewers, Prof. Andrea Tosin and Prof. Jean Clairambault, for reading the manuscript of this thesis and for writing the corresponding reports.

These pages would not have been possible without the support of my collaborators. Many thanks go to Dr. Sergio Casas-Tintó, Dr. Nadia Loy, and Prof. Maria Groppi. Vorrei spendere qualche parola in più per ringraziare Maria dal profondo del mio cuore. Non solo per tutti i consigli accademici, l'aiuto e la guida constante, specialmente nei momenti di maggiore difficoltà, ma sopratutto per il supporto personale che mi hai dato. Grazie per esserci sempre stata, sai quanto questo significhi per me.

This journey would have not been the same without all the amazing people from BCAM and from the university.

Thanks to all the present and former members of the MMB/MTB group, Nicole, Julia, Isabella, Gabriela, Marina, and Argyrios, for the friendly chats and the support, academic and non-academic. Thanks to Abolfazl and Javi, my office mates since my very first day in BCAM. Thanks to Mikel, Diana, Lore, Vittoria, Havva, Sandeep, Marco, Mauricio, for sharing thousands of coffee breaks and lunches and for making BCAM such a pleasant work environment. Un agradecimiento especial a Lorenzo,

Martín y Tomás por haber significado tanto en tan poco tiempo. I would also like to thank the entire staff of BCAM. En especial, muchísimas gracias a Miguel por la ayuda al resolver cualquier cuestión administrativa y el apoyo durante todo el doctorado.

Muchas gracias a todo el grupo de estudiantes de doctorado del departamento de matemáticas de la UPV, aunque la mayoría de ellos ya sean doctores, por el tiempo que hemos compartido, sin el cual estos años no habrían sido lo mismo. Un agradecimiento particular a Iker, por la compañía en las noches en las que Morfeo se olvida de nosotros. Aunque no tuvimos suficiente tiempo, seguiré esperando nuestra clase de salsa.

During the Ph.D. I have deeply grasped the truthfulness of this: it is not about the amount of time you spent with somebody, it is about the quality of time spent. For this reason, I would like to dedicate a few more words to some special people that I was lucky to meet along the way. Thanks so much to Julia, not only for the incredible help in the revision of this manuscript and her valuable scientific advice, but mostly for the numerous calls, the closeness, and the friendship. Un grazie speciale a Nicole. Sei stata per me molto più che un'amica durante questi anni, sei stata una guida, un supporto constante, una buona dose di razionalità quando tutto sembrava cosí caotico. Ci sei sempre stata, e per me questo é tutt'altro che scontato. Isa, un ringraziamento particolare a te. Apparentemente cosí diverse, eppure sappiamo quanto possiamo essere simili. Grazie per la comprensione, il supporto, i momenti speciali che abbiamo condiviso. Aunque lo haya intentado mucho, Dani, no encuentro las palabras adecuadas para agradecerte tu amistad. Eres una persona muy especial, como creo no quedan muchas hoy en día, y significas para mí mucho más de lo que parece. Javi, se me hace imposible condensar en palabras lo que hemos vividos en estos tres años, y me perdonarás por esto. Gracias por tu sincera amistad, por estar siempre ahí, especialmente en mis peores momentos, por aguantar mis cambios de humor, mis mezclas de italiano y español y, a veces, solo de italiano, sobre todo cuando el día se nos hacía muy largo.

Un trocito de mi corazón se queda aquí en Bilbao, en las comidas que hemos compartido, en los bares del Casco, entre una copa de Txakoli y un pincho de tortilla, en las excursiones por Euskadi, en el frío Cantábrico, en las sidrerías de Gipuzkoa, en Aste Nagusia. No puedo esperar a poder volver a celebrarla todos juntos.

The Ph.D. gave me the possibility of traveling quite a lot, and I am really glad about that. Above all, I am glad for the people that I had the chance to meet during these trips and the pleasure to consider them my friends now. Un grazie dal profondo del mio cuore a Nadia e Giada, per aver significato tanto in cosí poco tempo e nella speranza di poter condividere con voi molti altri momenti in un futuro non troppo lontano. E grazie a te, Fede, ovunque tu sia!

Last but not least, I am especially grateful for my family and friends from home that, even from many kilometres far away, always make me feel loved.

Grazie agli amici di una vita, gli amici più cari, che mi sopportano e supportano da troppi anni ormai. Grazie a quelli che hanno fatto tutto il cammino insieme me e anche a quelli che ho avuto il piacere di ritrovare dopo qualche incrocio al quale avevamo scelto direzioni diverse. Grazie a Fede, un pezzo di cuore lasciato nella mia amata Parma. Grazie, pulci, per essere una amica, una sorella, una confidente, per le nostre risate e i nostri silenzi, per capirmi e accettarmi meglio di quanto riesca a fare io stessa, per il nostro cinismo e l'appoggio incondizionato.

Un immenso grazie a tutta la mia familia, per la sua vicinanza e il suo supporto. Non avrei mai potuto chiedere di far parte di una tribù migliore. Un grazie speciale

alla mia nonna, per il suo amore incondizionato, e a quelli che mi stanno guardando da lassù, che spero siano felici della strada che ho intrapreso E poi ci siete voi, mamma e papá. Che cosa posso dire? Grazie per essere il pilastro solido che sempre mi sostiene, per il vostro appoggio senza riserve, per il vostro aiuto in qualsiasi momento ne senta il bisogno. Spero possiate essere orgogliosi del mio percorso. Vi amo tanto!

During these years I had the luck of being supported by so many amazing people. To everyone that was part of my journey, thank you.

Martina
Bilbao, November 2020

Abstract

Mathematical models for glioma growth and migration inside the brain

Martina CONTE

Gliomas are the most prevalent, aggressive, and invasive subtype of primary brain tumors, characterized by rapid cell proliferation and great infiltration capacity. Despite the advances of clinical research, these tumors are often resistant to treatment, the median survival ranges between 9 and 12 months, and recurrence is the main cause of mortality. Glioma migration and invasion into the brain tissue is a complex phenomenon and little is still known about the underlying mechanisms that lead to tumor progression.

In this thesis, we propose several mathematical models studying various aspects of glioma progression in relation to the microscopic and macroscopic scales characterizing this process. Exploiting the inherently multiscale nature of glioma evolution allows to define models based on dynamical systems, kinetic equations, and macroscopic PDEs with different roles depending on the considered phenomena. The integration of biological and clinical data with the mathematical models is one of the key objectives of this thesis. The experimental data at hand are obtained from magnetic resonance and diffusion tensor images of the human brain and from *in-vivo* immunofluorescence analysis of protein distributions in *Drosophila*, a reliable model for the study of glioblastoma dynamics.

We analyze the anisotropic characteristics of the brain tissue, using the diffusion tensor data, and the influence of the fiber structures on tumor cell dynamics. We show how the fiber network directs cell migration along preferential paths, reproducing the branched and heterogeneous patterns typical of glioma evolution, and how multimodal treatments can reduce this behavior.

We study the interdependency of microenvironmental acidity and vasculature in tumor angiogenesis, defining a model capable of reproducing their influence on the emergence of phenotypic heterogeneity and hypoxia-related features (like necrosis) typical of glioma progression. This study enables the testing of a necrosis-based tumor grading and the investigation of multi-modal therapies with anti-angiogenic effects.

We investigated the role of cell protrusions from a non-local perspective. We explore their influence on the contact guidance phenomenon and on the emergence of collaborative or competitive effects between two cues driving cell velocity changes.

Using the experimental analysis of protein distributions, we evaluate cell protrusion relationship with integrins and proteases as leading mechanisms of glioblastoma progression. We show how the biochemical and biomechanical interactions of these agents result in the emergence of tumor propagation fronts, which can feature a dynamical and heterogenous evolution in relation to environmental changes.

Sinopsis

Modelos matemáticos para el crecimiento y migración de gliomas en el cerebro

Martina CONTE

Los gliomas forman el subtipo más prevalente, agresivo e invasivo de tumores cerebrales primarios, caracterizados por una rápida proliferación celular y una elevada capacidad de infiltración. A pesar de los avances de la investigación clínica, estos tumores suelen ser resistentes al tratamiento; la supervivencia media oscila entre 9 y 12 meses, siendo la recurrencia la principal causa de mortalidad. La migración y la invasión de los gliomas en el cerebro son fenómenos complejos y aún se desconocen varios de los mecanismos subyacentes que guían la progresión de estos tumores.

En esta tesis, proponemos varios modelos matemáticos para estudiar diversos aspectos de la progresión del glioma en relación con las escalas microscópicas y macroscópicas que caracterizan este proceso. Considerar el carácter intrínsico multiescala de la evolución del glioma permite definir modelos basados en sistemas dinámicos, ecuaciones cinéticas y EDP macroscópicas con diferentes roles dependiendo de los fenómenos a estudiar. Uno de los objetivos principales de esta tesis es integrar datos biológicos y clínicos con los modelos matemáticos. Los datos experimentales utilizados se han obtenido de imágenes por resonancia magnética, de imágenes con tensor de difusión del cerebro humano y de análisis de inmunofluorescencia *in-vivo* de distribuciones de varias proteínas en *Drosophila*, un modelo fiable para el estudio de la dinámica del glioblastoma.

Analizamos las características de anisotropía del tejido nervioso, utilizando los datos del tensor de difusión, y la influencia de la estructura de las fibras en la dinámica de las células tumorales. Mostramos cómo la red de fibras guía la migración celular a lo largo de rutas preferenciales, reproduciendo los patrones ramificados y heterogéneos típicos de la evolución del glioma; asimismo, demostramos cómo los tratamientos multimodales pueden reducir este comportamiento.

Estudiamos la interdependencia entre la acidez del microambiente y la vascularización en el proceso de angiogénesis tumoral. Para ello, construimos un modelo capaz de reproducir la influencia de estos mecanismos en el desarrollo de la heterogeneidad intratumoral y de características típicas de la progresión del glioma relacionadas con la hipoxia (e.g. la necrosis). Este estudio permite formular una clasificación de los tumores basada en el nivel de necrosis, así como la investigación de terapias multimodales que incluyan efectos anti-angiogénicos.

Investigamos la influencia de las protrusiones celulares desde una perspectiva no local. Analizamos su rol en el fenómeno de la guía por contacto y en la manifestación de efectos colaborativos o competitivos entre dos estímulos que determinan cambios de dirección de la velocidad celular.

Utilizando el análisis experimental de las distribuciones de varias proteínas, evaluamos la relación de las protrusiones celulares con las integrinas y las proteasas como principales mecanismos de progresión del glioblastoma. Mostramos cómo las interacciones bioquímicas y biomecánicas de estos agentes dan como resultado el desarrollo de frentes de propagación tumoral, que pueden presentar una evolución dinámica y heterogénea en relación a los cambios ambientales.

Laburpena

Garunaren barruko gliomaren hazkunde eta migraziorako eredu matematikoak

Martina CONTE

Glioma burmuin tumore primario motarik nagusiena, agresiboena eta inbasiboena da, haren ezaugarririk garrantzitsuenak zelulen ugaltze azkarra eta infiltrazio gaitasun handia izanik. Nahiz eta ikerketa klinikoan aurrerapen ugari egon, tumore hauek tratamenduei erresistentzia egiten diote maiz, biziraupen mediana 9 eta 12 hilabeten artekoa da, eta tumorearen berragerpena mortalitatearen kausa nagusia da. Gliomaren inbasioa eta migrazioa garun ehunetan zehar fenomeno konplexua da eta tumorearen progresioa bultzatzen duten mekanismoei buruz gutxi dakigu oraindik.

Tesi honetan, hainbat eredu matematiko proposatzen ditugu, gliomaren migrazio prozesua aztertzeko honen eskala makroskopiko eta mikroskopikoetan. Glioma eboluzioaren izaera multieskalarra erabiliz, eredu desberdinak definituko ditugu, sistema dinamikoetan, ekuazio zinetikoetan edota DPE makroskopikoetan oinarrituta, kontuan hartutako fenomenoaren arabera. Tesi honen helburu nagusia eredu matematikoen eta datu biologiko eta klinikoen arteko integrazioa da. Erabilitako datu esperimentalak erresonantzia magnetiko eta difusio-tensore irudietatik ateratakoak dira, bai eta *Drosophila* espezimeneko proteina banaketen *in-vivo* inmunofluoreszentzia analisietatik. Azken hau glioblastomaren dinamikak ikertzeko eredu fidagarria da.

Difusio tensorearen datuak erabiliz, garun ehunaren ezaugarri anisotropikoak ikasiko ditugu, bai eta zuntzen egiturek tumore zelulen dinamikan daukaten eragina ere. Ikusiko dugu nola zuntza-sareak zelulen migrazioa zuzentzen duen lehentasunezko bideetan, eta nola tratamendu multimodalek jokabide hau gutxiagotu dezaketen.

Azidotasun mikroanbientala eta baskulaturaren arteko menpekotasuna aztertuko dugu. Horretarako, haiek duten eragina erreproduzitzeko gai den eredu bat proposatuko dugu, bai fenotipoen heterogeneotasunaren agerpenan bai gliomaren aurreratzearen tipikoak diren hipoxia motako ezaugarrietan, hala nola nekrosia. Azterketa honek bidea ematen digu tumoreak sailkatzeko nekrosi graduaren arabera, bai eta ondorio anti-angiogenikoak duten terapia multimodalak ikertzeko ere.

Zelulen protrusioek daukaten rola ikertzen dugu ikuspuntu ez-lokal batetik. Haien eragina esploratuko dugu bi eremutan: alde batetik, kontakatu bidezko bideraketa fenomenoan; bestetik, zelulen abiadura aldaketa baimentzen duen bi seinalen arteko efektu kolaboratibo edo konpetitiboen agerpenetan.

Proteina banaketen analisi esperimentala erabiliz, zelulen protrusioaren integrinekiko eta protreasarekiko erlazioa ebaluatuko dugu glioblastomaren garapenaren mekanismo nagusi gisa identifikatuz. Erakutsiko dugu nola agente hauen elkarreragin biokimiko eta biomekanikoek tumorearen hedapena agerrarazten duten. Hedapen honetan ikus daiteke eboluzio dinamiko eta heterogeneoa, ingurumenaren aldaketen arabera.

Summary

Gliomas are the most prevalent subtype of primary brain tumors originating from mutations of the glia cells in the central nervous system. Classified by the World Health Organization into three main types and four grades depending on the degree of tumor differentiation, their most common and aggressive malignant variety is called glioblastoma (GB). Gliomas, and especially GBs, are characterized by fast cell growth, strong invasion capability, and well-developed tumor vasculature. This vasculature originates from hypoxia-driven mechanisms and supplies glioma cells with the nutrients necessary to sustain their proliferation and spread. Although the research advances and the clinical trials testing the efficacy of novel combined therapies have allowed significant progress in the comprehension and treatment of gliomas, these tumors are characterized by a poor prognosis, with a median survival range between 9 and 12 months. Therefore, the research on the mechanisms driving glioma progression remains an emerging field.

Biological motivations and main objectives

The advancements in technology have created a considerable amount of clinical and biological data concerning the mechanisms that drive glioma evolution. However, the high complexity of the invasion process remains a challenge to face in the research on glioma development, and several important questions are still unanswered. Moreover, there is a need to integrate the theoretical and empirical acquired knowledge towards the investigation of the mechanisms that contribute to tumor growth and invasion. In this context, mathematical models emerge as powerful tools to face these challenges, as they can provide significant insights into the processes characterizing tumor progression. In this dissertation, we propose different mathematical models for the description of some relevant mechanisms involved in glioma growth and spread inside the brain, with a special interest in integrating clinical and biological data in the model settings.

The objective of this thesis is to study the processes involved in cell migration and invasion, tumor angiogenesis, and the application of possible therapeutic treatments. The capability of ***cell invasion*** into the healthy brain tissue represents one of the most prominent glioma features and it combines both intracellular and intercellular mechanisms. In particular, the interactions between tumor cells and the extracellular matrix (ECM) have a central role in leading tumor progression. The anisotropic *fiber structure* characterizing the brain tissue influences the direction of cell migration determining preferential paths along which the cells move. These cell-ECM interactions are mediated by the *cell protrusions*, extensions of the plasma membrane outside of the cell body that capture external stimuli to activate downstream pathways leading to migration. Precisely, the external signals are detected by transmembrane receptors located on the protrusions. *Integrins* are the most common family of membrane receptors involved in glioma-ECM adhesion and they have been demonstrated to facilitate tumor infiltration in normal tissue. Besides the cell membrane receptors, further mediators of

cell migration are *proteases*, enzymes localized in specific tumor regions that modulate and remodel the ECM. This remodeling process allows creating space for tumor cells to migrate. Increased levels of proteases have been shown to correlate with tumor invasiveness and aggressiveness. ***Angiogenesis***, consisting in the growth of new blood vessels from the existing vasculature, is another core mechanism in tumor progression. Tumor vasculature, constituted by endothelial cells (ECs), provides the necessary nutrients for the cells to grow and spread, and the higher the degree of vascularization, the more advanced the tumor grade. Vascular proliferation is sustained by *angiogenic growth factors* secreted by tumor cells and especially over-expressed in the surrounding of necrotic regions. The lack of nutrients, in fact, as well as an excessive environmental *acidity*, determines the formation of *necrotic matter* and encourages a more active migration of the cells towards more favorable brain regions. Concerning the treatment of glioma patients, different ***multi-modal therapies*** have been tested and are currently applied in the clinical practice. The standard combination of the *surgical resection* of the most possible extended area interested by the tumor, the *radiotherapy*, and the *chemotherapy* with temozolomide (the most common chemotherapeutic agent) is supported by new therapeutic targets. We focus on the emerging therapies that target integrin function and tumor angiogenesis. The *integrin inhibitors* reduces the cell-ECM binding capability, while angiogenesis is impaired by *anti-angiogenic factors* that decrease the vascular proliferation and the affinity between pro-angiogenic factors and endothelial cells.

Mathematical framework

The process of glioma evolution features an inherently multiscale nature due to characteristic phenomena that occur on different spatial and temporal scales. Therefore, in this thesis, we use a ***multiscale mathematical framework*** based on three specific levels of description to characterize glioma progression. The *subcellular level*, generally defined in terms of ODE systems, describes the processes taking place at the single cell level, such as the interactions between molecules and membrane receptors. The *cellular level*, modeled by kinetic equations, describes the interactions between the tumor cells and the extracellular environment. These interactions influence cell invasion (in terms of velocity changes), cell proliferative, phenotypic switches, or blood vessel formation. The *tissue level*, involving PDEs for the macroscopic quantities, describes diffusive or drift phenomena leading to tumor progression and reflects the main features of tumor evolution that are observed in the clinical context. The equations at this level can be properly derived from lower levels of description via asymptotic methods or can be directly stated at the macroscopic scale when the nature of the involved mechanisms does not allow for a formal derivation from first principles.

In this dissertation, we propose different approaches relying on both the deduction of the continuous macroscopic systems from a kinetic description of the cell behavior (Chapters 3-6) and on their definition directly at the macroscopic level (Chapter 7). As the presented settings assess the problem of cell migration from different perspectives, important ingredients in the models concern the description of diffusive and dispersive cell dynamics. The description of these dynamics can be stated in either a linear or a nonlinear form. While the deduction of the linear form from a kinetic level is well-established and has been largely investigated, the definition of a proper deduction for the nonlinear form is still a pending issue, currently under investigation. However, the use of nonlinear diffusive terms (especially in their flux-saturated form) allows to account for additional properties of the solution, such as a finite speed of propagation,

the definition of invasion fronts, and the preservation of the initial profile characteristics (compactness of the support or possible jump discontinuities). Therefore, in this dissertation, we rely on a linear description of the diffusive terms in the kinetic-based settings (Part II), while we use a nonlinear description in the macroscopic setting (Part III).

Description of the thesis contents and the main achievements

This thesis is structured in seven main chapters divided into three parts. An introduction to both the biological and the mathematical concepts of this dissertation is provided in Chapter 1. Here, we first discuss the biological aspects related to the study of glioma progression. We focus on three central topics that represent the cores of the proposed models: *glioma invasion* in the brain tissue and its main mediators, namely cell protrusions (subjects of Chapters 6 and 7), membrane receptors (subjects of Chapters 3-5 and 7), and proteases (subjects of Chapter 7); *tumor angiogenesis*, with its characteristic features associated with tissue hypoxia, acidity and necrosis (subjects of Chapters 4 and 5); *clinical treatments*, combining standard and novel therapeutic agents (subjects of Chapters 3 and 5). Moreover, we discuss the biological and clinical data that we include in the models. Namely, we describe the commonly used medical imaging techniques, with a special focus on *MRI* and *DTI*, which allow the reconstruction of the brain geometry and the diffusion-tensor data used in Chapters 3-5, and the *immunostaining techniques*, which provide the protein distribution data used in Chapter 7. Then, we introduce the mathematical aspects of the thesis. We discuss the inherent multiscale nature of our problem, introduce the basic concepts of the two modeling frameworks we rely on, namely multiscale models stated in terms of kinetic equations and macroscopic models, and highlight their main peculiarities.

Part I accounts for the preliminary studies, proposed in Chapter 2, that concern some of the ***characteristics of the brain tissue***. The features described in this chapter are subsequently taken into account in all the model settings. Precisely, we discuss the *anisotropic characteristics* of the brain fiber network that are responsible for the macroscopic heterogeneous patterns observed in glioma images. Accounting for this aspect of fiber alignment is fundamental to obtain reliable mathematical models. We provide insight into the diffusion tensor imaging (DTI) technique and the provided tensor data, which describe the molecular diffusivity in the different directions. In particular, we discuss the quantification of these data employing scalar maps (e.g. the *fractional anisotropy* (FA)). Then, since the tensor describing cell diffusivity is derived from the DTI tensor data, we comment on some methodologies that have been identified to include the DTI information into the macroscopic and the kinetic-based modeling frameworks. Referring to the kinetic framework, we comment on the use of a distribution function to describe the fiber network and build the tensor characterizing cell diffusivity. Moreover, we perform a *comparison between the three main used expressions for this function* (Peanut distribution, von Mises-Fisher distribution (VMF), and orientation distribution function (ODF) [3, 216]), using processed DTI data and the fractional anisotropy (Figures 2.7-2.11). The results highlight strengths and weaknesses of each of these distributions, providing proper arguments to motivate the choices of one of them instead of another. The Peanut distribution is easy to compute, although it partially loses the anisotropic information originating from the DTI data, while the VMF distribution is more accurate, but requires a proper tuning of the parameters involved in its expression. The computation of the ODF is more complex and costly, but this distribution shows a good degree of accuracy. This analysis represents a preparatory work for the settings proposed in Part II, in which the distribution functions have a

central role in the modeling of the contact guidance phenomenon.

Part II comprises the kinetic-based models in which the macroscopic settings are formally derived from systems of kinetic transport equations. Precisely, the models in Chapters 3-5 are built using a micro-meso formulation that combines the description of microscopic dynamics with mesoscopic kinetic equations from which the macroscopic settings are derived via parabolic limit and the Hilbert expansion method. Chapter 6 presents a class of non-local kinetic models only stated at the mesoscopic level on which both parabolic and hyperbolic limits are applied to derive the macroscopic settings in the appropriate regime. Macroscopically, the models proposed in these chapters feature linear diffusion and multiple taxis, the latter carrying information about the microscopic dynamics (when applicable). The ***influence of the brain tissue architecture on tumor cell migration*** represents the core of the DTI-based model proposed in Chapter 3. In line with the studies in [74, 126], we model the role of the *brain fibers* as the cue guiding cell migration and we describe the dynamics of *integrins* as mediators of cell-ECM interactions. These interactions are also responsible for tumor proliferation. The macroscopic equation is derived via parabolic scaling and simulated on a 2D brain slice, which is reconstructed from the MRI data processing and accounts for DTI data. The numerical tests analyze the impact of the different expressions of the fiber distribution functions and of the microscopic dynamics on the emergence of anisotropic macroscopic patterns in the tumor evolution (Figures 3.3-3.5). For instance, when the Peanut distribution is included in the model, we notice a more homogenous tumor spreading, different from the branched patterns observed in the case of the ODF. Analogous differences are shown comparing the inclusion and the exclusion of the microscopic dynamics in the model. Moreover, we incorporate in the model the description of a *combined therapy based on integrin inhibitors and radiation*, showing numerically the reduction of tumor infiltration due to the integrin inhibitors and the radiation impact on the cell density (Figures 3.6-3.7).

The first extension of this multiscale setting is proposed in Chapter 4, where the description of tumor evolution is coupled with the modeling of the interdependency of ***acidity and vascularity***, two key ingredients in the process of tumor angiogenesis. In this setting, tumor evolution involves, at the microscale, the dynamics of two types of membrane receptors, mediating cell interactions with the ECM and the extracellular protons determining the environmental acidity. Moreover, we introduce a component of ***intratumor heterogeneity*** in the description of glioma evolution. We rely on the *go-or-growth hypothesis* asserting that a cell can either move or proliferate and the respective behavior is transient. The switching between growth and migration depends on the nutrient availability (supplied by vasculature), the extracellular pH (determined by the acidity), and the crowding of the environment. Angiogenesis is necessary to sustain tumor proliferation and is described in terms of the evolution of the EC density. ECs are characterized by a migratory behavior towards tumor cells in response to the pro-angiogenic growth factors that tumor produces to satisfy the energy demand. The macroscopic equations for tumor and ECs are derived via parabolic scaling of the kinetic formulation, which involves the microscopic dynamics, and feature multiple taxis phenomena. We first couple this macroscopic setting with the dynamics of protons, regulating the extracellular pH and, consequently, the acidification of the tumor microenvironment. For this model, we lump together the two mechanisms of *hypoxia* (due to low oxygenation) and *acidosis* (due to hypoxia-driven metabolism shift), evaluating directly the resulting level of *extracellular pH* and modeling its influence on tumor dynamics. The numerical simulations show the nonlinear nature of the dynamics that arise from the repellent pH-taxis (tumor cells tend to avoid highly acidic regions) and the ability of the model to capture *hypoxia-related*

histopathological features (Figures 4.3-4.4). Moreover, with these simulations we analyze the influence of the go-or-growth dichotomy on the overall behavior, noticing a general slowdown of the tumor dynamics compared to the case in which this dichotomy is neglected (Figures 4.5-4.6). Then, we extend the setting to include the dynamics of tissue and necrotic matter, caused by the acidity. With these two additional elements, we define a *necrosis-based tumor grading* that allows us to analyze the influence of intratumor heterogeneity and vasculature on the evolution of the tumor grade (Figure 4.10).

The ***influence of angiogenesis on the tumor response to the therapy*** is the central focus of Chapter 5. Here, we model the dynamics of tumor and endothelial cells at both the microscopic and the kinetic level, and then coupling the derived macroscopic equations with the description of *vascular endothelial growth factors* (VEGFs) evolution. These growth factors, whose effect on ECs was indirectly included in the setting of Chapter 4, are produced by tumor cells in hypoxic conditions to attract ECs towards the tumor mass and, thus, provide the nutrients to sustain tumor proliferation. Moreover, at the tissue level, we include the description of healthy tissue degradation and the growth of necrotic matter. In this model, we describe the effects of a treatment combining *radiation*, *chemotherapy* with temozolomide, and *anti-angiogenic therapy*. The former affects tumor, ECs, and healthy tissue, whose degradation also depends on the (acidity produced by) the activity of tumor cells. Chemotherapy is delivered by blood and only affects the tumor population, while the anti-angiogenic therapy impacts ECs. Anti-angiogenic therapy reduces ECs proliferation and the affinity between ECs and VEGFs. The preliminary numerical results analyze the effects of this multi-modal treatment, which mainly depletes tumor density and degrades the healthy tissue, with respect to the situation without any therapies (Figures 5.2 and 5.4). Moreover, we study the effect of the only anti-angiogenic therapy in decreasing EC migration and the vasculature supply to the tumor (Figure 5.5). This model lays the basis for a study of the *therapy efficacy* based on real data of glioma patients (which is the subject of a forthcoming work).

In the previous chapters, the proposed settings assume a single cue to drive the velocity changes at the kinetic level. This cue can be either the fiber network (as for tumor cells in Chapters 3-5) or the gradient of a population or an external signal (as for ECs in Chapter 4). In Chapter 6, we analyze the ***effect of multiple cues influencing cell migration*** at the kinetic level. In line with [173], we propose a kinetic-based model for the description of the influence of *chemotaxis* and *contact guidance* (driven by the tissue fiber network) on the cell velocity changes and, thus, on cell migration. The model includes *non-local terms*, that describe the sensing of the environment and allow to incorporate the effects of the extension of cell protrusions for exploring the neighborhood around a cell. At the kinetic level, we introduce two classes of models, depending on whether the cells perform an independent sensing of the two cues or average them with the same sensing kernel. According to the characteristic lengths of variation of the cues and the adopted sensing strategy, we derive different macroscopic limits of the two transport models and simulate them to illustrate the behavior of the solution in the various cases. The results highlight the impact of the double-cue environment (with respect to a single cue) that, even for locally sensed and non-oriented fibers, ensures a preferential sense of motion to the cells (Figure 6.1). The simulations show how the model captures *collaborative or competitive effects* of the two cues, which can sustain or contrast cell movement (Figures 6.9-6.10). Moreover, we analyze how these effects are influenced by the angle between their relative orientations and their relative strengths, in terms of *degree of alignment of the fiber* and *steepness of the chemoattractive gradient*. Mono-directional cues (like chemotaxis) compete when this

angle is π, whereas they collaborate when this angle is 0, while for bi-direction cues (like contact guidance) competition requires an angle of $\pi/2$. Between these values, many intermediate scenarios can happen (Figures 6.4-6.8).

The last part (Part III) accounts for the macroscopic setting proposed in Chapter 7. We analyze the ***dynamics of the tumor invasion front*** and the biochemical and biomechanical aspects related to it, with a focus on the role of *cell protrusions* (called tumor microtubes in the context of GB) in glioma progression. We model at the macroscopic level the evolution of the tumor population, using nonlinear terms that allow an effective study of the propagation front, together with the equations for the description of *integrins*, *proteases*, and *ECM dynamics*. The proposed framework integrates the mathematical description of the population dynamics with experimental data about protein distribution studies. The experiments are performed in a *Drosophila* model, which is a suitable platform for the study of molecular and cellular mechanisms implicated in GB progression. The results of the performed data analysis are useful to determine the localization and the profile of protease and integrin distributions in different brain regions. Precisely, integrins are divided into two subfamilies, whether these receptors are actively bound to the ECM or not. The resulting macroscopic setting is characterized by flux-saturated descriptions of the diffusive fluxes that allow a direct control on the front velocity and the emergence of a sharp front profile. This macroscopic model shows a strong coupling between the different populations and it is simulated in a 1D scenario, which enables the comparison with the experimental data. The numerical results are in good agreement with experimental measurements and they show the dynamical evolution of the GB front and the emergence of organized patterns in the population profiles (Figure 7.12). We analyze the influence of the tactic processes and of possible porosity changes in the appearance of front heterogeneities and separations. We propose and test two possible approaches for the description of heterogeneous proliferation, which can either enhance or reduce the front separation (Figures 7.13-7.17). These tests explore the potential of the proposed setting in reproducing phenomena related to front heterogeneity, even though these aspects will better express their impact in a 2D extension of the model.

The proposed settings show several advances in the study of the processes driving glioma progression, especially from the viewpoint of cell migration. Nevertheless, different extensions and improvements of these settings can be proposed (Chapter 8). We are currently working on the definition of a stochastic extension of the model described in Chapter 5 to study the efficacy of the therapeutic treatments on real patient data. Concerning the framework defined in Chapter 6, we are going to extend it to the case of external cues affecting also cell speed. Moreover, we are going to use the models as a platform to quantify directed cell migration and to set its efficiency in the case of competitive cues on a realistic domain. This can mimic *in-vivo* or *in-vitro* cell migration in the extracellular matrix. Finally, we are going to extend the macroscopic model of Chapter 7 in the 2D spatial case to study the effect of the fiber directions on the tumor front dynamics and to analyze the phenomena described above (heterogeneous proliferation and porosity changes) in a more complex and realistic environment.

We conclude this dissertation with three explicative appendices. Appendix A provides a basic introduction to the processing of MRI and DTI data, while Appendix B gives a detailed overview about the main mathematical concepts behind the finite element method, the time advancing method, and the numerical integration used to solve the macroscopic models. Finally, Appendix C contains a description of the experimental procedures performed to obtain the experimental data included in Chapter 7 and the corresponding data analysis.

Resumen

Los ***gliomas*** forman el subtipo más prevalente de tumores cerebrales primarios que se originan a partir de mutaciones de las células gliales en el sistema nervioso central. Clasificados por la Organización Mundial de la Salud en tres tipos principales y cuatro grados según la evaluación de la diferenciación tumoral, su variedad maligna más común y más agresiva se llama glioblastoma (GB). Los gliomas, y especialmente los GB, se caracterizan por un rápido crecimiento celular, una marcada capacidad de invasión y un sistema vascular bien desarrollado. Este sistema vascular se origina a partir de mecanismos impulsados por la hipoxia y proporciona a las células de glioma los nutrientes necesarios para mantener su proliferación y propagación. Aunque los avances en la investigación y los ensayos clínicos, que evalúan la eficacia de nuevas terapias combinadas, han permitido progresos significativos en la comprensión y en el tratamiento de los gliomas, estos tumores se caracterizan por un mal pronóstico, con una supervivencia media entre 9 y 12 meses. Por lo tanto, la investigación sobre los mecanismos que impulsan la progresión de los gliomas sigue siendo un campo emergente.

Motivaciones biológicas y objetivos principales

Los avances tecnológicos han creado una cantidad considerable de datos clínicos y biológicos sobre los mecanismos que impulsan la evolución del glioma. Sin embargo, la elevada complejidad del proceso de invasión sigue siendo un desafío a afrontar en la investigación sobre el desarrollo del glioma, y varias preguntas importantes aún siguen sin respuesta. Además, es necesario combinar los conocimientos teóricos y empíricos adquiridos para desarrollar la investigación de los mecanismos que contribuyen al crecimiento y a la invasión tumoral. En este contexto, los modelos matemáticos emergen como una importante herramienta para afrontar estos desafíos, ya que pueden proporcionar información significativa sobre los procesos que caracterizan la progresión tumoral. En esta tesis, proponemos diferentes modelos matemáticos para la descripción de algunos de los mecanismos más importantes implicados en el crecimiento y en la diseminación del los gliomas en el cerebro, con un interés especial en integrar datos clínicos y biológicos en la estructura del modelo.

El principal objetivo de esta tesis es estudiar los procesos implicados en la migración y en la invasión celular, la angiogénesis en el tumor y la aplicación de posibles tratamientos terapéuticos. La capacidad de ***invasión celular*** en el tejido cerebral sano representa una de las características más relevantes del los gliomas y combina mecanismos intracelulares con intercelulares. En particular, la interacción entre las células tumorales y la matriz extracelular (MEC) tiene un papel central en la guía de la progresión del tumor. La *estructura anisotrópica de las fibras nerviosas* influye en la dirección de migración celular determinando rutas preferenciales a lo largo de las cuales se mueven las células. Estas interacciones célula-MEC están mediadas por las *protrusiones celulares*, que son extensiones de la membrana plasmática fuera del cuerpo celular y que capturan los estímulos externos para activar las vías subyacentes de la

migración. Concretamente, las señales externas son detectadas por receptores transmembrana ubicados en las protrusiones. Las *integrinas* son la familia más común de receptores de membrana involucrados en la adhesión entre células de glioma y MEC y se ha demostrado que estos receptores facilitan la infiltración tumoral en el tejido normal. Además de los receptores de la membrana celular, otros mediadores de la migración celular son las *proteasas*, enzimas localizadas en regiones tumorales específicas que modulan y remodelan la MEC. Este proceso de remodelación permite crear espacio para que las células tumorales migren. Se ha demostrado que los niveles elevados de proteasas se correlacionan con la agresividad y la invasividad del tumor. La ***angiogénesis***, que consiste en la formación de vasos sanguíneos nuevos a partir de los vasos preexistentes, es otro mecanismo clave en la progresión del tumor. La vasculatura del tumor, constituida por células endoteliales (CE), proporciona los nutrientes necesarios para que las células crezcan y se diseminen, y cuanto mayor es el grado de vascularización, más avanzado es el grado del tumor. La proliferación vascular se sostiene por *factores de crecimiento angiogénicos* secretados por las células tumorales y principalmente sobreexpresados en el entorno de las regiones necróticas. De hecho, la falta de nutrientes, así como una excesiva *acidez* del ambiente, determinan la formación de *tejido necrótico* e impulsan una migración más activa de las células hacia regiones cerebrales más favorables. En cuanto al tratamiento de pacientes con gliomas, se han evaluado diferentes ***terapias multimodales*** que actualmente se aplican en la práctica clínica. La práctica estándar de *resección quirúrgica* de la mayor área tumoral posible, *radioterapia* y *quimioterapia* con temozolomida (el agente quimioterapéutico más común) se combina con nuevos objetivos terapéuticos. En esta tesis, nos centramos en las terapias emergentes dirigidas a influir en la actividad de las integrinas y en la angiogénesis tumoral. Los *inhibidores de integrinas* reducen la capacidad de unión de las células y la MEC, mientras que la angiogénesis se ve afectada por *factores anti-angiogénicos* que disminuyen la proliferación vascular y la afinidad entre los factores pro-angiogénicos y las células endoteliales.

Contexto matemático

El proceso de evolución de un glioma tiene un carácter intrínsico multiescala debido a fenómenos peculiares que ocurren en diferentes escalas tanto espaciales como temporales. Por lo tanto, en esta tesis, utilizamos un ***contexto matemático multiescala*** basado en tres niveles de descripción específicos para caracterizar la progresión de los gliomas. El *nivel subcelular*, comúnmente definido en términos de sistemas de EDO, describe los procesos que tienen lugar a nivel de una sola célula, como las interacciones entre moléculas y receptores de membrana. El *nivel celular*, modelado por ecuaciones cinéticas, describe las interacciones entre las células tumorales y el entorno extracelular. Estas interacciones influyen en la invasión celular (en términos de cambios de velocidad), en la proliferación celular, en los cambios fenotípicos y en la formación de vasos sanguíneos. El *nivel del tejido*, formulado por EDP para las cantidades macroscópicas, describe los fenómenos de difusión y de transporte, que guían la progresión del tumor, y refleja las principales características de la evolución del tumor observadas en el contexto clínico. Las ecuaciones de este nivel pueden derivarse adecuadamente de los niveles inferiores de descripción mediante métodos asintóticos o pueden ser definidos directamente a la escala macroscópica cuando la complejidad de los mecanismos involucrados no permite una derivación formal desde primeros principios.

En esta tesis, proponemos diferentes modelos que se basan tanto en la deducción

de los sistemas macroscópicos continuos a partir de una descripción cinética del comportamiento celular (Capítulos 3-6) como en su definición directa desde el punto de vista macroscópico (Capítulo 7). Como los modelos presentados evalúan el problema de la migración celular desde diferentes perspectivas, las descripciones de las dinámicas celulares de difusión y de dispersión son componentes importantes de estos modelos. La descripción de estas dinámicas puede ser formulada en forma lineal o no lineal. Si bien la deducción de la forma lineal a partir de un nivel cinético está bien establecida y extensamente investigada, una adecuada deducción para la forma no lineal sigue siendo un tema abierto y está actualmente en desarrollo. Sin embargo, el uso de términos difusivos no lineales (sobre todo en la versión de flujo saturado) permite tener en cuenta propiedades adicionales de la solución, como una velocidad finita de propagación, la definición de frentes de invasión y la preservación de las características del perfil inicial (compacidad del soporte o posibles discontinuidades de tipo salto). Por lo tanto, en esta tesis, nos basamos en una descripción lineal de los términos difusivos en los modelos con base cinética (Parte II), mientras que usamos una descripción no lineal en el modelo macroscópico (Parte III).

Descripción del contenido de la tesis y los logros principales

Esta tesis está estructurada en siete capítulos principales divididos en tres partes. En el Capítulo 1 se presenta una introducción a los conceptos biológicos y matemáticos de esta tesis. Primero discutimos los aspectos biológicos relacionados con el estudio de la progresión de los gliomas. Nos centramos en tres temas principales que representan los núcleos de los modelos presentados: la *invasión de un glioma* en el tejido cerebral y los principales mediadores de este mecanismo, es decir protrusiones celulares (tema de los Capítulos 6 y 7), receptores de membrana (tema de los Capítulos 3-5 y 7), y proteasas (tema del Capítulo 7); la *angiogénesis tumoral*, con sus características distintivas asociadas con la hipoxia del tejido, la acidez y la necrosis (temas de los Capítulos 4 y 5); los *tratamientos clínicos*, que combinan agentes terapéuticos estándares y novedosos (temas de los Capítulos 3 y 5). Además, discutimos los datos biológicos y clínicos que incluimos en los modelos. Concretamente, describimos las técnicas de imágenes médicas de uso común, con un enfoque particular en las *imágenes por resonancia magnética* (IRM), en las *imágenes por resonancia magnética con tensores de difusión* (DTI), que permiten la reconstrucción de la geometría del cerebro y del tensor de difusión utilizados en los Capítulos 3-5, y en las *técnicas de inmunotinción*, utilizadas en el Capítulo 7 y que proporcionan información sobre la distribución de varias proteínas. Luego, presentamos los aspectos matemáticos de la tesis. Discutimos el carácter intrínsico multiescala de nuestro problema, presentamos los conceptos básicos de los dos marcos de modelado en los que nos basamos, es decir modelos multiescala formulados en términos de ecuaciones cinéticas y modelos macroscópicos, y recalcamos sus principales peculiaridades.

La parte I explica los estudios preliminares presentados en el capítulo 2 relativos a las ***características del tejido cerebral***. Los aspectos descritos en este capítulo se tienen en cuenta posteriormente en todos los modelos formulados. Precisamente, discutimos las *características de anisotropía* de la red de fibras nerviosas que son responsables de los patrones macroscópicos heterogéneos observados en las imágenes de gliomas. Tener en cuenta este aspecto de alineamiento de las fibras es fundamental para obtener modelos matemáticos fiables. Proporcionamos información sobre la técnica de imagen por resonancia magnética con tensor de difusión (DTI) y los datos que esta aporta, relativos a la difusividad molecular en diferentes direcciones. En particular, discutimos la cuantificación de estos datos utilizando mapas escalares (por ejemplo, la *anisotropía*

fraccional (AF)). Luego, dado que el tensor que describe la difusividad celular se deriva de los datos proporcionados por la DTI, comentamos algunas metodologías que se han identificado para incluir la información de la DTI en los modelados macroscópico y cinético. Con referencia al marco cinético, comentamos el uso de una función de distribución para describir la red de fibras y construir el tensor que caracteriza la difusividad celular. Además, realizamos una *comparación entre las tres formulaciones principales utilizadas para esta función* (distribución Peanut, distribución de von Mises-Fisher (VMF) y función de distribución de orientación (ODF) [3, 216]), utilizando datos de DTI y la anisotropía fraccional (Figuras 2.7-2.11). Los resultados subrayan los puntos fuertes y débiles de cada una de estas distribuciones, proporcionando argumentos adecuados para motivar la elección de una de ellas en lugar de otra. La distribución Peanut es fácil de calcular, aunque falla parcialmente en preservar la información sobre la anisotrópia que se deduce de los datos de DTI, mientras que la distribución VMF es más precisa, pero requiere un ajuste adecuado de los parámetros involucrados en su formulación. El cálculo de la ODF es más complejo y costoso, pero esta distribución muestra un mayor grado de precisión. Este análisis representa un estudio preparatorio para los modelos presentados en la Parte II, en la que las funciones de distribución tienen un papel central en el modelado del fenómeno de la guía de contacto.

La Parte II comprende los modelos basados en una formulación cinética en los que las configuraciones macroscópicas se derivan formalmente de sistemas de ecuaciones cinéticas de transporte. Concretamente, los modelos presentados en los Capítulos 3-5 se construyen utilizando una formulación *micro-meso*. Esta formulación combina la descripción de la dinámica microscópica con ecuaciones cinéticas mesoscópicas a partir de las cuales se derivan los modelos macroscópicos mediante el uso del límite parabólico y del método de expansión de Hilbert. El capítulo 6 presenta una clase de modelos cinéticos no locales que se formulan a nivel mesoscópico al que se aplican límites tanto parabólicos como hiperbólicos para derivar las ecuaciones macroscópicas en el régimen apropiado. Macroscópicamente, los modelos propuestos en estos capítulos presentan difusión lineal y varios fenómenos de taxia que transmiten la información sobre la dinámica microscópica (cuando corresponda). La ***influencia de la arquitectura del tejido cerebral en la migración de las células tumorales*** representa el núcleo principal del modelo propuesto en el Capítulo 3 y basado en datos de DTI. Sobre la base de los estudios en [74, 126], modelamos la función de las *fibras nerviosas* como estímulo que guía la migración celular y describimos la dinámica de las *integrinas* como mediadoras de las interacciones célula-MEC. Estas interacciones son también responsables de la proliferación del tumor. La ecuación macroscópica se deriva a través de un limite parabólico y se simula en un dominio constituido por un corte 2D de cerebro. Este se reconstruye a partir del procesamiento de imágenes de resonancia magnética y tiene en cuenta la información de DTI. Las pruebas numéricas analizan el impacto de las diferentes formulaciones de la función de distribución de las fibras. También muestran el efecto de la dinámica microscópica sobre la manifestación de patrones macroscópicos en la evolución tumoral debidos a la anisotrópia del tejido (Figuras 3.3-3.5). Por ejemplo, cuando se incluye la distribución Peanut en el modelo, notamos una extensión tumoral más homogénea, diferente a los patrones ramificados observados en el caso de la ODF. Se muestran diferencias análogas comparando la inclusión y la exclusión de la dinámica microscópica en el modelo. Además, incorporamos en el modelo la descripción de una *terapia combinada basada en inhibidores de integrinas y radiación*, que muestra numéricamente la reducción de la infiltración tumoral debido a los inhibidores de integrinas y el impacto de la radiación en la densidad celular (Figuras 3.6-3.7).

La primera extensión de este modelo multiescala se plantea en el Capítulo 4, donde

la descripción de la evolución del tumor se combina con el modelado de la interdependencia entre ***acidez*** y ***vascularización***, dos aspectos clave en el proceso de angiogénesis tumoral. En este contexto, la evolución del tumor incluye, a nivel microscópico, la dinámica de dos tipos de receptores de membrana que median las interacciones celulares con la MEC y con los protones presentes en el espacio extracelular y que determinan la acidez del ambiente. Además, introducimos un componente de ***heterogeneidad intratumoral*** en la descripción de la evolución del glioma. Nos basamos en la *hipótesis de ir-o-crecer* (*go-or-grow hypothesis*), afirmando que una célula puede moverse o proliferar y el respectivo comportamiento es transitorio. La transición entre crecimiento y migración depende de la disponibilidad de nutrientes (aportados por la vasculatura), del pH extracelular (determinado por la acidez del ambiente) y del hacinamiento de células en el ambiente. La angiogénesis es necesaria para mantener la proliferación tumoral y se describe en términos de la evolución de la densidad de CE. Las CE se caracterizan por un comportamiento migratorio hacia las células tumorales en respuesta a los factores de crecimiento pro-angiogénicos producidos por el tumor para satisfacer la demanda energética. Las ecuaciones macroscópicas del tumor y las CE se derivan a través del límite parabólico de la formulación cinética, que involucra la dinámica microscópica y presenta varios fenómenos de taxia. Primero, acoplamos el modelo macroscópico con la dinámica de los protones, responsables del pH extracelular y, en consecuencia, de la acidificación del microambiente tumoral. Para este modelo, consideramos los dos mecanismos de *hipoxia* (debida a la baja oxigenación) y *acidosis* (debido al cambio metabólico impulsado por la hipoxia), evaluando directamente el nivel resultante de *pH extracelular* y modelando su influencia en la dinámica tumoral. Las simulaciones numéricas muestran el carácter no lineal de la dinámica que surge desde la formulación del termino de quimiotaxia pH-repelente (las células tumorales tienden a evitar las regiones altamente ácidas) y también muestran la capacidad del modelo de capturar *las características histopatológicas relacionadas con la hipoxia* (Figuras 4.3-4.4). Además, con estas simulaciones analizamos la influencia de la dicotomía ir-o-crecer en el comportamiento macroscópico, notando una desaceleración generalizada de la dinámica tumoral en comparación con el caso en el que se ignora esta dicotomía (Figuras 4.5-4.6). Luego, ampliamos el modelo para incluir la dinámica de tejido sano y del tejido necrótico, provocada por la acidez. Con estos dos elementos adicionales, definimos una *clasificación tumoral basada en el nivel de necrosis* que nos permite analizar la influencia de la heterogeneidad intratumoral y de la vasculatura en la evolución del grado tumoral (Figura 4.10).

La ***influencia de la angiogénesis en la respuesta del tumor a la terapia*** es el enfoque del Capítulo 5. En este capitulo, modelamos la dinámica de las células tumorales y de las células endoteliales tanto a nivel microscópico como cinético, y luego acoplamos las ecuaciones macroscópicas que se derivan con la descripción de la evolución de *factores de crecimiento endotelial vascular* (VEGF). Estos factores de crecimiento, cuyo efecto sobre las CE se incluyó indirectamente en el modelo descrito en el Capítulo 4, son producidos por células tumorales en condiciones hipóxicas para atraer las CE hacia la masa tumoral y, así, proporcionar los nutrientes necesarios para mantener la proliferación tumoral. Además, a nivel macroscópico, incluimos la descripción de la degradación del tejido sano y el crecimiento del tejido necrótico. En este modelo, describimos los efectos de un tratamiento que combina *radiación* y *quimioterapia* con temozolomida y *terapia anti-angiogénica*. El primer tratamiento afecta al tumor, a las CE y al tejido sano, cuya degradación también depende de la (acidez producida por la) actividad de las células tumorales. La quimioterapia se administra en vena y solo afecta a la población tumoral, mientras que la terapia anti-angiogénica afecta a las CE. La terapia anti-angiogénica reduce la proliferación de CE y la afinidad entre CE y

VEGF. Los resultados numéricos preliminares analizan los efectos de este tratamiento multimodal, que principalmente disminuye la densidad tumoral y degrada el tejido sano, con respecto a la situación sin terapias (Figuras 5.2 y 5.4). Además, estudiamos el efecto de la única terapia anti-angiogénica en la disminución de la migración de CE y la disponibilidad de vasculatura para el tumor (Figura 5.5). Este modelo asienta la base para un estudio de la *eficacia de la terapia* basado en datos reales de pacientes con glioma (que será el tema de un trabajo futuro).

En los capítulos anteriores, los modelos propuestos consideran una única señal como impulso para los cambios de velocidad a nivel cinético. Esta señal puede ser la red de fibras (como para las células tumorales en los Capítulos 3-5) o el gradiente de una población o de una señal externa (como para las CE en el Capítulo 4). En el capítulo 6, analizamos el ***efecto de diferentes señales que influyen al mismo tiempo en la migración celular*** a nivel cinético. Partiendo de la base de [173], proponemos un modelo basado en ecuaciones cinéticas para la descripción de la influencia de la *quimiotaxis* y de la *guía de contacto* (impulsada por la red de fibras nerviosas) en los cambios de dirección de velocidad de las células y, por tanto, en la migración celular. El modelo incluye *términos no locales*, que describen el rastreo del ambiente alrededor de las células y que permiten incorporar los efectos de la extensión de protrusiones celulares para explorar este entorno. A nivel cinético, presentamos dos clases de modelos, dependiendo de si las células realizan una detección independiente de las dos señales o las promedian con el mismo núcleo que caracteriza el operador de detección. Dependiendo de las longitudes características de variación de las señales y de la estrategia de detección adoptada, derivamos diferentes límites macroscópicos de los dos modelos de transporte y los simulamos para ilustrar el comportamiento de la solución en diferentes casos. Los resultados muestran el impacto sobre el comportamiento celular de una doble señal (con respecto al caso de una única señal) que, incluso para fibras detectadas localmente y no orientadas, asegura un sentido preferencial de movimiento a las células (Figura 6.1). Las simulaciones muestran cómo el modelo captura los *efectos colaborativos o competitivos* de las dos señales, que pueden sostener o contrastar el movimiento celular (Figuras 6.9-6.10). Además, analizamos cómo estos efectos están influenciados por el ángulo entre las orientaciones y las fuerzas relativas de las dos señales, en términos de *nivel de alineamiento de las fibras* y *pendiente del gradiente quimioatractivo*. Las señales unidireccionales (como la quimiotaxis) compiten cuando este ángulo es π, mientras que colaboran cuando este ángulo es 0; en cambio, para las señales bidireccionales (como la guía de contacto) la competición requiere un ángulo de $\pi/2$. Entre estos valores, pueden ocurrir muchos escenarios intermedios entre competición y colaboración (Figuras 6.4-6.8).

La última parte (Parte III) explica el modelo macroscópico presentado en el Capítulo 7. Analizamos la ***dinámica del frente de invasión tumoral*** y los aspectos bioquímicos y biomecánicos relacionados con ella, prestando particular atención a la influencia de las *protrusiones celulares* (denominadas microtúbulos tumorales en el contexto de GB) en la progresión del glioma. Modelamos a nivel macroscópico la evolución del tumor, utilizando términos no lineales que permiten un estudio eficaz del frente de propagación, junto con las ecuaciones para la descripción de las *integrinas*, las *proteasas* y la *MEC*. El modelo propuesto integra la descripción matemática de la dinámica de estas especies con datos experimentales sobre estudios de las distribuciones de varias proteínas. Los experimentos se realizan en un modelo de *Drosophila*, que es una plataforma adecuada para el estudio de los mecanismos moleculares y celulares implicados en la progresión de GB. Los resultados del análisis de datos experimentales realizado son útiles para determinar la localización y el perfil de las distribuciones de proteasas e integrinas en diferentes regiones del cerebro. Precisamente, dividimos las

integrinas en dos subgrupos, dependiendo de si estos receptores están activamente unidas a la MEC o no. El modelo macroscópico resultante se caracteriza por la descripción de los flujos difusivos por medio de flujos saturados que permiten un control directo de la velocidad de frente y el desarrollo de un perfil frontal con una pendiente muy elevada. Este modelo macroscópico muestra un fuerte acoplamiento entre las diferentes especies y lo simulamos en el caso 1D, lo que permite la comparación con los datos experimentales. Los resultados numéricos son coherentes con los datos experimentales y muestran la evolución dinámica del frente de GB y el desarrollo de patrones en los perfiles de las diferentes especies (Figura 7.12). Analizamos la influencia de los procesos de taxia y de posibles cambios en porosidad del tejido sobre la manifestación de heterogeneidades y separaciones en el perfil del frente. Proponemos y estudiamos dos posibles formulaciones de la descripción de la proliferación heterogénea, que pueden aumentar o reducir la separación del frente (Figuras 7.13-7.17). Estas simulaciones exploran el potencial del modelo presentado en reproducir fenómenos relacionados con la heterogeneidad del frente, aunque estos aspectos expresarán más su impacto en la extensión 2D del modelo.

Los modelos presentados muestran varios avances en el estudio de los procesos que impulsan la progresión del glioma, sobre todo desde el punto de vista de la migración celular. Sin embargo, se pueden proponer diferentes extensiones y mejorías de estas formulaciones (Capítulo 8). Actualmente estamos trabajando en la definición de una extensión estocástica del modelo descrito en el Capítulo 5 para estudiar la eficacia de los tratamientos con datos de pacientes reales. Con respecto a los modelos presentados en el Capítulo 6, la idea es extenderlos al caso de señales externas que afecten también el modulo de velocidad celular y no simplemente su dirección. Además, queremos utilizar estos modelos como una plataforma para cuantificar la migración celular dirigida y establecer su eficiencia en el caso de señales que compiten en un dominio realista. Esto podría imitar la migración celular *in-vivo* o *in-vitro* en la matriz extracelular. Por ultimo, queremos extender el modelo macroscópico del Capítulo 7 en el caso 2D para estudiar el efecto de la dirección de las fibras en la dinámica del frente tumoral y analizar los fenómenos descritos anteriormente (proliferación heterogénea y cambios de porosidad) en un contexto más complejo y realista.

Concluimos esta tesis con tres apéndices explicativos. El Apéndice A proporciona una introducción básica al procesamiento de datos de IRM y DTI, mientras que el Apéndice B ofrece una descripción detallada de los principales conceptos matemáticos detrás del método de los elementos finitos, los métodos de avance en tiempo y de integración numérica utilizados para resolver numéricamente los modelos macroscópicos. Por ultimo, el Apéndice C presenta una descripción de los métodos utilizados para obtener los resultados experimentales incluidos en el Capítulo 7 y el análisis de datos correspondiente.

Contents

1 Introduction

"Nothing in biology makes sense except in the light of evolution."

T. Dobzhansky

The human body is composed of many millions of cells that interact and coordinate to form tissues and organs. They grow and divide for a specific period of time, reproducing themselves to replace defective or dying cells. Failure in the control mechanism of cell reproduction is one of the fundamental peculiarity of cancer cells. Unlike normal cells, in fact, cancer cells continuously grow and divide, in an uncontrolled, uncoordinated and abnormal cell division process, invading adjacent tissues and, eventually, spreading to other organs. This ability to sustain chronic proliferation has been identified by Hanahan and Weinberg as one of the ***hallmarks of cancer*** [109], together with five other distinctive characteristics that enable tumor growth and dissemination. In the following, we briefly discuss these six hallmarks of cancer, represented in Figure 1.1.

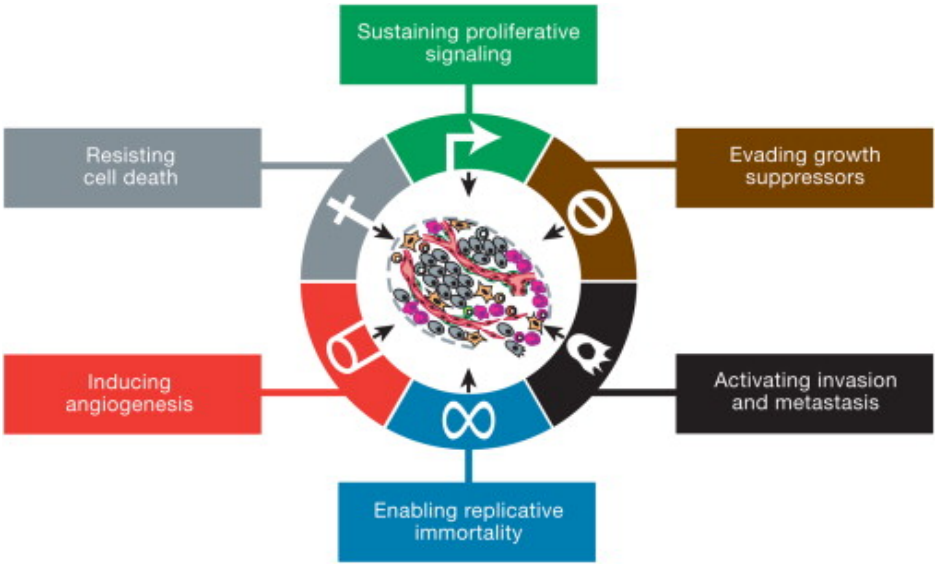

FIGURE 1.1: **Hallmarks of cancer.** Schematic representation of the six *hallmarks of cancer*, originally proposed by Hanahan and Weinberg. (Reprinted from [110] by permission from Elsevier)

The first four hallmarks concern the alteration of the cell cycle. Cancer cells ***sustain proliferative signaling*** with different strategies. One way to do so is to increase the level of receptor proteins on their cell surface, making the cancer cell hyperresponsive to growth factor ligands. Another strategy is to produce growth factor ligands themselves, resulting in an autocrine proliferative stimulation [220, 298]. These strategies can result from somatic mutations of genes that initiate the proliferation process or

from the attenuation or inhibition of cell senescence mechanisms by oncogenic signals [208, 306]. In addition to sustain proliferation, cancer cells circumvent powerful processes that negatively regulate cell division, i.e., they typically ***evade growth suppressors***. These processes typically depend on tumor suppressor genes. Two well-known tumor suppressors are retinoblastoma protein (RB) and tumor protein p53. The former regulates the growth-and-division cycle by integrating intra- and extracellular signals. The latter controls the cell cycle progression in response to inputs from stress and abnormality sensors, blocking the cell cycle if the degree of genome damage is excessive [257]. Clearly, each of these pathways operates as part of a larger network. Alterations of the apoptosis pathway represent a further hallmark of tumor development, enabling ***resistance to cell death***. In normal conditions, this pathway drives the activation of protease, responsible for the cell progressive disassembling and consumption [172]. Tumor cells, instead, develop several strategies to limit or circumvent apoptosis, one among all is the loss of p53 function. The last hallmark related to the alteration of the cell cycle describes the unlimited replicative potential of cancer cells, as opposed to the finite number of division of a normal cell before reaching mortality. This phenomenon is called ***replicative immortality*** and it enables tumor cells to continue dividing and prevent senescence and apoptosis [114].

Concerning cancer cell interactions with the extracellular environment, Hanahan and Weinberg highlight the role of angiogenesis and active migration as hallmarks of the tumor cells. ***Angiogenesis*** describes the formation of new blood capillaries from existing blood vessels. This process provides substances, such as nutrients or oxygen, to the cells and it enables the removal of metabolic waste. Cancer cells stimulate nearby host stroma cell proliferation by releasing growth factors (mainly VEGFs, i.e., vascular endothelial growth factors). This way, the tumor is provided with the blood vessels and the supplies needed for faster growth. A typical blood vessel produced within a tumor is distorted and enlarged, with erratic blood flux or microhemorrhages [200]. It has been shown that continuous activation and sprout of new vessels are characteristics of advanced cancers. In particular, the switch from low vascularization to high vascularization is considered an essential capability for tumor progression. Angiogenesis is fundamental for active invasion and metastasis [11]. Cancer ***invasion***, with consequent growth of ***metastasis***, is a complex process, involving several factors [10, 42] and taking place as both an individual and a collective process. Among individual cell migration mechanisms, for instance, we find the epithelial-mesenchymal transition (EMT) process, which allows individual cells to acquire abilities to prevent apoptosis, invade tissue, and disseminate. It can be activated transiently or stably, and it involves transcription factors that orchestrate most of the steps of the invasion-metastasis cascade [227]. Some mesenchymal cells remain in the tumor stroma to sustain invasion by supplying matrix-degrading enzymes. Another example of individual cell invasion process is the amoeboid migration, characterized by individual cell morphological plasticity that enables a cell to slither through existing interstices of the extracellular matrix (ECM) rather than clearing a path for itself [91].

These six characteristics, firstly introduced in [109], provide a solid framework for understanding the biology of cancer. In a later work [110], Hanahan and Weinberg added some additional elements to the list of features characterizing cancel cells: two ***enabling characteristics***, which allow the cancer cells to survive, proliferate, and disseminate, and two ***emerging hallmarks***, complementary to the six features above described. The most prominent of the two enabling characteristics is the ***development of genome instability***, i.e., the acquisition of successive genome alterations that provide a selective advantage to tumor cells [80]. The second enabling characteristic concerns the ***tumor-promoting inflammation***. The tumor area, in fact, is characterized

by infiltrated cells of the immune system that have tumor-promoting effects. More specifically, immune cells are able to supply bioactive molecules to the tumor microenvironment, such as growth and pro-angiogenic factors, or actively mutagenic chemicals that accelerate the genetic evolution [104]. On the other hand, the two emerging hallmarks are the ability of reprogramming the energy metabolism, the first, and of evading the immune destruction, the second. ***Reprogramming the energy metabolism*** is necessary to support continuous cell growth and proliferation. An example of this reprogramming in cancer cells is the process of aerobic glycolysis. Already observed by Otto Warburg in 1956 [291], even in the presence of oxygen cancer cells tend to reprogram their glucose metabolism and their energy production performing anaerobic glycolysis. This glycolytic process converts glucose first to pyruvate and then to lactate, released in the extracellular space, and it produces 2 molecules of ATP (adenosine triphosphate). Despite the anaerobic glycolysis producing less ATP than the other energy conversion processes (the complete cell respiration cycle produces 36-38 ATP molecules), the production is faster and allows cells to adapt at intermittently hypoxic conditions, prevalently in poorly vascularized tumor or in presence of unstable neovasculature [63]. It is not rare, for instance, to identify in the tumor two subpopulations working in symbiosis: hypoxic cells, glucose-dependent and secreting lactate, and normoxic cells that utilize lactate as the main source of energy [256]. The second emerging hallmark is the ability of cancer cells to ***evade immune destruction***. How this process can occur is still an open question. In fact, little is know about the role of the immune system in tumor formation and the development of deficiencies in some tumor-suppressors that underlie the mechanism. Furthermore, downstream these hallmark capabilities of cancer cells, there are several ***circuits and signaling pathways***, both intracellular and intercellular, that constitute a large and complex network [110], supporting cancer progression.

With this brief overview, we want to show why cancer is classified as a multifactorial and multistage disease that exhibits several structural, biochemical, molecular, and genotypic alterations. The magnitude and nature of the consequences of such modifications strongly depend on the affected tissue and on the subtype of cancer. For these reasons, in this dissertation, we focus our study on a specific type of brain tumor, which is, the ***glioma***. This strategy enables to pay exclusive attention to its peculiar characteristics, to develop more specific and targeted models, and to interpret the results by comparing them with experimental data concerning glioma cells, when this is possible.

We proceed to present in Section 1.1 the biological features that characterize glioma cells and allow to distinguish between the different grades of tumor progression. With regard to the mathematical content of the dissertation, we focus on the inherent multiscale nature of the processes of tumor growth and progression, developing different model settings. Thus, in Section 1.2, we provide a general and introductory description of this mathematical multiscale modeling framework.

1.1 *Biological aspects of gliomas*

Brain tumors are neuroepithelial solid neoplasias that are classified depending on the cells from which they derive [69]. Malignant gliomas are the most prevalent subtype of primary malignant brain tumors, accounting for almost 80% of them [210]. They originate from mutations of glia cells of the central nervous system (CNS). Glia cells are supporting cells in the human brain, which means that they provide nourishment, protection, and structural support to the neurons. Such cells are responsible for the

electrical isolation of the nervous tissue, as well as for the digestion of dead cells and pathogens. Depending on their main function, glia cells are divided into astrocytes, oligodendrocytes, ependymal cells, and radial glia [263].

The widely used scheme for classifying gliomas is the World Health Organization (WHO) classification [145]. Based on this classification, gliomas are sorted by type and grade. The type (three in total) indicates whether the glioma displays features of astrocytic, oligodendroglial, or ependymal cells. Whereas, the grade qualitatively determines the degree of differentiation of the tumor:

- grade I brain tumors are biologically benign, with long-term survival, limited invasive capacity, and possibly curable via surgery alone (e.g. pilocytic astrocytoma);
- grade II brain tumors are low-grade malignancies that are not curable by surgery alone and might recur as higher grade (e.g. diffuse astrocytoma or pure oligodendroglioma);
- grade III brain tumors are malignant and infiltrative, often recurring as higher grade and potentially leading to death within a few years (e.g. anaplastic astrocytoma);
- grade IV brain tumors are highly malignant, usually not well responding to therapies, and lethal within 9-12 months (e.g. glioblastoma (GB), also known as glioblastoma multiforme (GBM)).

Almost 70% of grade II gliomas evolve into grade III and IV tumors within 5 to 10 years from diagnosis [180]. According to the WHO, the most common and aggressive primary brain neoplasm is glioblastoma, a grade IV brain tumor with a median survival range within 9 to 12 months [171]. It is characterized by rapid cell proliferation, great infiltration capacity, and neurological impairment [120]. Typically, tumors of this type present a radial growth rate of 10 times greater than the lower-grade gliomas. Glioblastoma is characterized by a hypoxia-driven mechanism that determines the formation of a necrotic core surrounded by pseudopalisade cells (described in the next section). These cells, in response to hypoxia, stimulate diffusion, migration, and angiogenesis [34]. In Figure 1.2, histological samples of brain tumors show the main differences between the various tumor grades.

Recently, new research tools and refined experimental models have allowed great progress in understanding and treating glioma. However, little is still known about the mechanism used by glioma cells to grow, migrate, and spread in the tissue. In this dissertation, we focus our study on the description of the intercellular mechanisms that lead to glioma progression. Precisely, we analyze and model the processes driving ***glioma invasion***, specifically relating to cell membrane dynamics and cell-ECM interactions, and the processes involved in ***tumor angiogenesis***.

The following sections are organized as follows. In Sections 1.1.1-1.1.3, we present a detailed description of the mechanisms triggering tumor invasion and angiogenesis. These two processes, together with possible therapeutic approaches described in Section 1.1.4 are the main focus of this dissertation. We continue, in Section 1.1.5, to investigate the clinical aspect of this study by including a detailed description of the biological and clinical data that are used in several proposed model settings.

1.1.1 *Glioma invasion*

Gliomas have a remarkable capacity of infiltrating surrounding brain tissues. The invasive ability is present in low-grade as well as in high-grade tumors, implying that

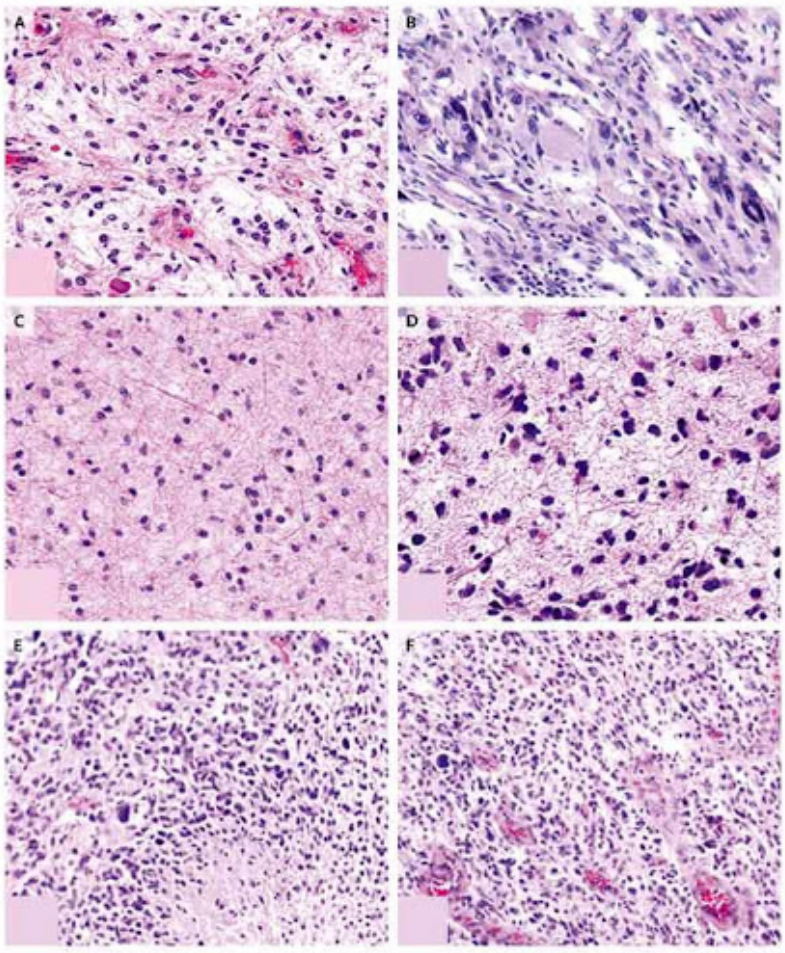

FIGURE 1.2: **Histological samples of brain tumors.** Panels A and B show circumscribed astrocytomas, specifically *pilocytic astrocytomas* (grade *I* tumors) in A, and *pleomorphic xanthoastrocytomas* (grade *II* tumor) in B. Both partially show cellular pleomorphism - variations in cell size and shape - with limited invasion capacity, and, for the case A, microvascular hyperplasia is also visible, despite its designation as grade *I*. Panels C-F show *diffuse-type astrocytomas*: in C a grade *II* astrocytoma is shown with mild-to-moderate nuclear pleomorphism; in D, a grade *III* astrocytoma presents the mitotic figures characteristic of a high proliferation rate; E and F show the case of *glioblastoma multiforme*, (grade *IV* tumor) with the distinctive features of palisading necrosis (E) and microvascular hyperplasia (F). (Reprinted with permission from `www.aboutcancer.com`).

an invasive tumor phenotype is acquired early in tumorigenesis. Glioma invasion is a multifactorial process driven by biochemical intracellular mechanisms, which support the active cell movement, and by cell interactions with both the ECM and the adjacent cells. In particular, glioma invasion can be viewed as a combination of the ability to migrate and the ability to modulate the extracellular space, with a dynamical interplay between cell adhesion to the ECM and the remodeling of the ECM itself.

Brain tissue consists predominantly of closely apposed neurons and glia, leaving little room for the extracellular matrix of the brain. Moreover, the ECM that is located in the intercellular space between neurons and glia is substantially different from the one present in other organs of the body. Brain ECM can be divided into two main parts: the *parenchymal ECM*, which surrounds prevalently neurons and glia cells, and the *basal membrane*, which is found around blood vessels and at the pial surface [239].

The former is mainly composed of glycosaminoglycans (GAGs), glycosaminoglycan hyaluronic acid (HA), proteoglycans of the lectican family, and other glycoproteins. The latter consists of a mixture of specialized collagens, glycoproteins, and adhesion molecules. Among them, collagen type IV, laminin, and entactin (a glycoprotein) are the main components [307]. Tumor cells invade the brain parenchyma following preferential routes [296]. Initially observed by Scherer [254], glioma cells follow preferentially white matter tracts to migrate. Many tumors cross the corpus callosum to form butterfly lesions, while others remain simply confined to the white matter; moreover, they grow mostly around neurons and spread along vessels [84, 170, 207]. The influence of peculiar brain structures on tumor migration can be included in the modeling framework, as discussed in Chapter 2.

The invasion process and, more generally, most of the tumor-ECM interactions are mediated by ***cell protrusions***, which are extensions of the plasma membrane outside of the cell body. The cell protrusions are highly dynamic structures involved in several fundamental processes, including collective cell migration and invasion through the tissue matrix. Different types of protrusions have been identified to contribute to cell spreading depending on context, cell type, and microenvironment [224, 246]. Protrusive structures formed by migrating and invading cells are named filopodia, lamellopodia, podosomes, and invadopodia based on their morphological, structural, and functional characteristics [5]. These protrusions have a significant role in mediating intercellular communications and in modulating cell-cell and cell-ECM adhesion processes.

The most common receptors that allow glioma cells to adhere to the ECM are ***integrins***. Integrins are dimeric transmembrane glycoproteins that mediate dynamic interactions of cells and ECM and, to a lesser extent, cell-to-cell adhesion [127], involving the actin cell cytoskeleton. Integrins are composed of α and β subunits that initiate intracellular signaling cascades by binding to adapter proteins. The binding specificity is determined by the integrin extracellular domain, which allows integrins to recognize different matrix ligands (fibronectin, collagen, laminin) or other cell surface receptors [279]. In glioma cells, integrins are involved in cell motility and migration [73], but affect also cell growth, division, and proliferation through the interaction with extracellular proteins and enzymes controlling the cell cycle [64, 127]. Extensive data show that the expression of integrins facilitates the infiltration of tumor cells through normal brain tissue. For this reason, these transmembrane receptors are one of the major contributors to the invasive phenotype of gliomas [61]. For instance, $\alpha 3\beta 1$ integrins are consistently over-expressed in invading glioma cells and is a key regulator of glioma cell migration [311]. Therefore, integrins have emerged as a marker for brain tumor malignancy [106], and a promising anti-glioblastoma target.

The modulation and remodeling of the ECM, which is directly involved in tumor invasion, is mediated by several enzymes, known as ***proteases*** or ***proteinases*** [175, 191]. Proteases are enzymes that catalyze the breakdown of proteins into smaller polypeptides or single amino acids (proteolysis), facilitating tumor cell dissemination. To allow this process, proteases must be located extracellularly or concentrated in specialized regions of the plasma membrane [175]. In addition to ECM regulation, proteases can also activate para- and autocrine growth and chemotactic factors, as well as intracellular pathways related to glioma cell survival and invasion. Proteases can be classified into several classes according to their catalytic site. The most common class of proteases involved in the degradation of the ECM due to invading glioma cells consists of matrix metalloproteinases (MMPs). In particular, increased MMP levels and tumor invasiveness in human gliomas are strongly correlated [72, 238], highlighting the role of proteases as a prerequisite for glioma malignant invasion. Like integrins,

MMPs have acquired an emerging role as tumor markers. Several clinical studies have shown promising beneficial effects in combining inhibitors of MMPs with other treatments [191].

A schematic representation of the main mechanisms involved in glioma cells invasion at the intercellular level is presented in Figure 1.3.

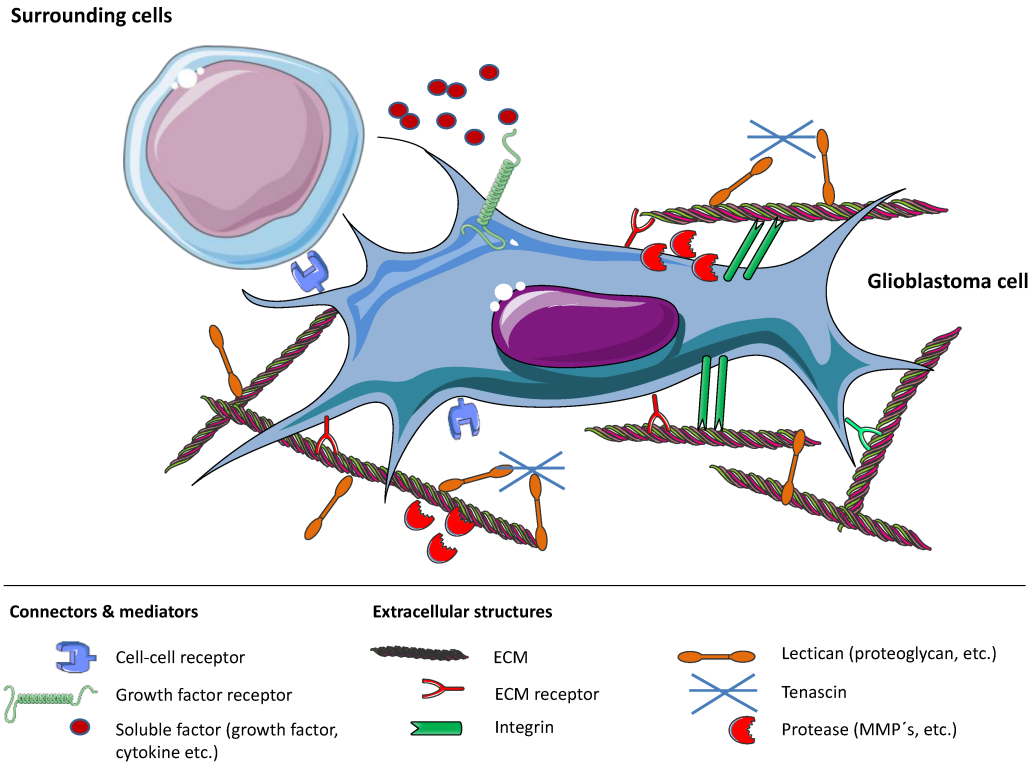

FIGURE 1.3: **Intercellular invasion mechanisms.** Schematic representation of the mechanisms that drive glioma invasion. Processes involve glioma cells and ECM, as well as connecting molecules, like integrins, proteases, soluble factors, and surrounding cells. (Source [288]; used under the terms and permission of MDPI and Creative Commons Attribution License).

The role of integrins in mediating glioma invasion along the white matter tracts of the brain is the focus of the preliminary model described in Chapter 3. Further extensions of this study, including - among other mechanisms - the degradation of the ECM, are presented in Chapter 4. Moreover, a direct analysis of the role of cell protrusions in glioma progression, and their interplay with integrins, proteases, and ECM is presented in Chapters 6 and 7.

1.1.2 *Angiogenesis in glioma*

Angiogenesis is a key event in the progression of malignant gliomas. This term refers to the formation of new blood vessels by rerouting or remodeling existing ones, and it is believed to be the primary method of vessel formation in gliomas. Angiogenesis requires three distinct steps: blood vessel breakdown; degradation of the vessel basement membrane and the surrounding ECM by proteases activity; migration of endothelial cells toward tumor cells, which express pro-angiogenic compounds for the formation of new blood vessels [207]. ***Vascular proliferation*** is a hallmark of tumor aggressiveness, especially in the case of glioblastomas, and an increase in vascularization

significantly worsens prognosis. Glioblastomas (GBs) are among the most vascularized human tumors, displaying a high degree of vascular proliferation and endothelial cell hyperplasia [84], which is a form of angiogenesis morphologically recognized as endothelial proliferation within newly sprouted vessels. GBs show blood vessels of increased diameter with high permeability, thickened basement membranes, and highly proliferative endothelial cells. The most characteristic form of vascular proliferation is microvascular proliferation with glomerular-like capillary loops. These formations are complex structures composed of both proliferating endothelial and smooth muscle cells [170]. They are unique to high-grade gliomas and are used as a histopathological hallmark for these brain tumors [268]. Such intense vascularization has also been proposed as responsible for the peritumoral edema, another pathological feature of GB. Tumor vascular proliferation is sustained by many angiogenic growth factors. For example, vascular endothelial growth factors and their receptors are secreted by tumor cells, and they are especially upregulated in cells surrounding regions of necrotic tissue. They bind with the corresponding VEGF receptors on the endothelial cell membrane, playing a major role in angiogenesis.

Tissue hypoxia promotes and activates angiogenic mechanisms. One of these mechanisms is the HIF-1/VEGF-A pathway that drives endothelial cell proliferation and migration [207]. Hypoxia-inducible factor (HIF)-1 is a nuclear transcription factor influencing cell adaptive response to low oxygen. The microvascular proliferation in gliomas is characterized by the presence of ***pseudopalisade cells*** surrounding necrosis regions, protecting the cancer stem cells residing in these regions from therapeutic agents. Pseudopalisades are known to be hypoxic, as they show strong upregulation of HIF-1, and to affect hypoxia-mediated migration. Limitations in oxygen and nutrient supply, in fact, determine the movement of tumor cells that, if located at the furthermost distance from arterial supplies, become hypoxic and migrate towards viable vessels. As a consequence, pseudopalisades, surrounding necrotic regions, appear as a wave of actively migrating tumor cells moving away from areas of central hypoxia, vaso-occlusion, or thrombosis [249].

Another characteristic configuration in glioblastoma is ***necrosis*** surrounded by pseudopalisade cells. The necrotic areas are caused by many different factors, such as high metabolic demands, that exceed supply, or vascular thrombosis. Necrosis is determined by hypoxia that can encourage more active migration and result in a clear central region more susceptible to necrosis. Although cancer cells can survive in relatively acidic regions, which confers them an advantage against normal cells [293], they cannot survive in an extremely low pH environment created by the large amounts of lactate and alanine produced during anaerobic glycolysis. Thus, when the extracellular pH level goes below critical levels, necrotic areas form and cell migration towards more favorable regions is initiated.

The main pathologic features characterizing glioma angiogenesis are shown in several tissue samples collected in Figure 1.4. Angiogenesis in glioma is analyzed in Chapter 4. In that chapter, we show that the proposed model is able to capture the features of microvascular proliferation with glomerular-like capillary loops, and the creation of pH-driven necrotic areas. Moreover, a deep analysis of the role of VEGFs in driving tumor-endothelial cell dynamics is presented in Chapter 5.

1.1.3 *Brain tumor microenvironment*

The ***brain tumor microenvironment*** (TME) is a critical regulator of cancer progression [232]. It is characterized by many different non-cancerous cell types, such as immune

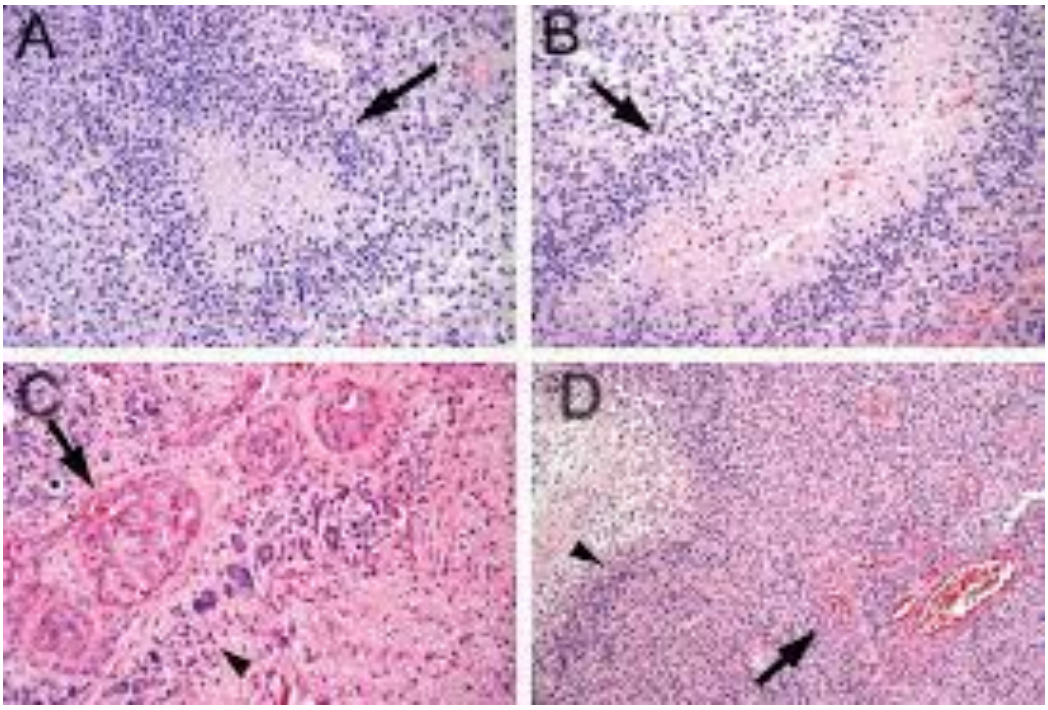

FIGURE 1.4: **Pathologic features of glioma angiogenesis.** In Panel A, pseudopalisade tumor cells (arrow) accumulate around a central clear zone, while in Panel B larger pseudopalisades contain regions of necrosis. In Panel C microvascular hyperplasia (arrow) is induced by hypoxic pseudopalisade cells (arrowhead), and in Panel D a low-magnification view of pseudopalisade necrosis (arrowhead) and microvascular hyperplasia (arrow) shows a wave of tumor cells migrating toward the emerging vasculature (left to right). (Reprinted from [249] by permission of Oxford University Press and the American Association of Neuropathologists).

cells, endothelial cells, pericytes, and fibroblasts, as well as several nutrients and unsoluble macromolecules constituting the brain ECM. Each of these cell types has a key role in tumor progression. The ***immune cell landscape*** of brain tumors consists of several, different cells belonging to both neuronal and immune systems. It includes tumor-associated macrophages (TAMs) and microglia, which have a significant bidirectional crosstalk with tumor cells, supplying them with pro-tumorigenic and pro-survival factors [107]. Several studies suggest that these factors regulate glioma stem cell pools and they seem to be involved in angiogenesis and resistance to therapy. Lymphoid cells are also part of this immune cell landscape and, together with dendritic cells (DCs), stimulate the anti-tumor immune response [217]. Moreover, neutrophils, a particular kind of white blood cells, are often associated with the development of drug resistance and often appear reprogrammed in high-grade gliomas. ***Endothelial cells*** and ***pericytes***, instead, constitute the brain vasculature. Specifically, they are involved in both tumor-associated vasculature and blood-brain barrier (BBB). The latter is a unique feature of the brain, used to prevent solutes in the blood from entering the central nervous system. The BBB blocks the transport of approximately 98% of molecules, representing a major challenge for treating brain tumors [1].

We want to remark that the different studies presented in this dissertation investigate the intercellular mechanisms influencing glioma invasion in the brain, with a special focus on the interaction of the tumor cells with their microenvironment. However, we are aware that glioma progression is a much more complex phenomenon that includes also a large variety of intracellular ***signaling pathways*** downstream the

individual cell behaviors, and is influenced by several mutations in the cell genome [180, 220]. For instance, one of the most commonly mutated pathways in GB tumorigenesis is the p53 pathway, a well-known tumor suppressor, that normally responds to DNA damage. Its loss is associated with GB progression and with more invasive and proliferative phenotypes. Several growth factors (e.g. epidermal growth factor (EGF) pathway) and transduction pathways (e.g. Wnt signaling or Hedgehog pathway) are also responsible for driving the transformation process toward GB, mediating cell communication, and influencing neovascularization, increased proliferation, and resistance to cell death. Moreover, the appearance of extensive hypoxic regions within the tumor, which is associated with tumor aggressiveness, is driven by the hypoxia-inducible factor (HIF) pathway. This phenomenon might explain the characteristic intense vascular hyperplasia observed in GB and triggers VEGF activation, proteases activity, and many other components involved in angiogenesis [220].

1.1.4 *Clinical therapies for glioma*

The treatment of gliomas for a human patient takes into account several aspects, such as tumor location, potential symptoms, and potential benefits versus risks of different treatment options. Over the past decades, the treatments have become more multi-modal, combining the three most used interventions (surgery, radiation, and chemotherapy) with new therapeutic targets.

The first approach to treat newly diagnosed gliomas is usually a maximal ***surgical resection***, whose benefits, for both high- and low-grade gliomas, have been extensively debated since it could cause neurologic deficits. As reported in [270], in the evaluation of resection quality with magnetic resonance imaging at 72 h post-operatively of 143 GBs, patients with no visible residual disease had a median survival longer than the follow-up period (24 months). For patients with residual disease (>1.5 cm) the median survival time was 13.9 months. Thus, postoperative neurologic status has been shown to be a good predictor for survival probability, even though any surgical resection should be approached cautiously to preserve it. In this context, it is worth mentioning that complete resection is often impossible. The highly infiltrative nature of the tumor cells and the brain tissue characteristics lead to heterogeneous often disconnected finger-like patterns and to an 'invisible' outer border of the tumor, undetectable with current medical imaging techniques. Magnetic resonance imaging (MRI) is frequently used to evaluate tumor invasion. However, only the central, more compact part of high-grade gliomas can be visualized in human glioma patients. The outer rims of the tumor, composed of cells infiltrating the surrounding normal brain tissue and protected by normal vasculature, are not visible. Although MRI is a powerful tool for high resolution *in-vivo* imaging, sub-millimeter lesions are not always detected by MRI and, consequently, they might not be removed by surgery. Therefore, alternative supporting treatments are usually used in combination with surgical resection.

One of these treatments is the ***radiation therapy*** (RT) that is based on ionizing radiation, normally delivered by a linear accelerator, used to control or kill malignant cells. In high-grade gliomas, the standard dose is 60 Gy delivered in 30-33 fractions. Here, Gy stands for *gray* that represents the ionizing radiation dose unit and is defined as the absorption of one joule of radiation energy per kilogram of matter. Specifically, the *conventional RT* refers to a daily radiation dose of 180-200 cGy, although other treatment plans are often used to reduce the toxicity potential of the treatment. RT in glioma patients is constantly evolving as a result of advances in imaging methods. More advanced techniques help to establish the margins of the gross tumor volume

(GTV) with higher accuracy and to better generate the planning treatment volume (PTV, i.e., the area to treat).

The last treatment is chemotherapy. The term ***chemotherapy*** refers to the use of intracellular drugs to inhibit or to slow down mitosis and cell division (both healthy or tumor cells) for the treatment of several types of tumors. Because most normal cells in an adult's body are not actively growing, they are not affected by chemotherapy. Exceptions are bone marrow cells, hair, and the lining of the gastrointestinal tract, which hence are more prone to the side effects of the treatment. In the case of gliomas, chemotherapy is standardly based on Temozolomide (TMZ), whose use was approved in 1999 for recurrent GB and 2005 for primary GB. Several studies showed beneficial effects of this therapy on decreasing the relative risk of death [51] and, compared with other chemotherapy regimens, TMZ is causing fewer side effects. To date, it appears to be the most efficacious alkylating agent for gliomas.

Together with the standard approaches, any of the hallmarks of glioma could virtually be a possible therapeutic target. New treatments are emerging to target molecules involved in various signaling pathways, with the goal of maximize the clinical efficacy and minimize toxicity (see [110, 253] and references therein). Among them, ***angiogenesis inhibitors*** have been tested as anti-migratory agents for GB. For instance, bevacizumab, a neutralizing monoclonal antibody against VEGFs, demonstrated promising responses in patients with recurrent malignant gliomas in combination with other drugs [242]. However, the role and efficacy of bevacizumab are still debated and a topic for ongoing research. Intravenous ***integrins inhibitors***, such as cilengitide, demonstrated efficacy in inducing apoptosis in U87, a particular type of glioma cells, while a broad spectrum ***MMP inhibitors*** (e.g. marimastat that acts against MMP-1,-2,-7,-9) combined with TMZ showed promising beneficial effects, whilst further investigations on their side effects are still needed.

In the next chapter, we consider some possible modeling approaches of the standard therapies used in the clinical context to treat glioma patients. We model a combination of radio- and chemotherapy in Chapter 3. In this setting, chemotherapy is target at inhibiting integrins activity, while radiotherapy is aimed at cell killing. Moreover, in Chapter 5, we investigate the effect of anti-angiogenic therapies, targeted at reducing VEGF beneficial effects, combined with chemotherapy and radiation treatment.

1.1.5 *Biological and clinical data*

Throughout this dissertation, we adopt the view that any mathematical model describing the evolution of a disease has to be connected in some way to the clinical setting. For this reason, when biological and clinical data, pertinent to the mechanisms we are interested in, are available, we extrapolate information from them use such information to tune the model. Traditionally, diseases were understood at the organ level. Advances in microscopy - including improved instruments and staining techniques - and progresses in molecular biology and omics technologies allow in-depth studies at all levels of the diseases. Therefore, it is now possible to study the biological organization, from organ systems, to the tissue and individual cell level, up to the molecular level.

In this dissertation, we incorporate two different types of clinical data to investigate glioma from a clinical and biological perspective. First, we include data from ***medical images*** in the modeling settings discussed in Chapters 3, 4 and 5 data from ***medical images***. In particular, we use magnetic resonance imaging and diffusion-tensor imaging to realistically describe the brain geometry and its anisotropic features, whose analysis will be proposed in Chapter 2. The second type of data is obtained by

implementing ***immunostaining techniques***, namely the immunofluorescence of several protein distributions on the cell membrane, to evaluate protein levels and profiles in specific regions of the tumor volume. We include the obtained information in the model proposed in Chapter 7.

Medical imaging

Magnetic resonance imaging is nowadays the standard imaging modality in the evaluation of brain tumors. It is a non-invasive medical imaging technique that uses strong magnetic fields and radio waves to generate images of the brain, by exploiting the sensitivity of water molecules in the body to magnetic fields. In the specific, several images with varying contrasts can be created by changing the intensity, timing, and duration of radiofrequency pulses and directional gradients. The two common sequences that are collected are the T1- and T2-weighted images, which display differently the features characterizing glioma progression. T1-weighted images, for instance, can highlight some vasculature-related characteristics of glioblastoma by acquiring the image after administration of gadolinium, a contrast agent that appears bright on T1-weighted images [159, 283]. These sequences are most commonly used for delineating tumor regions. However, as observed in Section 1.1.4, neither of them can provide a precise visualization of tumor abnormality due to the extensive invasiveness of the tumor cells.

Other advanced imaging techniques include vascular perfusion imaging, diffusion-weighted imaging (DWI) and diffusion tensor imaging (DTI), and proton magnetic resonance spectroscopy (MRS). ***Vascular perfusion imaging technique*** highlights regions of high vascularity and it is useful to predict the response to anti-angiogenic therapies. ***DWI*** and ***DTI*** are commonly used to quantify the apparent diffusion coefficient. Finally, ***MRS*** determines concentrations of selected water-soluble metabolites and it is often used to detect mutations in tumors or to study the intratumor heterogeneity. In addition to these techniques, we should mention the ***positron emission tomography*** (PET) scans. It consists of a functional imaging technique that is becoming a highly useful tool to provide deeper insights into metabolic and physiologic processes of glioma progression. This medical imaging technique uses radioactive substances to visualize the distribution of specific molecules in the human body at very high sensitivity [159]. An illustrative example of some of the described techniques is provided in Figure 1.5. None of the described techniques is designed to provide all the information about glioma progression, but each of them can highlight some specific features, while it can fail in others. Consequently, the complementary use of these techniques is required and advised. All the collected information should be viewed, in fact, as an ensemble and has to be combined to get the most comprehensive picture possible of the tumor state.

Microscopy and Immunostaining

Immunostaining refers to an antibody-based method that is used to detect a specific protein in a sample, and to study the distribution of protein signals in tissues [237]. The most commonly applied immunostaining technique is immunohistochemistry (IHC) staining that can be based on fluorescent dyes (immunofluorescence) or other non-fluorescent methods. *Immunofluorescence* relies on the usage of a fluorescence microscope, i.e., it analyzes the emission of light by a substance to study its properties. In the body, each antibody targets a specific antigen. The immunofluorescence technique exploits this specificity to target fluorescent dyes to specific biomolecules within

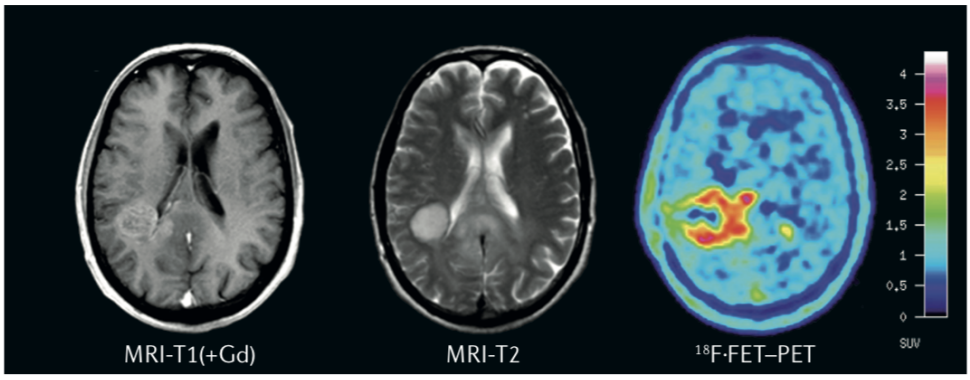

FIGURE 1.5: **Medical imaging.** Image of anaplastic astrocytoma (grade *III* tumors). From left to right: T1-weighted MRI, after application of gadolinium, T2-weighted MRI, and F-FET-PET (PET using the amino-acid O-(2-[^{18}F]fluoroethyl)-l-tyrosine). The last one, acquired 19 days after MRI, shows a larger mass of metabolically active tumor. (Reprinted by permission from Springer Nature Customer Service Centre GmbH: Springer Nature, Nature Reviews Neurology [159].

a cell. As a result, the distribution of the target molecules through the sample can be visualized. Figure 1.6 shows an example of the outcome of the immunofluorescence technique for targeting the distribution of two proteins in a sample of tumor tissue from a *Drosophila* brain.

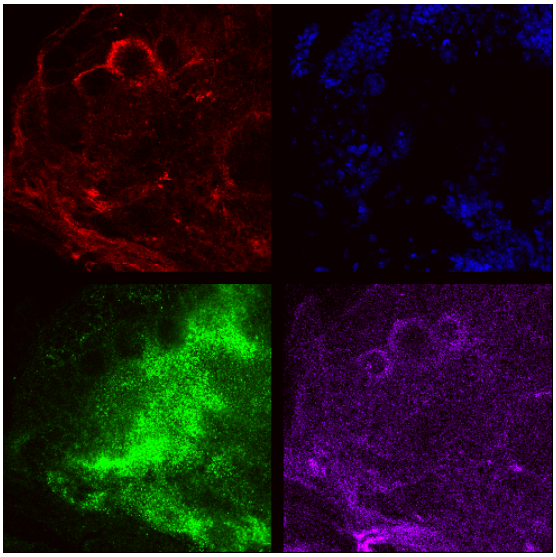

FIGURE 1.6: **Immunostaining of GB proteins.** Fluorescent confocal images of *Drosophila* 3rd instar larvae brain with GB: the GB cell membrane is marked in red, cell nuclei are marked in blue, focal adhesion kinase (FAK) and MMP-1 protein are marked in green and magenta, respectively. Images were obtained at Instituto Cajal CSIC, Madrid, Spain.

In contrast to that, *non-fluorescent methods* use enzymes that are capable of catalyzing reactions and give a colored outcome, easily detectable by light microscopy. One of the main difficulties with IHC staining is overcoming possible residual levels of immunofluorescence that are not directly emitted by the studied substance and can affect the interpretation of the immunologic reactions.

To this point, it is clear the need of mathematical models to extrapolate useful information from the large amount of data obtained with the most advanced imaging techniques. On the clinical side, these techniques bring along benefits for both prognosis, i.e., the estimation of the likely progression of a disease, and treatment.

As stated above, we mainly focus on these two described classes of clinical and biological data (medical imaging and immunostaining techniques), and we analyze them to obtain useful information to be included in the models. However, we know that further technological advances are available. In the last decades, several *omics technologies* have been largely applied. The term ***omics*** refers to the study of cancer as a whole entity focusing on various micro- and macro-molecules. Omics technologies include the study of DNA mutations, copy number variations, epigenetic changes, transcriptome analysis, and whole-genome DNA/RNA sequencing, providing a broad range of genomic information [309]. These techniques have unveiled some molecular mechanisms behind various cancers and assisted in the identification of next-generation molecular markers. For instance, in the case of glioma diagnosis and classification, IDH or TP53 mutations have been included as molecular signatures. Besides these technologies, advances in histopathological analysis, namely the microscopic examination of tissue sections, have provided an important contribution to the study of glioma progression, quantifying and classifying intra-tumoral heterogeneity, which is useful to determine glioma grading and assessing disease progression.

1.2 *Mathematical aspects of glioma modeling*

Although there is a considerable amount of information about the clinical and biological behavior of gliomas, the high complexity of the invasion mechanisms remains a major challenge in clinical neuro-oncology. From a biological and medical perspective, it is often difficult to investigate the connections between clinically observable glioma behaviors and the underlying molecular and cellular processes. Therefore, an important challenge consists in the integration of the theoretically and empirically acquired knowledge for a better understanding of the mechanisms that contribute to tumor invasion.

In this context, ***mathematical models*** emerge as powerful tools towards the investigation of how neoplasias become malignant - known as the carcinogenesis process - how tumors grow, migrate, invade adjacent tissues, and metastasize, and how this can be clinically managed. Ultimately, mathematical models could improve the overall clinical outcome by predicting the results of specific combinations of treatments, providing a theoretical and computational framework to perform in silico experiments. Numerous mathematical studies have been developed to describe cancer progression, and specifically glioma evolution. However, the exponential growth of the number of such models precludes any attempt for a comprehensive and exhaustive survey. A wide variety of modeling approaches has been proposed to investigate the mechanisms of glioma growth and invasion, varying from discrete to continuous methods, from the theory of dynamical systems to the study of models that include space-dependent components.

The biology that characterizes glioma progression, and cancer dynamics in general, is complex, and the evolution process is characterized by an ***inherently multiscale nature***. It involves several phenomena that occur at different spatial and temporal scales, ranging from processes at subcellular, up to cellular, and, finally, tissue levels. Therefore, the need of understanding the various mechanisms expressed at the different scales reflects on our choice of applying a multiscale mathematical approach

to the study of glioma evolution. The intrinsic multiscale nature of the biological system suggests focusing on the three natural scales related to the invasion dynamics. Thus, we consider three specific levels of description: subcellular level, cellular level, and tissue level.

- The ***subcellular level***, or microscopic scale, refers to processes happening at the level of a single cell. These are usually faster than the ones occurring at higher levels, and involve membrane receptors and/or intracellular pathways. This scale describes interactions between molecules and receptors on the cell membrane, which drive cell migration in response to external factors, as well as alterations of signaling cascades. The cell membrane, in fact, is characterized by a large number of receptors that interact with the external environment, receive signals from it, and transmit them to the cell, inducing the activation or suppression of downstream mechanisms. Depending on the nature of the involved receptors, these interactions can affect, for instance, cell migration, cell proliferation, or the angiogenesis process. In our study, we limit the microscopic scale to the description of the dynamics of some families of receptors triggering glioma migration (e.g. the integrin family, and proton-sensing receptors) and angiogenesis (e.g. VEGF receptors).

- The ***cellular level***, or mesoscopic scale, models the effect of several intercellular interactions. These interactions can occur between tumor cells and the extracellular environment (cell-ECM interactions), or among tumor cells themselves (cell-cell interactions). This level can be used to describe how such interactions affect cell invasion in terms of velocity changes, how they determine proliferative or lethal effects on the tumor population, how they drive phenotypic switches (due to crowded environments or to lack of nutrients) or blood vessel formation. In this dissertation, we mainly consider at this level the processes involved in the interactions between glioma cells and tumor microenvironment. This choice is justified by our aim to achieve a deeper understanding of how these mechanisms can explain features directly visible at the tissue level. One example of a mechanism studied at the cellular level is the typical anisotropic spreading. Observable at the macroscopic level, it characterizes glioma migration and is strongly related to the mesoscopic interactions between glioma cells and underlying brain fibers.

- The ***tissue level***, or macroscopic scale, directly describes the processes of proliferation and migration of tumor cells in terms of macroscopic density, reflecting the major aspects of tumor evolution observable in the clinical context. At this level, it is possible to describe the growth of avascular, or vascular, tumors with diffusive or drift phenomena related to the availability of external resources, such as fiber tracts on which cells can crawl, or nutrient and growth factor. Moreover, at this level tumor dynamics can be coupled with the evolution of other tissue/cell types to model intratumor heterogeneity, blood vessel evolution, or ECM remodeling.

Several mathematical approaches have been developed for the description of these different scales. The subcellular level is generally described in terms of *ordinary differential equations* (ODEs), modeling receptor dynamics in response to external fields or their position gradients, which can implicitly include a time or space dependency. The mesoscopic level can be modeled by *linear or nonlinear integro-differential equations*, referring to the kinetic theory used in the context of gas dynamics, and describing individual cell behaviors. For instance, in this dissertation, the mesoscopic settings,

which are described in Chapters 3-6, are based on the description of cell movement by means of kinetic equations. These equations can describe the so-called *velocity-jump process*, which characterizes a cell that moves with constant velocity in a straight line, stops after a certain time, chooses a new direction, and then continues running. This mechanism is also known as *run and tumble* [22]. Alternatively, cell velocity changes can be caused by contact guidance or other environmental cues. Macroscopic models, instead, are usually characterized by systems of *nonlinear partial differential equations* (PDEs). These can be derived with suitable scaling methods from lower levels of description, since individual cell behaviors are crucial to drive the macroscopic processes, stressing the need for connecting the multiple scales. Nevertheless, these models can be also stated directly at the macroscopic scale, employing mechanical or phenomenological assumptions. This possibility is often employed when the highly complex and nonlinear nature of some mechanisms included in the models does not allow for a properly stated and formal derivation of the macroscopic system from lower levels of description. We adopt this approach in Chapter 7, as nonlinearity is an intrinsic and essential feature of the modeling.

This dissertation aims to address questions related to glioma invasion in the tissue in relation to the external environment. Therefore, we strongly emphasize the multiscale nature of the biological problem and analyze processes belonging to different scales, making connections between them. Our approaches are all based on continuous systems stated in terms of partial differential equations. These equations describe the spatial and temporal evolution of the tumor population and additional external agents interacting with it. In the ***first part*** of our work, namely Chapters 3-5, we develop three-level multiscale models, where the macroscopic setting is formally derived from an individual level of description, based on kinetic transport equations. Macroscopically, these models characterize cell migration with a combination of linear diffusion and tactic terms, the latter carrying information about the subcellular dynamics. Precisely, we first model the cell-ECM interactions. We analyze the lower scale mechanisms taking into account the influence of fiber distribution on glioma spread and potential treatments (Chapter 3). Then, this study is extended to include the effect of vasculature and acidity on tumor proliferation and migration (Chapter 4), and, eventually, possible therapeutic approaches affecting tumor angiogenesis (Chapter 5). In the ***second part*** of this thesis, we dedicate our study to a deeper analysis of the cell membrane dynamics and the biochemical and biomechanical aspects related to it. In the specific, in Chapter 7 we present a macroscopic model to describe the evolution of cell protrusions linked to integrin and protease dynamics, and how the combination of these agents drives the propagation of the tumor invasion front. In doing so, we merge diffusive and drift-driven mechanisms for the description of cell migration. We assume that the drift-driven mechanism is governed by haptotactic and chemotactic processes, i.e., directed migration of cells towards gradients of soluble or unsoluble components of the ECM, induced by MMP and integrins, respectively. The definition of a sharp and well-defined propagation front for the tumor population, observed experimentally, requires the introduction of strong nonlinear operators for the diffusive and advective terms, leading to a complex coupled multicellular system. For these reasons, we directly state the model equations at the macroscopic level, relying on a priori phenomenological assumptions supported by biological data. The model deduction from lower scales and microscopic descriptions of the biological system is a future challenge of our research. Furthermore, in this dissertation, we include a further study, presented in Chapter 6. It illustrates an analysis of the relative relationship between cell response to chemotaxis and contact guidance. In particular, it relies on a kinetic framework (like the models described in Chapters 3-5), providing a mesoscopic

description of the cell population. However, unlike the other settings, this model does not include microscopic dynamics. Instead, it describes two distinct cues that simultaneously influence cell velocity changes. Moreover, it includes non-local terms, aimed at describing the effects of cell protrusions on the migration. In Chapter 7, we address the problems related to cell protrusion modeling at the macroscopic level in detail. Thus, the work presented in Chapter 6 originates from the idea of understanding the effect of a multi-cue environment on cell velocity in general, and it prepares the basis for a future and more precise application at glioma case.

In the following Sections 1.2.1 and 1.2.2, we present the main, general aspects of the mathematical formalisms in the modeling approaches that will be used in the forthcoming chapters.

1.2.1 *Multiscale models*

Multiscale models belong to the class of spatially structured models based on the idea of relating the macroscopic cell behavior with the dynamics at a subcellular and individual cell level. As above stated, all temporal and spatial scales are crucial to achieve a more comprehensive understanding of the glioma evolution. Therefore, the mathematical description of glioma progression fits in the framework of multiscale models. In this context, the macroscopic setting is derived from lower levels of description by using suitable asymptotic methods.

The multiscale approach has been widely analyzed for the case of movements of classical particles by asymptotic methods developed in kinetic theory. In particular, the asymptotic methods have been largely studied with respect to the so-called parabolic and hyperbolic limits. The parabolic or low field limit of a kinetic equation leads to a drift-diffusion type of system (or reaction-drift-diffusion system) in which the diffusion processes dominate the overall behavior. In the hyperbolic or high field limit, the influence of the diffusion terms is of lower (or equal) order of magnitude in comparison with other convective terms. Therefore, different macroscopic models can be obtained depending on the different scaling assumptions that are considered. The literature on asymptotic methods for classical particles is vast and well-documented (see [31, 222] and references therein), and numerous contributions apply the same methodology for multicellular models related to different biological problems (e.g. see [18, 43, 155, 213]). It is important to notice that some differences distinguish the study of classical particles, which are elements of inert matter, and the study of cells belonging to living organisms. While active particles are only characterized by position and velocity, cells can also present an additional microscopic state representing some biological functions at a subcellular level. Moreover, the microscopic interactions within a single cell may also take into account non-conservative proliferative and/or destructive phenomena.

In biological system in general, the distribution of cells is described at the mesoscopic scale by the distribution function $\rho(t, \mathbf{x}, \mathbf{v}, \mathbf{y})$, which depends on time $t \geq 0$, space $\mathbf{x} \in \Omega \subseteq \mathbb{R}^d$, microscopic velocity $\mathbf{v} \in \mathbf{V} \subseteq \mathbb{R}^d$, and internal variables $\mathbf{y} \in \mathbf{Y} \subseteq \mathbb{R}^p$. This kinetic approach is based on Boltzmann-type equations for the cell population density. Here, the usual collision operator describes the cell velocity changes. In particular, the cell movement is led by velocity jump processes, for which the cell's position changes are subjected to $d\mathbf{x} = \mathbf{v}dt$, and the new velocity is chosen according to a probability distribution, which depends on the cell's previous velocity, position, and internal variable. The internal variable dynamics are described using an evolutionary

equation, generally defined as

$$\frac{d\mathbf{y}}{dt} = G(t, \mathbf{x}, \mathbf{v}, \mathbf{y}) ,$$

where the vector field $G(\cdot)$ could also depend on the distribution function $\rho(t, \mathbf{x}, \mathbf{v}, \mathbf{y})$, as well as on the concentration of other mesoscopic or macroscopic quantities, and it could directly or indirectly involve the dependency on time, position and velocity. At the single cell level, the cell distribution density $\rho(t, \mathbf{x}, \mathbf{v}, \mathbf{y})$ satisfies the general kinetic transport equation

$$\begin{aligned} &\frac{\partial \rho}{\partial t}(t, \mathbf{x}, \mathbf{v}, \mathbf{y}) + v \cdot \nabla_{\mathbf{x}} \rho(t, \mathbf{x}, \mathbf{v}, \mathbf{y}) + \nabla_{\mathbf{y}} \cdot (G(t, \mathbf{x}, \mathbf{v}, \mathbf{y})\, \rho(t, \mathbf{x}, \mathbf{v}, \mathbf{y})) \\ &= \mathcal{L}[\rho](t, \mathbf{x}, \mathbf{v}, \mathbf{y}) + \mathcal{C}[\rho](t, \mathbf{x}, \mathbf{v}, \mathbf{y}) + \mathcal{D}[\rho](t, \mathbf{x}, \mathbf{v}, \mathbf{y}) . \end{aligned} \tag{1.1}$$

In this equation, $\mathcal{C}[\rho]$ and $\mathcal{D}[\rho]$ correspond to conservative and proliferative (or destructive) interactions, respectively, while $\mathcal{L}[\rho]$ represents a turning operator modeling the velocity changes. The application of an asymptotic method provides a macroscopic equation for the population density $n(t, \mathbf{x})$ defined as

$$n(t, \mathbf{x}) = \int_{\mathbf{Y}} \int_{\mathbf{V}} \rho(t, \mathbf{x}, \mathbf{v}, \mathbf{y}) d\mathbf{v} d\mathbf{y} .$$

Technically, an asymptotic method is based on the expansion of the distribution function ρ in terms of a small dimensionless parameter related to the spatial scale. The specific form of the macroscopic equations depends on which biological mechanisms are described at the individual cell level and which of them is assumed to be predominant in the dynamics. The first paper that addresses the study of a cellular system in the context of the kinetic theory is [211], followed by many contributions that apply this approach to various other biological systems (e.g. see [16, 18, 43, 78, 155] and references therein). The same modeling approach has been applied to the study of gliomas, connecting the modeling of the subcellular processes with the mesoscopic population-level description (e.g. see [57, 74, 75, 77, 216] and reference therein). The use of a subcellular level, in addition to the classical mesoscopic one, allows us to observe how the information emerging from this lower level introduces additional terms, or dependency, at the mesoscopic level, which consequently are reflected in the macroscopic equations.

1.2.2 *Macroscopic models*

Macroscopic models describe the evolution of the cell population at the tissue level, modeling the progression of the tumor mass by means of proliferative or migrative mechanisms. In this framework, an important and often-discussed aspect concerns cell diffusion dynamics. Several macroscopic mathematical models have been developed to describe the evolution of tumor cells due to diffusion processes. These models can be categorized primarily into two main classes depending on whether they relying on linear or nonlinear diffusion.

If we consider the macroscopic cell density $n(t, \mathbf{x})$, the general diffusion equation reads as

$$\frac{\partial n}{\partial t} = -\nabla_{\mathbf{x}} \cdot (D\, \mathcal{J}[n]) , \tag{1.2}$$

where $\mathcal{J}[n]$ is the diffusive flux and $D \in \mathbb{R}^{d\times d}$ the diffusion coefficient. Models for linear diffusion rely on *Fick's law* [85], which describes cell migration as a result of a flux of cells moving at rate D along a density gradient, i.e.,

$$\mathcal{J}[n] := -\nabla_{\mathbf{x}} n\,.$$

This provides an evolution equation for the tumor density of the form

$$\frac{\partial n}{\partial t} = \nabla_{\mathbf{x}} \cdot (D\nabla_{\mathbf{x}} n)\,.$$

Introductory literature [39, 280] describing the evolution of the glioma cell population is based on this approach. Relying on this framework, several models for tumor progression have been developed and extended to describe various additional morphological features characterizing glioma progression [275, 276], such as chemotactic and haptotactic processes [141, 142], or cell-cell and cell-ECM adhesion [218].

The concept of nonlinear diffusion originates from the study of the flow of an ideal gas in a homogeneous porous medium. Considering the density n and the pressure p, the velocity $\mathbf{V}$ of the flow can be expressed using the *Darcy's law* [286]

$$\mu\mathbf{V} := -k\nabla_{\mathbf{x}} p\,,$$

with μ representing the dynamic viscosity of the fluid and k the permeability of the medium. Taking into account the relation given by the *state equation* for perfect gases, namely

$$p = p_0 n^{\gamma}\,, \tag{1.3}$$

and the mass balance equation

$$\varepsilon\frac{\partial n}{\partial t} + \nabla_{\mathbf{x}} \cdot (n\,\mathbf{V}) = 0\,,$$

we can derive one expression for the porous medium equation (PME)

$$\frac{\partial n}{\partial t} = c\,\nabla_{\mathbf{x}} \cdot (n^{\gamma}\,\nabla_{\mathbf{x}} n)\,.$$

Here the coefficient c is given by $c = \frac{k\gamma}{\mu\,\varepsilon\,p_0}$, where p_0 is the reference pressure, ε the porosity of the medium, and $\gamma \geq 1$ the so-called polytropic exponent [286]. The nonlinear diffusion equation allows the definition of stationary profiles, possibly traveling waves, that have a sharp and finite front of propagation moving with constant speed and separating the regions $\{n > 0\}$ and $\{n = 0\}$. In contrast, in the linear diffusion case, diffusion is characterized by an infinite speed of propagation that determines the well-known infinitely long exponential tail. This feature is shown in a conceptual example Figure 1.7. In the context of glioma modeling, nonlinear models have been used to replicate the occurrence of these well-defined invasion fronts (e.g. see [181] and references therein).

A more sophisticated approach to the problem of nonlinear diffusion describes the diffusion operator using the so-called ***flux-saturated equation***, where the diffusive flux is given as

$$\mathcal{J}[n] := -\nu\,\frac{n^m}{\sqrt{n^2 + \left(\frac{\nu}{\mathrm{v}}\right)^2 |\nabla_{\mathbf{x}} n|^2}}\nabla_{\mathbf{x}} n\,. \tag{1.4}$$

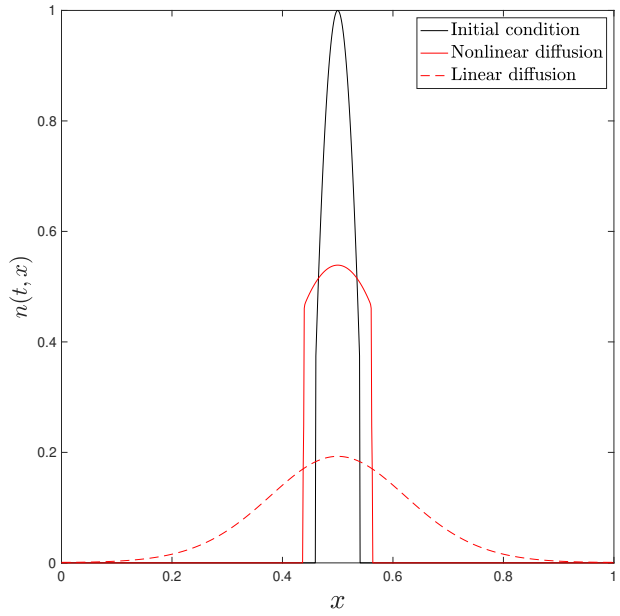

FIGURE 1.7: **Linear vs. Nonlinear Diffusion.** Example of the evolution of the cell density for linear (dashed line) and nonlinear (solid line) diffusion equation at time t=10. The equations have been solved numerically, choosing $D = \mathbb{I}_d$ in the linear case and $c = 1$ and $\gamma = 1$ in the nonlinear case.

Here ν is the kinematic viscosity of the medium, $\mathbf{v}$ is the front propagation velocity, and the exponent m is connected to the polytropic exponent γ in (1.3) and to the porosity of the medium. These models with saturated flows appear in the literature on wave propagation in a medium and in optimal mass transport as an alternative to linear diffusion. The flux-saturated equation, obtained plugging (1.4) into (1.2), is an equation in divergence form combining two nonlinear diffusion mechanisms: the one of porous-media equations on one hand, and the one for the flux saturation mechanism on the other. The latter component provides a flow that is saturated as long as the size of the gradients is large enough. This type of equation is characterized by an overall finite speed of propagation bounded by the explicit value of the velocity of the propagation front $\mathbf{v}$ incorporated in the operator (1.4). In particular, the value of the velocity of the front depends on the internal pressure and is exactly $\mathbf{v}$ for $m = 1$, while it is limited by $\mathbf{v}$ for $m > 1$ [40, 41]. The flux-saturated equation preserves, in its solution, the characteristics of the initial data, with respect to the compactness of the support and possible jump discontinuities, enabling the emergence of sharp invasion profiles.

In addition to the diffusive mechanisms leading to cell movement, several other components can be included in a macroscopic setting to describe the effect of cell-microenvironment interactions on the tumor population on proliferation and migration. For instance, a nonlinear description can be used to model the diffusive flux governing the tactic process supporting tumor migration (e.g. see [139] and references therein). A reasonable representation of this flux is given by

$$\mathcal{J}[n, S] := n \frac{a_S}{\sqrt{1 + |\nabla_{\mathbf{x}} S|^2}} \nabla_{\mathbf{x}} S \,,$$

with the tactic coefficient a_S and the agent S whose gradient drives the taxis. This

form reduces to the standard form $\mathcal{J}[n, S] = a_S\, n \nabla_{\mathbf{x}} S$ for a small gradient of S, while it saturates for large gradients.

Although our focus is on empathizing the multiscale nature of glioma progression, the ***mathematical literature*** in the oncologic field offers extensive and diverse modeling frameworks. Due to the vastness of the field, we simply report some examples of frameworks applied to the study of glioma progression: *compartmental models* are usually used to usually describe the dynamics related to intratumor heterogeneity or the tumor interplay with external agents (examples of this approach can be found in [105, 163, 190, 245] for the context of population dynamics, and in [90, 113, 141, 185, 276] for the spatial-dependent system); *multiphase mixture models*, are characterized by the description of the malignant mass as a saturated medium, with at least one liquid phase (e.g. water) and one solid phase (e.g. glioma cells, ECM, etc.) [52, 119]; *hybrid models* involve both discrete and continuous equations for the characterization of cell migration and the evolution of external factors [97, 140].

1.3 *Summary*

Throughout the previous introductory sections, we gave a biological overview of the peculiar features characterizing the development and evolution of brain tumors. We provided a detailed description of the aspects characterizing glioma progression on which we focus our study. In particular, we analyzed tumor invasion in the extracellular space, its interaction with the microenvironment, peculiar mechanisms of tumor angiogenesis, and some of the common therapeutic approaches used in the clinic. We explained which biological and clinical data can be included in the modeling approach, e.g. DTI and MRI data applied to the study of cell diffusion, and immunostaining techniques to track protein distribution in the tumor domain. Moreover, we discussed the mathematical purpose of developing models that describe tumor evolution as a multiple level process, emphasizing the need of connecting the different scales, and providing a general overview of the two frameworks on which our approaches are built.

In the following chapters, we present the analysis on the features characterizing the brain structures (Chapter 2), develop and analyze the multiscale kinetic-based models (Chapters 3-6), and describe the macroscopic setting (Chapter 7).

Part I

Preliminaries on brain data

2 The brain structure

The human brain consists of 86 billion neurons and, in addition, a similar number of other cells. Together with the spinal cord, it makes up the central nervous system. The brain controls most activities in the human body, processing the incoming information and sending instructions to the rest of the tissues and organs. The outer layer of the brain is called cerebral cortex and is composed of neural cell bodies referred to as *grey matter*. Internally, the myelinated axons of these cortical neurons extend into the cerebral hemispheres and, because of their whitish appearance, they are referred to as *white matter*. Consequentially, the *grey matter* is predominantly located on the cortical surface of the brain, while the *white matter* runs deep inside the two hemispheres into which the brain is divided. Topographically, the surface of the hemispheres has a series of elevations, called *gyri*, and infoldings, named *sulci*, that significantly increase the surface area of the brain. Structurally, each hemisphere is divided into four major anatomical lobes - frontal, parietal, occipital, and temporal - separated from each other by several sulci. The cerebral cortex and the different internal brain regions are connected through various white matter pathways. One example of an internal brain region is the *corpus callosum*, which is formed by myelinated axons horizontally linking the two hemispheres. Decades of anatomical studies have provided information on the fiber pathways and fiber bundles that link the different components of the neural system, yielding a considerable body of literature on the biology and pathology of myelinated axons (see [263] and references therein).

A deeper understanding of the white matter tracts is a pivotal step for further elaborations of the knowledge about brain structure and function, as well as for clinical purposes. In fact, tumor migration and dissemination in the brain largely depend on the orientation and spatial distribution of the brain fibers. As introduced in Section 1.1.1, glioma cells invade the brain following preferential pathways determined by the brain fibers. The structure and orientation of these brain fibers provide an anisotropic character to the brain tissue, meaning that different tissue properties, e.g. the diffusion of water molecules, change in different directions. This anisotropic property is directly reflected in the migratory cell dynamics. In particular, anisotropic invasion is a peculiarity of glioma cells, which crawl along the aligned structures in the brain fibers. The resulting infiltrative and heterogeneous patterns contribute to generate the glioma characteristic of not displaying well-delineated outer borders, as observed in Section 1.1.4. Therefore, taking into account the presence of fiber tracts in the brain is a central point for the development of realistic models. The reliability of mathematical models is a crucial factor when they are used to compare the simulated tumor evolution with patient data, or they are used to predict tumor progression.

The development of *diffusion tensor imaging* (DTI) has made possible a clearer *in-vivo* identification of some details related to the major white matter pathways [14], in both normal and damaged brains. An illustrative example of white matter tracts

originated from DTI data is given in Figure 2.1. Moreover, the development of MR tractography [12] and diffusion spectrum imaging [255] has allowed a greater degree of technical precision, although there are some important constraints upon tractography, which can sometimes fail in reconstructed the true fiber tract trajectory because of noise or cumulative error along the trajectory path.

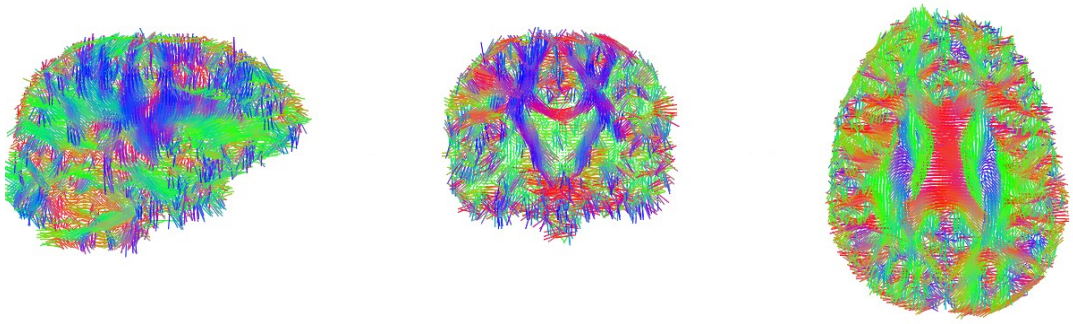

FIGURE 2.1: **Representation of white matter tracts.** From left to right: sagittal, coronal, and transversal plane. The colors refer to principal direction of the fiber tracts: Red for left-right direction, green for anterior-posterior direction, and blue for inferior-superior direction.

In the following sections, we introduce the basics of DTI imaging. In Section 2.1, we provide a detailed description of the data collected using the DTI technique and how they can be quantified. Thereafter, in Section 2.2 we specify how these data can be incorporated in the model, providing different options for the macroscopic and multiscale modeling settings. One of the methods described in this section is based on the idea that the information on tumor cell diffusivity can be extrapolated from the DTI data by introducing a distribution function that specifies the brain fiber orientation. Due to the relevance of such an approach to this thesis, we continue in Section 2.3 to present different well-known formulations of this fiber distribution function. We describe and compare such characterizations, highlighting their differences and their respective strengths and weaknesses.

2.1 *Diffusion tensor imaging*

Diffusion tensor imaging is a special type of diffusion-weighted imaging (DWI). DWI uses specific MRI sequences (see Section 1.1.5) to trace the diffusion of water molecules and to generate contrast in MR images. Since the diffusion of water within tissues is altered by changes in tissue microstructure and organization, DWI methods, including DTI, are potentially effective for characterizing the effects of diseases on the tissue structure. DTI is mainly used to study the architecture of white matter in human brains *in-vivo*. It allows us to map water molecule diffusion patterns, characterizing their three-dimensional diffusion as a function of the spatial location and revealing microscopic details about the tissue architecture, both in normal and pathological states. Therefore, the DTI method is a valuable instrument in the glioma prognosis since it provides information about the local brain tissue structure that influences cell spread. Moreover, it is used to estimate the white matter connectivity patterns, visualizing aligned structures and neural tracts.

Technically, DTI measures the apparent diffusivity of water molecules in different

directions per volume element, i.e. in each voxel of an image. The DTI technique relies on the basic physiological concept that, in the brain, the random diffusion-driven displacements of a molecule is influenced by the interaction with many tissue components. In a free medium, the molecular displacements during a given time interval Δt can be described with a three-dimensional Gaussian distribution $\mathcal{P}$, and the traveled distance is statistically well described by a diffusion coefficient, which can depend on the molecule size, or the viscosity and temperature of the medium [6]. Using the Einstein diffusion equation in n-dimension, the diffusion coefficient D (expressed in $\mathrm{mm}^2 \cdot \mathrm{s}^{-1}$) reads

$$D = \frac{\langle \Delta r^2 \rangle}{2\, n\, \Delta t},$$

where $\langle \Delta r^2 \rangle$ is the mean squared displacement, and the probability density $\mathcal{P}$ is given by

$$\mathcal{P}(\Delta r, \Delta t) = \frac{1}{\sqrt{(2\pi\, D \Delta t)^3}} \exp\left(-\frac{\Delta r^2}{4 D \Delta t}\right).$$

Pure water molecules, for instance, at 20°C diffuse freely with a diffusion coefficient of roughly $2 \cdot 10^{-3}$ $\mathrm{mm}^2 \cdot \mathrm{s}^{-1}$. In other words, they diffuse over 17 μm in 50 ms [162]. In biological tissues, obstacles modulate the free diffusion process: the actual diffusion distance is reduced and the displacement distribution is no longer Gaussian and closely reflects the tissue microstructure. In this case, the water diffusion can be measured by a pair of magnetic field gradient pulses that make the MR signal sensitive to diffusion. The first pulse dephases the magnetization across the sample (or voxel in imaging), "labeling" water nuclei according to their spatial location. The second pulse, introduced slightly later, rephases the magnetization to detect the changes in nuclei location along the gradient direction. This way, the second pulse collects the displacement history of nuclei occurring during the time interval (or *diffusion time*) between the two pulses. By acquiring data for various gradient pulse amplitudes, it is possible to obtain images with different degrees of sensitivity.

For raw DWI data, the signal intensity of an individual voxel in the image is essentially the cube root of the multiplied signal intensities of the three individual images acquired with a diffusion gradient in each of the three orthogonal directions. In the specific case of DTI, a minimum of six non-collinear directions is required to fully sample the directional tensor in space. Then, six individual diffusion-weighted images are generated and averaged to render the trace of diffusion or diffusion-weighted image. The anisotropic features in the brain can be recognized by looking at the differences in the signal intensity between brain regions in relation to the applied diffusion gradient.

2.1.1 *DTI data*

The DTI data used in this dissertation was acquired and published in [68] and previously used in [150]. Its acquisition was approved by the Ethics Committee at the Cruces University Hospital and all the methods employed were in accordance with approved guidelines. The DTI data was processed with the FSL software[1]. Specifically, an *Eddy Current Correction* was first applied to correct the changes produced by the variations in gradient field directions during the image acquisition, and possible head movements. Then, the non-brain tissue was removed from the images of the whole head with the *Brain Extraction Tool*. Finally, using the information about the gradient direction and diffusion weightings, for each voxel of the images, *DTIFIT toolbox*

[1] https://fsl.fmrib.ox.ac.uk

fitted a diffusion tensor model at each voxel, deriving the three eigenvectors - referring to the three principal directions - and the associated eigenvalues - referring to the corresponding diffusivities - of the diffusion of water molecules within brain tissues. A more detailed description of the DTI data processing can be found in Appendix A.

The tensor resulting from DTI data for a given voxel centered in $\mathbf{x} \in \mathbb{R}^3$ can be represented by a 3×3 symmetric matrix

$$\mathbf{D}(\mathbf{x}) = \begin{pmatrix} D_{xx} & D_{xy} & D_{xz} \\ D_{yx} & D_{yy} & D_{yz} \\ D_{zx} & D_{zy} & D_{zz} \end{pmatrix} , \tag{2.1}$$

where all the matrix elements are functions of $\mathbf{x}$. Although $\mathbf{D}$ is traditionally called ***diffusion tensor***, in this chapter we refer to it as ***directional tensor***[2]. Alternatively, the directional tensor $\mathbf{D}$ can be defined by its three eigenvalues $\lambda_1, \lambda_2, \lambda_3 \in \mathbb{R}$, and the corresponding normalized and orthogonal eigenvectors $\mathbf{v}_1, \mathbf{v}_2, \mathbf{v}_3 \in \mathbb{R}^3$ at each grid point as

$$\mathbf{D}(\mathbf{x}) = \lambda_1 \mathbf{v}_1 \mathbf{v}_1^T + \lambda_2 \mathbf{v}_2 \mathbf{v}_2^T + \lambda_3 \mathbf{v}_3 \mathbf{v}_3^T . \tag{2.2}$$

Eigenvalues and eigenvectors are space-dependent, i.e. $\lambda_i = \lambda_i(\mathbf{x})$ and $\mathbf{v}_i = \mathbf{v}_i(\mathbf{x})$ for $i = 1, 2, 3$. With the above notation, we refer to eigenvectors sorted according to the size of the corresponding eigenvalue (decreasing order), and we indicate with $\mathbf{v}_1$ the principal direction of the movement at point $\mathbf{x}$. In the case of anisotropy, these representations of the directional tensor provide a good approximation for the fiber alignment direction. For instance, the corpus callosum usually shows high diffusion in the D_{xx} direction and low diffusion on D_{yy} and D_{zz}. Considering that the x-axis is aligned with the right-left direction, the y-axis with the anterior-posterior direction, and the z-axis with the inferior-superior direction, this means that fibers in the corpus callosum run mainly transversely from left to right. For simplicity in the notation, in the following, we drop the dependency on $\mathbf{x}$ in the eigenvalues and eigenvectors of the tensor.

The application of the directional tensor to describe anisotropic behaviors was introduced in [14], where molecular diffusion in an anisotropic medium was represented as a Brownian random process characterized by a macroscopic Gaussian conditional probability density function $\mathcal{P}(\mathbf{x}|\mathbf{x}_0, t)$

$$\mathcal{P}(\mathbf{x}|\mathbf{x}_0, t) = \frac{1}{\sqrt{(2\pi t)^3 |\mathbf{D}|}} \exp\left(\frac{-(\mathbf{x} - \mathbf{x}_0)^T \mathbf{D}^{-1} (\mathbf{x} - \mathbf{x}_0)}{2t} \right) , \tag{2.3}$$

where $|\mathbf{D}|$ is the determinant of $\mathbf{D}$. This equation describes the probability that a molecule, located in $\mathbf{x}_0$ at $t = 0$, reaches position $\mathbf{x}$ at time t, where $\mathbf{D} = \mathbf{D}(t, \mathbf{x})$.

To visualize tensor data, the concept of *diffusion ellipsoids* was introduced in [14]. An ellipsoid is a three-dimensional representation of the average displacement in space of a molecule located in a particular spot in a given interval of time. The equation for the diffusion ellipsoid is built by considering a level set of the quadratic form in the exponent of $\mathcal{P}(\mathbf{x}|\mathbf{x}_0, t)$, i.e.,

$$\frac{-(\mathbf{x} - \mathbf{x}_0)^T \mathbf{D}^{-1} (\mathbf{x} - \mathbf{x}_0)}{2t} = 1 .$$

[2] In the mathematical literature that employs a multi-dimensional tensor in the description of the diffusive flux, this tensor is traditionally named *diffusion tensor*; however, it has much more implication than the simple modification of the constant diffusion coefficient. In particular, it is fundamental for the description of the spatial orientation of the movement. Therefore, as we are interested in the effect of the tissue orientation on the tumor behavior, we refer to it as *directional tensor*.

Considering the representation of $\mathbf{D}$ in (2.2), the ellipsoid equation results in

$$\left(\frac{\mathbf{v}_1^2}{\sqrt{2t\lambda_1}}\right)^2 + \left(\frac{\mathbf{v}_2^2}{\sqrt{2t\lambda_2}}\right)^2 + \left(\frac{\mathbf{v}_3^2}{\sqrt{2t\lambda_3}}\right)^2 = 1\,.$$

The main axes of the ellipsoid represent the mean effective diffusion distances, i.e.,

$$\sqrt{\langle \mathbf{x}_i^2 \rangle} = \sqrt{2t\lambda_i}$$

in the three principal directions in the time t. In the case of isotropic diffusion, as for homogenous media, the ellipsoid is simply a sphere, whose size is proportional to the unique diffusion coefficient. In the case of anisotropic diffusion, the ellipsoid becomes elongated if one direction predominates, or flat if one direction contributes less than the others. An illustrative example of the diffusion ellipsoids for isotropic and anisotropic scenarios is provided in Figure 2.2.

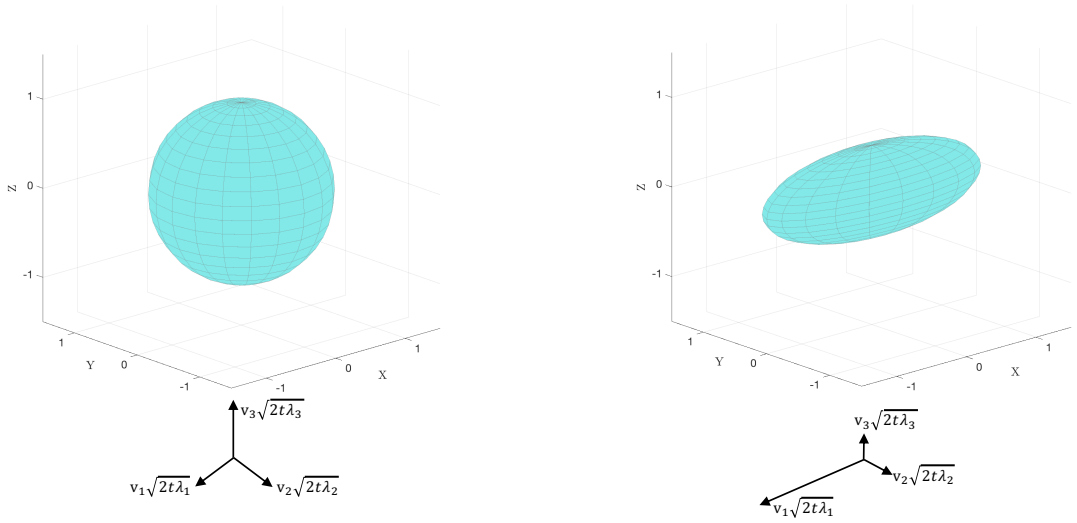

FIGURE 2.2: **Diffusion ellipsoids.** On the left, the sphere representing the isotropic case, where $\lambda_1 = \lambda_2 = \lambda_3$; on the right, the ellipsoid of an anisotropic case, where $\lambda_1 \gg \lambda_2, \lambda_3$. At the bottom of the two plots the main axis of the ellipsoids, indicated with $\mathbf{v}_i$, and their lengths are represented.

2.1.2 *Quantitative DTI information*

Diffusion ellipsoids are a meaningful way to display the DTI data and instantly get visual information from them. However, to provide information on tissue structures and, eventually, make comparisons, a quantification of the image information is necessary. This is commonly done by translating the information into simpler scalar maps. Three well-established ways to extract tissue microstructure and architecture information for each image voxel are based on the *mean diffusivity*, the *main direction of diffusivities*, and the *degree of anisotropy*.

The ***mean diffusivity*** (MD) characterizes the overall mean squared displacement of molecules and the magnitude of diffusion. This measure relates to the *average ellipsoid size* through the trace of the local tensor $\mathbf{D}$ in (2.1), or the mean of the eigenvalues

of **D** in (2.2):

$$MD(\mathbf{x}) = \frac{D_{xx} + D_{yy} + D_{zz}}{3} = \frac{1}{3}\sum_{i=1}^{3} \lambda_i \,. \tag{2.4}$$

For a generic point **x**, MD represents the mean of the eigenvalues of the directional tensor **D**, that we also denote as $\bar{\lambda}$. Physically, the trace of **D** measures intrinsic properties of the tissue and it is inherently insensitive to fiber orientation or gradient directions. Thus, changes in this measure can be ascribed to changes in the tissue's physiological state. The ***main direction of diffusivities*** relates to the main *ellipsoid axes*, i.e., to the mapping of the tissue structure orientation in space. In fact, the underlying assumption is that the direction of the fibers is coaligned with the direction of the eigenvector associated with the largest eigenvalue. Finally, the ***degree of anisotropy*** quantifies the spatial variation of the molecular displacement, namely the *ellipsoid eccentricity*, and, therefore, it relates to the presence of oriented structures.

Many measures for the degree of anisotropy have been proposed. They are called ***diffusion anisotropy indexes*** (DAIs) and can be calculated from the eigenvalues of **D**. The three main DAIs to which we refer are the *fractional anisotropy*, the *relative anisotropy*, and the *volume ratio*. We focus on these indices, even though other DAIs have been suggested in literature, including the *ultimate anisotropy indices* and the γ-variate anisotropy index. However, their expression can be recovered in terms of the three previously introduced DAIs [143]. ***Fractional anisotropy*** (FA) represents the fraction of the magnitude of the tensor that can be ascribed to anisotropic diffusion; it expresses the normalized variance of the eigenvalues as

$$FA(\mathbf{x}) = \sqrt{\frac{3}{2}} \frac{\sqrt{(\lambda_1 - \bar{\lambda})^2 + (\lambda_2 - \bar{\lambda})^2 + (\lambda_3 - \bar{\lambda})^2}}{\sqrt{\lambda_1^2 + \lambda_2^2 + \lambda_3^2}} \,.$$

FA is a positive quantity with values in the interval $[0, 1]$, where 0 represents a fully isotropic condition ($\lambda_1 = \lambda_2 = \lambda_3$) and 1 a fully anisotropic condition. ***Relative anisotropy*** (RA) is a normalized standard deviation representing the coefficient of variation of the eigenvalues

$$RA(\mathbf{x}) = \frac{\sqrt{(\lambda_1 - \bar{\lambda})^2 + (\lambda_2 - \bar{\lambda})^2 + (\lambda_3 - \bar{\lambda})^2}}{\sqrt{3}\bar{\lambda}} \,.$$

RA can also be interpreted as the ratio of the standard deviation of the eigenvalues to their mean, and it varies between 0 (full isotropy) and $\sqrt{2}$ (full anisotropy). Finally, the ***volume ratio*** (VR) is defined as

$$VR(\mathbf{x}) = \frac{\lambda_1 \lambda_2 \lambda_3}{\bar{\lambda}^3}$$

and it represents the ratio of the ellipsoid volume to the volume of a sphere of radius $\bar{\lambda}$. As for FA, the volume ratio takes values in the interval $[0, 1]$, but in this case, the volume of the ellipsoid approaches 0 as anisotropy increases, i.e., 0 indicates the highest anisotropy and 1 represents complete isotropy. These three DAIs (FA, RA, and VR) are rotationally invariant, i.e., independent of the orientation of the anisotropic structure with respect to the rotation of the coordinate system, and they are insensitive to the scheme by which the eigenvalues are ordered. The main application of DAIs is to determine whether two tissues have the same degree of anisotropy. In this regard, an important parameter for DAI comparisons is the contrast-to-noise ratio (CNR). Contrast is the difference between two measurements (DAI_i) of the same DAI, and the

noise is the square root of the sum of the variances (σ_i^2) in the two individual measurements. CNR is defined as

$$CNR = \frac{DAI_2 - DAI_1}{\sqrt{\sigma_1^2 + \sigma_2^2}}.$$

Several studies (e.g. see [112, 143]) have shown that there are significant differences between DAIs, especially in terms of sensitivity to the anisotropy and noise. In particular, FA seems to provide the most detailed representation of the anisotropy characterizing the tissue. It reveals well the various anisotropic structures, even for areas of mild and low anisotropy, providing good anatomical details of the anisotropic regions, even with increasing noise in the area of low anisotropy. On the contrary, VR has increasing noise contamination and a decreasing resolution for middle and low anisotropic regions, despite the fact that it provides the strongest contrast between low and high anisotropy areas. RA takes an intermediate position. It shows a significantly reduced intensity of the isotropic background when compared to the FA map, but better anatomical details and identification of the anisotropic region when compared to the VR map. In terms of noise, FA has a higher CNR between white matter tracks, neighboring cerebrospinal fluid, and grey matter compared to the RA map, while VR seems to be the index most susceptible to noise. However, these differences are not so evident, especially for small anisotropy variation, to justify an intrinsic advantage of one index on the others. All DAIs can be derived from a complete knowledge of the directional tensor or of its components.

In the following sections, we use the fractional anisotropy index for the comparisons of the fiber distribution functions specifying brain fiber orientation. In Figure 2.3 an example of visualization of the FA index on a transversal plane of the brain is presented. The degree of anisotropy of the tissue increases with the colors going from red to white, and, therefore, the brighter areas represent brain regions characterized by highly aligned fibers.

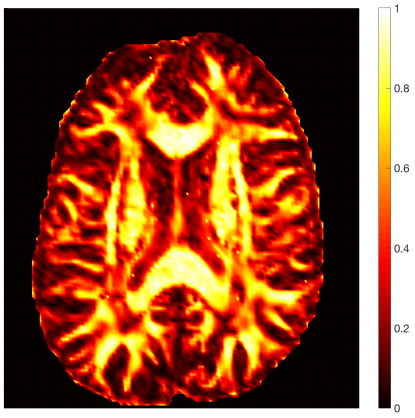

FIGURE 2.3: **Fractional anisotropy.** An illustrative example of FA on a real brain slice.

2.2 *Modeling anisotropic diffusion*

Previously, we have observed that the invasive pathways of glioma migration are largely dependent on white matter architecture. A variety of mathematical models for cell migration has been developed (e.g. see [30, 129, 148, 198]), where DTI data are incorporated to include the information about the brain structures and to simulate the directional movement of glioma cells in response to the anisotropy of the environment. In particular, this mechanism is called *contact guidance*. We provide a brief overview of some approaches proposed in the literature for including anisotropic information through DTI tensors into the mathematical setting for tumor evolution, either in macroscopic models or in kinetic-transport equations. More precisely, in the following description we refer to the *DTI tensor*, describing water molecule displacement, as $\mathbf{D}_W$, while we identify with $\mathbf{D}_T$ the *tumor directional tensor* related to cell migration. In general, $\mathbf{D}_T$ is not identify directly with $\mathbf{D}_W$, but it is calculated using the information that $\mathbf{D}_W$ provides. For our purpose, and considering the data available for our study, these tensors are space-dependent, but constant in time, i.e., $\mathbf{D}_i = \mathbf{D}_i(\mathbf{x})$, $i = T, W$.

In the context of ***macroscopic models***, as introduced in equation (1.2), a general way to describe the diffusion of glioma cell density $n(t, \mathbf{x})$, with $t \geq 0$, $\mathbf{x} \in \Omega \subseteq \mathbb{R}^d$ for $d \leq 3$, is

$$\frac{\partial}{\partial t} n(t, \mathbf{x}) = -\nabla_{\mathbf{x}} \cdot (\mathbf{D}_T(\mathbf{x}) \mathcal{J}[n])$$

where $\mathcal{J}[n]$ is the flux, which can be written in either a linear or a nonlinear form, as generally described in Section 1.2.2. In the case describe by equation 2.2, the diffusion rate is not a constant coefficient, but rather it is described with the tensor $\mathbf{D}_T(\mathbf{x})$, which directly models the impact of the complex tissue orientation on cell migration. The first attempt to include tissue anisotropy in a macroscopic model was proposed in [275], where the heterogeneity between grey and white matter is included by setting a significantly higher value for $\mathbf{D}_T$ in white than in grey matter. Specifically $\mathbf{D}_T(\mathbf{x}) = d_g$ in grey matter, while $\mathbf{D}_T(\mathbf{x}) = d_w > d_g$ in white matter, describing the faster invasion in white matter regions. Later on, further expansions of this model have been proposed; these connect directly $\mathbf{D}_T(\mathbf{x})$ to the anisotropic tensor $\mathbf{D}_W$ informed by DTI. One possible choice for $\mathbf{D}_T$ is described in [148], where the directional tensor is defined as

$$\mathbf{D}_T(\mathbf{x}) = \begin{cases} d_g \mathbb{I} & \text{for } \mathbf{x} \in \text{ grey matter} \\ d_w \mathbf{D}_W & \text{for } \mathbf{x} \in \text{ white matter}. \end{cases}$$

The authors of this paper use a brain atlas and real patient data to show the applicability of their model. However, no biological justifications are provided for such a relationship between the diffusion of water molecules and the diffusion of tumor cells. In [129], DTI data are used to connect $\mathbf{D}_W$ with $\mathbf{D}_T$ by means of a geometric argument. Specifically, the authors propose to modify the eigenvalues of the DTI tensor λ_i, but not its eigenvectors $\mathbf{v}_i$, preserving tensor orientation while changing the diffusivity. This modification is governed by a parameter r: $r = 1$ keeps the tensor unchanged; $r < 1$ decreases the anisotropy; $r > 1$ increases it. In particular, defining the linear, planar and spherical indices

$$c_l = \frac{\lambda_1 - \lambda_2}{\lambda_1 + \lambda_2 + \lambda_3}, \qquad c_p = \frac{2(\lambda_2 - \lambda_3)}{\lambda_1 + \lambda_2 + \lambda_3}, \qquad c_s = \frac{3\lambda_3}{\lambda_1 + \lambda_2 + \lambda_3}, \tag{2.5}$$

for which the eigenvalues are sorted in decreasing order, they introduce the vector $\mathbf{a}(r)$ as

$$\begin{pmatrix} a_1 \\ a_2 \\ a_3 \end{pmatrix} = \begin{pmatrix} r & r & 1 \\ 1 & r & 1 \\ 1 & 1 & 1 \end{pmatrix} \begin{pmatrix} c_l \\ c_p \\ c_s \end{pmatrix}$$

and defined $\bar{\lambda}_i(r) = a_i(r)\lambda_i$. Using these definitions, $\mathbf{D}_T(\mathbf{x})$ is given as

$$\mathbf{D}_T(\mathbf{x}) = \bar{\lambda}_1(r)\mathbf{v}_1\mathbf{v}_1^{\mathbf{T}} + \bar{\lambda}_2(r)\mathbf{v}_2\mathbf{v}_2^{\mathbf{T}} + \bar{\lambda}_3(r)\mathbf{v}_3\mathbf{v}_3^{\mathbf{T}}\,.$$

In [198], $\mathbf{D}_T$ is estimated as $\mathbf{D}_T(\mathbf{x}) = \alpha FA(\mathbf{x})\mathbf{D}_W(\mathbf{x})$ where FA represents the fractional anisotropy computed from DTI tensor data and α is a parameter (usually $\alpha = 1500$). By using this definition, the authors introduce an acceleration of the diffusion in white matter, while keeping the shape of the tensors (directionality distribution) the same as for $\mathbf{D}_W$, following the assumption that tumors evolve preferentially along white matter fibers.

An alternative has been developed for ***kinetic models***, which describe cell invasion at the individual level, to connect the tensor $\mathbf{D}_T$ with the DTI data encoded in $\mathbf{D}_W$ at the derived macroscopic scale (see [116, 216] and references therein). Considering a kinetic representation of the cell distribution $\rho(t, \mathbf{x}, \mathbf{v}, \mathbf{y})$, with $t \geq 0$, $\mathbf{x} \in \Omega \subseteq \mathbb{R}^d$, for $d \leq 3$, $\mathbf{v} \in \mathbf{V} = [s_1, s_2] \times \mathbb{S}^{d-1}$, where the minimum ($s_1$) and maximum ($s_2$) cell speeds satisfy $0 \leq s_1 \leq s_2 < \infty$ ($\mathbb{S}^{d-1}$ is the unit sphere in $\mathbb{R}^d$), and $\mathbf{y} \in \mathbf{Y} \subseteq \mathbb{R}^p$ an interval variable, cell migration can be model as in equation (1.1). In this equation $\mathcal{L}[\rho]$ represents the turning operator that describes the velocity changes of the individual cells. The influence of the brain fiber network on the velocity changes - the so-called *contact guidance* phenomenon - is modeled by introducing the distribution of fiber orientations at time t and location $\mathbf{x}$ by a *probability density* $q(t, \mathbf{x}, \hat{\mathbf{v}})$, where $\hat{\mathbf{v}} \in \mathbb{S}^{d-1}$ denotes the normalized fiber orientation (specifically, $\hat{\mathbf{v}} = \mathbf{v}/||\mathbf{v}||$). Defining the weight parameter ω as

$$\omega := \int_{\mathbf{V}} q(t, \mathbf{x}, \hat{\mathbf{v}}) d\mathbf{v} = \begin{cases} \dfrac{s_2^2 - s_1^2}{d} & \text{for } s_1 < s_2 \\ s^{d-1} & \text{for } s_1 = s_2 = s\,, \end{cases} \tag{2.6}$$

a candidate expression for the turning operator describing velocity changes due to the fiber network is given by

$$\mathcal{L}[\rho](t, \mathbf{x}, \mathbf{v}, \mathbf{y}) = -\mu\rho(t, \mathbf{x}, \mathbf{v}, \mathbf{y}) + \mu \int_V \frac{q(t, \mathbf{x}, \hat{\mathbf{v}})}{\omega} \rho(t, \mathbf{x}, \mathbf{v}', \mathbf{y}) \mathbf{v}' d\mathbf{v}' \tag{2.7}$$

with turning rate μ. Under the assumption of a constant cell speed s that refers to a population-averaged rate, i.e., $\mathbf{V} = s \times \mathbb{S}^{d-1}$, and a time-independent fiber distribution function, i.e., $q = q(\mathbf{x}, \hat{\mathbf{v}})$, a macroscopic scaling of equation (1.1) with (2.7) leads to an advection-diffusion equation, whose tensor for the tumor population is given by

$$\mathbf{D}_T(\mathbf{x}) = \frac{s^2}{\mu} \int_{\mathbb{S}^{d-1}} \hat{\mathbf{v}}\hat{\mathbf{v}}^T q(\mathbf{x}, \hat{\mathbf{v}}) d\hat{\mathbf{v}}\,. \tag{2.8}$$

It is worth noticing that this expression integrates the DTI information through the function $q(\mathbf{x}, \hat{\mathbf{v}})$. A proper description of the model characteristics and of the asymptotic method used for the derivation of the macroscopic equation will be addressed in the forthcoming Chapter 3. At this stage, we focus on the function $q(\mathbf{x}, \hat{\mathbf{v}})$, providing a more detailed description of its specificities and of the expressions used to

characterized it, pointing out how DTI-data are involved.

2.3 *Fiber distribution functions*

The last approach studied in the previous section describes how to map the information contained in $\mathbf{D}_W$ into the tumor cell tensor $\mathbf{D}_T$ by using the fiber distribution function related to the cell turning. This approach, which was first described in [216], yields to the definition of $\mathbf{D}_T$ described in equation (2.8). In this expression, the function $q(\mathbf{x}, \hat{\mathbf{v}})$ that represents the turning distribution function is left general. In this section, we investigate the nature of this distribution function. In particular, we study how such a function incorporates in the model the information about the diffusivity in the brain and how it describes the anisotropic characteristics of the nervous tissue. It is important to notice that to obtain reliable simulations of tumor dynamics from both qualitative and quantitative point of view, we need a detailed analysis on how the DTI data are processed and included in the model and how the information derived from these data is taken into account at the macroscopic level.

The ***fiber distribution density function*** $q(\mathbf{x}, \hat{\mathbf{v}})$ describes the probability of turning at point $\mathbf{x}$ and into a velocity of direction $\hat{\mathbf{v}}$. It represents the link between the raw DTI data, collected in the tensor $\mathbf{D}_W(\mathbf{x})$, and the information encoded in the tensor $\mathbf{D}_T(\mathbf{x})$, which describes tumor orientation and diffusivity at the macroscopic level. We assume the function q to be time-independent, leaving the generalization to the time-dependent case as a future task to address. We investigate how $\mathbf{D}_T(\mathbf{x})$ is derived from $\mathbf{D}_W(\mathbf{x})$ according to different possible expression of the underlying distribution function q. The three main choices of the fiber distribution most commonly used in the literature are the *Peanut distribution*, the *von Mises-Fisher distribution* (VMF), and the *orientation distribution function* (ODF).

In Sections 2.3.1, 2.3.2 and 2.3.3 we present an analysis of some theoretical aspects of these three distributions. Then, in Section 2.3.4 we compare them using synthetic data on a single spatial point $\mathbf{x}$ first, and then, using real brain data. In the last case, we analyze 1D and 2D scenarios, i.e., the comparison is done on brain slices obtained from transversal sections or coronal sections of the brain, respectively. We analyze and compare the results to better understand their main differences and drive a more informed choice between them.

2.3.1 *Peanut distribution*

The definition of the Peanut distribution relies on the concept of the apparent diffusion coefficient (ADC). This coefficient reflects the average diffusion coefficient in a voxel and is defined by taking the ratio of the mean squared displacement measured along a particular direction to the diffusion time of the experiment. In the case of the classical diffusion described with the use of a directional tensor $\mathbf{D}_W$, the mean-squared displacement in a given direction $\hat{\mathbf{v}}$ belonging to the unit sphere $\mathbb{S}^{d-1}$ is given by

$$\langle \mathbf{x}^2 \rangle = 2t\, \hat{\mathbf{v}}^T \mathbf{D}_W\, \hat{\mathbf{v}}$$

where t is the diffusion time. Thus, the apparent diffusion coefficient in the direction $\hat{\mathbf{v}}$ is defined as

$$ADC_{\hat{\mathbf{v}}} := \frac{\langle \mathbf{x}^2 \rangle}{2t} = \hat{\mathbf{v}}^T \mathbf{D}_W\, \hat{\mathbf{v}}\,.$$

As ADC is an indicator for the anisotropy of the tissue, the most straightforward idea presented in [216] is to define the fiber distribution function proportional to ADC.

More specifically, the fiber distribution function $q(\mathbf{x}, \hat{\mathbf{v}})$, called Peanut distribution, is given by

$$q(\mathbf{x}, \hat{\mathbf{v}}) := \frac{d}{|\mathbb{S}^{d-1}| Tr\left(\mathbf{D}_W(\mathbf{x})\right)} ADC_{\hat{\mathbf{v}}}(\mathbf{x}) \,. \tag{2.9}$$

This way, the cell turning results directly correlated to the apparent diffusion coefficient. Using (2.9) into equation (2.8), it is possible to generate an explicit expression of $\mathbf{D}_T$ in terms of $\mathbf{D}_W$:

$$\mathbf{D}_T(\mathbf{x}) = \frac{s^2}{(d+2)\mu} \left(\mathbb{I}_d + \frac{2}{Tr(\mathbf{D}_W(\mathbf{x}))} \mathbf{D}_W(\mathbf{x}) \right) . \tag{2.10}$$

This general expression in d-dimensions was derived in Lemma 1 of [216]. This expression reveals the direct relationship between the DTI-generated tensor $\mathbf{D}_W$ and the tumor tensor $\mathbf{D}_T$. The latter results in a combination of an isotropic component proportional to the identity matrix $\mathbb{I}_d$, and an anisotropic part proportional to $\mathbf{D}_W$. Theoretically, even in the case of a totally anisotropic background (e.g. the limit case of only one $\mathbf{D}_W$ eigenvalue different from 0), $\mathbf{D}_T$ would always keep an isotropic part, leading to a partial homogenization of the environment. Considering the particular case of $d = 2$ and fixing spatial point $\mathbf{x} \in \mathbb{R}^2$, it is possible to visualize the two tensors $\mathbf{D}_W$ and $\mathbf{D}_T$ as ellipses and immediately grasp the difference between the way they reproduce the anisotropic information. Figure 2.4 illustrates an example of $\mathbf{D}_W$ with bigger diffusion along the y-axis direction than along the x-axis direction and the resulting $\mathbf{D}_T$ in the same point $\mathbf{x}$.

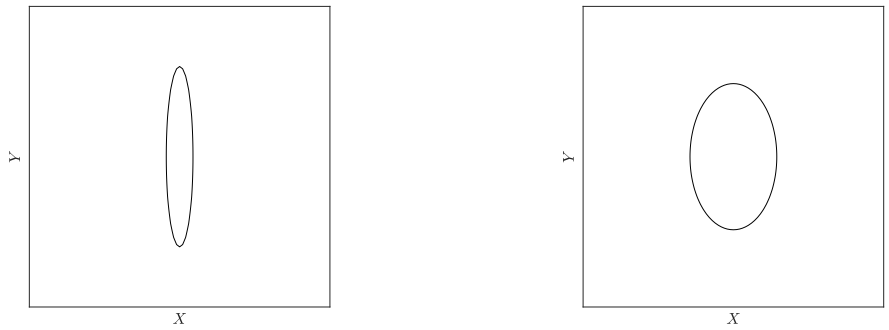

FIGURE 2.4: **Single point comparison for the Peanut distribution.** $\mathbf{D}_W$ (left plot) and $\mathbf{D}_T$ with the Peanut distribution (right plot) in a single data point.

The ellipse shown in the left plot of Figure 2.4 has a more elongated shape than the ellipse in the right plot. The partial homogenization of the anisotropy characterizes the Peanut distribution and can be mathematically shown by looking at the analytical relation between $FA(\mathbf{D}_W)$ and $FA(\mathbf{D}_T)$. In [216], it was proven that $FA(\mathbf{D}_T(\mathbf{x})) \leq FA(\mathbf{D}_W(\mathbf{x}))\ \forall \mathbf{x} \in \mathbb{R}^d$, for the spatial dimensions $d = 2$ and $d = 3$ (Lemma 2). The inequality shows that the anisotropy index of the tumor tensor is always lower than the one calculated from the DTI tensor. Moreover, referring to the linear, planar and spherical indices introduced in (2.5), the same Lemma shows that $\tilde{c}_l = \frac{2}{3} c_l$, $\tilde{c}_p = \frac{2}{3} c_p$, and $\tilde{c}_s = 1 + \frac{2}{3} c_s$, i.e., the tumor ellipsoids are less anisotropic and more spherically shaped ($\tilde{c}_l$, $\tilde{c}_p$, and $\tilde{c}_s$ are the indices of $\mathbf{D}_T$, while c_l, c_p, and c_s are those of $\mathbf{D}_W$). This result suggests that $\mathbf{D}_T$ partially fails in reproducing the brain structure with sufficient details, especially in the case of crossing fiber tracts.

2.3.2 *von Mises-Fisher distribution*

The von Mises-Fisher distribution belongs to a class of distributions used for describing data on the circle or on the sphere from the standpoint of statistical inference [182]. Considering the unit vector $\hat{\mathbf{v}} \in \mathbb{S}^{d-1}$, we denote by $\mathcal{M}_d(\boldsymbol{\mu}, \kappa)$ the $(d-1)$-dimensional von Mises-Fisher distribution with probability density function

$$f(\hat{\mathbf{v}}, \boldsymbol{\mu}, \kappa) = \frac{\kappa^{\frac{d}{2}-1}}{(2\pi)^{\frac{d}{2}} \mathrm{I}_{\frac{d}{2}-1}(\kappa)} \exp\left(\kappa \boldsymbol{\mu}^T \hat{\mathbf{v}}\right) . \tag{2.11}$$

The parameters $\kappa \geq 0$ and $\boldsymbol{\mu} \in \mathbb{S}^{d-1}$ represent the concentration parameter and the vector of mean direction, respectively, with $||\boldsymbol{\mu}|| = 1$, while I_ν is the modified Bessel function of the first kind and of order ν. In the equation, the fraction $\frac{\kappa^{d/2-1}}{(2\pi)^{d/2} \mathrm{I}_{d/2-1}(\kappa)}$ is a normalizing constant. The von Mises-Fisher distribution is symmetrical in $\boldsymbol{\mu}$ and its mean value reads

$$\mathbb{E}[\hat{\mathbf{v}}] = \frac{\mathrm{I}_{\frac{d}{2}}(\kappa)}{\mathrm{I}_{\frac{d}{2}-1}(\kappa)} \boldsymbol{\mu} .$$

This distribution is also rotationally symmetric in $\boldsymbol{\mu}$ and, for $\kappa > 0$, the distribution has mode at $\boldsymbol{\mu}$ and antimode at $-\boldsymbol{\mu}$. Moreover, the larger the value of the concentration parameter, the greater is the clustering around this direction, explaining the reason beyond naming κ concentration parameter. For $\kappa = 0$, $\mathcal{M}_d(\boldsymbol{\mu}, 0)$ reduces to a uniform distribution for all d. In the planar case ($d = 2$), the distribution is simply called *von Mises distribution* $\mathcal{M}_2(\boldsymbol{\mu}, \kappa)$. In this case, the density function f in equation (2.11) reduces to

$$f(\hat{\mathbf{v}}, \boldsymbol{\mu}, \kappa) = \frac{1}{2\pi \mathrm{I}_0(\kappa)} \exp\left(\kappa \cos(\hat{\mathbf{v}} - \boldsymbol{\mu})\right) . \tag{2.12}$$

This distribution is unimodal and symmetric in $\hat{\mathbf{v}} = \boldsymbol{\mu}$; the mode is at $\hat{\mathbf{v}} = \boldsymbol{\mu}$, while the antimode at $\hat{\mathbf{v}} = \boldsymbol{\mu} + \pi$. Once again, the concentration parameter regulates the clustering around the mode. In the spherical case ($d = 3$), the von Mises-Fisher distribution is also called *Fisher distribution* $\mathcal{F}(\boldsymbol{\mu}, \kappa)$ (or $\mathcal{M}_3(\boldsymbol{\mu}, \kappa)$). Starting from equation (2.11), it is possible to simplify the normalizing constant, obtaining the probability density function

$$f(\hat{\mathbf{v}}, \boldsymbol{\mu}, \kappa) = \frac{\kappa}{\sinh \kappa} \exp\left(\kappa \boldsymbol{\mu}^T \hat{\mathbf{v}}\right) . \tag{2.13}$$

The planar distribution was introduced by von Mises in 1918 [195] for the study of the deviation of measured atomic weights from integral values. R. A. Fisher extended it to the spherical case in the context of statistical mechanics to describe the distribution of the energies of weakly interacting dipoles [87]. The extension to $d > 3$ is based on the work of Watson and Williams [292].

The von Mises-Fisher distribution can be used for the definition of the fiber distribution function. Starting from the planar case $d = 2$ in equation (2.12) and considering the expression of the DTI tensor $\mathbf{D}_W$ in (2.2), one can consider the mean direction $\boldsymbol{\mu}$ as referring to the leading eigenvector $\mathbf{v}_1$ of $\mathbf{D}_W$. In fact, it is natural to assume that cell turning is more concentrated in the dominant direction of anisotropy. Since the brain fiber network is naturally non-polarized, i.e., there is no preferential sense of motion along a fiber, it is reasonable to consider the symmetric version of the distribution (2.12), namely the *bimodal von Mises distribution*. Thus, in this case, the function $q(\mathbf{x}, \hat{\mathbf{v}})$ can be defined as

$$q(\mathbf{x}, \hat{\mathbf{v}}) := \frac{1}{4\,\pi\,\mathrm{I}_0(\kappa)} \left(e^{\kappa\, \mathbf{v}_1 \cdot \hat{\mathbf{v}}} + e^{-\kappa\, \mathbf{v}_1 \cdot \hat{\mathbf{v}}}\right) . \tag{2.14}$$

With this definition, the fiber distribution function satisfies $q(\mathbf{x}, \hat{\mathbf{v}}) = q(\mathbf{x}, -\hat{\mathbf{v}})\ \forall \mathbf{x} \in \mathbb{R}^2$ and $\forall \hat{\mathbf{v}} \in \mathbb{S}^1$, and it has two maxima in the directions $\mathbf{v}_1$ and $-\mathbf{v}_1$, respectively. The concentration parameter κ, related to the level of concentration around the dominant direction, can be chosen to be proportional to $FA(\mathbf{D}_W)$. Intuitively, cells should become more aligned along the direction of greater anisotropy of the environment. Therefore, one can define the function $k(\mathbf{x}) := \kappa\, FA(\mathbf{D}_W(\mathbf{x}))$, where the constant factor κ describes the sensitivity of the cells to the directional information given by the environment, and use it as the concentration function in (2.14). Plugging (2.14) into equation (2.8) with these choices of the parameters, we obtain

$$\mathbf{D}_T(\mathbf{x}) = \frac{s^2}{\mu}\left(\frac{1}{2}\left(1 - \frac{\mathrm{I}_2(k(\mathbf{x}))}{\mathrm{I}_0(k(\mathbf{x}))}\right)\mathbb{I}_2 + \frac{\mathrm{I}_2(k(\mathbf{x})}{\mathrm{I}_0(k\mathbf{x})}\mathbf{v}_1\mathbf{v}_1^T\right). \tag{2.15}$$

The function $k(\mathbf{x})$ allows to control the relative weights of the isotropic and anisotropic components of the tensor. In fact, in the isotropic case ($FA(\mathbf{D}_W) = 0$), the von Mises distribution reduces to a uniform distribution. The same happens for cells that are not responding to the environmental anisotropy ($\kappa = 0$). For $FA(\mathbf{D}_W) = 1$, $k(\mathbf{x}) = \kappa$ and $\mathbf{D}_T(\mathbf{x})$ preserves only the anisotropic component when $\kappa \to \infty$,, i.e.,

$$\mathbf{D}_T(\mathbf{x}) = \frac{s^2}{\mu}\left(\frac{\mathrm{I}_2(k(\mathbf{x}))}{\mathrm{I}_0(k(\mathbf{x}))}\mathbf{v}_1\mathbf{v}_1^T\right)$$

since $\frac{\mathrm{I}_2(\kappa)}{\mathrm{I}_0(\kappa)} \to 1$ for $\kappa \to \infty$. Introducing a further parameter $\delta \in [0,1]$ to describe the inherent degree of randomized turning of the cell, it is possible to have an additional partial control on the size of the isotropic component in $\mathbf{D}_T$. In particular, the parameter δ represents the weight of the uniform distribution included in the following modified expression of $q(\mathbf{x}, \hat{\mathbf{v}})$:

$$q(\mathbf{x}, \hat{\mathbf{v}}) = \frac{\delta}{2\pi} + (1-\delta)\frac{1}{4\,\pi\,\mathrm{I}_0(k(\mathbf{x}))}\left(e^{k(\mathbf{x})\mathbf{v}_1\cdot\hat{\mathbf{v}}} + e^{-k(\mathbf{x})\mathbf{v}_1\cdot\hat{\mathbf{v}}}\right). \tag{2.16}$$

Plugging (2.16) into equation (2.8) gives

$$\mathbf{D}_T(\mathbf{x}) = \frac{s^2}{\mu}\left(\frac{1}{2}\left(\delta + (1-\delta)\left(1 - \frac{\mathrm{I}_2(k(\mathbf{x}))}{\mathrm{I}_0(k(\mathbf{x}))}\right)\right)\mathbb{I}_2 + (1-\delta)\frac{\mathrm{I}_2(k(\mathbf{x}))}{\mathrm{I}_0(k(\mathbf{x}))}\mathbf{v}_1\mathbf{v}_1^T\right).$$

As for the concentration function $k(\mathbf{x})$, the parameter δ influences the contribution of the isotropic and anisotropic components in $\mathbf{D}_T$. In particular, if $\delta = 1$ (or $k(\mathbf{x}) = 0$), $\mathbf{D}_T$ simply describes an isotropic environment

$$\mathbf{D}_T(\mathbf{x}) = \frac{s^2}{2\mu}\mathbb{I}_2\,.$$

On the contrary, when $\delta \to 0$, it reduces to (2.15). Similarly to what we did for the Peanut distribution, we consider anisotropic data at one particular spatial point $\mathbf{x} \in \mathbb{R}^2$, and we visualize $\mathbf{D}_T$ as an ellipse, analyzing how the variation of the parameters κ and δ in (2.16) affects size and shape of it, also with respect to the ellipse representing the DTI-tensor $\mathbf{D}_W$. The results are shown in Figures 2.5. As highlighted above, $\mathbf{D}_T$ has a higher degree of anisotropy for increasing value of κ or for decreasing value of δ. Analytically, if we compute directly the tensor $\mathbf{D}_T$ in the planar case, it is possible to obtain an explicit expression of its eigenvalues $\lambda_i = \frac{s^2}{2\mu}(1 + (-1)^{i+1}\gamma)$, for $i = 1, 2$,

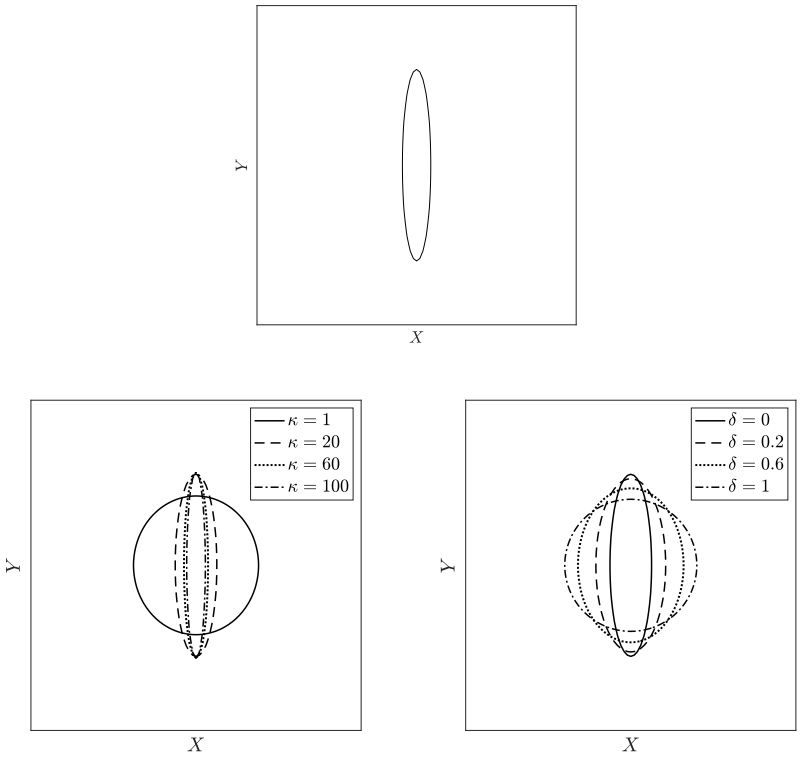

FIGURE 2.5: **Single point comparison for the von Mises-Fisher distribution.** $\mathbf{D}_W$ in a single data point (top row). $\mathbf{D}_T(\mathbf{x})$ in a single data point (bottom row). $\mathbf{D}_T(\mathbf{x})$ is calculated for different values of κ (left plot) and δ (right plot).

where $\gamma = (1-\delta)\frac{\mathrm{I}_2(k)}{\mathrm{I}_0(k)}$, and, therefore, of the FA index

$$FA(\mathbf{D}_T(\mathbf{x})) = \frac{2(1-\delta)\frac{\mathrm{I}_2(k(\mathbf{x}))}{\mathrm{I}_0(k(\mathbf{x}))}}{\sqrt{2+2(1-\delta)^2\left(\frac{\mathrm{I}_2(k(\mathbf{x}))}{\mathrm{I}_0(k(\mathbf{x}))}\right)^2}}.$$

Unlike in the case of Peanut distribution, there is a larger possibility of control on the anisotropy of the tumor tensor. In fact, for $\delta = 1$ or $k(\mathbf{x}) = 0$, $FA(\mathbf{D}_T) \to 0$, while for $\delta \to 0$ and $\kappa \to \infty$, $FA(\mathbf{D}_T) \to 1$. On the one side, this means that $\mathbf{D}_T$ can be calibrated in order to better reproduce the DTI data encoded in $\mathbf{D}_W$, but on the other side this makes $\mathbf{D}_T$ strongly dependent on κ (and eventually on δ), whose identification from the data is not totally clear. Although it seems reasonable to choose these two parameters by fitting the original data, their biological estimation remains uncertain. In the study presented in Section 2.3.4 we use a least square optimization to deduce their estimation from the fitting of $FA(\mathbf{D}_T)$ with $FA(\mathbf{D}_W)$ data.

The bimodal version of the VMF distribution in the spherical case $d = 3$ can be derived from equation (2.13), assuming the leading eigenvector $\mathbf{v}_1$ as mean direction. The fiber distribution in this case can be defined as

$$q(\mathbf{x}, \hat{\mathbf{v}}) := \frac{\kappa}{4\pi \sinh \kappa} \left(\cosh(\kappa)\mathbf{v}_1 \cdot \hat{\mathbf{v}}\right).$$

This equation, together with (2.8), provides

$$\mathbf{D}_T(\mathbf{x}) = \frac{s^2}{3\mu}\left[\left(\frac{\coth(\kappa)}{\kappa} - \frac{1}{\kappa^2}\right)\mathbb{I}_3 + \left(1 - \frac{3\coth(\kappa)}{\kappa} + \frac{3}{\kappa^2}\right)\mathbf{v}_1\mathbf{v}_1^T\right].$$

The same modifications previously discussed for the two-dimensional case concerning the introduction of the concentration function $k(\mathbf{x})$ and the parameter δ reflecting the predominance of random over oriented turning, can be considered in this spherical case. With respect to the changes in κ and δ, $\mathbf{D}_T$ in the spherical case behaves similar to the planar case.

2.3.3 *Orientation distribution function*

We recall that the probability density function (PDF) of diffusion $\mathcal{P}$ introduced in equation (2.3) gives the displacement probability for a molecule in $\mathbf{x}_0$ to reach the point $\mathbf{x}$ located inside a fiber bundle described by the generic tensor $\mathbf{D}$ in the time of the experiment t. Here, the ODF represents the marginal probability of movement in a given direction and it is used for mapping the orientation architecture of the tissue [3]. Assuming that the PDF is a symmetric function that does not depend on time and considering the standard spherical coordinates system, the probability of movement in a direction $\hat{\mathbf{v}}$ is given by

$$ODF(\hat{\mathbf{v}}) = \int_0^\infty \mathcal{P}(r\hat{\mathbf{v}})r^2 dr\,. \tag{2.17}$$

Precisely, being $\hat{\mathbf{v}}$ the direction of the vector $\mathbf{x} - \mathbf{x}_0$ and r is magnitude, the ODF is computed by integrating the displacement probabilities over all possible magnitude r, keeping the direction $\hat{\mathbf{v}}$ constant. The application of this distribution to fiber orientation analysis originates from experimental results that show the correspondence between the peaks of the ODF and the principal directions of the underlying fibers [221]. These studies also show a nonlinear, monotonically increasing, relationship between $FA(\mathbf{D}_W)$ and the mean principal curvature of the ODF at the principal direction of the fibers [29]. Therefore, considering the probability density function given in (2.3) with the above assumptions, and integrating it like in (2.17), the resulting orientation distribution function reads

$$ODF(\mathbf{x}, \hat{\mathbf{v}}) = \frac{1}{4\,\pi\,|\mathbf{D}(\mathbf{x})|^{\frac{1}{2}}(\hat{\mathbf{v}}^T\mathbf{D}(\mathbf{x})^{-1}\hat{\mathbf{v}})^{\frac{3}{2}}}\,. \tag{2.18}$$

Thus, setting the fiber distribution function

$$q(\mathbf{x}, \hat{\mathbf{v}}) := ODF(\mathbf{x}, \hat{\mathbf{v}})$$

with $\mathbf{D}(\mathbf{x}) = \mathbf{D}_W(\mathbf{x})$, we obtain the expression for the fiber distribution function applied to the study of DTI data. Unlike the previous cases, we do not calculate analytically the expression of $\mathbf{D}_T$. Instead, we substitute in equation (2.8) the fiber distribution function defined by the ODF in (2.18) and we obtain $\mathbf{D}_T$ by numerically approximating the integral term. Details about the applied quadrature schemes are provided in Appendix B. Following the approach used in Sections 2.3.1 and 2.3.2, we provide an visual example of the comparison between $\mathbf{D}_W$ and $\mathbf{D}_T$ in one spatial point $\mathbf{x}$ in Figure 2.6. The two ellipses have reasonably similar shape and proportions, showing good preservation of the anisotropic characteristics of the underlying tissue.

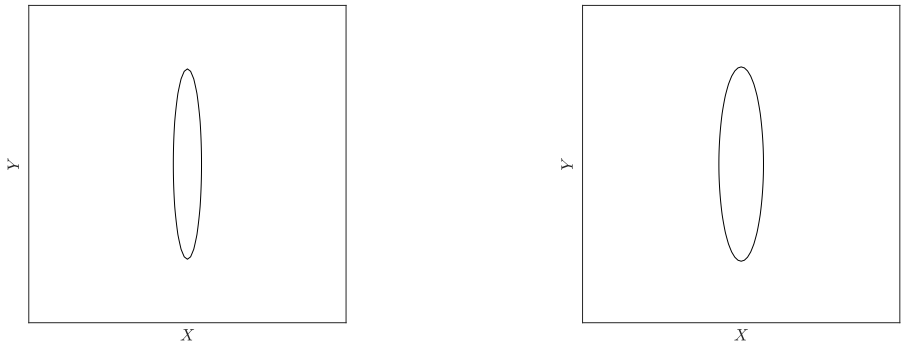

FIGURE 2.6: **Single point comparison for the ODF.** $\mathbf{D}_W$ (left plot) and $\mathbf{D}_T$ (right plot) with ODF in a single data point.

2.3.4 *Comparison of the fiber distribution functions*

For the sake of simplicity in visualization, we first consider the case of a single spatial point $\mathbf{x} \in \mathbb{R}^2$. We visualize and compare the ellipses related to the three distribution function $q(\mathbf{x}, \hat{\mathbf{v}})$ from the previous sections to the ellipsis related to $\mathbf{D}_W$. The overall comparison is shown in Figure 2.7.

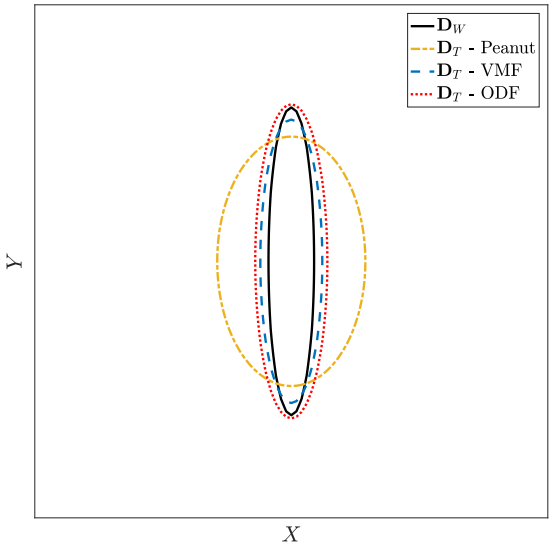

FIGURE 2.7: **Single-point comparison.** $\mathbf{D}_W$ and $\mathbf{D}_T$ at the point $\mathbf{x}$. For the VMF distribution we fix $\delta = 0.05$ and $\kappa = 46$.

It is evident that with the Peanut distribution (2.9) the anisotropy of $\mathbf{D}_W$ is in large part lost in $\mathbf{D}_T$, due to its strong isotropic component (see equation (2.10)). On the other hand, the tensor $\mathbf{D}_T$ obtained with the VMF distribution (2.16) shows a degree of anisotropy more similar to that of the original $\mathbf{D}_W$. The similarity also depends on the particular choice of the two parameters, κ and δ. Precisely, δ has been set at $\delta = 0.05$ (according to [216]), allowing a small effect of the randomized turning; instead, for κ we consider a least square optimization to fit $FA(\mathbf{D}_T)$ to the data from $FA(\mathbf{D}_W)$. In particular, the optimization procedure provides the value $\kappa = 46$ for the single-point case (Figure 2.7), and the value $\kappa = 5.775$ for the coronal and transversal section

(Figures 2.8 and 2.10). In both cases, the values minimize the norm of the residual

$$\|FA(\mathbf{D}_T) - FA(\mathbf{D}_W)\|_2 = \sqrt{\sum_{i=1}^{N} (FA(\mathbf{D}_T)_i - FA(\mathbf{D}_W)_i)^2},$$

with N being the number of data points. Finally, with the ODF (2.18), the resulting $\mathbf{D}_T$ has similar shape and proportions to the original $\mathbf{D}_W$, with more pronounced preservation of the anisotropic feature compared to the Peanut distribution case, and also independently from any further parameter selection. This choice of fiber distribution function can be considered beneficial in lack of real patient data that can be used for accurate parameter estimations.

As it is sufficiently representative for the proposed analysis, we consider real DTI data on a 2D slice obtained from a horizontal section of an entire brain DTI dataset and we compare the effect of the three fiber distribution functions computing the FA index. The results are shown in Figure 2.8.

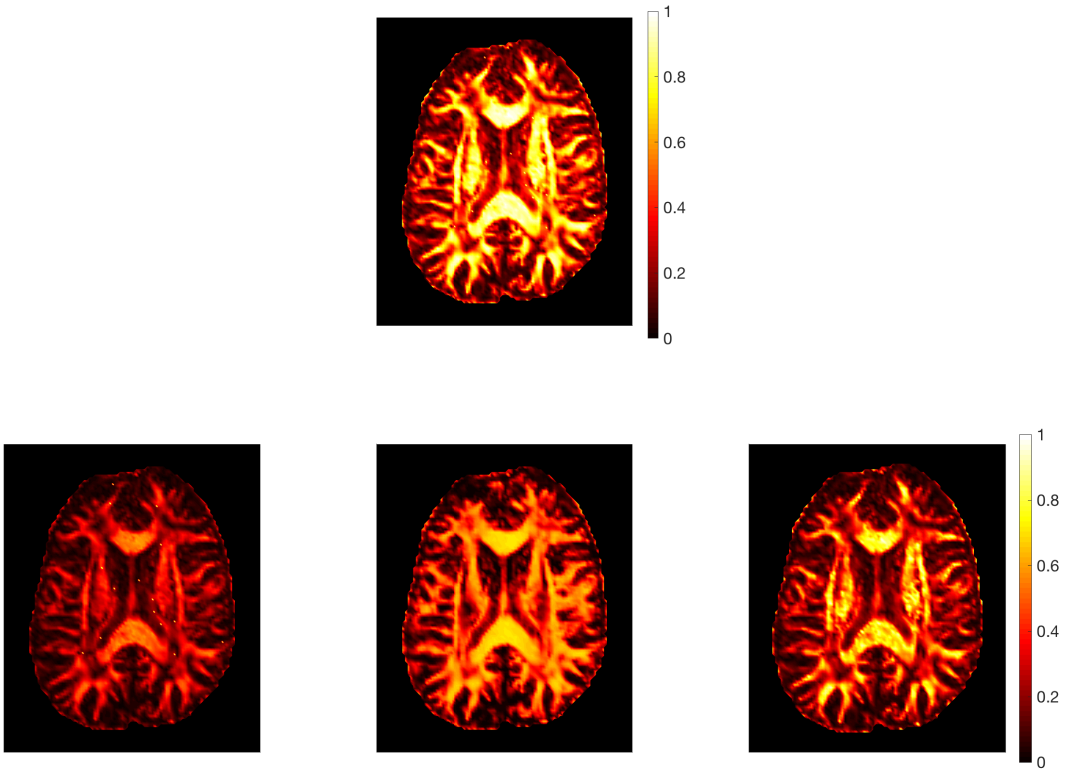

FIGURE 2.8: **FA comparison on a real brain slice.** $FA(\mathbf{D}_W)$ (top row). From left to right (bottom row): $FA(\mathbf{D}_T)$ with Peanut distribution, VMF distribution with $\delta = 0.05$ and $\kappa = 5.7753$, and ODF.

This example stresses again that the Peanut distribution identifies quite accurately the locations where the fibers are aligned or not, but it also provides some issues related to the degree of anisotropy emerge. In fact, the resulting tensor $\mathbf{D}_T$ has a generally lower degree of anisotropy than the original $\mathbf{D}_W$, with values for the fractional anisotropy almost halved in the areas of greater alignment. For the VMF distribution, provided that a suitable tuning of its parameters is performed, the results show a good preservation of FA. In particular, in Figure 2.9 we can observe how changing the values of κ and δ in the VMF distribution affects $FA(\mathbf{D}_T)$ on this 2D brain slice. Finally, although the use

of the ODF provides a general under-estimation of the degree of anisotropy, this distribution improves the results compared to the Peanut distribution, and it preserves with sufficient accuracy the description of the location of aligned and non-aligned fibers. A

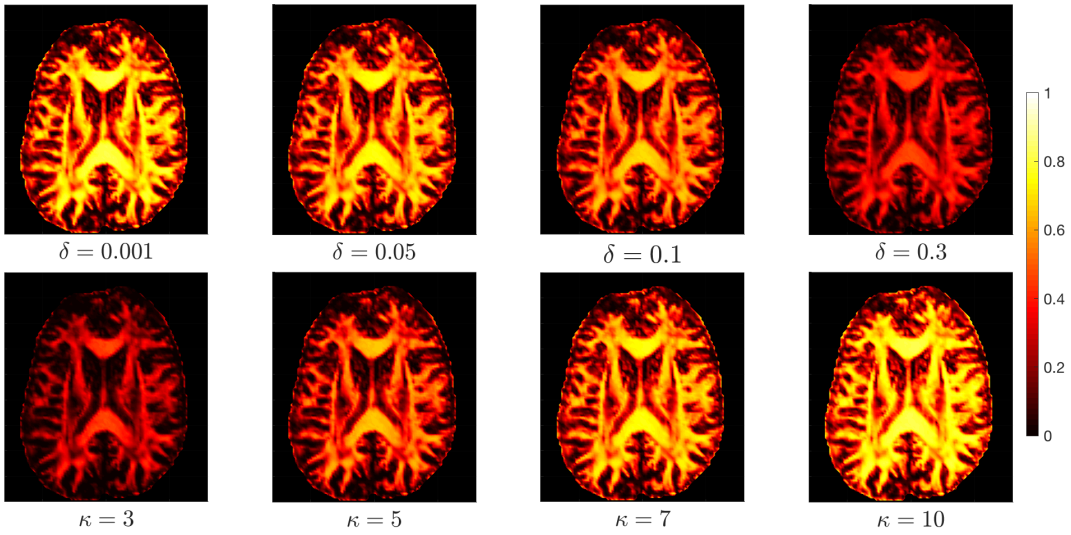

FIGURE 2.9: **Effect on FA of changing κ and δ on a real brain slice.** $FA(\mathbf{D}_T)$ built with the VMF on a brain slice for different values of δ (top row, $\kappa = 7$) and κ (bottom row, $\delta = 0.05$).

closer look at the differences between the three distribution is done by considering different coronal sections of this 2D slice and looking at the variation of the fractional anisotropy along them. Figure 2.10 illustrates the output for a representative coronal section.

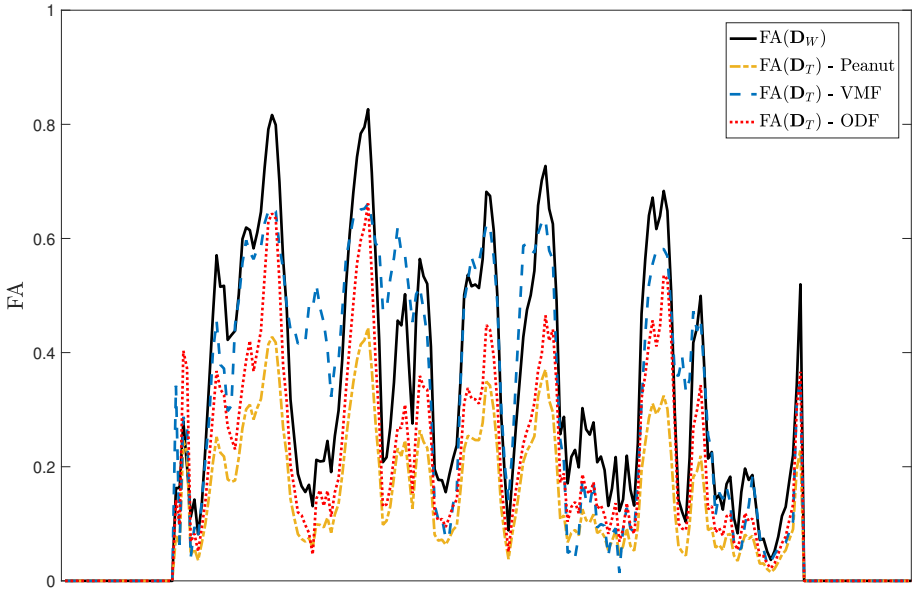

FIGURE 2.10: **FA comparison on a coronal plane.** Comparison between $FA(\mathbf{D}_W)$ and $FA(\mathbf{D}_T)$ along a coronal plane of the 2D brain slice with the Peanut distribution, the VMF distribution ($\delta = 0.05$ and $\kappa = 5.7753$), and the ODF.

Peanut distribution and ODF have an almost identical trend. As expected, the Peanut distribution almost halves the degree of anisotropy with respect to the DTI data, while the ODF preserves the information significantly better. VMF distribution, on the other hand, often provides an under-estimation of the fractional anisotropy at local maxima of $FA(\mathbf{D}_W)$ and an over-estimation of $FA(\mathbf{D}_W)$ at local minima. Changing the considered coronal section, the qualitative results do not change, and the highlighted differences in the fractional anisotropy remain essentially the same. These differences can be more clearly observed from a global perspective considering the relative difference $R(\mathbf{D})$ between the $FA(\mathbf{D}_W)$ and $FA(\mathbf{D}_T)$

$$R(\mathbf{D}) := \frac{FA(\mathbf{D}_W) - FA(\mathbf{D}_T)}{FA(\mathbf{D}_W)} . \tag{2.19}$$

Notice that in equation (2.19) we are not considering the absolute value of the numerator in order to visualize situations of both under-estimation and over-estimation of the fractional anisotropy. The results of this analysis are shown in Figure 2.11.

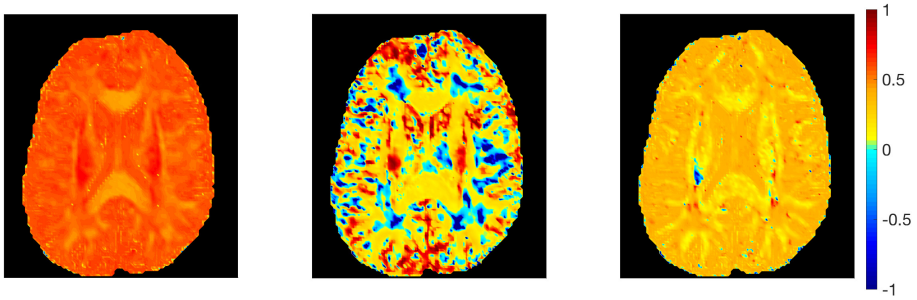

FIGURE 2.11: **$\mathbf{R}(\mathbf{D})$ comparison.** From left to right, $R(\mathbf{D})$ for Peanut distribution, VMF distribution ($\delta = 0.05$ and $\kappa = 5.7753$), and ODF.

In line with the results of Figure 2.10, we observe that the VMF distribution is the only one with a mixed trend. The only exceptions are given by some isolated blue areas in the ODF plot, possibly related to errors in the DTI measurements and/or to oscillations in the calculations. $R(\mathbf{D})$ for this distribution indicates that $FA(\mathbf{D}_T)$ pass from areas of over-estimation of the original anisotropy (colors from green to blue) to areas of under-estimation of the original FA (colors from green to red). An additional piece of information emerging from the comparison between the top row of Figures 2.8 and 2.11 is that in the highly anisotropic areas, where $FA(\mathbf{D}_W)$ is bigger (the brighter regions in Figure 2.8), the relative error made with any of the three distributions is generally smaller with respect to more isotropic regions. Moreover, in these highly anisotropic areas, the error is reduced as we pass from Peanut distribution to ODF and, even more, when we consider the VMF distribution.

Some of the simulations shown above involve very heavy computation. Therefore, it is worth discussing the ***computational cost*** of each of the three distributions. The cost for calculating of the fiber distribution functions and the resulting tensor $\mathbf{D}_T$ is almost identical for the Peanut and the VMF distribution. However, the construction of $\mathbf{D}_T$ via the Peanut distribution does not require any matrix multiplication, while one matrix product is needed for the calculation of $\mathbf{D}_T$ in each voxel with the VMF distribution. The ODF, on the other hand, requires more calculations and, therefore,

has a higher computational cost. For each voxel, it requires the numerical approximation of a spherical integral, whose cost depends on the chosen numerical method. In all cases, independently from the particular approximation used, the evaluation of the integrand function involves several matrix products and matrix inversions. If, for instance, the Gauss-Legendre quadrature formula for computing the integral is chosen, the computational cost for the calculation of $\mathbf{D}_T$ in each voxel of the 3D mesh grid is $\mathcal{O}(m^2)$, where m indicates the number of points of the quadrature formula.

2.4 *Summary*

Brain structures and mainly white matter tracts are critical factors involved in the highly anisotropic migratory dynamics of glioma cells. These structures enable the glioma cells to extensively invade the brain tissue. On the one side, this causes the macroscopic heterogeneous patterns of tumor mass observed in the images. On the other, it determines the formation of a not well-delineated outer tumor borders, i.e., regions of low glioma cell density outside the main tumor body that are not detectable with standard imaging techniques. These problems in detecting the actual tumor border often translate into negative effects on the outcome of clinical treatments. Therefore, it is essential to account for the characteristics of brain fibers in the development of reliable models for glioma progression in order to improve treatment strategies.

In this chapter, we discussed the details of the DTI technique for medical imaging, which allow an *in-vivo* identification of the features related to the major white matter pathways and to the cell diffusivity along them. We described the tensor representation of the DTI data and different scalar maps (FA, RA, and VR) that are used for the quantification of the DTI information. Many methods have been defined for both macroscopic and the kinetic-based frameworks to infer the anisotropic tumor tensor from the information obtained with the DTI technique. Among these approaches, we discussed the use of a distribution function to characterize the brain network. The advantage of this approach is that different $\mathbf{D}_T$ can be derived from the same expression simply changing the fiber distribution. We analyzed the main peculiarity of this function and carried out a comparison between the most common fiber distribution functions, namely the Peanut, the VMF, and the ODF distribution. We highlighted how the DTI information is translated by each of the distribution functions into the tensor $\mathbf{D}_T(\mathbf{x})$ characterizing tumor orientation and diffusion, and which are their main differences. This study represents the basis for the forthcoming models based on the kinetic framework that will be discussed in Chapters 3-5.

Part II

Kinetic-based models

3 *Tissue influence on glioma progression*

Glioma progression is a highly complex process that involves several biological aspects already introduced and discussed in Section 1.2. In this dissertation, we approach this problem introducing some of such features step by step. We define a first model focusing only on the evolution of glioma cells with the aim of investigating the impact of the brain fibers in the tumor overall dynamics. Cell interactions with the ECM are one of the mechanisms supporting active cell movement along the pre-existing brain structures. In particular, we consider the family of integrin receptors as only mediators of this process [61, 64, 127], and we rely on DTI data to identify the aligned structures along which cell migration is more likely to occur since this technique provides information about the microscopic tissue architecture [281].

The model presented in this chapter is based on a multiscale modeling approach for glioma cell migration and proliferation, relying on kinetic equations. The internal variable characterizing the tumor population is used to describe the binding process between cells and brain fibers, while the mesoscopic equation, modeling cell turning and proliferation in response to the underlying tissue structure, carries the microscopic information up to the macroscopic level. Moreover, we include in the model an integrated therapeutic treatment, a combination of radiation and chemotherapy based on integrins inhibitors. We incorporate this treatment at both microscopic and mesoscopic level. The macroscopic setting is derived via a parabolic limit and the Hilbert expansion method applied to the moment equations. More precisely, in Section 3.1 we elaborate on the transport model, its basic concepts, and its macroscopic limits, while in Section 3.2 we describe the model setting at the different scales. Finally, Section 3.3 is dedicated to the numerical results for different scenarios.

Some of the results presented in Chapter 2 and the content of this chapter have been published in the paper by Conte, Gerardo-Giorda, and Groppi [54].

3.1 *Preliminaries*

The multiscale framework described in this section is proposed for modeling biological systems using the characteristic methods of the kinetic theory [222]. This framework is essentially based on the definition of the microscopic state of the cells, the distribution function over that state, and the derivation of an evolution equation for this distribution. Cell migration is modeled by using kinetic transport equations featuring an integral operator for the characterization of velocity changes and additional terms for modeling proliferative/destructive dynamics. This framework originates from the so-called kinetic theory of active particles (KTAP) largely described in [19]. It was first applied in [8, 211] to describe the movement of organisms under the influence of a chemotactic signal and it was further extended in [116, 216] to model mesenchymal tumor invasion.

Recalling notation (1.1) introduced in Section 1.2.1, the distribution of tumor cells is described at the mesoscopic scale by the function $\rho(t, \mathbf{x}, \mathbf{v}, \mathbf{y})$, which is parametrized by the time $t \geq 0$, the position $\mathbf{x} \in \Omega \subseteq \mathbb{R}^d$, the microscopic velocity $\mathbf{v} \in \mathbf{V} \subseteq \mathbb{R}^d$, and the internal state, or internal activity, $\mathbf{y} \in \mathbf{Y} \subset \mathbb{R}^p$. The mesoscopic model consists of the following transport equation for the cell distribution:

$$\begin{aligned} &\frac{\partial \rho}{\partial t}(t, \mathbf{x}, \mathbf{v}, \mathbf{y}) + \mathbf{v} \cdot \nabla \rho(t, \mathbf{x}, \mathbf{v}, \mathbf{y}) + \nabla_{\mathbf{y}} \cdot (G(t, \mathbf{x}, \mathbf{v}, \mathbf{y}) \rho(t, \mathbf{x}, \mathbf{v}, \mathbf{y})) \\ &= \mathcal{L}[\rho](t, \mathbf{x}, \mathbf{v}, \mathbf{y}) + \mathcal{I}[\rho](t, \mathbf{x}, \mathbf{v}, \mathbf{y}) \,. \end{aligned} \tag{3.1}$$

From now on, with the notation ∇ we indicate the spatial gradient, unless otherwise indicated. The term $\mathcal{I}[\rho] := \mathcal{C}[\rho] + \mathcal{D}[\rho]$ include both to conservative ($\mathcal{C}[\rho]$) and proliferative or destructive ($\mathcal{D}[\rho]$) interactions. The dynamics of the internal state variable $\mathbf{y}$ are described by the ODE introduced in Section 1.2.1, namely

$$\frac{d\mathbf{y}}{dt} = G(t, \mathbf{x}, \mathbf{v}, \mathbf{y}) \,.$$

These dynamics determine the second transport term on the left hand side of the transport equation. Moreover, the right hand side of (3.1) is characterized by the presence of the turning operator $\mathcal{L}[\rho](t, \mathbf{x}, \mathbf{v}, \mathbf{y})$ describing the velocity changes. These velocity changes can originate from the classical run and tumble behaviors or result from a contact guidance phenomena, as introduced in (2.7). The general form of the turning operator implementing cell velocity changes as velocity jump process reads

$$\mathcal{L}[\rho](t, \mathbf{x}, \mathbf{v}, \mathbf{y}) = \mathbf{G}[\rho](t, \mathbf{x}, \mathbf{v}, \mathbf{y}) - \mathbf{L}[\rho](t, \mathbf{x}, \mathbf{v}, \mathbf{y}) \,, \tag{3.2}$$

where the gain term $\mathbf{G}$ and the loss term $\mathbf{L}$ are given by

$$\mathbf{G}[\rho](t, \mathbf{x}, \mathbf{v}, \mathbf{y}) = \int_{\mathbf{V}} \mu(\mathbf{x}, \mathbf{v}', \mathbf{y}) T[S](\mathbf{x}, \mathbf{v} | \mathbf{v}') \rho(t, \mathbf{x}, \mathbf{v}', \mathbf{y}) d\mathbf{v}' \tag{3.3}$$

$$\mathbf{L}[\rho](t, \mathbf{x}, \mathbf{v}, \mathbf{y}) = \int_{\mathbf{V}} \mu(\mathbf{x}, \mathbf{v}, \mathbf{y}) T[S](\mathbf{x}, \mathbf{v}'' | \mathbf{v}) \rho(t, \mathbf{x}, \mathbf{v}, \mathbf{y}) d\mathbf{v}'' \,, \tag{3.4}$$

respectively. Here, $\mathbf{v}'$ is the pre-turning velocity of the gain term and $\mathbf{v}''$ is the post-turning velocity of the loss term, while μ is a turning frequency that can depend on position, velocity, or internal state. $T[S](\mathbf{x}, \mathbf{v} | \mathbf{v}')$ is the turning kernel describing the probability for a cell in $\mathbf{x}$ to choose the velocity $\mathbf{v}$ after a reorientation biased by an eventual external field S and given the pre-turning velocity $\mathbf{v}'$. This kernel is a conditional probability satisfying

$$\int_{\mathbf{V}} T[S](\mathbf{x}, \mathbf{v} | \mathbf{v}') d\mathbf{v} = 1 \,, \quad \forall \mathbf{x} \in \Omega \,, \quad \forall \mathbf{v}' \in \mathbf{V} \tag{3.5}$$

and

$$T[S](\mathbf{x}, \mathbf{v} | \mathbf{v}') \geq 0 \quad \forall \mathbf{x} \in \Omega \,, \quad \forall \mathbf{v}, \mathbf{v}' \in \mathbf{V} \,.$$

Therefore, depending on the choice of the turning kernel, several environmental factors governing velocity changes and, consequently, cell migration can be described. In this chapter and in the forthcoming ones, we present the turning kernels describing either contact guidance or tactic processes. Considering the transport equation (3.1) and taking into account the dependency of the distribution function ρ on both microscopic velocity and internal state variable, the zero-th and first order moments of ρ

with respect to $\mathbf{y}$ are defined as

$$m(t,\mathbf{x},\mathbf{v}) := \int_{\mathbf{Y}} \rho(t,\mathbf{x},\mathbf{v},\mathbf{y})d\mathbf{y}$$

$$m^{y}(t,\mathbf{x},\mathbf{v}) := \int_{\mathbf{Y}} \mathbf{y}\rho(t,\mathbf{x},\mathbf{v},\mathbf{y})d\mathbf{y}\,.$$

The equations for m and m^{y} can be calculated from (3.1) by integration with respect to the internal variable $\mathbf{y}$. These equations form the basis for the derivation of the macroscopic setting with the cell density

$$n(t,\mathbf{x}) := \int_{\mathbf{V}}\int_{\mathbf{Y}} \rho(t,\mathbf{x},\mathbf{v},\mathbf{y})d\mathbf{y}d\mathbf{v}\,.$$

In particular, to establish the connection between the mesoscopic and the macroscopic level and derive the equations for the latter, several scaling arguments, based on biological assumptions and depending on the problem at hand, for the operators $\mathcal{L}$ and $\mathcal{I}$ are considered. These scaling arguments are used together with asymptotic methods. These methods highlight whether the driving macroscopic phenomenon is related to diffusion or convection processes.

As introduced in Section 1.2.1, the classical and commonly used asymptotic methods for multicellular system rely on parabolic (also called *diffusive*) or hyperbolic (also called *hydrodynamic*) limits, resulting from a proper non-dimensionalization of the model equations. Diffusive and hydrodynamic limits for transport equations with velocity jump processes have been widely analyzed (e.g. see [18, 43, 213] and reference therein). Formally, a small parameter $\varepsilon \ll 1$ is introduced to rescale the spatial variable as

$$\boldsymbol{\xi} = \varepsilon\mathbf{x}\,. \tag{3.6}$$

According to the other characteristic quantities of the system at hand, the macroscopic time scale τ is defined as

$$\tau = \varepsilon^2 t, \tag{3.7}$$

in the case of the parabolic scaling representing a diffusion dominated phenomenon, or

$$\tau = \varepsilon t, \tag{3.8}$$

in the case of the hyperbolic scaling representing a drift driven phenomenon. After the spatial scaling (3.6) of the moments equation, we have that the transition probability can be expanded as

$$T[S](\boldsymbol{\xi},\mathbf{v}|\mathbf{v}') = T_0[S](\boldsymbol{\xi},\mathbf{v}|\mathbf{v}') + \varepsilon T_1(\boldsymbol{\xi},\mathbf{v}|\mathbf{v}') + \mathcal{O}(\varepsilon^2)\,. \tag{3.9}$$

In both limits, the distribution function ρ (and its moments) is expanded in the form

$$\rho = \rho_0 + \varepsilon\rho_1 + \mathcal{O}(\varepsilon^2)\,. \tag{3.10}$$

The functional solvability condition that is necessary for performing a diffusive limit (i.e., for choosing (3.7)) is that

$$\int_{\mathbf{V}} T_0[S](\boldsymbol{\xi},\mathbf{v}|\mathbf{v}')\mathbf{v}\,d\mathbf{v} = 0\,. \tag{3.11}$$

This equation mean that the leading order of the drift vanishes, coherently with the diffusive time because the phenomenon macroscopically is diffusion-driven. If equation (3.11) does not hold, the hyperbolic scaling (3.8) is required, which gives a macroscopic advection equation modeling a drift driven phenomenon. In both cases, the macroscopic settings are derived by plugging the expansions of the different quantities in the moments equations, and comparing the equal orders of ε.

We describe, for the model introduced in Section 3.2 and for those of Chapters 4-6, the expressions of the operators involved in the kinetic equations and the modeling assumption for performing the macroscopic limits.

3.2 *Modeling setting*

The first modeling setting relying on the introduced kinetic framework is aimed at describing the growth and spread of glioma cells in the brain with a major focus on the influence of the underlying nervous fibers on the tumor evolution. In particular, we are interested in how the information about the fiber structure, obtained from the clinical data, is translated and encoded in the model to achieve a realistic description of glioma cell spread and migration. We connect the extracellular environment to the processes of cell proliferation and migration, describing the role of some membrane receptors in glioma evolution, and considering the tumor response to a possible combined treatment, affecting the tumor cell at both microscopic and macroscopic level.

Our setting is built on the framework proposed in [74, 126] and represents an extension of them. To briefly introduce our approach, we consider the three different levels to formulate the multiscale setting.

- At the microscopic scale, accounting for processes taking place at the subcellular level, we describe the dynamics of receptors on the tumor cell membrane, allowing cells to bind with the ECM fibers, by an ODE for their mass action kinetics. This approach involving cell receptor dynamics was first proposed in [136], where a multiscale model for tumor cell migration accounting for the receptor-mediated cell movement is described. This work was followed by several others in line with the above-mentioned KTAP and first directly applied to the study of glioma evolution in [77]. At this scale, the novelty with respect to [74, 77] is the addition of therapeutic effects on the receptor dynamics. In particular, following the idea in [126], we include at this level a specific chemotherapy treatment, based on integrins inhibitors, aimed at reducing the receptor capability to mediate the cell-ECM binding process, thus affecting cell migration.

- At the mesoscopic scale, the individual cell behavior is described using a kinetic transport equation, considering cell interactions with the surrounding tissue as mediators of the proliferation process, as well as a loss term, accounting for both natural cell death and the cell death due to the radiation treatment. In fact, integrin inhibitors are combined with radiotherapy, but, if the former is aimed only at reducing cell motility, the latter is directly aimed at cell killing.

- The macroscopic level is derived via parabolic scaling of the mesoscopic equation, yielding an evolution equation for the macroscopic cell density. At this stage, tumor progression is governed by anisotropic diffusion along the directions characterized by the fiber orientation, haptotaxis, i.e., migration in the direction of the gradient of the extracellular matrix, and tissue-mediated proliferation together with cell death.

In the following sections, we describe in detail the model derivation at the different scales.

3.2.1 *Subcellular level*

Here, we focus on the microscopic dynamics of cell surface receptors, belonging to the family of integrins. To understand the influence of integrin dynamics on the macroscopic movement, we denote by $y(t) \in \mathbf{Y} \subset \mathbb{R}$ the concentration of bound integrins, depending on time t. We assume that the binding between integrins and tissue occurs preferentially in regions of highly aligned tissue [77]. This process can be described as

$$(\bar{R}_0 - y) \; + \; Q \; \underset{k^-}{\overset{k^+}{\rightleftharpoons}} \; y \,,$$

where $\bar{R}_0$ is the total amount of receptors on a cell membrane, Q is a density field describing ECM components, and k^+ and k^- are reaction rates. Therefore, the mass action kinetics for the concentration $y(t)$ is governed by the following ODE

$$\frac{dy}{dt} = k^+(d_c)(\bar{R}_0 - y)Q(\mathbf{x})S(\alpha_2, d_r) - k^-(d_c)y \,. \tag{3.12}$$

Precisely, $Q(\mathbf{x})$ is a time-invariant density field depending on the position $\mathbf{x} \in \mathbb{R}^d$ and representing the fraction of the insoluble component of the ECM involved in the integrin binding [75, 77]. The therapy effect is modeled through the terms $k^+(d_c)$, $k^-(d_c)$, and $S(\alpha_2, d_r)$. As in [126, 164], $d_c(t)$ denotes the dose of chemotherapeutic agent for integrin inhibition that affects cell invasion influencing the interaction between integrins and ECM. This is modelled through the attachment and detachment rates $k^+(d_c)$ and $k^-(d_c)$. In particular, $d_c(t)$ reduces the capability of the cells to bind with the ECM. Moreover, $d_r(t)$ represents the dose of radiotherapy, directly aimed at cell killing. In line with the well-established linear-quadratic radiobiological model (L-Q) [36, 88], the surviving fraction of cells after radiotherapy is described as

$$S(\alpha, d_r) := exp(-\alpha d_r - \beta d_r^2) \,,$$

where α and β represent the lethal lesions produced by a single radiation track or by two radiation tracks, respectively. Therefore, in the binding process of the cell receptor with the ECM, we account only for the fraction of healthy tissue surviving the radiation, i.e., $Q(\mathbf{x})S(\alpha_2, d_r)$, that is available to the cells for attaching to it. We use different values for the parameters α and β to refer to the radiation effects on tumor cells (α_1 and β_1) or on healthy tissue (α_2 and β_2). In particular, we use the notations $S_1(d_r) := S(\alpha_1, d_r)$ and $S_2(d_r) := S(\alpha_2, d_r)$. Additionally, we assume $d_c(t)$ and $d_r(t)$ to be at least piecewise continuous functions of time, $d_c(t)$, $d_r(t)$, $k^+(d_c)$, $k^-(d_c) \geq 0$, and the parameters $\alpha, \beta \geq 0$.

Since the microscopic integrin dynamics are much faster than the macroscopic time scale, they are assumed to equilibrate rapidly [74]. Rescaling $y/\bar{R}_0 \rightsquigarrow y$ to simplify the notation, we consider the unique steady state y^* of equation (3.12), namely

$$y^* = \frac{k^+(d_c)S_2(d_r)Q(\mathbf{x})}{k^+(d_c)S_2(d_r)Q(\mathbf{x}) + k^-(d_c)} =: f\left(k^+(d_c), k^-(d_c), Q(\mathbf{x}), S_2(d_r)\right) \,.$$

Introducing a new internal variable $z(t) := y^* - y$, which measures the deviation of $y(t)$ from the steady state [77], we consider the path of a single cell moving from an initial position $\mathbf{x}_0$ with velocity $\mathbf{v}$ through the field $Q(\mathbf{x})$. With the notation $\mathbf{x} = \mathbf{x}_0 + \mathbf{v}t$,

equation (3.12) can be rewritten in terms of the deviation $z(t)$

$$\frac{dz}{dt} = -z(t)(k^+ S_2 Q + k^-) + F(t) + \frac{\partial f}{\partial Q}\,\mathbf{v}\cdot\nabla Q =: G(z, Q, d_c, d_r)\,.$$

Here, $F(t)$ represents the derivative of $f\,(k^+(d_c), k^-(d_c), Q(\mathbf{x}), S_2(d_r))$ with respect to $k^+(d_c)$, $k^-(d_c)$, and $S_2(d_r)$, i.e.,

$$F(t) := \frac{\partial f}{\partial k^+}\frac{\partial k^+}{\partial d_c}\dot{d}_c + \frac{\partial f}{\partial k^-}\frac{\partial k^-}{\partial d_c}\dot{d}_c + \frac{\partial f}{\partial S_2}\frac{\partial S_2}{\partial d_r}\dot{d}_r\,,$$

where the dot indicates the time derivative. The derivative of f with respect to Q reads

$$\frac{\partial f}{\partial Q} = \frac{k^+ k^- S_2}{(k^+ S_2 Q + k^-)^2}\,.$$

To simplify the notation, we define

$$B_\rho(Q) := k^+ S_2 Q + k^-.$$

We recall that in the model description and derivation we use the notation ∇ to indicate the spatial gradient unless otherwise indicated.

3.2.2 *Mesoscopic level*

Using the above characterization of the microscopic dynamics, we describe the cell behavior with the aid of velocity-jump processes. At this level, we base the description of the proliferation on the model formulated in [74], and we add an overall loss term taking into account natural and induced cell death.

Letting $\rho(t, \mathbf{x}, \mathbf{v}, z)$ be the glioma density function at time t, in position $\mathbf{x} \in \Omega \subseteq \mathbb{R}^d$, with velocity $\mathbf{v} \in \mathbf{V} \subset \mathbb{R}^d$, and the internal state $z \in \mathbf{Z} \subseteq (y^* - 1, y^*)$, the kinetic transport equation for tumor dynamics reads

$$\frac{\partial \rho}{\partial t} + \nabla_{\mathbf{x}}\cdot(\mathbf{v}\rho) - \frac{\partial}{\partial z}\left[G(z, Q, d_c, d_r)\rho\right] = \mathcal{L}[\lambda]\rho + P(\rho) - L(M, R_1, d_r)\rho\,. \tag{3.13}$$

Here, $\mathcal{L}[\lambda]\rho$, $P(\rho)$, and $L(M, R_1, d_r)\rho$ stand for the turning operator, the proliferation term, and the overall loss term, respectively. Precisely, $\mathcal{L}[\lambda]\rho$ denotes the turning operator for the description of the cell velocity changes due to contact guidance. This process describes the oriented motility response of cells to the anisotropy of the environment. As we analyzed in Chapter 2, in the case of glioma cells, the movement and spread are especially associated with white matter tracts, acting as highways for cell migration. $\mathcal{L}[\lambda]\rho$ is here defined via an integral operator of Boltzmann type

$$\mathcal{L}[\lambda]\rho = -\lambda(z)\rho + \lambda(z)\int_{\mathbf{V}} K(\mathbf{x}, \mathbf{v})\rho(\mathbf{v}')d\mathbf{v}'\,, \tag{3.14}$$

where $\lambda(z)$ is the turning rate and $K(\mathbf{x}, \mathbf{v})$ is the turning kernel. Precisely, $\lambda(z) := \lambda_0 - \lambda_1 z \geq 0$ depends on the microscopic variable $z(t)$, while λ_0 and λ_1 are positive constants. Due to the rescaling of $\mathbf{y}$, we have $\mathbf{Y} = (0, 1)$ and, consequently, $y^* < 1$ and $|z| < 1$. To ensure a positive turning rate, we assume that $\lambda_0 \geq \lambda_1$. The term $\lambda(z)\rho$ represents the rate at which cells change their velocity $\mathbf{v}$ to any other velocity. The integral term denotes the cell changing from any previous velocity $\mathbf{v}'$ to a new velocity $\mathbf{v}$ as a consequence of interacting with the tissue fibers. In order to model

the turning kernel $K(\mathbf{x}, \mathbf{v})$ in (3.14), we assume that the dominating directional cue is given by the oriented environment of the brain fibers and, consequently, cells choose their new direction according to the given fiber network. Moreover, we assume $K(\mathbf{x}, \mathbf{v})$ to be independent from the incoming velocity $\mathbf{v}'$. To describe the oriented structure of the environment we use the directional distribution $q(\mathbf{x}, \hat{\mathbf{v}})$ described in Section 2.3. In particular, we assume a constant cell speed s, namely $\mathbf{V} = s\mathbb{S}^{d-1}$, $s \geq 0$, and, being $\hat{\mathbf{v}} \in \mathbb{S}^{d-1}$, we have $\mathbf{v} = s\hat{\mathbf{v}}$. We also assume the tissue to be undirected, hence $q(\mathbf{x}, \hat{\mathbf{v}}) = q(\mathbf{x}, -\hat{\mathbf{v}})$ for all $\mathbf{x} \in \mathbb{R}^d$. Therefore, the turning kernel is modelled as

$$K(\mathbf{x}, \mathbf{v}) = \frac{q(\mathbf{x}, \hat{\mathbf{v}})}{\omega}, \tag{3.15}$$

with the scaling constant $\omega := \int_{\mathbf{V}} q(\mathbf{x}, \hat{\mathbf{v}}) d\mathbf{v} = s^{d-1}$ introduced in (2.6) [77, 216]. For later reference we introduce the notations

$$\mathbb{E}_q(\mathbf{x}) := \int_{\mathbb{S}^{d-1}} \hat{\mathbf{v}} q(\mathbf{x}, \hat{\mathbf{v}}) d\hat{\mathbf{v}} \tag{3.16}$$

$$\mathbb{V}_q(\mathbf{x}) := \int_{\mathbb{S}^{d-1}} (\hat{\mathbf{v}} - \mathbb{E}_q) \otimes (\hat{\mathbf{v}} - \mathbb{E}_q)\, q(\mathbf{x}, \hat{\mathbf{v}}) d\hat{\mathbf{v}} \tag{3.17}$$

for the mean fiber orientation and the variance-covariance matrix for the orientation distribution of tissue fibers, respectively. Notice that the above symmetry of q implies $\mathbb{E}_q(\mathbf{x}) = 0$. If we associate integrin activation with cell binding to the tissue, we can see the binding as the onset of proliferation and also of reorientation. In fact, the turning rate of the cells depends on the integrin state on the cell membrane. If many integrins are already bound, the cells will need to change their direction more often in order to escape from the densely packed fibers surrounding them [272], resulting in an increased rate $\lambda(z)$.

Following [74], we model proliferation as an effect of cell-tissue interactions via integrin binding. A way to include proliferation at the mesoscopic level is to consider in (3.13) the proliferation term $P(\rho)$ in the form

$$P(\rho) = \mu(M) \int_{\mathbf{Z}} \chi(\mathbf{x}, z, z') \rho(t, \mathbf{x}, \mathbf{v}, z') Q(\mathbf{x}) dz',$$

where $M = M(t, \mathbf{x})$ denotes the macroscopic cell density and is defined as

$$M(t, \mathbf{x}) = \int_{\mathbf{V}} \int_{\mathbf{Z}} \rho(t, \mathbf{x}, \mathbf{v}, z) dz d\mathbf{v},$$

while $\mu(M)$ is a general growth rate. We will specify the expression of $\mu(M)$, as well as the other coefficient function involved in the model formulation in the following Section 3.3. In the integral operator, the kernel $\chi(\mathbf{x}, z, z')$ characterizes the transition from state z' to state z during the proliferative process at position $\mathbf{x}$. No particular conditions are required for χ. We only assume that the nonlinear proliferative operator $P(\rho)$ is uniformly bounded in the L^2-norm, a reasonable biological condition linked to the space-imposed bounds on the cell division.

The overall loss is modeled by the last term in equation (3.13), as a combination of two parts: one term is related to the natural cell death $l(M)$ and the other term is related to the induced death due to radiotherapy $R_1(d_r)$. Thus, the overall loss term reads:

$$L(M, R_1, d_r)\rho = (l(M) + R_1(d_r))\rho.$$

In the clinical practice, the total dose of radiation is given in smaller fractions, to avoid toxic effects on healthy tissue. If ς is the number of fractions, the total effect of the radiation therapy protocol can be expressed as:

$$R(\alpha, d_r) = \sum_{i=1}^{\varsigma} (1 - S(\alpha, d_r))\eta_\delta(t - t_i)\,,$$

where η_δ is a C_0^∞ function with unit mass and support in $(-\delta, \delta)$, $\delta \ll 1$, and t_i denotes the time instants at which ionizing radiation are applied to the patient. Following the notation for the survival fraction introduced above, we indicate with $R_1(d_r) = R(\alpha_1, d_r)$. Global existence of a unique solution for equation (3.13) can be proved following the arguments in [169], under suitable growth conditions for the rate μ with respect to its third argument $\mathbf{v}$.

3.2.3 *Derivation of the macroscopic setting*

Considering the above description of the subcellular and mesoscopic dynamics for the tumor cell density $\rho(t, \mathbf{x}, \mathbf{v}, z)$, we introduce proper scaling arguments in order to apply the parabolic limit method and deduce the macroscopic density equation. Specifically, we consider the moments of the cell density ρ

$$m(t, \mathbf{x}, \mathbf{v}) = \int_{\mathbf{Z}} \rho(t, \mathbf{x}, \mathbf{v}, z) dz\,, \qquad M(t, \mathbf{x}) = \int_{\mathbf{V}} m(t, \mathbf{x}, \mathbf{v}) d\mathbf{v}\,,$$

$$m^z(t, \mathbf{x}, \mathbf{v}) = \int_{\mathbf{Z}} z\rho(t, \mathbf{x}, \mathbf{v}, z) dz\,, \qquad M^z(t, \mathbf{x}) = \int_{\mathbf{V}} m^z(t, \mathbf{x}, \mathbf{v}) d\mathbf{v}\,.$$

We do not consider higher order moments of ρ, as the subcellular dynamics is much faster than the events on the other scales, so that the deviation z is close to zero. We also assume the data to be compactly supported in the phase space $\mathbb{R}^d \times \mathbf{V} \times Z$. We first integrate equation (3.13) with respect to z, obtaining the following equation for m

$$\begin{aligned}\frac{\partial}{\partial t} m + \nabla_{\mathbf{x}} \cdot (\mathbf{v} m) = &- \lambda_0 m + \lambda_0 \frac{q}{\omega} M + \lambda_1 m^z - \lambda_1 \frac{q}{\omega} M^z \\ &+ \mu(M) \int_{\mathbf{Z}} \int_{\mathbf{Z}} \chi(\mathbf{x}, z, z') \rho(z') Q \, dz' dz - L(M, R_1, d_r) m\,.\end{aligned}$$

We then multiply all terms in (3.13) by z and repeat the integration procedure, obtaining the equation for m^z

$$\begin{aligned}\frac{\partial}{\partial t} m^z + \nabla_{\mathbf{x}} \cdot (\mathbf{v} m^z) = &- m^z B_\rho(Q) + F\, m + \frac{k^+ k^- S_2}{B_\rho(Q)^2}\, v \cdot \nabla Q\, m - \lambda_0 m^z + \lambda_0 \frac{q}{\omega} M^z \\ &+ \mu(M) \int_{\mathbf{Z}} \int_{\mathbf{Z}} z\chi(\mathbf{x}, z, z') \rho(z') Q \, dz' dz - L(M, R_1, d_r) m^z\,.\end{aligned}$$

We consider a parabolic scaling $\mathbf{x} \to \varepsilon \mathbf{x}$ and $t \to \varepsilon^2 t$ for the space and time variables, respectively, as described in Section 3.1. In particular, $F(t)$, which accounts for fast dynamics and involves the time derivatives of d_c, d_r ,and the cell survival fraction S, is scaled with ε^2. With a similar argument we scale the growth rate $\mu(M)$ and the loss

term $L(M, R_1, d_r)$. Therefore, we collect the equations for the moments m and m^z:

$$\begin{aligned}\varepsilon^2 \frac{\partial}{\partial t} m + \varepsilon \nabla_{\mathbf{x}} \cdot (\mathbf{v} m) = &-\lambda_0 m + \lambda_0 \frac{q}{\omega} M + \lambda_1 m^z - \lambda_1 \frac{q}{\omega} M^z \\ &+ \varepsilon^2 \mu(M) \int_{\mathbf{Z}} \int_{\mathbf{Z}} \chi(\mathbf{x}, z, z') \rho(z') Q \, dz' dz \\ &- \varepsilon^2 L(M, R_1, d_r) m \,, \end{aligned} \tag{3.18}$$

$$\begin{aligned}\varepsilon^2 \frac{\partial}{\partial t} m^z + \varepsilon \nabla_{\mathbf{x}} \cdot (\mathbf{v} m^z) = &-m^z B_\rho(Q) + \varepsilon^2 F m + \varepsilon \frac{k^+ k^- S_2}{B_\rho(Q)^2} v \cdot \nabla Q \, m - \lambda_0 m^z + \lambda_0 \frac{q}{\omega} M^z \\ &+ \varepsilon^2 \mu(M) \int_{\mathbf{Z}} \int_{\mathbf{Z}} z \chi(\mathbf{x}, z, z') \rho(z') Q \, dz' dz \\ &- \varepsilon^2 L(M, R_1, d_r) m^z \,. \end{aligned} \tag{3.19}$$

At this point, we apply the asymptotic Hilbert method [44, 212]. Proposed by D. Hilbert at the beginning of the last century, this method to resolve Boltzmann equations is based on the use of asymptotic series. It considers the *Hilbert expansions* of the moments of ρ, namely their expansions in power series of ε:

$$\begin{aligned} m &= \sum_{k=0}^{\infty} \varepsilon^k m_k \,, & M &= \sum_{k=0}^{\infty} \varepsilon^k M_k \,, \\ m^z &= \sum_{k=0}^{\infty} \varepsilon^k m_k^z \,, & M^z &= \sum_{k=0}^{\infty} \varepsilon^k M_k^z \,. \end{aligned} \tag{3.20}$$

Hilbert's approach is to insert the expressions (3.20), called Hilbert series, into (3.18) and (3.19) and to determine the unknown variables, namely m_k, m_k^z, M_k, and M_k^z for $k = 0, 1, 2$, by sorting the equations into ε-powers and using the identity principle. This upscaling strategy is aimed at obtaining the macroscopic equation for the leading coefficient M_0 of the Hilbert expansion of the macroscopic glioma density function $M(t, \mathbf{x})$. In order to obtain a closed form for the macroscopic equation, we need to Taylor expand some terms involved in the moment equations. Precisely, concerning the proliferation term $\mu(M)$ and its dependency on the macroscopic cell density M, we expand it with respect to M around M_0, i.e.,

$$\mu(M) = \mu(M_0) + \partial_M \mu(M_0)(M - M_0) + \mathcal{O}(|M - M_0|^2) \,. \tag{3.21}$$

In addition, we assume that $\chi(\mathbf{x}, z, z')$ is a probability kernel with respect to z and for all $(\mathbf{x}, z')$. This means that there exists a probability distribution, independent of the space variable and the integrin binding, that describes the state of the cell before a proliferation event. This allows us to write

$$\int_{\mathbf{Z}} \int_{\mathbf{Z}} \chi(\mathbf{x}, z, z') \rho(z') Q \, dz' dz = Q \int_{\mathbf{Z}} \rho(z') dz' = Q \, m_0 + \mathcal{O}(\varepsilon) \,. \tag{3.22}$$

Analogously, for the overall loss term $L(M, R_1, d_r)$, we expand it with respect to M around M_0:

$$\begin{aligned} L(M, R_1, d_r) &= l(M_0) + \partial_M l(M_0)(M - M_0) + \mathcal{O}(|M - M_0|^2) + R_1(d_r) \\ &= L(M_0, R_1, d_r) + \mathcal{O}(\varepsilon)\,. \end{aligned} \tag{3.23}$$

Therefore, taking into account (3.21), (3.22), and (3.23), and substituting (3.20) into (3.18) and (3.19) and collecting the coefficients of the different powers of ε, we obtain

ε^0 :

$$0 = -\lambda_0 \left(m_0 - \frac{q}{\omega} M_0\right) + \lambda_1 \left(m_0^z - \frac{q}{\omega} M_0^z\right)\,, \tag{3.24}$$

$$0 = -\lambda_0 \left(m_0^z - \frac{q}{\omega} M_0^z\right) - m_0^z\, B_\rho(Q)\,, \tag{3.25}$$

ε^1 :

$$\nabla_{\mathbf{x}} \cdot (\mathbf{v} m_0) = -\lambda_0 \left(m_1 - \frac{q}{\omega} M_1\right) + \lambda_1 \left(m_1^z - \frac{q}{\omega} M_1^z\right)\,, \tag{3.26}$$

$$\nabla_{\mathbf{x}} \cdot (\mathbf{v} m_0^z) = -\lambda_0 \left(m_1^z - \frac{q}{\omega} M_1^z\right) - m_1^z\, B_\rho(Q) + \frac{k^+ k^- S_2}{B_\rho(Q)^2}\, m_0\, \mathbf{v} \cdot \nabla Q\,, \tag{3.27}$$

ε^2 :

$$\begin{aligned} \frac{\partial}{\partial t} m_0 + \nabla_{\mathbf{x}} \cdot (\mathbf{v} m_1) = -\lambda_0 (m_2 - \frac{q}{\omega} M_2) + \lambda_1 (m_2^z - \frac{q}{\omega} M_2^z)\,, \\ + \mu(M_0) Q\, m_0 - L(M_0, R_1, d_r) m_0\,. \end{aligned} \tag{3.28}$$

We start integrating (3.25) with respect to the velocity $\mathbf{v}$. Considering the definition (2.6) of the parameter ω, we get $M_0^z = 0$ and, then, plugging this into the equations (3.25) and (3.24), we have

$$0 = m_0^z(-\lambda_0 - B_\rho(Q)) \Longrightarrow m_0^z = 0$$

and

$$0 = -\lambda_0 \left(m_0 - \frac{q}{\omega} M_0\right) \Longrightarrow m_0 = \frac{q}{\omega} M_0\,.$$

Then, we consider (3.27) and integrate it with respect to $\mathbf{v}$ obtaining

$$\begin{aligned} 0 &= -\lambda_0 M_1^z + \lambda_0 M_1^z - M_1^z B_\rho(Q) + \frac{k^+ k^- S_2}{B_\rho(Q)^2}\, \nabla Q \cdot \int_{\mathbf{V}} m_0 \mathbf{v} d\mathbf{v} \\ &= -M_1^z B_\rho(Q) + \frac{k^+ k^- S_2}{B_\rho(Q)^2}\, \nabla Q \cdot \int_{\mathbf{V}} \frac{q}{\omega} M_0 \mathbf{v} d\mathbf{v} = -M_1^z B_\rho(Q)\,. \end{aligned}$$

We use here the symmetry assumption on the fiber distribution function $q(\mathbf{x}, \hat{\mathbf{v}})$. Therefore, we have $M_1^z = 0$ that, plugged into (3.27), gives

$$0 = -m_1^z(\lambda_0 + B_\rho(Q)) + \frac{q}{\omega} M_0 \frac{k^+ k^- S_2}{B_\rho(Q)^2} \mathbf{v} \cdot \nabla Q$$

$$\Longrightarrow m_1^z = \frac{1}{B_\rho(Q) + \lambda_0} \left(\frac{q}{\omega} M_0 \frac{k^+ k^- S_2}{B_\rho(Q)^2} \mathbf{v} \cdot \nabla Q \right) .$$

Considering (3.26) with the above deduction leads to

$$\nabla_{\mathbf{x}} \cdot (\mathbf{v} m_0) = -\lambda_0 \left(m_1 - \frac{q}{\omega} M_1 \right) + \lambda_1 m_1^z = \mathcal{L}[\lambda_0] m_1 + \lambda_1 m_1^z .$$

In order to deduce an expression for m_1, we need to invert $\mathcal{L}[\lambda_0]$. For this, we recall the definition of the functional space $L^p_\vartheta(\mathbf{W})$ and of the *Hilbert-Schmidt operator*.

Definition 3.1. A weighted L^p-space, with weight function ϑ, indicated with $L^p_\vartheta(\mathbf{W})$, is defined as

$$L^p_\vartheta(\mathbf{W}) := \left\{ f : \mathbf{W} \to \mathbb{R} \,\middle|\, f \text{ is measurable and } \left(\int_{\mathbf{W}} |f(\mathbf{w})|^p \vartheta(\mathbf{w}) d\mathbf{w} \right)^{\frac{1}{p}} < \infty \right\} .$$

Definition 3.2. A bounded operator $\mathcal{T}$ defined on an Hilbert space $\mathcal{H}$ is called *Hilbert-Schmidt operator* if and only if $\text{trace}(\mathcal{T}^* \mathcal{T}) < \infty$, where $\mathcal{T}^*$ is the self-adjoint operator. Notice that every Hilbert-Schmidt operator is compact [243].

For our purpose, we consider $p = 2$, $\vartheta := (q/\omega)$ and $\mathbf{W} := \mathbf{V}$, such that the space $L^2_q(\mathbf{V})$ is also a function of the space-time point $(t, \mathbf{x})$. For each pair $(t, \mathbf{x})$, we analyze the kernel of the operator $\mathcal{L}[\lambda_0]$, which is a compact Hilbert-Schmidt operator [212]:

$$\mathcal{L}[\lambda_0] m_1 = 0 \Longleftrightarrow m_1 = \frac{q}{\omega} M_1 .$$

This kernel is the linear subspace of $L^2_q(\mathbf{V})$ spanned by q/ω, i.e. $\langle q/\omega \rangle$. Therefore, we can write $L^2_q(\mathbf{V}) = \langle q/\omega \rangle \oplus \langle q/\omega \rangle^\perp$. Restricting $\mathcal{L}$ to the subspace $\langle q/\omega \rangle^\perp$, we can define its pseudo-inverse $\mathcal{F}$:

$$\mathcal{F} := \left(\mathcal{L}_{|\langle q/\omega \rangle^\perp} \right)^{-1} .$$

Assuming $\psi \in \langle q/\omega \rangle^\perp$ and solving $\mathcal{L}[\lambda_0](m_1) = \psi$, we get

$$\mathcal{L}[\lambda_0](m_1) = \psi \Leftrightarrow m_1 = -\frac{1}{\lambda_0} \psi + \frac{q}{\omega} M_1 .$$

Since $m_1 \in \langle q/\omega \rangle^\perp$, we obtain

$$M_1 = 0 \quad \text{and} \quad m_1 = \frac{1}{\lambda_0} \left[\frac{\lambda_1}{\lambda_0 + B_\rho(Q)} \frac{k^+ k^- S_2}{B_\rho(Q)^2} \nabla Q \cdot \mathbf{v} \frac{q}{\omega} M_0 - \nabla_{\mathbf{x}} \cdot (\mathbf{v}\, m_0) \right] .$$

Finally, we integrate (3.28) with respect to $\mathbf{v}$, resulting in

$$\frac{\partial}{\partial t}\int_{\mathbf{V}} m_0\, d\mathbf{v} + \int_{\mathbf{V}} \nabla_{\mathbf{x}}\cdot(\mathbf{v}m_1)\, d\mathbf{v} = \int_{\mathbf{V}} -\lambda_0\left(m_2 - \frac{q}{\omega}M_2\right) + \lambda_1\left(m_2^z - \frac{q}{\omega}M_2^z\right) d\mathbf{v} + \int_{\mathbf{V}} \mu(M_0)\, Q\, m_0\, d\mathbf{v} - \int_V L(M_0, R_1, d_r) m_0\, d\mathbf{v}\,.$$

In view of $M_1 = 0$, the ε-correction terms for M can be neglected and, ignoring the higher order terms, we get the following evolution equation characterizing the macroscopic glioma density M

$$\begin{aligned}\frac{\partial}{\partial t}M = \nabla_{\mathbf{x}}\cdot(\mathbf{D}_T(\mathbf{x})\nabla M) - \nabla_{\mathbf{x}}\cdot((g(Q(\mathbf{x}))\mathbf{D}_T(\mathbf{x})\nabla Q - u(\mathbf{x}))M) \\ + \mu(M)Q(\mathbf{x})M - L(M, R_1, d_r)M\,.\end{aligned} \tag{3.29}$$

Here, we denote by

$$g(Q(\mathbf{x})) := \frac{\lambda_1}{\lambda_0 + B_\rho(Q)}\frac{k^+k^-S_2}{B_\rho(Q)^2}$$

the function carrying the information about the influence of the subcellular dynamics. The macroscopic tensor for the tumor population is expressed, analogously to (2.8), as

$$\mathbf{D}_T(\mathbf{x}) := \frac{1}{\omega\lambda_0}\int_{\mathbf{V}} \mathbf{v}\otimes\mathbf{v}\, q(\mathbf{x}, \hat{\mathbf{v}}) d\mathbf{v}\,,$$

while the tumor drift velocity is given by

$$u(\mathbf{x}) := \frac{1}{\omega\lambda_0}\int_{\mathbf{V}} \mathbf{v}\otimes\mathbf{v}\,\nabla q(\mathbf{x}, \hat{\mathbf{v}})\, d\mathbf{v}\,.$$

It is important to stress that, even though the similarity between the macroscopic setting proposed in [74] and equation (3.29) is evident, there are substantial differences in the modeling of the therapeutic approach. More precisely, therapy has been introduced at the microscale, as explained in Section 3.2.1, and its effects on the macroscopic equation (3.29) are collected in the terms $L(M, R_1, d_r)$ and $g(Q(\mathbf{x}))$. Equation (3.29) can written in the equivalent form

$$\frac{\partial}{\partial t}M - \nabla\nabla : (\mathbf{D}_T(\mathbf{x})M) + \nabla\cdot(g(Q(\mathbf{x}))\mathbf{D}_T(\mathbf{x})\nabla Q\, M) = \mu(M)Q(\mathbf{x})M - L(M, R_1, d_r)M\,,$$

where the operator $\nabla\nabla :$ is a short form of the full second derivative. When expanded, this operator gives rise to a Fickian diffusion part (second term on the left-hand side of (3.29)) plus an additional advection term (fourth term on the left-hand side of (3.29)) related to the tumor drift velocity. This form of the diffusive operator is also referred to as the *fully-anisotropic advection-diffusion model*. In fact, this expression is derived from individual cell-movement and, as such, is a more biologically relevant form compared to Fickian diffusion only [74, 216, 274]).

Well-posedness of the macroscopic setting

Using the theory of monotone operators for nonlinear parabolic equations and following a well-known approach [251, 258], it is possible to prove the existence, uniqueness and non-negativity of the solution of the parabolic problem (3.29) with homogeneous Neumann boundary conditions.

Let $\Omega \subset \mathbb{R}^3$ be a Lipschitz domain and $\hat{n}$ the normal vector to $\partial\Omega$. Let $\bar{T} > 0$ be finite and consider the following nonlinear parabolic initial-boundary-value problem related to equation (3.29):

$$\begin{cases} \dfrac{\partial}{\partial t} M - \nabla \cdot (\mathbf{D}_T(\mathbf{x}) \nabla M) + \nabla \cdot (Y(Q, \mathbf{D}_T) M) + \Gamma(M) = 0 \quad \text{in } [0, \bar{T}] \times \Omega \\ \nabla M \cdot \hat{n} = 0 \quad \text{on } [0, \bar{T}] \times \partial\Omega \\ M(0, \mathbf{x}) = \bar{M}_0(\mathbf{x}) \quad \text{in } \Omega \end{cases} \tag{3.30}$$

where

$$Y(Q, \mathbf{D}_T) = g(Q(\mathbf{x})) \mathbf{D}_T(\mathbf{x}) \nabla Q - u(\mathbf{x})$$

$$\Gamma(M) = ((l(M) + R_1(d_r)) - \mu(M) Q(\mathbf{x}))\, M\,.$$

Adapting the proof proposed in Appendix A.1 of [74], it is possible to prove the following theorem.

Theorem 3.1. Assume:

A.1 The tensor $\mathbf{D}_T(\mathbf{x})$ is uniformly positive definite, it belongs to the Sobolev space $W^{1,\infty}(\Omega)$ and its smallest eigenvalue is larger than a constant $\alpha > 0$;

A.2 $\Gamma(M)$ is continuous in time and M and it satisfies the growth condition

$$|\Gamma(s)| \leq c\,(1 + |s|^{r-1})$$

for some $r \geq 1$ (with a constant c independent of time and space) and the coercivity condition $\inf_{s \in \mathbb{R}^+} \Gamma(s) s > -\infty$;

A.3 The function $Q(\mathbf{x})$ belongs to the space $W^{1,\infty}(\Omega)$;

A.4 The rates k^+ and k^- are continuous in the variable d_c (which in turn has to be continuous in time) and uniformly bounded;

A.5 The term $Y(Q, \mathbf{D}_T)$ is in $L^\infty(\Omega)$.

Let $U = H^1(\Omega)$, $H = L^2(\Omega)$, $X = L^2(0, T; U)$ and define the functional space

$$W := \{\omega \in L^2(0, T; U) \,:\, \partial_t \omega \in L^2(0, T; U^*)\} \subseteq X\,.$$

Let $\bar{M}_0 \in H$ and let $\Gamma : \mathbb{R} \to \mathbb{R}$ be a continuous function that satisfies the condition A.2 above with $1 \leq r < \frac{10}{3}$. Then, there exists a weak solution $M \in W$ of the problem (3.30), i.e., there exists $M \in W$ such that for all $\varphi \in C_0^\infty([0, T] \times \Omega)$:

$$\int_0^T \langle \partial_t M, \varphi \rangle_{H^1(\Omega)}\, dt + \int_0^T \int_\Omega (\mathbf{D}_T \nabla M - Y(Q, D_T) M) \nabla \varphi d\mathbf{x} dt + \int_0^T \int_\Omega \Gamma(M) \varphi d\mathbf{x} dt = 0\,.$$

It is also possible to prove uniqueness and non-negativity of the solution, using classical estimates, parabolic comparison principle [83] and theorems from Section III.4.1. in [258].

Proposition 3.1. The solution of the macroscopic problem (3.30) is unique if $\Gamma(M)$ is strictly monotone. In addition, if $\bar{M}_0 \geq 0$, the solution of (3.30) is non-negative.

3.3 *Numerical results*

The macroscopic setting (3.29) consists of an advection-diffusion-reaction equation for the description of glioma cell growth and migration in the brain. In this section, we show some numerical experiments representing various scenarios that the model is able to reproduce. First, in Section 3.3.1, we specify the expressions of the coefficient functions involved in the macroscopic setting and the value for the constant parameters. Then, in Section 3.3.2, we briefly describe how the data on the computational domain and the DTI information are taken into account. Finally, the numerical results of the model simulations are shown in Section 3.3.3.

3.3.1 *Assessment of the coefficients*

First, we define the expression we consider for the function $Q(\mathbf{x})$ describing the fraction of unsoluble components of the ECM interacting at point $\mathbf{x}$ with the tumor population, as introduced in Section 3.2.1. We choose it to be proportional to the fractional anisotropy of the tissue itself. This approach, introduced in [77], is motivated by the fact that the fractional anisotropy is a measure for the alignment of the brain fibers and, since in this setting the fiber alignment is guiding cell migration, the function $Q(\mathbf{x})$ expresses higher values where the tissue is strongly aligned. Hence, we set

$$Q(\mathbf{x}) := FA(\mathbf{D}_W(\mathbf{x})) .$$

However, other possible choices can be considered and we will address one of them in the forthcoming chapter.

The growth rate $\mu(M)$, which we assumed to depend on the macroscopic tumor density, can be defined following different growth models and its choice should be motivated by biological evidence. A logistic term, as well as Gompertzian or exponential growth, can be a reasonable choice in the absence of biological data. Following several previous works (see for instance [74, 129]), we employ a logistic growth term, defined as

$$\mu(M) := c_g \left(1 - \frac{M}{K_M}\right) ,$$

with a constant growth coefficient c_g and the tumor carrying capacity K_M. For the natural death term we set $l(M) = \bar{c}_l M$, with tumor death rate $\bar{c}_l$.

The integrin binding and unbinding rates, k^+ and k^-, respectively, are modelled to satisfy the assumption made on the chemotherapeutic term in Section 3.2.1. Namely, we consider the function k^+ monotonically decreasing with respect to the given dose d_c, while the function k^- is monotonically increasing with d_c. In this way, the chemotherapy treatment, by modeling integrin inhibitors, directly affects cell migration, reducing the cell capability of binding with the ECM. Precisely, we set

$$k^+(d_c) := 0.1 \left(1 + \frac{d_c}{1 + d_c^2}\right)$$

$$k^-(d_c) := 0.1 \left(1 + d_c\right) .$$

In Table 3.1 we report the range of the values for the constant parameters involved in the macroscopic setting (3.29). In particular, the simulations shown in Section 3.3.3 are performed using the average values of the reported intervals.

Parameter	Description	Value (unit)	Source
s	speed of tumor cells	$0.21 \cdot 10^{-3}$ (mm$\cdot$ s^{-1})	[49]
λ_0	turning frequency in $\mathcal{L}_\rho[\lambda(z)]$	0.1 (s^{-1})	[259]
λ_1	turning frequency in $\mathcal{L}_\rho[\lambda(z)]$	0.01 (s^{-1})	[77]
c_g	tumor proliferation rate	$[0.32, 0.72] \cdot 10^{-5}$ (s^{-1})	[193]
$\bar{c}_l$	tumor death rate	$[0.32, 0.72] \cdot 10^{-7}$ (s^{-1})	estimated, based on [75]
K_M	tumor carrying capacity	$\approx 10^6$ (cells$\cdot$ mm^{-3})	[81]
α_1	one radiation track tumor lesions	$[0.018, 0.401]$ (Gy^{-1})	[27]
α_2	one radiation track tissue lesions	$[0.373, 0.389]$ (Gy^{-1})	[27]
β_1	two radiation tracks tumor lesions	$[0.023, 0.091]$ (Gy^{-2})	[27]
β_2	two radiation tracks tissue lesions	$[0.016, 0.052]$ (Gy^{-2})	[27]

TABLE 3.1: **Tissue influence on glioma progression: model parameters.**

3.3.2 *Reconstruction of the computational domain*

In Section 1.1.5 we stressed the importance of including patient data in the model (if available) to which extend they can be useful to obtain realistic outcomes and, eventually, contribute to reliable predictions based on this model. In the context of the setting presented in this chapter, we processed data from an MRI scan of a healthy brain and used this data to derive a realistic description of the computational domain. Moreover, for the same tissue, the given DTI data provided information about the diffusivity and the fiber tracts.

We process the brain geometry with the FreeSurfer Software Suite[1], an open-source software for the analysis and visualization of structural and functional neuroimaging data from cross-sectional or longitudinal studies [86]. The processing of MRI data with FreeSurfer provides surface and volume information about the two hemispheres of the brain. From this information, we extract a 2D slice that constitutes the computational domain. A completed and detailed description of the MRI data processing is provided in Appendix A. Examples of the processing outputs are shown in Figure 3.1, where both the entire surface of the left hemisphere and the outer border of the considered 2D slice are visualized.

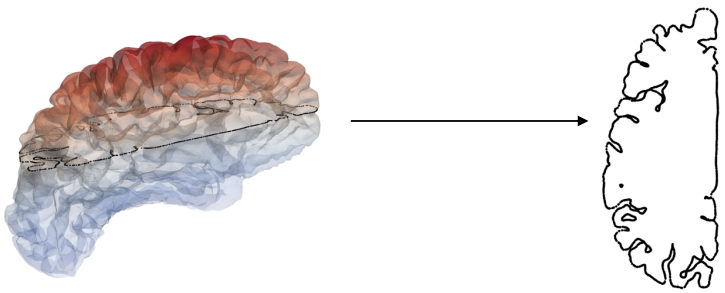

FIGURE 3.1: **Brain slice reconstruction.** The left hemisphere visualized with Paraview[2](left); contour of a 2D slice of the hemisphere (right).

[1] https://surfer.nmr.mgh.harvard.edu

This computational domain was, then, triangulated with the mesh generator Gmsh[3]. It is important to mention that this spatial mesh does not coincide with the voxel mesh of the DTI dataset. In particular, the former is much finer than the latter and, thus, a registration between the two meshes is required. This registration is performed with different visualization programs (Paraview and FSLeyes[4], the FSL image viewer), allowing to combine different data and obtaining the overall brain information on the computational domain. Further details on the mesh registration are provided in Appendix A. In Figure 3.2, the fractional anisotropy values of the DTI data, $FA(\mathbf{D}_W(\mathbf{x}))$, and the underlying fiber structures are visualized on the 2D brain slice of the left hemisphere. The latter, which highly influences tumor dynamics, is visualized in a

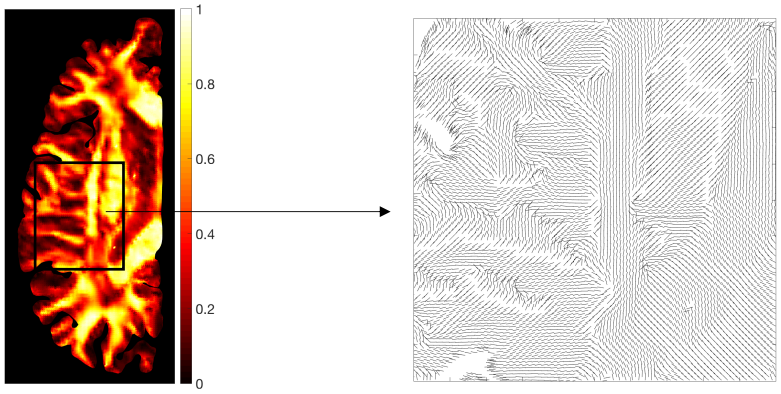

FIGURE 3.2: **FA and fiber representation.** Fractional anisotropy of $\mathbf{D}_W(\mathbf{x})$ (left) and visualization of the fiber tracts in a selected subdomain (right).

selected subdomain, where the leading eigenvector of the tensor $\mathbf{D}_W(\mathbf{x})$ is plotted in each point $\mathbf{x}$. The processing of this DTI data allows the calculation of the macroscopic tensor $\mathbf{D}_T(\mathbf{x})$ with the three fiber distribution functions introduced in Section 2.3. We will use the different macroscopic tensors obtained with the three distributions for comparing the evolution of the tumor mass in the next section.

The simulation presented in Section 3.3.3 refers to the 2D version of the macroscopic setting (3.29). For simplicity in the visualization, the simulations are performed on one hemisphere only. However, no constraints exist to extend the numerical calculations to the entire brain slice. The numerical simulations are performed with a self-developed code in Matlab (MathWorks Inc., Natick, MA), where a Galerkin finite element scheme for the spatial discretization is considered, together with an implicit Euler scheme for the time discretization. Details about the numerical schemes are provided in Appendix B.

3.3.3 *Numerical experiments*

Considering the parameters given in Table 3.1 and the functions defined in Section 3.3.1, we simulate different scenarios on the computational domain shown in Figure 3.1. We recall the macroscopic setting (3.29) in its equivalent form

$$\begin{aligned}\frac{\partial}{\partial t}M = \nabla\nabla : (\mathbf{D}_T(\mathbf{x})M) - \nabla_{\mathbf{x}} \cdot (g(Q(\mathbf{x}))\mathbf{D}_T(\mathbf{x})\nabla Q\, M) \\ + \mu(M)Q(\mathbf{x})M \,-\, L(M, R_1, d_r)M\,.\end{aligned} \tag{3.31}$$

[2] https://www.paraview.org
[3] http://gmsh.info
[4] https://fsl.fmrib.ox.ac.uk/fsl/fslwiki/FSLeyes

For the initial conditions we take a constant distribution of tumor cells on the circle with radius $r_{0,M} = 0.5$ and centered at $(\mathbf{x}_{0,M}, \mathbf{y}_{0,M}) = (-36, -32)$, situated in the left-bottom part of the brain slice representing the illustrative computational domain, i.e.,

$$M(\mathbf{x}, \mathbf{y}) = 1 \qquad \text{for } \left((\mathbf{x} - \mathbf{x}_{0,M})^2 + (\mathbf{y} - \mathbf{y}_{0,M})^2\right) < r_{0,M}\,.$$

We present the numerical results of these different scenarios:

(A) we consider the model without therapy and we compare the tumor evolution obtained with the three different fiber distribution functions;

(B) after selecting one of the distributions, we compare the model outputs in the cases with and without the advective term;

(C) we add the therapeutic term and simulate its effects on the tumor evolution with the same fiber distribution used in **(B)**.

Figure 3.3 shows the comparison of scenario **(A)**: the tumor evolution over time with the three different fiber distribution functions, in the absence of a therapeutic strategy. Columns in this figure refer to three different time instants: the solution is shown after 40 days, 80 days, and 120 days. On the other hand, rows refer to the three different fiber distribution functions: Peanut distribution, VMF distribution, and ODF. Some similarities can be observed between the tumor dynamics with the different fiber distribution functions, especially in qualitative terms. For all the three distributions, cell displacement inside the tissue covers an area of comparable extension and similarly reflects the underlying fiber orientation. Nevertheless, we see that the ODF distribution can reproduce anisotropic pattern and branched structures of tumor evolution arising from the underlying tissue structure, in contrast to the smoothed effect observed for VMF and Peanut distribution. This smoothing effect is mainly due to the isotropic component in the tensor $\mathbf{D}_T$ (2.10).

For our second set of numerical experiments, scenario **(B)**, we select the ODF for the description of the fiber. With this choice, we avoid on the one hand the isotropic component independent from the DTI data that characterized the Peanut distribution, and on the other hand, the estimation of the parameters κ and δ necessary for a proper use of the VMF distribution, as done for instance in [274]. Unfortunately, for this study, we did not have access to data from oncologic patients in order to run a patient-specific estimation. Therefore, we decided to rely on the fiber description provided by the ODF. In Figure 3.4 we illustrate case **(B)**, i.e., the numerical simulations of the tumor evolution with and without the advective term and in the absence of therapy. The advective term originates from the subcellular dynamics and involves also a component related to the divergence of $\mathbf{D}_T$, which differentiates the fully anisotropic model for the simpler Fickian diffusion, named in the following as the pure diffusive model. Significant anisotropic behaviors, which are evident in the simulations of the model with advection (bottom row), are not reproduced by the pure diffusive model (top row). In the purely diffusive case, the tumor evolution still shows the influence of the anisotropic diffusion in driving cell movements preferentially along the major fiber tracts, but it is not able to reproduce branched patterns and more heterogeneous distribution of the tumor density in the domain. On the other hand, the introduction of the haptotactic drift leads to more branched structures, closer to the ones observed in clinical imaging (e.g. see [312]). The mechanism that drives cell migration along the tissue structure is visualized in detail in Figure 3.5, where the leading eigenvector of the tensor $\mathbf{D}_T(\mathbf{x})$ is plotted together with the tumor density at 140 days in the two cases. The figure shows the aligned structures characterizing the brain tissue, by

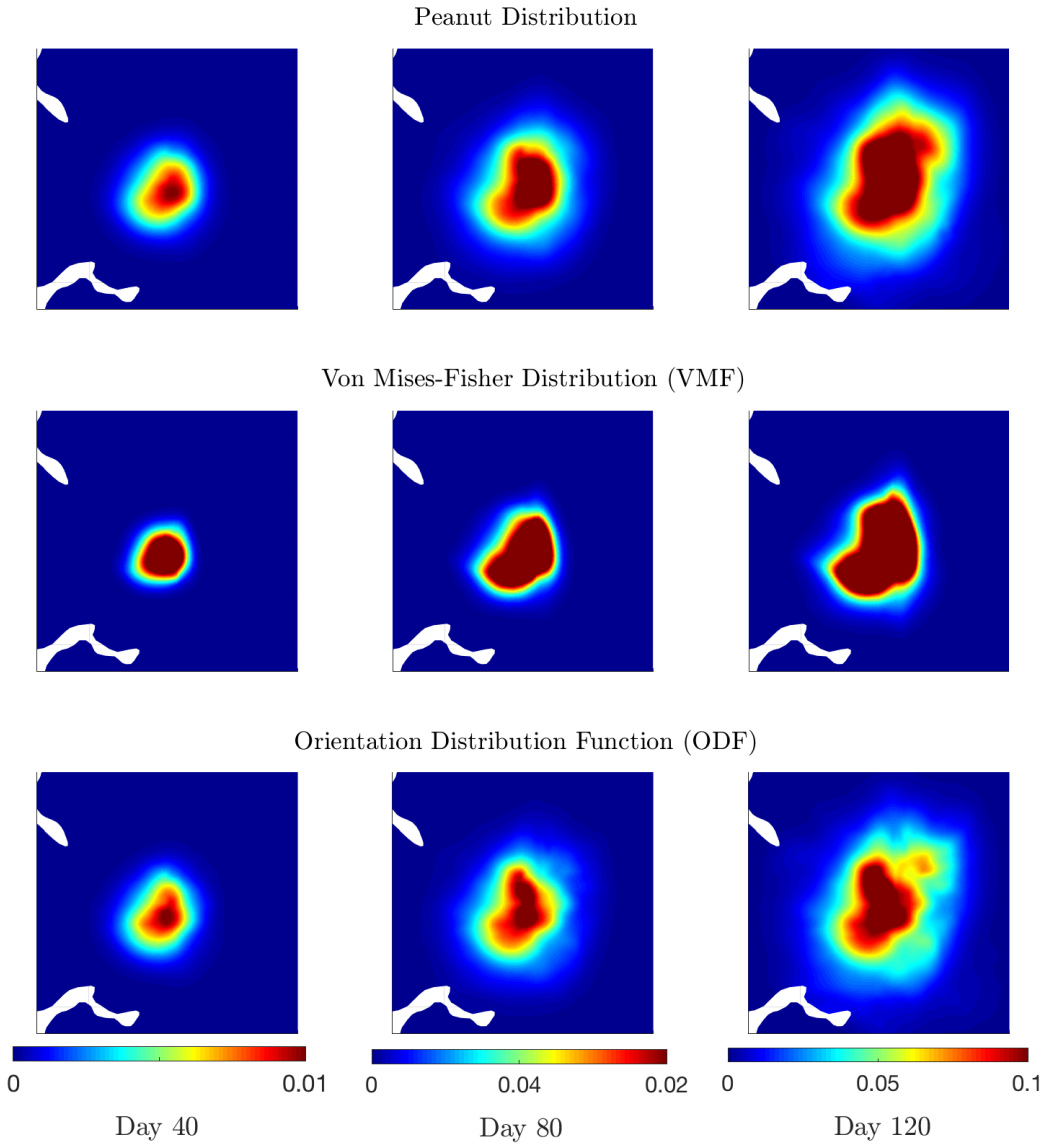

FIGURE 3.3: **Scenario (A).** Simulation of the evolution equation (3.31) without therapy, with the three different choices for the fiber distribution function.

means of the $\mathbf{D}_T(\mathbf{x})$ eigenvector, and their influence on the tumor dynamics. The diffusion in both cases is anisotropic, due to the presence of tensor $\mathbf{D}_T(\mathbf{x})$, and along the main fiber tracts the diffusion seems to be similarly fast, although slightly faster in the pure diffusion case. However, the cells in the purely diffusive model seem to be slower or less able to change direction and adapt to the tissue, especially in the region with crossing fibers and at the tumor edges. To conclude scenario **(B)**, Figures 3.4 and 3.5 show that taking subcellular processes into account leads to a non-negligible influence on the spatial distribution of the tumor cells. However, real patient data would be necessary to clarify which of the modeling approaches better explains the clinically observed tumor behavior.

In our third and final set of simulations, scenario **(C)**, we test our model considering a therapeutic strategy used in the case of newly diagnosed malignant glioma. It is based on a combination of chemotherapy and radiotherapy for a period of 6 weeks. Radiotherapy at a dose $d_r = 2$ Gy is given once per day, 5 days per week from weeks 1

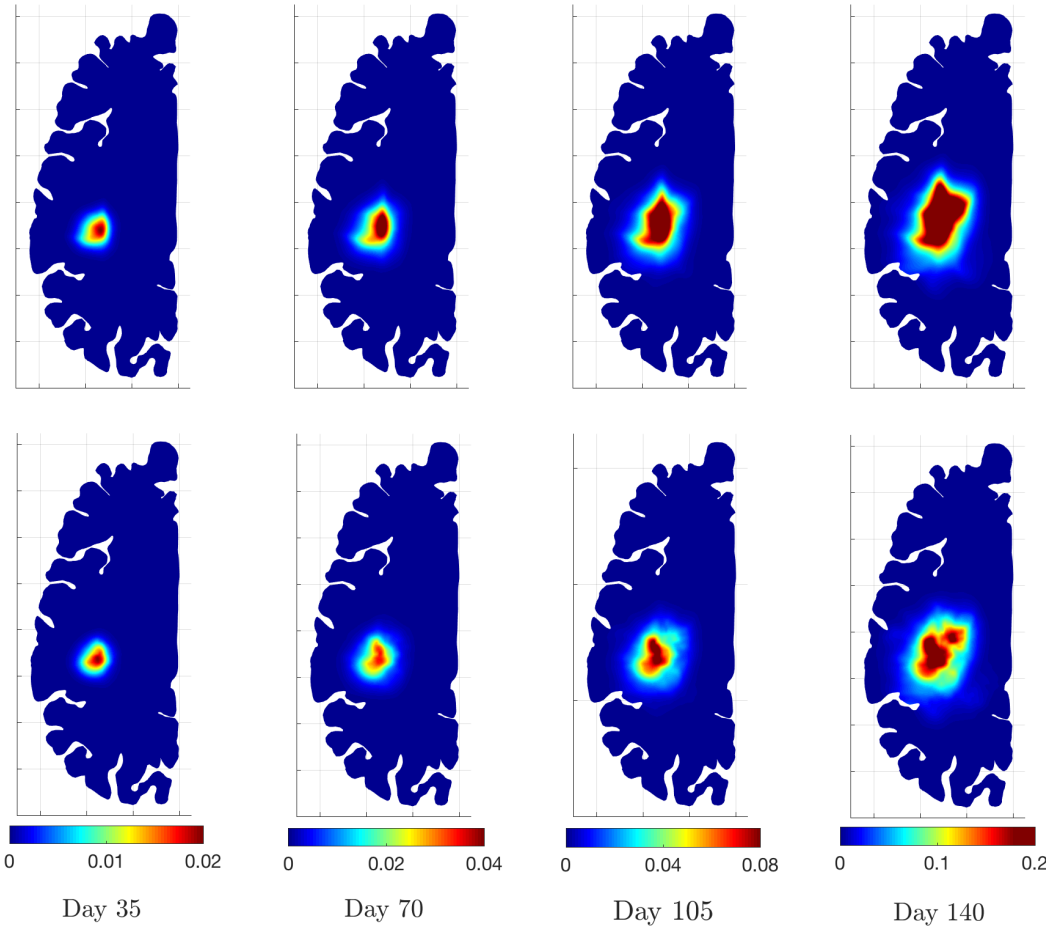

FIGURE 3.4: **Scenario (B).** Simulation of the pure diffusion model (top row) and of the complete model (3.31) without therapy (bottom row). In both cases, the ODF is used for the fiber description.

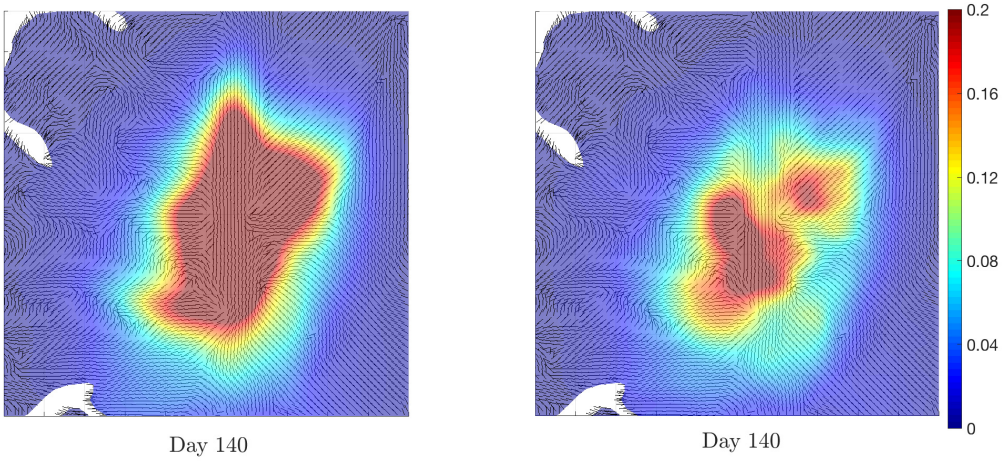

FIGURE 3.5: **Details of scenario (B).** Tumor evolution after 140 days in the case of the pure diffusion model (left) and the complete model (3.31) without therapy (right), together with the fiber direction.

to 6, with a total dose of 60 Gy, while chemotherapeutic agents for integrins inhibition at a normalized dose of $d_c = 5$ [126] is administered once per day from weeks 1 to 6. In particular, concerning chemotherapy, as we described in Section 3.2.1, we concentrate on the reduction of tumor invasion affecting the integrin/ECM bindings [73, 271]. Different types of integrin inhibitors, such as cilengitide (targeting the families of $\alpha_v\beta_3$ or $\alpha_v\beta_6$ integrins) or ATN 161 (targeting $\alpha_5\beta_1$ integrins), have been evaluated in preclinical or clinical studies. We consider the action of such chemotherapeutic agents, motivated by different reported trials (e.g., see trials NCT00689221 and NCT01165333[5]). As initial condition for the simulation with therapy, we consider the tumor density obtained running the model without therapy for 5 weeks. We first observe the effect of chemotherapy as the only applied treatment, setting the dose of radiation to $d_r = 0$. Results are shown in Figure 3.6 where we plot the difference between the solution for the model without any therapeutic treatment and the one with chemotherapy.

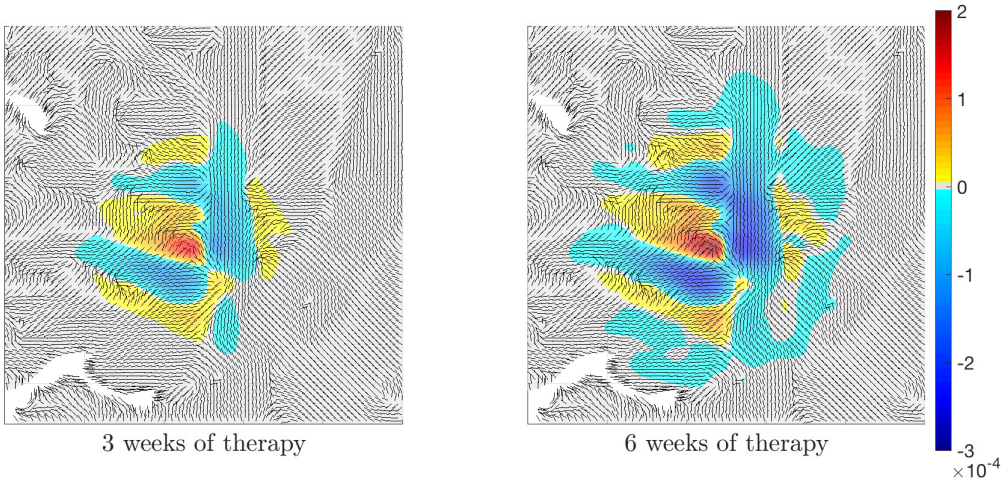

FIGURE 3.6: **Scenario (C).** Difference between the tumor density in the model without therapy and in the case of chemotherapy. The difference is plotted together with the fiber direction. For the construction of $\mathbf{D}_T$ the ODF is used.

In both cases, $\mathbf{D}_T$ is calculated using the ODF. As chemotherapy does not aim at killing cells, but at reducing their mobility, no changes in the tumor mass are observed. On the other hand, the tumor cells are less invasive than in the case without therapy, and at the end of the simulation, namely after the 6 weeks of therapy, they show a larger concentration in the neighborhood of their initial location. In Figure 3.6 also the main fiber direction is shown. We observe that, when chemotherapy is considered, the cells tend to remain clustered in the area of high alignment of the fibers, being less able to change direction and spread inside the brain due to the effect of the therapy on the integrin/ECM binding. Finally, we test the effect of radiotherapy, whose objective is killing cells. The results are shown in Figure 3.7, where the difference in the cell density between the model without any therapy and the complete model with both chemo- and radiotherapy is considered. After 6 weeks one can observe a stronger reduction of the tumor density with respect to the situation 3 weeks before, represented by larger areas of positive difference. This is particularly evident in the areas where, due to the chemotherapy effects observed in Figure 3.6, the cells are more concentrated (i.e., the blue areas of Figure 3.6).

[5]Reports on the clinical trials are provided at https://clinicaltrials.gov

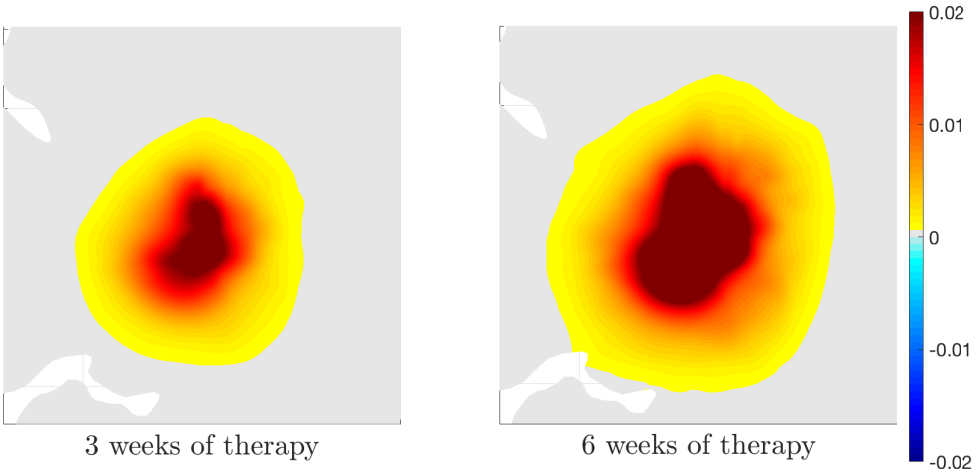

FIGURE 3.7: **Scenario (C).** Difference between the tumor density in the no-therapy model and in the case in which both chemo- and radiotherapy are considered. For the construction of $\mathbf{D}_T$ the ODF is used.

3.4 *Summary*

The influence of the brain tissue architecture on tumor cell migration, described in Chapter 2, represents the central focus of the DTI-based multiscale model setting proposed in this chapter. Starting from the works proposed in [74, 126], we described the influence of brain fibers on glioma growth and spread and elaborated on the effects of combined treatments of chemo- and radiotherapy on tumor evolution. The multiscale formulation integrates, within the same framework, the dynamics of integrins receptors, the mesoscopic description of cell-ECM interactions as the onset of tumor proliferation, and a specific therapeutic approach including inhibitors of cell-tissue bindings. The macroscopic equation for the tumor cell density - derived from the mesoscale via a parabolic scaling - accounts for real data of the brain structure through the tensor $\mathbf{D}_T$ that depends on a local fiber distribution function. In particular, the comparison between the different fiber distribution functions, performed in Section 2.3.4, was here further investigated, analyzing the response of the tumor cells to the different descriptions of the fiber network.

The simulations show how different choices of this distribution can influence the results, in terms of extension of the neoplastic area, shape, tumor infiltration, and emergence of heterogenous patterns (as shown in Figures 3.3 and 3.4). The role of the fibers in guiding cell movement and glioma invasion clearly emerges, as shown in Figure 3.5. In line with previous approaches based on a multiscale framework (see for instance [74, 75, 77]), this figure also shows the importance of including in the model the microscopic dynamics that allow the emergence of evident anisotropic behaviors as the tumor progresses. The resulting tumor evolution reflects the features (e.g. branched patterns or heterogeneous distribution) that are often observed in the clinic. Moreover, the proposed multiscale framework gives the possibility of including, at various levels in the model formulation, emerging treatments, related to integrins inhibition, combined with standard approaches, whose effect on tumor invasion and migration in the tissue are clearly shown in Figures 3.6 and 3.7.

The validation of the results related to the fiber distribution choice, via comparison of the simulated tumor evolution with longitudinal clinical data, as well as of the results from combined treatments remains a future objective since only data for healthy

brain structures were available for this study. In fact, the acquisition of the desired data presents several issues, mainly related to the fast evolution characterizing this disease, often discovered already at a late stage of progression. However, for the global aim of this dissertation, the proposed setting in this chapter represents an important base, on which the following models will be built. In fact, several processes have not been included so far, such as intratumor heterogeneity or micro-environmental factors evolving together with cancer cells. In the forthcoming Chapters 4 and 5, we will see how this setting can be extended to include some of these aspects, mainly related to intratumor heterogeneity and tumor-associated angiogenesis.

4 Intratumor heterogeneity, vasculature, and acidity

Glioma development, growth, and invasion are influenced by a multitude of intrinsic and extrinsic factors. In Chapter 3, we mainly focused on the contribution of the fiber network to the contact guidance phenomenon driving cell migration. Conversely, in this chapter we describe the impact of tumor heterogeneity, tissue acidity, and the vasculature component of the tumor microenvironment on the cell growth and migration.

The ***phenotypic heterogeneity*** of the glioma population is a highly debated topic. Several experiments with cultures of glioma cells suggest mutual exclusion of migratory and proliferative behavior, as reviewed e.g. in [21, 100, 303]; this characteristic is known as *go-or-grow dichotomy* [98, 99]. Biological evidence indicates that migratory and proliferative processes share common signaling pathways, suggesting a unique intracellular mechanism that regulates both phenotypes [100]. However, the biological community is divided, and this issue is still under investigation, especially for the case of neoplasms at an advanced stage. Concerning tumor microenvironment, ***hypoxia is*** one of its prominent traits, especially for glioma neoplasms, as we described in Section 1.1.2. It has been suggested (see e.g. [123, 303] and references therein) that hypoxia is putatively influencing the phenotypic switch between migrating and proliferating behavior along with other regulating factors, like angiogenesis or ECM production and degradation. Inconsistent intratumor oxygenation, caused by capillary occlusion, leads to the formation of highly hypoxic sites, acidosis, and necrosis [197]. Hypoxia is responsible for inducing acidosis through a shift in cellular metabolism generating a high acid load in the tumor microenvironment. ***Acidification of the tumor microenvironment*** from abnormal metabolism along with angiogenesis are both hallmarks of malignant brain tumors [103, 122, 290]. Acidosis (and the consequent low pH conditions) facilitate tumor invasion by producing growth factors, angiogenic factors, and proteases that degrade the extracellular matrix and promote tumor cell migration. Moreover, highly hypoxic sites determine the formation of the so-called pseudopalisade patterns, typical especially in the case of glioblastoma [33, 34, 297]. These patterns have garland-like shapes exhibiting central necrotic zones surrounded by stacks of tumor cells, most of which are actively migrating. As tumor cell proliferation is impaired at lower ***pH level***, this seems to endorse the antagonistic relationship between (transiently) migratory and proliferative phenotypes [196]. Even though cancer cells can survive in relatively hypoxic regions by anaerobic glycolysis[63, 293], the large amounts of lactate and alanine produced during this process decrease the pH below critical levels. As a consequence, cancer cells initiate re-vascularization by expressing pro-angiogenic factors, in order to provide an adequate supply with blood-transported nutrients [207, 290]. Cancer cells can deter proliferation for migration towards more favorable areas [186, 293], and the above mentioned pseudopalisade

formation represents one aspect of this complex behavior.

In this chapter, we develop a multiscale model for the description of glioma invasion relying on the go-or-grow dichotomy, representing intratumor heterogeneity, and the influence of vasculature, acidity, and brain tissue anisotropy on tumor progression. In the previous chapter (Chapter 3), we proposed a mesoscopic description of glioma density in interaction with the anisotropic brain tissue that took into account the subcellular dynamics of receptor binding to tissue fibers. In what follows, we extend this setting by including two tumor phenotypes, the dynamics of endothelial cells developing vasculature and the acidity (caused by hypoxia), where the two latter are responsible for the phenotypic switch. The microscopic dynamics of tumor membrane receptors responsible for the interaction with both tissue and extracellular protons are included in a system of kinetic transport PDEs for glioma and endothelial cells, whose upscaling of the kinetic transport PDEs leads, in the parabolic limit, to a system of advection-diffusion-reaction equations. These equations feature several types of taxis, nonlinear myopic diffusion of glioma, and elaborate coupling between the variables of the model. The multiscale character of the setting is clearly shown in the taxis coefficients, which encode information from the lower modeling levels.

Concerning the mechanisms related to intratumor heterogeneity, tumor angiogenesis, and the emergence of hypoxic and necrotic regions, the mathematical literature mainly characterizes to model types, purely macroscopic or multiscale models. Some examples of the macroscopic models describing the evolution of glioma cell density in relation to angiogenic events, and consequently hypoxia-driven phenomena can be found e.g. in [185, 276], while proper references on mathematical models for cancer invasion and patterning under acidic conditions were introduced in [94, 189, 261]. Tumor heterogeneity in the continuous setting has been modeled by defining the dynamics of the corresponding subpopulations of cells, e.g. hypoxic/normoxic/necrotic cells [185, 276] or moving/proliferating cells [96, 225]. The main multiscale settings proposed for addressing the problem of the intratumor heterogeneity are described in [75, 126, 192, 265, 310], while analysis of acid-mediated tumor development, directly related or applicable to pH-influenced glioma spread, as well as some aspects of tumor-associated hypoxia, can be found in [76, 152, 192, 264].

The content of this chapter is organized as follows. In Section 4.1, we describe the setup of the model on the subcellular and mesoscopic scales and the deduction of the macroscopic PDEs. Then, in Section 4.2, we concretize the coefficient functions involved in the macroscopic setting, providing a proper estimation of the model parameters and the non-dimensionalization of the setting. In Section 4.3, we present the numerical simulations of the macroscopic model analyzing different scenarios. The goal of these simulations is to study the sensitivity of the models to special parameters and the influence of the go-or-growth dichotomy on the overall system dynamics. Moreover, to facilitate the evaluation of the tumor burden in relation to the necrotic and the normal tissue, in Section 4.4 we include a model extension accounting for the dynamics of the latter. In particular, the model extension is helpful for the analysis of a necrosis-based tumor grading scheme, which we is used for the evaluation of the tumor stage in different conditions.

The results of this chapter have been collected in the paper by Conte and Surulescu submitted for publication [56].

4.1 *Modeling setting*

Relying on the go-or-grow dichotomy, which states that a single cell can either proliferate, without moving, or migrate, and can switch between the two phenotypes, we consider a tumor containing these two mutually exclusive subpopulations of cells, named as migrating cells and proliferating cells. The respective states are transient and the tumor can change dynamically its composition, according to the signals received by the cells from their surroundings. From the large variety of chemical and physical cues present in the extracellular space [110], we investigate the association between microenvironment acidification and angiogenesis, both hallmarks of malignant glioma [122, 290]. Since acidity and angiogenesis are tightly interrelated and crucial for the tumor evolution, we also model vascularization, by way of endothelial cell dynamics. Starting on the framework presented in the previous chapter, the extension proposed here considers three different levels.

- The microscopic level, where we recall the dynamics of the integrin receptors on the tumor cell membrane, mediating cells binding with the brain fibers, and we couple them with a second class of receptors responsible for the interaction with the extracellular protons. In particular, the interactions between cells and soluble as well as unsoluble ligands follow the idea of building a micro-meso model for tumor invasion with multiple tactic terms revisited in several works for cell-tissue interactions (see e.g. [54, 74, 75, 169] and references therein) and for cell-proton interactions [152].

- The mesoscopic level, where the corresponding kinetic transport equations for glioma cells of the two phenotypes and endothelial cells are described; these equations model the interactions between the two subpopulations of tumor cells as well as between tumor, vasculature, pH levels, and tissue.

- The macroscopic level, which is deduced via the parabolic limit of the mesoscopic equation, leading to a macroscopic system of advection-diffusion-reaction PDEs for the involved quantities: total tumor burden (moving and proliferating cells), endothelial cells, and pH level (expressed through the concentration of protons). The resulting system includes anisotropic diffusion along the directions characterized by the fiber orientation, several types of taxis, such as haptotaxis or pH-taxis. The latter is a repellent mechanism describing the tendency of tumor cells to move away from hypoxic regions, where the cellular metabolic shift determines a decrease in the pH level. The macroscopic setting also features the phenomena of tissue- and acid-mediated proliferation and death processes.

4.1.1 *Subcellular level*

On the microscopic scale, we describe the interaction of glioma cells with the extracellular space, more precisely with tissue fibers and protons. As we described in the introductory chapter, cells exchange information with their environment through various transmembrane entities, e.g. cell surface receptors and ion channels. In particular, in the modeling, the former is used to account for cell-tissue interactions, while both are employed for the cell-proton exchange. In addition to ion channels and membrane transporters which have been extensively studied in the context of intra- and extracellular pH regulation, there also exist proton-sensing receptors [121], e.g. the G protein-coupled receptors (GPCRs) involved among others in regulating the migration and proliferation of cells in tumor development and wound healing [133, 294].

We neglect here the details of the intracellular machinery activated by receptor binding and channel opening and closing. Instead, we see the events of occupying such transmembrane units as triggering the cellular processes leading to migration, proliferation, and phenotypic switch.

We denote by $y_1(t)$ the amount of receptors bound to tissue fibers and by $y_2(t)$ that of transmembrane entities (ion channels, pH-sensing receptors) occupied by protons. The corresponding binding/occupying dynamics are characterized by simple mass action kinetics:

$$\bar{R}_0 - (y_1 + y_2) \; + \; \frac{Q}{Q^*} \underset{k_1^-}{\overset{k_1^+}{\rightleftharpoons}} \; y_1$$

$$\bar{R}_0 - (y_1 + y_2) \; + \; \frac{S}{S_{c,0}} \underset{k_2^-}{\overset{k_2^+}{\rightleftharpoons}} \; y_2.$$

Here, $\bar{R}_0$ is the total amount of receptors on a cell membrane, $Q(\mathbf{x})$ denotes the macroscopic tissue density, depending on the position $\mathbf{x} \in \mathbb{R}^d$, $Q^*(\mathbf{x})$ is the reference tissue density, while $S(t, \mathbf{x})$ is the macroscopic concentration of protons and $S_{c,0}(\mathbf{x})$ the reference proton concentration. Accordingly, we get the ODE system

$$\begin{aligned} \dot{y_1} &= \frac{k_1^+}{Q^*} Q \left(\bar{R}_0 - (y_1 + y_2)\right) - k_1^- y_1 \\ \dot{y_2} &= \frac{k_2^+}{S_{c,0}} S \left(\bar{R}_0 - (y_1 + y_2)\right) - k_2^- y_2 \,, \end{aligned}$$

where k_1^+ and k_1^- represent the attachment and detachment rates of cells to tissue, respectively, while k_2^+ and k_2^- are the corresponding rates in the process of proton binding. As in [76], we define the *activity variable* $y := y_1 + y_2$ as the total amount of transmembrane entities occupied by tissue or protons, which allows us to lump together the two ODEs into

$$\dot{y} = \left(\frac{k_1^+}{Q^*} Q + \frac{k_2^+}{S_{c,0}} S \right) \left(\bar{R}_0 - y\right) - k_1^- y_1 - k_2^- y_2 \,.$$

Assuming that $k_1^- = k_2^- = k^-$, we obtain the microscopic equation for the subcellular dynamics

$$\dot{y} = \left(\frac{k_1^+}{Q^*} Q + \frac{k_2^+}{S_{c,0}} S \right) \left(\bar{R}_0 - y\right) - k^- y \,.$$

Since processes on this scale are much faster than those happening on the macroscopic time scale, they can be assumed to equilibrate rapidly. Moreover, on this scale we can ignore the time dependence of S. Rescaling $y/\bar{R}_0 \rightsquigarrow y$ will further simplify the notation. Then, the unique steady state of the above equation is given by:

$$y^* = \frac{\frac{k_1^+}{Q^*} Q + \frac{k_2^+}{S_{c,0}} S}{\frac{k_1^+}{Q^*} Q + \frac{k_2^+}{S_{c,0}} S + k^-} =: \bar{f}\left(Q, S\right) \,.$$

In line with the first setting introduced in Chapter 3, the activity variable y can be seen as characterizing the overall cell internal state. In the sequel, we consider the mesoscopic densities $\rho(t, \mathbf{x}, \mathbf{v}, y)$ and $r(t, \mathbf{x}, y)$ of migrating and respectively non-moving and proliferating glioma cells, hence both depending on such activity variable y.

Further, we assume that the glioma cells follow the tissue gradient, but move away from highly acidic areas. Therefore, we look at the path of a single cell starting at position $\mathbf{x}_0$ and moving to position $\mathbf{x}$ with velocity $\mathbf{v}$ in the (locally) time-invariant density fields Q and S, so that $Q(\mathbf{x}) = Q(\mathbf{x}_0 + \mathbf{v}t)$, while $S(\mathbf{x}) = S(\mathbf{x}_0 - \mathbf{v}t)$. Defining by $z := y^* - y$ the deviation of y from its steady state, we have:

$$\dot{z} = \frac{\partial \bar{f}}{\partial Q}\,\mathbf{v}\cdot\nabla Q - \frac{\partial \bar{f}}{\partial S}\,\mathbf{v}\cdot\nabla S - z\left(\frac{k_1^+}{Q^*}Q + \frac{k_2^+}{S_{c,0}}S + k^-\right),$$

with

$$\frac{\partial \bar{f}}{\partial Q} = \frac{1}{Q^*}\frac{k_1^+ k^-}{\left(\frac{k_1^+}{Q^*}Q + \frac{k_2^+}{S_{c,0}}S + k^-\right)^2}$$
$$\frac{\partial \bar{f}}{\partial S} = \frac{1}{S_{c,0}}\frac{k_2^+ k^-}{\left(\frac{k_1^+}{Q^*}Q + \frac{k_2^+}{S_{c,0}}S + k^-\right)^2}.$$

Thus the equation for z is given by:

$$\dot{z} = -z\left(\frac{k_1^+}{Q^*}Q + \frac{k_2^+}{S_{c,0}}S + k^-\right) + \frac{k^-}{\left(\frac{k_1^+}{Q^*}Q + \frac{k_2^+}{S_{c,0}}S + k^-\right)^2}\left(\frac{k_1^+}{Q^*}\mathbf{v}\cdot\nabla Q - \frac{k_2^+}{S_{c,0}}\mathbf{v}\cdot\nabla S\right)$$
$$=: G(z, Q, S)\,.$$

For reason of simplicity we define $B(Q,S) := \left(\frac{k_1^+}{Q^*}Q + \frac{k_2^+}{S_{c,0}}S + k^-\right)$.

4.1.2 *Mesoscopic level*

We model the mesoscale behavior of glioma and endothelial cells with the aid of kinetic transport equations (KTEs) taking into account the subcellular dynamics. Concretely, we consider the following cell density functions:

- $\rho(t, \mathbf{x}, \mathbf{v}, y)$ for moving glioma cells;
- $r(t, \mathbf{x}, y)$ for non-moving, hence (in virtue of the go-or-grow dichotomy) proliferating glioma cells;
- $w(t, \mathbf{x}, \vartheta)$ for endothelial cells (ECs) forming capillaries,

with the time and space variables $t > 0$ and $\mathbf{x} \in \mathbb{R}^d$, velocities $\mathbf{v} \in \mathbf{V} = s\mathbb{S}^{d-1}$ and $\vartheta \in \Theta = \sigma\mathbb{S}^{d-1}$, and the activity variable $y \in \mathbf{Y} = (0,1)$. These choices mean that we assume for glioma and ECs constant speeds $s > 0$ and $\sigma > 0$, respectively, where $\mathbb{S}^{d-1}$ denotes the unit sphere in $\mathbb{R}^d$. As in the previously introduced model, in the sequel we work with the deviation $z = y^* - y \in \mathbf{Z} \subseteq (y^* - 1, y^*)$ rather than with y. The corresponding macroscopic cell densities are denoted by $M(t,\mathbf{x})$, $R(t,\mathbf{x})$ and $W(t,\mathbf{x})$, respectively, and we use the notation $N(t,\mathbf{x}) := M(t,\mathbf{x}) + R(t,\mathbf{x})$ for the space-time varying macroscopic total tumor burden.

The kinetic transport equation for the ***motile glioma phenotype*** is given by:

$$\frac{\partial \rho}{\partial t} + \nabla\cdot(\mathbf{v}\rho) + \frac{\partial}{\partial z}\left(G(z,Q,S)\rho\right) = \mathcal{L}_\rho[\lambda(z)]\rho + \beta(S)\frac{q}{\omega}r - \alpha(w,S)\rho - l_m(N)\rho\,, \quad (4.1)$$

where $\mathcal{L}_\rho[\lambda(z)]$ is the turning operator, while $\beta(S)\frac{q}{\omega}$, $\alpha(w,S)$, and $l_m(N)$ are the terms describing the phenotypic switches. Precisely, $\mathcal{L}_\rho[\lambda(z)]\rho$ denotes the turning operator describing velocity changes. As for the previous model, the dominating directional cue is related to the contact guidance phenomenon, given by the orientation of tissue fibers: the cells have a tendency to align to the white matter tracts, mainly associated with the brain tissue anisotropy. $\mathcal{L}_\rho[\lambda]\rho$ is a Boltzmann-like integral operator of the form

$$\mathcal{L}_\rho[\lambda(z)]\rho = -\lambda(z)\rho + \lambda(z)\int_{\mathbf{V}} K(\mathbf{x},\mathbf{v})\,\rho(\mathbf{v}')\,d\mathbf{v}'\,,$$

where $\lambda(z) := \lambda_0 - \lambda_1 z \geq 0$ is the cell turning rate depending on the microscopic variable z, while λ_0 and λ_1 are positive constants. The integral term, describing the reorientation of cells, is controlled by the turning kernel $K(\mathbf{x},\mathbf{v})$, whose expression (3.15) has been provided in Section 3.2.2. We recall that $\hat{\mathbf{v}} = \frac{\mathbf{v}}{|\mathbf{v}|} \in \mathbb{S}^{d-1}$ and $q(\mathbf{x},\hat{\mathbf{v}})$ is the orientational distribution of the fibers; moreover, we still assume the tissue network to be unpolarized and, in the subsequent, we use the symmetry property on $q(\mathbf{x},\hat{\mathbf{v}})$ together with the notations (3.16) and (3.17) introduced in the previous chapter.

The term $\beta(S)\frac{q}{\omega}r$ in (4.1) describes the phenotypic switch from the proliferation to the motile state, namely the transition $r \to \rho$; the rate β depends on S, since hypoxic and, consequently, too acidic environment the cells are supposed to stop proliferation and migrate towards regions with higher pH. Therefore, we assume that $\beta(S)$ is an increasing function of the proton concentration S and we require $\beta(S) > 0$, since there will always be some proliferating cells switching into a migratory regime, otherwise the tumor would stay confined, which is not the case for gliomas, and especially glioblastomas.

The terms $\alpha(w,S)\rho$ and $l_m(N)\rho$ model the phenotypic switch $\rho \to r$ due to environmental signals. Thus, the former depends on the proton concentration S and on the mesoscopic EC density w and describes the adoption of a proliferative phenotype when there are enough oxygen and nutrient supplies, while the pH level remains below a certain threshold. The latter models the switch to proliferation caused by the glioma cell population being too crowded to allow effective migration (but still allowing some limited proliferation).

The evolution of ***proliferating tumor cells*** is characterized by the integro-differential equation

$$\begin{aligned}\frac{\partial r}{\partial t} =&(\alpha(w,S)+l_m(N))\int_{\mathbf{V}}\rho(t,\mathbf{x},\mathbf{v},z)\,d\mathbf{v} + \mu(W,N,S)\int_{\mathbf{Z}}\chi(\mathbf{x},z,z')\frac{Q(\mathbf{x})}{Q^*}r(t,\mathbf{x},z')dz' \\ &-(\beta(S)+\gamma(S))r\,,\end{aligned} \tag{4.2}$$

where, additionally to the already described switch terms, we model intrinsic proliferation and death. In particular, the growth term

$$\mathcal{P}(r) := \mu(W,N,S)\int_{\mathbf{Z}}\chi(\mathbf{x},z,z')\frac{Q(\mathbf{x})}{Q^*}r(z')dz'$$

describes, as in the previous setting, proliferation triggered by cell receptor binding to tissue. The kernel $\chi(\mathbf{x},z,z')$ has the same properties as described in Section 3.2.2, but, in this model, the proliferation rate $\mu(W,N,S)$ depends on the total macroscopic tumor density N, on the concentration of protons S, and on the vasculature W.

The last term $-\gamma(S)r$ describes acid-induced death of glioma cells when the pH

value drops below a certain threshold. Even if cancer cells have developed a strong resistant phenotype that allows them to survive in an acidic environment, where healthy cells normally die, below a much lower pH threshold also cancer cells undergo apoptosis and consequently death. In particular, while in normal circumstances cells start to die when the pH drops below values of approximately 6.7, cancer cells are able to survive until pH-values of 6.4-6.5. The precise threshold values is discussed in Section 4.2.

The KTE for ***endothelial cells*** is given by:

$$\frac{\partial w}{\partial t} + \nabla \cdot (\vartheta w) = \mathcal{L}_w[\eta]w + \mu_W(W, Q)w\,, \tag{4.3}$$

where the turning operator $\mathcal{L}_w[\eta]w$ describes changes in the orientation of ECs. It is well-established (see e.g. [110]) that tumor cells produce angiogenic signals acting as chemoattractants for ECs. Less known is whether such signals are expressed by proliferating rather than moving cells or by both phenotypes. There is, however, evidence that hypoxia induces the production of VEGF and other angiogenic cytokines (see e.g. [50, 207, 304] and references therein). Since cancer cells are highly glycolytic - which leads to acidification - and increased glucose metabolism is selected in proliferating cells [176], we assume that pro-angiogenic signals are mainly produced by proliferating cells. Intending to avoid the introduction of a new variable for the concentration of such chemoattractants, we let the ECs be attracted by the proliferating glioma cells as main sources therewith. This translates into the following form of the turning operator acting on the right-hand side in (4.3):

$$\mathcal{L}_w[\eta]w = -\eta(\mathbf{x}, \vartheta, R)w(t, \mathbf{x}, \vartheta) + \int_\Theta \frac{1}{|\Theta|}\eta(\mathbf{x}, \vartheta', R)w(\vartheta')d\vartheta'\,,$$

where, for the turning kernel modeling ECs reorientations, we simply take a uniform density function over the unit sphere $\mathbb{S}^{d-1}$ and

$$\eta(\mathbf{x}, \vartheta, R) = \eta_0(\mathbf{x})e^{-a(R)D_tR} \tag{4.4}$$

represents the turning rate of ECs. It depends on the macroscopic density of proliferating tumor cells R and on the pathwise gradient $D_tR = \partial_t R + \vartheta \cdot \nabla R$, where D_tR denote the total derivate of R with respect to time. The coefficient function $a(R)$ is related to the interactions between ECs and proliferating glioma, more precisely ECs and pro-angiogenic signals produced by the latter. This can be described for instance via equilibrium of EC receptor binding. This way to include directional bias provides an alternative to that using a transport term with respect to the activity variable z in (4.1) and it has been introduced in [213] in the context of bacteria movement. Under certain conditions, the relation between the two approaches was established rigorously for bacteria chemotaxis in [223] and investigated more formally for glioma repellent pH-taxis in [152].

Finally, $\mu_W(W, Q)w$ is the proliferation term for ECs. Besides the total population of ECs irrespective of their orientation, μ_W is supposed to depend on the available macroscopic tissue Q. The concrete choices of the coefficient functions involved in (4.1), (4.2), and (4.3) are provided in Section 4.2.

4.1.3 *Parabolic scaling of the mesoscopic model*

Considering that clinicians are interested in the macroscopic evolution of the tumor along with its vascularization and acidity profile, we decide to deduce effective equations for the macroscopic dynamics of ECs and the total tumor burden $N = R + M$, instead of considering the simulations of the high dimensional KTE system (4.1), (4.2), and (4.3). In particular, we assume that the PDE for the proton concentration S is already macroscopic and, therefore, does not need to be upscaled. In fact, it is not necessary to include microscopic or mesoscopic variables (such as the microscopic velocity) in the protons equation, since the protons do not undergo particular velocity dynamics.

First we define the moments for the mesoscopic variables ρ, r, and w as

$$
\begin{aligned}
m(t,\mathbf{x},\mathbf{v}) &= \int_{\mathbf{Z}} \rho(t,\mathbf{x},\mathbf{v},z)dz\,, & m^z(t,\mathbf{x},\mathbf{v}) &= \int_{\mathbf{Z}} z\rho(t,\mathbf{x},\mathbf{v},z)dz\,,\\
R(t,\mathbf{x}) &= \int_{\mathbf{Z}} r(t,\mathbf{x},z)dz\,, & R^z(t,\mathbf{x}) &= \int_{\mathbf{Z}} zr(t,\mathbf{x},z)dz\,,\\
M(t,\mathbf{x}) &= \int_{\mathbf{V}} m(t,\mathbf{x},\mathbf{v})d\mathbf{v}\,, & M^z(t,\mathbf{x}) &= \int_{\mathbf{V}} m^z(t,\mathbf{x},\mathbf{v})d\mathbf{v}\,,\\
W(t,\mathbf{x}) &= \int_{\Theta} w(t,\mathbf{x},\vartheta)d\vartheta\,,
\end{aligned}
$$

and we neglect the higher order moments with respect to the variable z, in virtue of the subcellular dynamics being much faster than the events on the higher scales, hence $z \ll 1$. We assume the functions ρ and r to be compactly supported in the phase space $\mathbb{R}^d \times \mathbf{V} \times \mathbf{Z}$ and w to be compactly supported in $\mathbb{R}^d \times \Theta$.

We first integrate equation (4.1) with respect to z, obtaining the following equation for $m(t,\mathbf{x},\mathbf{v})$:

$$
\frac{\partial m}{\partial t} + \nabla\cdot(\mathbf{v}m) = -\lambda_0\left(m - \frac{q}{\omega}M\right) + \lambda_1\left(m^z - \frac{q}{\omega}M^z\right) + \beta(S)\frac{q}{\omega}R - \alpha(w,S)m - l_m(N)m\,. \tag{4.5}
$$

Then, integrating equation (4.2) with respect to z we get

$$
\frac{\partial R}{\partial t} = (\alpha(w,S) + l_m(N))\,M + \int_{\mathbf{Z}} \mu(W,N,S)\int_{\mathbf{Z}} \chi(z,z',\mathbf{x})r(z')\frac{Q}{Q^*}dz'dz - (\beta(S)+\gamma(S))\,R\,.
$$

Using the fact that $\chi(z,z',\mathbf{x})$ is a probability kernel with respect to z, the previous equation for $R(t,\mathbf{x})$ reduces to:

$$
\frac{\partial R}{\partial t} = (\alpha(w,S) + l_m(N))\,M + \mu(W,N,S)\frac{Q}{Q^*}\,R - (\beta(S)+\gamma(S))\,R\,. \tag{4.6}
$$

We proceed by multiplying equation (4.1) by z and integrating with respect to z, obtaining

$$
\begin{aligned}
\frac{\partial m^z}{\partial t} = &-\nabla\cdot(\mathbf{v}m^z) + \int_{\mathbf{Z}} z\frac{\partial}{\partial z}\left[\left(zB(Q,S) + \frac{k^-}{B(Q,S)^2}\left(\frac{k_1^+}{Q^*}\mathbf{v}\cdot\nabla Q - \frac{k_2^+}{S_{c,0}}\,\mathbf{v}\cdot\nabla S\right)\right)\rho(z)\right]dz\\
&+ \int_{\mathbf{Z}} z\mathcal{L}_\rho[\lambda(z)]\rho(z)dz + \beta(S)\frac{q}{\omega}R^z - (\alpha(w,S)+l_m(N))m^z\,.
\end{aligned}
$$

The calculation of the integral terms leads to the following equation for $m^z(t, \mathbf{x}, \mathbf{v})$:

$$\begin{aligned}\frac{\partial m^z}{\partial t} =& -\nabla\cdot(\mathbf{v}m^z) - B(Q,S)m^z + \frac{k^-}{B(Q,S)^2}\left(\frac{k_1^+}{Q^*}\mathbf{v}\cdot\nabla Q - \frac{k_2^+}{S_{c,0}}\mathbf{v}\cdot\nabla S\right)m \\ & -\lambda_0 m^z + \lambda_0\frac{q}{\omega}M^z + \beta(S)\frac{q}{\omega}R^z - (\alpha(w,S)+l_m(N))m^z\,.\end{aligned} \tag{4.7}$$

Applying the same procedure to equation (4.2) we obtain the following equation for $R^z(t, \mathbf{x})$:

$$\begin{aligned}\frac{\partial R^z}{\partial t} =& \left(\alpha(w,S)+l_m(N)\right)M^z + \mu(W,N,S)\frac{Q}{Q^*}\int_{\mathbf{Z}}\int_{\mathbf{Z}} z\chi(\mathbf{x},z,z')r(z')dz'dz \\ & -\left(\beta(S)+\gamma(S)\right)R^z\,.\end{aligned} \tag{4.8}$$

Considering, now, the derived equations (4.5), (4.6), (4.7), (4.8), and the KTE for ECs (4.3), we rescale the time and space variables as $t \to \varepsilon^2 t$ and $\mathbf{x} \to \varepsilon\mathbf{x}$. In particular, the proliferation terms in (4.2) and (4.3) and the death term in (4.2) are scaled by ε^2 in order to account for the mitotic and apoptotic events taking place on a much larger time scale than migration and switching from moving to non-moving regimes. Hence, collecting the resulting equations we have:

$$\begin{aligned}\varepsilon^2\frac{\partial m}{\partial t} + \varepsilon\nabla\cdot(\mathbf{v}m) =& -\lambda_0\left(m - \frac{q}{\omega}M\right) + \lambda_1\left(m^z - \frac{q}{\omega}M^z\right) + \beta(S)\frac{q}{\omega}R \\ & -\alpha(w,S)m - l_m(N)m\,,\end{aligned} \tag{4.9}$$

$$\varepsilon^2\frac{\partial R}{\partial t} = \left(\alpha(w,S)+l_m(N)\right)M + \varepsilon^2\mu(W,N,S)\frac{Q}{Q^*}R - \left(\beta(S)+\varepsilon^2\gamma(S)\right)R\,, \tag{4.10}$$

$$\begin{aligned}\varepsilon^2\frac{\partial m^z}{\partial t} =& -\varepsilon\nabla\cdot(\mathbf{v}m^z) - B(Q,S)m^z + \frac{\varepsilon k^-}{B(Q,S)^2}\left(\frac{k_1^+}{Q^*}\mathbf{v}\cdot\nabla Q - \frac{k_2^+}{S_{c,0}}\mathbf{v}\cdot\nabla S\right)m \\ & + \int_{\mathbf{Z}} z\mathcal{L}_\rho[\lambda(z)]\rho(z)dz + \beta(S)\frac{q}{\omega}R^z - (\alpha(w,S)+l_m(N))m^z\,,\end{aligned} \tag{4.11}$$

$$\begin{aligned}\varepsilon^2\frac{\partial R^z}{\partial t} =& \left(\alpha(w,S)+l_m(N)\right)M^z + \varepsilon^2\mu(W,N,S)\frac{Q}{Q^*}\int_{\mathbf{Z}}\int_{\mathbf{Z}} z\chi(\mathbf{x},z,z')r(z')dz'dz \\ & -\left(\beta(S)+\varepsilon^2\gamma(S)\right)R^z\,,\end{aligned} \tag{4.12}$$

$$\varepsilon^2\frac{\partial w}{\partial t} + \varepsilon\nabla\cdot(\vartheta w) = \mathcal{L}_w[\eta^\varepsilon]w + \varepsilon^2\mu_W(W,Q)w\,, \tag{4.13}$$

with

$$\eta^\varepsilon(\mathbf{x},\vartheta,R) = \eta_0(\mathbf{x})\exp\Big(-a(R)(\varepsilon^2\partial_t R + \varepsilon\vartheta\cdot\nabla R)\Big).$$

Considering the Hilbert expansions for the introduced moments:

$$m(t,\mathbf{x},\mathbf{v}) = \sum_{k=0}^{\infty} \varepsilon^k m_k, \qquad m^z(t,\mathbf{x},\mathbf{v}) = \sum_{k=0}^{\infty} \varepsilon^k m_k^z, \qquad R(t,\mathbf{x}) = \sum_{k=0}^{\infty} \varepsilon^k R_k,$$

$$M(t,\mathbf{x}) = \sum_{k=0}^{\infty} \varepsilon^k M_k, \qquad M^z(t,\mathbf{x}) = \sum_{k=0}^{\infty} \varepsilon^k M_k^z, \qquad R^z(t,\mathbf{x}) = \sum_{k=0}^{\infty} \varepsilon^k R_k^z,$$

$$w(t,\mathbf{x},\vartheta) = \sum_{k=0}^{\infty} \varepsilon^k w_k, \qquad W(t,\mathbf{x}) = \sum_{k=0}^{\infty} \varepsilon^k W_k,$$

we first define the Taylor-expansion of the coefficient functions involving any of w, W, R, M or N in the scaled equations (4.9), (4.10), (4.11), (4.12), and (4.13):

$$\alpha(w,S) = \alpha(w_0,S) + \partial_w\alpha(w_0,S)\,(w-w_0) + \frac{1}{2}\partial_{ww}^2\alpha(w_0,S)\,(w-w_0)^2 + \mathcal{O}(|w-w_0|^3),$$

$$l_m(N) = l_m(N_0) + l_m'(N_0)\,(N-N_0) + \frac{1}{2}l_m''(N_0)\,(N-N_0)^2 + \mathcal{O}(|N-N_0|^3),$$

$$\mu(W,N,S) = \mu(W_0,N_0,S) + \partial_W\mu(W_0,N_0,S)(W-W_0) + \partial_N\mu(W_0,N_0,S)(N-N_0) + \mathcal{O}(\varepsilon^2),$$

$$\mu_W(W,Q) = \mu_W(W_0,Q) + \partial_W\mu_W(W_0,Q)(W-W_0) + \mathcal{O}(|W-W_0|^2),$$

$$\eta^\varepsilon(\mathbf{x},\vartheta,R) = \eta_0(\mathbf{x})\Big[1 - \varepsilon a(R)\vartheta\cdot\nabla R + \varepsilon^2\Big(-a(R)\partial_t R + \frac{1}{2}(a(R))^2(\vartheta\cdot\nabla R)^2\Big) + \mathcal{O}(\varepsilon^3)\Big],$$

$$a(R) = a(R_0) + a'(R_0)(R-R_0) + \frac{1}{2}a''(R_0)(R-R_0)^2 + \mathcal{O}(|R-R_0|^3).$$

Then, equating the powers of ε in the scaled equations (4.9), (4.10), (4.11), (4.12), and (4.13), we obtain:

ε^0 terms:

$$0 = -\lambda_0\left(m_0 - \frac{q}{\omega}M_0\right) + \lambda_1\left(m_0^z - \frac{q}{\omega}M_0^z\right) + \beta(S)\frac{q}{\omega}R_0 - \alpha(w_0,S)m_0 - l_m(N_0)m_0, \tag{4.14}$$

$$0 = \Big(\alpha(w_0,S) + l_m(N_0)\Big)M_0 - \beta(S)R_0, \tag{4.15}$$

$$0 = -\Big(B(Q,S) + \lambda_0 + \alpha(w_0,S) + l_m(N_0)\Big)m_0^z + \lambda_0\frac{q}{\omega}M_0^z + \beta(S)\frac{q}{\omega}R_0^z, \tag{4.16}$$

$$0 = \Big(\alpha(w_0,S) + l_m(N_0)\Big)M_0^z - \beta(S)R_0^z, \tag{4.17}$$

$$0 = \eta_0(\mathbf{x})(S_d^\sigma W_0 - w_0), \tag{4.18}$$

where $S_d^\sigma := \dfrac{1}{|\Theta|} = \dfrac{\sigma^{1-d}}{|\mathbb{S}^{d-1}|}$.

ε^1 terms:

$$\nabla\cdot(\mathbf{v}m_0) = -\lambda_0\left(m_1 - \frac{q}{\omega}M_1\right) + \lambda_1\left(m_1^z - \frac{q}{\omega}M_1^z\right) + \beta(S)\frac{q}{\omega}R_1 - \Big(\alpha(w_0,S) + l_m(N_0)\Big)m_1 - \Big(\partial_w\alpha(w_0,S)w_1 + l_m'(N_0)N_1\Big)m_0, \tag{4.19}$$

$$0 = \Big(\alpha(w_0,S) + l_m(N_0)\Big)M_1 + \Big(\partial_w\alpha(w_0,S)w_1 + l_m'(N_0)N_1\Big)M_0 - \beta(S)R_1, \tag{4.20}$$

$$\nabla\cdot(\mathbf{v}m_0^z) = -B(Q,S)m_1^z + \frac{k^-}{B(Q,S)^2}\left(\frac{k_1^+}{Q^*}\mathbf{v}\cdot\nabla Q - \frac{k_2^+}{S_{c,0}}\mathbf{v}\cdot\nabla S\right)m_0 - \lambda_0\Big(m_1^z - \frac{q}{\omega}M_1^z\Big) + \beta(S)\frac{q}{\omega}R_1^z - \Big(\alpha(w_0,S) + l_m(N_0)\Big)m_1^z - \Big(\partial_w\alpha(w_0,S)w_1 + l_m'(N_0)N_1\Big)m_0^z, \tag{4.21}$$

$$0 = \Big(\alpha(w_0,S) + l_m(N_0)\Big)M_1^z + \Big(\partial_w\alpha(w_0,S)w_1 + l_m'(N_0)N_1\Big)M_0^z - \beta(S)R_1^z, \tag{4.22}$$

$$\nabla\cdot(\vartheta w_0) = \eta_0(\mathbf{x})\Big(S_d^\sigma W_1 - w_1\Big) + \eta_0(\mathbf{x})a(R_0)\vartheta\cdot\nabla R_0\, w_0 - S_d^\sigma\eta_0(\mathbf{x})a(R_0)\int_\Theta w_0(\vartheta')\vartheta' d\vartheta'\cdot\nabla R_0. \tag{4.23}$$

ε^2 terms:

$$\frac{\partial m_0}{\partial t} + \nabla\cdot(\mathbf{v}m_1) = -\lambda_0\left(m_2 - \frac{q}{\omega}M_2\right) + \lambda_1\left(m_2^z - \frac{q}{\omega}M_2^z\right) + \beta(S)\frac{q}{\omega}R_2 - \left(\alpha(w_0,S) + l_m(N_0)\right)m_2 - \left(\partial_w\alpha(w_0,S)w_1 + l_m'(N_0)N_1\right)m_1 - \left(\partial_w\alpha(w_0,S)w_2 + l_m'(N_0)N_2\right)m_0 - \frac{1}{2}\left(\partial_{ww}^2\alpha(w_0,S)w_1^2 + l_m''(N_0)N_1^2\right)m_0, \tag{4.24}$$

$$\frac{\partial R_0}{\partial t} = \left(\alpha(w_0,S) + l_m(N_0)\right)M_2 + \left(\partial_w\alpha(w_0,S)w_1 + l_m'(N_0)N_1\right)M_1 + \frac{1}{2}\left(\partial_{ww}^2\alpha(w_0,S)w_1^2 + l_m''(N_0)N_1^2\right)M_0 + \left(\partial_w\alpha(w_0,S)w_2 + l_m'(N_0)N_2\right)M_0 + \mu(W_0,N_0,S)\frac{Q}{Q^*}R_0 - \beta(S)R_2 - \gamma(S)R_0, \tag{4.25}$$

$$\frac{\partial w_0}{\partial t} + \nabla\cdot(\vartheta w_1) = \eta_0(\mathbf{x})\Bigg[\Bigg(a(R_0)\partial_t R_0 + a(R_0)\vartheta\cdot\nabla R_1 + a'(R_0)R_1\vartheta\cdot\nabla R_0 - \frac{1}{2}(a(R_0)\vartheta\cdot\nabla R_0)^2\Bigg)w_0 + a(R_0)\vartheta\cdot\nabla R_0\, w_1 - w_2\Bigg] + S_d^\sigma\eta_0(\mathbf{x})\Bigg[W_2 - a(R_0)\int_\Theta \vartheta' w_1(\vartheta')d\vartheta'\cdot\nabla R_0 - a(R_0)\partial_t R_0 W_0 - \int_\Theta \vartheta' w_0(\vartheta')d\vartheta'\cdot\left(a(R_0)\nabla R_1 + a'(R_0)R_1\nabla R_0\right)$$

$$+\frac{1}{2}\int_{\Theta}(a(R_0)\vartheta'\cdot\nabla R_0)^2 w_0(\vartheta')d\vartheta'\Big] + \mu_W(W_0,Q)w_0\,. \tag{4.26}$$

We start the deduction of the macroscopic setting considering (4.15) that gives

$$R_0(t,\mathbf{x}) = \frac{\alpha(w_0,S)+l_m(N_0)}{\beta(S)}M_0(t,\mathbf{x})\,, \tag{4.27}$$

and (4.17), from which we get

$$R_0^z(t,\mathbf{x}) = \frac{\alpha(w_0,S)+l_m(N_0)}{\beta(S)}M_0^z(t,\mathbf{x})\,. \tag{4.28}$$

Then, integrating equation (4.16) with respect to the velocity $\mathbf{v}$, we have

$$0 = -B(Q,S)M_0^z + \beta(S)R_0^z - \alpha(w_0,S)M_0^z - l_m(N_0)M_0^z,$$

from which, by using (4.28), we obtain

$$\begin{aligned} M_0^z &= 0\,, \\ R_0^z &= 0\,. \end{aligned} \tag{4.29}$$

Plugging them into (4.16) leads to

$$m_0^z = 0\,. \tag{4.30}$$

Using (4.27), (4.29), and (4.30) into (4.14), we obtain:

$$\begin{aligned} 0 &= -\lambda_0 m_0 + \lambda_0\frac{q}{\omega}M_0 + \Big(\alpha(w_0,S)+l_m(N_0)\Big)\frac{q}{\omega}M_0 - \Big(\alpha(w_0,S)-l_m(N_0)\Big)m_0 \\ \Rightarrow\quad 0 &= \Big(\frac{q}{\omega}M_0 - m_0\Big)\Big(\lambda_0+\alpha(w_0,S)+l_m(N_0)\Big)\,. \end{aligned}$$

Since $\lambda_0 > 0$ and the functions $\alpha(w_0,S)$ and $l_m(N_0)$ are nonnegative for any N_0, S, w_0, we have $(\lambda_0+\alpha(w_0,S)+l_m(N_0)) \neq 0$ and, thus, we obtain

$$m_0 = \frac{q}{\omega}M_0\,. \tag{4.31}$$

From equation (4.18) we see that

$$w_0 = S_d^\sigma W_0, \tag{4.32}$$

thus, w_0 depends on the (constant) speed σ, but not on the direction $\theta \in \mathbb{S}^{d-1}$.

Now, turning to the equations stemming from the ε^1-terms, from (4.22) we get:

$$R_1^z(t,\mathbf{x}) = \frac{\alpha(w_0,S)+l_m(N_0)}{\beta(S)}M_1^z(t,\mathbf{x})\,. \tag{4.33}$$

Integrating, (4.21) with respect to the variable $\mathbf{v}$ and using (4.31) and (4.30), we obtain

$$\begin{aligned} 0 = &-B(Q,S)M_1^z + \frac{k^-}{B(Q,S)^2}M_0\, s^d\, \mathbb{E}_q\cdot\left(\frac{k_1^+}{Q^*}\nabla Q - \frac{k_2^+}{S_{c,0}}\nabla S\right) + \beta(S)R_1^z \\ &- \left(\alpha(w_0,S)+l_m(N_0)\right)M_1^z. \end{aligned}$$

Recalling that we assume the fiber network to be unpolarized, i.e., $\mathbb{E}_q = 0$, and (4.33), the previous equation leads to:

$$M_1^z = 0 \tag{4.34}$$

and hence

$$R_1^z = 0\,.$$

Now plugging these results into (4.21) we get

$$\begin{aligned} 0 = &-B(Q,S)m_1^z + \frac{k^-}{B(Q,S)^2}\left(\frac{k_1^+}{Q^*}\,\mathbf{v}\cdot\nabla Q - \frac{k_2^+}{S_{c,0}}\,\mathbf{v}\cdot\nabla S\right)m_0 - \lambda_0 m_1^z \\ &- \Big(\alpha(w_0,S) + l_m(N_0)\Big)m_1^z \\ \Rightarrow\; & m_1^z\left[B(Q,S) + \lambda_0 + \alpha(w_0,S) + l_m(N_0)\right] = \frac{k^-}{B(Q,S)^2}\left(\frac{k_1^+}{Q^*}\,\mathbf{v}\cdot\nabla Q - \frac{k_2^+}{S_{c,0}}\,\mathbf{v}\cdot\nabla S\right)m_0\,. \end{aligned}$$

We define

$$F(Q,S) := \frac{k^-}{B(S,Q)^2\left[B(Q,S) + \lambda_0 + \alpha(w_0,S) + l_m(N_0)\right]} \tag{4.35}$$

and obtain therewith the following expression for m_1^z:

$$m_1^z = F(Q,S)\left(\frac{k_1^+}{Q^*}\,\mathbf{v}\cdot\nabla Q - \frac{k_2^+}{S_{c,0}}\,\mathbf{v}\cdot\nabla S\right)m_0. \tag{4.36}$$

From equation (4.20) we have

$$R_1 = \frac{\alpha(w_0,S) + l_m(N_0)}{\beta(S)}M_1 + \frac{\partial_w\alpha(w_0,S)w_1 + l_m'(N_0)N_1}{\beta(S)}M_0. \tag{4.37}$$

Using (4.19) with (4.34) and (4.37) we derive

$$\begin{aligned} \nabla\cdot(\mathbf{v}m_0) = &-\lambda_0\left(m_1 - \frac{q}{\omega}M_1\right) + \lambda_1 m_1^z + \left(\alpha(w_0,S) + l_m(N_0)\right)\frac{q}{\omega}M_1 \\ &+ \left(\partial_w\alpha(w_0,S)w_1 + l_m'(N_0)N_1\right)m_0 - \left(\alpha(w_0,S) + l_m(N_0)\right)m_1 \\ &- \left(\partial_w\alpha(w_0,S)w_1 + l_m'(N_0)N_1\right)m_0, \end{aligned}$$

thus, we can write

$$\begin{aligned} \bar{\mathcal{L}}_m[\lambda_0 + \alpha(w_0,S) + l_m(N_0)]m_1 := &-\Big(\lambda_0 + \alpha(w_0,S) + l_m(N_0)\Big)m_1 \\ &+ \Big(\lambda_0 + \alpha(w_0,S) + l_m(N_0)\Big)\frac{q}{\omega}M_1 \\ = &\,\nabla\cdot(\mathbf{v}m_0) - \lambda_1 m_1^z\,. \end{aligned} \tag{4.38}$$

In order to get an explicit expression for m_1, we would like to invert the operator $\bar{\mathcal{L}}_m[\lambda_0 + \alpha(w_0,S) + l_m(N_0)]$. As explained in the model derivation of Section 3.2.3, we define this operator on the weighted L^2-space $L^2_q(\mathbf{V})$, in which the measure $d\mathbf{v}$ is

weighted by $q(\mathbf{x},\hat{\mathbf{v}})/\omega$. In particular, $L^2_q(\mathbf{V})$ can be decomposed as

$$L^2_q(\mathbf{V}) = < q/\omega > \oplus < q/\omega >^{\perp} .$$

Due to the properties of the chosen turning kernel, $\bar{\mathcal{L}}_m[\lambda_0 + \alpha(w_0,S) + l_m(N_0)]$ is a compact Hilbert-Schmidt operator with kernel $< q/\omega >$. We can, therefore, calculate its pseudo-inverse on $< q/\omega >^{\perp}$. Thus, to determine m_1 from (4.38) we need to check the solvability condition

$$\int_{\mathbf{V}} [\nabla\cdot(\mathbf{v}m_0) - \lambda_1 m_1^z]\, d\mathbf{v} = 0\,.$$

This condition holds thanks to (4.36) and to the symmetry of $q(\mathbf{x},\hat{\mathbf{v}})$. Therefore, we obtain from (4.38) the expression m_1

$$m_1 = -\frac{1}{\lambda_0 + \alpha(w_0,S) + l_m(N_0)}\left[\nabla\cdot(\mathbf{v}m_0) - \lambda_1 F(Q,S)\left(\frac{k_1^+}{Q^*}\,\mathbf{v}\cdot\nabla Q - \frac{k_2^+}{S_{c,0}}\,\mathbf{v}\cdot\nabla S\right) m_0\right]$$

and

$$M_1 = 0\,. \tag{4.39}$$

On the other hand, (4.23) and (4.32) give:

$$\nabla\cdot(\vartheta w_0) = -\eta_0(\mathbf{x})w_1 + \eta_0(\mathbf{x})a(R_0)\vartheta\cdot\nabla R_0 w_0 + S_d^{\sigma}\eta_0(\mathbf{x})W_1\,. \tag{4.40}$$

Likewise, we observe that the operator $\bar{\mathcal{L}}_w[\eta_0]w_1 := -\eta_0(\mathbf{x})w_1 + S_d^{\sigma}\eta_0(\mathbf{x})W_1$ can be inverted, so that (4.40) leads to

$$w_1 = -\frac{1}{\eta_0(\mathbf{x})}\nabla\cdot(\vartheta w_0) + w_0 a(R_0)\vartheta\cdot\nabla R_0 \tag{4.41}$$

and

$$W_1 = 0\,. \tag{4.42}$$

From (4.25), we derive the following expression for $\frac{\beta(S)}{\omega}R_2$:

$$\begin{aligned}\frac{\beta(S)}{\omega}R_2 = {}& \frac{1}{\omega}\Big(\alpha(w_0,S) + l_m(N_0)\Big)M_2 + \frac{1}{2\omega}\Big(\partial^2_{ww}\alpha(w_0,S)w_1^2 + l_m''(N_0)N_1^2\Big)M_0 \\ & + \frac{1}{\omega}\Big(\partial_w\alpha(w_0,S)w_2 + l_m'(N_0)N_2\Big)M_0 + \frac{\mu(W_0,N_0,S)}{\omega}\frac{Q}{Q^*}R_0 - \frac{\gamma(S)}{\omega}R_0 - \frac{1}{\omega}\frac{\partial R_0}{\partial t}.\end{aligned}$$

Plugging the previous equation into (4.24) we get

$$\begin{aligned}\frac{\partial m_0}{\partial t} = {}& -\nabla\cdot(\mathbf{v}m_1) - \lambda_0\left(m_2 - \frac{q}{\omega}M_2\right) + \lambda_1\left(m_2^z - \frac{q}{\omega}M_2^z\right) + \frac{q}{\omega}\left(\alpha(w_0,S) + l_m(N_0)\right)M_2 \\ & + \frac{q}{2\omega}\left(\partial^2_{ww}\alpha(w_0,S)w_1^2 + l_m''(N_0)N_1^2\right)M_0 + \frac{q}{\omega}\left(\partial_w\alpha(w_0,S)w_2 + l_m'(N_0)N_2\right)M_0 \\ & + \frac{q}{\omega}\mu(W_0,N_0,S)\frac{Q}{Q^*}R_0 - \frac{q}{\omega}\gamma(S)R_0 - \frac{q}{\omega}\frac{\partial R_0}{\partial t} - \left(\alpha(w_0,S) + l_m(N_0)\right)m_2 \\ & - \left(\partial_w\alpha(w_0,S)w_1 + l_m'(N_0)N_1\right)m_1 - \left(\partial_w\alpha(w_0,S)w_2 + l_m'(N_0)N_2\right)m_0\end{aligned}$$

$$- \frac{1}{2}\left(\partial^2_{ww}\alpha(w_0,S)w_1^2 + l_m''(N_0)N_1^2\right) m_0.$$

Integrating with respect to $\mathbf{v}$ we get

$$\begin{aligned}\frac{\partial M_0}{\partial t} + \int_{\mathbf{V}} \nabla\cdot(\mathbf{v}m_1)d\mathbf{v} = &\frac{1}{2}\left(\partial^2_{ww}\alpha(w_0,S)w_1^2 + l_m''(N_0)N_1^2\right) M_0 \\ &+ \left(\partial_w\alpha(w_0,S)w_2 + l_m'(N_0)N_2\right) M_0 + \mu(W_0,N_0,S)\frac{Q}{Q^*}R_0 \\ &- \gamma(S)R_0 - \partial_t R_0 - \left(\partial_w\alpha(w_0,S)w_2 + l_m'(N_0)N_2\right) M_0 \\ &- \frac{1}{2}\left(\partial^2_{ww}\alpha(w_0,S)w_1^2 + l_m''(N_0)N_1^2\right) M_0\end{aligned}$$

$$\Rightarrow \quad \frac{\partial M_0}{\partial t} + \int_{\mathbf{V}} \nabla\cdot(\mathbf{v}m_1)d\mathbf{v} = \mu(W_0,N_0,S)\frac{Q}{Q^*}R_0 - \gamma(S)R_0 - \frac{\partial R_0}{\partial t}, \tag{4.43}$$

where

$$\begin{aligned}\int_{\mathbf{V}} \nabla\cdot(\mathbf{v}m_1)d\mathbf{v} = &\int_{\mathbf{V}} \nabla\cdot\left[\mathbf{v}\left(-\frac{1}{\lambda_0+\alpha(w_0,S)+l_m(N_0)}\left(\nabla\cdot(\mathbf{v}m_0)\right.\right.\right. \\ &\left.\left.\left. - \lambda_1 F(Q,S)\left(\frac{k_1^+}{Q^*}\,\mathbf{v}\cdot\nabla Q - \frac{k_2^+}{S_{c,0}}\,\mathbf{v}\cdot\nabla S\right) m_0\right)\right)\right] d\mathbf{v} \\ = &\nabla\cdot\left[\int_{\mathbf{V}} -\frac{1}{\lambda_0+\alpha(w_0,S)+l_m(N_0)}\mathbf{v}\otimes\mathbf{v}\,\nabla\left(\frac{q}{\omega}M_0\right)\right] d\mathbf{v} \\ &+\nabla\cdot\left[\frac{\lambda_1 F(Q,S)}{\omega(\lambda_0+\alpha(w_0,S)+l_m(N_0))}\int_{\mathbf{V}}\mathbf{v}\otimes\mathbf{v}q(\mathbf{x},\hat{\mathbf{v}})d\mathbf{v}\left(\frac{k_1^+}{Q^*}\nabla Q - \frac{k_2^+}{S_{c,0}}\nabla S\right)M_0\right].\end{aligned} \tag{4.44}$$

With the notation

$$\mathbf{D}_T(\mathbf{x}) := \frac{1}{\omega}\int_{\mathbf{V}} \mathbf{v}\otimes\mathbf{v}\,q(\mathbf{x},\hat{\mathbf{v}})d\mathbf{v} = s^2\int_{\mathbb{S}^{d-1}} \hat{\mathbf{v}}\otimes\hat{\mathbf{v}}\,q(\mathbf{x},\hat{\mathbf{v}})d\hat{\mathbf{v}} = s^2\mathbb{V}_q(\mathbf{x})\,, \tag{4.45}$$

where $\mathbb{V}_q(\mathbf{x})$ is provided in (3.17), and recalling that $N_0(t,\mathbf{x}) = M_0(t,\mathbf{x}) + R_0(t,\mathbf{x})$, i.e.,

$$N_0 = \left(1 + \frac{\alpha(w_0,S)+l_m(N_0)}{\beta(S)}\right) M_0\,,$$

from (4.43) and (4.44), we obtain the following macroscopic equation for $N_0(t,\mathbf{x})$:

$$\begin{aligned}\frac{\partial N_0}{\partial t} = &\nabla\cdot\left[\frac{1}{\lambda_0+\alpha(w_0,S)+l_m(N_0)}\nabla\cdot\left(\frac{\beta(S)}{\beta(S)+\alpha(w_0,S)+l_m(N_0)}\mathbf{D}_T(\mathbf{x})N_0\right)\right] \\ &-\nabla\cdot\left[\frac{\lambda_1 F(Q,S)\beta(S)}{\lambda_0+\alpha(w_0,S)+l_m(N_0)}\mathbf{D}_T(\mathbf{x})\frac{\frac{k_1^+}{Q^*}\nabla Q - \frac{k_2^+}{S_{c,0}}\nabla S}{\beta(S)+\alpha(w_0,S)+l_m(N_0)}N_0\right]\end{aligned}$$

$$+\frac{\alpha(w_0,S)+l_m(N_0)}{\alpha(w_0,S)+l_m(N_0)+\beta(S)}N_0\left(\mu(W_0,N_0,S)\frac{Q}{Q^*}-\gamma(S)\right). \tag{4.46}$$

We denote

$$\varphi(w_0,N,S):=\frac{\beta(S)}{\beta(S)+\alpha(w_0,S)+l_m(N)}, \tag{4.47}$$

$$\varrho(w_0,N,S):=(\lambda_0+\alpha(w_0,S)+l_m(N)). \tag{4.48}$$

It is important to notice that, due to (4.18), these are, in fact, purely macroscopic quantities. Moreover, because of (4.18), equation (4.26) can be written as

$$\begin{aligned}\frac{\partial w_0}{\partial t}+\nabla\cdot(\vartheta w_1)=\eta_0(\mathbf{x})\Bigg[&\Big(a(R_0)\partial_t R_0+a(R_0)\vartheta\cdot\nabla R_1+a'(R_0)R_1\vartheta\cdot\nabla R_0\\&-\frac{1}{2}(a(R_0)\vartheta\cdot\nabla R_0)^2\Big)w_0+a(R_0)\vartheta\cdot\nabla R_0\,w_1-w_2\Bigg]\\&+S_d^\sigma\eta_0(\mathbf{x})\Bigg[W_2-a(R_0)\int_\Theta\vartheta' w_1(\vartheta')d\vartheta'\cdot\nabla R_0-a(R_0)\partial_t R_0 W_0\\&+\frac{1}{2}\int_\Theta(a(R_0)\vartheta'\cdot\nabla R_0)^2 w_0(\vartheta')d\vartheta'\Bigg]+\mu_W(W_0,Q)w_0\,.\end{aligned} \tag{4.49}$$

Integrating (4.49) with respect to $\vartheta\in\Theta$ gives

$$\frac{\partial W_0}{\partial t}+\nabla\cdot\int_\Theta\vartheta w_1 d\vartheta=\mu_W(W_0,Q)W_0,$$

Recalling the deduced expression for w_1 in (4.41), we calculate the expression of the integral term on the left hand side as

$$\begin{aligned}\int_\Theta\nabla\cdot(\vartheta w_1)d\vartheta&=\int_\Theta\nabla\cdot\left[\vartheta\left(-\frac{1}{\eta_0(\mathbf{x})}\nabla\cdot(\vartheta w_0)\right)+\vartheta\, w_0\, a(R_0)\,\vartheta\cdot\nabla R_0\right]d\vartheta\\&=-\nabla\cdot\left(\int_\Theta\frac{1}{\eta_0(\mathbf{x})}\,\vartheta\otimes\vartheta\,\nabla w_0\,d\vartheta\right)+\nabla\cdot\left(\int_\Theta\vartheta\otimes\vartheta\, w_0\,d\vartheta\,(a(R_0)\,\nabla R_0)\right)\\&=-\nabla\cdot\left[\frac{\sigma^2}{d\,\eta_0(\mathbf{x})}\,\mathbb{I}_d\,\nabla W_0\right]+\nabla\cdot\left[\frac{\sigma^2 a(R_0)}{d}\,\mathbb{I}_d\,W_0\nabla R_0\right].\end{aligned}$$

This leads to the following macroscopic equation for the density W_0 of endothelial cells:

$$\frac{\partial W_0}{\partial t}-\nabla\cdot\Big(\mathbf{D}_{EC}\nabla W_0\Big)+\nabla\cdot\Big(\chi_a(R_0)W_0\nabla R_0\Big)=\mu_W(W_0,Q)W_0, \tag{4.50}$$

where

$$\mathbf{D}_{EC}(\mathbf{x}):=\frac{\sigma^2}{d\eta_0(\mathbf{x})}\mathbb{I}_d$$

and

$$\chi_a(R_0):=\frac{\sigma^2 a(R_0)}{d}\mathbb{I}_n=\eta_0(\mathbf{x})a(R_0)\mathbf{D}_{EC}(\mathbf{x})\,.$$

The two macroscopic equations obtained in (4.46) and (4.50) for the evolution of the tumor and ECs, respectively, are coupled with the diffusion-reaction equation for proton concentration dynamics:

$$\frac{\partial S}{\partial t} = D_S \Delta S + g(S, N_0, W_0, Q)\,, \tag{4.51}$$

where $D_S \in \mathbb{R}$ denotes the diffusion coefficient of protons and $g(S, N_0, W_0, Q)$ is a reaction term. This term involves the processes of proton production by tumor cells and the buffering by vasculature and normal tissue and it will be defined in the next section. We do not explicitly account for the dynamics of the oxygen in order to maintain a low number of solution components and we rather focus on environmental acidification and pH level. However, the influence of oxygen on glioma cells is indirectly included, as ECs are responsible to provide nutrient and oxygen to the tumor cells and influence the phenotypic switch. Moreover, the consequence of low oxygen conditions (i.e., hypoxia) are also taken into account, as hypoxia determines the described acidosis [48] and the reductions in the pH level (described by means of the proton concentration).

Considering the results in (4.27), (4.37), (4.39), and (4.42), the ε-correction terms for N and W can be neglected. Ignoring the higher order terms, we get the following closed PDE system characterizing the macroscopic evolution of the tumor under the influence of tissue, vasculature, and acidity:

$$\begin{cases} \dfrac{\partial N}{\partial t} = \nabla \cdot \left[\dfrac{1}{\varrho(W,N,S)} \nabla \cdot \left(\varphi(W,N,S)\, \mathbf{D}_T(\mathbf{x}) N \right) \right] \\ \qquad\qquad -\nabla \cdot \left[\lambda_1 \dfrac{F(Q,S)\,\varphi(W,N,S)}{\varrho(W,N,S)}\, \mathbf{D}_T(\mathbf{x}) \left(\dfrac{k_1^+}{Q^*} \nabla Q - \dfrac{k_2^+}{S_{c,0}} \nabla S \right) N \right] \\ \qquad\qquad +\varphi(W,N,S) \dfrac{\alpha(W,S) + l_m(N)}{\beta(S)} N \left(\mu(W,N,S) \dfrac{Q}{Q^*} - \gamma(S) \right), \\ \dfrac{\partial W}{\partial t} = \nabla \cdot (\mathbf{D}_{EC} \nabla W) - \nabla \cdot (\eta_0 a(R) \mathbf{D}_{EC} W \nabla R) + \mu_W(W,Q) W, \\ \dfrac{\partial S}{\partial t} = D_S \Delta S + g(S,N,W,Q), \end{cases} \tag{4.52}$$

with $F(Q,S)$ given in (4.35), the tensor $\mathbf{D}_T$ from (4.45), and with the coefficients φ and ρ from (4.47) and (4.48), respectively. For the derivation of this macroscopic system we use $w = \frac{W}{|\Theta|}$, in virtue of (4.32).

For the numerical simulations of Section 4.3, this system has to be supplemented with adequate initial and boundary conditions. Although the deduction of the PDE system has been carried out for $\mathbf{x} \in \mathbb{R}^d$, we consider it to be set in a bounded, sufficiently regular domain $\Omega \subset \mathbb{R}^d$ and endow it with no-flux boundary conditions.

4.2 *Assessment of coefficients and parameters*

We dedicate this section to the definition of the coefficient functions involved in the macroscopic setting and to the estimation of the constant parameters. In addition to

that, we introduce the non-dimensionalization of the macroscopic system. In particular, the large number of constant parameters involved in the model and the difficulties in getting a clear estimation for some of the parameters from biological experiments require particular attention. For this reason, we dedicate Section 4.2.2 to the description of the parameter estimation and, in Sections 4.2.1 and 4.2.3 we address the assessment of the coefficient functions and the details of the non-dimensionalization procedure, respectively.

4.2.1 *Definition of the coefficient functions*

First, we determine the expression for $\mathbf{D}_T(\mathbf{x})$ in (4.45) providing a concrete form for the (mesoscopic) orientational distribution of tissue fibers $q(\mathbf{x}, \hat{\mathbf{v}})$. Considering the analysis performed in Chapter 2, we use the orientation distribution function (ODF):

$$q(\mathbf{x}, \hat{\mathbf{v}}) = \frac{1}{4\pi |\mathbf{D}_W(\mathbf{x})|^{\frac{1}{2}} (\hat{\mathbf{v}}^T (\mathbf{D}_W(\mathbf{x}))^{-1} \hat{\mathbf{v}})^{\frac{3}{2}}}, \tag{4.53}$$

where $\mathbf{D}_W(\mathbf{x})$ is, as usual, the water diffusion tensor obtained from processing the patient-specific DTI data.

Concerning the macroscopic tissue density $Q(\mathbf{x})$, for the simulations shown in Chapter 3 we rely on the assumption that Q is proportional to $FA(\mathbf{D}_W)$; this is reasonable for highly anisotropic regions, but some issues might arise in regions of isotropic and dense tissue. Therefore, here we consider the idea introduced in [74] and based on the definition of the characteristic diffusion length l_c. This length is defined as an estimation of the free path length of a molecule diffusion in a medium and, generally, l_c relates to the diffusion coefficient D and the characteristic (diffusion) time t_c. For the assessment of D, a possible option is to consider the trace $Tr(\mathbf{D}_W)$, or alternatively, to choose the mean diffusivity defined in (2.4). To deduce an estimation for t_c, as introduced in Chapter 2, we discuss about the process beyond the measurements of $\mathbf{D}_W$. This process is the Brownian motion. It has been shown [205] that the expected exit time from a ball with radius r in a three-dimensional space is given as $\frac{r^2}{3}$. Therefore, for the minimal ball containing a DTI voxel with side length h, i.e., of radius $h\frac{\sqrt{3}}{2}$, this exit time is $\frac{h^2}{4}$. However, this estimation is valid for $\mathcal{N}(0, t-s)$-distributed increments and, here as in [74], the increments are $\mathcal{N}(0, \sigma(t-s))$-distributed for some diffusion speed σ, thus a rescaling is necessary. Setting $\sigma := \bar{\lambda}_1$, where $\bar{\lambda}_1$ is the leading eigenvalue of $\mathbf{D}_W$, we define the characteristic diffusion length as

$$l_c(\mathbf{x}) := \sqrt{\frac{Tr(\mathbf{D}_W(\mathbf{x}))h^2}{4\bar{\lambda}_1(\mathbf{x})}}.$$

Since $l_c(\mathbf{x})$ is aimed at estimating the length of the mean free space in every direction, we get the occupied volume as

$$Q(\mathbf{x}) := 1 - \frac{l_c^3(\mathbf{x})}{h^3}. \tag{4.54}$$

For the rate $\alpha(w, S)$ describing the cell phenotypic switch $\rho \to r$ from migration to proliferation, we choose a combination of an increasing function of w and a decreasing function of S. As explained in Section 4.1.2, this rate is influenced by the pH of the environment and by the availability of nutrient, provided by vasculature for sustaining the processes involved in the cell cycle. The dynamical balance of these factors

decides the migratory or mitotic state of a cell. Recalling (4.32), we set

$$\alpha(W,S) := \alpha_0 \frac{S_n^\sigma \frac{W}{W_{c,0}}}{S_n^\sigma + S_n^\sigma \frac{W}{W_{c,0}}} \frac{1}{1+\frac{S}{S_{c,0}}}, \tag{4.55}$$

where $W_{c,0}$ and $S_{c,0}$ are reference values for EC density and proton concentration, respectively.

The second rate of the phenotypic switch $\rho \to r$, namely $l_m(N)$, describing the influence of a crowed environment on cell phenotype changes, is chosen as

$$l_m(N) := l_{m,0}\left(1+\tanh\left(\frac{N}{N_{c,0}} - \frac{N^*}{N_{c,0}}\right)\right),$$

where N^* represents a threshold value for glioma density: when it is exceeded, the cells are not able to move anymore. The constant $N_{c,0}$ denotes a reference value for the density of (moving and proliferating) glioma cells.

The switching rate $r \to \rho$ given by the function $\beta(S)$ controls the acidity-triggered motility enhancement of formerly proliferating cells. We set

$$\beta(S) := \beta_0\left(\epsilon + \left(\frac{S}{S_{c,0}} - \frac{S_{T,1}}{S_{c,0}}\right)_+\right)$$

with $\epsilon \ll 1$ used to endorse the positivity of $\beta(S)$ and $(\cdot)_+$ denotes the positive part. $S_{T,1}$ is the pH threshold which, when underrun, induces the cells to switch from a proliferative to a migrative phenotype.

Although tumor cells can live in an environment with substantially lower pH than that for normal tissue [94, 293], when the pH value drops below a certain threshold (which in terms of proton concentration we denote by $S_{T,2}$) the cancer cells become necrotic [95, 293]. This suggests the following cell death coefficient $\gamma(S)$:

$$\gamma(S) := \gamma_0\left(\frac{S}{S_{c,0}} - \frac{S_{T,2}}{S_{c,0}}\right)_+.$$

The growth rate $\mu(W,N,S)$ can be defined in different ways and the choice should be motivated by biological evidence. As stated for the previous model, we choose a logistic-like function to describe the growth. We include an growth-enhancing factor depending on the vascularization W and a growth-limiting term related to environmental acidity, like that employed in (4.55). Thus, $\mu(W,N,S)$ is defined as

$$\mu(W,N,S) := \mu_{N,0}\left(1 - \frac{N}{K_N} - c_e\frac{N_e}{K_{N_e}}\right)\frac{W}{W_{c,0}}\frac{1}{1+\frac{S}{S_{c,0}}}.$$

Here, K_N is the tumor carrying capacity and $\mu_{N,0}$ is the constant proliferation rate. The term $-c_e\frac{N_e}{K_{N_e}}$ is related to the extension of the model described in Section 4.4. In particular, $c_e = 0$ when we consider the evolution of system (4.52), while $c_e = 1$ when the dynamics of healthy tissue and necrotic matter (N_e) are included. K_{N_e} represents the carrying capacity for the necrotic component.

Similarly, for the term $\mu_W(W,Q)$ describing the proliferation of ECs we take

$$\mu_W(W,Q) := \mu_{W,0}\left(1 - \frac{W}{K_W}\right)\frac{Q}{Q^*},$$

with constant proliferation rate $\mu_{W,0}$ and carrying capacity for ECs K_W.

For the tactic sensitivity $\chi_a(R) = \eta_0 a(R)\mathbf{D}_{EC}$ of ECs towards proliferating glioma

cells, we specify the function $a(R)$ involved in the definition (4.4) of the EC turning rate as

$$a(R) := \chi_{a_0} \frac{K_N}{(K_N + R)^2} .$$

This function corresponds to the rate of change of the expression $\zeta(R) = \frac{R}{R+K_N}$ representing the equilibrium of the interactions between ECs and proliferating glioma cells R, scaled by a constant χ_{a_0} that is used to account for changes in the turning rate per unit of change in $d\zeta/dt$. Thereby, we assume that the attachment and the detachment of ECs and R-cells happen with the same rates.

The reaction term in the PDE for acidity dynamics is chosen as

$$g(S, N, W, Q) := g_s \frac{N}{N_{c,0}} - g_d \left(\frac{W}{W_{c,0}} + \frac{Q}{Q^*} \right) S .$$

This reaction term consists of a source term for the production of protons by the tumor at rate g_s and a decay term with rate g_d, as the protons are buffered by healthy tissue and also uptaken by the capillary network.

4.2.2 *Parameter estimation*

In this section, we provided a detailed description of the estimation of the parameters involved in the PDF system (4.52). In particular, the highly nonlinear and coupled structure of this system requires a careful analysis.

Turning rates and diffusion related parameters: λ_0, λ_1, s, σ, η_0, D_S

λ_0, λ_1: In [259] the authors presented experiments on the migratory behavior and turning frequency of metastatic cancer cells from rat mammary adenocarcinoma cell line, reporting values for λ_0 in the range $[0.01, 0.1]$ s^{-1}. Considering the highly aligned brain structures which influence cell migration enhancing cell persistence in the favorable direction of motion, we assume a reduction of the turning likelihood and take the range $[10^{-4}, 10^{-2}]$ s^{-1} for the parameter λ_0. The choice of λ_1 is, unfortunately, rather imprecise, due to the lack of data and references. In [77] variations of this parameter by $\pm 50\%$ were tested in a similar context. As proposed there, we consider the same order of magnitude for λ_0 and λ_1.

s: Different references are available for the tumor cell speed. In a recent work [65], four types of typical GBM cell lines were cultured in a microfabricated 3D model to study their *in-vitro* behavior. According to this study, we consider for glioma cell speed the range $[10.2, 30]$ $\mu\mathrm{m} \cdot \mathrm{h}^{-1}$. A further upper limit for this parameter can be found in [230], where a maximum speed of $54 - 60$ $\mu\mathrm{m} \cdot \mathrm{h}^{-1}$ was reported for glioma cells.

σ: For the average speed of ECs, in [60] the range $\sigma \in [10, 50]$ $\mu\mathrm{m} \cdot \mathrm{h}^{-1}$ was reported for individual cells in several culture conditions. *In-vivo*, the registered mean speed for motile endocardial and endothelial cells is of approximately 20 $\mu\mathrm{m} \cdot \mathrm{h}^{-1}$.

η_0: For reason of simplicity, we assume a constant coefficient η_0 for the turning rate in (4.4) for ECs. In [277], the authors analyzed the statistical properties of the random streaming behavior for endothelial cell cultures. In particular, they estimated a period of $T = 5$ min to alter cell polarity and influence the cell turning. With this value, they obtained a cell speed estimation in the range of $[20, 40]$ $\mu\mathrm{m} \cdot \mathrm{h}^{-1}$ within

monolayers of ECs. Following their results, we consider $\eta_0 \in [0.0001, 0.003]$ s^{-1}.

D_S: From [168], we get an average value of $[0.3, 10] \cdot 10^{-3}$ mm$^2\cdot$ s^{-1} estimation of the diffusion coefficient for different ions. We test the model for different values of this parameter and we chose $D_S = 0.5 \cdot 10^{-3}$ mm$^2\cdot$ s^{-1}. D_S was rescaled in the simulations in order to account for the fast dynamics characterizing proton evolution.

Phenotypic switch related parameters: α_0, β_0, $l_{m,0}$, N^*, $S_{T,1}$, $S_{T,2}$, γ_0

α_0, β_0, $l_{m,0}$: For the estimation of reasonable ranges for the values of the phenotypic switch parameters α_0 and β_0 there are no specific data or measurements available. However, considering the experiments performed in [146, 219], it is possible to define a wide range for the duration of the glioma cell cycle that translates into $\alpha_0, \beta_0 \in [0.09, 1] \cdot 10^{-4}$ s^{-1}. Analogous arguments apply for the rate $l_{m,0}$, for which there are not estimations directly derived from biological data. For this reason we test the model for several values of α_0, β_0, $l_{m,0}$ of order of magnitude 10^{-4} to fix the value of $l_{m,0}$.

N^*: Due to the lack of biological data, for the estimation of this parameter related to the total tumor density level that still allows cell movement, we choose it to be proportional to the estimated tumor carrying capacity, namely in the range $[0.6, 0.9] \cdot K_N$ proposed in [28, 225].

$S_{T,1}$, $S_{T,2}$: Following the pH range $[6.4, 7.3]$ proposed in [285, 293] for the brain tumor microenvironment, we choose the threshold values that determine the phenotypic switch from proliferating to migrating cells ($S_{T,1}$) and the acid-mediated death of the resting cells ($S_{T,2}$) as $S_{T,1} = 1.995 \cdot 10^{-7}$ M (referring to a pH $= 6.7$), and $S_{T,2} = 3.98 \cdot 10^{-7}$ M (referring to a pH $= 6.4$).

γ_0: In [276], the authors assumed the cell necrosis rate to be proportional to the metabolic rate $\mu_{N,0}$. This estimation appears reasonable, considering also our assumption in the parabolic scaling procedure about having similar time scales for birth and death processes. Therefore, we set $\gamma_0 = \mu_{N,0}/50$.

Adhesion related parameters: k_1^+, k_2^+, k^-, χ_{a_0}

k_1^+, k_2^+: For the estimation of the attachment rates between tumor cell and ECM or protons, we refer to [161]. In particular, for both the cell-ECM attachment rate and the cell-protons interaction rate, we set $k_1^+ = k_2^+ = 10^4$ (M $\cdot$ s)$^{-1}$. Then, assuming that the main ECM component is collagen, with a molecular weight of approximately 300 kDa, and taking into account the reference value Q^* in Table 4.2, we deduce $k_1^+ = 0.034$ s^{-1}. Analogously, considering the reference value for the protons concentration $S_{c,0}$ in Table 4.2, we get $k_2^+ = 0.01$ s^{-1}.

k^-: For the estimation of the cells-ECM and cells-protons detachment rate, referring to [161], we set $k^- = 0.01$ s^{-1}.

χ_{a_0}: We estimate the parameter χ_{a_0} by considering the values reported in [267] and [266] for the chemotactic sensitivity. In particular, in [267] the authors analyzed

the chemotactic coefficient of migrating endothelial cells in gradients of growth factors, measuring a maximum chemotactic response of 2600 $cm^2 \cdot (M \cdot s)^{-1}$ at a concentration of growth factors around 10^{-10} M. In the work [266], the authors analyzed the changes of this parameter in response to cell speed and persistence time. Taking into account the above-described range for the EC speed, we set $\chi_{a_0} \in [3.09, 4.5]$ d.

Proliferation related parameters: $\mu_{N,0}$, K_N, $\mu_{W,0}$, K_W

$\mu_{N,0}$: For the estimation of glioma growth rate, we analyze the doubling times reported in [135] for several glioma cell lines. Therein, the authors reported a range of variability between 21.1 h and 46 h for the doubling time, which translates into $\mu_{N,0} \in [0.42, 0.9] \cdot 10^{-5}\ s^{-1}$.

K_N, K_W: Considering that the mean diameter of a glioma cell is around $[12, 14]$ μm [81], we estimate a value for the tumor carrying capacity K_N of approximately 10^6 cells $\cdot\ mm^{-3}$. In the same way, considering a mean diameter for an endothelial cell of $[10, 20]$ μm [82], we set K_W approximately to 10^6 cells $\cdot\ mm^{-3}$.

$\mu_{W,0}$: The doubling time of EC density has been estimated in several experiments to vary between the different phases of an endothelial colony growth until the formation of a monolayer. In [7, 203], the authors gave a range of variability for the value of the EC doubling time of $[0.5, 13]$ d. This leads to $\mu_{W,0} \in [0.62, 5.7] \cdot 10^{-6}\ s^{-1}$.

Production and consumption related parameters: g_s, g_d, $d_{0,Q}$, $S_{T,Q}$

g_s: In [94], the authors estimated the rate of proton production due to tumor cell activity by fitting their equation for proton dynamics (analogous to our PDE (4.51)) to a converted form of the data in [183]. In particular, in [183] pH measurements were taken at a variety of points within both the tumor and surrounding healthy tissue for four composite cases, giving a geometric mean for the production rate of $2.2 \cdot 10^{-20}\ M \cdot mm^3 \cdot (s \cdot cell)^{-1}$.

g_d: Following [94, 184], for the rate of proton uptake by tissue and vasculature we consider the range of variability given by $[0.66, 1.1] \cdot 10^{-4}\ s^{-1}$. As we did for D_S, proton production and consumption rates were rescaled in the simulations to account for the fast dynamics characterizing proton evolution.

$d_{0,Q}$: For the rate of tissue degradation due to the acidic environment, in [276] the authors proposed an estimation choosing the parameter $d_{0,Q}$ such that 10% necrosis allow the tissue for 50-day half-life. Starting from the value proposed in [276], we test a wider range of possible estimations, which translates into $d_{0,Q} \in [0.005, 0.07]\ d^{-1}$.

$S_{T,Q}$: In [285], tissue pH values in normal brain tissue and in brain tumors were reported. Specifically, considering that these values vary depending on the type of brain tissue (i.e., grey matter, white matter, cerebellum), the minimum pH required for the normal cell activity is in the range of $[6.94, 6.74]$. For these reasons, we set $S_{T,Q} = 1.995 \cdot 10^{-7}$ M (referring to pH $= 6.7$). In particular, these last two parameters, i.e., $d_{0,Q}$ and $S_{T,Q}$, are involved in the model extension described in Section 4.4.

We resume in Table 4.1 the values for the constant parameters we use in system (4.52), as well as the main references to which we refer.

Parameter	Description	Value (unit)	Source
λ_0	turning frequency in $\mathcal{L}_\rho[\lambda(z)]$	0.001 (s^{-1})	[259]
λ_1	turning frequency in $\mathcal{L}_p[\lambda(z)]$	0.001 (s^{-1})	[77, 259]
α_0	phenotype switch rate $p \to r$	0.0001 (s^{-1})	[146, 219]
β_0	phenotype switch rate $r \to p$	0.0002 (s^{-1})	[146, 219]
$l_{m,0}$	overcrowding switch rate $p \to r$	0.0005 (s^{-1})	[146, 219]
N^*	optimal N-value for cell movement	$0.75 \cdot K_N$	[28, 225]
s	speed of tumor cells	$0.0084 \cdot 10^{-3}$ (mm $\cdot$ s^{-1})	[65]
k_1^+	cell-ECM attachment rate	0.034 (s^{-1})	[161]
k_2^+	cell-protons interaction rate	0.01 (s^{-1})	[161]
k^-	detachment rate	0.01 (s^{-1})	[161]
$\mu_{N,0}$	tumor proliferation rate	$9.26 \cdot 10^{-6}$ (s^{-1})	[135]
K_N	tumor carrying capacity	$\sim 10^6$ (cells $\cdot$ mm^{-3})	[81]
γ_0	acid-induced death rate for tumor cells	$0.19 \cdot 10^{-6}$ (s^{-1})	[276]
$S_{T,1}$	S-concentration threshold for $r \to p$	$1.995 \cdot 10^{-7}$ (M)	[285, 293]
$S_{T,2}$	S-concentration threshold for tumor cell death	$3.98 \cdot 10^{-7}$ (M)	[285, 293]
η_0	turning frequency of ECs in $\mathcal{L}_w[\eta]$	0.001 (s^{-1})	[277]
χ_{a_0}	duration between R-damped EC turnings	4.5 (d)	[266, 267]
σ	speed of ECs	$0.0056 \cdot 10^{-3}$ (mm $\cdot$ s^{-1})	[60]
K_W	carrying capacity for ECs	$\sim 10^6$ (cells $\cdot$ mm^{-3})	[82]
$\mu_{W,0}$	EC proliferation rate	$0.58 \cdot 10^{-6}$ (s^{-1})	[7, 203]
D_S	diffusion coefficient of protons	$0.5 \cdot 10^{-3}$ ($mm^2 \cdot s^{-1}$)	[168]
g_s	proton production rate	$2.2 \cdot 10^{-20}$ (M $\cdot$ $mm^3 \cdot$ (cells $\cdot$ s)$^{-1}$)	[183]
g_d	proton removal rate	$0.8 \cdot 10^{-4}$ (s^{-1})	[184]

TABLE 4.1: **Intratumor heterogeneity, vasculature and acidity: model parameters.**

4.2.3 *Non-dimensionalization*

This last section, before presenting the numerical results of the model, concerns the non-dimensionalization of system (4.52). In particular, we first observe that the variables N, W, and N_e involved in system (4.52) (and in its extension (4.56), presented in the following Section 4.4) are expressed in cells $\cdot$ mm^{-3}, the tissue density Q in g $\cdot$ mm^{-3}, while the concentration of protons S is given in mol $\cdot$ l^{-1}(=:M). The reference values we use for the non-dimensionalization are listed in Table 4.2. In particular, we rescale the variables accounting for tumor cell, EC cell, and necrotic matter (including dead cells and tissue) densities with respect to their carrying capacities, i.e., $N_{c,0} = K_N$,

$W_{c,0} = K_W$, and $N_{e,0} = K_N$, assuming a similar carrying capacity for tumor cells and necrotic s.

Parameter	Description	Value (unit)	Source
T	time	1 (d)	
L	length	0.875 (mm)	
$N_{c,0}$	tumor cell density	10^6 (cells $\cdot$ mm^{-3})	this work
$W_{c,0}$	EC density	10^6 (cells $\cdot$ mm^{-3})	this work
$S_{c,0}$	proton concentration	10^{-6} (M)	[285]
Q^*	healthy tissue density	10^{-3} (mg $\cdot$ mm^{-3})	[134]
$N_{e,0}$	density of necrotic matter	10^6 (cells $\cdot$ mm^{-3})	this work

TABLE 4.2: **Intratumor heterogeneity, vasculature and acidity: reference variables for the non-dimensionalization.**

We non-dimensionalize the partial differential equations as follows:

$$\tilde{t} = \frac{t}{T}, \quad \tilde{\mathbf{x}} = \frac{\mathbf{x}}{L}, \quad \tilde{N} = \frac{N}{K_N}, \quad \tilde{W} = \frac{W}{K_W}, \quad \tilde{S} = \frac{S}{S_{c,0}}, \quad \tilde{Q} = \frac{Q}{Q^*}, \quad \tilde{N}_e = \frac{N_e}{K_N}.$$

The proper scaling of the parameters involved in the macroscopic setting then reads

$$\tilde{\alpha}_0 = \frac{\alpha_0}{\lambda_0}, \quad \tilde{l}_{m,0} = \frac{l_{m,0}}{\lambda_0}, \quad \tilde{\lambda}_1 = \frac{\lambda_1}{\lambda_0}, \quad \tilde{\mathbf{D}}_T = \frac{1}{\lambda_0}\frac{T}{L^2}\mathbf{D}_T,$$

$$\tilde{N}^* = \frac{N^*}{K_N}, \quad \tilde{\beta}_0 = \frac{\beta_0}{\lambda_0}, \quad \tilde{\mathbf{D}}_{EC} = \frac{T}{L^2}\mathbf{D}_{EC}, \quad \tilde{D}_S = \frac{T}{L^2}D_S,$$

$$\tilde{k}_2^+ = \frac{k_2^+}{\lambda_0}, \quad \tilde{k}_1^+ = \frac{k_1^+}{\lambda_0}, \quad \tilde{\chi}_{a_0} = \frac{\chi_{a_0}}{K_N}, \quad \tilde{S}_{T,j} = \frac{S_{T,j}}{S_{c,0}} \ (j = 1,2),$$

$$\tilde{k}^- = \frac{k^-}{\lambda_0}, \quad \tilde{S}_{T,Q} = \frac{S_{T,Q}}{S_{c,0}}, \quad \tilde{g}_s = g_s\frac{T}{S_{c,0}}, \quad \tilde{g}_d = g_d\,T,$$

$$\tilde{\gamma}_0 = \gamma_0\,T, \quad \tilde{\mu}_{N,0} = \mu_{N,0}\,T, \quad \tilde{d}_{0,Q} = d_{0,Q}\,T, \quad \tilde{\mu}_{W,0} = \mu_{W,0}\,T.$$

Dropping the tilde in the new variables and parameters, the differential equations in system (4.52) maintain the same form, with the following rescaled functions:

$$\tilde{\mu}(\tilde{W},\tilde{N},\tilde{S}) = \tilde{\mu}_{N,0}\,(1-\tilde{N}-\tilde{N}_e)\,\tilde{W}\frac{1}{1+\tilde{S}}, \qquad \tilde{\alpha}(\tilde{W},\tilde{S}) = \tilde{\alpha}_0\,\frac{\tilde{W}}{1+\tilde{W}}\,\frac{1}{1+\tilde{S}},$$

$$\tilde{\mu}_W(\tilde{W},\tilde{Q}) = \tilde{\mu}_{W,0}\,(1-\tilde{W})\,\tilde{Q}, \qquad \tilde{\beta}(\tilde{S}) = \tilde{\beta}_0(\epsilon + (\tilde{S}-\tilde{S}_{T,1})_+),$$

$$\tilde{B}(\tilde{Q},\tilde{S}) = \left(\tilde{k}_1^+\tilde{Q} + \tilde{k}_2^+\tilde{S} + \tilde{k}^-\right), \qquad \tilde{\gamma}(\tilde{S}) = \tilde{\gamma}_0(\tilde{S}-\tilde{S}_{T,2})_+,$$

$$\tilde{g}(\tilde{N},\tilde{S},\tilde{W},\tilde{Q}) = \tilde{g}_s\tilde{N} - \tilde{g}_g(\tilde{W}+\tilde{Q})\tilde{S}, \qquad \tilde{l}_m(\tilde{N}) = \tilde{l}_{m,0}(1+\tanh(\tilde{N}-\tilde{N}^*)),$$

$$\tilde{\varrho}(\tilde{W},\tilde{N},\tilde{S}) = 1 + \tilde{\alpha}(\tilde{W},\tilde{S}) + \tilde{l}_m(\tilde{N}), \qquad \tilde{a}(\tilde{R}) = \frac{\tilde{\chi}_{a_0}}{(1+\tilde{R})^2},$$

$$\tilde{\varphi}(\tilde{W},\tilde{N},\tilde{S}) = \frac{\tilde{\beta}(\tilde{S})}{\tilde{\beta}(\tilde{S}) + \tilde{\alpha}(\tilde{W},\tilde{S}) + \tilde{l}_m(\tilde{N})}$$

and

$$\tilde{F}(\tilde{Q},\tilde{S}) = \frac{\tilde{k}^-}{\tilde{B}(\tilde{S},\tilde{Q})^2\left[\tilde{B}(\tilde{Q},\tilde{S}) + 1 + \tilde{\alpha}(\tilde{W},\tilde{S}) + \tilde{l}_m(\tilde{N})\right]}.$$

4.3 *Numerical simulations*

Considering the parameters given in Table 4.1 and the functions defined in Section 4.2.1, we perform 2D simulations of the resulting macroscopic setting of coupled advection - diffusion - reaction equations (4.52). For the initial conditions we take a Gaussian - like aggregate of proliferating tumor cells centered in $(x_{0,N}, y_{0,N}) = (-17, 5)$, situated in the upper-left part of the brain slice representing our illustrative computational domain Ω (in the following, $(x, y) \in \Omega \subseteq \mathbb{R}^2$)

$$R_0(x,y) = e^{-\frac{(x-x_{0,N})^2+(y-y_{0,N})^2}{8}},$$

and a ring-like profile for the migrating tumor cells centered at the same location:

$$M_0(x,y) = 0.5\, e^{-\left(\sqrt{(x-x_{0,N})^2+(y-y_{0,N})^2}-2\right)^2}.$$

The initial distribution of the total tumor population is given by $N_0 = R_0 + M_0$. For the ECs we consider $x_{0,W} = -6$ and

$$W_0(x,y) = 0.5\, e^{-\frac{(x-x_{0,W})^2}{0.2}} \sin^6\left(\frac{\pi}{8}y\right) \qquad \forall\, y \in [-5, 15],$$

reproducing the representative situation of three blood vessels close to the neoplastic region. Finally, for the acidity profile we consider a Gaussian distribution, centered in the same point as tumor cells $(x_{0,S}, y_{0,S}) = (-17, 5)$, as a capillary occlusion would have caused acidification of the extracellular space around the glioma cell. This distribution is given by:

$$S_0(x,y) = 0.65\, e^{-\frac{(x-x_{0,S})^2+(y-y_{0,S})^2}{10}}.$$

The initial pH distribution is calculated considering that $\mathrm{pH}_0 = -\log_{10}(S_0)$. We are more interested in visualizing the changes in the pH level rather than in the proton concentration as advanced techniques have been recently developed to obtain high-resolution pH-weighted images [111] and study tumor acidity and vascularity association. Figure 4.1 shows the plots for the initial conditions on the entire 2D brain slice, zooming then on the region $\bar{\Omega} = [-35, 5] \times [-15, 25] \subseteq \Omega$. Figure 4.2 shows the initial tissue density estimated with (4.54).

The numerical simulations are performed with a self-developed code in Matlab (MathWorks Inc., Natick, MA). The computational domain is a horizontal brain slice reconstructed from the processing of an MRI scan. The macroscopic tensor $\mathbf{D}_T(x)$ is precalculated using DTI data and the ODF for the fiber distribution function (4.53).

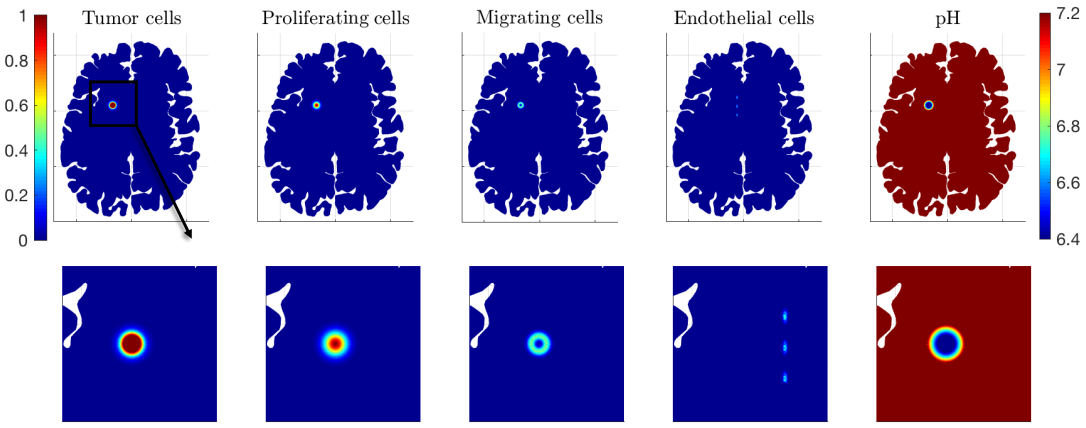

FIGURE 4.1: **Initial conditions for system (4.52).** The five columns refers to total tumor density, proliferating cells, migrative cells, ECs, and pH level, respectively. The bottom row shows a close up of the initial densities on the domain $\bar{\Omega} = [-35, 5] \times [-15, 25]$.

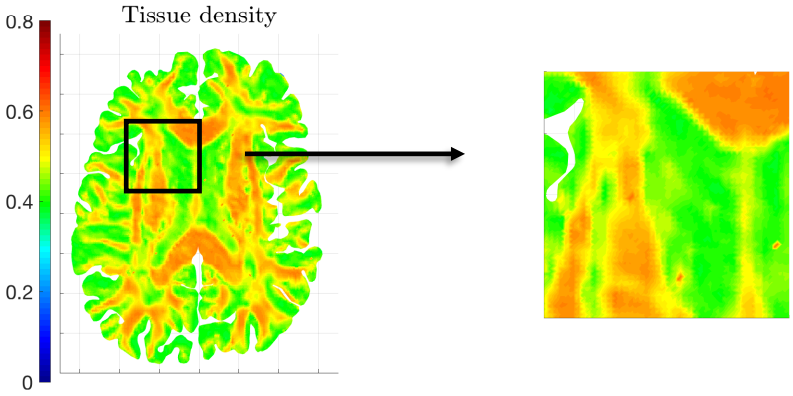

FIGURE 4.2: **Healthy tissue density for system (4.52).**

We consider a Galerkin finite element scheme for the spatial discretization of the equations for tumor cells, ECs, and proton concentration, together with an implicit Euler scheme for the time discretization. More detail descriptions and definitions of the numerical methods are provided in Appendix B.

We present a series of simulations addressing several aspects of the system dynamics:

(A) we study the behavior of species involved in system (4.52) for the parameters listed in Table 4.1;

(B) we compare the model behaviors upon varying some of the parameters: the turning rate of glioma cells λ_0 and the two speeds for tumor and endothelial cells (s, σ);

(C) we study the effect of the go-or-grow dichotomy, comparing the evolution of the system (4.52) with a setting in which the tumor cells migrate and proliferate without deterring one of these phenotypes for the other. We referee to this setting as *Model NGG*.

The simulation results for study **(A)** are shown in Figure 4.3, where the five columns report the evolution of the whole tumor mass (N), the two subpopulations of proliferating (R) and migrating (M) tumor cells, the endothelial cells (W), and the pH (computed from S). The tumor spread, which seems to mainly depend on EC evolu-

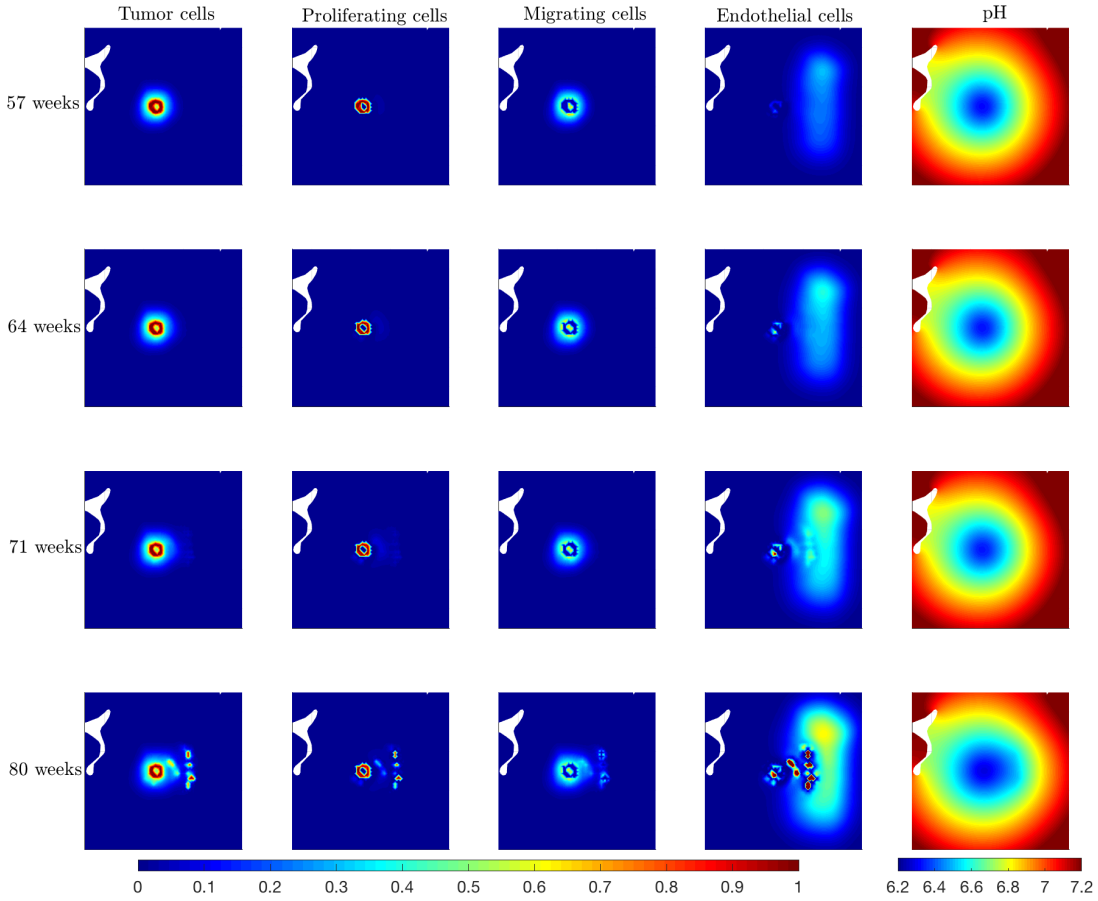

FIGURE 4.3: **Scenario (A).** Numerical simulation of system (4.52) with parameters listed in Table 4.1.

tion and on the parameters λ_0 and s, is rather slow, with a partial exchange between the two subpopulations of tumor cells in relation to the pH values at the center of the tumor mass, where proliferating cells are more initially concentrated. The tumor cells increasingly adopt the proliferating phenotype when they approach ECs, as these provide the necessary nutrient and oxygen to sustain glioma proliferation. ECs diffuse and grow, with a higher accumulation around the first of the three vessels situated in the upper part of the domain and where there is more healthy tissue available to sustain proliferation (as can be observed in Figure 4.2). They clearly exhibit a tactic behavior towards the (pro-angiogenic growth factors released by) proliferating tumor cells. The subplots for the evolution of ECs at later times (e.g. the last two rows of Figure 4.3) show an increasing amount of high EC aggregates developing towards the tumor. This behavior can be associated with the phenomenon of microvascular hyperplasia and glomeruloid bodies. The latter are tumor-associated vascular structures that develop in the presence of high levels of VEGF and are important histopathological features of glioblastoma [248, 268]. Globally, Figure 4.3 shows the strong dependency of tumor evolution on EC dynamics. The chosen illustrative initial condition for ECs (shown in Figure 4.1) is effective to demonstrate how the model is able to reproduce the phenomena of microvascular hyperplasia and glomeruloid bodies,

typical of GB, although the limited amount of vessels provided initially affects the tumor extension. However, it has been proved that tumor volume has no influence on the overall survival (OS) in GB patients, while there is a high significance of necrosis and hypoxia-related histopathological features (like microvascular hyperplasia and glomeruloid bodies) for OS (see [115] and references therein) and, thus, we focus on these latter aspects.

Figure 4.4 show the comparison described in **(B)** between the simulations performed for different values of the parameter λ_0, referring to the turning rate of glioma cells, and different values of the two speeds (s, σ) for tumor and ECs with the aim to illustrate how sensitive the model predictions are with respect to these parameters. The tumor and EC densities are plotted after 80 weeks of evolution for three different values of λ_0 (expressed in s^{-1}), i.e., 10^{-4}, 10^{-3} and 10^{-2}, and for four pairs (s, σ) of speed values (expressed in $\mu m \cdot h^{-1}$), i.e., $(15, 20)$, $(20, 15)$, $(30, 20)$, and $(30, 25)$. The simulations suggest that vascularization at the tumor site requires a sufficiently large glioma turning rate λ_0 accompanied by relatively large EC speed σ. Too small values of λ_0 trigger the tumor cells to shift from their original location to the site of blood vessels, where they switch to the proliferative phenotype. The faster the glioma cells are, the more this behavior occurs, obviously dominated by migration during the first stage and subsequent proliferation. Increasing λ_0 by one or two orders of magnitude leads to more realistic behaviors of tumor cells and ECs, with less sensitivity towards variations in λ_0. Naturally, wide-spread hyperplasia and strong tumor invasion occur for higher cell speeds.

Moreover, to test the effect of the go-or-grow dichotomy on the evolution of the cell populations involved in system (4.52), we compare the model with a setting in which the tumor cells migrate and proliferate without deterring one of these phenotypes for the other, namely the *Model NGG* described in **(C)**. In particular, we do not differentiate between proliferating and migrating cells and accordingly let the ECs be biased by the density gradient of the whole tumor. Using a scaling argument similar to the one described in Section 4.1.3, we obtain a system of three partial differential equations for tumor cells (N_1), ECs (W_1), and protons (S_1), which is analogous to (4.52) with $\alpha_0 = 0$ and $l_{m,0} = 0$. This choice of parameters reduces the former coefficient functions to $\varphi(w_0, N, S) = 1$ and $\varrho(w_0, N, S) = \lambda_0$. Figure 4.5 shows the solution behavior for this new setting. The initial conditions for the three populations are the same as those shown in Figure 4.1. Comparing Figures 4.3 and 4.5 we observe that the go-or-growth model predicts - as expected - a slower tumor spread, with lower cell density, which, consequently, induces lower acidity concentrations in the environment, and the differences between the two settings become more accentuated with time. Moreover, the tactic phenomenon driving ECs towards the tumor mass is stronger for the case shown in Figure 4.5, and accumulations of ECs indicating microvascular hyperplasia are now earlier formed and become larger. To enable a direct assessment of the two settings we plot in Figure 4.6 the differences (at 57 and 80 weeks) between the (overall) densities of tumor and endothelial cells for the model with go-or-grow and its *NGG* counterpart (the quantities for the latter are marked by the index 1), as well as between the respective pH distributions, the latter illustrated on a larger domain $\tilde{\Omega} = [-40, 10] \times [-20, 30]$. The described features concerning tumor/EC spread and aggregation along with acidity distribution can be clearly observed. The larger tumor spread in the *NGG* model with respect to the go-or-growth model is highlighted by the presence of extensive blu-areas in the corresponding plots (first columns); in turn, the tactic force driving EC migration is stronger, leading to an earlier and more enhanced accumulation of ECs in the core region of the tumor mass (indicated by the central dark blue spot in the second column). Due to the higher production of protons for

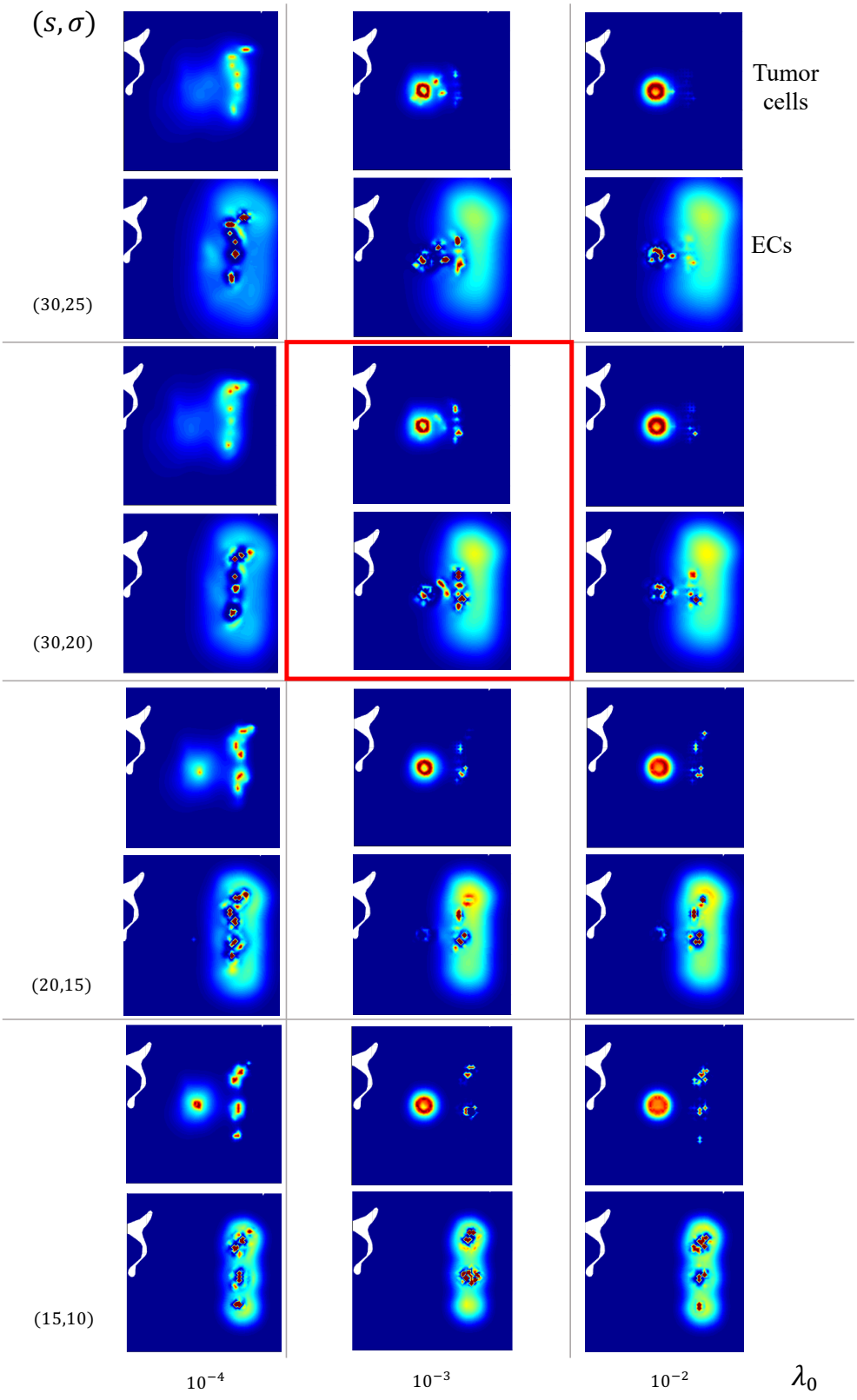

FIGURE 4.4: **Scenario (B).** Comparison between the evolution of tumor (first row of each box) and endothelial cells (second row of each box) for three different values of λ_0 (s^{-1}): 10^{-4}, 10^{-3} and 10^{-2}, and four pairs (s,σ) of speed values ($\mu m \cdot h^{-1}$): $(15,20)$, $(20,15)$, $(30,20)$, and $(30,25)$. All values belong to the parameter ranges reported in Section 4.2.2.

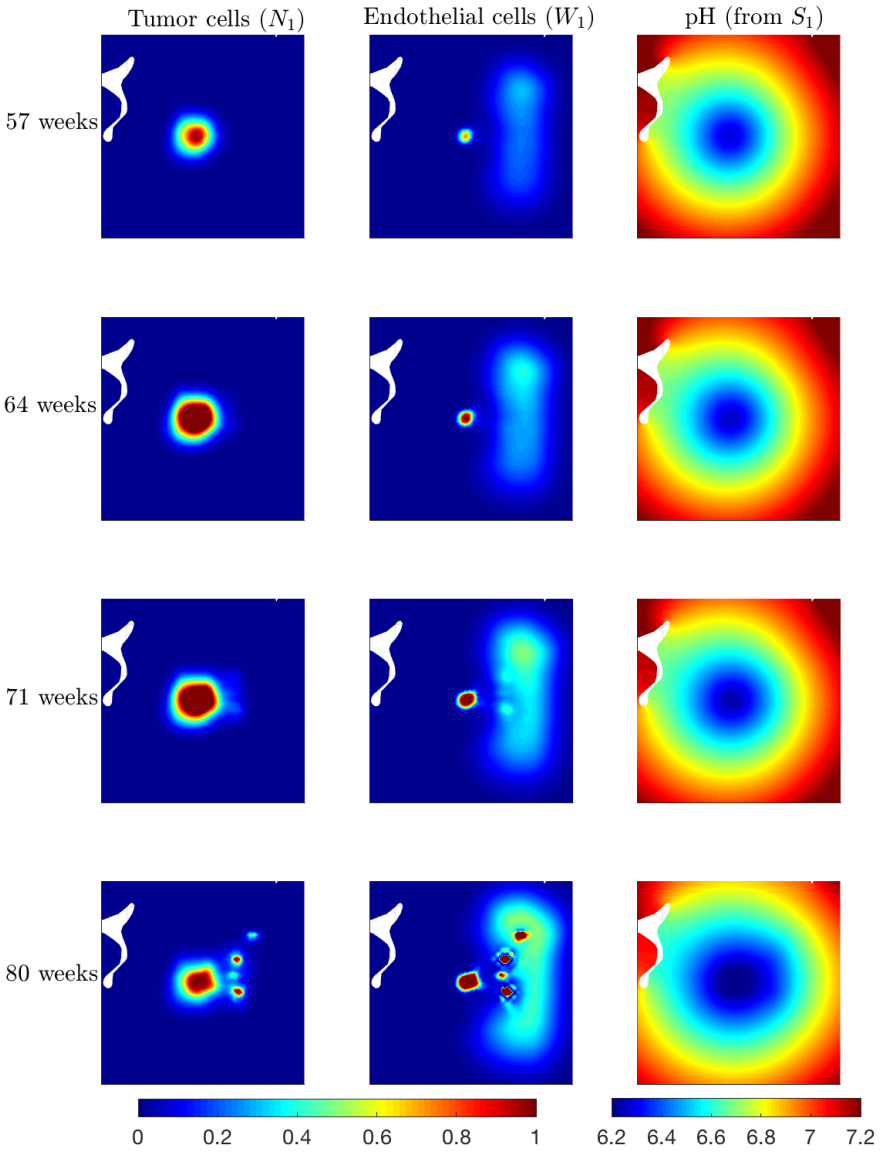

FIGURE 4.5: **Scenario (C).** Numerical simulation of *Model NGG*, i.e., with simultaneously moving and proliferating cancer cells. The employed parameter values are listed in Table 4.1, except for $\alpha_0 = 0$ and $l_{m,0} = 0$.

the *NGG* model, the difference in the pH level is nonnegative everywhere, indicating a less acidic environment.

4.4 *Model extension: tissue degradation, necrosis, and tumor grading*

In the last step, we extend our model by considering the evolution of the macroscopic tissue density Q and that of necrotic matter N_e, the latter including tissue as well as glioma cells degraded by hypoxia. The whole system consists of the equations of system (4.52) together with the following ODEs:

$$\begin{cases} \partial_t Q = -d_Q(S)Q \\ \partial_t N_e = d_Q(S)Q + \varphi(w,N,S)\dfrac{\alpha(w,S)+l_m(N)}{\beta(S)}\gamma(S)\,N, \end{cases} \tag{4.56}$$

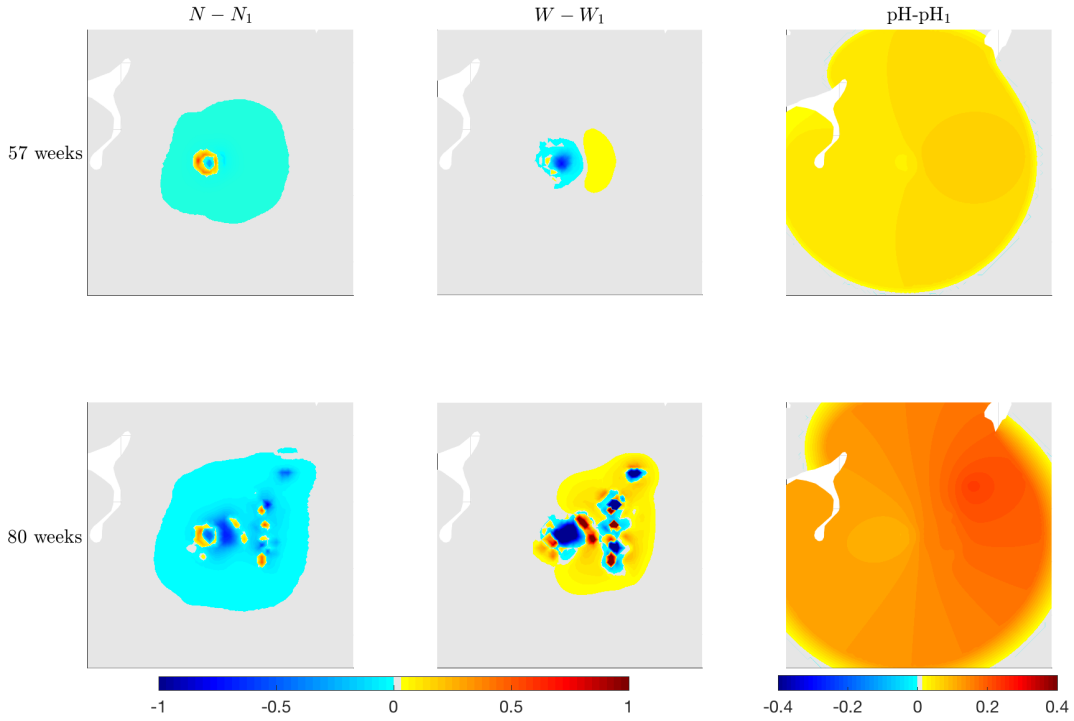

FIGURE 4.6: **Detail of scenario (C).** Differences between the respective solution components of system (4.52) and of *Model NGG* at 57 (top row) and 80 (bottom row) weeks.

where the coefficient $d_Q(S)$ models the pH-triggered tissue degradation occurring when a certain acidity threshold $S_{T,Q}$ is exceeded, namely

$$d_Q(S) = d_{0,Q}\left(\frac{S}{S_{c,0}} - \frac{S_{T,Q}}{S_{c,0}}\right)_+ .$$

Thereby $d_{0,Q} > 0$ describes the tissue degradation rate and $(\cdot)_+$ denotes as usual the positive part. In particular, the details on the estimation of $d_{Q,0}$ and $S_{T,Q}$ have been provided in Section 4.2.2.

The numerical simulations for the model (4.52) extended with (4.56) are shown in Figure 4.8, corresponding to the initial conditions of Figure 4.7.
In Figure 4.9 we illustrate the evolution of proliferating and migrating glioma cells. Although the qualitative behavior of glioma and endothelial cells is comparable with the one shown in Figure 4.3, the degradation of tissue due to the environmental acidity affects both tumor and EC proliferation, as less healthy tissue is available to sustain growth. Therefore, the simulations in Figures 4.8 and 4.9 show lower densities for both species and, particularly, tumor cell growth is affected by the reduction of vasculature and the depletion of healthy tissue, as clearly shown by the evolution of the proliferating tumor cells in Figure 4.9 (first row). As stated above, we remark our attention for the necrosis significance on the tumor progression and the patient OS, rather than on the reproduced tumor volume.

The above model extension enables us to perform necrosis-based tumor grading, which is essential for assessing patient survival and treatment planning. Other indicators of tumor aggressiveness can be employed as well (e.g. histological patterns [297] or tumor size [226]). Here, we rely on the grading based on the amount of necrosis

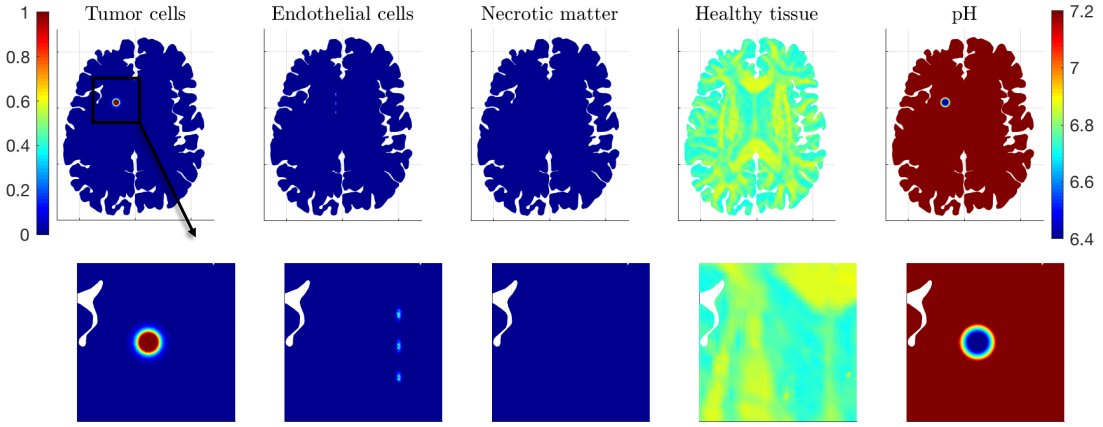

FIGURE 4.7: **Initial conditions for system (4.52) extended with (4.56).** The five columns refers to total tumor density, ECs, necrotic matter, healthy tissue, and pH level, respectively. The bottom row shows a close up of the initial densities on the domain $\bar{\Omega} = [-35, 5] \times [-15, 25]$.

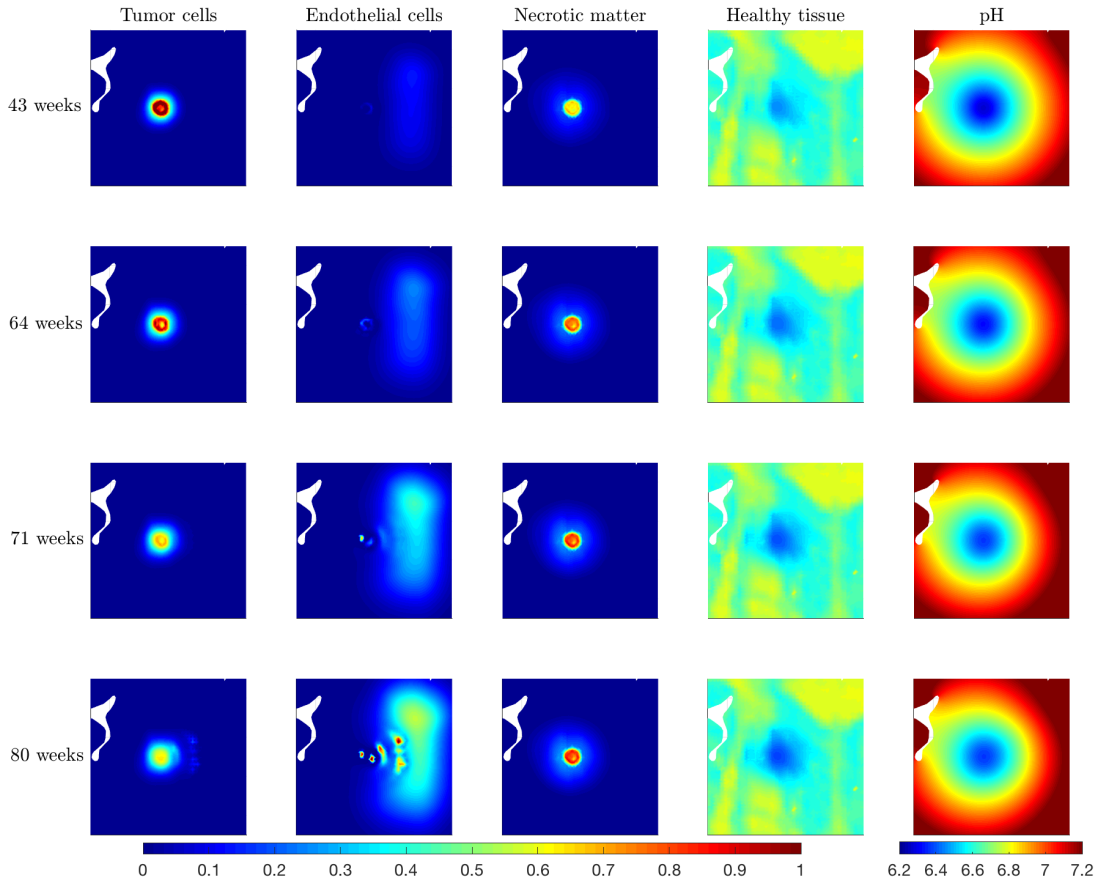

FIGURE 4.8: **Evolution of system (4.52) extended with (4.56).** The parameters used in this simulation are listed in Table 4.1 and the value of ECs speed is here set to $\sigma = 0.0069 \cdot 10^{-3}$ mm $\cdot$ s^{-1}.

relative to the whole tumor volume in view of [108, 115], where the authors show that the tumor volume by itself has no influence on the overall survival. Following [58],

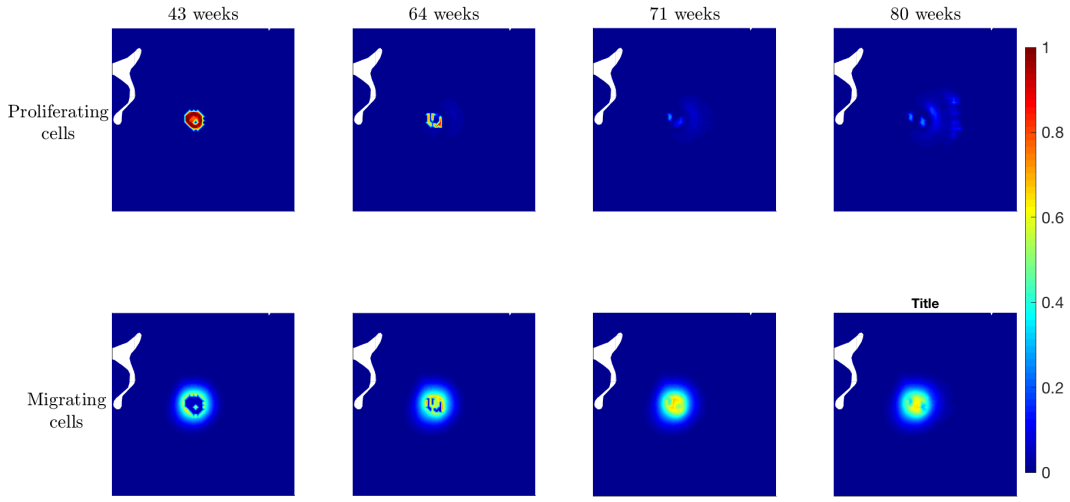

FIGURE 4.9: **Evolution of proliferating and of the migrating tumor cells for the system (4.52) extended with (4.56).**

we define the time-dependent grade $G(t) \in [0,1]$ of the simulated tumor via:

$$G(t) := \frac{V_{Ne}(t)}{V_{Ne}(t) + V_N(t)}, \tag{4.57}$$

where $V_{Ne}(t)$ and $V_N(t)$ denote the fraction of necrosis and the fraction of living cell densities in the visible tumor volume, respectively. They are defined as the integrals of the densities N_e and N over the domain defined by the level sets of the tumor population for a detection threshold of 80% of the carrying capacity, which corresponds to the detection threshold for T1-Gd images [276]. We represent in Figure 4.10 the temporal evolution of G, guided by the percentage classification in [108], i.e., $0 < G < 25\%$: grade 1, $25\% \leq G < 50\%$: grade 2, and $G \geq 50$: grade 3. The highest grade corresponds to the most aggressive tumor and the poorest survival prognosis. With the word grade, we do not refer to the WHO scheme for classifying gliomas, which divides them into four grades depending on the degree of tumor differentiation. We use this terminology following the work in [108], where the grade indicates the amount of necrosis measured mainly from the T1 images. In particular, we compare the effect of four different scenarios on the necrosis-based tumor grading: the grey curves therein refer to the model (4.52) extended with (4.56) involving vascularization, i.e., with the population W (solid line: go-or-grow (*GoG* in the legend of Figure 4.10), dotted line: *Model NGG*), while the red curves illustrate the evolution of the grade G for the corresponding variants of the extended model without EC dynamics (i.e., without W). First, Figure 4.10 shows that assuming the go-or-grow dichotomy leads to slower progression of neoplasia, due to the cells deterring one phenotype for the other. In the long run, the full go-or-grow model with vascularization predicts a slower advancement towards high tumor grades. When considering EC dynamics, the differences between the model with or without go-or-grow are rather small; when ECs are not included, these differences increase. The vascularization seems to have a significant impact on the evolution of the grade: focusing e.g. on *Model NGG* (dotted curves) we see that during the first simulated 14-15 weeks the vascularization ensures a higher percentage of necrosis, after which the situation reverses, with differences becoming larger while time is advancing. The early phase (which is supposed to correspond to a lower tumor

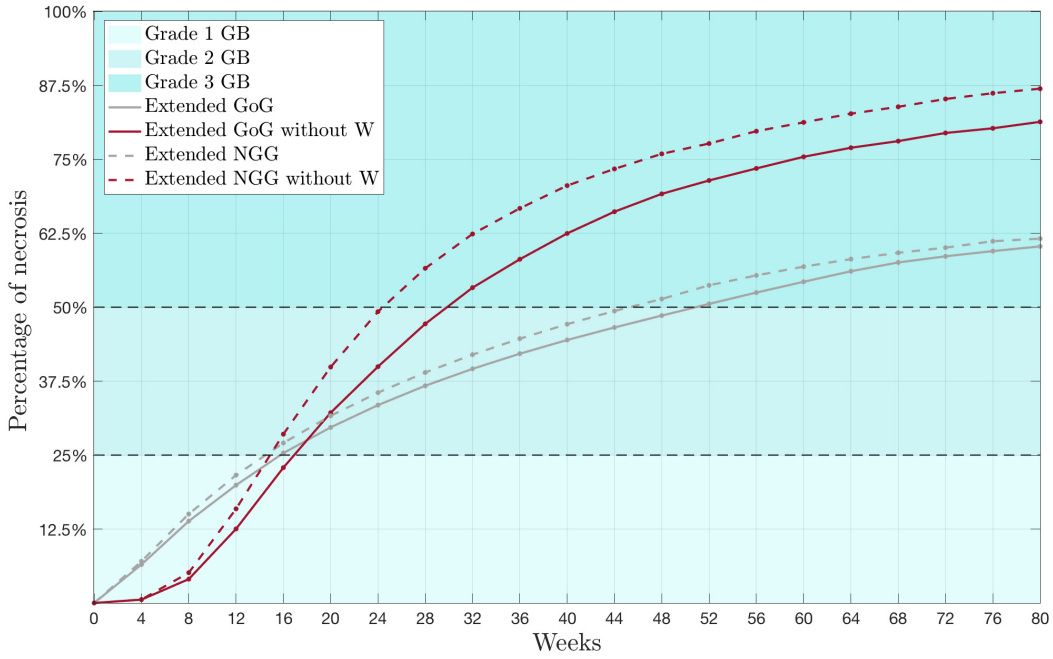

FIGURE 4.10: **Tumor grading.** Evolution of the grade function $G(t)$ given in (4.57). Grey curves relate to the extended full model (i.e., including dynamics of endothelial cells) in the case with go-or-grow (solid line, model (4.52), (4.56)) and without the migration-proliferation dichotomy (dotted line, *Model NGG*). The red curves refer to the same model variants, but without vascularization. In both cases we set $\mu_{N,0} = 5.79 \cdot 10^{-6}\ \mathrm{s}^{-1}$.

grade) can seem somehow paradoxical when thinking about blood capillaries buffering the acidity and reducing necrosis. It is, however, well-known that a tumor usually develops angiogenesis when it has reached a more advanced phase in its development and begun to get increasingly hypoxic, which leads to enhanced VEGF expression and capillary formation. The small amount of vessels prior to such stage is on the one side supporting the growth of tumor cells, while on the other side it is not able to buffer the ever-increasing proton concentration triggered by the exuberant growth. Without a substantial enhancement of angiogenesis, the tumor will develop a larger necrotic component, thus receiving a higher grade. Therefore, omitting the dynamics of endothelial cells from the model can overestimate the tumor growth and spread, which for brain tumors can have a significant therapeutic impact.

4.5 *Summary*

On the basis of the multiscale framework set up in Chapter 3 concerning the influence of the brain tissue on tumor progression, we extended in this chapter this description to include intratumor heterogeneity aspects and the impact of the tumor microenvironment. Precisely, we defined a multiscale mathematical model - to our knowledge, the first one of this type - with pH- and vasculature-induced phenotypic switch between moving and proliferating tumor cells that analyze the interdependency of tumor acidity and vascularity. In particular, intratumor heterogeneity, describing two tumor cell types, is modeled by means of two tumor subpopulations evolving under

mutual, direct, and indirect interactions. As such, it can be seen as a further development of the models in [75, 126], but several novelties have been introduced here, leading to a highly nonlinear and coupled system.

Starting from the description of single-cell dynamics for glioma, we formulated the corresponding kinetic transport equations for glioma and EC density distribution functions on the mesoscopic scale (Section 4.1.2) and employed a parabolic scaling to deduce the population-level behavior for the model variables (Section 4.1.3), i.e., glioma density, acid concentration (that determines the pH level), EC density, and - for the extended model - densities of normal tissue and necrotic matter. We considered a heterogeneous tumor and, using the go-or-grow dichotomy, we asserted that glioma cells can either move or proliferate and the respective behavior is transient and switches according to nutrient availability (supplied by vasculature), to pH (determined by proton production and buffering), as well as to crowded environments. In particular, the differences in relying on the go-or-growth dichotomy or assuming a uniform tumor population were analyzed in the simulations and the results are shown in Figures 4.5 and 4.6.

The microscopic dynamics, together with the mesoscopic description of the tumor and ECs velocity changes, allowed for the derivation of a macroscopic setting, which addresses multiple tactic phenomena. The macroscopic scale is characterized by nonlinear, myopic self-diffusion, involving the anisotropic tensor $\mathbf{D}_T$ which takes into account the local tissue structure, and also by multiple taxis (haptotaxis, chemotaxis, repellent pH-taxis) for both tactic populations, i.e., glioma cells and ECs. In particular, the haptotactic and pH-tactic processes, carrying information from the microscopic scale, direct glioma migration towards increasing tissue gradients, and away from highly (hypoxic and, thus,) acidic regions. Furthermore, ECs migrate by a combination of diffusion and drift terms, described indirectly the response of ECs to pro-angiogenic growth factors (e.g. VEGFs). In particular, in order not to maintain a low number of solution components, we described this response biasing EC migration towards proliferating tumor cells, which are assumed to produced VEGF. For the same reason, we implicitly include the effect of oxygen dynamics through EC-sustained tumor proliferation and the (hypoxia-caused) tumor acidosis. Analytically, ECs bias was described in an alternative manner with respect to the bias leading glioma cell migration. In particular, the effect of the multiple taxis and their dependency on the model parameters were shown and analyzed in Figures 4.3 and 4.4. The nonlinear nature of the dynamics arises also from the modeling of the chemorepellent taxis. In fact, the chemorepellent is produced by glioma cells which, in turn, try to avoid it. At the same time, the chemorepellent is degraded by the other tactic actor (ECs), which is directionally biased by a subpopulation of the glioma cells, namely the proliferating tumor cells. These mechanisms render the repellent acidity taxis of glioma cells both direct and indirect and make the coupling of the equations nonlinear. Moreover, Figures 4.3 and 4.4 highlight the capability of the model to reproduce hypoxia-related histopathological features typical of GB evolution. This aspect, together with the choice of a more realistic initial condition for ECs (preferably taken from vascular perfusion imaging data), would allow to improve our results and replicate the typical GB dynamics, in terms of both tumor extensions, hypoxia-related features, and acidosis.

The extension of the model, introduced in the last Section 4.4 and involving dynamics of tissue and necrotic matter, determined an additional indirect kind of haptotaxis, with even more complex coupled equations. In particular, this extension opened the way for necrosis-based tumor grading, which we used for determining the evolution of the tumor in different scenarios and the influence of the tumor heterogeneity and the vasculature supply on it, as shown by Figure 4.10. In particular, this extension

is highly relevant for diagnosis and therapy planning, several aspects of which will be discussed in detail in the forthcoming chapter.

5 *Vasculature, VEGFs, and therapy effects*

The development of a glioma in the brain and, especially, of its more advanced subtype (glioblastoma) is accompanied by strong angiogenic processes. Angiogenesis, driven by hypoxia-dependent and independent mechanisms, is primarily mediated by vascular endothelial growth factors (VEGFs) expressed by tumor cells. The angiogenic process generates blood vessels that are often distorted, enlarged, and with erratic blood flux or microhemorrhages. These features of the blood vessels determine leaky and unstable blood flow, despite increased vessel density. The vessel network is essential to supply the tumor cells with oxygen and nutrients necessary, among others, for cell growth and migration. In Chapter 4, we focused on some aspects involved in the relationship between tumor and endothelial cells, the latter being responsible for the capillary formation. In the specific, we analyzed intratumor heterogeneity and acidity dynamics in response to endothelial cell evolution, while the role of VEGFs was indirectly accounted for by the EC chemotactic term. In this chapter, we look closely at the VEGF-driven angiogenesis and at the possible effects of combined treatments affecting tumor, ECs, and tissue.

The standard treatments for glioma patients includes, after the maximum safe resection, radiation therapy, and chemotherapy with temozolomide. This protocol usually achieves a median progression-free survival varying from 6.9 to 14.7 months. Angiogenesis is a complex and critical feature involved in tumor progression and, thus, offers several potential strategies for therapeutic exploitation. In the last decades, clinical studies in glioma patients have shown improved progression-free survival in response to combined treatments of radiation, chemotherapy with temozolomide, and anti-angiogenic therapy with bevacizumab, a humanized monoclonal antibody targeting vascular endothelial growth factors [92, 149]. VEGFs typically localize adjacent to necrotic regions and within glioma pseudopalisades [207, 249], and their expression increases with the tumor grade. Many strategies are under clinical evaluation to therapeutically target multiple aspects of VEGF activation. For instance, direct suppression of VEGF receptor activation can be achieved by targeting either the corresponding ligand or the receptor, and ligand inactivation can be achieved by sequestering VEGF to either antibodies or soluble decoy receptors, preventing effective receptor binding [242]. More than 50 clinical trials[1] are evaluating bevacizumab alone or in combination with other treatments for patients with recurrent glioblastoma (see [242] and references therein). These studies with bevacizumab show that VEGF/VEGFR-targeting agents can be safely used in patients with glioblastoma. Moreover, anti-VEGF antibody treatment has been shown to inhibit angiogenesis and glioblastoma growth. However, many additional aspects of anti-angiogenic therapy require further insights. There are still several difficulties in assessing the body response after anti-VEGF therapies and in identifying effective treatments after bevacizumab failure. For instance, a

[1] www.clinicaltrials.gov

better understanding of the mechanisms of resistance to VEGF/VEGFR therapeutics is paramount to implementing more effective strategies and to improve patient survival.

The content of this chapter is organized as follows. In Section 5.1, we describe the model setup and the deduction of the macroscopic PDEs from the lower scales. Then, in Section 5.2, we provide the explicit expressions of the coefficient functions involved in the macroscopic setting along with a proper assessment of the model parameters and non-dimensionalization. Finally, in Section 5.3, we present the numerical simulations of both scenarios (without and with therapy) in order to understand the therapy effects on tumor progression.

5.1 *Modeling setting*

Aiming at understanding the efficacy of combinations of standard therapies used for treating glioma patients with new anti-angiogenic agents, we consider here a new multiscale framework describing the evolution of the tumor population in interaction with several environmental factors. On the basis of the extended model proposed in Section 4.4, we modify some of the assumptions previously stated, moving the central focus on the therapy modeling and the consequent effects on tumor progression.

Glioma cells, considered as one tumor population, migrate along tissue fibers and blood vessels. In order to meet nutrient and oxygen supply demands, a tumor produces and releases in the extracellular environment growth factors, such as VEGFs, that attract endothelial cells. These cells, in turn, enhance tumor growth and lead to a more vascularized and advanced neoplasm. Standard therapy with radiation is usually combined with chemotherapy. Here, we consider chemotherapy with *temozolomide*, which is administered by blood and is directly aimed at killing cells. This choice for the chemotherapy differs from the model proposed in Chapter 3, where the chemotherapeutic agent consists of integrin inhibitors, affecting tumor-ECM interactions. Recently, the combination of radio- and chemotherapy has been studied in association with several complementary treatments. In this context, *anti-angiogenic factors*, such as *bevacizumab*, have been used to reduce the affinity between VEGF and endothelial cells and, consequently, to affect the tumor vasculature supply. Thus, starting from the general multiscale framework described in the previous chapters, we specify here the three scales of the new model setting.

- The microscopic level describes the interactions that drive both tumor and endothelial cell migration. Tumor cells bind with tissue and vasculature through the integrin receptors located on their cell membrane and they use these bindings to crawl along fibers and vessels. Similarly, endothelial cells respond to the chemotactic cue determined by the tumor-produced growth factors upon binding such ligands to their corresponding membrane receptors. We model these two processes by also including the effects of two treatment components. We consider the role of the anti-angiogenic therapy on the VEGF-EC interactions and the effect of radiation on the available healthy tissue and vessels with which the glioma cells interact. Thus, for this setting, we follow the idea of building a micro-meso model for both tumor and EC populations.

- On the mesoscopic level, we describe the corresponding kinetic transport equations for the density function of glioma and endothelial cells. These equations

model the interactions between tumor cells, vasculature, tissue, and growth factors. Moreover, we include the description of the effects of radio- and chemotherapy on glioma and ECs, as well as the effect of anti-angiogenic therapy on the EC proliferation ability.

- The macroscopic level, deduced via a parabolic limit of the mesoscopic equations, consists of a macroscopic system of advection-diffusion-reaction PDEs for the involved quantities: density of glioma and endothelial cells, and VEGF concentration. The resulting system includes anisotropic diffusion along the directions of the brain fibers, several types of taxis, tissue-mediated proliferation, and death processes due to the treatment. Moreover, we include at this level the formation and evolution of necrotic regions due to the treatment and the dynamics of the healthy tissue. The latter degrades due to the acidity produced by tumor cells and due to the effect of the radiotherapy, which affects tumor and healthy matter, although to different extents.

5.1.1 *Subcellular level*

On the microscopic scale, we describe the interactions of glioma cells with the unsoluble components of the ECM and the vessels. Moreover, we consider the interactions between ECs and VEGFs, which diffuse in the extracellular space. As we described in the introductory chapter, for both tumor and ECs the exchange of information between the cells and their extracellular microenvironment is mediated by through various transmembrane entities. In this model, these are integrin receptors for the tumor population and VEGF receptors for the exchange between VEGFs and ECs. We neglect the details about the intracellular machinery activated by receptor binding, as we assume that the events of occupying such transmembrane units trigger the cellular processes, which lead to migration and proliferation. This assumption follows the idea revisited in the previous chapters and in a large series of works in the literature, especially for the case of cell-tissue interactions (e.g. see [77, 136, 169]).

We denote by $y_1(t)$ the amount of glioma receptors bound to the tissue fibers and by $y_2(t)$ that receptors bound to the vessels, irrespective of how these are oriented. Concerning endothelial cells, we denote by $\zeta(t)$ the amount of EC receptors bound to VEGF molecules. The corresponding binding dynamics is characterized by simple mass action kinetics:

$$\begin{aligned} (\bar{R}_0 - y_1 - y_2) \; + \; \frac{W}{W_{c,0}} \underset{k_W^-}{\overset{k_W^+}{\rightleftharpoons}} y_1 \\ (\bar{R}_0 - y_1 - y_2) \; + \; \frac{Q}{Q^*} \underset{k_Q^-}{\overset{k_Q^+}{\rightleftharpoons}} y_2 \\ (\bar{R}_\zeta - \zeta) \; + \; \frac{H}{H_{c,0}} \underset{k_H^-}{\overset{k_H^+}{\rightleftharpoons}} \zeta \, . \end{aligned} \tag{5.1}$$

Here, $\bar{R}_0$ and $\bar{R}_\zeta$ represent the total amount of receptors on a tumor cell and on an endothelial cell, respectively. Both values are assumed to be constant. $Q(t, \mathbf{x})$ denotes the macroscopic brain tissue density, $W(t, \mathbf{x})$ the macroscopic density of ECs, and $H(t, \mathbf{x})$ the concentration of VEGFs. These three populations depend on the position $\mathbf{x} \in \mathbb{R}^d$ and the time $t > 0$. Further, $W_{c,0}$, Q^*, and $H_{c,0}$ denote the reference density/concentration values for ECs, tissue, and VEGFs, respectively. The corresponding

equations for the microscopic dynamics read

$$\dot{y}_1 = k_W^+ \frac{W}{W_{c,0}} S_W(d_r, \alpha_W)\,(\bar{R}_0 - y_1 - y_2) - k_W^- y_1\,,$$

$$\dot{y}_2 = k_Q^+ \frac{Q}{Q^*} S_Q(d_r, \alpha_Q)(\bar{R}_0 - y_1 - y_2) - k_Q^- y_2\,,$$

$$\dot{\zeta} = k_H^+(d_b) \frac{H}{H_{c,0}} (\bar{R}_\zeta - \zeta) - k_H^-(d_b)\zeta\,,$$

where k_W^+ and k_W^-, k_Q^+ and k_Q^- represent the attachment and the detachment rates of glioma cells to vessels and tissue, respectively, while k_H^+ and k_H^- are the corresponding coefficient functions in the process of VEGF-EC binding. As stated above, at this level, we include the effect of the anti-angiogenic therapy on the EC receptors and, also, the effect of radiotherapy on the tumor receptor dynamics. Precisely, we model the effect of radiotherapy, which reduces the available healthy tissue and vasculature to which glioma cells interact by way of their receptors. We recall the L-Q model introduced in Chapter 3 defining the function

$$S(d_r, \alpha) := \exp\left(-\alpha d_r - \beta d_r^2\right)$$

that is used to describe the fraction of cells that survive to a dose d_r of radiotherapy. Each population affected by radiotherapy has different values for the parameters α and β, referring to the lethal lesions produced by a single radiation track or by two radiation tracks. The parameter pairs (α_W, β_W) and (α_Q, β_Q) refer to the effects of radiotherapy on the vasculature W and on the brain tissue Q, respectively. In the following, we indicate with S_W and S_Q the survival fractions of W and Q, neglecting in the writing their dependency on the parameters α, β, and d_r. The interactions between ECs and VEGFs are influenced by the anti-angiogenic drug, delivered at a dose d_b. This drug reduces the binding affinity of VEGF molecules with its corresponding receptors on the EC membrane. Thus, we model this effect in the attachment/detachment coefficient functions, i.e.,

$$k_H^+(d_b) := \bar{k}_H^+ l^+(d_b)\,,$$

$$k_H^-(d_b) := \bar{k}_H^- l^-(d_b)\,,$$

where $l^+(d_b)$ and $l^-(d_b)$ are a decreasing and an increasing function of d_b, respectively.

As we did in the previous chapter, we define $y := y_1 + y_2$ to be the total amount of transmembrane entities on the tumor cells occupied by tissue or ECs. With this we can lump together the two ODEs for the tumor receptors, obtaining

$$\dot{y} = \left(k_W^+ \frac{S_W}{W_{c,0}} W + k_Q^+ \frac{S_Q}{Q^*} Q\right)(\bar{R}_0 - y) - k_W^- y_1 - k_Q^- y_2\,.$$

Assuming that $k_W^- = k_Q^- = k^-$, we get the following microscopic equation for the subcellular dynamics

$$\dot{y} = \left(k_W^+ \frac{S_W}{W_{c,0}} W + k_Q^+ \frac{S_Q}{Q^*} Q\right)(\bar{R}_0 - y) - k^- y\,. \tag{5.2}$$

Rescaling $y/\bar{R}_y \rightsquigarrow y$ and $\zeta/\bar{R}_\zeta \rightsquigarrow \zeta$ we can further simplify the notation. Thus, the unique steady states of equations (5.2) and (5.1) are given by:

$$y^* = \frac{\left(k_W^+ \frac{S_W}{W_{c,0}} W + k_Q^+ \frac{S_Q}{Q^*} Q\right)}{k_W^+ \frac{S_W}{W_{c,0}} W + k_Q^+ Q \frac{S_Q}{Q^*} + k^-},$$

$$\zeta^* = \frac{k_H^+ \frac{H}{H_{c,0}}}{k_H^+(d_b)\frac{H}{H_{c,0}} + k_H^-(d_b)}.$$

In line with the models proposed in the previous chapters, the variable y characterizes the overall internal tumor state, while ζ characterizes the internal EC state. In the following sections, we consider the mesoscopic densities $\rho(t, \mathbf{x}, \mathbf{v}, y)$ and $w(t, \mathbf{x}, \vartheta, \zeta)$ of tumor and endothelial cells, that are hence depending on such internal variables y and ζ. Moreover, we assume that glioma cells follow the gradients of tissue and vasculature. Thus, we look at the path of a single cell starting at position $\mathbf{x}_0$ and moving to position $\mathbf{x}$ with velocity $\mathbf{v}$ in the density fields $Q(t, \mathbf{x})$ and $W(t, \mathbf{x})$, so that $Q(t, \mathbf{x}) = Q(t, \mathbf{x}_0 + \mathbf{v}t)$ and $W(t, \mathbf{x}) = W(t, \mathbf{x}_0 + \mathbf{v}t)$. Denoting by $z := y^* - y$ the deviation of y from its steady state, we have:

$$\dot{z} = \frac{k^-}{\left(k_W^+ \frac{S_W}{W_{c,0}} W + k_Q^+ \frac{S_Q}{Q^*} Q + k^-\right)^2} \left(k_W^+ \frac{S_W}{W_{c,0}} \mathbf{v} \cdot \nabla W + k_Q^+ \frac{S_Q}{Q^*} \mathbf{v} \cdot \nabla Q + \bar{F}_W(t) + \bar{F}_Q(t)\right)$$

$$- z \left(k_W^+ \frac{W}{W_{c,0}} S_W + k_Q^+ \frac{S_Q}{Q^*} Q + k^-\right) =: G(z, W, Q)$$

with

$$\bar{F}_W(t) := k_W^+ \frac{S_W}{W_{c,0}} \partial_t W,$$

$$\bar{F}_Q(t) := k_Q^+ \frac{S_Q}{Q_{c,0}} \partial_t Q.$$

To simplify the notation, we define

$$B_\rho(W, Q) := \left(k_W^+ \frac{S_W}{W_{c,0}} W + k_Q^+ \frac{S_Q}{Q^*} Q + k^-\right).$$

With an analogous argument, denoting by $u := \zeta^* - \zeta$ the deviation of ζ from its steady state, we assume that ECs follow the gradient of the growth factors. Thus, we look at the path of a single cell starting at position $\mathbf{x}_0$ and moving to position $\mathbf{x}$ with velocity ϑ in the density fields H, so that $H(t, \mathbf{x}) = H(t, \mathbf{x}_0 + \vartheta t)$. The equation for u is given by:

$$\dot{u} = \frac{\frac{k_H^+}{H_{c,0}} k_H^-}{\left(\frac{k_H^+}{H_{c,0}} H + k_H^-\right)^2} (\partial_t H + \vartheta \cdot \nabla H) - u \left(\frac{k_H^+}{H_{c,0}} H + k_H^-\right) =: \Gamma(u, H).$$

To simplify the notation, we define

$$B_w(H) := \left(\frac{k_H^+}{H_{c,0}} H + k_H^- \right) .$$

5.1.2 *Mesoscopic level*

We model the behavior of glioma and endothelial cells at the mesoscopic level with the aid of kinetic transport equations (KTEs) describing velocity-jump processes and taking into account the subcellular dynamics proposed in the previous section. In the specific, we consider the following cell density functions:

- $\rho(t, \mathbf{x}, \mathbf{v}, y)$ for glioma cells;
- $w(t, \mathbf{x}, \vartheta, \zeta)$ for endothelial cells (ECs) forming capillaries and blood vessels.

These density functions depend on the time and the space variables $t > 0$ and $\mathbf{x} \in \mathbb{R}^d$, the velocities $\mathbf{v} \in \mathbf{V} = s\mathbb{S}^{d-1}$ and $\vartheta \in \Theta = \sigma\mathbb{S}^{d-1}$ ($\mathbb{S}^{d-1}$ denotes the unit sphere in $\mathbb{R}^d$), and the internal variables $y \in \mathbf{Y} = (0,1)$ and $\zeta \in \mathbf{Z} = (0,1)$. These choices mean that we assume for glioma and ECs constant speeds $s > 0$ and $\sigma > 0$, respectively. As in the previous chapters, for the derivation of this model we work with the deviations $z = y^* - y \in Z \subseteq (y^* - 1, y^*)$ rather than y for glioma cells and $u = \zeta^* - \zeta \in U \subseteq (\zeta^* - 1, \zeta^*)$ rather than ζ for ECs. We denote by $M(t, \mathbf{x})$ and $W(t, \mathbf{x})$ the corresponding space-time varying macroscopic cell densities for tumor and ECs, respectively.

The kinetic transport equation for ***glioma cells*** is given by

$$\frac{\partial \rho}{\partial t} + \nabla \cdot (\mathbf{v}\rho) + \frac{\partial}{\partial z}(G(z, W, Q)\rho) = \mathcal{L}_\rho[\lambda(z)]\rho + \mathcal{P}(\rho) - R_M(d_r)\rho + C_M(d_c)\rho , \quad (5.3)$$

where $\mathcal{L}_\rho[\lambda(z)]$ denotes the turning operator, $\mathcal{P}(\rho)$ is the proliferation term, and $R_M(d_r)$ and $C_M(d_c)$ are therapy-related terms. Precisely, the turning operator describes the tumor velocity changes. Such changes are due to contact guidance, determined by orientation of the underlying brain network of fibers. As in the previous models of this type, $\mathcal{L}_\rho[\lambda(z)]\rho$ is a Boltzmann-like integral operator of the form

$$\mathcal{L}_\rho[\lambda(z)]\rho = -\lambda(z)\rho + \lambda(z) \int_{\mathbf{V}} K(\mathbf{x}, \mathbf{v})\, \rho(\mathbf{v}')\, d\mathbf{v}' ,$$

with the cell turning rate $\lambda(z) := \lambda_0 - \lambda_1 z \geq 0$ depending on the microscopic variable z, while λ_0 and λ_1 are positive constants. The integral term describes the reorientation of cells from any previous velocity $\mathbf{v}'$ to a new velocity $\mathbf{v}$ after interacting with the tissue. The turning kernel $K(\mathbf{x}, \mathbf{v})$, describing the likelihood of the cells to adopt the velocity $\mathbf{v}$ after being in the velocity regime $\mathbf{v}'$, has the same properties we discussed in Chapters 2-4. We simply recall that its expression is given in (3.15), with the orientational distribution of the undirected fiber network $q(\mathbf{x}, \hat{\mathbf{v}})$. In the sequel, we use the symmetry property of $q(\mathbf{x}, \hat{\mathbf{v}})$ together with the notations (3.16) and (3.17) previously introduced.

The proliferation process, described with the term $\mathcal{P}(\rho)$, is triggered by glioma cell receptor binding with the brain tissue and it also depends on the availability of nutrients and oxygen (supplied by ECs). The proliferation term reads

$$\mathcal{P}(\rho) := \mu_M(M, W, N_e) \int_Z \chi(\mathbf{x}, z, z') \frac{Q(t, \mathbf{x})}{Q^*} \rho(t, \mathbf{x}, \mathbf{v}, z') dz' .$$

The proliferation rate $\mu_M(M, W, N_e)$ depends on the macroscopic densities of tumor cells M and endothelial cells W, as well as on the necrotic matter N_e. In the integral operator, the kernel $\chi(\mathbf{x}, z, z')$ characterizes the transition from state z' to state z during a proliferation event originating from the interaction at position $\mathbf{x}$. This kernel satisfies the same properties as described in Section 3.2.2.

The last terms in equation (5.3) describe the negative effects of radiotherapy and chemotherapy on the tumor population. In the specific, $R_M(d_r)$ describes the radiation effect on tumor cells by means of the L-Q model. $R_M(d_r)$ is expressed in terms of the survival fraction $S(d_r, \alpha)$ introduced above, i.e.,

$$R_M(d_r) = 1 - S(d_r, \alpha_M) \tag{5.4}$$

with d_r being the dose of radiotherapy and α_M a parameter referring to the lesions caused by the radiation on the neoplastic tissue. Chemotherapy is modeled using the coefficient function $C_M(d_c)$, with mortality rate d_c. Several cell-kill models have been proposed in the literature and applied to the study of the chemotherapy effects on tumor growth (e.g. see [147] and references therein). Here, we rely on the log-kill hypothesis stating that cell killing is proportional to the tumor population [260], i.e., a given dose of chemotherapy kills a fixed fraction of cells. Therefore, a linear increase in the dose causes a log increase in the cell death. A standard treatment plan for glioma patients consists in a phase of concurrent radio- and chemotherapy, followed by a resting period and, then, one or more phases of adjuvant chemotherapy alone. Usually, the dosages in the different phases are not equal. We choose the mortality rate d_c to be proportional to a chemotherapy dose of 75 mg $\cdot$ m^{-2} (the standard dose of the concurrent phase) and, then, the other dosages will be appropriate fractions of d_c [229]. For instance, if we assume three different phases of administration of the treatment ($[t_0, t_1]$,$[t_2, t_3]$ and $[t_4, t_5]$) and two resting periods $[t_1, t_2]$ and $[t_3, t_4]$, then $C_M(d_c)$ can be modeled as

$$C_M(d_c) := d_c(t) = \begin{cases} d_{c_1} & t_0 \leq t \leq t_1 \\ d_{c_3} & t_2 \leq t \leq t_3 \\ d_{c_5} & t_4 \leq t \leq t_5 \\ 0 & t \text{ not in the intervals}. \end{cases}$$

Here, the parameters d_{c_i}, for $i = 1, 3, 5$ represents the mortality rate of the chemotherapy administrated in $[t_{i-1}, t_i]$.In the following, we indicate with

$$L_M(d_r, d_c) := R_M(d_r) + C_M(d_c)$$

the overall tumor loss term due to the combination of radio- and chemotherapy.

The KTE for ***endothelial cells*** is given by:

$$\frac{\partial w}{\partial t} + \nabla \cdot (\vartheta w) + \frac{\partial}{\partial u}(\Gamma(u, H)w) = \mathcal{L}_w[\gamma(u)]w + \mathcal{P}_w(w) - R_W(d_r)w\,. \tag{5.5}$$

In this equation, the turning operator $\mathcal{L}_w[\gamma(u)]w$ describes the changes in the orientation of ECs due to their chemotactic response to the concentration of the growth factors H produced by the tumor cells. Differently from Chapter 4 where we indirectly described the EC response to VEGFs modeling their tactic motion towards the tumor cells producing these growth factors, we directly include here the VEGF dynamics. These growth factors determine an angiogenic signal, which stimulates the nearby host stroma cells to proliferate. These cells provide the tumor with vasculature and, hence, with the means for a faster growth. For the description of the EC turning

dynamics, we consider here a Boltzmann-like integral operator similar to the one used for tumor cells, but with a different turning kernel, namely

$$\mathcal{L}_w[\gamma(u)]w = -\gamma(u)w + \gamma(u)\int_\Theta \frac{1}{|\Theta|} w(\vartheta')d\vartheta' ,$$

where $|\Theta|$ represents the measure of the set $\Theta = \sigma \mathbb{S}^{d-1}$. For the turning kernel modeling EC reorientations, we use here for simplicity a uniform distribution. The EC turning rate $\gamma(u) := \gamma_0 - \gamma_1 u \geq 0$ depends on the microscopic variable u and, consequently, on the concentration of VEGFs. γ_0 and γ_1 are positive constants.

The proliferation term $\mathcal{P}_w(w)$ related to ECs describes proliferation as the result of the interactions between the endothelial cells and growth factors:

$$\mathcal{P}_w(w) := \mu_W(W, Q, d_b)\int_U \chi_W(\mathbf{x}, u, u')\frac{H(t,\mathbf{x})}{H_{c,0}} w(t, \mathbf{x}, \vartheta, u')du' .$$

The source rate $\mu_W(W, Q, d_b)$ depends on the macroscopic density of ECs W and on the unsoluble component of the brain tissue $Q(t, \mathbf{x})$. Moreover, we include at this level an additional effect of the anti-angiogenic therapy. Besides affecting the EC affinity with the VEGFs, this treatment influences the proliferation of ECs, reducing or inhibiting the mitotic capability of these cells. Thus, we include the dependency of the proliferation rate on the anti-angiogenic dose d_b.

Finally, the last term $R_W(d_r)$ of equation (5.5) describes the death of ECs due to radiation. In fact, capillaries and tumor cells have similar cell cycle time scale and, for this reasons, they are similarly affected by radiotherapy treatments. In this case,

$$R_W(d_r) := 1 - S(d_r, \alpha_W) ,$$

with α_W a parameter related to the lesions caused by radiation on the capillaries. The concrete choices for the coefficient functions involved in (5.3) and (5.5) are provided in Section 5.2.

5.1.3 *Parabolic scaling of the mesoscopic model*

We deduce the effective equations for the macroscopic dynamics of ECs W and glioma cells N, since clinicians are typically interested in the analysis of the macroscopic evolution of the tumor mass along with vasculature and necrotic matter. We couple the equations deduced from the mesoscale with PDEs for VEGF concentration H, tissue degradation Q, and necrotic tissue N_e. These equations are stated directly at the macroscopic level and do not need to be upscaled. In fact, as we already mentioned in Chapter 4 for the proton dynamics, it is not necessary to include microscopic or mesoscopic variables (such as the microscopic velocity) in the VEGF equation, since the VEGF concentration does not undergo velocity changes; same applies to the equations for the healthy tissue and necrotic matter.

We first define the moments for the mesoscopic variables ρ and w as

$$m(t,\mathbf{x},\mathbf{v}) = \int_Z \rho(t,\mathbf{x},\mathbf{v},z)dz, \qquad m^z(t,\mathbf{x},\mathbf{v}) = \int_Z z\rho(t,\mathbf{x},\mathbf{v},z)dz ,$$

$$M(t,\mathbf{x}) = \int_\mathbf{V} m(t,\mathbf{x},\mathbf{v})d\mathbf{v}, \qquad M^z(t,\mathbf{x}) = \int_\mathbf{V} m^z(t,\mathbf{x},\mathbf{v})d\mathbf{v} ,$$

$$\bar{w}(t,\mathbf{x},\vartheta) = \int_U w(t,\mathbf{x},\vartheta,u)du, \qquad \bar{w}^u(t,\mathbf{x},\vartheta) = \int_U u\, w(t,\mathbf{x},\vartheta,u)du ,$$

$$W(t,\mathbf{x}) = \int_\Theta w(t,\mathbf{x},\vartheta)d\vartheta, \qquad W^u(t,\mathbf{x}) = \int_\Theta w^u(t,\mathbf{x},\vartheta)d\vartheta\,,$$

neglecting the higher order moments with respect to the variables z and u, as the subcellular dynamics is assumed to be much faster than the events on the higher scales, hence $z \ll 1$ and $u \ll 1$. We assume the functions ρ and w to be compactly supported in the phase spaces $\mathbb{R}^d \times \mathbf{V} \times Z$ and $\mathbb{R}^d \times \Theta \times U$, respectively.

We integrate equation (5.3) with respect to z, getting the following equation for $m(t,\mathbf{x},\mathbf{v})$:

$$\begin{aligned}\frac{\partial m}{\partial t} + \nabla\cdot(\mathbf{v}m) = &-\lambda_0\left(m - \frac{q}{\omega}M\right) + \lambda_1\left(m^z - \frac{q}{\omega}M^z\right)\\ &+ \int_Z \mu_M(M,W,N_e)\int_Z \chi(\mathbf{x},z,z')\rho(z')\frac{Q}{Q^*}dz'dz - L_M(d_r,d_c)m\,.\end{aligned}$$

Using the fact that $\chi(\mathbf{x},z,z')$ is a probability kernel with respect to z for all pairs $(\mathbf{x},z^{'})$, the previous equation for $m(t,\mathbf{x},\mathbf{v})$ reduces to:

$$\frac{\partial m}{\partial t}+\nabla\cdot(\mathbf{v}m) = -\lambda_0\left(m-\frac{q}{\omega}M\right)+\lambda_1\left(m^z-\frac{q}{\omega}M^z\right)+\mu_M(M,W,N_e)\frac{Q}{Q^*}m-L_M(d_r,d_c)m\,. \tag{5.6}$$

Then, we multiply equation (5.3) by z and integrate it with respect to z, obtaining

$$\begin{aligned}\frac{\partial m^z}{\partial t} &= -\nabla\cdot(\mathbf{v}m^z) + \int_Z z\frac{\partial}{\partial z}\left[zB_\rho(W,Q)\,\rho(z)\right]dz\\ &- \int_Z z\frac{\partial}{\partial z}\left[\frac{k^-}{B_\rho(W,Q)^2}\left(\left(k_W^+\frac{S_W}{W_{c,0}}\mathbf{v}\cdot\nabla W + k_Q^+\frac{S_Q}{Q^*}\mathbf{v}\cdot\nabla Q\right) + (\bar{F}_W+\bar{F}_Q)\right)\rho(z)\right]dz\\ &+ \int_Z z\mathcal{L}_\rho[\lambda(z)]\rho(z)dz + \int_Z z\,\mu_M(M,W,N_e)\int_Z\chi(\mathbf{x},z,z')\rho(z')\frac{Q}{Q^*}dz'dz - L_M(d_r,d_c)m^z.\end{aligned}$$

The integral terms can be calculated, leading to the following equation for $m^z(t,\mathbf{x},\mathbf{v})$:

$$\begin{aligned}\frac{\partial m^z}{\partial t} = &-\nabla\cdot(\mathbf{v}m^z) - B_\rho(W,Q)m^z\\ &+\frac{k^-}{B_\rho(W,Q)^2}\left(\left(k_W^+\frac{S_W}{W_{c,0}}\mathbf{v}\cdot\nabla W + k_Q^+\frac{S_Q}{Q^*}\mathbf{v}\cdot\nabla Q\right) + (\bar{F}_W+\bar{F}_Q)\right)m\\ &-\lambda_0\left(m^z-\frac{q}{\omega}M^z\right)+\mu_M(M,W,N_e)\int_Z\int_Z z\chi(\mathbf{x},z,z')\rho(z')\frac{Q}{Q^*}dz'dz - L_M(d_r,d_c)m^z.\end{aligned} \tag{5.7}$$

Applying the same procedure to equation (5.5) considering the integration with respect to u, we obtain the following equation for the moment $\bar{w}$:

$$\frac{\partial\bar{w}}{\partial t} + \nabla\cdot(\vartheta\bar{w}) = -\gamma_0\left(\bar{w} - S_d^\sigma W\right) + \gamma_1\left(\bar{w}^u - S_d^\sigma W^u\right) + \mu_W(W,Q,d_b)\frac{H}{H_{c,0}}\bar{w} - R_W(d_r)\bar{w}\,, \tag{5.8}$$

assuming $\chi_W(\mathbf{x},u,u^{'})$ to be a probability kernel with respect to u for all $(\mathbf{x},u^{'})$. Multiplying by u and integrating again (5.5) with respect to u, we get the following equation

for $\bar{w}^u$:

$$\frac{\partial \bar{w}^u}{\partial t} = -\nabla\cdot(\vartheta \bar{w}^u) + \int_U u \frac{\partial}{\partial u}\left[\left(uB_w(H) - \frac{\frac{k_H^+}{H_{c,0}}k_H^-}{B_w(H)^2}(\vartheta\cdot\nabla H + \partial_t H)\right)w(u)\right]du \tag{5.9}$$
$$+\int_U u\mathcal{L}_w[\gamma(u)]w(u)du + \int_U u\mu_W(W,Q,d_b)\int_U \chi_W(\mathbf{x},u,u')\frac{H}{H_{c,0}}w(u')du'du - R_W(d_r)\bar{w}^u\,.$$

After calculating the integral term, equation (5.9) reduces to

$$\begin{aligned}\frac{\partial \bar{w}^u}{\partial t} =& -\nabla\cdot(\vartheta\bar{w}^u) - B_w(H)\bar{w}^u + \frac{\frac{k_H^+}{H_{c,0}}k_H^-}{B_w(H)^2}(\vartheta\cdot\nabla H + \partial_t H)\bar{w} - \gamma_0\left(\bar{w}^u - S_d^\sigma W^z\right)\\ &+ \mu_W(W,Q,d_b)\int_U\int_U u\chi_W(\mathbf{x},u,u')\frac{H}{H_{c,0}}w(u')du'du - R_W(d_r)\bar{w}^u\,.\end{aligned} \tag{5.10}$$

Considering the derived equations (5.6), (5.7), (5.8), and (5.10), we rescale the time and space variables as $t \to \varepsilon^2 t$ and $\mathbf{x} \to \varepsilon\mathbf{x}$. In particular, the proliferation and death terms in (5.3) and (5.5) are scaled by ε^2 in order to account for mitotic and apoptotic events taking place on a much slower time scale than migration. Hence, the resulting rescaled equations read

$$\begin{aligned}\varepsilon^2\frac{\partial m}{\partial t} + \varepsilon\nabla\cdot(\mathbf{v}m) =& -\lambda_0\left(m - \frac{q}{\omega}M\right) + \lambda_1\left(m^z - \frac{q}{\omega}M^z\right) + \varepsilon^2\mu_M(M,W,N_e)\frac{Q}{Q^*}m\\ &- \varepsilon^2 L_M(d_r,d_c)m\,,\end{aligned} \tag{5.11}$$

$$\begin{aligned}\varepsilon^2\frac{\partial m^z}{\partial t} =& -\varepsilon\nabla\cdot(\mathbf{v}m^z) - B_\rho(W,Q)m^z - \varepsilon^2 L_M(d_r,d_c)m^z\\ &+ \frac{k^-}{B_\rho(W,Q)^2}\left(\varepsilon\left(k_W^+\frac{S_W}{W_{c,0}}\mathbf{v}\cdot\nabla W + k_Q^+\frac{S_Q}{Q^*}\mathbf{v}\cdot\nabla Q\right) + \varepsilon^2\left(\bar{F}_W + \bar{F}_Q\right)\right)m\\ &- \lambda_0\left(m^z - \frac{q}{\omega}M^z\right) + \varepsilon^2\mu_M(M,W,N_e)\int_Z\int_Z z\chi(\mathbf{x},z,z')\rho(z')\frac{Q}{Q^*}dz'dz\,,\end{aligned} \tag{5.12}$$

$$\begin{aligned}\varepsilon^2\frac{\partial \bar{w}}{\partial t} + \varepsilon\nabla\cdot(\vartheta\bar{w}) =& -\gamma_0\left(\bar{w} - S_d^\sigma W\right) + \gamma_1\left(\bar{w}^u - S_d^\sigma W^u\right) + \varepsilon^2\mu_W(W,Q,d_b)\frac{H}{H_{c,0}}\bar{w}\\ &- \varepsilon^2 R_W(d_r)\bar{w}\,,\end{aligned} \tag{5.13}$$

$$\begin{aligned}\varepsilon^2\frac{\partial \bar{w}^u}{\partial t} =& -\varepsilon\nabla\cdot(\vartheta\bar{w}^u) - B_w(H)\bar{w}^u + \frac{\frac{k_H^+}{H_{c,0}}k_H^-}{B_w(H)^2}(\varepsilon\vartheta\cdot\nabla H + \varepsilon^2\partial_t H)\bar{w} - \gamma_0\left(\bar{w}^u - S_d^\sigma W^z\right)\\ &+ \varepsilon^2\mu_W(W,Q,d_b)\int_U\int_U u\chi_W(\mathbf{x},u,u')\frac{H}{H_{c,0}}w(u')du'du - \varepsilon^2 R_W(d_r)\bar{w}^u\,.\end{aligned} \tag{5.14}$$

We recall that $S_d^\sigma := \frac{1}{|\Theta|} = \frac{\sigma^{1-d}}{|\mathbb{S}^{d-1}|}$. We consider the Hilbert expansions for the previously introduced moments:

$$m(t,\mathbf{x},\mathbf{v}) = \sum_{k=0}^{\infty} \varepsilon^k m_k, \qquad m^z(t,\mathbf{x},\mathbf{v}) = \sum_{k=0}^{\infty} \varepsilon^k m_k^z$$

$$M(t,\mathbf{x}) = \sum_{k=0}^{\infty} \varepsilon^k M_k, \qquad M^z(t,\mathbf{x}) = \sum_{k=0}^{\infty} \varepsilon^k M_k^z$$

$$\bar{w}(t,\mathbf{x},\vartheta) = \sum_{k=0}^{\infty} \varepsilon^k \bar{w}_k, \qquad \bar{w}^u(t,\mathbf{x},\vartheta) = \sum_{k=0}^{\infty} \varepsilon^k \bar{w}_k^u,$$

$$W(t,\mathbf{x}) = \sum_{k=0}^{\infty} \varepsilon^k W_k, \qquad W^u(t,\mathbf{x}) = \sum_{k=0}^{\infty} \varepsilon^k W_k^u\,.$$

Moreover, for the subsequent calculations it is useful to define the Taylor-expansion of the coefficient functions involving W or M in the scaled equations (5.11), (5.12), (5.13), and (5.14):

$$\begin{aligned}\mu_M(M,W,N_e) &= \mu_M(M_0,W_0,N_e) + \partial_M\mu_M(M_0,W_0,N_e)(M-M_0)\\ &\quad + \partial_W\mu_M(M_0,W_0,N_e)(W-W_0) + \mathcal{O}(\varepsilon^2)\,,\\ \mu_W(W,Q,d_b) &= \mu_W(W_0,Q,d_b) + \partial_W\mu_W(W_0,Q,d_b)(W-W_0) + \mathcal{O}(|W-W_0|^2)\,.\end{aligned}$$

Moreover, we observe that

$$B_\rho(W,Q) = B_\rho(W_0,Q) + k_W^+\frac{S_W}{W_{c,0}}(W-W_0) + \frac{k_W^+}{2}\frac{S_W}{W_{c,0}}(W-W_0)^2 + \mathcal{O}(|W-W_0|^3)$$

and

$$\begin{aligned}\frac{1}{B_\rho(W,Q)^2} =& \frac{1}{B_\rho(W_0,Q)^2} - 2k_W^+\frac{S_W}{W_{c,0}}\frac{1}{B_\rho(W_0,Q)^3}(W-W_0)\\ &+ 3\left(k_W^+\frac{S_W}{W_{c,0}}\right)^2\frac{1}{B_\rho(W_0,Q)^4}(W-W_0)^2 + \mathcal{O}(|W-W_0|^3)\,.\end{aligned}$$

Therefore, equating the powers of ε in the scaled equations (5.11), (5.12), (5.13), and (5.14), we obtain:

ε^0 terms:

$$0 = -\lambda_0\left(m_0 - \frac{q}{\omega}M_0\right) + \lambda_1\left(m_0^z - \frac{q}{\omega}M_0^z\right)\,, \tag{5.15}$$

$$0 = -B_\rho(W_0,Q)m_0^z - \lambda_0\left(m_0^z - \frac{q}{\omega}M_0^z\right)\,, \tag{5.16}$$

$$0 = -\gamma_0(\bar{w}_0 - S_d^\sigma W_0) + \gamma_1(\bar{w}_0^u - S_d^\sigma W_0^u)\,, \tag{5.17}$$

$$0 = -B_w(H)\bar{w}_0^u - \gamma_0\left(\bar{w}_0^u - S_d^\sigma W_0^u\right)\,. \tag{5.18}$$

ε^1 terms:

$$\nabla \cdot (\mathbf{v} m_0) = -\lambda_0 \left(m_1 - \frac{q}{\omega} M_1 \right) + \lambda_1 \left(m_1^z - \frac{q}{\omega} M_1^z \right) , \tag{5.19}$$

$$\begin{aligned} \nabla \cdot (\mathbf{v} m_0^z) = & -B_\rho(W_0, Q) m_1^z - k_W^+ \frac{S_W}{W_{c,0}} W_1 m_0^z - \lambda_0 \left(m_1^z - \frac{q}{\omega} M_1^z \right) \\ & + \frac{k^-}{B_\rho(W_0, Q^2} \left(k_W^+ \frac{S_W}{W_{c,0}} \mathbf{v} \cdot \nabla W_0 + k_Q^+ \frac{S_Q}{Q^*} \mathbf{v} \cdot \nabla Q \right) m_0 , \end{aligned} \tag{5.20}$$

$$\nabla \cdot (\vartheta \bar{w}_0) = -\gamma_0 (\bar{w}_1 - S_d^\sigma W_1) + \gamma_1 (\bar{w}_1^u - S_d^\sigma W_1^u) , \tag{5.21}$$

$$\nabla \cdot (\vartheta \bar{w}_0^u) + B_w(H) \bar{w}_1^u - \frac{\frac{k_H^+}{H_{c,0}} k_H^-}{B_w(H)^2} \vartheta \cdot \nabla H \bar{w}_0 = -\gamma_0 \left(\bar{w}_1^u - S_d^\sigma W_1^u \right) . \tag{5.22}$$

ε^2 terms:

$$\begin{aligned} \frac{\partial m_0}{\partial t} + \nabla \cdot (\mathbf{v} m_1) = & -\lambda_0 \left(m_2 - \frac{q}{\omega} M_2 \right) + \lambda_1 \left(m_2^z - \frac{q}{\omega} M_2^z \right) \\ & + \mu_M(M_0, W_0, N_e) \frac{Q}{Q^*} m_0 - L_M(d_r, d_c) m_0 , \end{aligned} \tag{5.23}$$

$$\begin{aligned} \frac{\partial \bar{w}_0}{\partial t} + \nabla \cdot (\vartheta \bar{w}_1) = & -\gamma_0 (\bar{w}_2 + S_d^\sigma W_2) + \gamma_1 (\bar{w}_2^u - S_d^\sigma W_2^u) \\ & + \mu_W(W_0, Q, d_b) \frac{H}{H_{c,0}} \bar{w}_0 - R_W(d_r) \bar{w}_0 . \end{aligned} \tag{5.24}$$

We start the deduction of the macroscopic setting by integrating (5.16) with respect to $\mathbf{v}$ and obtaining

$$0 = -M_0^z B_\rho(W_0, Q) ,$$

i.e.,

$$M_0^z = 0 \tag{5.25}$$

as $B_\rho(W_0, Q) \neq 0$ for $k^- > 0$. Plugging this result into (5.16) leads to

$$m_0^z = 0 . \tag{5.26}$$

Using (5.25) and (5.26) in equation (5.15), we obtain:

$$0 = -\lambda_0 m_0 + \lambda_0 \frac{q}{\omega} M_0 \quad \Longrightarrow m_0 = \frac{q}{\omega} M_0 \tag{5.27}$$

since $\lambda_0 > 0$. Integrating equation (5.18) with respect to ϑ, we get

$$0 = -W_0^u B_w(H) ,$$

i.e.,

$$W_0^u = 0 . \tag{5.28}$$

as $B_w(H) \neq 0$ for $k_H^- > 0$. Then, plugging this result back into equation (5.18), we obtain

$$\bar{w}_0^u = 0\,. \tag{5.29}$$

Considering equations (5.17), (5.28), and (5.29) we obtain:

$$0 = -\gamma_0 \bar{w}_0 + \gamma_0 S_d^\sigma W_0 \quad \Longrightarrow \bar{w}_0 = S_d^\sigma W_0\,, \tag{5.30}$$

since $\gamma_0 > 0$. Thus, $\bar{w}_0$ depends on the (constant) speed σ, but not on the direction $\vartheta \in \mathbb{S}^{n-1}$.

Now, we focus on the equations stemming from the ε^1-terms. Integrating equation (5.22) with respect to ϑ and using (5.29) and (5.30), we obtain

$$0 = -B_w(H) W_1^u + \frac{k_H^- \frac{k_H^+}{H_{c,0}}}{B_w(H)^2} \int_\Theta \vartheta\, \bar{w}_0\, \nabla H\, d\vartheta\,,$$

i.e.,

$$W_1^u = 0\,. \tag{5.31}$$

due to (5.30). Plugging this result into equation (5.22) we get

$$\begin{aligned} 0 &= -(B_w(H) + \gamma_0)\bar{w}_1^u + \frac{k_H^- \frac{k_H^+}{H_{c,0}}}{B_w(H)^2} \vartheta \cdot \nabla H\, \bar{w}_0 \\ \Rightarrow \quad \bar{w}_1^u &= \frac{k_H^- \frac{k_H^+}{H_{c,0}}}{(B_w(H) + \gamma_0)\, B_w(H)^2}\, \vartheta \cdot \nabla H\, \bar{w}_0\,. \end{aligned} \tag{5.32}$$

Considering equation (5.21) and the result from (5.31), we derive

$$\begin{aligned} &\nabla \cdot (\vartheta \bar{w}_0) = -\gamma_0 \left(\bar{w}_1 - S_d^\sigma W_1\right) + \gamma_1 \bar{w}_1^u \\ &\Rightarrow -\gamma_0 \bar{w}_1 = \nabla \cdot (\vartheta \bar{w}_0) - \gamma_0 S_d^\sigma W_1 - \gamma_1 \bar{w}_1^u \\ &\Rightarrow \bar{\mathcal{L}}_w[\gamma_0]\bar{w}_1 := -\gamma_0 \bar{w}_1 + \gamma_0 S_d^\sigma W_1 = \nabla \cdot (\vartheta \bar{w}_0) - \gamma_1 \bar{w}_1^u\,. \end{aligned} \tag{5.33}$$

In order to get an explicit expression for w_1, we would like to invert the operator $\bar{\mathcal{L}}_w[\gamma_0]$. As described in previous chapters, we define this operator on the weighted L^2-space $L^2_{S_d^\sigma}(\Theta)$, in which the measure $d\vartheta$ is weighted by $S_d^\sigma(\vartheta)$. In particular, $L^2_{S_d^\sigma}(\Theta)$ can be decomposed as

$$L^2_{S_d^\sigma}(\Theta) = < S_d^\sigma > \oplus < S_d^\sigma >^\perp\,.$$

Due to the properties of the the turning kernel of $\bar{\mathcal{L}}_w[\gamma_0]$. this turning operator is a compact Hilbert-Schmidt operator with kernel $< S_d^\sigma >$. We can therefore calculate its pseudo-inverse on $< S_d^\sigma >^\perp$. To determine $\bar{w}_1$ from equation (5.33) we check the solvability condition, which holds thanks to the results obtained above for $\bar{w}_0$. Thus, from equations (5.32) and (5.33) we obtain

$$\bar{w}_1 = -\frac{1}{\gamma_0}\left[\nabla \cdot (\vartheta \bar{w}_0) - \gamma_1 \frac{\frac{k_H^+}{H_{c,0}} k_H^-}{(B_w(H) + \gamma_0) B_w(H)^2} \vartheta \cdot \nabla H\, \bar{w}_0\right]$$

and

$$W_1 = 0\,. \tag{5.34}$$

Concerning equation (5.20), we integrate it with respect to $\mathbf{v}$ and, upon using (5.26), and (5.27) we obtain

$$0 = -B_\rho(W_0, Q)M_1^z + \frac{k^-}{B_\rho(W_0, Q)^2} M_0 s^d \mathbb{E}_q \cdot \left(k_W^+ \frac{S_W}{W_{c,0}} \nabla W_0 + k_Q^+ \frac{S_Q}{Q^*} \nabla Q \right) .$$

Recalling that the fiber network is assumed to be unpolarized, i.e., $\mathbb{E}_q = 0$ (with $\mathbb{E}_q$ defined in (3.16)), the previous equation leads to

$$M_1^z = 0 .$$

Plugging these results into equation (5.20) we obtain

$$0 = -(B_\rho(W_0, Q) + \lambda_0)m_1^z + \frac{k^-}{B_\rho(W_0, Q)^2} \left(k_W^+ \frac{S_W}{W_{c,0}} \mathbf{v} \cdot \nabla W_0 + k_Q^+ \frac{S_Q}{Q^*} \mathbf{v} \cdot \nabla Q \right) m_0 ,$$

i.e.,

$$m_1^z = \frac{k^-}{(B_\rho(W_0, Q) + \lambda_0)\, B_\rho(W_0, Q)^2} \left(k_W^+ \frac{S_W}{W_{c,0}} \mathbf{v} \cdot \nabla W_0 + k_Q^+ \frac{S_Q}{Q^*} \mathbf{v} \cdot \nabla Q \right) m_0 .$$

Using equation (5.19), we derive

$$\begin{aligned} &\nabla \cdot (\mathbf{v} m_0) = -\lambda_0 \left(m_1 - \frac{q}{\omega} M_1 \right) + \lambda_1 m_1^z \\ &\Rightarrow -\lambda_0 m_1 = \nabla \cdot (\mathbf{v} m_0) - \lambda_0 \frac{q}{\omega} M_1 - \lambda_1 m_1^z \\ &\Rightarrow \bar{\mathcal{L}}_M[\lambda_0] m_1 := -\lambda_0 m_1 + \lambda_0 \frac{q}{\omega} M_1 = \nabla \cdot (\mathbf{v} m_0) - \lambda_1 m_1^z . \end{aligned}$$

Likewise, we observe that the operator $\bar{\mathcal{L}}_M[\lambda_0] m_1$ can be inverted, thanks to the symmetry properties of $q(\mathbf{x}, \hat{\mathbf{v}})$. Thus, we have

$$\begin{aligned} m_1 = &- \frac{1}{\lambda_0} \nabla \cdot (\mathbf{v} m_0) \\ &- \frac{\lambda_1}{\lambda_0} \frac{k^-}{(B_\rho(W_0, Q) + \lambda_0) B_\rho(W_0, Q)^2} \left(k_W^+ \frac{S_W}{W_{c,0}} \mathbf{v} \cdot \nabla W_0 + k_Q^+ \frac{S_Q}{Q^*} \mathbf{v} \cdot \nabla Q \right) m_0 \end{aligned}$$

and

$$M_1 = 0 . \tag{5.35}$$

Finally, integrating equation (5.23) with respect to $\mathbf{v}$ we get

$$\frac{\partial M_0}{\partial t} + \int_{\mathbf{V}} \nabla \cdot (\mathbf{v} m_1) d\mathbf{v} = \mu_M(M_0, W_0, N_e) \frac{Q}{Q^*} M_0 - L_M(d_r, d_c) M_0 \tag{5.36}$$

where

$$\int_{\mathbf{V}} \nabla \cdot (\mathbf{v} m_1) d\mathbf{v} = \int_{\mathbf{V}} \nabla \cdot \left(-\frac{1}{\lambda_0} \mathbf{v} \nabla \cdot (\mathbf{v} m_0) \right) d\mathbf{v}$$

$$+\int_{\mathbf{V}}\nabla\cdot\left(\frac{\lambda_1}{\lambda_0}\frac{k^-}{(B_\rho(W_0,Q)+\lambda_0)B_\rho(W_0,Q)^2}\mathbf{v}\left(k_W^+\frac{S_W}{W_{c,0}}\mathbf{v}\cdot\nabla W_0+k_Q^+\frac{S_Q}{Q^*}\mathbf{v}\cdot\nabla Q\right)\,m_0\right)d\mathbf{v}$$

$$=\nabla\cdot\left[\int_{\mathbf{V}}-\frac{1}{\lambda_0}\mathbf{v}\otimes\mathbf{v}\,\nabla\cdot\left(\frac{q}{\omega}M_0\right)\right]d\mathbf{v}$$

$$+\nabla\cdot\left[\frac{\lambda_1 k^-}{\omega\lambda_0(B_\rho(W_0,Q)+\lambda_0)B_\rho(W_0,Q)^2}\int_{\mathbf{V}}\mathbf{v}\otimes\mathbf{v}qd\mathbf{v}\left(k_W^+\frac{S_W}{W_{c,0}}\nabla W_0+k_Q^+\frac{S_Q}{Q^*}\nabla Q\right)M_0\right].$$

Defining

$$\mathbf{D}_T(\mathbf{x}):=\frac{1}{\omega}\int_{\mathbf{V}}\mathbf{v}\otimes\mathbf{v}\,q(\mathbf{x},\hat{\mathbf{v}})d\mathbf{v}=s^2\int_{\mathbb{S}^{d-1}}\hat{\mathbf{v}}\otimes\hat{\mathbf{v}}\,q(\mathbf{x},\hat{\mathbf{v}})d\hat{\mathbf{v}}=s^2\mathbb{V}_q(\mathbf{x})\,, \tag{5.37}$$

with $\mathbb{V}_q$ given in (3.17), we obtain from equation (5.36) the following macroscopic equation for $M_0(t,\mathbf{x})$:

$$\begin{aligned}\frac{\partial M_0}{\partial t}=&\nabla\cdot\left[\frac{1}{\lambda_0}\nabla\cdot(\mathbf{D}_T(\mathbf{x})M_0)\right]\\&-\nabla\cdot\left[\frac{\lambda_1 k^-}{\lambda_0(B_\rho(W_0,Q)+\lambda_0)B_\rho(W_0,Q)^2}\mathbf{D}_T(\mathbf{x})\,\left(k_W^+\frac{S_W}{W_{c,0}}\nabla W_0+k_Q^+\frac{S_Q}{Q^*}\nabla Q\right)M_0\right]\\&+\left(\mu_M(M_0,W_0,N_e)\frac{Q}{Q^*}-L_M(d_r,d_c)\right)M_0\,.\end{aligned} \tag{5.38}$$

Then, for the EC dynamics, we integrate (5.24) with respect to $\vartheta\in\Theta$, obtaining

$$\frac{\partial W_0}{\partial t}+\int_\Theta\nabla\cdot(\vartheta\bar{w}_1)d\vartheta=\mu_W(W_0,Q,d_b)\frac{H}{H_{c,0}}W_0-R_W(d_r)W_0\,,$$

where

$$\begin{aligned}\int_\Theta\nabla\cdot(\vartheta\bar{w}_1)d\vartheta=&\int_\Theta\nabla\cdot\vartheta\left(-\frac{1}{\gamma_0}\nabla\cdot(\vartheta\bar{w}_0)\right)d\vartheta\\&+\int_\Theta\nabla\cdot\vartheta\left(\frac{\gamma_1}{\gamma_0}\frac{\frac{k_H^+}{H_{c,0}}k_H^-}{(B_w(H)+\gamma_0)B_w(H)^2}\vartheta\cdot\nabla H\,\bar{w}_0\right)d\vartheta\\=&\nabla\cdot\left[\int_\Theta-\frac{1}{\gamma_0}\vartheta\otimes\vartheta\,\nabla\bar{w}_0\right]d\vartheta\\&+\nabla\cdot\left[\frac{\gamma_1\frac{k_H^+}{H_{c,0}}k_H^-}{\gamma_0(B_w(H)+\gamma_0)B_w(H)^2}\int_\Theta\vartheta\otimes\vartheta\,d\vartheta\,\nabla H\,W_0\right].\end{aligned}$$

Recalling (5.30),we obtain the following macroscopic equation for the density W_0 of endothelial cells:

$$\begin{aligned}\frac{\partial W_0}{\partial t} &= \nabla \cdot (\mathbf{D}_{EC} \nabla W_0) - \nabla \cdot \left(\mathbf{D}_{EC} \frac{\gamma_1 k_H^+ k_H^-}{H_{c,0}(B_w(H) + \gamma_0) B_w(H)^2} \nabla H \, W_0 \right) \\ &+ \left(\mu_W(W_0, Q, d_b) \frac{H}{H_{c,0}} - R_W(d_r) \right) W_0 \,.\end{aligned} \tag{5.39}$$

The tensor related to the ECs is given by

$$\mathbf{D}_{EC} := \frac{\sigma^2}{d\gamma_0} \mathbb{I}_d. \tag{5.40}$$

The two macroscopic equations obtained in (5.38) and (5.39) for the evolution of glioma cells and ECs, respectively, are coupled with the equations for the dynamics of VEGF, healthy tissue, and necrotic matter. In the specific, the evolution of the ***VEGF concentration*** $H(t, \mathbf{x})$ is described as

$$\frac{\partial H}{\partial t} = D_H \Delta H + f(M_0, W_0, H) \,,$$

where $D_H \in \mathbb{R}$ is the VEGF constant diffusion coefficient, while $f(M_0, W_0, H)$ is a reaction term describing the processes of VEGF production by tumor cells and its consumption by ECs. The concrete form of the reaction term is defined in the next section. The degradation of the ***healthy tissue*** (of density $Q(t, \mathbf{x})$) is due to both the (acidity produced by) tumor cells activity and the effects of the radiotherapy treatment. Thus, we describe the evolution of the healthy tissue by means of the following ODE

$$\frac{\partial Q}{\partial t} = -d_Q \frac{M_0}{M_{c,0}} Q - R_Q(d_r) Q \,,$$

where $M_{c,0}$ denotes the reference density for tumor cells and d_Q the tissue degradation rate. $R_Q(d_r)Q$ collects the effects of the radiation on the healthy tissue and is described with the L-Q model like defined in Chapter 3 (and also in equation (5.4)) as

$$R_Q(d_r) := 1 - S(d_r, \alpha_Q) \,.$$

Finally, the ODE describing the evolution of the ***necrotic tissue*** (of density $N_e(t, \mathbf{x})$) takes into account both tissue degradation and therapy effects on tumor, endothelial cells, and tissue i.e.,

$$\frac{\partial N_e}{\partial t} = L_M(d_r, d_c) M + R_W(d_r) W_0 + d_Q \frac{M_0}{M_{c,0}} Q + R_Q(d_r) Q \,.$$

In view of (5.34)and (5.35), the ε-correction terms for M and W can be left out and, ignoring the higher order terms, we get the following PDE system characterizing the macroscopic evolution of the tumor under the influence of tissue, vasculature, and growth factors:

$$
\begin{cases}
\dfrac{\partial M}{\partial t} = \nabla \cdot \left[\dfrac{1}{\lambda_0} \nabla \cdot (\mathbf{D}_T(\mathbf{x}) M) \right] \\
\qquad -\nabla \cdot \left[\dfrac{\lambda_1 k^-}{\lambda_0 (B_\rho(W,Q) + \lambda_0) B_\rho(W,Q)^2} \mathbf{D}_T(\mathbf{x}) \left(k_W^+ \dfrac{S_W}{W_{c,0}} \nabla W + k_Q^+ \dfrac{S_Q}{Q^*} \nabla Q \right) M \right] \\
\qquad + \left(\mu_M(M,W,N_e) \dfrac{Q}{Q^*} - L_M(d_r,d_c) \right) M \,, \\
\dfrac{\partial W}{\partial t} = \nabla \cdot (\mathbf{D}_{EC} \nabla W) - \nabla \cdot \left(\mathbf{D}_{EC} \dfrac{\gamma_1 k_H^+ k_H^-}{H_{c,0} (B_w(H) + \gamma_0) B_w(H)^2} \nabla H \, W \right) \\
\qquad + \left(\mu_W(W,Q,d_b) \dfrac{H}{H_{c,0}} - R_W(d_r) \right) W \,, \\
\dfrac{\partial H}{\partial t} = D_H \Delta H + f(M,W,H) \,, \\
\dfrac{\partial Q}{\partial t} = -d_Q \dfrac{M}{M_{c,0}} Q - R_Q(d_r) Q \,, \\
\dfrac{\partial N_e}{\partial t} = L_M(d_r,d_c) M + R_W(d_r) W + d_Q \dfrac{M}{M_{c,0}} Q + R_Q(d_r) Q \,.
\end{cases}
\tag{5.41}
$$

Here, the tumor tensor $\mathbf{D}_T$ is given by (5.37) and the EC diffusion tensor $\mathbf{D}_{EC}$ by (5.40). For the numerical simulations, the macroscopic system needs to be supplemented with adequate initial and boundary conditions. Although the deduction has been carried out for $\mathbf{x} \in \mathbb{R}^d$, the numerical simulations presented in Section 5.3 are performed in a bounded, sufficiently regular domain $\Omega \subset \mathbb{R}^d$. We endow the system with no-flux boundary conditions.

5.2 *Assessment of coefficients and parameters*

The definition of the coefficient functions involved in the macroscopic setting, the estimation of the constant parameters, and the non-dimensionalization of the macroscopic system are the three aspects addressed in this section. Most of the constant are taken from the parameter study we performed in Chapter 4. In the sequel, we collect the parameter values in Table 5.1. Sections 5.2.1 and 5.2.2 are dedicated to assess the coefficient functions involved in the macroscopic equations and to describe the details of the non-dimensionalization procedure, respectively.

5.2.1 *Definition of the coefficient functions*

To determine the tumor tensor $\mathbf{D}_T(\mathbf{x})$ in (5.37) we provide a concrete form for the (mesoscopic) orientational distribution of tissue fibers $q(\mathbf{x}, \hat{\mathbf{v}})$. Following the analysis performed in Chapter 2 (specifically, in Section 2.3.4), here we use the orientation

distribution function:

$$q(\mathbf{x}, \hat{\mathbf{v}}) = \frac{1}{4\pi |\mathbf{D}_W(\mathbf{x})|^{\frac{1}{2}} (\hat{\mathbf{v}}^T (\mathbf{D}_W(\mathbf{x}))^{-1} \hat{\mathbf{v}})^{\frac{3}{2}}}, \tag{5.42}$$

where $\mathbf{D}_W(\mathbf{x})$ is the water diffusion tensor obtained from processing the DTI data.

Concerning the growth rate $\mu(M, W, N_e)$ we consider a logistic-like function to describe the growth of tumor cells. In the specific, tumor proliferation is limited by the tumor cells themselves and the necrotic tissue N_e, and it is influenced by the vasculature availability:

$$\mu(M, W, N_e) := \mu_{M,0} \left(1 - \frac{M}{K_M} - \frac{N_e}{K_{Ne}}\right) g(W) .$$

Here, K_N and K_{Ne} are the carrying capacities of tumor cells and of the necrotic matter, respectively, while $\mu_{M,0}$ is the constant proliferation rate. We model vasculature effects on the tumor growth by means of the function $g(W)$. We assume

$$g(W) := \left(1 + \frac{W}{W_{c,0}}\right) ,$$

describing the ECs enhancing tumor proliferation in the region where the vasculature is developing. Other choices of the function $g(W)$ are possible. For instance, one can assume $g(W) := \frac{W}{W_{c,0}}$ that describes tumor proliferation as an effect of the binary interactions between tumor and ECs, as we did in the setting proposed in Chapter 4. In this way, tumor proliferation would be completely dependent on the availability of vasculature.

Similarly, the EC proliferation term $\mu_W(W, Q, d_b)$ is described by means of a logistic-like function for ECs in which we include the influence of the healthy tissue on EC proliferation. The availability of healthy tissue allows, in fact, EC growth. The proliferation term is described as

$$\mu_W(W, Q, d_b) := \mu_{W,0}(d_b) \left(1 - \frac{W}{K_W}\right) \frac{Q}{Q^*} ,$$

where we include the effect of the anti-angiogenic therapy at dose d_b on EC proliferation. In the proliferation term, K_W represents the carrying capacity of ECs, while $\mu_{W,0}(d_b)$ is the proliferation rate. This proliferation rate is modeled as a decreasing function in d_b, as the anti-angiogenic treatment limits EC affinity to VEGF and reduces EC capability to growth. We set

$$\mu_{W,0}(d_b) := \bar{\mu}_{W,0} \left(\frac{1}{2} + \frac{1}{2(1 + d_b^2)}\right) .$$

Similar expressions are considered to describe the effects of the anti-angiogenic therapy on the attachment/detachment functions, which read

$$k_H^+ := \bar{k}_H^+ l^+(d_b) := \bar{k}_H^+ \left(\frac{1}{2} + \frac{1}{2(1 + d_b^2)}\right) ,$$

$$k_H^- := \bar{k}_H^- l^-(d_b) := \bar{k}_H^- (1 + d_b) .$$

Concerning the radiation treatment, we recall from the previous section the general expression related to the L-Q model, i.e.,

$$S(d_r, \alpha) = \exp\left(-\alpha d_r - \beta^2 d_r\right),$$

where d_r is the total dose of radiation. In clinical practice, radiotherapy is usually administered in daily smaller fractions of d_r, in order to avoid excessive toxic effects on the healthy tissue. For this reason, the radiation death terms for tumor cells, endothelial cells, and tissue fraction are described as

$$R_i(d_r) := \sum_{k=1}^{\xi} (1 - S(\bar{d}_r, \alpha_i))\eta_\delta(t - t_k)$$

for $i = M, W, Q$. $\bar{d}_r$ is the fraction of the total dose d_r administered at time instants t_k at which an ionizing radiation is applied to the patient. In the expression of $R_i(d_r)$, ξ represents the number of administered fractions and η_δ is a C_0^∞ function with unit mass and support in $(-\delta, \delta)$, with $\delta \ll 1$. We describe the therapy plans tested in the simulations in the next section.

Finally, the reaction term in the PDE for the VEGF dynamics is chosen as

$$f(M_0, W_0, H) := c_1 \frac{M_0}{M_{c,0}} - c_2 \frac{W_0}{W_{c,0}} H,$$

where the parameters $c_1 > 0$ and $c_2 > 0$ represent the production and uptake rates of VEGFs, respectively. VEGFs are produced by tumor cells in order to enhance the vascularization and the nutrient and oxygen supplies. Then, ECs are attracted by the VEGF gradient and consume VEGFs to sustain the growth of the capillary network.

In Table 5.1 we report the ranges of the constant parameters involved in system (5.41), as well as the references they are drawn from.

5.2.2 *Non-dimensionalization*

Before presenting the numerical results, we perform the non-dimensionalization of system (5.41). Recalling that we express the variables N, W, N_e, and Q involved in system (5.41) in cells $\cdot$ mm^{-3}, while the concentration H of VEGFs is given in mol $\cdot$ l^{-1}(=:M), we list the reference values used for the non-dimensionalization in Table 5.2. In the specific, we rescale the tumor, EC, necrotic matter, and tissue densities with respect to their carrying capacities, i.e., $M_{c,0} = K_M$, $W_{c,0} = K_W$, $N_{e,0} = K_M$, and $Q^* = K_Q$, assuming a similar carrying capacity for tumor cells and necrotic tissue. We non-dimensionalize the partial and ordinary differential equations introduced above as follows:

$$\tilde{t} = \frac{t}{T}, \quad \tilde{\mathbf{x}} = \frac{\mathbf{x}}{L}, \quad \tilde{M} = \frac{M}{M_{c,0}}, \quad \tilde{W} = \frac{W}{W_{c,0}}, \quad \tilde{N}_e = \frac{N_e}{N_{e,0}}, \quad \tilde{Q} = \frac{Q}{Q^*}, \quad \tilde{H} = \frac{H}{H_{c,0}}.$$

A proper scaling of the parameters involved in the macroscopic setting leads to:

$$\tilde{k}_W^+ = \frac{k_W^+}{\lambda_0}, \qquad \tilde{k}_H^- = \frac{\bar{k}_H^-}{\gamma_0}, \qquad \tilde{\mathbf{D}}_T = \frac{1}{\lambda_0}\frac{T}{L^2}\mathbf{D}_T,$$

$$\tilde{k}_Q^+ = \frac{k_Q^+}{\lambda_0}, \qquad \tilde{\lambda_1} = \frac{\lambda_1}{\lambda_0}, \qquad \tilde{\mathbf{D}}_{EC} = \frac{T}{L^2}\mathbf{D}_{EC},$$

Parameter	Description	Value (unit)	Source
λ_0	turning frequency in $\mathcal{L}_p[\lambda(z)]$	10^{-3} (s^{-1})	[56, 259]
λ_1	turning frequency in $\mathcal{L}_p[\lambda(z)]$	10^{-3} (s^{-1})	[56, 259]
s	tumor cells speed	$[0.0042, 0.0084] \cdot 10^{-3}$ ($mm \cdot s^{-1}$)	[56, 65]
k_Q^+	tumor-ECM attachment rate	0.034 (s^{-1})	[56, 161]
k_W^+	tumor-EC attachment rate	0.034 (s^{-1})	[161]
k^-	detachment rate	0.01 (s^{-1})	[161]
$\mu_{M,0}$	tumor proliferation rate	$[0.35, 0.9] \cdot 10^{-5}$ (s^{-1})	[135]
K_M	tumor carrying capacity	$\sim 10^5$ ($cells \cdot mm^{-3}$)	[81]
K_{Ne}	necrotic matter carrying capacity	$\sim 10^5$ ($cells \cdot mm^{-3}$)	[81]
K_Q	healthy tissue carrying capacity	$\sim 10^5$ ($cells \cdot mm^{-3}$)	[276]
α_M	single radiation track lesion on tumor	$[0.04, 0.11]$ (Gy^{-1})	[13, 231]
α_Q	single radiation track lesion on tissue	0.001 (Gy^{-1})	[151]
α_W	single radiation track lesion on ECs	0.0025 (Gy^{-1})	[151]
β_M	two radiation tracks lesions on tumor	$[0.004, 0.011]$ (Gy^{-2})	[13, 231]
β_Q	two radiation tracks lesions on tissue	0.0001 (Gy^{-2})	[151]
β_W	two radiation tracks lesions on ECs	0.0003 (Gy^{-2})	[132, 151]
d_c	chemotherapy killing rate	$0.023 \cdot 10^{-6}$ (s^{-1})	[229]
d_r	radiotherapy dose	60 (Gy)	this work
γ_0	turning frequency in $\mathcal{L}_w[\gamma(u)]$	$2 \cdot 10^{-4}$ (s^{-1})	[56, 277]
γ_1	turning frequency in $\mathcal{L}_w[\gamma(u)]$	0.001 (s^{-1})	this work
σ	ECs speed	$[0.0028, 0.0069] \cdot 10^{-3}$ ($mm \cdot s^{-1}$)	[56, 60]
$\bar{k}_H^+$	EC-VEGF attachment rate	0.03 (s^{-1})	[177, 278]
$\bar{k}_H^-$	EC-VEGF detachment rate	$[0.001, 0.01]$ (s^{-1})	[177, 178]
K_W	EC carrying capacity	$\sim 10^5$ ($cells \cdot mm^{-3}$)	[82]
$\bar{\mu}_{W,0}$	EC proliferation rate	$[0.62, 5.7] \cdot 10^{-6}$ (s^{-1})	[7, 203]
d_b	anti-angiogenic therapy dose	10 ($mg \cdot kg^{-1}$)	this work
D_H	VEGF diffusion coefficient	$[10^{-7}, 10^{-5}]$ ($mm^2 \cdot s^{-1}$)	[9, 167]
c_1	VEGF production rate	$[0.21, 8.34] \cdot 10^{-4}$ (s^{-1})	[4, 97, 138]
c_2	VEGF consumption rate	$2.28 \cdot 10^{-7}$ (s^{-1})	[97]
d_Q	tissue degradation rate (by acidity)	$0.58 \cdot 10^{-7}$ (s^{-1})	[56]

TABLE 5.1: **Vasculature, VEGFs and therapy effects: model parameters.**

$$\tilde{k}^- = \frac{k^-}{\lambda_0}, \qquad \tilde{\gamma}_1 = \frac{\gamma_1}{\gamma_0}, \qquad \tilde{D}_H = \frac{T}{L^2} D_H,$$

$$\tilde{k}_H^+ = \frac{\bar{k}_H^+}{\gamma_0}, \qquad \tilde{\mu}_{M,0} = \bar{\mu}_{M,0} T, \qquad \tilde{c}_1 = c_1 \frac{T}{H_{c,0}},$$

$$\tilde{d}_Q = d_Q\, T, \qquad \tilde{\mu}_{W,0} = \bar{\mu}_{W,0}\, T, \qquad \tilde{c}_2 = c_2\, T$$

Parameter	Description	Value (unit)	Source
T	time	1 (d)	
L	length	0.875 (mm)	
$M_{c,0}$	tumor cell density	10^5 (cells $\cdot$ mm^{-3})	this work
$W_{c,0}$	ECs density	10^5 (cells $\cdot$ mm^{-3})	this work
$N_{e,0}$	necrotic matter density	10^5 (cells $\cdot$ mm^{-3})	this work
Q^*	healthy tissue density	10^5 (cells $\cdot$ mm^{-3})	this work
$H_{c,0}$	VEGF concentration	10^{-9} (M)	[278]

TABLE 5.2: **Vasculature, VEGFs and therapy effects: reference variables for the non - dimensionalization.**

and $\tilde{d}_c = d_c\, T$. Dropping the tildes in the new variables and parameters, the differential equations in system (5.41) keep the same form, however with the following rescaled functions:

$$\tilde{\mu}(\tilde{M},\tilde{W},\tilde{N}_e) = \tilde{\mu}_{M,0}\ \left(1-\tilde{M}-\tilde{N}_e\right) g(\tilde{W}), \qquad \tilde{k}_H^- = \tilde{k}_H^- l^-(d_b),$$

$$\tilde{\mu}_W(\tilde{W},\tilde{Q},\tilde{d}_b) = \tilde{\mu}_{W,0}(d_b)(1-\tilde{W})\tilde{Q}, \qquad \tilde{k}_H^+ = \tilde{k}_H^+ l^+(d_b),$$

$$\tilde{B}_\rho(\tilde{W},\tilde{Q}) = \left(\tilde{k}_W^+ S_W \tilde{W} + \tilde{k}_Q^+ S_Q \tilde{Q} + \tilde{k}^-\right), \qquad \tilde{f}(\tilde{M},\tilde{W},\tilde{H}) = \tilde{c}_1\tilde{M} - \tilde{c}_2\,\tilde{W}\tilde{H},$$

$$\tilde{B}_w(\tilde{H}) = (\tilde{k}_H^+\tilde{H} + \tilde{k}_H^-), \qquad \tilde{\mu}_{W,0}(d_b) = \tilde{\mu}_{W,0}\left(\frac{1}{2} + \frac{1}{2(1+d_b^2)}\right).$$

5.3 *Preliminary numerical simulations*

We perform numerical simulations in 2D of the non-dimensionalized macroscopic setting (5.41) with the parameters listed in Table 5.1. For the initial conditions we choose a Gaussian-like aggregate of tumor cells centered in $(x_{0,M}, y_{0,M}) = (-17, 5)$, in the upper-left part of the brain slice representing our illustrative computational domain Ω (in the following, $(x,y) \in \Omega \subseteq \mathbb{R}^2$):

$$M_0(x,y) = e^{-\frac{(x-x_{0,M})^2+(y-y_{0,M})^2}{8}}.$$

For the initial distribution of the healthy tissue, we consider

$$Q_0(x,y) = 1 - \frac{l_c^3(x,y)}{h^3}.$$

This configuration was introduced in the previous chapter for the description of the macroscopic tissue density. We recall that $l_c(x,y)$ represents the estimation of the length of the mean free space in every direction, while h is the side length of a DTI voxel. For the ECs, we consider the situation of several blood vessels located in the regions close to the tumor and where there is a high tissue density. From MRI and DTI scans it is not possible to distinguish between vessels and ECM. Therefore, we assume

the vasculature to be located in the areas where more tissue is available. Defining

$$W_1(x,y) = 2\,e^{-\frac{(x+2)^2}{0.5}}\,\sin^6\left(\frac{\pi}{8}y\right) \qquad \forall\, y \in [-5,15]\,,$$

$$W_2(x,y) = 2\,e^{-\frac{(x+12)^2}{0.5}}\,\sin^4\left(\frac{\pi}{8}y\right) \qquad \forall\, y \in [-35,-15]\,,$$

$$W_3(x,y) = 2\,e^{-\frac{(x+5)^2+(y-15)^2}{0.75}} + 2\,e^{-\frac{(x+5)^2+(y-20)^2}{0.75}} + 2\,e^{-\frac{(x+10)^2+(y-20)^2}{0.75}}\,,$$

we set $W_0(x,y) = W_1(x,y) + W_2(x,y) + W_3(x,y)$. For the VEGF initial profile, we consider a Gaussian distribution, centered in the same point as tumor cells $(x_{0,H}, y_{0,H}) = (-17,5)$ and given by:

$$H_0(x,y) = 0.5\,e^{-\frac{(x-x_{0,H})^2+(y-y_{0,H})^2}{4}}\,.$$

Finally, we do not initially consider any necrotic matter, setting the initial value to zero everywhere in the domain. Figure 5.1 shows the initial conditions on the zooming region $\bar{\Omega} = [-35,5] \times [-15,25] \subseteq \Omega$ of the entire 2D brain slice.

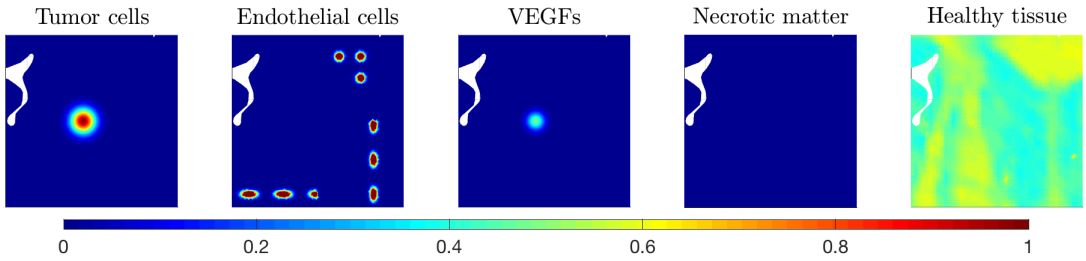

FIGURE 5.1: **Initial conditions of system** (5.41)**.** The five columns refer to tumor density, ECs, VEGFs, necrotic matter, and healthy tissue, respectively. The initial densities are visualized on the zoomed domain $\bar{\Omega} = [-35,5] \times [-15,25]$.

The numerical simulations are performed with a self-developed code in Matlab (MathWorks Inc., Natick, MA). The computational domain is a horizontal brain slice reconstructed from the processing of an MRI scan. The macroscopic tensor $\mathbf{D}_T(\mathbf{x})$ is precalculated using DTI data and the ODF for the fiber distribution function (5.42). We consider a Galerkin finite element scheme for the spatial discretization of the equations and an implicit Euler scheme for the time discretization. More details about the numerical methods are provided in Appendix B. We present two main sets of simulations:

(A) we study the dynamics of the five species involved in the macroscopic setting (5.41) in the absence of treatment. This means that the therapy doses (d_r and d_b) and the chemotherapy killing rate (d_c) are set to zero and the tumor is letting grow and spread without any external impediment.

(B) we include the three described treatment components in the population dynamics and analyze the effects of the different therapies on the overall evolution.

We start with scenario **(A)**, simulating system (5.41) for the parameters listed in Table 5.1. Starting to investigate the behavior of the involved populations in the absence of therapy, we preliminary set $d_c = d_r = d_b = 0$. This choice allow us to observe the tumor evolution over time without external intervention and to study the possible progression of the disease. The corresponding simulation results are shown in Figure

5.2, where the five columns report the evolution of the whole tumor mass M, the endothelial cells W, the VEGFs H, the necrotic matter N_e, and the healthy tissue Q.

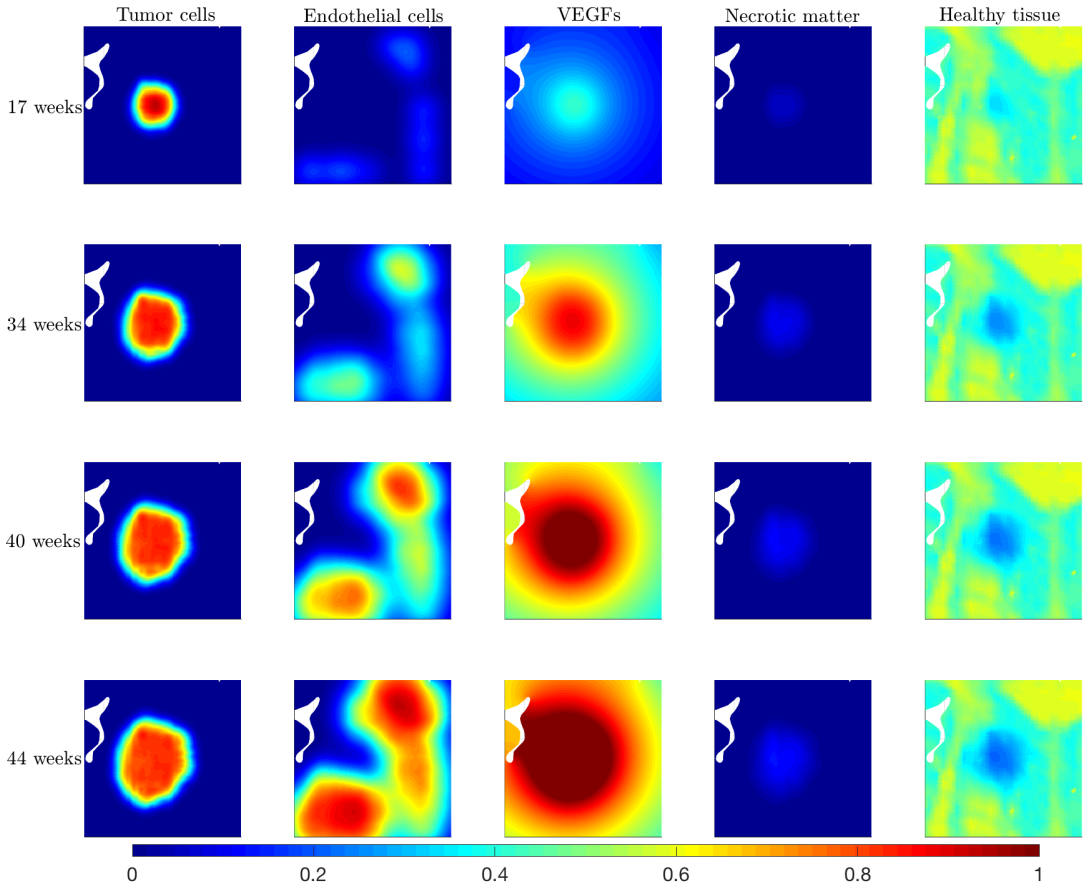

FIGURE 5.2: **Scenario (A).** Numerical simulation of system (5.41) with the parameters listed in Table 5.1 and without any treatment.

Tumor growth and spread, which mainly depend on the choice of the parameters λ_0 and s, as observed in Chapter 4, seem to be reasonably fast, as we are not relying on the go-or-growth hypothesis in this setting to describe any intratumor heterogeneity. Moreover, the influence of the EC evolution on the tumor proliferation is highly related to the choice of the function $g(W)$, which, in this setting, describes ECs as simply enhancing tumor proliferation and not directly controlling it. In Figure 5.2, ECs grow and diffuse, showing an evident migration toward the tumor population, due to the produced VEGFs. These factors are expressed by tumor cells and represent the chemotactic agent guiding ECs migration and, thus, mediating the vasculature supply to the tumor. In this case, since no therapy is included, the healthy tissue (last column of Figure 5.2) is degraded due to the (acidity produced by the) tumor cell activity, and the necrotic compartment only collects this portion of degraded tissue. We remark that in this setting we infer the degrading effect of excessive environmental acidity on the healthy tissue without directly including the evolution of the protons. However, the tissue degradation shows an overall behavior comparable to the one in Figure 4.8, where we explicitly included proton dynamics.

Then, in scenario **(B)**, we analyze the effects of the different therapeutic components on the tumor population. We let the tumor grow and spread for 34 weeks, allowing it to form a considerable neoplastic mass. Afterwards, we apply a therapeutic

plan consisting of a combination of radiation, chemotherapy with temozolomide, and anti-angiogenic therapy with bevacizumab for 6 weeks. This choice is motivated by different reported trials (e.g., see trials NCT01209442 and NCT01390948[2]). Precisely, chemotherapy is administered intravenously every day at a standard constant dose of 75 mg $\cdot$ m^{-2}. Radiotherapy is applied 5 days per week (from Monday to Friday) for 6 weeks, and the total dose of 60 Gy is fractionated into smaller doses of 2 Gy per day. Anti-angiogenic therapy is usually administered at dose 10 mg $\cdot$ kg^{-1} intravenously on Monday every 2 weeks, thus, providing a total of 3 doses in the whole treatment period of 6 weeks. For the anti-angiogenic treatment, we test a slightly different therapeutic plan, dividing the dose of 10 mg $\cdot$ kg^{-1}, administered every 2 weeks, into 10 smaller fractions of 1 mg $\cdot$ kg^{-1} administered at the same time as radiotherapy. This choice would not change the total amount of anti-angiogenic drugs administered to the patient. At the end of the treatment, we let the patient rest for 4 weeks and analyze how the tumor eventually reorganizes and evolves. A schematic representation of the therapy plan is provided in Figure 5.3.

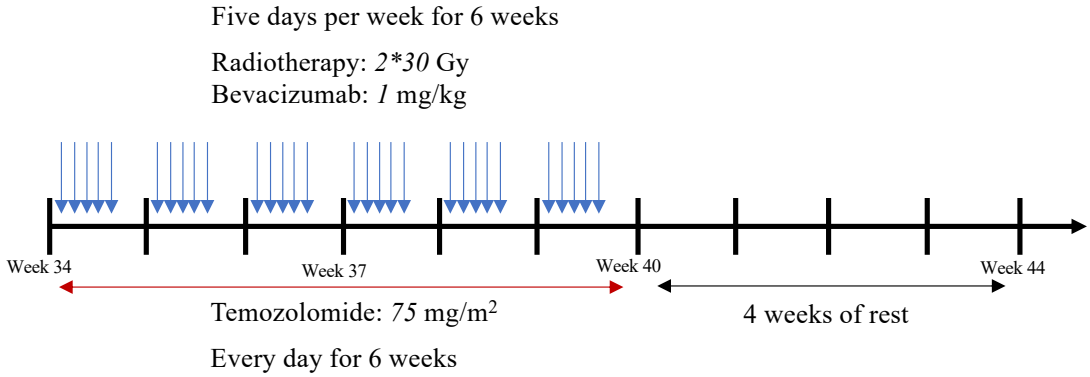

FIGURE 5.3: **Schematic representation of the therapeutic plan.**

With the same choice of parameters considered in Figure 5.2 for scenario **(A)**, we test the effect of the therapeutic treatment illustrated in Figure 5.3. The results of this scenario **(B)** are shown in Figure 5.4. The first row of Figure 5.4 (that also corresponds to the second row of Figure 5.2) represents the state of the five populations at the beginning of the treatments, while the second and third rows correspond to the situation after 3 and 6 weeks, respectively. Precisely, the third row represents the population state at the end of the combined treatment. In the last row, we show the system evolution after the resting period of 4 weeks, during which no therapies are applied. Comparing Figures 5.2 and 5.4, we immediately grasp the effects of the radio- and chemotherapy on the tumor population, whose density highly decreases during the treatment period, while the density of the necrotic matter increases, as this component collects the effects of the therapy on tumor, ECs, and healthy tissue. The reduction in the tumor density consequently affects VEGF production, with a decrease in the expression of these factors. The impact of radiation is also evident in the evolution of the healthy tissue. In turn, the reduction of tissue density affects tumor and endothelial cell proliferation processes. Tumor and EC proliferation, in fact, depend on the availability of healthy tissue and, when the latter is excessively degrades, proliferation is impaired. This effect can be observed by comparing the last two row of Figures 5.2 and 5.4 that relate to the system evolution at 40 (at the end of the treatment) and 44 (follow-up)

[2] https://www.clinicaltrials.gov

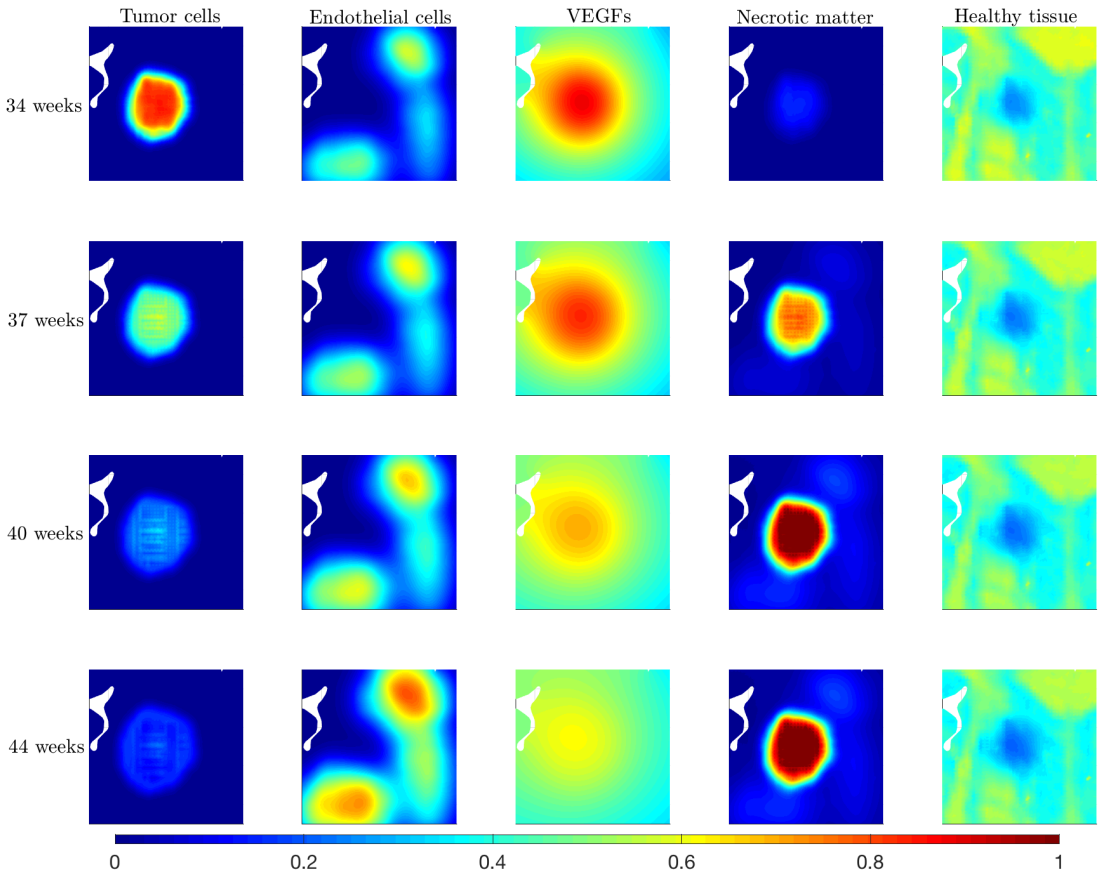

FIGURE 5.4: **Scenario (B).** Numerical simulation of system (5.41) with the parameters listed in Table 5.1 and for the therapeutic plan schematized in Figure 5.3.

weeks, respectively. ECs seem to proliferate slower, after having been affected by the multi-modal treatment, and the surviving tumor cells do not show strong growth dynamics. The anti-angiogenic therapy has also an impact on EC migration. To better evaluate the effect of the single anti-angiogenic drug, we simulate system (5.41) when only this treatment is applied. We consider the therapy plan illustrated in Figure 5.3, but we set $d_r = 0$ and $d_c = 0$. We focus on the evolution of tumor cells, ECs, and VEGFs, as these are the species more affected by anti-angiogenic therapy. To better appreciate the changes in their evolution, we plot the differences between the solution of system (5.41) without any therapy, i.e., $d_r = d_b = d_c = 0$ (whose variables are indicated by M_{NT}, W_{NT}, and H_{NT}) and the solution of the model where only anti-angiogenic treatment is included (whose variables are indicated by M_{AT}, W_{AT}, and H_{AT}). The results are shown in Figure 5.5. We notice that the most affected specie are the endothelial cells. The positivity of the difference $W_{NT} - W_{AT}$ highlights the negative effect of the anti-angiogenic drug on the EC proliferation, which appears reduced during the treatment. When the drug is suspended and the dynamics is let evolve without intervention during the next 4 weeks, we observe that the ECs start again to proliferate and the difference $W_{NT} - W_{AT}$ reduces. This is more evident in the upper-right and bottom-left areas of the domain, where ECs are initially located (as shown in Figure 5.1) and where, during the treatment period, they tend to remain more concentrated rather than spreading towards tumor cells, as shown by the EC evolution during treatment (37-40 weeks) in Figure 5.4. This EC behavior can be explained considering that, apart from impaired proliferation, anti-angiogenic drugs also affect the

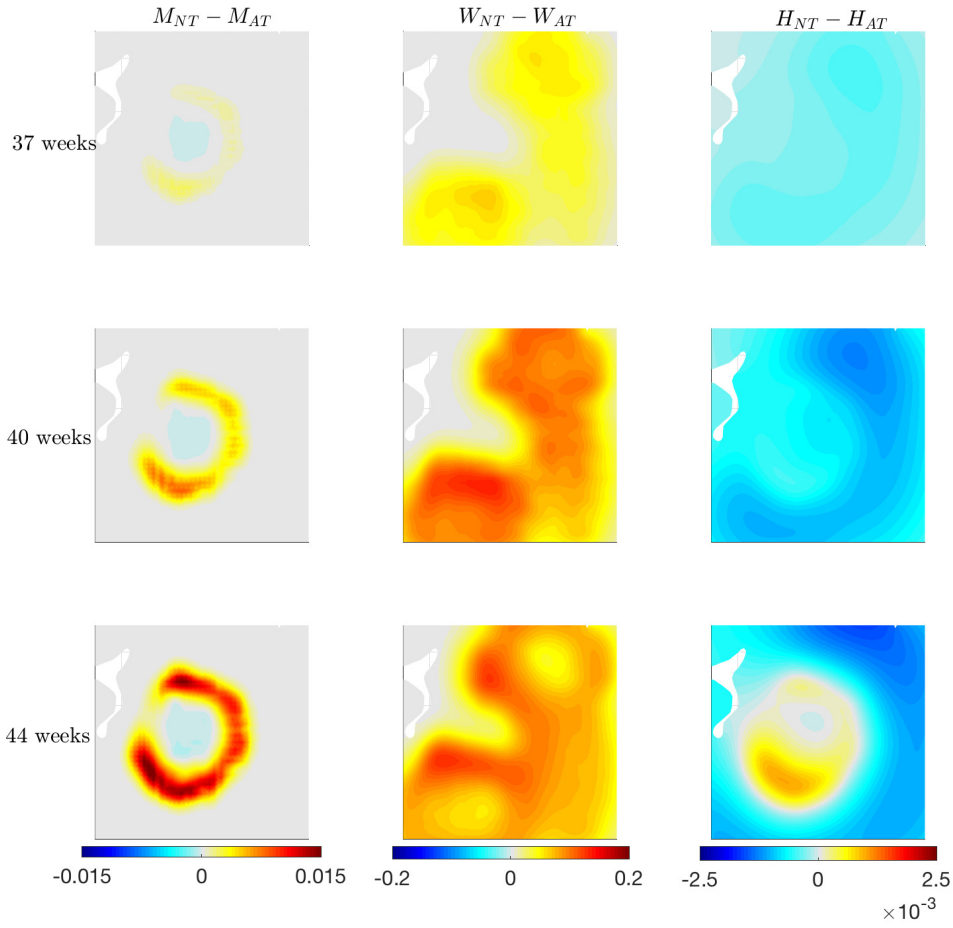

FIGURE 5.5: **Detail of scenario (B).** Differences between the solution components of system (5.41) without any therapy (M_{NT}, W_{NT}, and H_{NT}) and the solution component with only anti-angiogenic therapy administered (M_{AT}, W_{AT}, and H_{AT}). The results are shown after 3 weeks of treatment (top row), at the end of the treatment (middle row), and at the follow-up after 4 weeks without therapy (bottom row).

mobility of ECs upon inhibiting the VEGF/EC affinity. Thus, the chemotactic phenomenon characterizing ECs is less evident. These changes in the EC dynamics also affect the VEGFs. The angiogenic factor concentration is reduced where, due to the limitation in the EC migration, ECs tend to remain more concentrated and to uptake VEGFs. However, the differences in the VEGF concentration are not as strong as in the EC density. As for as tumor cells are concerned, they are not directly affected by the drug but feel its effects in a rather indirect manner. The reduction of EC migration towards glioma cells determines a decrease in the tumor proliferation in the regions around its outer rim having a better access to ECs. Thus, the difference $M_{NT} - M_{AT}$ is positive in those areas.

5.4 *Summary*

On the basis of the results concerning the influence of the vasculature on tumor progression obtained from the model in Chapter 4, we presented in this chapter a complementary study centered on the tumor and ECs response to multi-modal therapies. In

the specific, we modified the previous model taking into account several new features. We first included a micro-meso formulation for the EC population, describing the dynamics of the membrane receptors on ECs mediating VEGF-EC interactions. Then, we directly modeled the dynamics of VEGFs, which are produced by the tumor cells to attract new vasculature towards the tumor mass and, thus, to provide nutrients to sustain proliferation. Tumor, EC, and VEGF dynamics were coupled with the evolution equations for healthy tissue and necrotic matter, in line with the extended model presented in Section 4.4. In this model, we did not directly describe acidity evolution, but we indirectly accounted for its impact on tissue degradation. This degradation was described as a consequence of (the acidity produced by) tumor activity. Similar to Chapters 3 and 4, the macroscopic equations for tumor and ECs were derived via parabolic scaling of the kinetic transport equations including the microscopic receptor dynamics. The central focus of this study was on including in the model a multi-modal treatment based on a combination of standard radiation, chemotherapy with temozolomide, and anti-angiogenic therapy with bevacizumab. While chemo- and radiotherapy are directly aimed at killing the tumor cells, affecting also healthy tissue and vasculature by the ionizing radiation, anti-angiogenic therapy influences ECs and VEGFs dynamics. Specifically, anti-angiogenic therapy reduces the affinity between the VEGFs and the corresponding receptors on the EC membrane, decreasing their binding capability and, thus, affecting the migratory behavior of ECs. Moreover, we modeled the effect of this treatment on the reduction of EC proliferation.

We compared the macroscopic outcomes of the setting when no treatment was considered and when the multi-modal therapy described above was applied. In Figure 5.4 we showed the response of the different species to the combined therapy, with a detailed discussion about the effects of the anti-angiogenic therapy on tumor, ECs, and VEGFs dynamics (Figure 5.5).

The numerical results proposed in Section 5.3 represent a preliminary study of the macroscopic solution behavior and a stochastic extension of the model aimed at evaluating the efficacy of the treatment is work in progress. In this context, we will introduce a stochastic variable in the tumor equation of the model in order to calculate three common quality measures that quantify the success of a treatment schedule, namely the tumor control probability (TCP), the normal tissue complication probability (NTCP), and uncomplicated tumor control probability (UTCP). Moreover, we plan to simulate the therapy outcome based on clinical data. We will use glioma patient data to define the domain geometry, the tumor tensor, and the initial conditions of the tumor population and we will reproduce the administered treatment (possibly different from the one we used in the preliminary simulations) to analyze its possible outcome.

6 Non-local sensing in a multi-cue environment

Cell migration is a fundamental mechanism and a key aspect of tumor progression. We have seen across the different settings proposed in the previous chapters that cell migration, and in particular, glioma migration, can be led by several different guidance cues with biochemical or biophysical characters. In Chapter 3, the biophysical phenomenon of tissue fiber alignment has been shown to stimulate *contact guidance*, i.e., the mechanism by which cells tend to migrate crawling on the fibers, thus following the directions imposed by the network structure of the ECM. Nevertheless, several biochemical cues have been shown to guide *chemotactic movements* of tumor cells towards, for instance, sources of nutrients or growth factors (Chapter 5) or less acidic regions (Chapter 4). These directional cues can have either a *mono-directional* or a *bi-directional* nature: for example, the assumption of considering an unpolarized fiber network, on which there is not a preferential *sense of migration*, makes contact guidance a bi-directional cue, while the stimuli governing chemotaxis are usually mono-directional. In this chapter, we illustrate a deeper analysis of possible relationships between mono- and bi-directional stimuli in driving cell migration. The framework we rely on is defined in terms of kinetic-based models, and we introduce some novelties that were not included in the previous settings, one among all the role of cell protrusions. As briefly introduced in Section 1.1.1, ***cell protrusions*** have an important role in driving the migration. Precisely, these extensions of the cell membrane outside of the cell body can reach the dimension of several cell diameters and are involved in a large variety of mechanisms. Here, we focus on the description of how cells measure the external signals by transmembrane receptors located on their protrusions and use the captured stimuli to activate downstream pathways leading to migration. We particularly refer to the cell polarization process by which a cell chooses its direction of motion. This polarization process determines the formation of a *head* and a *tail* in the cell body and the activation of adhesion molecules and traction forces leading to motion [2]. In the framework of kinetic models, we consider the hypothesis of having an environmental sensing of the cells (i.e., the cell's ability to recognize and respond to external cues) over a finite radius in their neighborhood to model these protrusions-mediated mechanisms. Recalling the decomposition of cell velocity into the direction of motion and the speed, we analyze chemotaxis and contact guidance as non-local directional cues guiding cell polarization and, thus, influencing the cell's choice of the motion direction. Although the analysis is described for the general process of cell migration, the application to the case of glioma cell movement is straightforward.

There exists an extensive literature on ***mathematical models for cell migration*** concerning chemotaxis and contact guidance. The most famous example of a macroscopic models for chemotaxis was proposed by Keller and Segel [137]. Their model is based

on a drift-diffusion setting and several approaches to derive it from a lower scale have been proposed (see e.g [117, 213, 215] and references therein). In the context of mesoscopic models, examples of settings for the description of cell chemotactic motion can be found in [43, 71], while the two major contact guidance settings were proposed in [116] and [66]. These last two models are both local in the physical space. Interestingly, few models describing a multiple cues setting have been published. In [289], the authors propose one of the first models for both contact guidance and chemotaxis, derived from microscopic dynamics, while a recent review for macroscopic PDEs including multiple-taxis was proposed in [199].

As already stated, in this chapter, we want to include chemotaxis and contact guidance as directional cues guiding cell polarization, and we analyze two possible sensing strategies that a cell could apply to explore its neighborhood. A possibility for the cell is to measure the guidance cues independently, and, then, choose the new orientation using the collected information, eventually weighted in different ways. Another option is to measure the two-directional stimuli, weighting them equally, and assuming a conditioning of one cue on the other. It is evident that the cell response is related to the choice of the sensing strategy implemented and the macroscopic overall effect of the two cues would also be affected. On the basis of the non-local kinetic model with a double biasing cue proposed in [173], we model here - for the first time - non-local sensing of the fibers distribution, together with a chemotactic cue, both defined at a mesoscopic level. This allows us to study many intermediate scenarios in the analysis of the collaborative or competitive effect of the cues, depending also on the cell size and, thus, on the maximum protrusion length. Precisely, in Section 6.1, we describe the mathematical framework and the characteristic aspects of the non-local transport model. In Sections 6.2 and 6.3, we describe and analyze the two classes of models related to the different strategies for the sensing of the two cues, along with the corresponding macroscopic limits in various regimes, depending on the cell size and on the variability of the external cues. Finally, in Section 6.4, several numerical simulations of the kinetic models are presented to qualitatively investigate various scenarios in a two-dimensional setting.

The results of this chapter have been collected in the paper by Conte and Loy submitted for publication [55].

6.1 *Mathematical framework*

In many cellular processes, there are involved several directional cues that may induce different simultaneous stimuli. While the cell response to each of them has been largely studied, from both intracellular and a migrative points of view, cell responses to a multi-cue environment are less understood. The combination of chemotaxis and contact-guidance happens *in-vivo* in a variety of situations, for instance, the spread of cancer cells in the metastatic process. The fundamental issue is the way cells rank, integrate or hierarchize multiple cues, especially when these give conflicting stimuli, because, for example, they are not co-aligned [235]. Some studies have shown that there may be competition or cooperation between different stimuli. Moreover, many intermediate scenarios may happen and guidance stimuli submit or prevail according to other factors. Among these factors we highlight the role of the average concentration and intensity of the cues (fiber density or molecule concentration), which relate to the steepness of the gradient for taxis processes or to the degree of alignment for contact guidance. Unfortunately, there are only a few experimental and quantitative studies concerning chemotaxis and contact guidance (a few examples are provided in [37,

273, 295]), as well as other combinations of directional guidances cues [247]. One of the latest works concerning the competition between chemotaxis and contact guidance shows that less contractile cells are dominated by chemotaxis, while contact guidance might dominate in more contractile cells [244]. Considering that amoeboid cells are less contractile, while mesenchymal cells are more contractile, and that there can be a switching between amoeboid and mesenchymal migration, the result in [244] suggests that there can also be a switching between the dominance of chemotaxis (amoeboid migration) and contact guidance (mesenchymal migration) [300]. This large window of opened questions motivates our deep study on the understanding of multi-cue migrational responses.

In line with the approach from the previous chapters, we consider cells moving by ***contact guidance***: cells encounter the fiber and then move along the direction of the fiber itself. It has been shown experimentally, for example in the case of glioma cancer cells [131], that randomly disposed fibers imply isotropic movement of cells, while aligned fibers cause anisotropic movement of cells along the preferential direction of the fibers themselves, as we described in details in Chapter 2. This was translated into mathematical models firstly for contact guidance in [116] and, then, applied to the study of glioma in several works (see the settings proposed in Chapters 3-5 and the corresponding references).

We first recall the notation for the ***distribution of fibers*** on the space of directions, given by the unit sphere $\mathbb{S}^{d-1} \subset \mathbb{R}^d$,

$$q = q(\mathbf{x}, \hat{\mathbf{v}}), \qquad \mathbf{x} \in \Omega, \quad \hat{\mathbf{v}} \in \mathbb{S}^{d-1}$$

that satisfies

Q1: $q(\mathbf{x}, \hat{\mathbf{v}}) > 0, \quad \forall \mathbf{x} \in \Omega,\ \hat{\mathbf{v}} \in \mathbb{S}^{d-1}$,

Q2: $\displaystyle\int_{\mathbb{S}^{d-1}} q(\mathbf{x}, \hat{\mathbf{v}})\, d\hat{\mathbf{v}} = 1, \quad \forall \mathbf{x} \in \Omega$,

Q3: $q(\mathbf{x}, \hat{\mathbf{v}}) = q(\mathbf{x}, -\hat{\mathbf{v}}), \quad \forall \mathbf{x} \in \Omega,\ \hat{\mathbf{v}} \in \mathbb{S}^{d-1}$.

The the mean direction of the fibers is given by

$$\mathbb{E}_q(\mathbf{x}) = \int_{\mathbb{S}^{d-1}} q(\mathbf{x}, \hat{\mathbf{v}})\, \hat{\mathbf{v}}\, d\hat{\mathbf{v}},$$

and the tensor related to the fibers, determined by the variance-covariance matrix of q, is

$$\mathbb{V}_q(\mathbf{x}) = \int_{\mathbb{S}^{d-1}} q(\mathbf{x}, \hat{\mathbf{v}})\, (\hat{\mathbf{v}} - \mathbb{E}_q) \otimes (\hat{\mathbf{v}} - \mathbb{E}_q)\, d\hat{\mathbf{v}}\,.$$

As we consider a non polarized fiber network, we have

$$\mathbb{E}_q(\mathbf{x}) = 0, \tag{6.1}$$

meaning that there is no mean direction in the dynamics. Concerning ***chemotaxis***, we consider a chemoattractant in the domain Ω defined by a strictly positive definite function

$$\mathcal{S} : \Omega \longmapsto \mathbb{R}_+.$$

6.1.1 *The transport model*

For our analysis, we describe the cell population at a mesoscopic level through the distribution density $\rho = \rho(t, \mathbf{x}, \sigma, \hat{\mathbf{v}})$ that, for every time $t > 0$ and position $\mathbf{x} \in \Omega \subseteq \mathbb{R}^d$,

gives the statistical distribution of the speeds $\sigma \in [0, U]$, where U is the maximal speed a cell can achieve, and of the polarization directions $\hat{\mathbf{v}} \in \mathbb{S}^{d-1}$, being $\mathbb{S}^{d-1}$ the unit sphere in $\mathbb{R}^d$. Thus, the velocity vector is given by $\mathbf{v} = \sigma\hat{\mathbf{v}}$. Differently to what we did in Chapters 3-5, here we exclude the microscopic internal variable for the cell population density, but we consider the variation of both cell speed σ and orientation $\hat{\mathbf{v}}$, without assuming the former to be constant. Recalling the general modeling framework described in Section 3.1, and specifying it for the special case of a distribution function that does not depend on any internal variable $\mathbf{y}$, we can write the corresponding transport equation for the cell distribution as

$$\frac{\partial \rho}{\partial t}(t, \mathbf{x}, \sigma, \hat{\mathbf{v}}) + \mathbf{v} \cdot \nabla \rho(t, \mathbf{x}, \sigma, \hat{\mathbf{v}}) = \mathcal{L}[\rho](t, \mathbf{x}, \sigma, \hat{\mathbf{v}}) \,. \tag{6.2}$$

Compared to the general equation proposed in (3.1), here we do not consider any conservative or non-conservative interaction (modeled in (3.1) with the term $\mathcal{I}[\rho]$), but only the velocity changes described with the turning operator $\mathcal{L}[\rho](t, \mathbf{x}, \sigma, \hat{\mathbf{v}})$. This operator describes the scattering of the microscopic velocity in direction and speed, related to the typical microscopic dynamics of the cell and described with the *run and tumble* phenomenon [22]. $\mathcal{L}[\rho]$ is classically modeled by a velocity jump process [269], characterized by a *turning frequency* μ and a *transition probability* T. The general form of the turning operator which implements a velocity jump process at a kinetic level was provided in (3.2) with (3.3) and (3.4). Assuming the turning rate to be independent of the velocity variable and explicitly expressing the dependence of the turning probability on cell speed and orientation, the turning operator reads

$$\begin{aligned}\mathcal{L}[\rho](t, \mathbf{x}, \sigma, \hat{\mathbf{v}}) = \mu(\mathbf{x}) \int_{\mathbb{S}^{d-1}} \int_0^U \Big[& T[q, \mathcal{S}](\mathbf{x}, \sigma, \hat{\mathbf{v}} | \sigma', \hat{\mathbf{v}}') \rho(t, \mathbf{x}, \sigma', \hat{\mathbf{v}}') \\ & - T[q, \mathcal{S}](\mathbf{x}, \sigma', \hat{\mathbf{v}}' | \sigma, \hat{\mathbf{v}}) \rho(t, \mathbf{x}, \sigma, \hat{\mathbf{v}}) \Big] \, d\sigma' d\hat{\mathbf{v}}' \,.\end{aligned}$$

The turning kernel $T[q, \mathcal{S}](\mathbf{x}, \sigma, \hat{\mathbf{v}} | \sigma', \hat{\mathbf{v}}')$, which now depends on the two directional cues for chemotaxis $\mathcal{S}$ and contact guidance q, respectively, satisfies the condition (3.5), for all $\mathbf{x} \in \Omega$, $\sigma' \in [0, U]$, and $\hat{\mathbf{v}}' \in \mathbb{S}^{d-1}$. We also assume that the transition probability only depends on the post-tumbling velocity, i.e., $T[q, \mathcal{S}](\mathbf{x}, \sigma, \hat{\mathbf{v}} | \sigma', \hat{\mathbf{v}}') = T[q, \mathcal{S}](\mathbf{x}, \sigma, \hat{\mathbf{v}})$, which is in line with the pioneering work concerning kinetic equations for velocity jump processes [8, 116, 269]. This assumption is due to the fact that we consider directional cues which are sensed non-locally, and, therefore, the most relevant aspect will be the measured preferential direction instead of the incoming velocity. With this assumption, the turning operator reduces to

$$\mathcal{L}[\rho](t, \mathbf{x}, \sigma, \hat{\mathbf{v}}) = \mu(\mathbf{x}) \left(n(t, \mathbf{x}) T[q, \mathcal{S}](\mathbf{x}, \sigma, \hat{\mathbf{v}}) - \rho(t, \mathbf{x}, \sigma, \hat{\mathbf{v}}) \right) \tag{6.3}$$

where, $n(t, \mathbf{x})$ denotes again the macroscopic cell population density, namely

$$n(t, \mathbf{x}) = \int_{\mathbb{S}^{d-1}} \int_0^U \rho(t, \mathbf{x}, \sigma, \hat{\mathbf{v}}) \, d\sigma \, d\hat{\mathbf{v}} \,. \tag{6.4}$$

For later reference, we introduce the notations for the mean macroscopic velocity after a tumble event, as

$$\mathbf{U}_T(\mathbf{x}) = \int_{\mathbb{S}^{d-1}} \int_0^U \mathbf{v} \, T[q, \mathcal{S}](\mathbf{x}, \sigma, \hat{\mathbf{v}}) \, d\sigma \, d\hat{\mathbf{v}} \,, \tag{6.5}$$

that is the average of T, and for the corresponding tensor

$$\mathbf{D}_T(\mathbf{x}) = \int_{\mathbb{S}^{d-1}} \int_0^U T[q,\mathcal{S}](\mathbf{x},\sigma,\hat{\mathbf{v}})(\mathbf{v}-\mathbf{U}_T)\otimes(\mathbf{v}-\mathbf{U}_T)d\sigma\, d\hat{\mathbf{v}}\,, \tag{6.6}$$

which is the variance-covariance matrix of T. To link these notations with the notations in the previous settings, where the turning kernel T describing the contact guidance phenomenon was given by (3.15), the mean macroscopic velocity (6.5) corresponds to (3.16) and (6.6) reduces to (3.17). As remarked in [173], T is the local asymptotic equilibrium steady state of the system (6.2) with (6.3) and, therefore, $\mathbf{U}_T$ and $\mathbf{D}_T$ are the mean velocity and macroscopic tensor of the cell population at equilibrium.

In order to investigate the overall trend of the system (6.2) with (6.3), we analyze the macroscopic behavior. To obtain a closed evolution equation for $n(t,\mathbf{x})$ in the emerging regime of the system, we consider diffusive or a hydrodynamic scaling of the transport equation (6.2) with (6.3), resulting from a proper non-dimensionalization of the system. In particular, we discussed these limits and the procedure to get a closed macroscopic equation (or system of equations) in Section 3.1, and we used the parabolic scaling for the settings of Chapters 3-5. In addition to the notation introduced for the expansion of the turning kernel (3.9) and of the distribution function (3.10), for later reference we also define the expansions of $\mathbf{U}_T(\mathbf{x})$ and $\mathbf{D}_T(\mathbf{x})$

$$\mathbf{U}_T^i(\boldsymbol{\xi}) = \int_{\mathbb{S}^{d-1}} \int_0^U T_i[\mathcal{S},q](\boldsymbol{\xi},\sigma,\hat{\mathbf{v}})\mathbf{v}\, d\sigma d\hat{\mathbf{v}}$$

and

$$\mathbf{D}_T^i(\boldsymbol{\xi}) = \int_{\mathbb{S}^{d-1}} \int_0^U T_i[\mathcal{S},q](\boldsymbol{\xi},\sigma,\hat{\mathbf{v}})(\mathbf{v}-\mathbf{U}_T^i)\otimes(\mathbf{v}-\mathbf{U}_T^i)d\sigma\, d\hat{\mathbf{v}}\,,$$

where $i = 0,1,2,..$ and $\boldsymbol{\xi} = \varepsilon\mathbf{x}$. The functional solvability condition introduced in Section 3.1 and necessary for performing a diffusive limit, here, reads

$$\mathbf{U}_T^0 = 0 \qquad \text{for a.e.} \quad \boldsymbol{\xi}.$$

6.1.2 *Non-local aspects*

We consider that the sensing performed by the cells is non-local, as they may extend their protrusions, through which they sense the environment, up to several cell diameters [23]. The maximum length R of a protrusion is called *sensing radius* and it has been first introduced in [213] for modeling a non-local gradient of a chemical and, then, used in a number of works (see [45, 173] for a review and references therein) for describing the sensing of macroscopic quantities. In the present model, both $\mathcal{S}$ and q are sensed non-locally by a cell that, starting from its position $\mathbf{x}$, extends its protrusions in every direction $\hat{\mathbf{v}} \in \mathbb{S}^{d-1}$ up to the distance R. Assuming a non-local sensing of the fiber network allows to reproduce a wider range of migration strategies (with respect to a local sensing) that a cell can perform in order to cleverly reach the chemoattractant. Therefore, we consider the quantities:

$$\mathcal{S}(\mathbf{x}+\lambda\hat{\mathbf{v}}), \qquad q(\mathbf{x}+\lambda\hat{\mathbf{v}},\hat{\mathbf{v}}), \qquad \forall\,\mathbf{x}\in\Omega, \quad \forall\,\hat{\mathbf{v}}\in\mathbb{S}^{d-1}, \quad \lambda\in\mathbb{R}, \quad \lambda\le R.$$

We notice that, next to the border of the domain Ω, we consider λ such that $\mathbf{x}+\lambda\hat{\mathbf{v}}\in\Omega$.

In order to analyze qualitatively the impact of the non-locality at the macroscopic

level, we study, in the spirit of [173], the impact of the directional cues $\mathcal{S}$ and q with respect to the size of the cell. This size is related to the cell sensing radius R. Thus, we introduce the characteristic length of variation of $\mathcal{S}$ as

$$l_{\mathcal{S}} := \frac{1}{\max\limits_{\mathbf{x}\in\Omega} \frac{|\nabla \mathcal{S}(\mathbf{x})|}{\mathcal{S}(\mathbf{x})}} .$$

This notation allows to approximate $\mathcal{S}(\mathbf{x}+\lambda\hat{\mathbf{v}})$ with a positive quantity

$$\mathcal{S}(\mathbf{x}+\lambda\hat{\mathbf{v}}) \sim \mathcal{S}(\mathbf{x}) + \lambda \nabla \mathcal{S}(\mathbf{x})\cdot\hat{\mathbf{v}} \geq 0 \quad \forall \lambda \leq R \quad \text{if} \quad R < l_{\mathcal{S}} , \tag{6.7}$$

where we neglect higher order terms in λ.

Beside the above defined characteristic length of variation $l_{\mathcal{S}}$ of the chemoattractant $l_{\mathcal{S}}$, we analogously define a quantity for the fibers distribution. We choose

$$l_q := \frac{1}{\max\limits_{\mathbf{x}\in\Omega} \max\limits_{\hat{\mathbf{v}}\in\mathbb{S}^{d-1}} \frac{|\nabla q(\mathbf{x},\hat{\mathbf{v}})\cdot\hat{\mathbf{v}}|}{q(\mathbf{x},\hat{\mathbf{v}})}} .$$

In this case, we can approximate $q(\mathbf{x}+\lambda\hat{\mathbf{v}},\hat{\mathbf{v}})$ with a positive quantity

$$q(\mathbf{x}+\lambda\hat{\mathbf{v}},\hat{\mathbf{v}}) \sim q(\mathbf{x},\hat{\mathbf{v}}) + \lambda \nabla q(\mathbf{x},\hat{\mathbf{v}})\cdot\hat{\mathbf{v}} \geq 0 \quad \forall \lambda < R \quad \text{if} \quad R < l_q . \tag{6.8}$$

This definition of l_q takes into account the variation of directionality of the fibers in space, which influences the cell orientation, more than the spatial variation of the density of the extracellular matrix.

We analyze the possible scenarios depending on the relation between R, $l_{\mathcal{S}}$ and l_q. For this we introduce the parameters

$$\eta_{\mathcal{S}} := \frac{R}{l_{\mathcal{S}}} \tag{6.9}$$

and

$$\eta_q := \frac{R}{l_q} , \tag{6.10}$$

that quantify the cell capability to measure the guidance cues q and $\mathcal{S}$ with respect to their characteristic lengths of variation. In particular, $\eta_i < 1,\ i = \mathcal{S}, q$, means that the sensing radius is smaller than the characteristic length of variation of $\mathcal{S}$ (or q, respectively), meaning that a single instantaneous sensing of the cell is not capable of catching the total spatial variability of $\mathcal{S}$ (or q, respectively). In turn, if $\eta_i > 1,\ i = \mathcal{S}, q$, the sensing radius is large enough in order to capture the spatial variability of $\mathcal{S}$ (or q, respectively). If we consider only one of the two cues at the time, in the first case ($\eta_i < 1$) we expect that the sensing of $\mathcal{S}$ (or q, respectively) induces a diffusive behavior, while in the second scenario ($\eta_i > 1$) the overall behavior induced by $\mathcal{S}$ (or q, respectively) is drift-driven.

As we are considering the two guidance cues simultaneously affecting the cell polarization, we take into account four limit cases:

i) $\eta_{\mathcal{S}}, \eta_q \gg 1$;

ii) $\eta_{\mathcal{S}}, \eta_q \ll 1$;

iii) $\eta_{\mathcal{S}} \ll 1, \eta_q \gg 1$;

iv) $\eta_{\mathcal{S}} \gg 1, \eta_q \ll 1$.

In order to quantify the relative contribution of chemotaxis to contact guidance, we introduce a further parameter

$$\eta := \frac{\eta_q}{\eta_{\mathcal{S}}}\,, \tag{6.11}$$

that is larger than 1 if contact guidance prevails, whilst it is smaller than 1 if chemotaxis dominates. Due to (6.9) and (6.10), we have that, despite its definition, η does not depend on the size and sensing capability of the cell, as $\eta = \frac{\eta_q}{\eta_{\mathcal{S}}} = \frac{l_{\mathcal{S}}}{l_q}$. In particular, if $l_{\mathcal{S}}$ is larger than l_q, i.e., $\eta > 1$, this implies that the gradient of q is steeper than the one of $\mathcal{S}$, thus forcing a stronger effect of contact guidance on the dynamics. We can also observe that in case *iii*) we always have $\eta > 1$ while in case *iv*) we always have $\eta < 1$, i.e., contact guidance is weaker than chemotaxis.

6.1.3 *Definition of the turning probability*

We propose two different transition probabilities that model the changes in the cell polarization, in order to describe two different sensing strategies of the cells: in a first model the sensings of q and $\mathcal{S}$ are independent, while in a second model their sensing are dependent.

For the first model, we define the transition probability as the product of two different independent sensings, namely

$$T[q,\mathcal{S}](\mathbf{x},\sigma,\hat{\mathbf{v}}) = c(\mathbf{x})\,\psi(\sigma)\int_{\mathbb{R}_+}\gamma_{\mathcal{S}}(\lambda)\mathcal{S}(\mathbf{x}+\lambda\hat{\mathbf{v}})\,d\lambda\int_{\mathbb{R}_+}\gamma_q(\lambda)\,q(\mathbf{x}+\lambda\hat{\mathbf{v}},\hat{\mathbf{v}})\,d\lambda\,. \tag{6.12}$$

This transition probability models a cell located in position $\mathbf{x}$ that measures along the direction $\hat{\mathbf{v}}$ the field $\mathcal{S}(\mathbf{x}+\lambda\hat{\mathbf{v}})$ weighted by $\gamma_{\mathcal{S}}$, and, independently, the quantity $q(\mathbf{x}+\lambda\hat{\mathbf{v}},\hat{\mathbf{v}})$, weighted by γ_q. The *sensing functions* $\gamma_{\mathcal{S}}$ and γ_q have compact support in $[0,R]$ and can be Dirac delta functions centered in R, if the cell only measures the guidance cues on its membrane (only on $\mathbf{x}+R\hat{\mathbf{v}}$ for every $\hat{\mathbf{v}}$). Another possible choice for the sensing functions can be Heaviside functions if the cell gives the same weight to q and $\mathcal{S}$ from $\mathbf{x}$ to $\mathbf{x}+R\hat{\mathbf{v}}$ in every direction. Formally the transition probability can be seen as the product of the independent probabilities of q and $\mathcal{S}$, i.e., $T[q,\mathcal{S}] = \hat{T}[q]\,\hat{T}[\mathcal{S}]$.

The second model prescribes a simultaneous averaging of the guidance cues $\mathcal{S}$ and q, i.e.,

$$T[q,\mathcal{S}](\mathbf{x},\sigma,\hat{\mathbf{v}}) = c(\mathbf{x})\,\psi(\sigma)\int_{\mathbb{R}_+}\gamma(\lambda)\mathcal{S}(\mathbf{x}+\lambda\hat{\mathbf{v}})\,q(\mathbf{x}+\lambda\hat{\mathbf{v}},\hat{\mathbf{v}})d\lambda\,. \tag{6.13}$$

This transition probability describes a cell in position $\mathbf{x}$ that measures in the direction $\hat{\mathbf{v}}$ the two quantities $\mathcal{S}(\mathbf{x}+\lambda\hat{\mathbf{v}})$ and $q(\mathbf{x}+\lambda\hat{\mathbf{v}})$, weighting both with γ, which is a sensing function. Formally, as the two sensings are not independent and, thus, factorized, we have a conditioning of $\mathcal{S}$ given q and viceversa, i.e., $T[q,\mathcal{S}] = \tilde{T}[\mathcal{S}|q]\,\tilde{T}[q] = \tilde{T}[q|\mathcal{S}]\,\tilde{T}[\mathcal{S}]$.

In (6.12) and (6.13), $c(\mathbf{x})$ is a normalization coefficient, while $\psi(\sigma)$ is a probability density. This probability density is the distribution of the speed in the interval $[0,U]$ and satisfies

$$\int_0^U \psi(\sigma)d\sigma = 1\,,$$

with the mean speed

$$\bar{U} = \int_0^U \sigma\,\psi(\sigma)\,d\sigma$$

and the second moment

$$D = \int_0^U \sigma^2 \, \psi(\sigma) \, d\sigma \,, \tag{6.14}$$

such that the variance of ψ is given by $\frac{1}{2}(D - \bar{U}^2)$.

We refer to the transport model (6.2)-(6.3) with (6.12) as *non-local independent sensing model*, in which the cell averages the two cues independently according to two different sensing functions γ_S and γ_q. In turn, the transport model (6.2)-(6.3) with (6.13) is refereed to as *non-local dependent sensing model*, describing cells that sense the two cues at the same time and average them with one sensing kernel γ. In the next sections, we analyze the macroscopic limits of the two models for the cases $i) - iv)$ and we compare the two sensing strategies.

6.2 *Non-local independent sensing model*

We first consider the non-local independent sensing case (6.2)-(6.3) with (6.12). We recall the expression of the transition probability

$$T[q,\mathcal{S}](\mathbf{x},\sigma,\hat{\mathbf{v}}) = c(\mathbf{x}) \, \psi(\sigma) \int_{\mathbb{R}_+} \gamma_S(\lambda) \mathcal{S}(\mathbf{x}+\lambda\hat{\mathbf{v}}) \, d\lambda \int_{\mathbb{R}_+} \gamma_q(\lambda) \, q(\mathbf{x}+\lambda\hat{\mathbf{v}},\hat{\mathbf{v}}) \, d\lambda \,.$$

The average of T, which is the equilibrium velocity of the cell population, is given by

$$\mathbf{U}_T(\mathbf{x}) = c(\mathbf{x}) \, \bar{U} \int_{\mathbb{S}^{d-1}} \hat{\mathbf{v}} \left(\int_{\mathbb{R}_+} \gamma_S(\lambda) \mathcal{S}(\mathbf{x}+\lambda\hat{\mathbf{v}}) \, d\lambda \int_{\mathbb{R}_+} \gamma_q(\lambda) \, q(\mathbf{x}+\lambda\hat{\mathbf{v}},\hat{\mathbf{v}}) \, d\lambda \right) d\hat{\mathbf{v}} \,. \tag{6.15}$$

Case $i)$

In this case, we choose the scaling parameter as

$$\varepsilon = \min\left\{ \frac{1}{\eta_q}, \frac{1}{\eta_S} \right\} .$$

As a consequence of the fact that T cannot be expanded in powers of ε, after the re-scaling (3.6), we have that $\mathbf{U}_T^0 = \mathbf{U}_T$ given by (6.15). Therefore, we have to perform the hyperbolic scaling (3.8) that leads to the following macroscopic equation for the cells macroscopic density:

$$\frac{\partial}{\partial\tau} n(\tau,\boldsymbol{\xi}) + \nabla \cdot (n(\tau,\boldsymbol{\xi}) \mathbf{U}_T(\boldsymbol{\xi})) = 0 \,, \tag{6.16}$$

with $\mathbf{U}_T(\boldsymbol{\xi})$ given by the re-scaling of (6.15) with (3.6).

Case $ii)$

In this case, we can expand both $\mathcal{S}(\mathbf{x}+\lambda\hat{\mathbf{v}})$ and $q(\mathbf{x}+\lambda\hat{\mathbf{v}},\hat{\mathbf{v}})$ and consider the approximations (6.7) and (6.8) for $\lambda < \min\{l_q, l_S\}$. Therefore, we approximate the transition probability by substituting (6.7) and (6.8) in (6.12), and, thus, we obtain the following approximation for the turning kernel $T[q,\mathcal{S}]$, which reads

$$T[q,\mathcal{S}](\mathbf{x},\sigma,\hat{\mathbf{v}}) = c(\mathbf{x})\psi(\sigma) \left[\Gamma_0^{\mathcal{S}} \Gamma_0^q \, \mathcal{S}(\mathbf{x}) \, q(\mathbf{x},\hat{\mathbf{v}}) + \Gamma_0^{\mathcal{S}} \Gamma_1^q \mathcal{S}(\mathbf{x}) \, \nabla q \cdot \hat{\mathbf{v}} + \Gamma_1^{\mathcal{S}} \Gamma_0^q \, q(\mathbf{x},\hat{\mathbf{v}}) \nabla \mathcal{S} \cdot \hat{\mathbf{v}} \right]$$

where we neglected higher orders terms in λ. In the previous equation for the turning kernel we set

$$c(\mathbf{x}) = \frac{1}{\mathcal{S}(\mathbf{x})\,\Gamma_0^{\mathcal{S}}\,\Gamma_0^q}$$

and define

$$\Gamma_i^q := \int_{\mathbb{R}_+} \lambda^i \gamma_q(\lambda)\, d\lambda \qquad i = 0, 1\,,$$

$$\Gamma_i^{\mathcal{S}} := \int_{\mathbb{R}_+} \lambda^i \gamma_{\mathcal{S}}(\lambda)\, d\lambda \qquad i = 0, 1\,.$$

The quantities $\Gamma_0^q, \Gamma_0^{\mathcal{S}}$ are the weighted (by γ_q, γ_s) measures of the sensed linear tracts in every direction, while $\Gamma_1^q, \Gamma_1^{\mathcal{S}}$ are the averages of γ_q, γ_s on $[0, R]$. Then, we introduce the small parameter

$$\varepsilon = \min\{\eta_q, \eta_{\mathcal{S}}\}$$

and re-scale the space variable with (3.6), getting at the order zero

$$T_0[q, \mathcal{S}](\boldsymbol{\xi}, \sigma, \hat{\mathbf{v}}) = q(\boldsymbol{\xi}, \hat{\mathbf{v}})\psi(\sigma) \tag{6.17}$$

meaning that the equilibrium is determined by the fibers distribution, and at the first order

$$T_1[q, \mathcal{S}](\boldsymbol{\xi}, v, \hat{\mathbf{v}}) = \left[\Gamma^q\, \nabla q \cdot \hat{\mathbf{v}} + \Gamma^{\mathcal{S}}\, q(\boldsymbol{\xi}, \hat{\mathbf{v}})\, \frac{\nabla \mathcal{S}}{\mathcal{S}(\boldsymbol{\xi})} \cdot \hat{\mathbf{v}}\right] \psi(\sigma)\,,$$

where

$$\Gamma^q := \frac{\Gamma_1^q}{\Gamma_0^q}\,, \qquad \Gamma^{\mathcal{S}} := \frac{\Gamma_1^{\mathcal{S}}}{\Gamma_0^{\mathcal{S}}}\,.$$

Because of (6.1) and (6.17), we have that $\mathbf{U}_T^0(\boldsymbol{\xi}) = 0$, meaning that we are in a diffusive regime, and the diffusive limits (3.7) leads to the advection-diffusion equation

$$\frac{\partial}{\partial \tau} n + \nabla \cdot \left(\mathbf{U}_T^1 n\right) = \nabla \cdot \left[\frac{1}{\mu} \nabla \cdot \left(\mathbf{D}_T^0 n\right)\right]\,,$$

with zero-order macroscopic tensor given by

$$\mathbf{D}_T^0(\boldsymbol{\xi}) = D \int_{\mathbb{S}^{d-1}} q(\boldsymbol{\xi}, \hat{\mathbf{v}}) \hat{\mathbf{v}} \otimes \hat{\mathbf{v}}\, d\hat{\mathbf{v}} = D\, \mathbb{V}_q(\boldsymbol{\xi})\,, \tag{6.18}$$

and macroscopic first-order velocity

$$\begin{aligned}
\mathbf{U}_T^1(\boldsymbol{\xi}) &= \bar{U} \int_{\mathbb{S}^{d-1}} \left(\Gamma^q\, \nabla q \cdot \hat{\mathbf{v}} + \Gamma^{\mathcal{S}}\, \frac{\nabla \mathcal{S}}{\mathcal{S}(\boldsymbol{\xi})} \cdot \hat{\mathbf{v}}\, q(\boldsymbol{\xi}, \hat{\mathbf{v}})\right) \hat{\mathbf{v}} d\hat{\mathbf{v}} \\
&= \bar{U}\, \Gamma^q \int_{\mathbb{S}^{d-1}} (\nabla q \cdot \hat{\mathbf{v}})\, \hat{\mathbf{v}} d\hat{\mathbf{v}} + \bar{U}\, \Gamma^{\mathcal{S}}\, \frac{\nabla \mathcal{S}}{\mathcal{S}} \int_{\mathbb{S}^{d-1}} \hat{\mathbf{v}} \otimes \hat{\mathbf{v}}\, q(\boldsymbol{\xi}, \hat{\mathbf{v}}) d\hat{\mathbf{v}} \\
&= \bar{U} \left[\Gamma^q\, \nabla \cdot \mathbb{V}_q + \Gamma^{\mathcal{S}}\, \mathbb{V}_q\, \frac{\nabla \mathcal{S}}{\mathcal{S}}\right].
\end{aligned} \tag{6.19}$$

We recall that D is defined in (6.14), while $\mathbb{V}_q$ (namely, the variance-covariance matrix for the orientation distribution of tissue fibers) is defined in (3.17). Therefore, the complete advection-diffusion equation reads (dropping the dependencies)

$$\frac{\partial}{\partial \tau} n + \nabla \cdot \left[\left(\chi^{\mathcal{S}}\, \mathbb{V}_q \nabla \mathcal{S} + \chi^q \nabla \cdot \mathbb{V}_q\right) n\right] = \nabla \cdot \left[\frac{1}{\mu}\, \nabla \cdot \left(D\, \mathbb{V}_q\, n\right)\right]\,, \tag{6.20}$$

where

$$\chi^{\mathcal{S}}(\boldsymbol{\xi}) := \frac{\bar{U}\,\Gamma^{\mathcal{S}}}{\mathcal{S}(\boldsymbol{\xi})} \quad , \quad \chi^{q} := \bar{U}\,\Gamma^{q} \tag{6.21}$$

are the sensitivities related to chemotaxis and contact guidance. The diffusion represented by the tensor (6.18) only depends on the fibers distribution, while the advective term has two contributions differently weighted by the sensitivities (6.21). We remark that, in this regime, we obtain the same macroscopic behavior as postulated by Keller and Segel [137], with the logarithmic chemotactic sensitivity $\chi_{\mathcal{S}}$ given in (6.21). The term $\mathbb{V}_q \nabla \mathcal{S}$ depends on both the fibers distribution and the chemotactic field; it never vanishes if $\nabla \mathcal{S}$ is not the null vector, since it can be proved that the matrix $\mathbb{V}_q$ is invertible. In the case of randomly disposed fibers, corresponding to the isotropic case, i.e., when $\mathbb{V}_q$ is proportional to the identity matrix, then $\mathbb{V}_q \nabla \mathcal{S}$ is parallel to $\nabla \mathcal{S}$, which, thus, represents the anisotropy direction. Conversely, when $\mathbb{V}_q$ is anisotropic, if $\nabla \mathcal{S}$ is not parallel to the eigenvector corresponding to the highest eigenvalue of $\mathbb{V}_q$, then the migration does not follow the dominant direction of the fibers, but rather its projection on $\nabla \mathcal{S}$. Moreover, the second part of the drift term, i.e., $\nabla \cdot \mathbb{V}_q$, is a measure of the velocity field induced by the spatial variation of the fiber direction distribution, which determines the microscopic cell velocities. This term vanishes if the fiber distribution is homogeneous in space. Therefore, if q is homogeneous in space, even in case of competing cues, i.e., $\mathbb{E}_q \perp \nabla \mathcal{S}$, in general the advective term $\mathbf{U}_T^1$ does not vanish. While, in case of cooperating cues, i.e., $\nabla \mathcal{S}$ is an eigenvector of $\mathbb{V}_q$ with eigenvalue $\lambda_{\nabla \mathcal{S}}$, migration is in direction $\nabla \mathcal{S}$ with a kinetic factor $\chi_{\mathcal{S}} \lambda_{\nabla \mathcal{S}}$. In intermediate scenarios, i.e., when there is not complete cooperation or competition, migration happens in the projection $\mathbb{V}_q \nabla \mathcal{S}$, but, if q is not homogeneous, the dynamics is more complex and, even in case of cooperation, we cannot conclude anything about additivity effects.

Case *iii*)

In this case, we can only expand the chemoattractant, approximated in (6.7), with Taylor series and can, thus, rewrite the turning kernel (6.12) as

$$T[q,\mathcal{S}](\mathbf{x},\sigma,\hat{\mathbf{v}}) = \psi(\sigma)\Big[c_0(\mathbf{x})\,\mathcal{S}(\mathbf{x})\,\Gamma_0^{\mathcal{S}} \int_{\mathbb{R}_+} \gamma_q(\lambda) q(\mathbf{x}+\lambda\hat{\mathbf{v}},\hat{\mathbf{v}})\,d\lambda$$

$$+ c_1(\mathbf{x})\,\Gamma_1^{\mathcal{S}}\,(\nabla\mathcal{S}\cdot\hat{\mathbf{v}}) \int_{\mathbb{R}_+} \gamma_q(\lambda) q(\mathbf{x}+\lambda\hat{\mathbf{v}},\hat{\mathbf{v}})\,d\lambda\Big]$$

where we neglect higher order terms in λ. Here, the normalization coefficients are given by

$$c_0(\mathbf{x}) := \left(2\int_{\mathbb{S}^{d-1}} \Gamma_0^{\mathcal{S}}\,S(\mathbf{x}) \int_{\mathbb{R}_+} \gamma_q(\lambda) q(\mathbf{x}+\lambda\hat{\mathbf{v}},\hat{\mathbf{v}})\,d\lambda\,d\hat{\mathbf{v}}\right)^{-1}$$

and

$$c_1(\mathbf{x}) := \left(2\int_{\mathbb{S}^{d-1}} \Gamma_1^{\mathcal{S}}\,(\nabla S\cdot\hat{\mathbf{v}}) \int_{\mathbb{R}_+} \gamma_q(\lambda) q(\mathbf{x}+\lambda\hat{\mathbf{v}},\hat{\mathbf{v}})\,d\lambda\,d\hat{\mathbf{v}}\right)^{-1},$$

both different from zero. In this case, we choose

$$\varepsilon = \min\left\{\frac{1}{\eta_q}, \eta_{\mathcal{S}}\right\},$$

and, re-scaling the space variable as in (3.6),we get $T[q,\mathcal{S}] = T_0[q,\mathcal{S}]$. Let us now define

$$\mathbb{V}_q^\lambda(\boldsymbol{\xi}) = \int_{\mathbb{S}^{d-1}} q(\boldsymbol{\xi}+\lambda\hat{\mathbf{v}},\hat{\mathbf{v}})\,\hat{\mathbf{v}}\otimes\hat{\mathbf{v}}\,d\hat{\mathbf{v}}\,,$$

that, for each point $\boldsymbol{\xi}$, is the diffusion tensor of the fibers on a circle of radius λ, and

$$\bar{\mathbb{V}}_q^0(\boldsymbol{\xi}) = \frac{1}{\Gamma_0^q}\int_{\mathbb{R}_+}\gamma_q(\lambda)\mathbb{V}_q^\lambda(\boldsymbol{\xi})\,d\lambda\,,$$

that is a weighted directional tensor of the fibers in the whole neighbourhood sensed by the cells. Analogously we define

$$\mathbf{E}_q^\lambda(\boldsymbol{\xi}) = \int_{\mathbb{S}^{d-1}} q(\boldsymbol{\xi}+\lambda\hat{\mathbf{v}},\hat{\mathbf{v}})\,\hat{\mathbf{v}}\,d\hat{\mathbf{v}}\,,$$

that, for each point $\boldsymbol{\xi}$, is the mean direction of the fiber on a circle of radius λ, and

$$\bar{\mathbf{E}}_q^0(\boldsymbol{\xi}) = \frac{1}{\Gamma_0^q}\int_{\mathbb{R}_+}\gamma_q(\lambda)\mathbf{E}_q^\lambda\,d\lambda\,,$$

the mean fiber direction in the whole neighbourhood sensed by the cells. Hence, in this case, $\mathbf{U}_T^0(\boldsymbol{\xi})$ does not vanish in Ω, as it is given by

$$\begin{aligned}\mathbf{U}_T^0(\boldsymbol{\xi}) &= c_0(\boldsymbol{\xi})\,\bar{U}\,\Gamma_0^{\mathcal{S}}\,S(\boldsymbol{\xi})\int_{\mathbb{R}_+}\gamma_q(\lambda)\int_{\mathbb{S}^{d-1}}\hat{\mathbf{v}}\,q(\boldsymbol{\xi}+\lambda\hat{\mathbf{v}},\hat{\mathbf{v}})\,d\hat{\mathbf{v}}\,d\lambda\\ &\quad + c_1(\boldsymbol{\xi})\,\bar{U}\,\Gamma_1^{\mathcal{S}}\,\nabla\mathcal{S}\int_{\mathbb{R}_+}\gamma_q(\lambda)\int_{\mathbb{S}^{d-1}}\hat{\mathbf{v}}\otimes\hat{\mathbf{v}}\,q(\boldsymbol{\xi}+\lambda\hat{\mathbf{v}},\hat{\mathbf{v}})\,d\hat{\mathbf{v}}\,d\lambda,\\ &= c_0(\boldsymbol{\xi})\,\bar{U}\,\Gamma_0^{\mathcal{S}}\,\Gamma_0^q\,\mathcal{S}(\boldsymbol{\xi})\;\bar{\mathbf{E}}_q^0 + c_1(\boldsymbol{\xi})\,\bar{U}\,\Gamma_1^{\mathcal{S}}\,\Gamma_0^q\,\nabla\mathcal{S}\;\bar{\mathbb{V}}_q^0\,.\end{aligned} \tag{6.22}$$

The macroscopic equation is given by the drift equation (6.16) with mean velocity (6.22). Precisely, the advection velocity is related to a non-local average of the diffusion tensor of the fibers $\bar{\mathbb{V}}_q^\lambda$ projected on $\nabla\mathcal{S}$, and a non-local average of the mean fiber velocity depending on the local chemoattractant $\mathcal{S}$. In this case the additivity effect of the two cues is not evident and there are several possible scenarios.

Remark 6.1. If we consider $\gamma_q = \delta(\lambda-0)$ we obtain a local sensing of fibers. In this case, $\mathbf{U}_T^0(\boldsymbol{\xi})$ would vanish in Ω and we get a diffusion-advection equation with macroscopic velocity induced by both the spatial variation of the chemoattractant $\nabla\mathcal{S}$ and the diffusion tensor of the fiber $\mathbb{D}_q$ and with the same sensitivity $\chi^{\mathcal{S}}$ as in (6.21). Without chemotaxis, this case would reduce to the classical model for contact guidance [116].

Case *iv*)

The last case allows only a Taylor expansion of the distribution function q, as in (6.8). Therefore, the turning kernel can be approximated as

$$\begin{aligned}T[q,\mathcal{S}](\mathbf{x},\sigma,\hat{\mathbf{v}}) = \psi(\sigma)\Big[&c_0(\mathbf{x})\,\Gamma_0^q\,q(\mathbf{x},\hat{\mathbf{v}})\int_{\mathbb{R}_+}\gamma_s(\lambda)\mathcal{S}(\mathbf{x}+\lambda\hat{\mathbf{v}})\,d\lambda\\ &+ c_1(\mathbf{x})\Gamma_1^q\,(\nabla q\cdot\hat{\mathbf{v}})\int_{\mathbb{R}_+}\gamma_s(\lambda)\mathcal{S}(\mathbf{x}+\lambda\hat{\mathbf{v}})\,d\lambda\Big]\,,\end{aligned} \tag{6.23}$$

where the coefficient functions are defined as

$$c_0(\mathbf{x}) := \left(2\int_{\mathbb{S}^{d-1}} \Gamma_0^q\, q(\mathbf{x},\hat{\mathbf{v}}) \int_{\mathbb{R}_+} \gamma_{\mathcal{S}}(\lambda)\mathcal{S}(\mathbf{x}+\lambda\hat{\mathbf{v}})\, d\lambda\, d\hat{\mathbf{v}}\right)^{-1}$$

and

$$c_1(\mathbf{x}) := \left(2\int_{\mathbb{S}^{d-1}} \Gamma_1^q\, (\nabla q\cdot\hat{\mathbf{v}}) \int_{\mathbb{R}_+} \gamma_{\mathcal{S}}(\lambda)\mathcal{S}(\mathbf{x}+\lambda\hat{\mathbf{v}})\, d\lambda\, d\hat{\mathbf{v}}\right)^{-1},$$

both different from zero. In this case, we choose

$$\varepsilon = \min\left\{\frac{1}{\eta_{\mathcal{S}}}, \eta_q\right\}$$

and, by re-scaling (6.23) with (3.6), we get $T[q,\mathcal{S}] = T_0[q,\mathcal{S}]$. Hence $\mathbf{U}_T^0(\boldsymbol{\xi})$ does not vanish in Ω, as it is given by

$$\begin{aligned}\mathbf{U}_T^0(\boldsymbol{\xi}) = c_0(\boldsymbol{\xi})\,\bar{U}\,\Gamma_0^q \int_{\mathbb{S}^{d-1}} \hat{\mathbf{v}}\, q(\boldsymbol{\xi},\hat{\mathbf{v}}) \int_{\mathbb{R}_+} \gamma_{\mathcal{S}}(\lambda)\,\mathcal{S}(\boldsymbol{\xi}+\lambda\hat{\mathbf{v}})\, d\lambda\, d\hat{\mathbf{v}} \\ + c_1(\boldsymbol{\xi})\,\bar{U}\,\Gamma_1^q \int_{\mathbb{S}^{d-1}} \hat{\mathbf{v}}\otimes\hat{\mathbf{v}}\,\nabla q \int_{\mathbb{R}_+} \gamma_{\mathcal{S}}(\lambda)\,\mathcal{S}(\boldsymbol{\xi}+\lambda\hat{\mathbf{v}})\, d\lambda\, d\hat{\mathbf{v}},\end{aligned} \tag{6.24}$$

and the macroscopic drift equation is given by (6.16) with mean velocity (6.24). This is a linear combination of a non-local measure of the chemoattractant $\mathcal{S}$ over the fibers network and a non-local measure of $\mathcal{S}$ weighted by the directional average of the spatial variability of the fiber direction.

Remark 6.2. If we consider a local sensing for the chemoattractant, i.e., $\gamma_{\mathcal{S}} = \delta(\lambda - 0)$, we obtain a macroscopic advection-diffusion equation, where the macroscopic velocity is induced by the spatial variation of the distribution of fiber directions $\nabla\cdot\mathbb{V}_q$, and the measure of $\mathcal{S}$ does not affect the choice of the direction. In this case, if ∇q vanishes, the model reduces to a fully anisotropic diffusive equation [116].

6.3 *Non-local dependent sensing model*

Concerning the non-local dependent sensing case (6.2)-(6.3) with (6.13), we recall the expression of the transition probability

$$T[q,\mathcal{S}](\mathbf{x},\sigma,\hat{\mathbf{v}}) = c(\mathbf{x})\,\psi(\sigma)\int_{\mathbb{R}_+}\gamma(\lambda)\mathcal{S}(\mathbf{x}+\lambda\hat{\mathbf{v}})\,q(\mathbf{x}+\lambda\hat{\mathbf{v}},\hat{\mathbf{v}})d\lambda\,,$$

with

$$c(\mathbf{x}) := \int_{\mathbb{S}^{d-1}}\int_{\mathbb{R}_+}\gamma(\lambda)\mathcal{S}(\mathbf{x}+\lambda\hat{\mathbf{v}})\,q(\mathbf{x}+\lambda\hat{\mathbf{v}},\hat{\mathbf{v}})d\lambda\,.$$

The macroscopic velocity is here given by

$$\mathbf{U}_T(\mathbf{x}) = c(\mathbf{x})\,\bar{U}\int_{\mathbb{S}^{d-1}}\hat{\mathbf{v}}\int_{\mathbb{R}_+}\gamma(\lambda)\mathcal{S}(\mathbf{x}+\lambda\hat{\mathbf{v}})\,q(\mathbf{x}+\lambda\hat{\mathbf{v}},\hat{\mathbf{v}})d\lambda\,d\hat{\mathbf{v}}\,. \tag{6.25}$$

The macroscopic limits can be performed as in the previous section and the choice of the parameter ε will be the same for the cases $i)-iv)$, since it does not depend on the type of model (independent or dependent sensing), but only on $\eta_{\mathcal{S}}$ and η_q.

Case i)

In this case, we cannot consider the expansions (6.7) and (6.8), and, thus, we cannot expand the turning kernel, whose nonvanishing average is given by (6.25). Therefore, we perform a hyperbolic limit leading to an equation analogous to (6.16) with macroscopic velocity (6.25).

Case ii)

When the maximum sensing radius R is smaller than both characteristic lengths, we may consider the positive expansions (6.7) and (6.8) and substitute them in (6.13). Neglecting the higher order terms in λ, we get the approximation

$$T[q,\mathcal{S}](\mathbf{x},\sigma,\hat{\mathbf{v}}) = c(\mathbf{x})\,\psi(\sigma)\Big[\mathcal{S}(\mathbf{x})\,\Gamma_0\,q(\mathbf{x},\hat{\mathbf{v}}) + \mathcal{S}(\mathbf{x})\,\Gamma_1\,\nabla q\cdot\hat{\mathbf{v}} + \Gamma_1\,q(\mathbf{x},\hat{\mathbf{v}})\,\nabla\mathcal{S}\cdot\hat{\mathbf{v}}\Big]$$

with

$$c(\mathbf{x}) = \frac{1}{\mathcal{S}(\mathbf{x})\,\Gamma_0}$$

and

$$\Gamma_i := \int_0^R \lambda^i\gamma(\lambda)\,d\lambda\,, \qquad i = 0,1\,.$$

Re-scaling the space variable as in (3.6), we find

$$T_0[q,\mathcal{S}](\boldsymbol{\xi},v,\hat{\mathbf{v}}) = q(\boldsymbol{\xi},\hat{\mathbf{v}})\psi(\sigma)$$

and

$$T_1[q,\mathcal{S}](\boldsymbol{\xi},\sigma,\hat{\mathbf{v}}) = \Gamma\,\psi(\sigma)\Big[\nabla q\cdot\hat{\mathbf{v}} + q(\boldsymbol{\xi},\hat{\mathbf{v}})\,\frac{\nabla\mathcal{S}}{\mathcal{S}}\cdot\hat{\mathbf{v}}\Big]$$

with

$$\Gamma := \frac{\Gamma_1}{\Gamma_0}.$$

Therefore, $\mathbf{U}_T^0(\boldsymbol{\xi}) = 0$ because of (6.1), and we can perform a diffusive scaling that leads to the zero-order macroscopic tensor

$$\mathbf{D}_T^0(\boldsymbol{\xi}) = D\,\mathbb{V}_q(\boldsymbol{\xi})\,,$$

and to the macroscopic first-order velocity

$$\mathbf{U}_T^1(\boldsymbol{\xi}) = \bar{U}\,\Gamma\,\nabla\cdot\mathbb{V}_q(\boldsymbol{\xi}) + \bar{U}\,\Gamma\,\mathbb{V}_q(\boldsymbol{\xi})\,\frac{\nabla\mathcal{S}}{\mathcal{S}}\,. \tag{6.26}$$

The macroscopic advection-diffusion equation reads (dropping the dependencies)

$$\frac{\partial}{\partial\tau}n + \nabla\cdot\left[\chi\left(\nabla\cdot\mathbb{V}_q + \mathbb{V}_q\frac{\nabla\mathcal{S}}{\mathcal{S}}\right)n\right] = \nabla\cdot\left[\frac{1}{\mu}\nabla\cdot\left(D\,\mathbb{V}_q\,n\right)\right]$$

where

$$\chi := \bar{U}\Gamma\,.$$

Here, we can make observations about the macroscopic model similar to those discussed in case ii) of the non-local independent sensing model. The only difference is that, in this non-local dependent sensing model, there is only one sensitivity χ that weights the two contributions equally in the drift term (6.26).

Case *iii*)

In this case, we expand only the chemoattractant $\mathcal{S}(\mathbf{x}+\lambda\hat{\mathbf{v}})$, as defined in (6.7), so that the turning kernel (6.13) can be approximated as

$$T[q,\mathcal{S}](\mathbf{x},\sigma,\hat{\mathbf{v}}) = \psi(\sigma)\Big[c_0(\mathbf{x})\,\mathcal{S}(\mathbf{x})\int_{\mathbb{R}_+}\gamma(\lambda)q(\mathbf{x}+\lambda\hat{\mathbf{v}},\hat{\mathbf{v}})\,d\lambda \\ + c_1(\mathbf{x})\,(\nabla\mathcal{S}\cdot\hat{\mathbf{v}})\int_{\mathbb{R}_+}\lambda\,\gamma(\lambda)q(\mathbf{x}+\lambda\hat{\mathbf{v}},\hat{\mathbf{v}})\,d\lambda\Big]$$

with

$$c_0(\mathbf{x}) := \left(2\int_{\mathbb{S}^{d-1}}\mathcal{S}(\mathbf{x})\int_{\mathbb{R}_+}\gamma(\lambda)q(\mathbf{x}+\lambda\hat{\mathbf{v}},\hat{\mathbf{v}})\,d\lambda\,d\hat{\mathbf{v}}\right)^{-1}$$

and

$$c_1(\mathbf{x}) := \left(2\int_{\mathbb{S}^{d-1}}(\nabla\mathcal{S}\cdot\hat{\mathbf{v}})\int_{\mathbb{R}_+}\lambda\gamma(\lambda)q(\mathbf{x}+\lambda\hat{\mathbf{v}},\hat{\mathbf{v}})\,d\lambda\,d\hat{\mathbf{v}}\right)^{-1},$$

both different from zero. Re-scaling the space variable as in (3.6), we find $T[q,\mathcal{S}] = T_0[q,\mathcal{S}]$. Hence, in this case, $\mathbf{U}^0_T(\boldsymbol{\xi})$ does not vanish in Ω, as it is given by

$$\begin{aligned}\mathbf{U}^0_T(\boldsymbol{\xi}) &= c_0(\boldsymbol{\xi})\,\bar{U}\,\mathcal{S}(\boldsymbol{\xi})\int_{\mathbb{R}_+}\gamma(\lambda)\int_{\mathbb{S}^{d-1}}\hat{\mathbf{v}}\,q(\boldsymbol{\xi}+\lambda\hat{\mathbf{v}},\hat{\mathbf{v}})\,d\hat{\mathbf{v}}\,d\lambda \\ &\quad + c_1(\boldsymbol{\xi})\,\bar{U}\,\nabla\mathcal{S}\int_{\mathbb{R}_+}\lambda\,\gamma(\lambda)\int_{\mathbb{S}^{d-1}}\hat{\mathbf{v}}\otimes\hat{\mathbf{v}}\,q(\boldsymbol{\xi}+\lambda\hat{\mathbf{v}},\hat{\mathbf{v}})\,d\hat{\mathbf{v}}\,d\lambda, \\ &= c_0(\boldsymbol{\xi})\,\bar{U}\,\Gamma_0\,\mathcal{S}(\boldsymbol{\xi})\,\bar{\mathbf{E}}^0_q(\boldsymbol{\xi}) + c_1(\boldsymbol{\xi})\,\bar{U}\,\Gamma_0\,\nabla\mathcal{S}\,\bar{\mathbb{V}}^1_q(\boldsymbol{\xi})\,.\end{aligned} \tag{6.27}$$

where we defined

$$\bar{\mathbb{V}}^1_q(\boldsymbol{\xi}) = \frac{1}{\Gamma_0}\int_{\mathbb{R}_+}\lambda\,\mathbb{V}^\lambda_q(\boldsymbol{\xi})\,\gamma(\lambda)d\lambda$$

as an average of the weighted diffusion tensor of the fibers in the whole neighborhood sensed by the cells, differently form the case *iii*) of the non-local independent model. Therefore, the macroscopic advection equation has an expression analogous to (6.16) with macroscopic velocity (6.27).

Case *iv*)

In this case, again, we can only consider the positive approximation (6.8), and the transition probability rewrites as

$$T[q,\mathcal{S}](\mathbf{x},\sigma,\hat{\mathbf{v}}) = \psi(\sigma)\left[c_0(\mathbf{x})q(\mathbf{x},\hat{\mathbf{v}})\int_{\mathbb{R}_+}\gamma(\lambda)\,\mathcal{S}(\mathbf{x}+\lambda\hat{\mathbf{v}})\,d\lambda \right. \\ \left. + c_1(\mathbf{x})\nabla q\cdot\hat{\mathbf{v}}\int_{\mathbb{R}_+}\lambda\,\gamma(\lambda)\,\mathcal{S}(\mathbf{x}+\lambda\hat{\mathbf{v}})\,d\lambda\right] \tag{6.28}$$

where

$$c_0(\mathbf{x}) := \left(2\int_{\mathbb{S}^{d-1}}q(\mathbf{x},\hat{\mathbf{v}})\int_{\mathbb{R}_+}\gamma(\lambda)\mathcal{S}(\mathbf{x}+\lambda\hat{\mathbf{v}})\,d\lambda\,d\hat{\mathbf{v}}\right)^{-1}$$

and

$$c_1(\mathbf{x}) := \left(2\int_{\mathbb{S}^{d-1}}(\nabla q\cdot\hat{\mathbf{v}})\int_{\mathbb{R}_+}\lambda\,\gamma(\lambda)\mathcal{S}(\mathbf{x}+\lambda\hat{\mathbf{v}})\,d\lambda\,d\hat{\mathbf{v}}\right)^{-1},$$

both different from zero. As before, by re-scaling (6.28) with (3.6), we get $T[q,\mathcal{S}] = T_0[q,\mathcal{S}]$ and we have that the average velocity $\mathbf{U}_T^0 = \mathbf{U}_T \neq 0$. In the specific, the average velocity is given by

$$\begin{aligned}\mathbf{U}_T(\boldsymbol{\xi}) = {} & c_0(\boldsymbol{\xi})\,\bar{U}\int_{\mathbb{S}^{d-1}}\hat{\mathbf{v}}\,q(\boldsymbol{\xi},\hat{\mathbf{v}})\int_{\mathbb{R}_+}\gamma(\lambda)\,\mathcal{S}(\boldsymbol{\xi}+\lambda\hat{\mathbf{v}})\,d\lambda\,d\hat{\mathbf{v}}\\ & + c_1(\boldsymbol{\xi})\,\bar{U}\int_{\mathbb{S}^{d-1}}\hat{\mathbf{v}}\otimes\hat{\mathbf{v}}\,\nabla q(\boldsymbol{\xi},\hat{\mathbf{v}})\int_{\mathbb{R}_+}\lambda\,\gamma(\lambda)\mathcal{S}(\boldsymbol{\xi}+\lambda\hat{\mathbf{v}})\,d\lambda\,d\hat{\mathbf{v}}\end{aligned} \tag{6.29}$$

and, thus, we perform a hyperbolic limit leading to (6.16) with mean velocity (6.29). The mean velocity is a linear combination of a non-local measure of the chemoattractant $\mathcal{S}$ over the fibers network and a non-local average of $\mathcal{S}$ weighted by the directional average of the spatial variability of the fiber direction.

We summarize the macroscopic equations for the two sensing strategies in the four cases in Table 6.1.

Case	Non-local independent sensing (6.2)-(6.3) with (6.12)	Non-local dependent sensing (6.2)-(6.3) with (6.13)
i)	drift dominated $\mathbf{U}_T = c\bar{U}\int_{\mathbb{S}^{d-1}}\hat{\mathbf{v}}\int_0^R \gamma_{\mathcal{S}}(\lambda)\mathcal{S}(\boldsymbol{\xi}+\lambda\hat{\mathbf{v}})d\lambda\int_0^R \gamma_q(\lambda)\,q(\boldsymbol{\xi}+\lambda\hat{\mathbf{v}},\hat{\mathbf{v}})d\lambda d\hat{\mathbf{v}}$	drift dominated $\mathbf{U}_T = c\bar{U}\int_{\mathbb{S}^{d-1}}\hat{\mathbf{v}}\int_0^R \gamma(\lambda)\mathcal{S}(\boldsymbol{\xi}+\lambda\hat{\mathbf{v}})q(\boldsymbol{\xi}+\lambda\hat{\mathbf{v}},\hat{\mathbf{v}})d\lambda\, d\hat{\mathbf{v}}$
ii)	drift-diffusion $\mathbf{D}_T^0 = D\,\mathbb{V}_q$ $\mathbf{U}_T^1 = \bar{U}\left[\Gamma^q\nabla\cdot\mathbb{V}_q + \Gamma^{\mathcal{S}}\mathbb{V}_q\dfrac{\nabla\mathcal{S}}{\mathcal{S}}\right]$	drift-diffusion $\mathbf{D}_T^0 = D\,\mathbb{V}_q$ $\mathbf{U}_T^1 = \bar{U}\Gamma\left[\nabla\cdot\mathbb{V}_q + \mathbb{V}_q\dfrac{\nabla\mathcal{S}}{\mathcal{S}}\right]$
iii)	drift dominated $\mathbf{U}_T := c_0\,\bar{U}\,\Gamma_0^q\,\Gamma_0^{\mathcal{S}}\,\mathcal{S}\,\bar{\mathbf{E}}_q^0 + c_1\,\bar{U}\,\Gamma_0^q\,\Gamma_1^{\mathcal{S}}\,\nabla\mathcal{S}\,\bar{\mathbb{V}}_q^0$	drift dominated $\mathbf{U}_T := c_0\,\bar{U}\,\Gamma_0\,\mathcal{S}\,\bar{\mathbf{E}}_q^0 + c_1\,\bar{U}\,\Gamma_0\,\nabla\mathcal{S}\,\bar{\mathbb{V}}_q^1$
iv)	drift dominated $\mathbf{U}_T = c_0\,\bar{U}\,\Gamma_0^q\int_{\mathbb{S}^{d-1}}\hat{\mathbf{v}}\,q\int_0^R\gamma_{\mathcal{S}}(\lambda)\,\mathcal{S}(\boldsymbol{\xi}+\lambda\hat{\mathbf{v}})\,d\lambda\,d\hat{\mathbf{v}}$ $+c_1\,\bar{U}\,\Gamma_1^q\int_{\mathbb{S}^{d-1}}\hat{\mathbf{v}}\otimes\hat{\mathbf{v}}\,\nabla q\int_0^R\gamma_{\mathcal{S}}(\lambda)\,\mathcal{S}(\boldsymbol{\xi}+\lambda\hat{\mathbf{v}})\,d\lambda\,d\hat{\mathbf{v}}$	drift dominated $\mathbf{U}_T = c_0\,\bar{U}\int_{\mathbb{S}^{d-1}}\hat{\mathbf{v}}\,q\int_0^R\gamma(\lambda)\,\mathcal{S}(\boldsymbol{\xi}+\lambda\hat{\mathbf{v}})\,d\lambda\,d\hat{\mathbf{v}}$ $+c_1\,\bar{U}\int_{\mathbb{S}^{d-1}}\hat{\mathbf{v}}\otimes\hat{\mathbf{v}}\,\nabla q\int_0^R\lambda\,\gamma(\lambda)\mathcal{S}(\boldsymbol{\xi}+\lambda\hat{\mathbf{v}})\,d\lambda\,d\hat{\mathbf{v}}$

TABLE 6.1: **Summary of the derived models.** We report the average velocity and the zero-order macroscopic tensor for the non-local independent and dependent sensing models for cases *i*)-*iv*). The local dependencies in $\boldsymbol{\xi}$ was dropped.

Remark 6.3. We can observe that, if $\gamma_q = \gamma_s = \gamma = \delta(\lambda - R)$, the two non-local transport models for independent and dependent sensing are the same, while, if the sensing kernels are not Dirac deltas (even if $\gamma_q = \gamma_s = \gamma$), the transport models are always different. At the macroscopic level, with any choice of the sensing functions the models coincide only in case *ii*). In this case, the macroscopic limits are different only if $\gamma_q \neq \gamma_s$, while in the cases *iii*) and *iv*) they are different if the sensing kernels are not Dirac deltas (even if $\gamma_s = \gamma_q = \gamma$). The relevant difference concerns the macroscopic transport velocities (see (6.22) and (6.27) for the case *iii*), and (6.24) and (6.29) for the case *iv*)). In fact, in the cases *iii*) and *iv*), for the non-local dependent sensing model, as only one cue is considered non-locally and both cues are averaged with the same sensing function γ, we have a weighted average on λ of the non-local quantities, which results in the weighted averages in the second terms of (6.27) and (6.29). These results are summarized in Table 6.2.

	$\gamma_q = \gamma_s = \gamma = \delta$	$\gamma_q = \gamma_s = \gamma \neq \delta$	$\gamma_q \neq \gamma_s$
Meso models (6.2)-(6.3) with (6.12) or (6.13)	✓	✗	✗
Macro models case *i*)	✓	✗	✗
Macro models case *ii*)	✓	✓	✗
Macro models case *iii*)	✓	✗	✗
Macro models case *iv*)	✓	✗	✗

TABLE 6.2: **Summary of the comparison between the models for different choices of the sensing functions.** The symbol ✓ indicates the cases in which the models coincide, while the symbol ✗ the ones in which the models are different.

6.4 *Numerical tests*

On the basis of the models derived in the previous sections and summarized in Table 6.1, we propose here two-dimensional numerical simulations to illustrate the behavior of the kinetic transport models for non-local independent sensing and non-local dependent sensing, i.e., (6.2)-(6.3) with (6.12) or (6.13). In contrast to the previous chapters, we here integrate numerically the transport equation, in line with [173] and, then, we compute the macroscopic density (6.4).

Concerning the ***boundary conditions***, since we are going to consider 2D bounded domains without loss of cells and no cells coming in, we assume conservation of mass. Therefore, we choose no-flux boundary conditions:

$$\int_{\mathbb{S}^{d-1}} \int_0^U \rho(t, \mathbf{x}, \sigma, \hat{\mathbf{v}}) \hat{\mathbf{v}} \cdot \mathbf{n}(\mathbf{x}) \, d\sigma \, d\hat{\mathbf{v}} = 0, \quad \forall \mathbf{x} \in \partial\Omega, \quad t > 0,$$

where $\mathbf{n}(\mathbf{x})$ is the outward normal to the boundary $\partial\Omega$ in point $\mathbf{x}$. This class of boundary conditions is part of the wider class of non-absorbing boundary conditions. Precisely, in this analysis, we consider specular reflection boundary conditions, i.e.,

$$\rho(t, \mathbf{x}, \sigma', \hat{\mathbf{v}}') = \rho\left(t, \mathbf{x}, \sigma, \frac{\hat{\mathbf{v}} - 2(\hat{\mathbf{v}} \cdot \mathbf{n})\mathbf{n}}{|\hat{\mathbf{v}} - 2(\hat{\mathbf{v}} \cdot \mathbf{n})\mathbf{n}|}\right), \qquad \mathbf{n} \cdot \hat{\mathbf{v}} \leq 0,$$

that means that cells are reflected with an angle of $\pi/2$ when they reach the domain boundary.

With respect to the ***fibers network***, we decide here to rely on the von Mises distribution described in detail in Section 2.3.2. In fact, its expression with the concentration coefficient $k(\mathbf{x})$ allows us to perform simulations for several different scenarios and compare them. We recall the expression of q in its bimodal version, since we are dealing with cell migrating on a non-polarized network of fibers (see assumption Q3 in Section 6.1)

$$q\left(\mathbf{x}, \hat{\mathbf{v}}\right) = \frac{1}{4\pi I_0(k(\mathbf{x}))} \left(e^{k(\mathbf{x})\,\mathbf{u}(\mathbf{x})\cdot\hat{\mathbf{v}}} + e^{-k(\mathbf{x})\,\mathbf{u}(\mathbf{x})\cdot\hat{\mathbf{v}}}\right), \tag{6.30}$$

where $I_\nu(k)$ is the modified Bessel function of first kind of order ν and

$$\mathbf{u}(\mathbf{x}) := (\cos(\theta_q(\mathbf{x})), \sin(\theta_q(\mathbf{x}))) \tag{6.31}$$

where $\theta_q(\mathbf{x})$ is the mean direction, belonging to the interval $[0, 2\pi)$, of the fibers located at point $\mathbf{x}$. Moreover, its variance can be calculated as in [118] and it reads

$$\mathbb{V}_q(\mathbf{x}) = \frac{1}{2}\left(1 - \frac{I_2(k)}{I_0(k)}\right)\mathbb{I}_2 + \frac{I_2(k)}{I_0(k)}\mathbf{u}\otimes\mathbf{u},$$

where $\mathbb{I}_2$ is the identity matrix in $\mathbb{R}^{2\times 2}$, while k and $\mathbf{u}$ are functions of $\mathbf{x}$. Moreover, the variance in $[0, 2\pi)$ is the scalar

$$D_q(\mathbf{x}) = \frac{1}{2}\int_0^{2\pi} q(\theta - \theta_q)^2\, d\theta = \left(1 - \frac{I_1(k)}{I_0(k)}\right)$$

that represents the degree of alignment of the fibers at point $\mathbf{x}$.

We perform four different sets of numerical tests on the bounded domain $\Omega = [0, 5]^2$.

Test 1. We present the case in which the sensing of the tissue architecture, described by q, is local, showing only the effect of having two directional cues driving cell polarization.

Test 2. We consider non-local sensing of both cues and we compare the non-local independent sensing model and the non-local dependent sensing model for different expressions of the sensing functions γ_S and γ_q.

Test 3. We consider the non-local independent sensing model and we perform a comparison of the macroscopic behaviors of the cells in the cases *i*)-*iv*), i.e., depending on the relation between R, l_S, and l_q.

Test 4. Still considering the non-local independent sensing model, we divided the computational domain Ω into several regions, each of them characterized by a different average direction of the fibers, and we analyze the overall cell behavior.

6.4.1 Test 1: local ECM sensing and non-local chemotaxis

As a first test, we present the particular case in which the sensing of q is local. This case illustrates the effect of a second directional cue when dealing with a cell population migrating by contact guidance and evaluating the local alignment of the fibers over a non-polarized network. Formally, we are dealing with (6.12) with $\gamma_q = \delta(\lambda - 0)$. We

consider the region

$$\Omega_q = \{\mathbf{x} = (x, y) \in \Omega \quad s.t. \quad x_1 \leq x \leq x_2\}$$

with $x_1 = 1.8$ and $x_2 = 3.2$ in which the fibers are strongly aligned along the direction identified by $\theta_q = \pi/2$. In particular, for $(x, y) \in \Omega_q$ we set $k(x, y) = 700$, such that $D_q = 5 \cdot 10^{-3}$. In the rest of the computational domain $\Omega - \Omega_q$ fibers are uniformly distributed. The chemoattractant has a Gaussian profile

$$\mathcal{S}(x, y) = \frac{m_{\mathcal{S}}}{\sqrt{2\pi\sigma_{\mathcal{S}}^2}} e^{-\frac{(x-x_{\mathcal{S}})^2+(y-y_{\mathcal{S}})^2}{2\sigma_{\mathcal{S}}^2}}. \tag{6.32}$$

In the simulations shown in Figure 6.1, we choose $(x_{\mathcal{S}}, y_{\mathcal{S}}) = (4, 4)$, $m_{\mathcal{S}} = 10, \sigma_{\mathcal{S}}^2 = 0.1$. The initial condition for the cell population is also a Gaussian

$$\rho_0(x, y) = r_0 e^{-\frac{(x-x_0)^2+(y-y_0)^2}{2\sigma_0^2}} \tag{6.33}$$

with $r_0 = 0.1$ and $\sigma_0^2 = 0.1$. In this first test, the initial condition for the cell population is centered in $(x_0, y_0) = (2.5, 2.5)$, i.e., the center of the region Ω_q, as shown in Figure 6.1(a), and we set $R = 0.5$. The dynamics of the cell population is shown in Figure 6.1, together with the evolution of cell polarization and the trajectory of the center of mass.

Without chemoattractant, because of the presence of highly aligned fibers, we would expect that cells diffuse anisotropically in the preferential direction of the fibers (i.e., $\pm\pi/2$), forming the well-known ellipsis [214], which represents cells moving with the same probability along direction $\pi/2$ and $-\pi/2$. Here, due to the presence of a chemoattractant, the symmetry is broken, and, even if q describes a non-polarized fiber network, there is a preferential sense of motion (see Figures 6.1(d)-6.1(f)). Precisely, cells migrate along the fibers in the direction identified by $\theta_q = \pi/2$, corresponding to the preferential sense imposed by the presence of the chemoattractant in the upper-right corner of the domain Ω. Given this directional setting, the cell population dynamics is also greatly affected by the strength of the chemoattractant, which depends on $m_{\mathcal{S}}$ and $\sigma_{\mathcal{S}}^2$, the degree of the alignment D_q, which depends on $k(x, y)$, and by the sensing radius R. Another important aspect is the sensing function γ_s, which influences the transient dynamics and, especially, the relaxation time. This relaxation time appears to be double in the case of a Heaviside function since the kernel γ_s doubles when computed with a Heaviside function instead of a Dirac delta (see [173] for more details). We also analyzed the ***average polarization*** of the cells at every position $\mathbf{x}$ in Figures 6.1(b) and 6.1(g)-6.1(i), which is given by the momentum

$$n(t, \mathbf{x})\mathbf{U}(t, \mathbf{x}) = \int_{\mathbb{S}^{d-1}} \int_0^U \mathbf{v}\, \rho(t, \mathbf{x}, \sigma, \hat{\mathbf{v}})\, d\sigma\, d\hat{\mathbf{v}}\,.$$

The microscopic directions of cells are initially randomly distributed and they start from a vanishing initial speed, as shown in Figure 6.1(b). Then, they start to align along the fibers and to migrate in the direction identified by the mean direction $\theta_q(\mathbf{x}) = \pi/2$, since cells sense the chemoattractant (see Figures 6.1(g)-6.1(h)). Eventually when cells reach the position identified by $y = 4$, the microscopic directions polarize towards the chemoattractant (see Figure 6.1(i)). The ***center of mass*** plotted in Figure 6.1(c) stays in the region Ω_q during the migration of cells along the fibers bundle in Ω_q, and this center moves out of Ω_q only when it reaches the position identified by

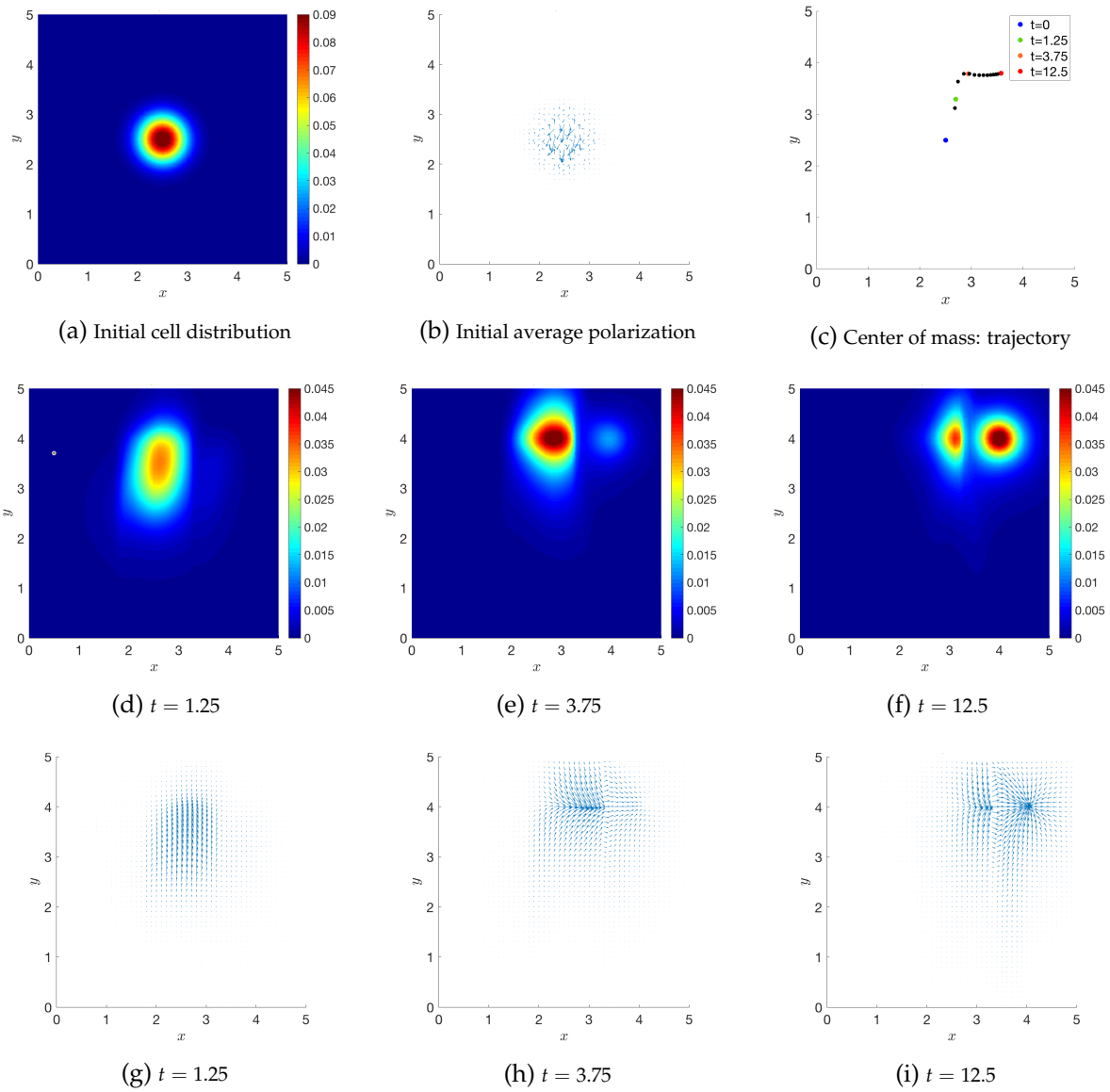

(a) Initial cell distribution (b) Initial average polarization (c) Center of mass: trajectory

(d) $t = 1.25$ (e) $t = 3.75$ (f) $t = 12.5$

(g) $t = 1.25$ (h) $t = 3.75$ (i) $t = 12.5$

FIGURE 6.1: **Test 1.** Evolution of the initial distribution given in (a) for the case of local q and non-local chemoattractant $\mathcal{S}$ with sensing function $\gamma_S = \delta(\lambda - R)$. The chemoattractant is a Gaussian centered in $(4, 4)$, with $m_S = 10$ and $\sigma_S^2 = 0.1$. The sensing radius of the cells is set to $R = 0.5$. (b): the initial average polarization of the cells. (c): trajectory of the center of mass of the cell population, where each black dot is plotted every $\Delta t = 1$. (d)-(f): evolution of the macroscopic density. (g)-(i): evolution of the polarizations of the cells.

$y = 4$. The black dots are plotted every $\Delta t = 1$ and it is clear that the highest acceleration happens when cells are on the bundle of fibers, while they are slowed down when they start to move out of the fibers stripe Ω_q.

6.4.2 Test 2: non-local ECM sensing and chemotaxis

As a second test, we present both the non-local independent sensing model and the non-local dependent sensing model. Differently from the previous test, we now consider a non-local sensing of the distribution of fibers. We assume fibers distributed similarly to the previous test, i.e., the fibers are highly aligned in the region Ω_q characterized by $x_1 = 2.1$ and $x_2 = 2.9$ and illustrated in Figure 6.2(b). Here, for $(x, y) \in \Omega_q$, we set $k(x, y) = 100$, which corresponds to $D_q = 0.0025$, and $\theta_q(x, y) = \pi/2$. In the

region $\Omega - \Omega_q$ fibers are uniformly distributed. The initial condition of the cell population is (6.33) with $r_0 = 0.1$, $\sigma_0^2 = 0.1$, and centered in $(x_0, y_0) = (1, 0.5)$, as shown in Figure 6.2(a), while the chemoattractant is located as in Test 1, with $m_S = 10$ and $\sigma_S^2 = 0.05$. We compare the dynamics of the cells in four settings:

1. local fiber distribution and non-local chemoattractant, as in Test 1, i.e., (6.12) with $\gamma_q = \delta(\lambda - 0)$ and $\gamma_S = \delta(\lambda - R)$;
2. non-local sensing with a Dirac delta for both q and S; this corresponds to both (6.12) and (6.13) with $\gamma_q = \gamma_S = \gamma = \delta(\lambda - R)$;
3. non-local independent sensing with Heaviside sensing functions for both S and q, i.e., (6.12) with $\gamma_q = \gamma_S = H(R - \lambda)$;
4. non-local dependent sensing for q and S, dealing with (6.13) and $\gamma = H(R - \lambda)$.

The results of the simulations for setting 1-4 are shown in Figure 6.2.

We can observe that, in the 1-4 settings, cells start from $(1, 0.5)$, they are attracted by the chemoattractant and, on their way towards S, they cross the aligned fibers region Ω_q and climb up this region in the direction $\pi/2$. Eventually, in all the cases, cells reach the chemoattractant, but the dynamics, as well as the transient time, are influenced by the different sensing kernels, even though the differences are not extremely appreciable, and by the local or non-local sensing strategy. Although settings 3 and 4 in Figure 6.2, which are related to the case of independent and dependent cues, respectively, do not show very strong differences, in setting 3 (see Figures 6.2(k)-6.2(n)) the tendency of moving in both the directions $\pi/2$, determined by the fibers, and $\pi/4$, determined by the chemoattractant, appears more evident because of the independent sensing. This behavior is the least evident when cells deal with a local sensing of the fibers (setting 1), resulting also in a general slow down of the dynamics.

6.4.3 Test 3: comparison of the cases $i) - iv)$

In this section, we present a comparison of the macroscopic behaviors of the cells depending on the relation between the parameters R, l_S and l_q, which define the differences between the models obtained in the cases $i)$, $ii)$, $iii)$ and $iv)$. For this comparison we consider the non-local independent sensing model (6.2)-(6.3) with (6.12) and we choose $\gamma_q = \gamma_S = H(R - \lambda)$, as this is the case in which the transport model is different from the dependent sensing model. We simulate the independent-case model because the independence of the two sensings allows to visualize more efficiently the two distinct directional effects (contact guidance and chemotaxis), as we observed with the comparison performed with the **Test 2**.

The initial distribution of cells for all the tests presented in Figures 6.4-6.8 is given by (6.33) with $(x_0, y_0) = (1.5, 1.5)$, $r_0 = 0.1$, and $\sigma_0^2 = 0.1$. The chemoattractant profile is given by (6.32) with $(x_S, y_S) = (4.5, 4.5)$ and $m_S = 10$. In the simulations, we consider three different values for the variance of the chemoattractant σ_S^2 in order to obtain different values of l_S. We choose $\sigma_S^2 = 0.05$ that corresponds to $l_S = 0.002$ in Figure 6.3(a), $\sigma_S^2 = 0.25$ that corresponds to $l_S = 0.055$ in Figure 6.3(b) and $\sigma_S^2 = 1.8$ corresponding to $l_S = 0.25$ in Figure 6.3(c). In order to have a direct control on the strength of fiber alignment and to modulate its relation to the other parameters, we consider the turning kernel describing contact guidance lead by q with mean direction $\theta_q = 3\pi/4$ and the coefficient function $k(x, y)$ given by a Gaussian distribution as

$$k(x, y) = m_k e^{-\frac{(x - x_k)^2 + (y - y_k)^2}{2\sigma_k^2}}. \tag{6.34}$$

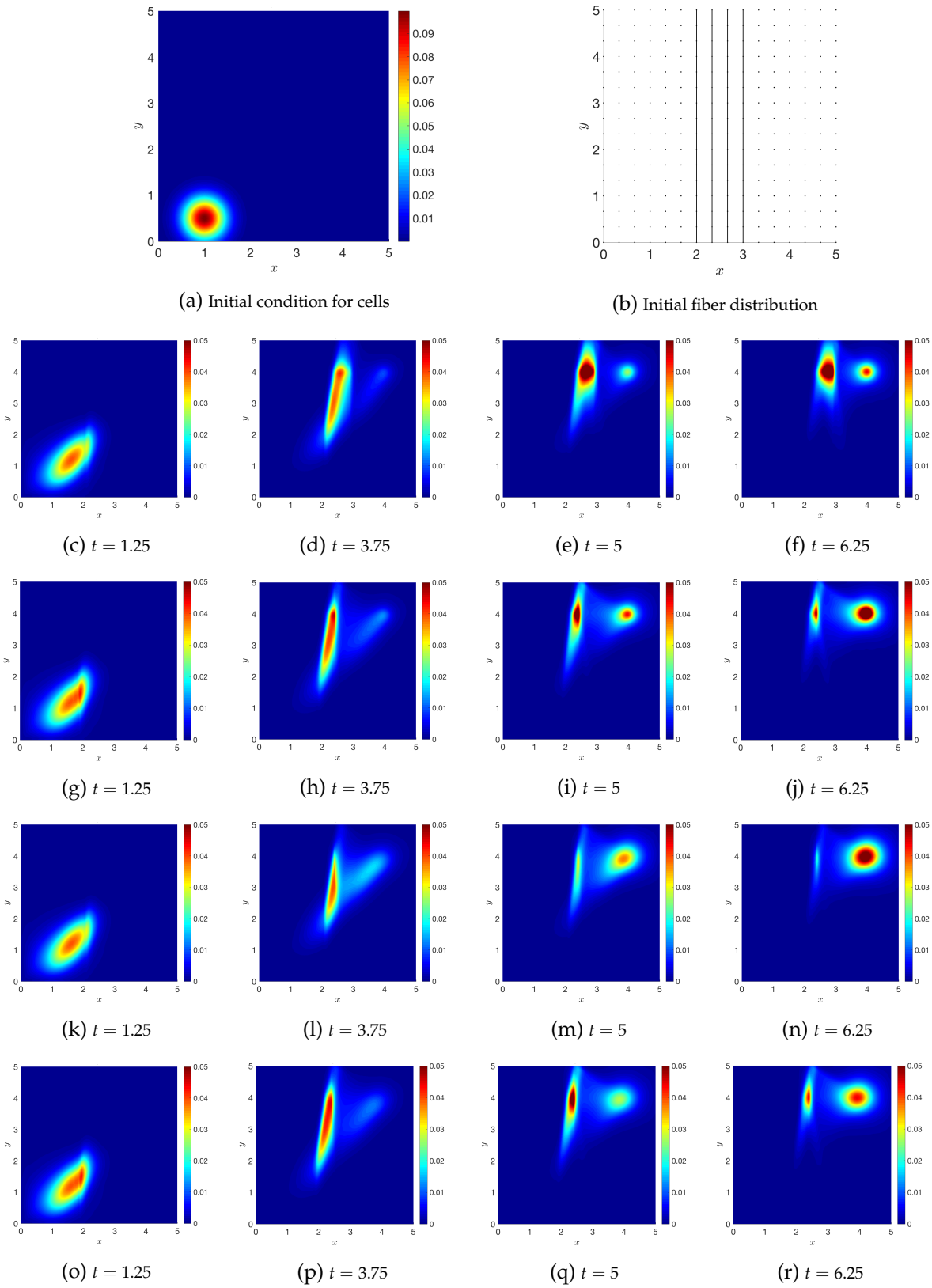

(a) Initial condition for cells

(b) Initial fiber distribution

(c) $t = 1.25$ (d) $t = 3.75$ (e) $t = 5$ (f) $t = 6.25$

(g) $t = 1.25$ (h) $t = 3.75$ (i) $t = 5$ (j) $t = 6.25$

(k) $t = 1.25$ (l) $t = 3.75$ (m) $t = 5$ (n) $t = 6.25$

(o) $t = 1.25$ (p) $t = 3.75$ (q) $t = 5$ (r) $t = 6.25$

FIGURE 6.2: **Test 2.** Time evolution of the initial distribution given in 6.2(a) in the settings 1-4. The sensing radius of the cells is $R = 0.5$ and the chemoattractant is defined in (6.32) with $m_{\mathcal{S}} = 10, \sigma^2_{\mathcal{S}} = 0.05$ and $(x_{\mathcal{S}}, y_{\mathcal{S}}) = (4,4)$. Setting 1 is represented in Figures (c)-(f): local q and non-local chemoattractant, $\gamma_{\mathcal{S}} = \delta(\lambda - R)$. Setting 2 is represented in Figures (g)-(j): non-local q and $\mathcal{S}$ with sensing functions $\gamma_q = \gamma_{\mathcal{S}} = \delta(\lambda - R)$. Setting 3 is represented in Figures (k)-(n): non-local q and $\mathcal{S}$, independent sensing with $\gamma_q = \gamma_{\mathcal{S}} = H(R - \lambda)$. Setting 4 is represented in Figures (o)-(r): non-local q and $\mathcal{S}$, dependent sensing with $\gamma = H(R - \lambda)$.

Here, we choose $(x_k, y_k) = (2.5, 2.5)$ and $\sigma_k^2 = 0.15$. The function $k(x, y)$ driving the strength of the alignment is represented in Figure 6.3(d). This function mimics the situation of fibers more aligned in the central circular region and uniformly disposed in the rest of the domain. Besides, we consider different values of m_k in order to obtain different values of l_q: $m_k = 10$ corresponds to $l_q \approx 0.031$ and $m_k = 100$ corresponds to $l_q \approx 0.0031$. We derive the estimation for the range of variability of the characteristic length l_q of the corresponding bimodal Von Mises Fisher q (given in (6.30)) in the case of a general concentration function $k(\mathbf{x}) \in \mathcal{C}^1(\Omega)$. Details are provided in the following observation.

Observation 6.1. Estimation of l_q
We recall the definition of the characteristic length l_q:

$$l_q := \frac{1}{\max\limits_{\mathbf{x}\in\Omega} \max\limits_{\hat{\mathbf{v}}\in\mathbb{S}^{d-1}} \frac{|\nabla q(\mathbf{x},\hat{\mathbf{v}})\cdot\hat{\mathbf{v}}|}{q(\mathbf{x},\hat{\mathbf{v}})}}\,.$$

Since $\frac{\partial I_0}{\partial k} = \frac{I_1(k)}{I_0(k)}$, we have that

$$\begin{aligned}
\nabla q &= \nabla\left(\frac{1}{4\pi I_0(k(\mathbf{x}))}\right)\left(e^{k(\mathbf{x})\,\mathbf{u}\cdot\hat{\mathbf{v}}} + e^{-k(\mathbf{x})\,\mathbf{u}\cdot\hat{\mathbf{v}}}\right) + \frac{1}{4\pi I_0(k(\mathbf{x}))}\nabla\left(e^{k(\mathbf{x})\,\mathbf{u}\cdot\hat{\mathbf{v}}} + e^{-k(\mathbf{x})\,\mathbf{u}\cdot\hat{\mathbf{v}}}\right)\\
&= \frac{e^{k(\mathbf{x})\,\mathbf{u}\cdot\hat{\mathbf{v}}} - e^{-k(\mathbf{x})\,\mathbf{u}\cdot\hat{\mathbf{v}}}}{4\pi I_0(k(\mathbf{x}))}\nabla k\,(\mathbf{u}\cdot\hat{\mathbf{v}}) - \frac{e^{k(\mathbf{x})\,\mathbf{u}\cdot\hat{\mathbf{v}}} + e^{-k(\mathbf{x})\,\mathbf{u}\cdot\hat{\mathbf{v}}}}{4\pi I_0^2(k(\mathbf{x}))}\frac{\partial I_0}{\partial k}\nabla k\\
&= \frac{e^{k(\mathbf{x})\,\mathbf{u}\cdot\hat{\mathbf{v}}} - e^{-k(\mathbf{x})\,\mathbf{u}\cdot\hat{\mathbf{v}}}}{4\pi I_0(k(\mathbf{x}))}\nabla k\,(\mathbf{u}\cdot\hat{\mathbf{v}}) - \frac{e^{k(\mathbf{x})\,\mathbf{u}\cdot\hat{\mathbf{v}}} + e^{-k(\mathbf{x})\,\mathbf{u}\cdot\hat{\mathbf{v}}}}{4\pi I_0(k(\mathbf{x}))}\frac{I_1(k(\mathbf{x}))}{I_0(k(\mathbf{x}))}\nabla k
\end{aligned}$$

Since $q(\mathbf{x}, \hat{\mathbf{v}}) > 0$ and $||\hat{\mathbf{v}}|| = 1$, we have:

$$\frac{\nabla q\cdot\hat{\mathbf{v}}}{q} = \left|\frac{e^{k(\mathbf{x})\,\mathbf{u}\cdot\hat{\mathbf{v}}} - e^{-k(\mathbf{x})\,\mathbf{u}\cdot\hat{\mathbf{v}}}}{e^{k(\mathbf{x})\,\mathbf{u}\cdot\hat{\mathbf{v}}} + e^{-k(\mathbf{x})\,\mathbf{u}\cdot\hat{\mathbf{v}}}}(\mathbf{u}\cdot\hat{\mathbf{v}}) - \frac{I_1(k(\mathbf{x}))}{I_0(k(\mathbf{x}))}\right| ||\nabla k||\cos(\nabla k\cdot\hat{\mathbf{v}})\,,$$

where $||\cdot||$ denotes the L_2-norm. Thus,

$$\left|\frac{\nabla q\cdot\hat{\mathbf{v}}}{q}\right| = \left|\frac{e^{k(\mathbf{x})\,\mathbf{u}\cdot\hat{\mathbf{v}}} - e^{-k(\mathbf{x})\,\mathbf{u}\cdot\hat{\mathbf{v}}}}{e^{k(\mathbf{x})\,\mathbf{u}\cdot\hat{\mathbf{v}}} + e^{-k(\mathbf{x})\,\mathbf{u}\cdot\hat{\mathbf{v}}}}(\mathbf{u}\cdot\hat{\mathbf{v}}) - \frac{I_1(k(\mathbf{x}))}{I_0(k(\mathbf{x}))}\right| ||\nabla k||\,|\cos(\nabla k\cdot\hat{\mathbf{v}})|\,.$$

Recalling that $|a-b| \le |a| + |b|$, $-1 \le \frac{e^{k(\mathbf{x})\,\mathbf{u}\cdot\hat{\mathbf{v}}} - e^{-k(\mathbf{x})\,\mathbf{u}\cdot\hat{\mathbf{v}}}}{e^{k(\mathbf{x})\,\mathbf{u}\cdot\hat{\mathbf{v}}} + e^{-k(\mathbf{x})\,\mathbf{u}\cdot\hat{\mathbf{v}}}} \le 1$, and $|\cos(\cdot)| \le 1$, we get

$$\left|\frac{\nabla q\cdot\hat{\mathbf{v}}}{q}\right| \le \left(1 + \left|\frac{I_1(k(\mathbf{x}))}{I_0(k(\mathbf{x}))}\right|\right)||\nabla k||\,.$$

Using the results from [156] (see equation (1.12) for $\nu = 1$), we obtain that $\left|\frac{I_1}{I_0}\right| < 1$, and, therefore,

$$\left|\frac{\nabla q\cdot\hat{\mathbf{v}}}{q}\right| < 2||\nabla k||$$

which implies

$$\max_{\mathbf{x}\in\Omega}\max_{\hat{\mathbf{v}}\in\mathbb{S}^{d-1}}\left|\frac{\nabla q(\mathbf{x},\hat{\mathbf{v}})\cdot\hat{\mathbf{v}}}{q(\mathbf{x},\hat{\mathbf{v}})}\right| < 2\max_{\mathbf{x}\in\Omega}||\nabla k(\mathbf{x})||.$$

This inequality translates into

$$l_q \geq \frac{1}{2 \max\limits_{\mathbf{x}\in\Omega} ||\nabla k(\mathbf{x})||} . \tag{6.35}$$

In particular, if there exists $\mathbf{x}$ such that $\nabla k(\mathbf{x}) \cdot \hat{\mathbf{v}} = 1$ and, at the same time, also satisfies $\nabla k(\mathbf{x}) \parallel \mathbf{u}$, where $\mathbf{u}$ is defined in (6.31), then (6.35) is true with the equal sign. For the symmetry of (6.32) and (6.34) in our numerical test we assume

$$l_q \approx \frac{1}{2 \max\limits_{\mathbf{x}\in\Omega} ||\nabla k(\mathbf{x})||} .$$

In this section we present five different simulations that are summarized in Table 6.3.

l_S	l_q	R	Case	η	Figure
0.002	0.0031	0.7	*i*)	< 1	6.4
0.25	0.0031	0.7	*i*)	$\gg 1$	6.5
0.055	0.031	0.02	*ii*)	> 1	6.6
0.25	0.0031	0.02	*iii*)	$\gg 1$	6.7
0.002	0.031	0.02	*iv*)	< 1	6.8

TABLE 6.3: **Summary of the five simulations presented in Test 3.** The parameter choices for l_S, l_q, and R, the corresponding case number, the parameter η, and the figure number of the visualization are indicated.

In Figure 6.4, we consider the case *i*) in which $\eta_S, \eta_q \gg 1$. The macroscopic behavior is strongly hyperbolic with the macroscopic velocity given by (6.15). In fact, in Figure 6.4 we can observe that the behavior is not diffusive and the cluster of cells is quite compact. Moreover, when cells reach the region in which fibers are strongly aligned in the direction $3\pi/4$ (as shown in Figure 6.3(d)), which is perpendicular to the favorable direction $\pi/4$ induced by the chemoattractant, they surround that region inducing strong alignment and move towards the chemoattractant. In this setting, the parameter η defined in (6.11) is slightly smaller than 1 and, thus, chemotaxis prevails in the overall dynamics, as the stationary state is clearly peaked on the chemoattractant profile, but the fibers structure influences the transient cell behavior.

In Figure 6.5, we consider $\mathcal{S}$ with $\sigma_S^2 = 1.8$, as shown in Figure 6.3(c), and, consequently, $l_S = 0.25$. Concerning the fibers, we have $m_k = 100$, so that $l_q \approx 0.0031$, and the sensing radius is $R = 0.7$. This setting belongs to case *i*), but the behavior is different with respect to the previous simulation in Figure 6.4. The chemoattractant in Figure 6.3(c) is spread out across the whole domain and the quantity l_S is almost 10^2 times the value of l_S considered in Figure 6.3(a) and used for the simulation in Figure 6.4. Even though this is a strongly hyperbolic case and cells are guided by the strong drift term (6.15), as R is slightly larger then l_S and l_S is large, the cell cluster diffuses a bit more in the domain. When it reaches the region of strongly aligned fibers, it starts to surround that region (as shown in Figures 6.5(a)-6.5(c)), but, as $\eta_S = 2.8 = \mathcal{O}(1)$, some cells, which do not surround the region, are slowed down and partially tend to align along the fibers. In Figure 6.5(d) we have a high density of cells both in the

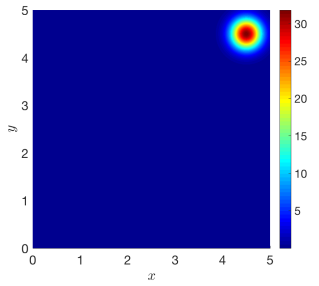

(a) Chemoattractant $\mathcal{S}$ with $\sigma^2_{\mathcal{S}} = 0.05$

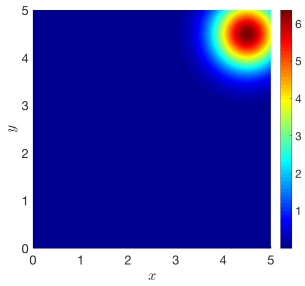

(b) Chemoattractant $\mathcal{S}$ with $\sigma^2_{\mathcal{S}} = 0.25$

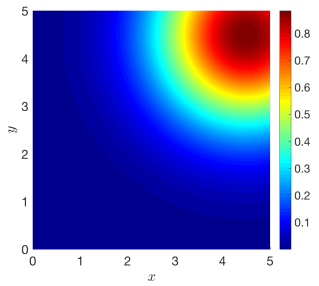

(c) Chemoattractant $\mathcal{S}$ with $\sigma^2_{\mathcal{S}} = 1.8$

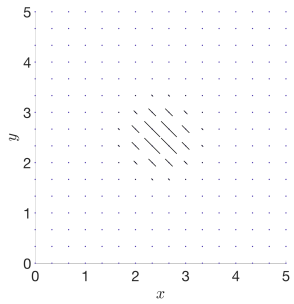

(d) Fibers distribution

FIGURE 6.3: **Test 3.** Three different chemoattractants used for comparing cases *i*)-*iv*). The chemoattractant profile is given by (6.32) with $m_{\mathcal{S}} = 10$ and (a) $\sigma^2_{\mathcal{S}} = 0.05$, corresponding to $l_{\mathcal{S}} = 0.002$, (b) $\sigma^2_{\mathcal{S}} = 0.25$, corresponding to $l_{\mathcal{S}} = 0.055$, and (c) $\sigma^2_{\mathcal{S}} = 1.8$, corresponding to $l_{\mathcal{S}} = 0.25$. The fibers distribution is visualized in (d).

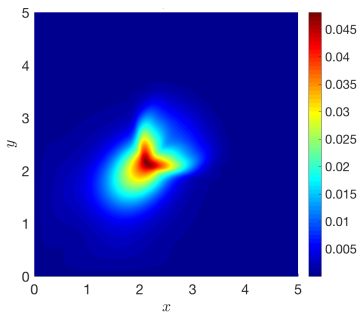

(a) $t = 1.25$

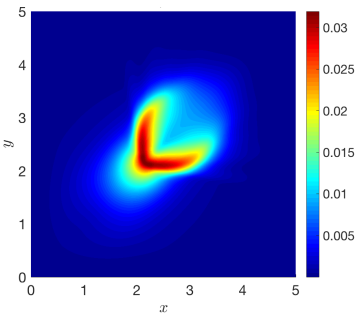

(b) $t = 1.875$

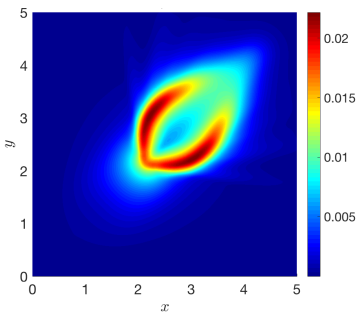

(c) $t = 2.5$

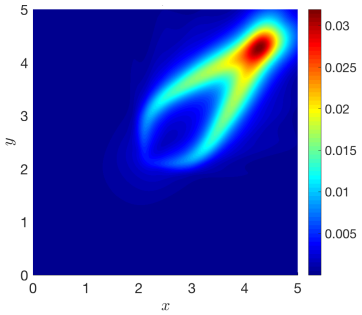

(d) $t = 3.75$

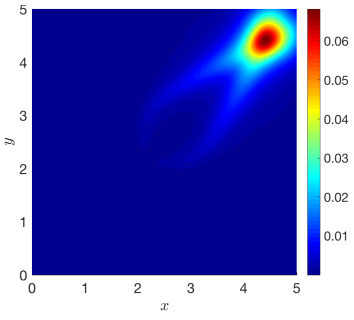

(e) $t = 5$

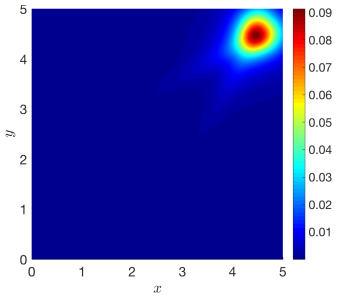

(f) $t = 6.25$

FIGURE 6.4: **Test 3.** Case *i*) with non-local q and $\mathcal{S}$, sensed independently with $\gamma_q = \gamma_{\mathcal{S}} = H(R - \lambda)$. $\mathcal{S}$ is given in Figure 6.3(a) with $m_{\mathcal{S}} = 10$ and $\sigma^2_{\mathcal{S}} = 0.05$, so that $l_{\mathcal{S}} = 0.002$. The fibers distribution q has a space dependent parameter k given by (6.34) with $m_k = 100$, so that $l_q \approx 0.0031$. The sensing radius of the cells is $R = 0.7$.

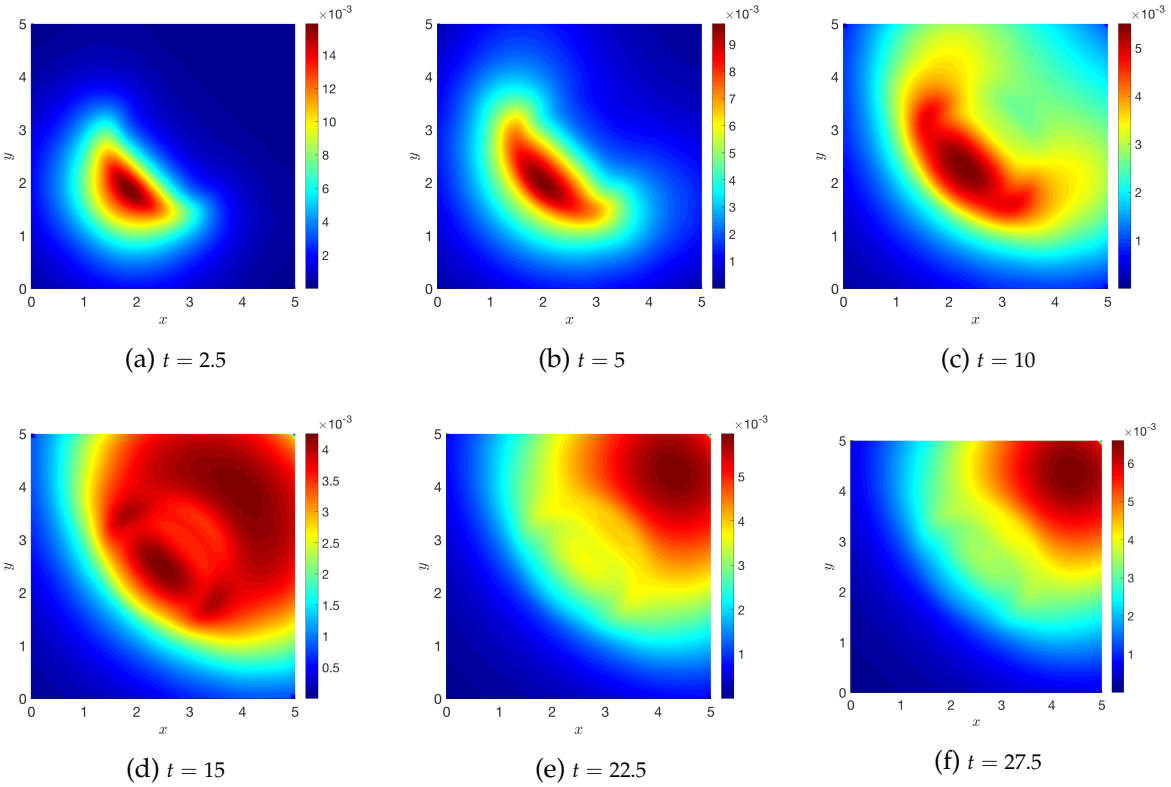

(a) $t = 2.5$ (b) $t = 5$ (c) $t = 10$

(d) $t = 15$ (e) $t = 22.5$ (f) $t = 27.5$

FIGURE 6.5: **Test 3.** Case i) with non-local q and $\mathcal{S}$, sensed independently with $\gamma_q = \gamma_S = H(R - \lambda)$. $\mathcal{S}$ is given in Figure 6.3(c), which corresponds to $l_{\mathcal{S}} = 0.25$, while for the fiber distribution $m_k = 100$, so that $l_q \approx 0.0031$. The sensing radius of the cells is $R = 0.7$.

strongly aligned fiber region and in the region of high density of chemoattractant. Eventually, the cells manage to overcome the area of highly aligned fibers and they converge to the chemoattractant profile (as in Figures 6.5(e)-6.5(f)). This demonstrates that the overall dynamics is greatly affected by the fibers and, in fact, this is expressed by the fact that the value of the parameter η in this case is $\eta \gg 1$.

The second scenario, illustrated in Figure 6.6, refers to the case ii), since the sensing radius $R = 0.02$ is smaller than both $l_{\mathcal{S}} = 0.055$ and $l_q \approx 0.031$. At the macroscopic level, the behavior of the system is described by the advection-diffusion equation (6.20) with macroscopic velocity (6.19). In Figure 6.6, we observe a highly diffusive behavior, as the macroscopic density of cells has invaded almost the half of the domain before even starting to be influenced by the fibers. If we compare the same time step in Figures 6.6(b) and 6.5(b), we see that the cells are in both cases reaching the fibers and reacting to the region in which fibers are aligned the most. However, in Figure 6.5(b) the cell cluster is much more compact than in Figure 6.6(b), where cells already occupy half of the domain, because of diffusion. In addition, we can observe a high density of cells both close to the strongly aligned fiber region and around the initial position. Therefore, cells start surrounding the central region of strongly aligned fibers, because they already sense the chemoattractant, and, once they have passed this area, they are attracted to the chemoattractant profile (see Figures 6.6(c)-6.6(f)). In the transient time, cells accumulate the most at the sides of the region with highly aligned fibers. In this specific setting, we observe that the parameter $\eta > 1$ that is characteristic of a scenario in which contact guidance highly affects the dynamics.

The third scenario, illustrated in Figure 6.7, refers to the case iii), where the sensing

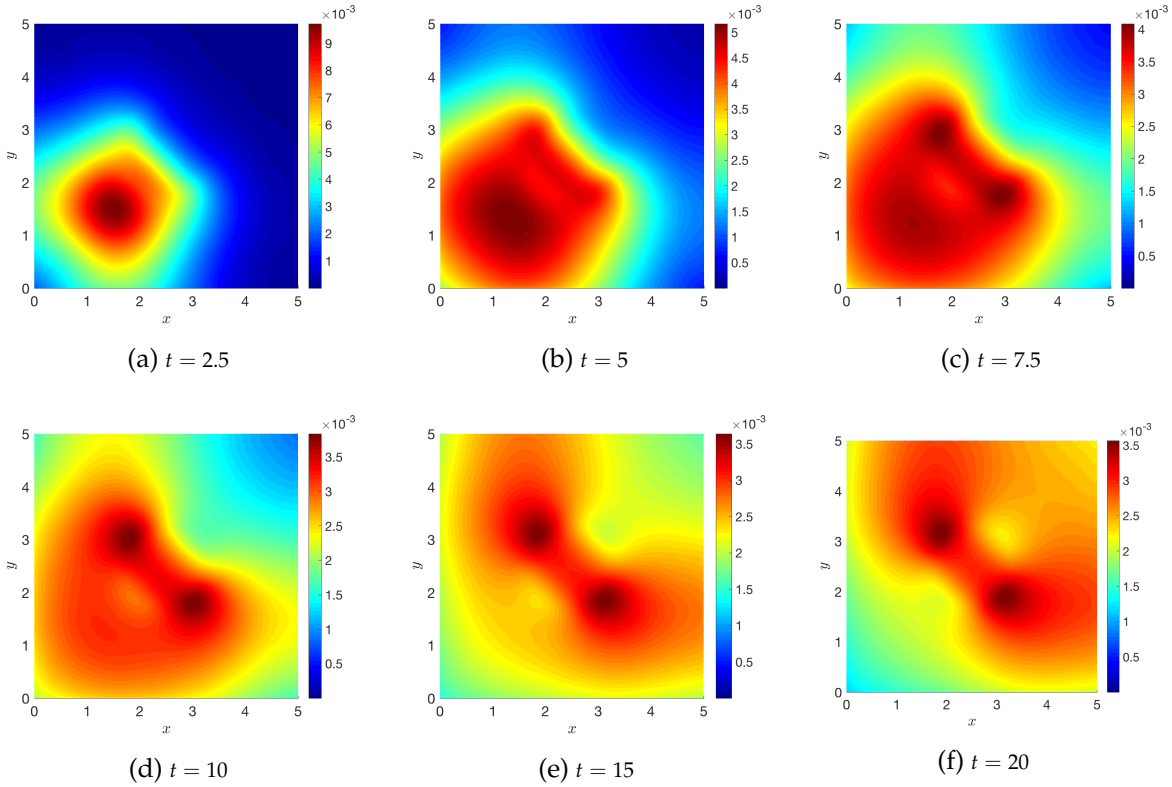

(a) $t = 2.5$ (b) $t = 5$ (c) $t = 7.5$

(d) $t = 10$ (e) $t = 15$ (f) $t = 20$

FIGURE 6.6: **Test 3.** Case *ii*) with non-local q and $\mathcal{S}$, sensed independently with $\gamma_q = \gamma_S = H(R - \lambda)$. $\mathcal{S}$ is given in Figure 6.3(b), which corresponds to $l_{\mathcal{S}} = 0.055$, while $m_k = 10$, so that $l_q \approx 0.031$. The sensing radius of the cells is $R = 0.02$.

radius $R = 0.02$ is smaller than $l_{\mathcal{S}} = 0.25$ but it is larger then $l_q \approx 0.0031$. The macroscopic setting is described by an advection equation with macroscopic velocity given by (6.22). As $\eta_{\mathcal{S}} < 1$, the chemoattractant induces a strong diffusivity, but because of $\eta_q > 1$, the alignment of fibers strongly affects the dynamics, as illustrated in Figures 6.7(c)-6.7(d). Comparing Figures 6.6(b) and 6.7(b), we can observe that the highest cell concentration is in the mean fiber direction $\theta_q = 3\pi/4$ in the region surrounding the center of the domain, where the fibers are aligned with a higher degree. As already observe in Section 6.1.2, this scenario prescribes $\eta \gg 1$ that characterizes the situation in which contact guidance dominates the dynamics.

Eventually, for a sensing radius $R = 0.02$ smaller than $l_q \approx 0.031$, but larger than $l_{\mathcal{S}} = 0.002$, the macroscopic behavior is approximated by a hyperbolic equation with drift velocity given in (6.24). Results of the simulation are presented in Figures 6.8. Here, the chemoattractant has the profile shown in Figure 6.3(a). Cells diffuse in the domain because η_q is smaller than 1, and they start moving in a region with randomly disposed fibers (see Figure 6.8(a)). Then, they mainly follow the preferential direction $\pi/4$ due to the presence of the chemoattractant. In fact, the chemoattractant induces a strong drift because of the high non-locality, determining $\eta_{\mathcal{S}} \gg 1$. Here, chemotaxis is slightly dominating the dynamics and this scenario is characterized by values for the parameter η such that $\eta < 1$.

6.4.4 Test 4: heterogeneous ECM environment

As last numerical test, we consider the domain Ω divided in several regions, each of them characterized by a different average direction of the fibers. We analyze this

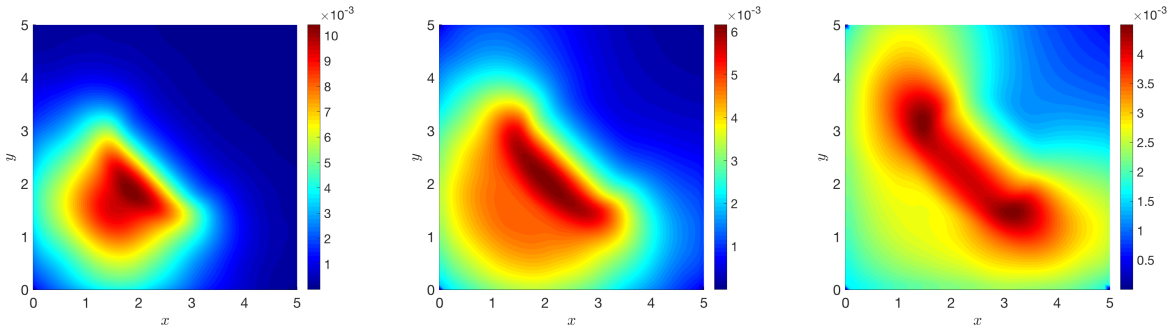

(a) $t = 2.5$ (b) $t = 5$ (c) $t = 10$

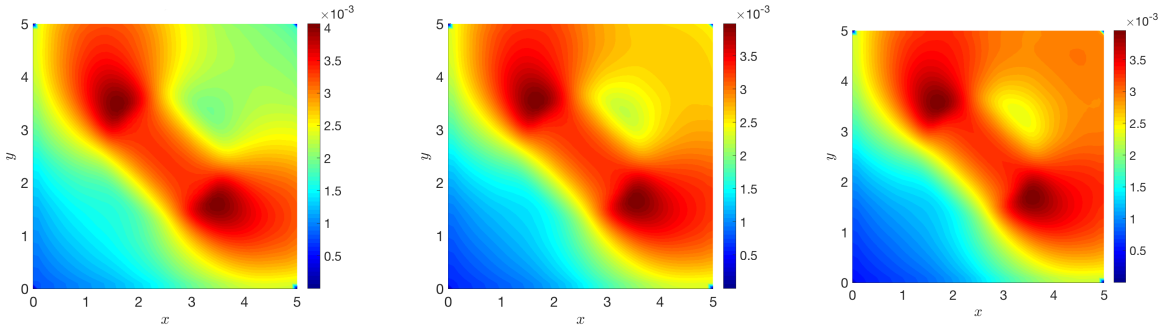

(d) $t = 20$ (e) $t = 30$ (f) $t = 60$

FIGURE 6.7: **Test 3.** Case *iii)* with non-local q and $\mathcal{S}$, sensed independently with $\gamma_q = \gamma_S = H(R - \lambda)$. $\mathcal{S}$ is given in Figure 6.3(c), so that $l_{\mathcal{S}} = 0.25$, while for the fiber distribution $m_k = 100$, corresponding to $l_q \approx 0.0031$. The sensing radius of the cells is $R = 0.02$.

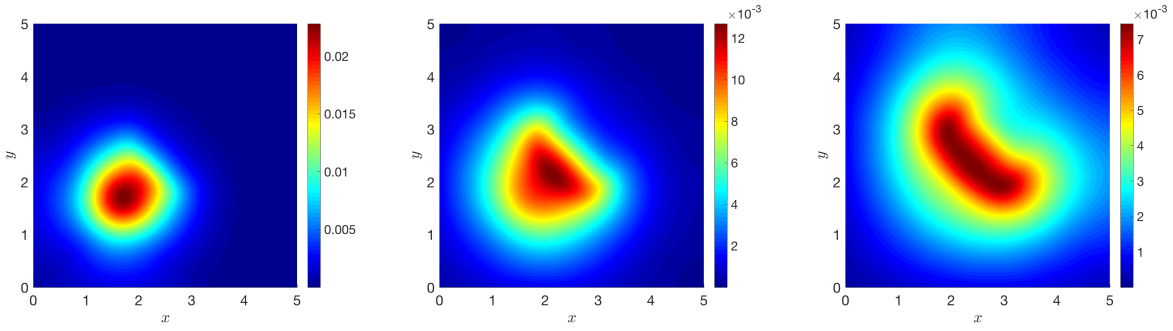

(a) $t = 1.25$ (b) $t = 2.5$ (c) $t = 5$

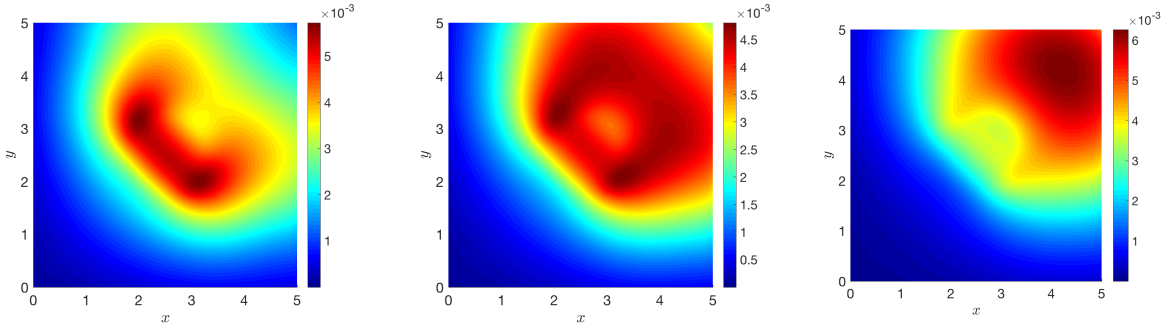

(d) $t = 7.5$ (e) $t = 10$ (f) $t = 15$

FIGURE 6.8: **Test 3.** Case *iv)* with non-local q and $\mathcal{S}$, sensed independently with $\gamma_q = \gamma_S = H(R - \lambda)$. $\mathcal{S}$ is given in Figure 6.3(a), which corresponds to $l_{\mathcal{S}} = 0.002$, while $m_k = 10$, so that $l_q \approx 0.031$. The sensing radius of the cells is $R = 0.02$.

scenario in the case of independent sensing model (6.2)-(6.3) with (6.12), choosing $\gamma_q = \gamma_{\mathcal{S}} = H(R - \lambda)$, similar to **Test 3**. As observed above, the independence of the two sensings allows to visualize more efficiently the two distinct directional effects.

As a ***first scenario***, we consider the domain characterized by two regions of different fiber orientation and schematized in Figure 6.9(a). In each subdomain we have $k(x, y) = 50$, which corresponds to $D_q = 0.005$. The initial condition of the cells is represented in Figure 6.9(c), with initial density $r_0 = 0.1$, while the chemoattractant has the Gaussian profile (6.32) centered in $(x_{\mathcal{S}}, y_{\mathcal{S}}) = (4, 4)$, with $m_{\mathcal{S}} = 10$ and $\sigma^2_{\mathcal{S}} = 0.5$, as shown in Figure 6.9(b).

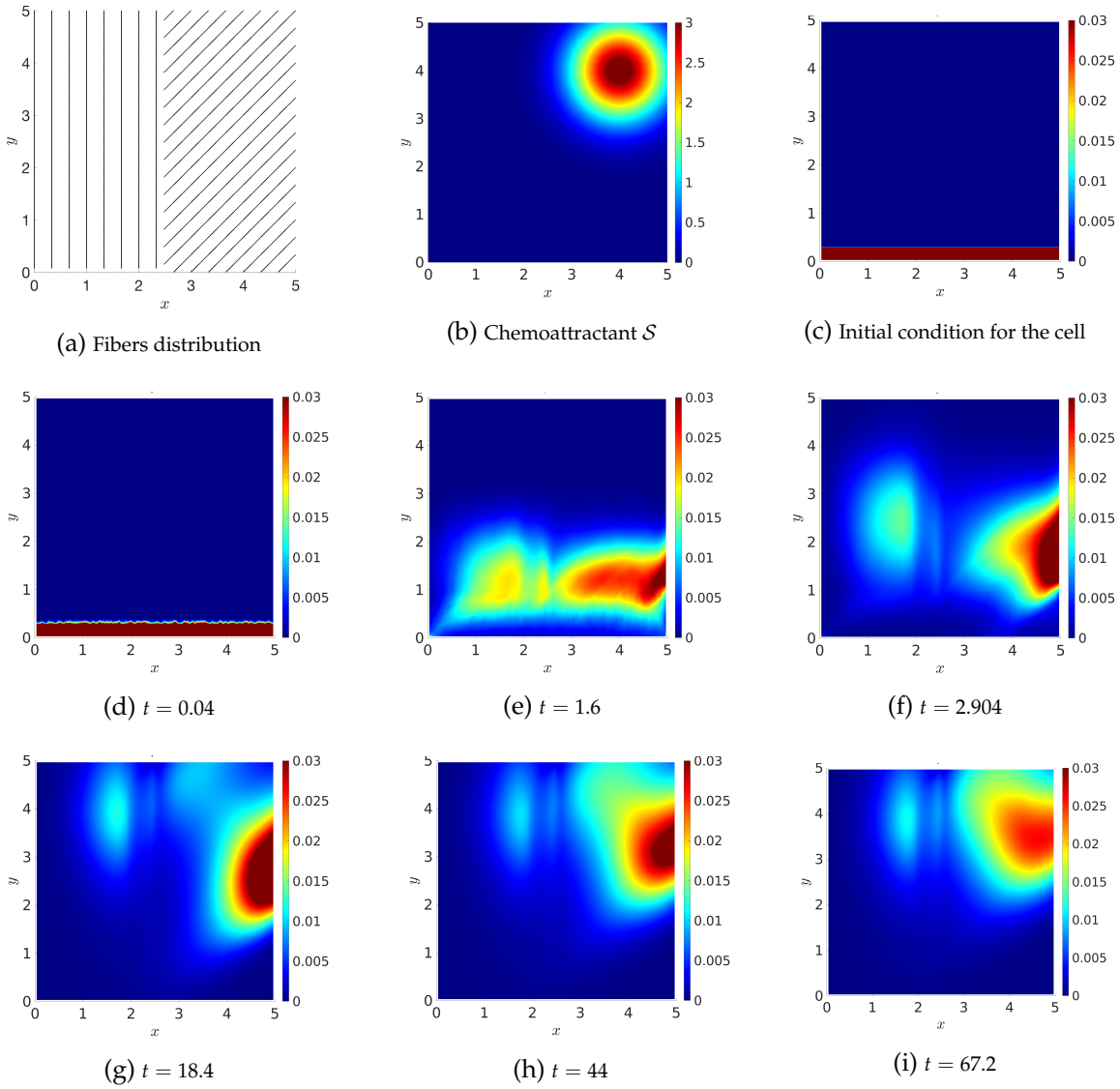

(a) Fibers distribution (b) Chemoattractant $\mathcal{S}$ (c) Initial condition for the cell

(d) $t = 0.04$ (e) $t = 1.6$ (f) $t = 2.904$

(g) $t = 18.4$ (h) $t = 44$ (i) $t = 67.2$

FIGURE 6.9: **Test 4.** Migration of cells in a heterogenous domain as illustrated in (a). The sensing radius of the cells is $R = 0.8$. The chemoattractant (b) is (6.32) with $m_{\mathcal{S}} = 10$ and $\sigma^2_{\mathcal{S}} = 0.5$. The initial cell profile (c) evolves in time as illustrated in (d)-(i).

We observe that the cells do not migrate collectively towards the chemoattractant, but they divide into two main separated clusters, as illustrated in Figures 6.9(f)-6.9(h). Although the sensing radius $R = 0.8$ is quite large, the cells that are closer to the left boundary remain trapped in the first subdomain, showing a loss of adhesion with the rest of the cell population. As shown in Figure 6.9(i), even though the cells that are in the left subdomain horizontally align to the chemoattractant, the high degree of alignment of the fiber does not allow them to escape this region, even for large times.

As a ***second scenario***, we consider the domain represented in Figure 6.10(a); in each subdomain, we set the parameter $k(x, y) = 50$. The initial condition of the cell population is given in (6.33) with $(x_0, y_0) = (4, 0.5)$ and $r_0 = 0.1$, while the chemoattractant has the Gaussian profile (6.32) centered in $(x_S, y_S) = (2, 4.5)$ with $m_S = 10$ and $\sigma_S^2 = 0.05$, as shown in Figure 6.10(c) and 6.10(b), respectively.

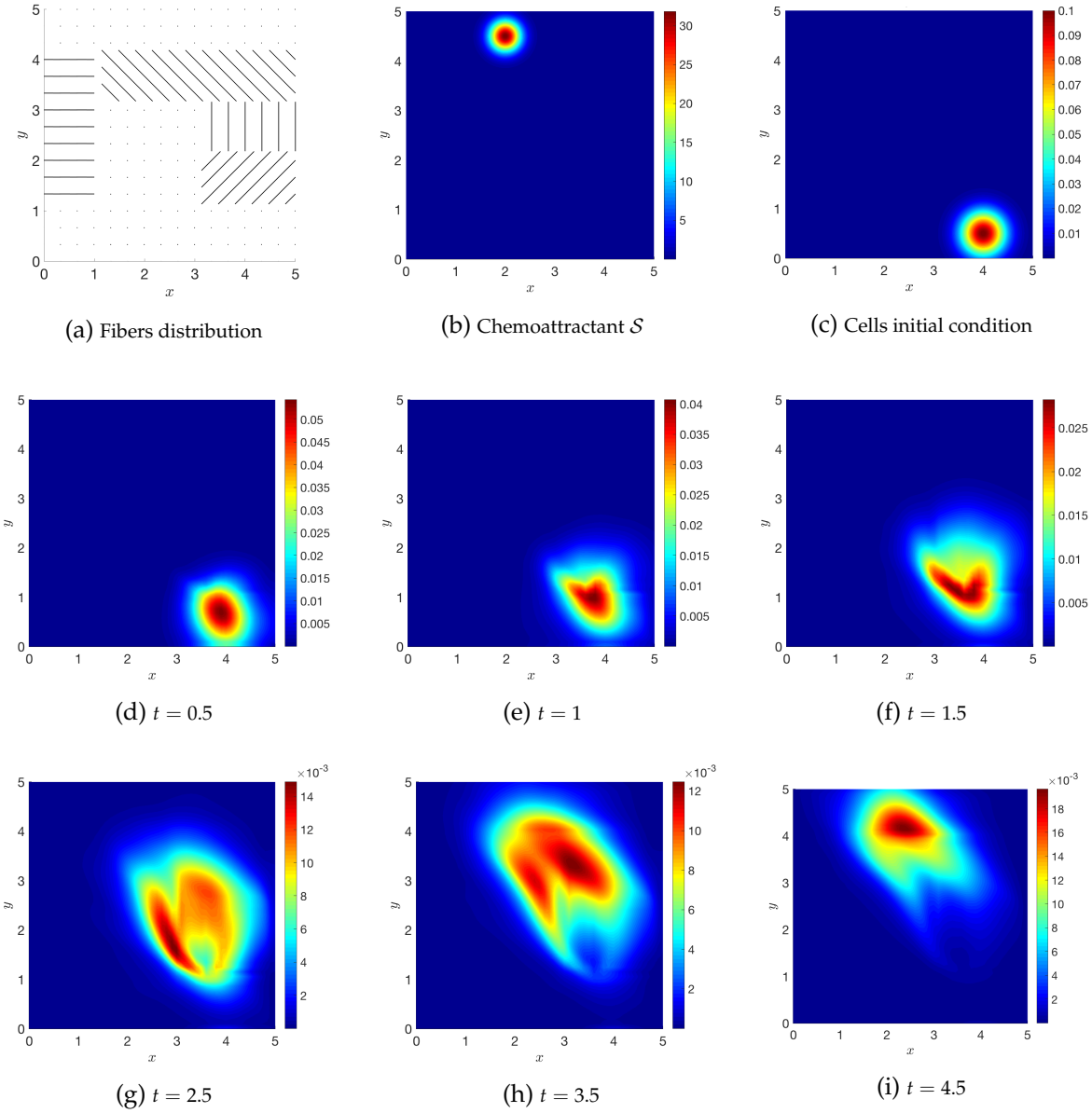

(a) Fibers distribution (b) Chemoattractant $\mathcal{S}$ (c) Cells initial condition

(d) $t = 0.5$ (e) $t = 1$ (f) $t = 1.5$

(g) $t = 2.5$ (h) $t = 3.5$ (i) $t = 4.5$

FIGURE 6.10: **Test 4.** Migration of cells in a heterogenous domain as illustrated in (a). The sensing radius of the cells is $R = 0.7$. The chemoattractant (b) is (6.32) with $m_S = 10$ and $\sigma_S^2 = 0.05$. The initial cell profile (c) evolves in time as illustrated in (d)-(i).

We observe that the cells do not migrate directly towards the chemoattractant, as they sense the heterogeneous fiber environment and, consequently, adapt their migration to the fiber network. In particular, cells that are able to reach and sense the isotropic subdomain where the fibers are uniformly distributed (for $1 \leq x \leq 3$ and $0 \leq y \leq 3$), move in the direction imposed by the gradient of the chemoattractant. In the subdomain, $3 \leq x \leq 5$, and $1 \leq y \leq 2$, cells follow the direction of the fiber alignment, which is $\pi/4$, perpendicular to the favorable direction imposed by $\mathcal{S}$. However, the sensing radius $R = 0.7$ allows the cells that are closer to the right boundary to escape quite fast the disadvantageous (in terms of preferential direction) subdomains and, following first the direction $\pi/2$ in $2 \leq y \leq 3$ and, then, $3\pi/4$ in $3 \leq y \leq 4$, they reach the chemoattractant.

6.5 *Summary*

In this chapter, we proposed a kinetic-based model for the description of cell migration in a multi-cue environment. Although we considered a general cell population, leaving the idea of specifying this analysis at the concrete case of glioma migration as a future task, prominent and novel aspects emerged in relation to the effects of the two cues, the non-locality of the sensings and their characterization. If in the previous chapters we assumed at the kinetic level a single cue driving the velocity changes and consisting either in the fiber network (as for tumor cells in Chapters 3-5) or in a chemotactic gradient (as for ECs in Chapter 4), here we analyzed the combined effect of two cues simultaneously guiding cell migration. Precisely, these two guidance cues, affecting cell polarization, and, thus, the direction of motion, consist of the fiber network, which is a bi-directional cue inducing contact guidance, and a chemical gradient, which is a mono-directional cue. Moreover, complementary to the previous chapters, we included here the mechanism of cell protrusion extension driving cell migration. Cells extend protrusions up to several cell diameters to mediate their interaction with the extracellular environment, for instance, the crawling along brain fibers or the tactic movement toward a chemoattractant source. Here, the effects of cell protrusion extension on cell migration were described by means of non-local terms characterizing the sensing of the environment. Therefore, we combined these non-local aspects with the description of two guidance cues and, for the first time, we considered a non-local sensing in the physical space of the mesoscopic distribution of fibers.

We introduced two classes of models: in the first one, cells performed an independent sensing of the fibers and the chemical in its neighborhood, while in the second class of models cells average the chemical and the fibers with the same sensing kernel. In the two cases, particular attention was devoted to the identification of the proper macroscopic limit according to the properties of the turning operator. We detected two parameters, η_q and $\eta_{\mathcal{S}}$, that measure the relationship between the cell sensing radius and the characteristic lengths of variation, $l_{\mathcal{S}}$ and l_q, of the two cues, and discriminate between a diffusion-driven regime with an advective correction and a drift-driven regime. In particular, when the sensing radius does not exceed the characteristic length of the chemoattractant, the bi-directional nature of the fibers allows for a diffusive regime; otherwise, the hyperbolic scaling leads to macroscopic drift. A common feature in the different cases is the dependency of the macroscopic velocity on both the fiber network and the chemoattractant. This aspect highlights the non-trivial influence of contact guidance on the cell drift, although we considered a non-polarized fiber network. This interdependence is in accordance with the model

proposed in [289]. Moreover, in the absence of a chemoattractant, this impact on the drift term can persist for spatial heterogeneous fiber distributions. This is in accordance to what is observed in [116] and it represents a step forward with respect to [289], in which the drift is a function of contact guidance only depending on the presence of a chemical gradient, i.e., without chemoattractant, there will be no drift.

The numerical simulations of the transport model pointed out the main features characterizing the two classes of models and the possible scenarios that they are able to reproduce. We observed that, even when the fibers are sensed locally (like in the models presented in the previous chapters), the presence of two cues influencing cell polarization ensures a preferential sense of motion for cells laying in regions of highly aligned non-oriented fibers, as shown in Figure 6.1. The results in Figures 6.4-6.8 showed the importance of deriving the macroscopic equations from an underlying microscopic dynamics: a directly postulated drift-diffusion equation could not capture the exact dynamics in all the possible regimes. Moreover, these results showed the importance of performing the model derivation in the appropriate regime. The competitive or collaborative effects of the cues depend, in a first instance, on the angle between their relative orientations, i.e., the direction of fiber alignment θ_q and the gradient of the chemoattractant. Especially for the cases of competitive cues, determining which one is the dominant cue depends on their relative strengths, in terms of both concentration and intensity (degree of alignment of the fiber $k(\mathbf{x})$ or steepness of the chemoattractive gradient). Moreover, we introduced the parameter $\eta = l_S/l_q$ that, independently of the cell size or the cell's sensing capability, quantifies the relative contribution of guidance to chemotaxis and provides a first classifier between the cases of fiber-dominating and chemotaxis-dominating dynamics ($\eta \gg 1$ or $\eta \ll 1$, respectively).

The non-locality, which is used for the mesoscopic description of cell protrusion effects and differentiates this setting from the previous ones, brought a further level of detail to the model, allowing us to obtain different macroscopic behaviors depending on the characteristics of the two sensings. In the previous chapters, the macroscopic settings were all derived in a diffusion-driven regime due to the symmetry properties of the cue guiding the velocity changes and the local interactions. Here, the presence of non-local terms and the combination of the two cues allow to capture drift-driven phenomena (e.g. see Figures 6.4 or 6.8), where we observed the migration of compact groups of cells in response to the guiding cues. We did not observe strong differences between the independent and the dependent sensing models, when we assumed in the former the same sensing kernel for fibers and chemoattractant, i.e., when $\gamma_q = \gamma_s$ (as shown in Test 2). However, if there are biological observations sustaining the possibility that a cell can implement different strategies for sensing the underlying fiber network and the chemoattractant, it would be possible to use the proposed framework, in its independent sensing version, to investigate this scenario and to compare the possible outcomes of this sensing approach with the case of a unique and common sensing strategy. Potentially, the case of competitive cues, combined with the non-local aspect of the model, could lead to interesting further analysis. As observed in the last numerical tests in Figures 6.9 and 6.10, the combination of heterogeneous landscapes of fibers (characteristic of the brain tissue) with chemoattractive agents shows how the cell density can divide and cross the domain using different migration strategies, while in the previous settings the diffusive dynamics induced by the fiber network had a stronger impact. This naturally leads to questions about the deeper mechanisms leading the competition between the two cues, considering, for instance, the possible role of cell adhesion in recovering collective migration.

This model setting constitutes a bridge between the kinetic-based model of Chapters 3-5, based on local interactions and a single cue driving velocity changes, and the macroscopic setting of Chapter 7, where the description of cell protrusions will be one of the core aspects we will analyze.

Part III

Macroscopic models

7 *Dynamics at the leading edge of glioblastomas*

So far in this dissertation, we have analyzed several aspects of glioma progression in a multiscale framework: from the influence of tissue anisotropy and membrane receptors on cell migration (Chapter 3) to the role of vasculature, acidity, and intratumor heterogeneity in the tumor evolution (Chapter 4), including the analysis of combined treatments (Chapter 5) and of the effect of protrusion dynamics (Chapter 6). Our next step is to explore the biochemical and biomechanical mechanisms that regulate the development of invasion fronts of glioma, the role of cell protrusions in this process, and the possibility of spatial heterogeneity characterizing the tumor activity.

In this chapter, we propose a novel multidisciplinary approach, based on a macroscopic mathematical model and *in-vivo* experiments in *Drosophila*, for the description of protein dynamics at the tumor front. The coordination of metalloprotease expression, extracellular matrix degradation, and integrin activity results in the extension of cell protrusions (known as tumor microtubes TMs), and emerges as the leading mechanism of glioma expansion and infiltration in healthy brain regions. Precisely, after providing in Section 7.1 the biological motivation that encouraged the study, in Section 7.2 we describe the novel mathematical elements used in the model and related to the flux terms. Then, in Section 7.3, we present the model setting together with the experimental results that sustain the modeling hypothesis. Finally, we provide some numerical results in Section 7.4.

The results of this chapter have been collected in the paper by Conte, Casas-Tintò, and Soler submitted for publication [53].

7.1 *Motivation*

GB growth and migration is driven by specific signaling pathways as well as interactions between the tumor cells and their extracellular microenvironment. Our main interest is to study the dynamics of the tumor cell membrane as driving factors of tumor progression involved in both the cell response to signaling gradients and the interplay with the ECM. The dynamics of tumor cell protrusions, in fact, are fundamental in several processes, particularly in cell transport and in the cell exposure to interactions with different molecular substrates during the tumor evolution.

As we briefly introduced in Section 1.1.1, ***cell protrusions*** are highly dynamic extensions of the plasma membrane, involved in cell migration and invasion through the ECM. Different types of protrusions have been identified; for instance, filopodia - thin, finger-like membrane extensions - have a significant role in mediating intercellular communication and in modulating cell adhesion. Cell protrusions appear to

be required for haptotaxis and chemotaxis [128]. We remind that these two mechanisms represent the cell response to the gradient of insoluble (haptotaxis) and soluble (chemotaxis) components of the tumor microenvironment. Cytonemes are one type of filopodia, first observed in the *Drosophila* wing imaginal disc [236] (see also [101, 102, 125, 287] for a detailed description), and they have a diameter of approximately 0.2 μm and an average length of 80 μm. Also known as TMs in the context of glioblastoma, cell protrusions have an important role in tumor development [228]. We focus our study on TM involvement in the progression of the tumor front and on TM relationship with integrins and proteases. Tumor propagation is characterized by sharp ***invasion fronts*** located in the front area of cell progression, where TMs are mostly concentrated. The tumor front represents the parts of the tumor region, in contact with the healthy tissue, that collect a wide activity related to cellular communication signals and cell-ECM interactions. The agents involved in GB invasion, such as integrins, proteases, or the tumor cells themselves, are not scattered or randomly moving, but rather there is self-organization between these agents that determines invasion patterns around the tumor front. This organization is important in the description of tumor progression and it can be observed in Figure 7.6, where proteases and integrins are shown to co-localize with the TMs in the region of the GB front. Thus, the majority of the tumor activity is concentrated in this area. We analyze the formation of these expansion patterns in order to predict GB dynamics. The ***integrin*** role in mediating the dynamic interactions between the ECM and the actin cell cytoskeleton during cell motility has been largely described in Section 1.1.1 and in Chapters 3-5. These receptors, generally present on the cell membrane, concentrate the most of their activity at the tumor front, where they are directly in contact with the ECM. In the *Drosophila* model we used for the experimental results, integrin function was studied considering the distributions of focal adhesion kinase (FAK) and talin. Details about these proteins and the experimental procedures are provided in Appendix C. ***Proteases***, enzymes that catalyze the proteolytic process, are also localized around the cell membrane and play a key role in promoting tumor invasion and tissue remodeling. They induce proteolysis of ECM components [305] and maintain a microenvironment that facilitates tumor cell survival. As observed in Section 1.1.1, increased MMP levels have been observed in high-grade astrocytoma and they have shown a strong correlation with GB invasiveness [228, 238]. Several studies reported their localization in the TM membrane [187, 204]. We schematize in Figure 7.1 the dynamics between these factors, which represent the core of this model.

Our interest in the TM role in glioma migration arises prevalently from studies on the effect of different drugs on TM structure and dynamics [25, 26]. It has been shown that the inhibition of TMs leads to a decrease in cell migration and proliferation, with obvious consequences on GB treatment [24–26]. The process of growth and retraction of TMs is an important binding platform for essential proteins that regulate tumor dynamics [93]. For instance, among these proteins, the presence of microtubule plus end-binding protein EB1 correlates with GB progression and poor survival [24, 46]. This has led to a great interest in the development of drugs aimed at affecting EB1 expression [26].

Therefore, with this model, we focus on the evolution of the tumor propagation front and we analyze the emergence of a strong nonlinear coordination between the self-organized collective processes characterizing the different agents involved in tumor progression. We exploit the ability of mathematical models to predict and guide biological experiments, supporting the mathematical hypothesis with the provided data on protein signaling, and we integrate this data in the modeling.

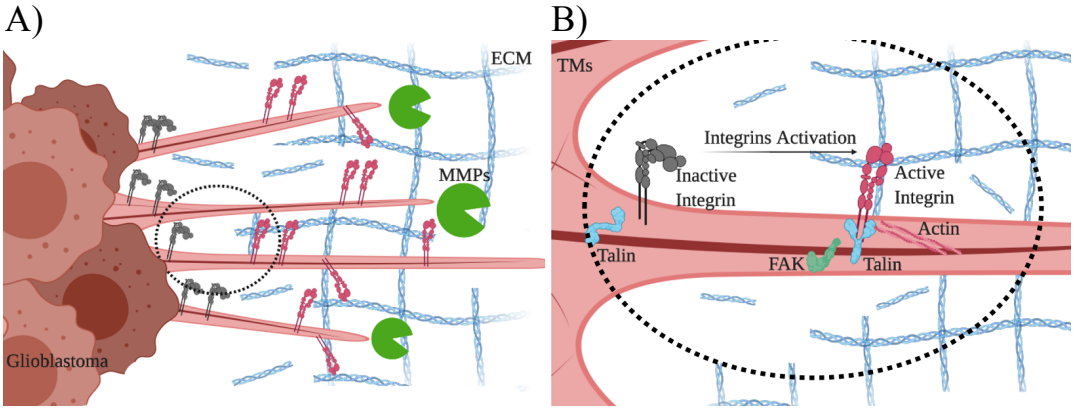

FIGURE 7.1: **Diagram of GB and protein dynamics.** Diagram of the interactions between the proteins involved in GB progression that give rise to the mathematical model. A): GB cells produce and release in the extracellular space MMPs that proteolyze the ECM components. B): Magnification of TMs. Integrins are activated in the TMs upon interaction with ECM. Active integrins, interacting with actin filaments and the talin adaptor protein, activate the FAK protein and promote cytoplasm dynamics.

7.2 *Preliminaries: the flux-saturated model*

Different mathematical models have been proposed to describe the invasion of tumors at the macroscopic level. As we briefly introduced in Section 1.2.2, these models can be divided into two main classes, whether they rely on linear or nonlinear diffusion. We recall that the former type of diffusion is based on the Fick's law and describes cell migration as a result of the flux from regions of higher to lower cell densities, while the latter can be derived from the application of the Darcy's law. We described in the previous chapters how to obtain a linear description of cell diffusion at the macroscopic scale from the mesoscopic scale of a two or a three-level setting. More complicated issues arise for deducing a nonlinear form of the diffusion term from a lower level of description. This is still an open and debated topic and a lot of effort has been recently focused on a formal and well-defined mathematical theory for this problem (e.g. see [20, 59] and reference therein). Here, we are interested in the analysis of sharp invasion profiles, not compatible with movements induced by linear diffusion. Moreover, the diffusive dynamics are coupled with several additional mechanisms. Thus, we define our setting directly at the macroscopic level, leaving the study of its derivation from a lower scale as a future task to address.

The core of the mathematical model presented in the next section is based on the description of the diffusion process by means of a more sophisticated form of the nonlinear diffusion operator, namely the ***flux-saturated diffusion operator*** for the density $n(t, \mathbf{x})$

$$\mathcal{J}[n] = \nu \frac{n^m}{\sqrt{n^2 + \left(\frac{\nu}{v}\right)^2 |\nabla n|^2}}.$$

In this definition, ν is the kinematic viscosity of the medium, v is the front propagation velocity, and the exponent m is connected to the porosity of the medium. To the best of our knowledge, models with saturated flows were introduced in the literature on Astrophysics [165, 166] in relation to particular instances of closure problems for radiative transfer theories. A further step in the use of these models was in the context of wave propagation [47, 154, 250], for deriving a model able to restore the finite speed

of propagation of signals in a medium and to sustain initially imposed sharp fronts (for instance, a jump discontinuity at the edge of the support). Besides this derivation of the flux-saturated operator, it was also formally derived, for the special case $m = 1$, in the context of optimal transport theory [35, 188], where the resulting flux-saturated equation was called a relativistic heat equation. For a extensive historical overview of the flux-saturated operator, we direct the reader to [40, 41].

The applications for this operator are divers. Several of them are applied in the biological context, as it has been suggested that flux-saturated mechanisms have the potential to reproduce some of the emerging behaviors that happen at the macroscopic level [17]. It is also important to understand how the saturation of the flux can compete or cooperate with other mechanisms involved in the dynamics, such as the porous media effect or reaction terms [40]. For instance, in [287] the authors show how the combination of different mechanisms can determine the gradient formation in morphogenesis and the development of propagation fronts. Flux-saturated models offer a novel dynamical framework to describe finite speed diffusion and front propagation phenomena in real media. The classical Gaussian-type traveling wave solutions of linear diffusion-reaction systems, in fact, are characterized by infinite tails which prevent the creation of fronts and by the phenomenon of infinite speed of propagation. In the context of this glioma model, a linear diffusion operator can be interpreted as an instantaneously reach and contamination of the healthy tissue by the neoplasia, to a greater or lesser extent. Therefore, to recover the concept of tumor front and to model the dynamics related to it, we develop our macroscopic setting on the basis of flux-saturated equations. In this context, the basic flux-saturated equation reads

$$\frac{\partial n}{\partial t} = \nu \nabla \left(\frac{n^m \nabla n}{\sqrt{n^2 + \left(\frac{\nu}{v}\right)^2 |\nabla n|^2}} \right), \tag{7.1}$$

where the parameter $\nu, v, m \in \mathbb{R}$, although this equation can be extend to the case in which some of these parameters depend on time or space. This equation arises from the combination of the porous-media equation with the flux saturation mechanism and provides a flow that is saturated as long as the size of the gradient is large enough. The flux-saturated equation enables a direct control on the finite speed of propagation of the front: this speed is bounded by v for $m > 1$, while it is exactly v for $m = 1$.

To practically understand the behavior of the solution of (7.1) we considering a 1D scenario, whose domain is defined by the interval $[0, 1]$. We assume no-flux boundary conditions and we center the initial concentration of n in the point $x_0 = 0.5$. The qualitative behavior of the solution of equation (7.1) for $\nu = 1$ and $v = 0.1$ is shown in Figure 7.2. In this example the preservation of the steepness of the initial profile is evident while the invasion front is advancing. We can better observe the direct control on the characteristic speed of front propagation in Figure 7.3. Here, the x-axis refers to the space variable x measured in mm, while the density $n(t, x)$ on the y-axis is normalized. ν is expressed in mm $\cdot$ h^{-2} and v in mm $\cdot$ h^{-1}. Precisely, we choose $v = 0.006$ mm $\cdot$ h^{-1} so that we can appreciate an exact displacement of 0.06 mm after 10 h of simulation. This well-defined distinction between the tumor internal region (left-side of the domain with respect to the front) and the external region (right-side of the domain with respect to the front) is important in our setting in order to define the TM region, where most of the tumor activity is localized. Moreover, we observe how changes in the speed v or in the viscosity ν determine modifications in the characteristics of the front, as shown in Figure 7.4. Precisely, in the left plot of Figure 7.4 we observe how decreasing or increasing the cell speed slows down

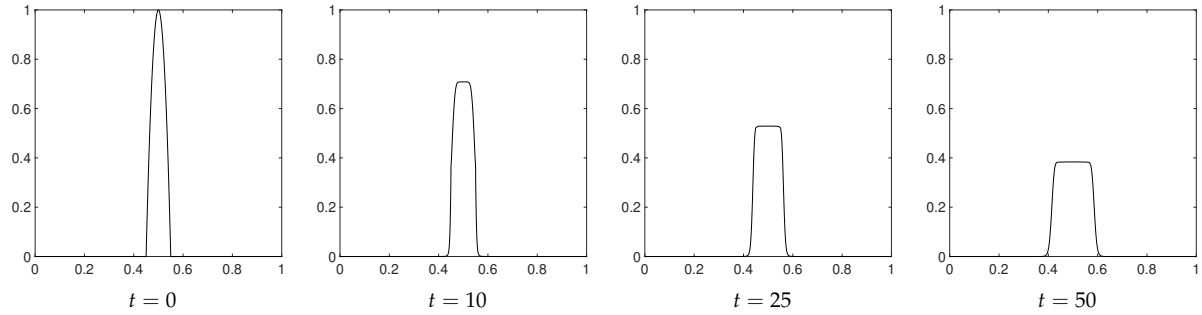

FIGURE 7.2: **Evolution of the solution of the flux-saturated equation.** Behavior of the solution of the 1D version of the flux-saturated equation (7.1) with $\nu = 1$, $v = 0.1$, and $m = 1$. The x-axis refers to the space variable x, while the y-axis describe the density $n(t, x)$.

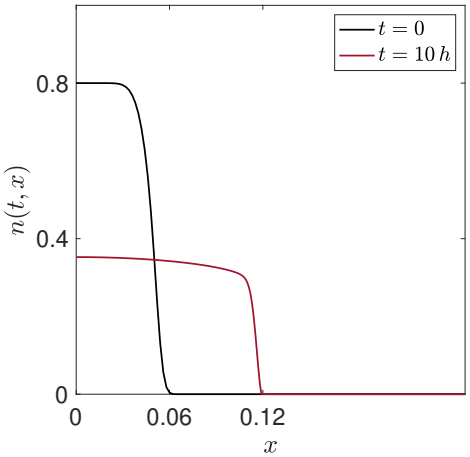

FIGURE 7.3: **Front speed.** Detail of the front speed for the solution of the 1D version of the flux-saturated equation (7.1) with $\nu = 1$, $v = 0.006$, and $m = 1$.

or accelerates the front propagation, respectively. In particular, since we use $m = 1$ in all the simulations, v represents the exact propagation speed and we can easily calculate the exact displacement of the invasion front. The right plot of Figure 7.4 shows how the changes in the viscosity coefficient affect the shape and the curvature of the solution profile. More distinct changes in the solution profile can be observed by considering the ratio $\frac{\nu}{v}$: for $\frac{\nu}{v} \geq 1$ (in Figure 7.4, the cases $\nu = 1$ and $\nu = 0.1$), the profiles are very similar, while for $\frac{\nu}{v} < 1$ (in Figure 7.4, the cases $\nu = 0.01$ or $\nu = 0.0005$) the profiles show significant different shapes. These results suggest that the ratio $\frac{\nu}{v}$ is the main parameter governing the shape of the solution, rather than the single value ν.

In line with the description of the diffusion operator, we adopt a similar approach for the description of the transport term $\mathcal{J}_{\text{tras}}[n, S]$ related to the signal pathway of an external source $S(t, \mathbf{x})$ (such as a chemoattractant). This transport term is usually assumed to be linear in the concentration gradient of the source, i.e., it can be described with the classical Keller-Segel model [137] as $\chi n \nabla S$, with a constant tactic sensitivity $\chi \geq 0$. However, this approach is not optimal in the optimal transportation sense. Thus, we include a modification in the transport term, which reads

$$\mathcal{J}_{\text{tras}}[n, S] = \chi n \frac{\nabla S}{\sqrt{1 + |\nabla S|^2}}\,. \tag{7.2}$$

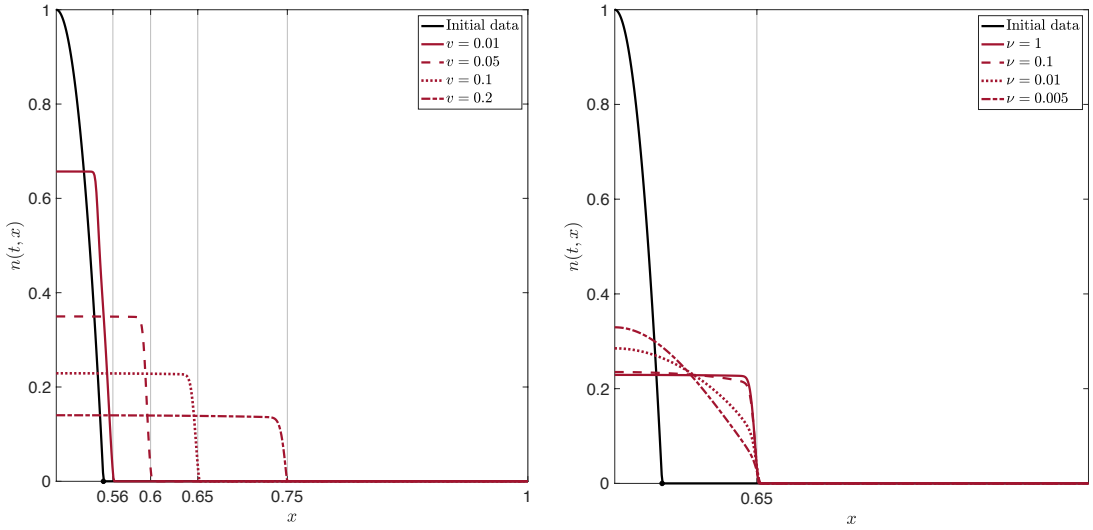

FIGURE 7.4: **Variation of the speed v and the viscosity ν.** Solution of the 1D flux-saturated model at $t = 1$ h for different values of v, while $\nu = 1$ is fixed (left). Solution of the 1D flux-saturated model at $t = 1$ h for different values of ν, while $v = 0.1$ is fixed (right). In the two plots the black dot is located at $x = 0.55$ mm and represents the front position at $t = 0$, while the values indicated on the x-axis represent the location of the front of the corresponding curve at $t = 1$ h. ν is expressed in mm $\cdot$ h^{-2} and v in mm $\cdot$ h^{-1}.

Similar to the the flux-saturated diffusion term, this expression is motivated by optimal transportation criteria, important for the propagation phenomena at hand from a qualitative viewpoint. This expression was proposed as a possible modification of the classical Keller-Segel model in order to optimize the density of the particles along the trajectory induced by the chemoattractant, namely to minimize the functional

$$\int \chi n(t,\mathbf{x}) dS = \int \chi n(t,\mathbf{x}) \sqrt{1 + |\nabla S(t,\mathbf{x})|^2} d\mathbf{x}$$

with respect to S, where dS is the measure of the curve defined by S. The term (7.2) coincides with the classical expression $\chi n \nabla S$ for very small $|\nabla S|$ [20].

In the following section, we describe how these flux-saturated operators are employed for the description of the transport terms characterizing the different populations involved in the dynamics.

7.3 *Model setup: theory and experiments*

We present here a novel mathematical model that covers specific evolutionary aspects that drive the dynamics at the leading edge of GB. From the modeling side, the most relevant novelties include the description of the tumor front evolution through the characterization of the TM region and the link of cell membrane movements with specific protein dynamics. In particular, this link involves both the protein concentration and the protein location in the TM region. In our setting, tumor evolution is governed by nonlinear diffusion and chemotactic and haptotactic phenomena, induced by proteases and integrin activity, respectively. All the tumor transport processes are described using flux-saturated operators that allow the incorporation of biological parameters related to tumor dynamics - namely, the viscosity of the medium and the propagation speed - and the definition of sharp invasion profiles [41]. The same

flux-saturated mechanisms are used in the description of proteases diffusion in the extracellular space, after the production of these enzymes by tumor cells. The integrin population is divided into two subpopulations accounting for active and inactive receptors: this distinction divides the receptors already bound to the ECM from the ones still not bound. In addition to the attachment/detachment processes with the ECM, active integrins are also subordinated to a transport term, as these receptors are constantly linked to the cell membrane and, thus, move with the cell. We complete the setting considering the description of ECM degradation driven by the protease proteolytic activity.

The positive ($\rightarrow$) and negative ($\dashv$) feedbacks of each population on the others is illustrated in the following scheme

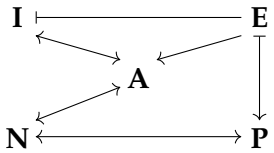

We notice that, both active integrins $A(t, \mathbf{x})$ and proteases $P(t, \mathbf{x})$ influence the process of tumor migration, and, in turn, GB cells $N(t, \mathbf{x})$ support integrin activation and proteases production. The mutual exchange between the active and the inactive $I(t, \mathbf{x})$ subpopulations of integrins is influenced by the presence of the ECM $E(t, \mathbf{x})$, which supports the activation at the expenses of the inactive integrins. Moreover, the ECM supports the MMP production and, eventually, it is degraded by proteases. All the population involved in the macroscopic setting are functions of time t and space $\mathbf{x}$.

In the following, we explore the dynamics of the active front of glioma cells. Precisely, we experimentally study the distributions of MMPs, integrins, and focal adhesions and analyze their localization in relation to the tumor membrane density. We hypothesize a spatial heterogeneity in the activity of tumor cells, referring to both proteolysis and binding receptor activation. This spatial heterogeneity determines the accumulation of MMPs and the activation of the integrins receptors at the tumor front.

7.3.1 *Description of the TM region*

Considering that the objective of our analysis is the study of the tumor front evolution, as first step we formulate the differential equations for the involved populations and we perform the numerical simulations in a 1D scenario. Therefore, we assume $(t, x) \in [0, T] \times \Omega$, with $T > 0$ and $\Omega = [0, b_\Omega]$, $b_\Omega \in \mathbb{R}$. For reasons of simplicity, we change the notation for the spatial variable from $\mathbf{x}$ to x, as $x \in \mathbb{R}$.

We first define and characterize the tumor microtubes region L_{TM}, where we expect to notice the well-defined tumor invasion front and the increased tumor activity. With *in-vivo* microscopy of different GB lines an abundant formation of ultra-long membrane protrusions has been shown to infiltrate the normal brain tissue at the invasive front. These membrane tubes have a unique composition and are a potent motility machinery [209] for glioma cells. In Figure 7.5 we can observe the extension of TMs at the tumor front and their invasion into the healthy tissue. Defining the tumor support as $Sup(N) = [0, b_N] \subseteq \Omega$, with $b_N \leq b_\Omega$, the TM region is described as:

$$L_{TM} = \{x \in \Omega \, : \, \exists \alpha \in [0, h_p] \text{ such that } x - \alpha = b_N\}\,, \tag{7.3}$$

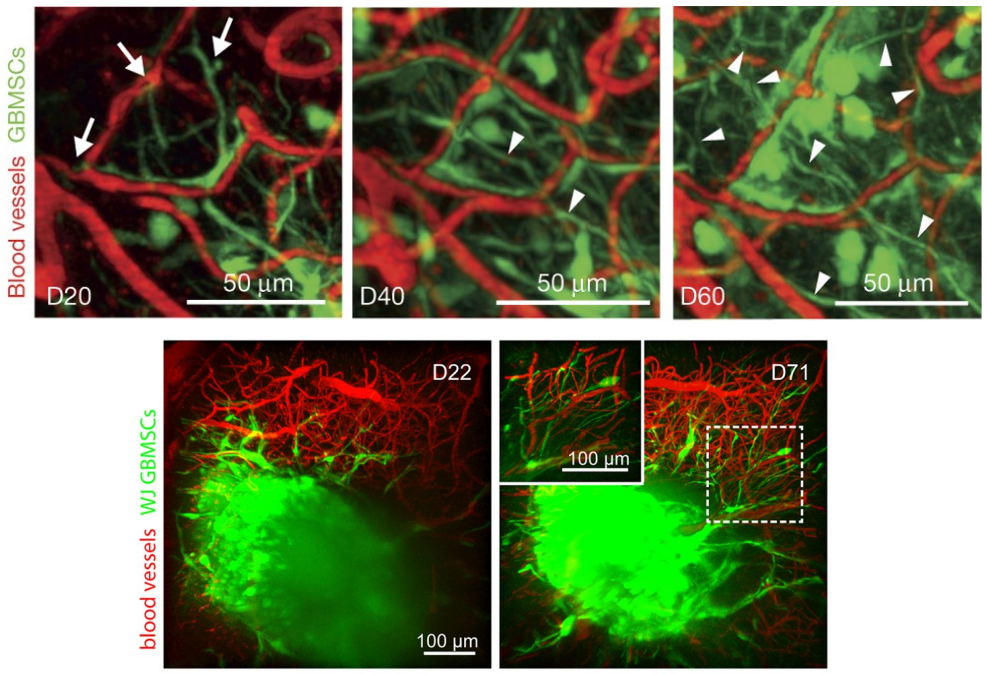

FIGURE 7.5: **Distinct microtubes of brain tumor cells.** *In-vivo* multiphoton laser-scanning microscopy of GBs growing in the mouse brain over 60 days (D) (top row). The arrows indicate thin cell protrusions extending into the normal brain tissue, while the arrowheads show long intratumoral protrusions. *In-vivo* microscopy (3D) reveals the abundant formation of ultra-long membrane protrusions in the mouse brain (bottom row). The inset shows the boxed areas in the corresponding images in higher magnification, covering a proportion of the z-dimension from $200 - 500$ μm depth. Reprinted by permission from Springer Nature Customer Service Centre GmbH: details in [209].

where $h_p \geq 0$ represents the maximum length of a microtube. Then, we define the functional $\mathcal{F}(N)$ describing the tumor activity across the tumor domain as

$$\mathcal{F}(N) = \frac{1}{\left(N * \mathbb{I}[-h_p, h_p] + \epsilon_{\mathcal{F}}\right)^{\alpha_{\mathcal{F}}}} . \tag{7.4}$$

Here, $*$ indicates the convolution operator, $\mathbb{I}[-h_p, h_p]$ the identity function on the interval of the semi-amplitude h_p, and $\epsilon_{\mathcal{F}}, \alpha_{\mathcal{F}} \in \mathbb{R}$ are two parameters used to modulate the tumor activity. These parameters are incorporated into the model on the basis of experimental results and they allow for a better fitting of the model results to the biological data. The presence of such differences in the levels of tumor activity across the domain, which motivate the definition of $\mathcal{F}(N)$, is shown in Figure 7.6.

7.3.2 *GB dynamics and localization of the front*

Initially, we focus on the description of glioma cell dynamics. The first experiments were performed in order to confirm the hypothesis on the co-localization of MMPs and active integrins with the tumor invasion front. These experiments were based on immunostaining with different antibodies of dissected third-instar larval brains with a genetically induced GB. We used anti-MMP antibodies the for proteases analysis, anti-FAK antibodies for the study of integrin activity, and anti-talin antibodies for the analysis of the inactive integrin distribution. To delimitate the front of the tumor, we induced the co-expression of a membrane bound version of the red fluorescent protein

(UAS-myrRFP) and, accordingly, all GB cell membranes were marked in red. Details on the experimental procedure and the materials used are provided in Appendix C. The results of this first immunostaining are shown in Figure 7.6.

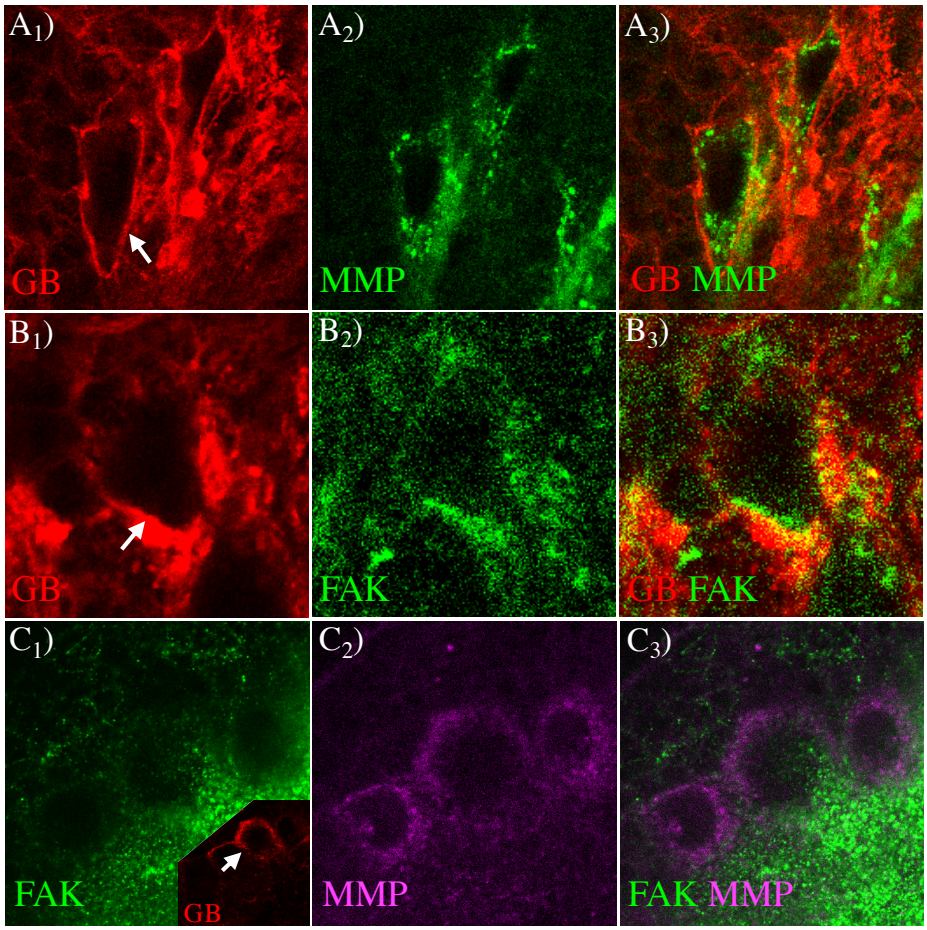

FIGURE 7.6: **Co-localization of MMP and FAK proteins at the GB front.** Fluorescent confocal images of a *Drosophila* third instar larval brain with GB. *A*) Glial membrane is shown in red (A_1), and MMP protein in green (A_2). MMP accumulation at the GB front is observed in the merged image A_3. *B*) Glial membrane (B_1, red) and FAK distribution (B_2, green) signals are shown in the brain sample. FAK accumulation at the GB front is detailed in the merged image B_3. *C*) Co-staining of FAK (C_1, green) and MMP (C_2, magenta) in the merged image (C_3). FAK and MMP signals accumulate in the same region of GB front (inset in C_1 in red). White arrows in the glial membrane images indicate the tumor front, where protein accumulation is observed

In Figures 7.6-A_1, 7.6-B_1, and in the inset of 7.6-C_1, the tumor membrane is marked in red. MMP proteins are represented in Figure 7.6-A_2 in green. The confocal microscopy images show that the MMP signal is heterogeneous throughout the brain and is stronger in specific regions around the GB front, where the marker for the tumor membrane is more expressed[1]. Then, we visualize the integrin activity with a marker for the FAK distribution, as shown in Figure 7.6-B_2 in green. As for MMP, the confocal images show that FAK staining concentrates mostly in the GB front. Finally,

[1]We recall that the red signal marks the cell membrane. Considering that the majority of the TMs are concentrated at the tumor front and they are large extension of the cell membrane, we expect to see a stronger red signal in the tumor front (region of higher tumor membrane density) than in the bulk tumor (region of higher tumor density).

we visualize on the same sample both MMP and FAK distribution to analyze their respective localization. Thus, we co-stain for FAK (Figure 7.6-C_1, green) and MMP (Figure 7.6-C_2, magenta) proteins, and visualize the active front of GB cells (Figure 7.6-C_1, red inset). The confocal fluorescent images show that MMP and FAK signals coincide at the tumor front. These results are compatible with our hypothesis that MMP and FAK are characteristic features of the leading edge of migrating cells, with a central role in the process of GB expansion. Thus, tumor activity results stronger in the TM region.

From the modeling side, we characterize the dynamics of glioma cells using the following equation:

$$\frac{\partial N}{\partial t} = -\frac{\partial}{\partial x}\,\mathcal{J}_N^{\text{tot}}(N,P,A) + \mathcal{P}_N(N)\,,$$

where $\mathcal{J}_N^{\text{tot}}$ indicates the total flux of GB cells, and $\mathcal{P}_N$ refers to the proliferation term. In the specific, we model the total flux of tumor cells by a combination of three main factors, i.e., $\mathcal{J}_N^{\text{tot}}(N,P,A) = \mathcal{J}_{\text{flux-sat}}(N) + \mathcal{J}_{\text{chemo}}(N,P) + \mathcal{J}_{\text{hapto}}(N,A)$. First, the dynamics that $\mathcal{J}_N^{\text{tot}}$ exerts on the cells include a flux-saturated mechanism, allowing to define the movement of a sharp profile [41] and to control propagation speed and porosity of the medium. As we described in Section 7.2,

$$\mathcal{J}_{\text{flux-sat}}(N) := -\nu_N \frac{N^m}{\sqrt{N^2 + \left(\frac{\nu_N}{v_N}\right)^2 \left|\frac{\partial N}{\partial x}\right|^2}} \frac{\partial N}{\partial x}\,. \tag{7.5}$$

Here, v_N stands for tumor speed, while ν_N relates to the viscosity of the medium with respect to the movement of tumor cells. All the parameters $v_N, \nu_N, m \in \mathbb{R}$. Moreover, $\mathcal{J}_N^{\text{tot}}$ collects the information about cell response to the gradient of soluble and insoluble components of the tumor microenvironment. We consider the gradient of MMPs as driving force for the chemotactic process and the gradient of active integrins for the haptotactic process. In fact, MMPs degrade the ECM and create space for the tumor to migrate, while active integrins mediate the attachment process between tumor cells and the ECM. The corresponding fluxes are described in the saturated form introduced in Section 7.2, i.e.,

$$\mathcal{J}_{\text{chemo}}(N,P) = N \frac{a_1}{\sqrt{1 + \left(\frac{\partial P}{\partial x}\right)^2}} \frac{\partial P}{\partial x}\,, \tag{7.6}$$

with chemotactic sensitivity $a_1 \in \mathbb{R}$, and

$$\mathcal{J}_{\text{hapto}}(N,A) = N \frac{a_2}{\sqrt{1 + \left(\frac{\partial A}{\partial x}\right)^2}} \frac{\partial A}{\partial x}\,, \tag{7.7}$$

with haptotactic sensitivity $a_2 \in \mathbb{R}$. Following the idea in [181], here integrins produce an explicit effect on the direction of motion, describing the migration toward the gradient of recognized adhesion sites. However, in contrast to [181], we use a nonlinear form of the haptotactic gradient. This choice permits to optimize the influence on cell dynamics of the measurements of the tactic force along the trajectories, providing nonlinear terms in the corresponding Euler-Lagrange equations (7.6) and (7.7). The proliferation term $\mathcal{P}_N(N)$ describes a logistic growth of glioma cells at rate a_3 and up

to the maximum carrying capacity K_N. This term reads

$$\mathcal{P}_N(N) = a_3 N \left(1 - \frac{N}{K_N}\right) . \tag{7.8}$$

Different improvements of this growth term can be taken into account. In Section 7.4.2, we numerically analyze the effects of heterogenous cell proliferation on the dynamical evolution of the front. Moreover, further improvement such as the influence of morphogenic signaling pathways on tumor proliferation, for instance Sonic Hedgehog (Shh) or Wnt (see [102, 125, 228, 287] for further details) are left as future tasks to address. Combining the described fluxes (7.5)-(7.7) and the proliferation term (7.8) leads to the following equation governing glioma cell evolution:

$$\begin{aligned}\frac{\partial N}{\partial t} =& \nu_N \frac{\partial}{\partial x}\left(\frac{N^m}{\sqrt{N^2 + \left(\frac{\nu_N}{v_N}\right)^2 \left|\frac{\partial N}{\partial x}\right|^2}} \frac{\partial N}{\partial x}\right) \\ &- \frac{\partial}{\partial x}\left(N \frac{a_1}{\sqrt{1 + \left(\frac{\partial P}{\partial x}\right)^2}} \frac{\partial P}{\partial x} + N \frac{a_2}{\sqrt{1 + \left(\frac{\partial A}{\partial x}\right)^2}} \frac{\partial A}{\partial x}\right) + a_3 N \left(1 - \frac{N}{K_N}\right) .\end{aligned} \tag{7.9}$$

Using this modeling approach, we want to show not only the role of MMPs and integrins in glioma motility, but also their co-localization and spatial distributions with respect to the location of the tumor front.

7.3.3 *Protease distribution and ECM dynamics*

MMPs facilitate the tumor invasion process by degrading the extracellular matrix. These enzymes are produced by the tumor cells and released in the extracellular space, mostly in the area around the tumor invasion front where TMs are present in large numbers. This results in an enhanced proteolytic activity in the TM regions. Thus, we propose the localization of the MMP production on the TMs and we model the MMP evolution in relation to the tumor front.

Experimentally, to analyze the MMP distribution in the tumor region, we quantify the MMP signal in the inner GB mass and at the GB border. We visualize *Drosophila* brains with induced GBs (Figures 7.7-A_1 and 7.7-B_1) and immunostained with anti-MMP antibodies (Figures 7.7-A_2 and 7.7-B_2). We quantify the marker signals using a self-developed code in Matlab based on the curve fitting toolbox (further details are provided in Appendix C). The results of these experiments are shown in Figures 7.7-A_3 and 7.7-B_3. Figure 7.7-A refers to a front region of the tumor mass, where the values of the cell membrane density are high (red curve in Figure 7.7-A_3). We observe from the green curve in Figure 7.7-A_3 that MMPs accumulate, showing a peak of concentration in the region corresponding to the TMs. Interestingly, this MMP maximum appears slightly shifted in the direction of GB migration with respect to the peak of the GB membrane density. Figure 7.7-B refers to the analysis of an inner region of the GB mass. The confocal images related to the measurements of MMP and GB densities show homogeneous lower levels of the GB membrane and the MMP protein in this inner region (Figure 7.7-B_1-B_3) compared to the front region (Figure 7.7-A_1-A_3). In the

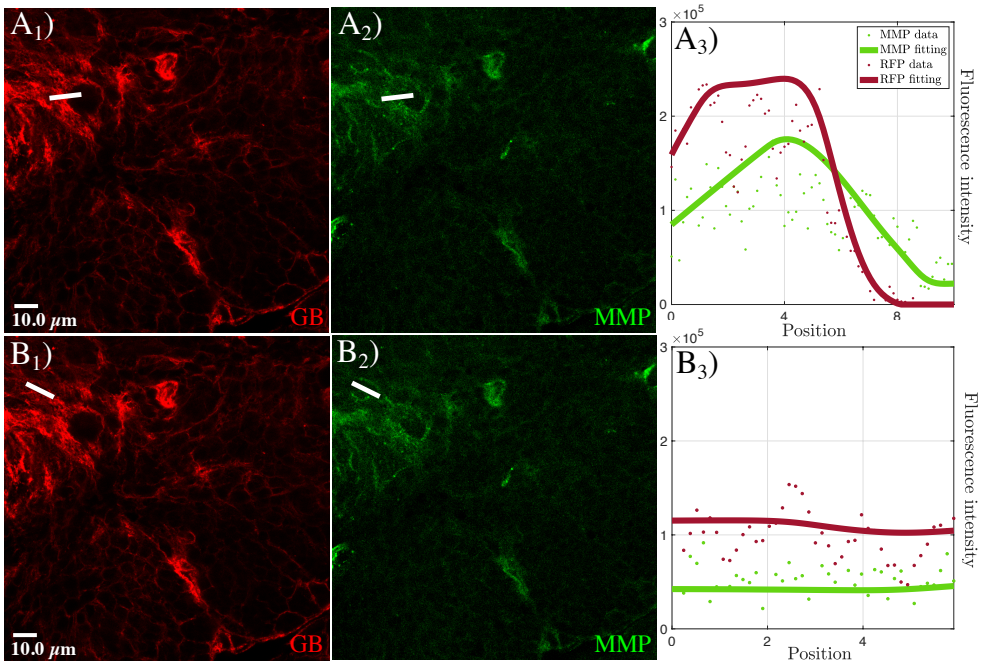

FIGURE 7.7: **MMP accumulation at the GB front and in the inner GB mass.** Fluorescent confocal images of a *Drosophila* third instar larval brain with GB marked with myristoylated-RFP in red (A_1 and B_1), and stained with anti-MMP in green (A_2 and B_2). A_3 and B_3 show the quantification and the graphical representation of the fluorescent intensity for GB and MMP signals along the white lines in A_1, A_2, B_1 and B_2. In A_3 and B_3 the dots represent the data and the lines represent the fitting. A_1-A_3 refer to a front region, while B_1-B_3 to an inner region.

following, we refer to these levels as basal levels. The results of these experiments enforces the idea of an enhanced protein accumulation in the front region of GB and this accumulation correlates with the peaks of the GB cell membrane density. Moreover, we notice that this phenomenon is not observed in inner tumor areas.

To mathematically model the dynamics and the distribution of MMPs, we take into account three main phenomena, collected in the following equation

$$\frac{\partial P}{\partial t} = -\frac{\partial}{\partial x}\,\mathcal{J}_P(P) + \mathcal{P}_P(N,E) - \mathcal{D}_P(P,N)\,.$$

We describe MMP production by tumor cells with the term $\mathcal{P}_P$, which is used to localize the production in the TM region, where the neoplastic tissue is in contact with the healthy tissue. Moreover, the proliferation term is directly dependent on the functional (7.4) describing the heterogeneous proteolytic activity of tumor cells. Precisely,

$$\mathcal{P}_P(N,E) = a_4\, E\, \mathcal{F}(N)\chi_{L_{TM}}\,,$$

where a_4 is the production rate and the functional $\mathcal{F}(N)$ is used to spatially weight the proliferation term. Moreover, $\chi_{L_{TM}}$ is the characteristic function of the TM region. After MMP production and release in the extracellular space, these enzymes diffuse in the ECM. In order to limit the MMP flux to the areas surrounding the tumor mass and to generate a sharp front of MMP ahead of the tumor, we model $\mathcal{J}_P$ by means of

a flux-saturated mechanism analogous to the flux term used for the cancer cells, i.e.,

$$\mathcal{J}_P(P) = -\nu_P \frac{P^m}{\sqrt{P^2 + \left(\frac{\nu_P}{v_P}\right)^2 \left|\frac{\partial P}{\partial x}\right|^2}} \frac{\partial P}{\partial x}\,.$$

Here, v_P is the speed of MMPs and ν_P the viscosity related to MMP diffusion. As the tumor front advances, the proteases that remains inside the tumor mass are degraded, but a basal level of MMP is maintained in the inner tumor regions. This degradation, with rate a_5, is described as

$$\mathcal{D}_P(P, N) = -a_5\, P\, N\,.$$

In particular, the preserved inner basal level of these proteins is related to the normal proteolytic activity of the cells in the inner tumor and is not directly aimed at sustaining the migration process. The overall equation governing the evolution of MMPs reads

$$\frac{\partial P}{\partial t} = \nu_P \frac{\partial}{\partial x}\left(\frac{P^m}{\sqrt{P^2 + \left(\frac{\nu_P}{v_P}\right)^2 \left|\frac{\partial P}{\partial x}\right|^2}} \frac{\partial P}{\partial x}\right) + a_4\, E\, \mathcal{F}(N)\chi_{L_{TM}} - a_5\, P\, N\,. \tag{7.10}$$

MMP evolution is strictly connected to the dynamics of the ECM and we describe the ECM degradation process due to the MMP proteolytic activity as

$$\frac{\partial E}{\partial t} = -\mathcal{D}_E(E, P)\,, \tag{7.11}$$

where, the degradation term is described as $\mathcal{D}_E(E, P) = a_6\, E\, P$ with the degradation rate a_6. Since, after the degradation process, some residual ECM material partially remains in the inner tumor region, we include in the model a basal level of ECM inside the main tumor mass.

7.3.4 *Integrin dynamics and distribution*

Integrins are transmembrane receptors located on the cell membrane. After activation, integrins mediate cell migration. If the receptors are not bound to the ECM, we refer to them as inactive integrins, otherwise we call them active integrins. In the tumor cells, the activation process occurs predominantly in the TM region, and active integrins are homogeneously distributed throughout the TMs. Moreover, the conversion into the inactive (not bound) state occurs in the proximal region of the TMs with respect to the main GB mass, as shown by our experimental and mathematical results.

To determine the molecular changes at the GB front in relation to the activity of integrins, we immunostained GB brain samples with talin, a mediator of integrin adhesion [144], and with FAK, a kinase involved in cytoskeleton dynamics associated to integrin activity [89, 179]. We analyze confocal microscopy images of different GB front regions, comparing fronts with low or high GB membrane signal. The results of this analysis are shown in Figure 7.8. Here, the top row refers to a low GB membrane signal, while the bottom row refers to a high GB membrane signal. The quantification of the signals for anti-talin and anti-FAK in Figure 7.8 shows that talin (black curve in Figures 7.8-A_4 and 7.8-B_4) decreases in the TM region, i.e., where the GB membrane signal is higher, while FAK (magenta in Figures 7.8-A_4 and 7.8-B_4) increases. This

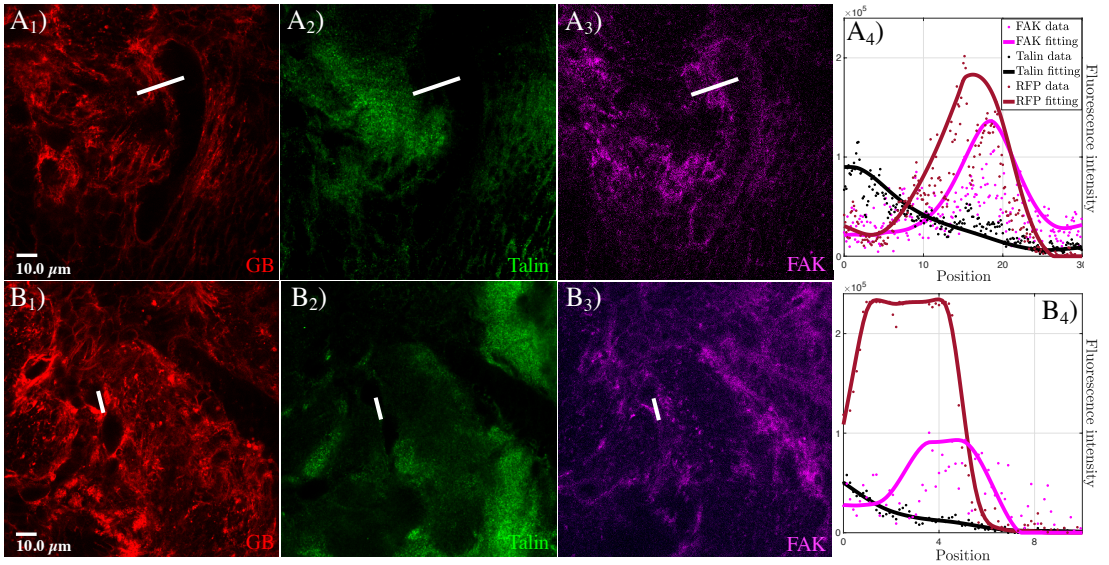

FIGURE 7.8: **Talin and FAK dynamics in the transition between GB front and healthy tissue.** Fluorescent confocal images of a *Drosophila* third instar larval brain with GB marked with myristoylated-RFP in red (A_1 and B_1), and stained with anti-talin (in green) and anti-FAK (in magenta) (A_2, A_3, B_2 and B_3). A_4 and B_4 show the quantification of the fluorescent signals and the graphical representation of the fluorescent intensity for GB, talin, and FAK signals along the white lines shown in the images A_1-A_3 and B_1-B_3. In A_4 and B_4 the dots represent the data and the lines represent the fitting.

means that talin and FAK expressions are inverted at the front, which is consistent with the relation between the two integrin subpopulation of active and inactive receptors. Additionally, GB membrane signal and FAK signal correlate. The GB/FAK correlation is maintained in different fronts, irrespective of their low (Figure 7.8-A) or high (Figure 7.8-A) level of GB membrane signal.

To confirm the inverse correlation between talin and FAK, we compared the measurements preformed in the inner GB mass and in GB front areas. The results are shown in Figure 7.9. The inner region of the GB mass in Figure 7.9-A has a higher talin levels (Figure 7.9-A_2) and lower FAK signal (Figure 7.9-A_3), as quantified in Figure 7.9-A_4. In line with our previous results, the relative concentration of talin and FAK is inverted in the front region of the GB samples, represented in Figure 7.9-B. The results indicate that talin concentration drops significantly (Figure 7.9-B_2 and B_4) and correlates with an increase of the FAK signal at the GB front (Figure 7.9-B_3 and B_4). These observations confirm that talin and FAK maintain an inverse correlation and they can be considered indicators of the migratory status of the GB cells.

Mathematically, we split the integrin population into two subpopulations, referring to the active $A(t,x)$ and the inactive $I(t,x)$ state of the integrin receptors. It is worth noticing that the former subfamily is responsible for the haptotactic movement of tumor cells. The corresponding dynamics for active integrins takes into account integrin activation, integrin inactivation and a flux term and reads

$$\frac{\partial A}{\partial t} = \mathcal{A}(E,I,N) - \mathcal{I}(A,N) + \mathcal{J}_A\,.$$

We model the binding between GB cells and the ECM through binary interactions of inactive integrins and the ECM at rate a_7. The binding depends on the heterogenous tumor activity and, thus, we weight this process with the functional $\mathcal{F}(N)$ defined in

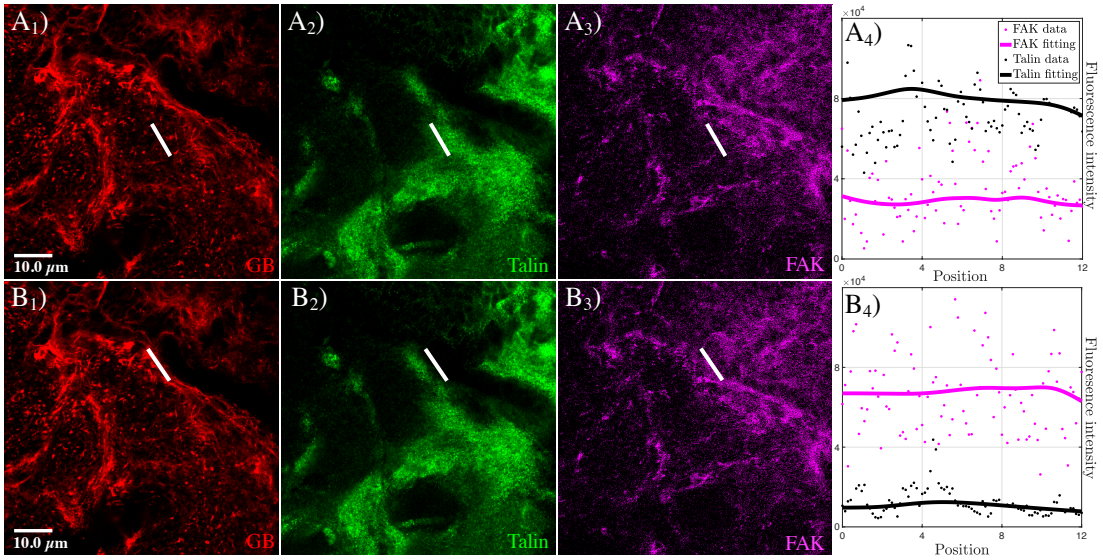

FIGURE 7.9: **Talin and FAK dynamics: comparison between the inner GB mass and the GB front.** Fluorescent confocal images of a *Drosophila* third instar larval brain with GB marked with myristoylated-RFP in red (A_1 and B_1), and stained with anti-talin in green and anti-FAK in magenta (A_2, A_3, B_2 and B_3). A_4 and B_4 show the quantification of the fluorescent signals and the graphical representation of the fluorescent intensity for GB, talin and FAK signals along the white lines shown in A_1-A_3, B_1-B_3. In A_4 and B_4 the dots represent the data and the lines represent the fitting.

(7.4), which supports the activation in the TM region, where tumor cells are in contact with the ECM. The term modeling integrin activation reads

$$\mathcal{A}(E, I, N) = a_7 \, E \, I \, \mathcal{F}(N) \, .$$

Once the tumor has crawled on the ECM and moved forward, inactivation occurs at rate a_8, namely

$$\mathcal{I}(A, N) = a_8 \, A \chi_{Sup(N)} \, .$$

Here, $\chi_{Sup(N)}$ represents the characteristic function of the support of N. Integrins are also subjected to a flux term describing the transport process due to the movement of GB cells. In fact, since integrin receptors are locate on the cell membrane, the receptors themselves are also transported during the process of cell migration, determining a flux of active and inactive integrins with estimated velocities (v_A and v_I) depending on the tumor one. Precisely, since we model the dynamics of the bulk tumor, these transport terms allow us to translate the tumor dynamics to the front, where the interaction between integrins and the ECM occurs. This transport term for the active subpopulation is given by

$$\mathcal{J}_A = v_A \frac{\partial A}{\partial x} \, . \tag{7.12}$$

The transport velocity v_A is defined through a nonlinear functional relationship that depends on the evolution of N, i.e., $v_A = v_A[N]$. This functional describes the propagation rate of the support of N by means of its evolution equation.

Concerning inactive integrins, apart from the attachment and detachment terms characterizing the dynamic interactions between the two subpopulations, we model the process of integrin production by exocytosis and the transport term J_I. Assuming that, initially, the inactive integrins on the cell membrane have not reached their

saturation value K_I, integrin production is described with the following term $\mathcal{P}_I$

$$\mathcal{P}_I = a_9 \left(K_I - A - I\right)(\chi_{L_{TM}} + \chi_{Sup(N)}) \,,$$

with the proliferation rate a_9, while the transport term $\mathcal{J}_I$ in the dynamics of inactive integrins that reads

$$\mathcal{J}_I = v_I \frac{\partial I}{\partial x} \,.$$

This term is analogous to (7.12) and we assume that $v_I = v_A$. Therefore, the equation for inactive integrin dynamics reads

$$\frac{\partial I}{\partial t} = -\mathcal{A}(E, I, N) + \mathcal{I}(A, N) + \mathcal{J}_I + \mathcal{P}_I \,.$$

With this choice, the dynamics of the whole population of integrin receptors $(A + I)$ will be governed by a transport term, with velocity corresponding to the front propagation rate, and the exocytosis process. In addition, considering the experimental results shown in the Figure 7.9, we include a basal level of active integrins in the inner tumor regions and a basal level of inactive integrins along the microtubules.

As we introduced in Chapter 1 and in Section 7.1, our interest in the role of integrins and proteases as key mechanisms of tumor progression arises from a series of experiments [106, 191, 201]. To confirm the functional contribution of integrins to GB progression, we used specific RNAi constructs to knockdown *myospheroid (mys)*, the *Drosophila* integrin B subunit, or *rhea*, the *Drosophila* talin. The results are shown in Figure 7.10. The data show that GB cells require integrins to progress and expand (Figure 7.10 A-C). Moreover, *mys* or *rhea* knockdown reduces the lethality caused by GBs, as it can be noticed in Figure 7.10-D.

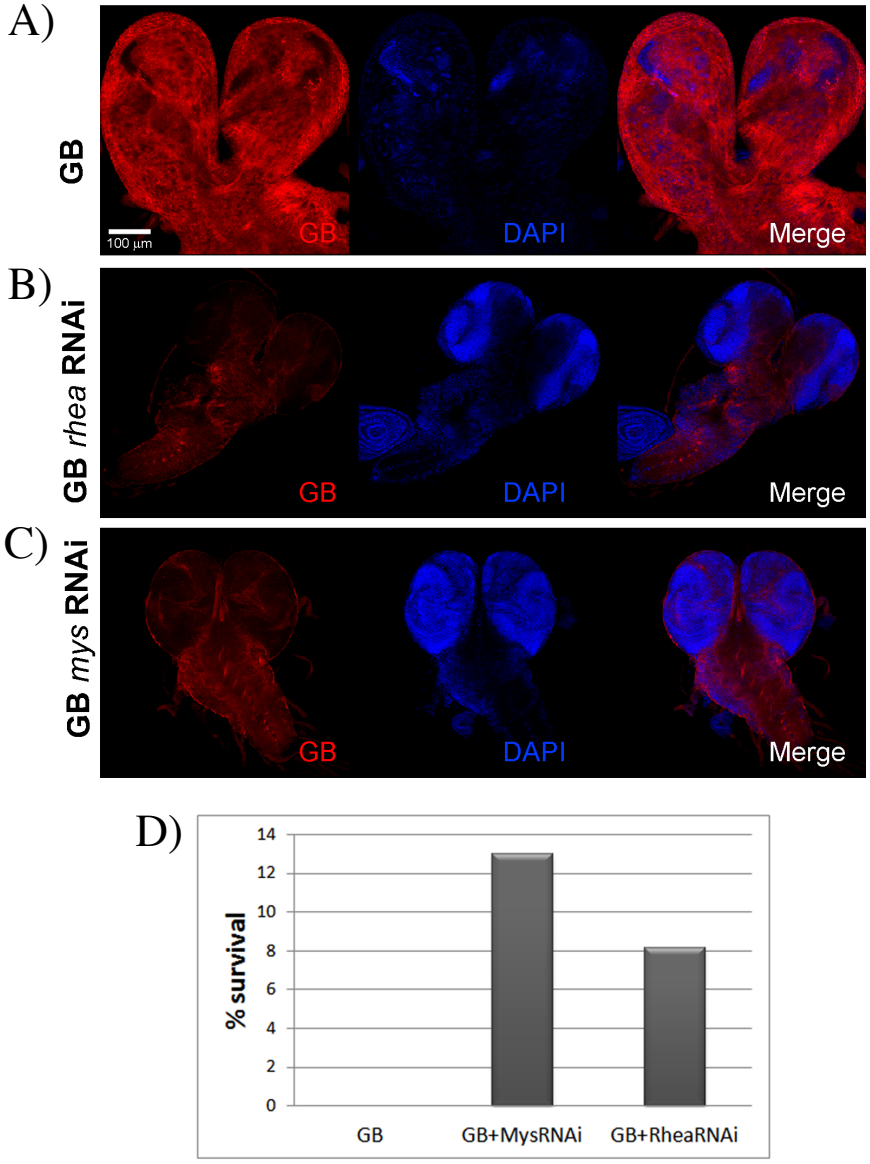

FIGURE 7.10: **Functional integrins are required for GB progression.** Low magnification confocal images of a *Drosophila* GB larval brain in A) and *rhea* knockdown (UAS-*rhea* RNAi) in B), and *mys* knockdown (UAS-*mys* RNAi) in C). The GB cell membrane is marked with myristoylated-RFP (in red) and neurons nuclei are marked with DAPI (in blue). The images show that *rhea* or *mys* knockdown prevents the expansion of GB and reduces the lethality. The percentage of cell survival with the different knockdowns is shown in D).

7.3.5 *Motility features of GB cells at the front*

We perform further analysis to characterize in more details the motility features of the tumor cells at the front in relation to the distribution of proteases and integrins. This analysis is aimed at supporting our hypothesis on the processes leading cell motility. Thus, experimentally, we analyze MMP concentration and focal adhesions distribution as cues for cell motility, invasiveness, and migration [62, 124]. We co-stained GB brain samples with anti-MMP and anti-FAK (Figure 7.11) and quantified the intensity of the fluorescent signals, comparing them for low and high tumor density fronts, shown in Figures 7.11-*A* and 7.11-*B*, respectively.

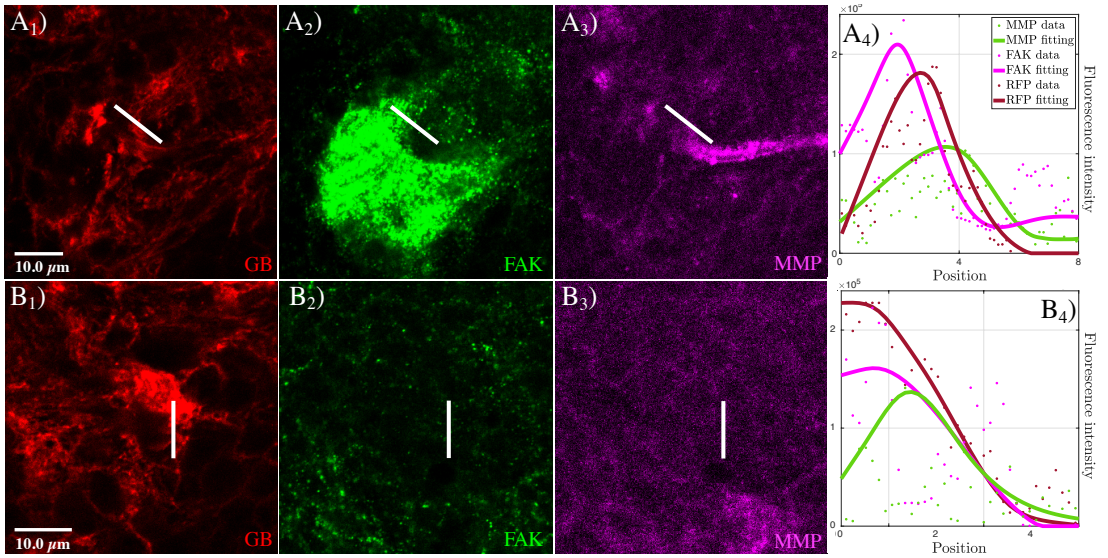

FIGURE 7.11: **FAK and MMP dynamics in the transition between GB front and healthy tissue.** Fluorescent confocal images of a *Drosophila* third instar larval brain with GB marked in red (A_1 and B_1), and stained with anti-FAK (green) and anti-MMP (magenta) (A_2, A_3, B_2 and B_3). A_4 and B_4 show the quantification of the fluorescent signals and the graphical representation of the fluorescent intensity for GB, FAK, and MMP signals along the white lines shown in the images A_1-A_3 and B_1-B_3. In A_4 and B_4 the dots represent the data and the lines represent the fitting.

The results quantified in Figures 7.11-A_4 and 7.11-B_4 show that, at the GB front (Figures 7.11-A_1 and 7.11-B_1), the maximum signal for FAK (Figures 7.11-A_2 and 7.11-B_2) occurs before the peak of MMP (Figures 7.11-A_3 and 7.11-B_3). This correlation occurs for both types of GB fronts, suggesting that this phenomenon is not a consequence of higher or lower GB membrane density. These results point towards a coordinated function between MMP activity and FAK dynamics and suggest that, at the front, FAK acts closer to GB mass than MMP. In contrast to that, MMP plays its role further away from the front. Mechanistically, these results indicate that MMP activity in the proteolysis of the ECM is prior to the increase of integrin dynamics, it is associated with the presence of FAK, and, thus, together they contribute to the motility of GB cells.

7.4 *Modeling results*

The whole system of five coupled differential equations we built on the basis of the experimental results reads:

$$
\begin{cases}
\dfrac{\partial N}{\partial t} = \nu_N \dfrac{\partial}{\partial x}\left(\dfrac{N^m}{\sqrt{N^2 + \left(\dfrac{\nu_N}{v_N}\right)^2 \left|\dfrac{\partial N}{\partial x}\right|^2}} \dfrac{\partial N}{\partial x}\right) \\
\qquad - \dfrac{\partial}{\partial x}\left(N \dfrac{a_1}{\sqrt{1 + \left(\dfrac{\partial P}{\partial x}\right)^2}} \dfrac{\partial P}{\partial x} + N \dfrac{a_2}{\sqrt{1 + \left(\dfrac{\partial A}{\partial x}\right)^2}} \dfrac{\partial A}{\partial x}\right) + a_3 N \left(1 - \dfrac{N}{K_N}\right), \\
\dfrac{\partial P}{\partial t} = \nu_P \dfrac{\partial}{\partial x}\left(\dfrac{P^m}{\sqrt{P^2 + \left(\dfrac{\nu_P}{v_P}\right)^2 \left|\dfrac{\partial P}{\partial x}\right|^2}} \dfrac{\partial P}{\partial x}\right) + a_4 E \mathcal{F}(N) \chi_{L_{TM}} - a_5 P N, \\
\dfrac{\partial E}{\partial t} - = -a_6 E P, \\
\dfrac{\partial A}{\partial t} = a_7 E I \mathcal{F}(N) - a_8 A \chi_{Sup(N)} + v_A \dfrac{\partial A}{\partial x}, \\
\dfrac{\partial I}{\partial t} = -a_7 E I \mathcal{F}(N) + a_8 A \chi_{Sup(N)} + v_I \dfrac{\partial I}{\partial x} + a_9 (K_I - A - I)(\chi_{L_{TM}} + \chi_{Sup(N)}).
\end{cases}
\tag{7.13}
$$

The evolution of the tumor population is coupled with the dynamics of proteases, integrins and ECM and, while GB cells, proteases, and active integrins are assumed to have both a temporal and a spatial evolution, ECM and inactive integrins only evolve temporally, with ODEs characterizing their dynamics. We analyze the evolution of the system and the emergence of specific evolutionary patterns in the TM region in Section 7.4.2. We also show additional numerical results focused on possible improvements of the model setting. Before presenting the numerical simulations of (7.13), in the next section we provide a detailed analysis of the parameter estimation.

7.4.1 *Parameter estimation*

We scale the five populations of system (7.13) with respect to their carrying capacities (K_N for tumor cells and K_I for integrins) or with respect to their typical concentrations/densities ($\hat{P}$ for proteases and $\hat{E}$ for ECM). We estimate the values for the parameters involved in the macroscopic setting. Keeping in mind that the experimental data we use for the comparison of our results are performed in a *Drosophila* model of GB, we adapt some of the values found in the literature to our particular cases. We dedicate a particular attention to the estimation of the parameters involved in the flux-saturated terms, i.e., speed and viscosity for both tumor cells and proteases, and to the carrying capacities of tumor cells and integrin receptors.

Speed and viscosity parameters: v_N, v_P, ν_N, ν_P

The maximum value reported in the literature for glioma cell speed in humans is 50 μm $\cdot$ h^{-1} [194]. Considering that our biological experiments are performed in a *Drosophila* model of GB, we need to deduce the value for the tumor speed v_N from the reported value. Therefore, we use the Stokes law that describes the frictional force F_d exerted on spherical objects of radius R with very small Reynolds numbers in a viscous fluid of dynamic viscosity μ. We recall that the Reynolds number represents the ratio of inertial forces to viscous forces within a fluid subjected to internal movement due to different fluid velocities. This number quantifies the relative importance of these two types of forces for given flow conditions. The Stokes law reads

$$F_d = 6\pi\mu\, R\, v \tag{7.14}$$

with the flow velocity v relative to the spherical object. Consequence from this is the relation between velocity v and radius R

$$v = \frac{2(n_p - n_f)}{9\mu}\, g\, R^2\,,$$

where n_p and n_f are the mass densities of the particles and the fluid, respectively, and g the gravitational field strength [157]. Considering that the average size of a human GB cell is $12 - 14$ μm [81], while for a GB cell in *Drosophila* this value drops to 5 μm (measurements taken from our experiments), we deduce the range $[6.4, 8.7]$ μm $\cdot$ h^{-1} for the parameter v_N. We notice that our model is built assuming a strong relation between MMPs and GB cells, in terms of their respective locations and the influence of one population on the other, and there is a lack of experimental data about protease propagation speed in the brain. For these reasons, we assume $v_P = v_N$.

For the tumor viscosity ν_N, we refer to [287], where an analogous description of the flux-saturated mechanism is used to model the dynamics of the protein Shh in *Drosophila*. In [287], the authors consider Shh aggregates moving along a protrusion. They consider the speed $v_{Shh} = 4.68 \cdot 10^{-3}$ mm $\cdot$ h^{-1} and the kinematic viscosity $\nu_{Shh} = 1.8 \cdot 10^{-3}$ mm$^2 \cdot$ h^{-1} for these Shh aggregates. We observed in Section 7.2 that, apart from the propagation speed, in the development of the invasion profiles characterizing the flux-saturated operator the ratio $\frac{\nu}{v}$ plays a key role. Thus, from [287] we deduce the information that $\frac{\nu_{Shh}}{v_{Shh}} = 0.4$ mm and we obtain $\nu_N \in [0.256, 0.348] \cdot 10^{-2}$ mm$^2 \cdot$ h^{-1}.

To deduce the protease viscosity ν_P, considering the similarity in size between the two proteins MMP and Shh, we use the Stokes-Einstein equation for diffusion of spherical particles [70]. For a spherical particle of radius R moving with uniform velocity in a continous fluid of viscosity μ, the frictional coefficient is given by $f_0 = 6\,\pi\,\mu\,R$, such that the Stokes law in (7.14) reads $F_d = f_0\, v$. Assuming that this result applies also to spherical molecules, the kinematic viscosity reads

$$\nu = \frac{\mathcal{K}\,\mathcal{T}}{6\,\pi\mu\,R} \tag{7.15}$$

with the Boltzmann constant $\mathcal{K}$ and the temperature $\mathcal{T}$ (in K). Moreover, considering that a vesicle containing Shh and moving along a cell protrusion has a radius of

$R_{Shh} \in [10, 100]$ nm and inserting this information in equation (7.15), we get the following estimation

$$\frac{\mathcal{K}\mathcal{T}}{6\,\pi\mu} = \nu_{Shh}\, R_{Shh} = 0.18 \cdot [10^{-7}, 10^{-6}] \text{ mm}^3 \cdot \text{h}^{-1}.$$

One molecule of MMP has a radius of $R_P = 0.066 M_P^{1/3}$ [79], with R_P expressed in nm and the mass M_P in Da. From [193], we know that $M_P \in [72, 92]$ kDa, therefore

$$R_P \in [2.75, 2.98] \cdot 10^{-6} \text{ mm}$$

and

$$\nu_P = \frac{\mathcal{K}\mathcal{T}}{6\,\pi\,\mu\,R_P} = \frac{0.18 \cdot [10^{-7}, 10^{-6}] \text{ mm}^3 \cdot \text{h}^{-1}}{[2.75, 2.98] \cdot 10^{-6} \text{ mm}}$$

$$= [0.34, 0.36] \cdot [10^{-2}, 10^{-1}] \text{ mm}^2 \cdot \text{h}^{-1}.$$

We set $\nu_P = 0.035$ mm$^2 \cdot$ h^{-1}.

Carrying capacities: K_N, K_I, ν_N, ν_P

The carrying capacity of tumor cells is estimated considering the mean diameter of a GB cell in *Drosophila*, i.e., 5 μm. This leads to an order of magnitude for the carrying capacity of K_N of approximately 10^6 cells $\cdot$ mm^{-3}.

For the integrin capacity, considering that there are approximately 10^5 integrin receptors per cell [15], we estimate a maximum of almost 10^{10} integrins $\cdot$ mm^{-3}.

Table 7.1 reports the values of the model parameters and the reference values used for the scaling. For some of the parameters, for which a large range of possible values is available, we indicate both the range and the exact value used in the simulations.

7.4.2 *Numerical results*

From the numerical viewpoint, we solve the whole system of partial differential equations (7.13) coupled with no flux boundary conditions and suitable initial conditions for the five populations. The initial conditions are displayed in Figure 7.12-*A* and are described below. The model was numerically solved with a self-developed code in Matlab (MathWorks Inc., Natick, MA). For the spatial discretization, we considered the Galerkin method on a spatial grid of 500 points. In particular, the flux-saturated terms were discretized using an IMEX version of the Galerkin scheme. Moreover, for the time discretization, we used an implicit Euler scheme for proteases and tumor equations, while a fourth-order Runge-Kutta method for the other involved populations over a total of $15 \cdot 10^6$ time points, with $\delta t = 10^{-6}$. This allows us to simulate the system evolution over 15 h. Details about the employed numerical methods are provided in Appendix B. For the numerical simulations presented in this section, we set the value $m = 1$ for the parameter involved in the flux-saturated terms.

The numerical tests are focused on showing specific features that characterize the developed setting:

(1) we numerically solve (7.13), with the parameters listed in Table 7.1 and we compare the numerical and the experimental results in term of development of invasion profiles for GB cells, integrins, and proteases;

Parameter	Description	Value (unit)	Source
ν_N	tumor viscosity	$[0.256, 0.348] \cdot 10^{-2}$ (mm$^2 \cdot$ h^{-1}) used value: 0.00348	see description
v_N	tumor speed	$[0.64, 0.87] \cdot 10^{-2}$ (mm $\cdot$ h^{-1}) used value: 0.0087	see description
a_1	chemotactic sensitivity	0.001 (mm$^2 \cdot$ h^{-1})	[139]
a_2	haptotactic sensitivity	0.0036 (mm$^2 \cdot$ h^{-1})	[139]
a_3	tumor proliferation rate	0.0345 (h^{-1})	[193]
K_N	tumor carrying capacity	10^6 (cells $\cdot$ mm^{-3})	see description
ν_P	MMPs viscosity	0.035 (mm$^2 \cdot$ h^{-1})	see description
v_P	MMPs speed	$[0.64, 0.87] \cdot 10^{-2}$ (mm $\cdot$ h^{-1}) used value: 0.0087	see description
a_4	MMPs production rate	$[3.6, 180]$ (h^{-1}) used value: 3.6	[153]
a_5	MMPs degradation rate	$[0.18, 18]$ (h^{-1}) used value: 18	[142]
a_6	ECM degradation rate	4.5 (h^{-1})	[206, 252]
a_7	integrin activation rate	$[1, 3] \cdot 36$ (h^{-1}) used value: 108	[161]
a_8	integrin inactivation rate	36 (h^{-1})	[161]
a_9	integrin exocytosis rate	$[0.36, 36]$ (h^{-1}) used value: 0.72	[67]
K_I	integrins carrying capacity	10^{10} (integrins $\cdot$ mm^{-3})	see description
$\hat{E}$	ECM reference value	10^{-3} (mg $\cdot$ mm^{-3})	[142]
$\hat{P}$	protease reference value	10^{-7} (mg $\cdot$ mm^{-3})	[142]

TABLE 7.1: **Dynamics at the leading edge of glioblastomas: model parameters.**

(2) we analyze the influence of the chemotactic process on the development of the invasion front and we show possible divisions of this front into two separated parts;

(3) we hypothesize two possible mechanisms of heterogeneous proliferation, testing them in a scenario with two separated invasion fronts;

(4) we analyze the effects on the tumor profile of possible changes in the porosity of the medium.

Starting from the analysis in **(1)**, we present the results of the evolution of system (7.13) after $t = 15$ h in Figure 7.12. The results show how the model is able to predict that the region of greatest interest for the whole GB development process is the front area where TMs are located (marked with a thick red line in Figure 7.12). These

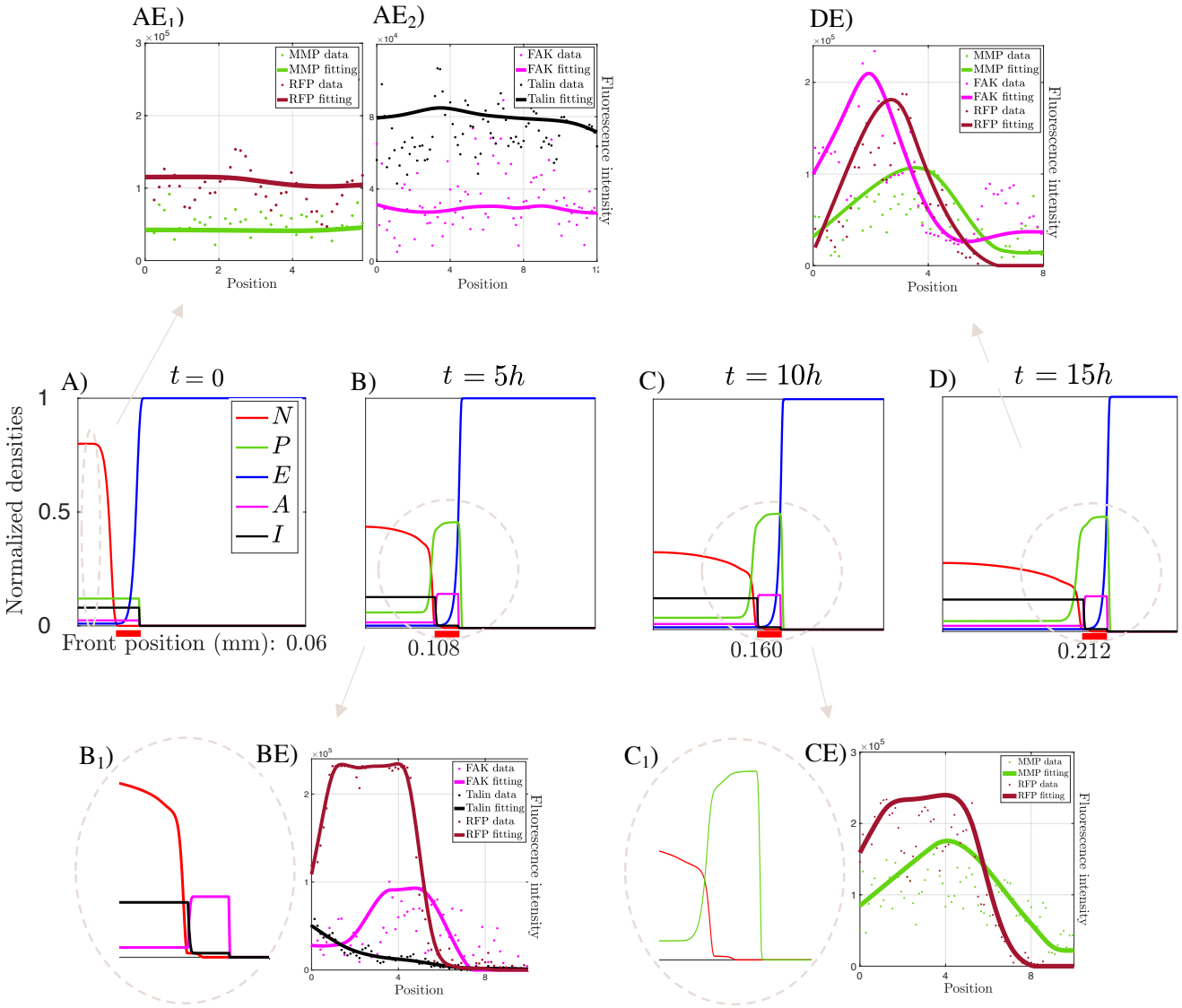

FIGURE 7.12: **Test (1): simulation results of system (7.13).** $A)$, $B)$, $C)$ and $D)$ are four snapshots of the numerical solution of our model at the initial state, after 5, 10, and 15 hours, respectively. The images show the evolution of tumor density (N), ECM (E), active (A) and inactive (I) integrins and MMPs (P). The thick red line below the figures indicates the front area with the highest concentration of TMs. Images $AE_1)$, $AE_2)$, $BE)$, $CE)$ and $DE)$ show the results of the analysis of the experimental data. Peaks in the RFP distribution indicate areas with high tumor membrane density, i.e., the TM regions, while analogous peaks in the numerical simulations refer to high tumor density areas, i.e., the main tumor mass. The images $B_1)$ and $C_1)$ are a magnification of the indicated regions and these images are correlated with the experimental data BE and CE, respectively. The parameters used in these simulations are listed in Table 7.1.

results also support the hypothesis that there is a collaborative relationship between the different agents for the generation and evolution of the migratory patterns characterizing the TM region. Precisely, Figure 7.12-A shows the initial conditions of the system. In particular, we choose a constant initial level for proteases, active and inactive integrins, taking these values from the experimental results shown in Sections 7.3.3 and 7.3.4. Figure 7.12-A is accompanied by the quantifications of the basal levels of MMPs with respect to the tumor density (Figure 7.12-AE_1), and the analogous

quantification of the active versus the inactive integrins (Figure 7.12-AE_2). In both cases, as we described previously, the measurements are taken in areas inside the bulk tumor (see Figure 7.7-B_1 and 7.9-A_1 for the localizations of the measurements). Figures 7.12-B and 7.12-C show the evolution after 5 and 10 hours, respectively. These numerical simulations show how the model predicts specific invasion profiles for the front evolution of each agent involved in the migration process. Precisely, Figures 7.12-B and 7.12-C first illustrate how the model collects the exchange between the active and inactive integrins (magenta and black curve, respectively) at the beginning of the tumor front area. This feature corresponds to the experimental results shown in Figure 7.12-BE. Moreover, a plateau-like profile arises for the active integrin population in the TM region. This reflects the idea that, along the TMs actively involved in the migration process, we expect to notice a homogenous distribution of active receptors. In addition, comparing Figure 7.12-B_1 with Figure 7.12-BE, we notice that the numerical results show a good agreement with the experimental data. Moreover, in Figures 7.12-B and 7.12-C the model predictions regarding the MMP front show a good correlation with the results obtained experimentally and shown in Figure 7.12-CE. MMP evolution is characterized, in fact, by an increased concentration along the TM region, indicating an enhanced tumor proteolytic activity in this area. Besides, MMPs show a steep profile in the direction of tumor migration. Besides, we observe that the MMP external front is slightly shifted with respect to the tumor front region. Although MMPs are produced along the protrusions, they are not located on the membrane (as the integrin receptors), but they are released in the extracellular space and can spread in the areas around the tumor front. Finally, in Figure 7.12-D we show the situation of the invasion patterns after 15 hours of tumor evolution. Figures 7.12-B, 7.12-C and 7.12-D show how the MMP and integrin invasion patterns are maintained over time. Moreover, we compare the experimental results in Figure 7.12-DE, about the motility features characterizing the GB front, with the simulation in Figure 7.12-D. Both numerical and experimental results show the distributions of GB, active integrins, and protease and highlight how these agents co-localize in the TM region. The results also show a displacement of the MMP distribution with respect to active integrin and tumor membrane distribution. We remark that the peaks in the GB membrane distribution in the experimental data indicate areas with high tumor membrane density, i.e., the TM regions, while analogous peaks of the red curve (for the tumor population) in the numerical simulations refer to high tumor density areas, i.e., the main tumor mass. In these simulations, the TM region is accentuated by the thick red line below the different plots. The previous considerations about the relative positions of GB front, MMP, and integrins can be seen as an indicator of the direction of tumor migration. In Figure 7.12-A-D we also indicate the position of the tumor front at the different time steps. We can notice that the tumor front speed never exceeds the estimated value v_N. For the simpler equation (7.1), when $m = 1$, we analytically know that the propagation speed is exactly v. For system (7.13), although we keep $m = 1$ in the simulations, the propagation speed is slightly lower than v_N. However, we notice that in our equations several additional terms are influencing the overall speed. We will address the issues of obtaining an analytical estimation of the relation between v_N and the overall tumor speed as future work.

As a second test, we analyze the influence of the chemotactic mechanism on the evolution of the invasion front, as described in **(2)**. Precisely, we reduce the system (7.13) to take into account only the evolution of tumor cells, proteases, and ECM, and also neglect the proliferation term in the tumor equation. Thus, we work with a diffusion-transport equation for N, where chemotaxis alone controls the drift, and the two equations (7.10) and (7.11) for proteases and ECM, respectively. We carry out

this analysis focusing on the chemotactic mechanisms, but analogous results can also be obtained considering the haptotactic process. In Figure 7.13 we analyze how different values of the chemotactic sensitivity a_1 can provide a different evolution of the invasion front and lead to a possible separation of the latter.

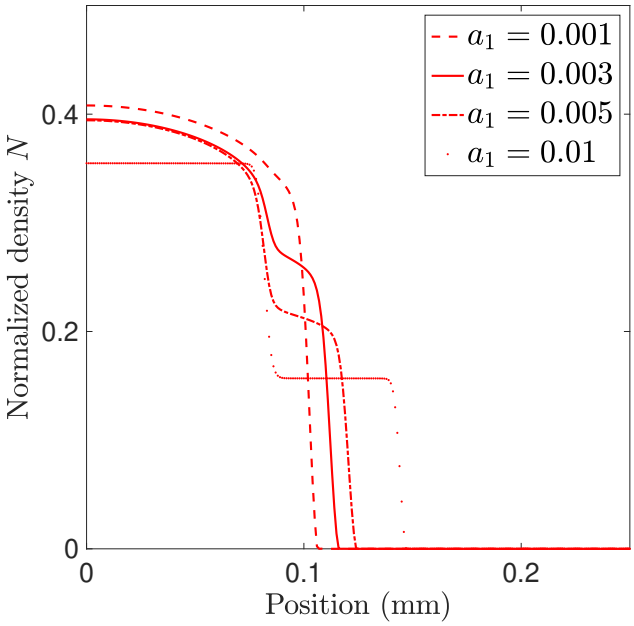

FIGURE 7.13: **Test (2): effects of chemotaxis strength on tumor profile.** The evolution of the tumor profile is shown after 5 hours of simulation for different values of the chemotactic sensitivity a_1.

Since the proteolytic activity and, consequently, the concentration of MMP is enhanced in the front area, the stronger the parameter a_1, the more evident the localization of the tactic effect. Tumor cells closer to the front acquire an increased overall speed (due to both $\mathcal{J}_{\text{flux-sat}}$ and $\mathcal{J}_{\text{chemo}}$ fluxes) which leads to a heterogenous front. Eventually, this process can determine the break of the tumor in two separated masses. This heterogeneity in the front can be observed experimentally, as shown in Figure 7.14. In this figure, neuron nuclei are marked in blue with DAPI, while the GB cell membrane is marked with mystoylated-RFP in red. Higher intensities of the GB membrane marker indicate areas of strong tumor invasion. We notice how there are regions where two parallel fronts evolve. Thus, depending on the concentration of MMPs, even in case of constant tumor cell speed, the front of the tumor can loose regularity and can split into two propagation fronts.

Several biological observations have suggested that within the areas occupied by the tumor mass, cell proliferation is not homogenous, but tumor cells can acquire a strong proliferative phenotype in specific regions. Thus, it is reasonable to suggest that a description of a heterogeneous proliferation could better reproduce the real cell behavior. Moreover, if the tumor growth is not homogeneous and there is a certain heterogeneity in the growth of the invasion fronts, modifications and splittings of the frontal structure can arise, similar to the results shown in Figure 7.13 and in agreement with the experimental evidence in Figure 7.14. When the front is separating into two parts, we hypothesize two possible mechanisms of heterogeneous proliferation that can happen. Cells closer to the inner front start to proliferate more in order to fill and reduce the distance between the two developed tumor fronts or cells closer to the

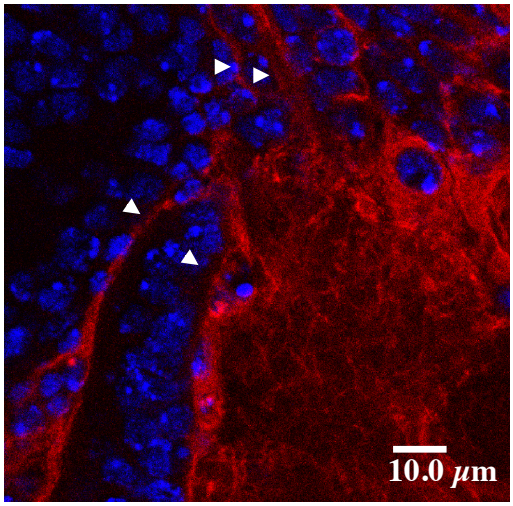

FIGURE 7.14: **Front heterogeneity.** GB membrane and cell nuclei are marked in red and blue, respectively. The arrowheads indicated the region where the front presents heterogeneities.

outer front proliferate more in order to create an autonomous front. As described in **(3)**, we simulate these two mechanisms. The numerical results of the former strategy are provided in the left plot of Figure 7.15, while the latter strategy is analyzed in the right plot of Figure 7.15.

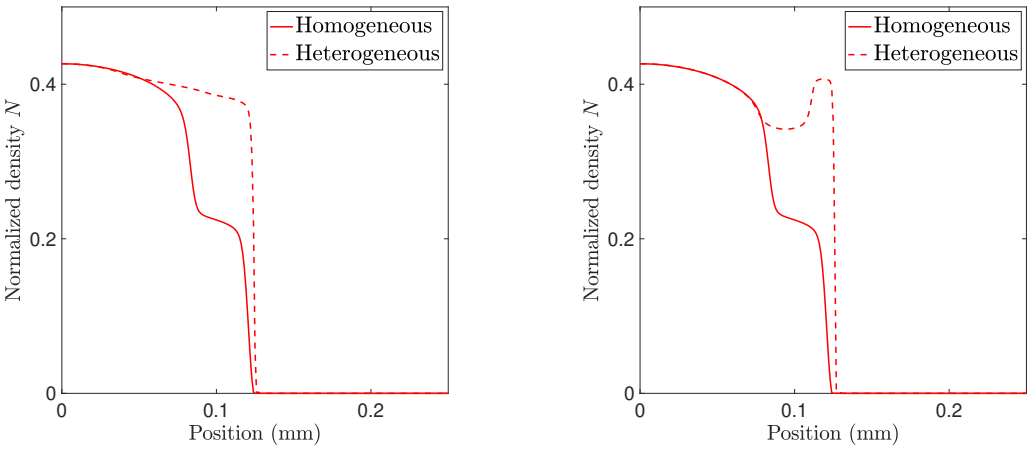

FIGURE 7.15: **Test (3): effects of heterogeneous proliferation on tumor profile.** The two plots show the evolution of the tumor profile after 5 hours in two specific cases of heterogeneous proliferation. We compare the proposed model with classical homogenous proliferation with the two possible models for heterogeneous proliferation. In both cases we set $a_1 = 0.005\ \text{mm}^2 \cdot \text{h}^{-1}$.

The heterogeneous proliferation will be further investigated in future works since this phenomenon has a major impact and relevance in the case of higher spatial dimensions.

The last tests **(4)** concerns the role of the tissue porosity on the evolution of the tumor front. The MMP activity modifies, in general, the porosity of the medium, facilitating cell spreading and, thus, the transport and progression of the tumor cells. This facilitation implies a modification in the tumor cell speed. This speed should not

be constant, but linearly dependent on the porosity of the medium. We study in a 1D setting this possibility and the resulting modifications of the front profile. As the proteases degrade the ECM, the porosity of the medium increases. This process can be modeled in two different ways. Using an equation for the degradation of the ECM (as (7.11)) and considering its influence on the dynamics of the protease in (7.10) and on the spread of the tumor described with (7.9) (which is the modeling approach we chose in the presented setting). Otherwise, an alternative way consists of modifying directly the porosity of the medium ϵ and modeling the effect of the porosity changes on the cell speed. Several experiments [301, 308] have shown the relation between the cell speed and the size of the pores of the ECM. Especially in the absence of proteolytic activity, too dense ECM does not allow cells to move inside it, since the pores are too narrow with respect to the cell capability of squeezing its nucleus and passing through the pores. At the same time, too large pores do not allow for cell migration either, since cell protrusions still need a certain amount of extracellular matrix around them in order to attach to it. Following the results of [308] (see, for instance, Figure 2.b in there), we consider a variability range for $\epsilon \in [0.5, 0.75]$, and we define a law of variability for v_N, assuming an optimal value for the tumor cell speed when ϵ has a value of approximately 0.67. Using an evolutionary law for ϵ analogous to the one proposed in [202], namely

$$\epsilon(t,x) = \epsilon_{max} - (\epsilon_{max} - \epsilon_0)\, e^{-\int_0^t a_6 P(\tau,x)\, d\tau}$$

with the initial porosity value $\epsilon_0 = 0.54$, and $\epsilon_{max} = 0.75$, we test the flux-saturated model for a scenario of non-constant v_N. The function representing the relation between ϵ and v_N is represented in Figure 7.16.

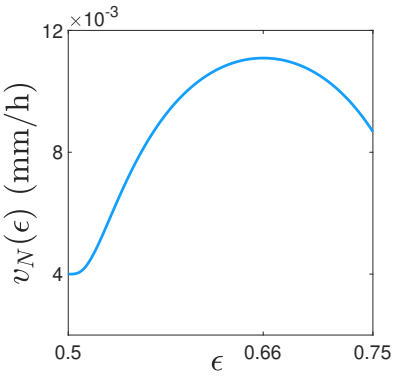

FIGURE 7.16: **Function describing the dependency of v_N on ϵ.**

Following [308], the minimum value for the speed relates to a porosity value of 0.5, while the maximum speed occurs around the porosity value of 0.66. The results of the study about the effects of the porosity changes on the front profile evolution are shown in Figure 7.17. For the simulation in Figure 7.17 we consider the tumor cell dynamics alone and driven only by the flux-saturated mechanism, without any transport term, i.e., $\frac{\partial N}{\partial t} = -\mathcal{J}_{\text{flux-sat}}(N)$. The red curve shows how cells closer to the front start moving faster than inner cells when the speed changes due to the ECM degradation process, which increases the medium porosity. These cell dynamics determine a heterogeneous modification of the invasion front, which slightly exceeds the homogeneous front related to the constant speed case (black curve). Eventually, the entire main tumor mass feels the changes in the speed, and a unique front is recovered. If there

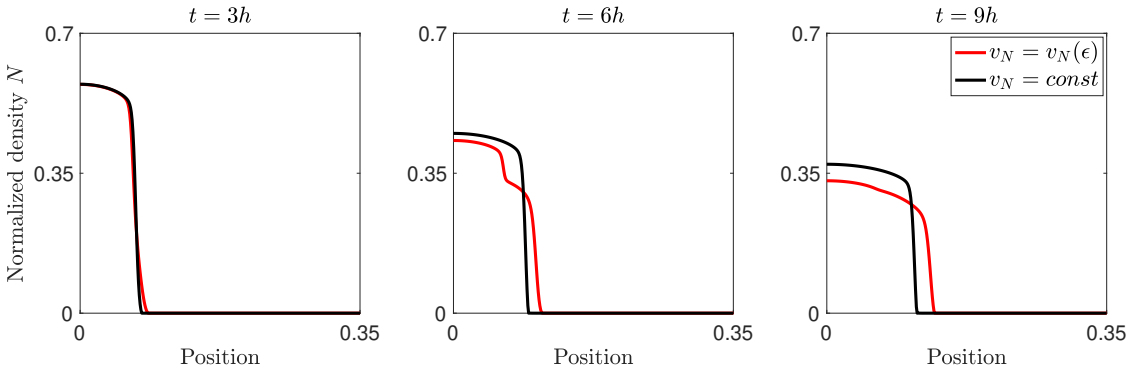

FIGURE 7.17: **Test (4): effects of porosity changes on tumor profile.** The results show the comparison between the tumor density profile in the case of flux-saturated model with constant speed v_N (in black) and with $v_N = v_N(\epsilon)$ (in red) after 3, 6, and 9 hours of tumor evolution.

is heterogeneity in the growth of the front, as we simulate in the previous test **(3)**, the profile might not unify and a new front can emerge from this disturbance.

7.5 *Summary*

Following the idea introduced in the kinetic-based model in Chapter 6, where non-local interactions were used to describe the contribution of cell protrusion in the migration, here we specifically focus on the key role played by tumor microtubes in mediating the dynamics of the glioblastoma front. We propose a novel multidisciplinary approach where data from protein signaling studies are integrated into a macroscopic mathematical setting. These data are used, on one side, to sustain the modeling hypothesis on MMP and integrin localization and, on the other side, to validate the numerical results about the invasion patterns that arise in the TM region and the relevance of these dynamics in the overall tumor progression process.

We started from the definition of the front region, named also TM region, where cell protrusions are localized and where we consider that the tumor activity, driving cell migration, is enhanced (Section 7.3.1). In the specific, for our analysis, with tumor activity we referred to the proteolytic activity leading to ECM degradation and to the binding processes between ECM and cell membrane receptors. We defined the functional $\mathcal{F}$ to describe the heterogeneous tumor activity within the tumor domain. We built the macroscopic setting in continuous feedback with the experimental results obtained from a *Drosophila* model, which represents a suitable platform to analyze the molecular and cellular mechanisms implicated in GB progression. Our mathematical model is based on the dynamical evolution of the agents involved in the front progression, as described in Section 7.3. In the specific, we described the dynamics of tumor cells with a combination of the proliferative process and the diffusive and tactic terms. The tactic phenomena are driven by protease and active integrin concentrations. Proteases, produced by tumor cells and releases in the extracellular space, where they freely diffuse, induce the degradation of the ECM. Active integrins operate in close relation with inactive integrins, mediating the binding/unbinding process with the ECM and, thus, driving the tumor's haptotactic mechanism. Tumor, active integrins, and proteases are described in terms of PDEs, while ODEs are used for the dynamics of inactive integrins and the ECM. The whole macroscopic system of differential equations shows highly nonlinear characteristics due to the strong coupling between

the different populations. The nonlinear nature is mainly due to the flux-saturated description of the fluxes leading GB cell and protease diffusion, as well as to the limited tactic terms. We described in detailed the characteristics of the basic flux-saturated equation, in terms of front profile and the influence of the parameters involved in its formulation (namely the propagation velocity and the medium viscosity) in Section 7.2. It is important to remark that the entire model derivation was performed in constant and strict relation with the experimental data shown in Figures 7.6-7.9.

The numerical tests first demonstrate that the tumor front is sharp and harbors a considerable biochemical activity. The relationship between inactive integrins, proteases, and focal adhesions drives GB dynamics and the front evolution and, moreover, the resulting patterns are in agreement with the experimental data (Figure 7.12). We also analyzed, even if with preliminary tests, the potential of the proposed model and some possible future directions of development. Precisely, we studied how the highly localized nature of the interactions can determine front heterogeneities and separations, as shown in Figure 7.13. Then, we explored the possibility of a heterogeneous description of the proliferation process of tumor cells, which can enhance the tumor front separation or restore the homogeneity (Figure 7.15). Moreover, the process of ECM degradation, which is essential for cell movement inside the matrix, at the same time produces biomechanical changes in the porosity and stiffness of the tissue. These changes affect the infiltration capacity of the tumor cells located closer to the TM area. We investigated this aspect considering a dynamic relation between cell speed and tissue porosity, as shown in Figure 7.16. The flux-saturated description of the diffusive term allows to directly include cell speed changes in the model and, thus, we noticed how the evolution of the tissue porosity can determine changes and heterogeneities in the tumor front progression. In conclusion, our results point out some of the main agents characterizing the leading edge of glioblastoma and also describe how mathematical models are able to predict the front dynamics. However, we want to remark that the features linked to front heterogeneity and tissue porosity modifications would express better their impact on tumor progression in a two-dimensional case that we will implement as a future extension of this work.

8 *Conclusions and future perspectives*

Throughout this dissertation, we presented several settings that address different aspects of the process of glioma growth and migration inside the brain. We relied on two major modeling frameworks: kinetic-based and macroscopic models, both featuring various aspects of tumor progression. In this final chapter, we summarize the contributions of this thesis (Section 8.1) and we discuss the main directions for future developments of the work (Section 8.2).

8.1 *Summary*

The central problem addressed in this thesis concerns the modeling of the complex dynamics driving tumor cell progression inside the brain. Specifically, referring to the case of gliomas, we analyzed cell growth and migration in relation to several factors, such as the brain fiber network, the brain vasculature, the membrane dynamics, and therapeutic treatments. We dedicated Chapter 1 to the description of the biology of gliomas, the most common therapeutic strategies, and the biological data we included in the models. Moreover, we introduced the two main mathematical frameworks used for our analysis, i.e., multiscale (kinetic-based) models and macroscopic model, and we described their fundamental characteristics. In Chapter 2, we presented a detailed study of the brain fiber network and its properties. We focused on the anisotropic characteristics of the brain tissue, showing how the information on the fiber alignment can be obtained from the DTI data and quantified. Following the theoretical description, we presented several approaches available in the literature to include DTI information in both macroscopic and multiscale settings in order to construct the tensor accounting for directed cell migration. In the multiscale setting, we focused on the distribution function to describe the fiber network. We introduce three different distribution functions, and for each of them we compute the degree of anisotropy in the resulting tensor. We then compare the three outputs in relation to the original information contained in the DTI data. This study represents a groundwork for all the settings presented in this thesis, especially for the kinetic-based models, where the introduced fiber distribution functions have an active role in describing the contact guidance phenomenon. The kinetic-based models (Chapters 3-5) follow the idea of building micro-meso models for glioma invasion with multiple taxis terms. Precisely, each of these settings represents an extension of the previous and considers additional, but different, mechanisms involved in tumor progression. In Chapter 6, the setting is still defined on the kinetic basis, but does not include details on the microscopic dynamics. We described the migration of the cells in a double-cue environment where the contact guidance phenomenon, characterizing the first three models, is combined with a chemotactic agent, both cues influencing cell velocity changes. Moreover, this setting contains a non-local description of the mesoscopic interactions to mimic the effects of

the extension of cell protrusion. Including the description for cell protrusions represents a bridge between the kinetic-based model and the macroscopic setting (Chapter 7). The latter, which provides a macroscopic description of the glioma cell migration, is focused on the dynamics of cell protrusions and is based on the integration of the model equations with biological measurements performed in a *Drosophila* model. Particular attention was devoted to the evolution of the tumor propagation front and the emergence of invasion patterns characterizing the different agents involved in tumor progression (i.e., ECM, proteases, and integrin receptors).

8.1.1 *Kinetic-based models*

The first kinetic-model we developed (Chapter 3) describes the influence of the brain tissue structure on tumor cell migration. Starting from the DTI-based approaches proposed in [74, 126], we built a multiscale model that integrates the microscopic dynamics of integrin receptors, a mesoscopic description of cell-ECM interactions (considered as the onset of cell proliferation), and the brain fibers driving contact guidance. Moreover, we included the description of a possible therapeutic treatment: radiotherapy, which aims to kill tumor cells, is combined with chemotherapy based on integrin inhibitor agents, which instead reduce the affinity between cell receptors and ECM. The macroscopic equation for the glioma cell density was derived via a parabolic scaling. The corresponding numerical simulations highlight how different fiber distribution functions determine differences in the emergence of heterogeneous patterns in the tumor dynamics (Figures 3.3 and 3.4) and how brain fibers influence the direction of cell migration (Figure 3.5). The numerical results show the effects of the modeled treatments in terms of reduction of both tumor invasion (due to integrin inhibitors, Figure 3.6) and tumor density (due to radiation, Figure 3.7). Despite its ability to reproduce some of the characteristic features of glioma progression, such as the spreading along the brain fibers, this setting has several limitations. For instance, it does not include the influence of the brain vasculature or the degradation of the healthy tissue due to the tumor activity. Nonetheless, this first setting represents a solid base on which we built the subsequent extensions.

In the first refinement of the model (Chapter 4) we add two populations to the setting: endothelial cells (ECs), which constitute the brain vasculature, and protons, which are produced by tumor cells and determine the acidification of the environment. Under hypoxic conditions, there is a shift in the cellular metabolism generating a high acidity in the tumor microenvironment. The resulting acidification together with angiogenesis is one of the hallmarks of malignant brain tumors and it facilitates tumor invasion and degrades the extracellular matrix. We derived the macroscopic setting from a micro-meso formulation of the population dynamics. At the microscopic level, we coupled the descriptions of integrin and proton-sensing receptors, considering both types of receptors located on the tumor cell membrane. Tumor and endothelial cell evolution were described at the mesoscopic level. Precisely, the description of the former is similar to the first model, but we characterized intratumor heterogeneity. Following the *go-or-growth* hypothesis, we split the tumor population into migrating and proliferating (and resting) cells. These behaviors are transient and the switch between these subpopulations happens according to the pH level (determined by the proton concentration), the vasculature availability, and the environmental crowding. The evolution of the EC population is mainly characterized by a tactic phenomenon towards pro-angiogenic factors (mainly vascular endothelial growth factors VEGFs) that are produced by the tumor cells. The effect of these factors on ECs was indirectly modeled as a biased migration of ECs towards tumor cells. The derived macroscopic

setting consists of a system of coupled advection-diffusion-reaction equations, characterized by anisotropic, nonlinear, myopic self-diffusion (for the tumor, in the model of Chapter 3) and multiple taxis (haptotaxis and pH-taxis for tumor cells, chemotaxis for ECs), which increase the level of complexity of the setting with respect to the previous model. To the best of our knowledge this is the first continuous mathematical model with pH- and vasculature-induced phenotypic switch between moving and proliferating cells where the two cell types are seen as distinct tumor subpopulations evolving under mutual, direct and indirect interactions. The numerical simulations highlight the nonlinear nature of the population dynamics, arising from the effect of the multiple taxis (especially the chemotaxis) and depending on the model parameters (Figures 4.3 and 4.4). Tumor evolution shows several different aspects compared to the previous setting. These differences are mainly related to the coupling between tumor and ECs, which have a strong impact on tumor proliferation, and to the modeled phenotypic heterogeneity (based on the *go-or-growth* mechanism), which makes the overall tumor evolution slower than the case where the tumor is considered as one population. This effect of the *go-or-growth* hypothesis on the tumor progression was analyzed (Figures 4.5 and 4.6). In Section 4.4, a further extension of the setting was introduced, involving the dynamics of the tissue and the necrotic matter due to the acid-mediated degradation. This extension allowed us to define a necrosis-based tumor grading that we used to determine the progression of the tumor stage in different scenarios and the influence of the tumor heterogeneity and the vasculature supply (Figure 4.10).

The tumor grading scheme can be particularly relevant for diagnosis and therapy planning and it provides the basis for the analysis proposed in Chapter 5. For the setting developed in this chapter, we mainly focused on the angiogenic process that characterizes glioma progression and on the effects of combined treatments directly affecting both tumor and endothelial cells. The model was built combining microscopic dynamics and mesoscopic descriptions for both tumor and vasculature. Unlike in Chapter 4, where VEGF effects were taken into account without including an evolution equation for this population, in this setting we directly described the evolution of the VEGFs. In our model, these factors are produced by the tumor cells, sustain the EC growth, and constitute also a chemotactic cue for the ECs themselves. Moreover, in this setting, we indirectly include the effect of the acidity produced by the tumor in hypoxic conditions. The derived macroscopic model for tumor, ECs, and VEGFs was coupled with evolution equations describing the healthy tissue degradation and the growth of the necrotic matter. The core of this study concerned the analysis of a therapeutic plan that combines radiation, affecting tumor, ECs, and healthy tissue, chemotherapy with temozolomide, and anti-angiogenic therapy with bevacizumab. The latter is specifically aimed at reducing EC growth and the affinity between VEGFs and EC, consequently affecting the supply of nutrients to the tumor cells. Preliminary simulations show the model dynamics both in the absence and presence of therapy (Figures 5.2, 5.4 and 5.5). In particular, the effect of integrin inhibitors on tumor migration (described in Chapter 3) is similar to the effect of anti-angiogenic drugs on EC migration (described in Chapter 5). Both treatments, in fact, reduce the motility of the affected population. However, the anti-angiogenic therapy is also able to indirectly affect the tumor evolution, reducing the availability of oxygen and nutrients that sustain its progression. Moreover, contrary to the previous setting (Chapter 4), we did not consider any intratumor heterogeneity, we initially provided more blood vessel to sustain tumor growth, and we reduced the dependence of tumor proliferation on ECs. The combination of these features determines a faster growth of the tumor mass with respect to the previous setting, as demonstrated in the numerical simulations. The model described in Chapter 5 represents a base to address the problem of studying

the efficacy of the multi-modal treatments, described in detail in Section 8.2.

The study proposed in Chapter 6 belongs to the family of kinetic-based models, but it slightly differs from both the previous settings (Chapters 3-5) and the forthcoming one (Chapter 7). In fact, the work presented in Chapter 6 was not directly applied to glioma migration. Nonetheless, it presents an extensive analysis of the effects of multiple cues guiding cell motion, whose specification in the case of glioma cells would be easy to achieve. Instead of describing the cell velocity changes in the transport equation due to a single cue, we considered the novelty of having the two mechanisms of contact guidance and chemotaxis as directional cues simultaneously driving cell polarization. A similarity with Chapter 7 is the inclusion of the effect of the cell protrusion extension for exploring the neighborhood around the cell. Based on the non-local kinetic model with a double biasing cue proposed in [173], this effect was described by means of non-local terms. We introduced two classes of models, analyzing two possible sensing strategies that a cell could apply. A cell can measure the guidance cues independently, and, then, choose the new orientation integrating the collected information, eventually weighted in different ways. Otherwise, it can measure the two-directional stimuli, weighting them equally, and assuming a conditioning of one cue on the other. To the best of our knowledge, this is the first time that a non-local sensing of the fibers distribution describing contact guidance is considered. The numerical simulations of the transport model show the effects of a double cue environment on cell polarization: even for locally sensed and non-oriented fibers, the influence of the chemotaxis on the polarization ensures a preferential sense of motion to the cells (Figure 6.1). The numerical tests displayed the effects of the implementation of different sensing strategies (Figure 6.2). We analyzed how these strategies affect the macroscopic dynamics of the system, determining different macroscopic limits depending on the strength of one cue on the other one (Figures 6.4-6.8). From these simulations, we observed the impact of the macroscopic adopted regime (derived from the choice of hydrodynamic or parabolic limit) on cell migration, while in the previous setting the derivation of the macroscopic models was always performed in the parabolic case. In contrast to the previous settings, for this study we only modeled cell migration, without any influence of proliferation processes. Finally, we built two heterogeneous landscapes of fibers and we observed how cells cross the domain and tend to reach the chemoattractant location. In the case of a stronger contact guidance cue compared to the chemotactic one, the two cues polarized the cells towards different directions and can failed to reach the chemoattractive agent (Figures 6.9 and 6.10).

8.1.2 *Macroscopic models*

The second framework we considered was the macroscopic models. In line with the idea introduced in Chapter 6 about the role of cell protrusions in driving cell migration, we developed a macroscopic model (Chapter 7) to identify the biochemical and biomechanical mechanisms involved in the tumor front progression and to investigate the role of cell protrusions (called tumor microtubes in the context of glioma) in this process. We proposed a novel multidisciplinary approach in which data collected *in-vivo* experiments in *Drosophila* are incorporates into the macroscopic mathematical model to provide a realistic description of the tumor evolution in relation to the dynamics of the proteins acting at the tumor front. In the specific, we introduced the concept of a tumor front and analyzed the dynamical evolution of proteases, active and inactive integrins, and the ECM. Proteases, produced by tumor cells and released in the extracellular space, diffuse in the area surrounding the tumor front and degrade the ECM, while integrins mediate the binding/unbinding process with the ECM. The

modeling assumptions were supported by biological experiments measuring the protein distributions in different regions of the brain (Figures 7.6-7.11). From the mathematical standpoint, the macroscopic setting of differential equations shows highly nonlinear characteristics due to the strong coupling between the different populations. This nonlinearity is greatly dependent on the flux-saturated model (Section 7.2). Used for the description of the fluxes characterizing glioma cell and proteases, this model allows to obtain sharp and well-defined invasion fronts and to directly control the front velocity. We performed several 1D *in-silico* experiments to test the model, each set-up describing a different scenario. Precisely, we first compared the evolution of our system with the results of the biological experiments, showing a good agreement between the patterns that arose at the front and the measured protein distributions (Figure 7.12). Then, we explored the potential of the proposed model to reproduce front heterogeneities or splittings due to both tactic cues leading cell migration and to the proliferation process (Figures 7.13 and 7.15, respectively). We also studied the effect of changes in the ECM porosity on the capacity of the tumor cells to invade the tissue (Figure 7.17), defining a dynamic relation between cell speed and tissue porosity. The two last aspects we analyzed (heterogeneous proliferation and tissue porosity) would better express their potential in a 2D extension of the setting. This extension would also allow us to make a comparison between the effects of the flux-saturate mechanisms used in Chapter 7 and the effects of the other dispersive dynamics introduced in Chapters 3-6. Although just in 1D, the numerical results highlighted how this model can represent a suitable platform for the study of the mechanisms driving the dynamics at the leading edge of GB progression.

8.2 *Future work*

The diverse settings proposed in this dissertation (the micro-meso models of Chapters 3-5, the non-local kinetic model of Chapter 6, and the macroscopic model of Chapter 7) show considerable advances in the glioma modeling field, being able to capture key reported experimental evidence of glioma progression. However, several extensions and improvements of these settings can be formulated and implemented. Here, we describe three main directions for future research.

Considering the multiscale model developed in Chapter 5, we performed preliminary numerical simulations showing the overall dynamics of the system and the effects of the different treatments on the populations involved. This analysis can be enriched by a stochastic extension to evaluate the efficacy of the treatment. A common quality measure for the success of a treatment schedule is the *tumor control probability* (TCP), which computes the probability that no clonogenic cells survive a radiation treatment. This measure takes into account complex interactions between tumor biology, tumor microenvironment, radiation dosimetry, and patient-related variables. *Normal tissue complication probability* (NTCP) and *uncomplicated tumor control probability* (UTCP) are other two measures of the success of a treatment, addressing its damaging influence on the normal tissue alone (NTCP) and jointly on tumor cells and normal tissue (UTCP). The former represents the probability that the functioning of normal tissues is impaired by radiation, while the latter generally gives the probability of achieving complication-free tumor control. Several approaches have been proposed to calculate these measures of therapy quality. As the tumor population is supposed to shrink drastically under the effect of the treatments, we plan to include in the equation for the tumor population a stochastic variable accounting for uncertainties in the

therapy outcomes. This stochastic extension will allow us to evaluate the quality measures described above. Moreover, we will consider patient-specific data and, for each patient, we will simulate the administered therapy treatment using the tumor segmentation obtained from the clinical data as the initial condition for the tumor population. This way, it will be possible to theoretically calculate the efficacy of the treatment and to compare the model outcomes with the real therapy results.

Concerning the non-local model presented in Chapter 6 and its general formulation, several further investigations are possible. This model represents a good platform to quantify directed cell migration and to assess its efficiency. For instance, mean square displacement, persistence time, directional persistence, or mean speed can be calculated [211] and compared with biological measurements of cell migration. Following the results of the last numerical test (Figures 6.9 and 6.10) it would be interesting to analyze in detail the case of competitive cues when a heterogeneous landscape of fibers is considered. This approach will allow us to investigate the mechanisms governing the competition between the two cues (such as the possible role of cell-cell adhesion). Moreover, similar to [174], we can enrich the model by introducing a non-constant sensing-radius, varying according to the spatial and directional variability of the external guidance cues, or by including the effect of the external cues on the cells speed (considered uniformly distributed in the setting of this thesis). As already mentioned, we are interested in the concrete application of this model to the study of tumors on a realistic domain for mimicking *in-vivo* or *in-vitro* cell migration in the extracellular matrix. For this purpose, the development of more sophisticated numerical approximation methods of the transport equation will be necessary.

The model described in Chapter 7 presents several characteristic features that, due to their spacial nature, would be better expressed in a 2D configuration. In the specific, we refer to the aspects related to the heterogeneous proliferation and the porosity changes. Thus, the first step will be the formulation and implementation of the setting in the 2D case. From the modeling side, the extension to a 2D scenario requires the introduction of the directional tensor describing both the fluxes that characterize the tumor population (defined in (7.5)-(7.7)) and the tumor microtube region (defined in (7.3)). From the numerical viewpoint, the implementation of the 2D extension requires to resort to more complex numerical methods to approximate of the flux-saturated terms, to preserve the characteristics of the invasion front, and to trace the front position. The first step in this direction will involve the implementation of an adaptive mesh refinement that can increase the accuracy of the system solution around the front region, where most of the dynamics are concentrated. The processes of cell protrusion extension and retraction as well as tumor proliferation are also influenced by several morphogenic signaling pathways. For instance, sonic hedgehog or Wnt pathways have been studied in relation to protrusion dynamics in both healthy and diseased cases. Therefore, a further development for this work will include the mathematical modeling of some signaling pathways and their coupling with the proposed macroscopic setting. Finally, we will analyze our system from a theoretical viewpoint. The idea is to define a kinetic formulation of the proposed macroscopic setting and formally derive this setting from a kinetic level. This approach will also define a stronger connection between this setting and the models presented in Chapters 3-6.

Appendices

A *A basic introduction to MRI and DTI data processing*

MRI techniques use the resonance of protons to generate images. Protons are excited by a radiofrequency pulse of an appropriate frequency and then, returning to their original state, they release energy that is recorded by sensors. Each tissue returns to its equilibrium state after excitation by the independent relaxation processes of T1 signal, a magnetization in the same direction as the static magnetic field, and T2 signal, a magnetization transverse to the static magnetic field. In particular, T1-weighted sequences allow distinguishing the tumor from the surrounding edema, while on T2-weighted sequences they cannot be distinguished. However, the latter sequence provides the most accurate measure of the outer margin of the neoplasia. DTI or diffusion tensor imaging is a special kind of diffusion-weighted magnetic resonance imaging that allows recording water molecule diffusion patterns, revealing microscopic details about tissue architecture, like the white matter neural tracts, either in a normal or a diseased state of the brain.

This appendix is conceived as a brief and basic introduction to the processing of MRI and DTI data to extract information on the brain geometry and the brain structure orientation. The purpose is to provide the essential information about the different processing steps and the proper references for in-depth studies of the presented topics and techniques. In particular, in Section A.1, we comment on the available data and their possible formats, which can require a preprocessing step. Then, in Section A.2.1, we describe the procedure to extract the brain geometry with the FreeSurfer Software Suite[1]. The DTI data extraction is based on the use of FSL[2] (FMRIB Software Library) and it is described in Section A.2.2. Finally, in Section A.3, we describe how we deal with the processed data within the Matlab environment.

A.1 *Raw data*

The raw data at hand encode different types of information. The anatomical details about the brain, derived from the MRI scans, are provided in the form of T1 or T2 images in the ***NIfTI*** (Neuroimaging Informatics Technology Initiative) format. They can be stored as a single file (`.nii`) or as dual file (`.hdr` & `.img`), including a header, that stores meta-information, and an image, i.e., the actual data. NIfTI is a common file format for neuroimages, commonly used in imaging informatics for neuroscience and neuroradiology research. In particular, when it is available, the meta-information file provides several details about the images, such as the brain orientation, the three spatial dimensions - x, y, and z -, the time points, the voxel dimensions, and other voxel-specific distributional parameters.

[1] `https://surfer.nmr.mgh.harvard.edu`
[2] `https://fsl.fmrib.ox.ac.uk`

The DTI measurements are also provided as NIfTI files. They are accompanied with the information about the gradient directions (`.bvecs`) and the diffusion weighting (`.bvals`). Precisely, the `.bvecs` file is a text file providing information about the gradient direction applied during diffusion-weighted volumes. The `.bvals` file contains the list of b-values applied during each volume acquisition, i.e., it measures the degree of diffusion weighting applied. The b-values vary between 750-1500 $s \cdot m^{-2}$ and it is usually set to 1000 $s \cdot m^{-2}$. The number of entries in this file has to match the entries of the `.bvecs` file, as well as the entry order, has to match the order of the volumes in the input data.

An alternative format for DTI and MRI raw data is the ***DICOM*** (Digital Imaging and Communications in Medicine) format, most commonly used for storing and transmitting medical images.

A.1.1 *Preprocessing steps*

If the raw data are provided in the DICOM format, a preprocessing step is required to convert the data into a standard file format, normally into NIfTI images, before applying any structural imaging method. The conversion into the NIfTI format can be done using the **dcm2nii**[3] software, a stand-alone program that converts images from the proprietary scanner format to the NIfTI format used by several brain imaging tools. Moreover, this program allows the modification of NIfTI file: with the option `Modify NIfTI`, choosing the output format `FSL(4D NIfTI nii)` and loading the `.hdr` data, we get a compressed file `.nii.gz` directly usable with FSL for the following steps of the DTI analysis.

A second preliminary control concerns the alignment between MRI and DTI raw data. It consists in checking if there is a coherent alignment between MRI and DTI in terms of image orientation. Information about the orientation can be obtained by loading the images with the viewer FSLeyes[4] and opening the image information window. An illustrative example of a non-aligned situation is given in Table A.1.

	MRI (T1 or T2)	DTI
Storage order	Radiological	Radiological
X voxel orientation	Anterior - Posterior	Right - Left
Y voxel orientation	Inferior - Superior	Posterior - Anterior
Z voxel orientation	Left - Right	Inferior - Superior

TABLE A.1: **Orientation of MRI and DTI data: an example of non-aligned data.**

In the case of not aligned images, we need to fix their orientation before the processing step with the FreeSurfer suit. In particular, it is possible to use the **fslswapdim**[5] command from the FSL toolbox. With respect to the example illustrated in Table A.1, the command line in the terminal of the FSL environment reads

```
fslswapdim T1.nii.gz -z -x y T1_reoriented.nii.gz
```

[3] https://people.cas.sc.edu/rorden/mricron/dcm2nii.html
[4] https://fsl.fmrib.ox.ac.uk/fsl/fslwiki/FSLeyes
[5] https://fsl.fmrib.ox.ac.uk/fsl/fslwiki/Fslutils

where `T1.nii.gz` refers to the T1-weighed image. Besides, using FSLeyes, it is also possible to get information about the number of voxels of the image and their dimensions. This information is useful for the definition of the computational mesh and for setting the spatial reference scale in our models. Once the MRI and DTI data are in the standard NIfTI format and coherent in their orientations, it is possible to start the FreeSurfer processing for the reconstruction of the brain geometry.

A.2 *Brain geometry reconstruction and DTI data*

The brain geometry reconstruction is based on the use of a T1 contrast image of the whole brain obtained from an MRI scan. This data shows white and grey matter, the former brighter than the latter. The overall processing consists of two main parts: the first one is based on the FreeSurfer software and processes the MRI files in the NIfTI format, while the second one uses FSL software to process the raw DTI data.

A.2.1 *FreeSurfer processing*

FreeSurfer is an open source software for the analysis and visualization of structural and functional neuroimaging data from MRI scans, developed by the Laboratory for Computational Neuroimaging in Charlestown, MA (for further details see [86]). To start working in the FreeSurfer environment, we first set the working directory and the directory for the FreeSurfer application itself. The corresponding line of code in the terminal reads:

```
tcsh
setenv ACT_DATA  "<path to the data>"
setenv SUBJECTS_DIR  $ACT_DATA
echo "SUBJECTS_DIR $SUBJECTS_DIR"
setenv FREESURFER_HOME "</Applications/freesurfer>"
source ${FREESURFER_HOME}/SetUpFreeSurfer.csh
```

In particular, the paths to the data and to the FreeSurfer application have to be specified by the user, while the variables SUBJECTS_DIR and FREESURFER_HOME are environment variables that have to be defined before using any FreeSurfer commands in order to find the right data for the processing. They represent the direction where the subject data are stored and the location where FreeSurfer is installed, respectively. The next step consists in the creation of an output folder with the command:

```
recon-all -s <output folder name> -i $SUBJECTS_DIR/<input file name.nii>
```

This defines an output folder with the name specified in <output folder name>, taking as input data the ones specified after `-i`, which are loaded in the directory of FreeSurfer. To start the whole process we use the following code in the terminal:

```
recon-all -s <output folder name> -all
```

The entire process creates 8 folders in the output folder. Among them, we are mainly interested in the ones collecting the data related to the volumetric processing (stored into `subjid/mri`) and to the surface processing (stored into `subjid/surf`). We briefly recall the main steps characterizing the acquisition process:

→ mri:

- *Motion correction*, correcting for small motions between multiple source volumes (`orig.mgz`);
- *Talairach*, computing the affine transform from the orig volume to the MNI305 atlas (`talairach.xfm`);
- *Nu intensity correction*, correcting non-uniformity in MR data (`nu.mgz`);
- *Normalization*, performing intensity normalization of the orig volume (`T1.mgz`);
- *Skullstrip*, removing the skull from `T1.mgz` (`brainmask.mgz`);
- *EM registration*, aligning `nu.mgz` volume to the default GCA atlas (`talairach.lta`);
- *CA normalize*, a further normalization (`norm.mgz`);
- *CA register*, a further nonlinear alignment with GCA atlas (`talairach.m3z`);
- *CA label*, labeling subcortical structures (`aseg.mgz`);
- *Normalization 2*, performing a second intensity correction (`brain.mgz`);
- *Mask brain final surface*, applying `brainmask.mgz` to `brain.mgz` (`brain.finalsurfs.mgz`);
- *WM segmentation*, separating white matter (`wm.mgz`);
- *Cut and Fill*, cutting the mid brain from the cerebrum and dividing the two hemispheres (`filled.mgz`).

→ surf:

- *Tessellation*, creating the orig surface for the two hemispheres (`?h.orig.nofix`);
- *Orig surface smoothing 1*, adjusting the vertex position on the surfaces (`?h.smoothwm.nofix`);
- *Inflation 1*, minimizing metric distortion (`?h.inflated.nofix`);
- *Qsphere*, fixing an automatic topology (`?h.qsphere.nofix`);
- *Automatic topology fixer*, mapping the unit sphere on the surface (`?h.orig`);
- *Final surfs*, generating surface files and curvature files (`?h.curv`, `?h.area`, and `?h.cortex.label`);
- *Orig surface smoothing 2*, performing a second smoothing (`?h.smoothwm`);
- *Inflation 2*, performing a second minimization of the metric distortion (`?h.inflated`);
- *Curve HK and Curve statistics*, calculating mean curvature and gaussian curvature of the cortical surface (`?h.curv.stats`);
- *Spherical inflation*, inflating the orig surface into a sphere (`?h.sphere`);
- *Ipsilateral surface registration*, registering the orig surface to the spherical atlas (`?h.sphere.reg`);
- *Jacobian*, computing white surface distortion (`?h.jacobian_white`);
- *Average curvature*, resampling the average curvature (`?h.avg_curv`);
- *Cortical parcellation 1, 2 and 3*, assigning neuroanatomical labels (`?h.aparc.annot`);

- *Pial and T2 pial*, generates surface files and curvature file (`?h.pial`, `?h.curv.pial`, `?h.area.pial` and `?h.thickness`);
- *Cortical ribbon mask*, creating binary volume masks (`ribbon.mgz`);
- *Parcellation statistics 1, 2 and 3*, creating a summary table of cortical parcellation statistics (`?h.aparc.stats`);
- *APARC to ASEG*, adding information in the volume parcellation (`aseg.mgz`);
- *Seg Stats*, computing statistics on the segmented subcortical structures (`aseg.stats`);
- *White matter parcellation*, adding white matter parcellation info into the `aseg` (`wmparc.mgz` and `wmparc.stats`);
- *Brodmann Area Maps and Hinds V1 Atlas*, labeling the different area of the brain with respect to a specific atlas (`?h.BA*_exvivo.label`, `?h.perirhinal_exvivo.label`, and `?h.entorhinal_exvivo.label`).

For each step, the output files are indicated between brackets. In particular, for the output of the surface processing `?h.` stays for `lh.` or `rh.` referring the left and right hemisphere, respectively.

When the processing ends, we can visualize some output files with the image viewer software FreeView[6]. In particular, this is useful for checking possible errors in the results of FreeSurfer. One example relates to the check of the output of the ***Talaraich registration*** that computes on the orig volume file a linear Talairach transformation: under some circumstances, the alignment can fail. To visualize the data in FreeView we use the following commands:

```
freeview -v $SUBJECTS_DIR/<output folder name>/mri/T1.mgz
    -v $SUBJECTS_DIR/<output folder name>/mri/brainmask.mgz:
    reg=$SUBJECTS_DIR/<output folder name>/mri/transforms/talairach.xfm
tkregister2 --mgz --s <output folder name> --fstal --surf orig
```

In FreeView we check the registration of the subject's volume and the Talairach volume and try to identify possible distortions and stretching of the latter from the position of the subject. If any misalignment is detected, it is necessary to correct the Talairach volume, stretching or rotating it until obtaining the correct alignment. A second example of errors during the processing is related to the construction of the ***pial surface***. This surface is created by expanding the white matter surface so that it closely follows the grey matter-cerebrospinal fluid (CSF) intensity gradient, as found in the `brainmask.mgz` volume. The pial surface boundary and white matter surface boundary should not cross. This can be visually checked by loading the pial surface into FreeView and visualizing it together with the `brainmask.mgz` volume:

```
freeview -v $SUBJECTS_DIR/<output folder name>/mri/T1.mgz \
  $SUBJECTS_DIR/<output folder name>/mr/brainmask.mgz \
  -f $SUBJECTS_DIR/<output folder name>/surf/lh.white:edgecolor=blue \
  $SUBJECTS_DIR/<output folder name>/surf/lh.pial:edgecolor=yellow \
  $SUBJECTS_DIR/<output folder name>/surf/rh.white:edgecolor=blue \
  $SUBJECTS_DIR/<output folder name>/surf/rh.pial:edgecolor=yellow
```

[6] https://surfer.nmr.mgh.harvard.edu/fswiki/FsTutorial/OutputData_freeview

If the surface appears not to follow the grey matter-CSF boundary in the volume, edits may be required. An example of a good construction of the pial surface is shown in Figure A.1.

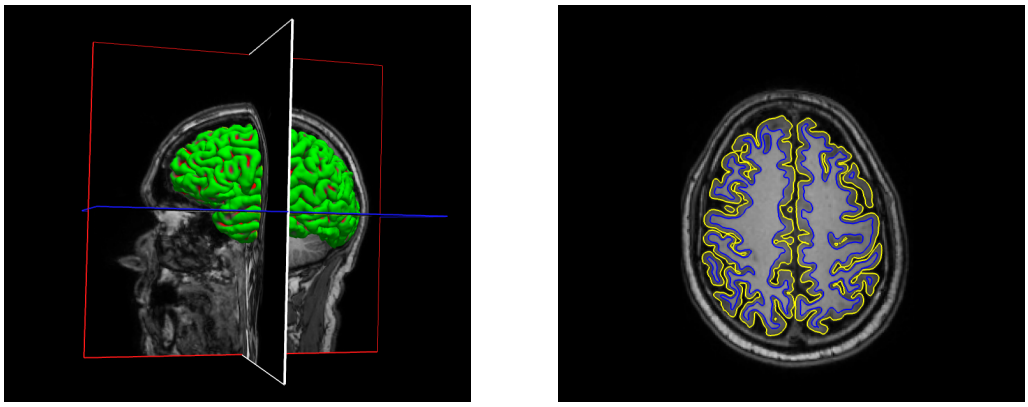

FIGURE A.1: **Visualization of volume and surface outputs of FreeSurfer.** Left plot: `lh.pial` and `rh.pial` surfaces in a 3D view. Right plot: `lh.pial` and `rh.pial` surfaces (in yellow) visualized together with `lh.white` and `rh.white` surfaces (in blue).

A.2.2 *FSL processing*

FSL is a comprehensive library of analysis tools for MRI, functional MRI, and DTI brain imaging data created by the FMRIB Group in Oxford, UK [130, 262, 302]. As explained for the MRI raw data, for the processing of the DTI data with FSL the NIfTI format is required. Moreover, it is also necessary to have access to the gradient direction (`.bvecs`) and b-values (`.bvals`) information. For our purpose, the processing of the DTI data includes

- the correction of eddy current distortions and simple head motions;
- the brain extraction from the DTI data;
- the application of the function DTIFIT;
- the registration of the DTI data with the T1 (MRI) space.
- the application of the inverse transformation to the DTI data and the check for alignment.

Therefore, after opening the FSL software in the terminal and setting the directory into the data folder (SUBJECTS_DIR), it is possible to use its interface to process the data or to directly type the following commands on the terminal window.

The first step consists in the correction of imaging distortion, using the ***eddy_correct*** toolbox function, which corrects for eddy current-induced distortions and subject movements [130]:

```
eddy_correct ${SUBJECTS_DIR}/DTI.nii  ${SUBJECTS_DIR}/DTI_correct.nii 0
```

This command defines an output file named `DTI_correct.nii` from the original data, which we name here `DTI.nii`. In particular, the setting `0` at the end of the command line indicates that we are using the reference volume, i.e. the volume with a b-value

of 0[7]. The corrected data are used as the input file for the brain extraction step.

This step is based on the ***brain extraction tool*** (BET) [262] of FSL that deletes non-brain tissue from the image of the whole head. The corresponding command in the terminal, which produces the output file `DTI_bet.nii`, reads:

```
bet ${SUBJECTS_DIR}/DTI_correct.nii ${SUBJECTS_DIR}/DTI_bet.nii -m -f 0.3
```

Here, `-f` indicates the fractional threshold and `-m` generates the binary brain mask. Precisely, the *fractional intensity threshold* is a parameter that controls the threshold of tissue distinction between what is considered part of the brain and what is not. Its default value is 0.5 and, changing it in the interval (0,1), causes the overall segmented brain estimation to become larger (< 0.5) or smaller (> 0.5).

The ***DTIFIT*** function consists in a diffusion tensor model that, for each voxel, fits a tensors to the previously processed diffusion weighed images. It typically runs on the data pre-processed with eddy current correction. Precisely, it uses the DTI data corrected with *eddy* (`DTI_correct.nii`), the *BET* binary brain mask (`DTI_bet.nii`), and gradient direction (`.bvecs`) and b-value (`.bvals`) information. The output file is `DTI_dtifit.nii`, whose name can be chosen by the user. The corresponding command line reads:

```
set bvecs=$SUBJECTS_DIR/*bvecs
set bvals=$SUBJECTS_DIR/*bvals
dtifit --data=$SUBJECTS_DIR/DTI_correct.nii
--out=$SUBJECTS_DIR/DTI_dtifit.nii
--mask=$SUBJECTS_DIR/DTI_bet.nii
--bvecs=$bvecs --bvals=$bvals
```

The output of this process consists of different files. The main ones we are interested in are:

- `DTI_dtifit_FA` for the fractional anisotropy;
- `DTI_dtifit_Li` and `DTI_dtifit_Vi` for the sorted eigenvalues and eigenvectors of the DTI tensor, respectively, with $i = 1, 2, 3$ (L1/V1 refers to the leading eigenvalue/eigenvector);
- `DTI_dtifit_MD` for the mean diffusivity.

Some of the output files (e.g. the tensor eigenvectors) are provided as a multi-volume (4D) file that can be visualize with FSLeyes. Entering the viewer software and selecting the desired image from the list, it is possible to open the image information window and to change the `DTIDisplay options` for the visualization. For instance, we can choose between `None`, `Lines` and `RGB` visualization. In particular, with the `Lines` option, the direction of each DTI eigenvector is represented as a small line for each voxel. For the DTI display option `RGB`, different colors express the different orientations: red is used for x-direction, green for y-direction, and blue for z-direction, while mixed colors refer to vector with significant non-zero components in more than one direction. This option allow also to modulate the intensity of the eigenvectors by the fractional anisotropy (FA). Examples of these visualization options are given in Figure A.2.

[7] dcm2nii should automatically ensure that the initial volume is the volume with b-value 0, although it is appropriate to verify this by viewing the volumes with MRIcron.

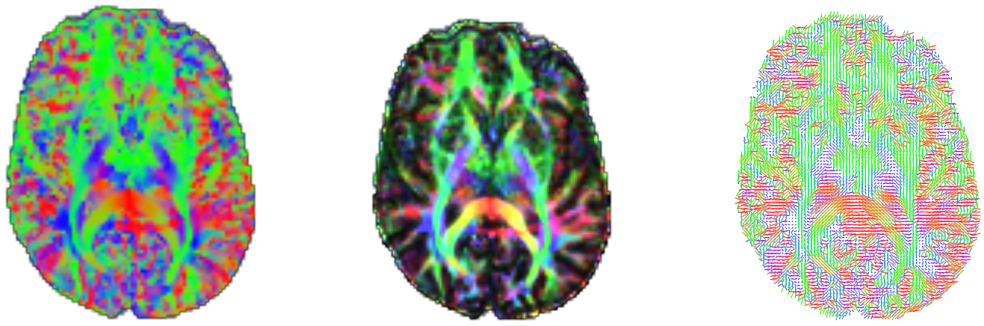

FIGURE A.2: **Visualization of the processed DTI images.** Leading eigenvector of DTI represented with `RGB` (left). Leading eigenvector represented with `RGB` and with intensity modulated by FA (middle). Leading eigenvector represented with `Lines` (right)

.

The registration of DTI data and T1 image is performed with a linear or a nonlinear transformation. An example of a software that performs linear registration is ***FLIRT***[8] (FMRIB's Linear Image Registration Tool), an accurate and robust tool for the registration of two single volumes together. Its main options are the input (`syntax:-in`) and the reference (`syntax:-ref`) volumes. The outputs consist in the affine transformation that registers the input to the reference, stored as a 4×4 affine matrix (`syntax:-omat`), and the output align volume (`syntax:-out`). Optional features, which might be set as options, are the number of *degrees of freedom* (`syntax:-dof <number of transform dofs>`) and the *cost functions* (`syntax:-cost`). The options for the latter include the predefined functions Least Squares (`leastsq`) and Normalized Correlation (`normcorr`), as well as the between-modality functions Correlation Ratio (`corratio`, by default), Mutual Information (`corratio`) and Normalized Mutual Information (`normmi`). The syntax of the transformation with FLIRT reads:

```
flirt [options] --in=${SUBJECTS_DIR}/MRI_data.nii
   --ref=${SUBJECTS_DIR}/DTI_data.nii
```

We use the illustrative names `MRI_data.nii` and `DTI_data.nii` to refer to the MRI and DTI data, respectively. A nonlinear transformation can be performed with the software ***FNIRT*** and is usually employed when the linear transform is not sufficient to achieve a good registration. Thus, the local deformations permitted by a nonlinear method may improve the results:

```
fnirt [options] --in=$SUBJECTS_DIR/<MRI_data.nii>
   --ref=$SUBJECTS_DIR/<DTI_data.nii>
   --cout=$SUBJECTS_DIR/struct2diffusion_warp
```

In this case, the options include an `-aff` file, containing the affine transformation obtained from the flirt command, an `-inwarp` file, containing initial nonlinear warps, or `-refmask`, the binary brain mask. Then, the function ***invwarp*** is used to reverse the nonlinear mapping. The corresponding command line reads

[8] https://fsl.fmrib.ox.ac.uk/fsl/fslwiki/FLIRT/UserGuide

```
invwarp --warp=$SUBJECTS_DIR/struct2diffusion_warp
   --ref=$SUBJECTS_DIR/<MRI_data.nii>
   --out=$SUBJECTS_DIR/struct2diffusion_warp_inv
```

where the `-warp` volume is obtained as output from the fnirt command. The output of invwarp is necessary for the following transformation of the DTI data to the T1 space. This transformation is performed with the function ***applywarp***, which applies the transformation estimated by FNIRT to the DTI image in order to align it with the MRI structural scan:

```
applywarp [options]  --in=$SUBJECTS_DIR/<DTI_data.nii>
   --out=$SUBJECTS_DIR/<output DTI file.nii>
   --ref=$SUBJECTS_DIR/<MRI_data.nii>
   --warp=$SUBJECTS_DIR/struct2diffusion_warp_inv
```

It is possible to specify, with the option `-interp`, the interpolation method (possibilities are `nn`, `trilinear`, `sinc`, `spline`). At this step it is important to check the registration and the alignment between DTI and MRI data, whose raw file are created with different systems of reference. Visualizing the MRI and DTI images the alignment can be confirmed, as shown in Figure A.3.

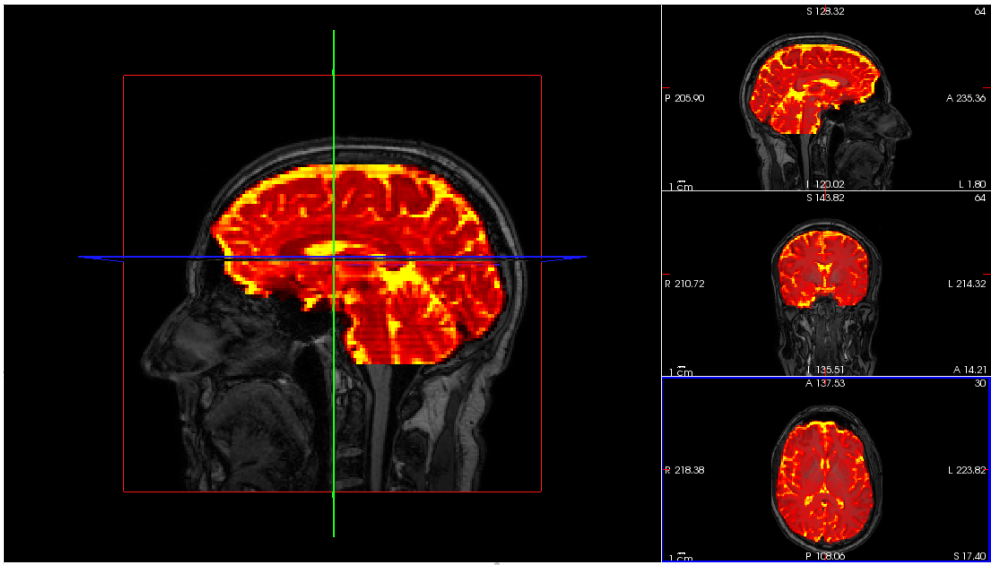

FIGURE A.3: **Example of correctly aligned data after the registration process.**

A.3 *Conversion to Matlab format*

Considering that we want to perform numerical simulations within the Matlab environment, we need to make the results of the raw data processing with FreeSurfer and FSL accessible with Matlab. In particular, we first have to extract the 2D boundary of the computational domain and define a fine mesh on it. Then, we need the corresponding DTI information on the chosen 2D slice and, finally, we have to define a way for matching the natural mesh of the DTI data, determined by its voxels, with the finer mesh defined on the domain. In fact, we do not use the former as a mesh for the

computational domain due to the voxel sizes[9].

We start from the data of the brain geometry, considering the two pial surface files `lh.pial` and `rh.pial` from the *Pial and T2 Pial* step of the FreeSurfer processing, which contain the information about the brain surface. The code for loading the data into the Matlab environment reads:

Algorithm 1.1 `?h.pial` loading in Matlab.

```
[vertices_l, faces_l] = freesurfer_read_surf('lh.pial');
[vertices_r, faces_r] = freesurfer_read_surf('rh.pial');
```

In particular, the function `freesurfer_read_surf.m` reads the vertex coordinates (expressed in *mm*) and the face list from the surface files and stores this information in the new variables `vertices_?` and `faces_?`, respectively, where `_?` stands for `_l` or `_r` and refers to the left and right hemisphere, respectively. These variables are defined as matrices containing vertex and face coordinates of the surface mesh defined by FreeSurfer. They also allow to visualize the surface in Matlab with the following code:

Algorithm 1.2 `?h.pial` visualization in Matlab.

```
Hp = patch('vertices', vertices, 'faces', faces(:, [1 3 2]), 'facecolor',....
.... [.5 .5 .5], 'edgecolor', 'none');
camlight('headlight', 'infinite');
```

An example of the brain surface visualization in Matlab is provided in Figure A.4.

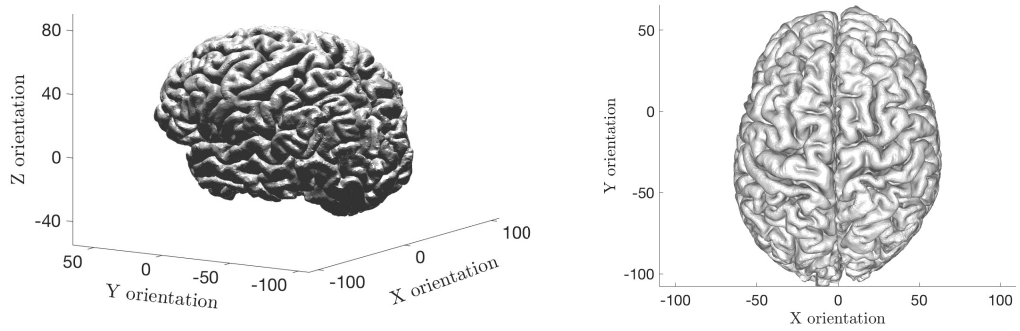

FIGURE A.4: **Illustrative example of the Matlab visualization of the brain surface.** 3D view of two hemisphere (left) and 2D superior view (right). In both plots, the axis labels refer to the orientation of the MRI data aligned with the DTI orientation of Table A.1. The three dimensions are expressed in *mm*.

To perform numerical simulations on a 2D slice of the brain, we need to extract from these data about the entire brain surface the information on the external contour of the 2D slice we are interested in. This procedure is performed with Paraview[10], a general open-source, multi-platform data analysis, and visualization application. This software reads `.vtk` files, which can be obtained from the above-defined matrices `vertices_?` and `faces_?`. In particular, once the files for the two hemispheres (`left_hemisphere_new.vtk` and `right_hemisphere_new.vtk`) are created, these are loaded

[9] The voxel dimensions of the DTI image are 1.5 mm $\times$ 1.5 mm $\times$ 1 mm. Considering the average speed of a glioma cell between $30 - 50\ \mu\text{m} \cdot \text{h}^{-1}$, we require a finer mesh for the computational domain to properly trace the cell movements.

[10] https://www.paraview.org

in Paraview and visualized. Using the `Contour` tool available in Paraview (from the drop-down menu `Filters/Alphabetical/Contour`), it is possible to extract the external contour of the chosen slice[11]. An example of visualization of the brain surface in 3D and the 2D contour with Paraview is provided in Figure A.5.

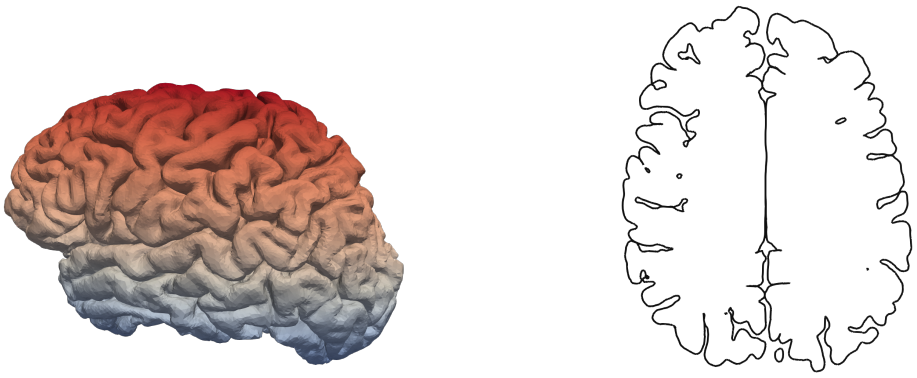

FIGURE A.5: **Illustrative example of the Paraview visualization.** 3D view of the brain (left) and contour plot of the chosen 2D slice (right).

The information about the contour is saved into an `ASCII` file, which provides the number of points, their coordinates, how many segments constitute the external boundary, and which points they connect. We store this information in two separate text files: `POINTS.txt`, with the number of boundary points and their coordinates; `SIDES.txt`, with the information about the segments. These files are read in Matlab and, once the points have been ordered, are used to create the file for the external boundary (`external_boundary.txt`). They can be visualized in Matlab with the simple code:

Algorithm 1.3 Visualization of the extracted contour in Matlab.

```
load external_boundary.txt
points = external_boundary;
plot (points(:, 1), points(:, 2), 'r*')
```

To mesh this 2D computational domain we use Gmsh[12], a free 3D finite element mesh generator, which provides a fast, light and user-friendly meshing tool with parametric input and advanced visualization capabilities. With the help of Gmsh, we define a fine unstructured mesh on the 2D domain we extracted. For this purpose, we use the code:

Algorithm 1.4 Preliminary step for Gmsh.

```
[IN,ON] = inpolygon(x_internal, y_internal, x_boundary, y_boundary);
j = 1;
for i = 1 : size(x_internal) do
    if ( IN(1,i) == 1 && ON(1,i) == 0 ) then
        C_in(1 : 2, j) = C_new(1 : 2, i);
```

[11] Since the DTI data have a different resolution than the MRI-T1 data, i.e., they differ in terms of the number of voxels and their dimensions, we need to ensure that we are extracting the same 2D slice from DTI and MRI processed data. Thus, one can visualize with FreeView both the DTI registration and the FreeSurfer output files `?h.pia` and, fixed in the desired slice on the DTI registration, read the corresponding value of the z-coordinate on the FreeSurfer outputs. Then, this information is used for the extraction of the external contour of the 2D slice with the `Contour` tool.

[12] `https://gmsh.info`

```
        j = j+1;
    end if
end for
```

where the coordinates `x_boundary` and `y_boundary` are taken from the text file `external_boundary.txt`, while `x_internal` and `y_internal` originate from the processing of the DTI data (they correspond to the first two row of the matrix `C_new`, which we will introduce later on and that contains information about the DTI voxel mesh). Algorithm 1.4 allows us to define the matrix `C_in`, containing the coordinates of the inner points of the DTI voxel mesh. Together with `external_boundary.txt`, this matrix is necessary to convert the `.txt` files in `.geo` format, the common format in Gmsh. The output of Gmsh is a Matlab structure that contains a series of information: the number of nodes of the new defined mesh (`.nbNod`), their coordinates (`.POS`), the maximum and minimum value between all the points of each of the coordinates (`.MAX` and `.MIN`), the segments that connect the points (`.LINES`) and the triangles constituting the mesh (`.TRIANGLES`).

Similarly to the processed MRI data, we have to make the FSL output files accessible in the Matlab environment. Thus, considering the files for the tensor eigenvalues (`DTI_dtifit_ Li`) and eigenvectors (`DTI_dtifit_Vi`), we first build a 5D structure collecting the DTI information. Precisely, for each voxel identified by (i, j, k), the structure $DTI(i, j, k, :, :)$ is a 3×3 matrix representing the DTI tensor corresponding to this voxel and built using the related eigenvalues $\lambda_{(i,j,k),l}$ and eigenvectors $v_{(i,j,k),l}$, for $l = 1, 2, 3$, i.e.,

$$DTI(i, j, k, :, :) = \sum_{l=1}^{3} \lambda_{(i,j,k),l}\, v_{(i,j,k),l}\, v^T_{(i,j,k),l}\,.$$

The corresponding algorithm to build this structure in Matlab reads:

Algorithm 1.5 DTI structure construction.

```
V1 = load_nii('ABU02_dti_V1.nii', [], 1);
V2 = load_nii('ABU02_dti_V2.nii', [], 1);
V3 = load_nii('ABU02_dti_V3.nii', [], 1);
L1 = load_nii('ABU02_dti_L1.nii', [], 1);
L2 = load_nii('ABU02_dti_L2.nii', [], 1);
L3 = load_nii('ABU02_dti_L3.nii', [], 1);
v1 = V1.img;
v2 = V2.img;
v3 = V3.img;
l1 = L1.img;
l2 = L2.img;
l3 = L3.img;

dim = size(v1);
Gamma1 = zeros(dim(1), dim(2), dim(3), 3, 3);
Gamma2 = zeros(dim(1), dim(2), dim(3), 3, 3);
Gamma3 = zeros(dim(1), dim(2), dim(3), 3, 3);

for i = 1 : dim(1) do
    for j = 1 : dim(2) do
        for k = 1 : dim(3) do
            w1 = squeeze(v1(i, j, k, :));
            w2 = squeeze(v2(i, j, k, :));
```

```
            w3 = squeeze(v3(i, j, k, :));

            Gamma1(i, j, k, :, :) = abs(l1(i, j, k))*w1*w1';
            Gamma2(i, j, k, :, :) = abs(l2(i, j, k))*w2*w2';
            Gamma3(i, j, k, :, :) = abs(l3(i, j, k))*w3*w3';
        end for
    end for
end for
DTI = Gamma1 + Gamma2 + Gamma3;

save ('DTI_constr.mat', 'DTI')
```

where the function `load_nii` is used to read a NIfTI file in Matlab. From this 5D structure, we extract the DTI information concerning the 2D slice for which we obtained the outer border with Paraview and that we meshed with Gmsh. As explained above, we do not use the natural and regular mesh provided by the DTI voxels because of its low resolution. Thus, we need to define a way to match the meshes and get, for each point $\mathbf{x}$ of the domain mesh the corresponding tensor. Referring to the chosen 2D slice with the index `k`, firstly we use the result of *BET*, i.e., `DTI_correct_brain.nii`, to build a reference geometry as:

Algorithm 1.6 Reference geometry extraction.

```
BET = load_nii('DTI_correct_brain.nii');
Bet = BET.img;
Bet = Bet(:, :, k);
save ('refer_geo_slicek.mat', 'Bet')
```

Using the function `slice_mesh`, we obtain the nodes (`points`) and the triangulation (`tri_new`) of the corresponding voxel mesh on this `k`-slice:

Algorithm 1.7 Algorithm for the function *slice_mesh*.

```
function [tri_new,points] = slice_mesh()
bet = load('refer_geo_slicek.mat');
bet = bet.Bet;
points = [];

for i = 1 : 128 do
    for j = 1 : 128 do
        if ( bet(i,j) > 0 ) then
            points = [points [i; j] ];
        end if
    end for
end for

Point_type = [];

level = 0;
a = find(points(1, :) == max(points(1, :)) & points(2, :) >= level);
Point_type = [Point_type; points(1, a)' points(2, a)' a'];
level = points(2, a(end));

for i = max(points(1, :))-1 : -1 : min(points(1, :))+1 do
```

```
    a = find(points(1, :) == i & points(2, :) >= level);
    if ( length(a) > 1 ) then
        a = a(2 : end);
    end if
    if ( length(a) == 0 ) then
        b = find(points(1, :) == i-1);
        a = find(points(1, :) == i & points(2, :) >= points(2, b(end)));
        if ( length(a) > 1 ) then
            a = a(end : -1 : 2);
        else if ( length(a) == 0 ) then
            a = find(points(1, :) == i);
            a = a(end);
        end if
    end if
    Point_type = [Point_type; points(1, a)' points(2, a)' a'];
    level = points(2, a(end));
end for

level = 0;
a = find(points(1, :) == min(points(1, :)) & points(2, :) >= level);
a = a(end : -1 : 1);
Point_type = [Point_type; points(1, a)' points(2, a)' a'];
level = points(2, a(end));

for i = min(points(1, :))+1 : max(points(1, :))-1 do
    a = find(points(1, :) == i & points(2, :) <= level);
    if ( length(a) > 1 ) then
        a = a(end-1 : -1 : 1);
    end if
    if ( length(a) == 0 ) then
        b = find(points(1, :) == i+1);
        a = find(points(1, :) == i & points(2, :) <= points(2, b(1)));
        u = points(2, a(2: end)) - points(2, a(1: end-1));
        if ( length(a) > 1 ) then
            a = a(1: end-1);
        end if
    end if
    Point_type = [Point_type; points(1, a)' points(2, a)' a'];
    level = points(2, a(end));
end for
bordo = Point_type(:, 3);
indexes = 1 : size(points, 2);
interni = setdiff(indexes, bordo);

tri = delaunay(points(1, :), points(2, :));
rubbish = [];
for i=1: size(tri,1) do
    if ( any(tri(i, 1) == bordo) | any(tri(i, 2) == bordo) | any(tri(i, 3) == bordo) ) then
        x = 0;
        for j=1 : 3 do
            if ( any(tri(i, j) == bordo) ) then
```

```
            x = x + 1;
        end if
    end for
    if (x == 3) then
        rubbish = [rubbish; tri(i, 1) tri(i, 2) tri(i, 3)];
    end if
  end if
end for

tri_new = setdiff(tri, rubbish, 'rows', 'stable');
```

From this voxel mesh we define the $5 \times N$ matrix `C_new`, with N total number of voxel mesh points, built with the following algorithm:

Algorithm 1.8 Construction of the structure containing the voxel mesh and the DTI tensor information.

```
C = points;
L = tri_new;
N = size(C, 2);
s = size(L);

DTI_2D = squeeze(DTI(:, :, k, 1:2, 1:2));
C_new = zeros(5, N);

for i=1 : N do
    x = C(1, i);
    y = C(2, i);
    DTI_temp = squeeze(DTI_2D(x, y, :, :));
    C_new(1:2, i) = C(1:2, i);
    C_new(3, i) = DTI_temp(1, 1);
    C_new(4, i) = DTI_temp(1, 2);
    C_new(5, i) = DTI_temp(2, 2);
end for
```

In particular, the first two rows of `C_new` contain the coordinates of each voxel mesh point, while the third, fourth and fifth rows contain respectively the values of $DTI_{1,1}$, $DTI_{1,2}$ and $DTI_{2,2}$ at the corresponding point. As the DTI tensor is symmetric, these values are sufficient. Once we have the unstructured mesh of the computational domain built with Gmsh and the voxel mesh and DTI information contained in `C_new`, for each point of the former mesh we look for the right voxel in which it falls and we assign the corresponding tensor values to it. This is done with the function `find_voxel` that used the `Pix` matrix defined as:

Algorithm 1.9 Construction of the `Pix` matrix.

```
N = size(C_new, 2);
Pix = zeros(2, N);
A = 0;
B = 0;

for i=1 : N do
    A = C_new(1, i)/h_vox;
    B = C_new(2, i)/h_vox;
```

```
    Pix(1, i) = A;
    Pix(2, i) = B;
end for
```

The `find_voxel` function determines in which voxel is located the point of (x, y)-coordinates, returning the number of the `C_new` column referring to the voxel in which the point falls. This function reads

Algorithm 1.10 Algorithm for the `find_voxel` function.

```
function [col] = find_voxel(x, y, Pix, h_vox)

pos_A = find( Pix(1, :) >= x/h_vox-1 & Pix(1, :) <= x/h_vox+1 );
i = 1;
flag = false;

while ( i <= size(pos_A, 2) & flag == false ) do
    j = pos_A(i);
    if ( Pix(2, j) >= y*2/h_vox-1 & Pix(2, j) <= y*2/h_vox+1 ) then
        col = j;
        flag = true;
    end if
    i = i + 1;
end while
if (flag == false) then
    col = 0;
end if

return
```

In both cases, `h_vox` indicated the x (or y)-dimension of the voxel. These algorithms provide a way to match the DTI and the MRI information within the Matlab environment.

B Mathematical compendium

Throughout this dissertation, we referred to some mathematical concepts and numerical methods used in the approximation of the solution of the PDE systems, in the numerical integration of the directional tensors as well as in the data analysis. In this appendix, we first comment, in Section B.1, on the finite element approximation method for a PDE system and on the space and time approximations used in Chapters 3-5 and 7. Then, in Section B.2, we describe the numerical integration methods, mainly used in Chapter 2 for the construction of the directional tensor $\mathbf{D}_T$.

B.1 *Introduction to the finite element method*

For the numerical solution of the PDE systems describing the evolution of tumor cells and eventual additional populations coupled with them, we use the finite element approximation method. We provide here a short introduction to the mathematical theory of the finite element method for the space approximation of macroscopic systems. Moreover, we describe some possible techniques for their temporal discretization. In the following, we mainly refer to [160, 234].

B.1.1 *Triangulation, finite-dimensional subspace, and shape functions*

The three basic aspects characterizing the finite element method consist in the definition of a triangulation, the construction of a finite dimensional subspace of piecewise-polynomials, and the description of its basis of shape functions.

Let the set $\Omega \in \mathbb{R}^d$ be a polygonal domain, i.e., an open bounded connected subset of $\mathbb{R}^d$ such that its closure $\bar{\Omega}$ is the union of a finite number of polyhedra. A ***triangulation***, or mesh, $\mathcal{T}_h$ of $\bar{\Omega}$ is a set of polyhedra such that

$$\bar{\Omega} = \bigcup_{\mathcal{K} \in \mathcal{T}_h} \mathcal{K}.$$

It satisfies the following assumptions:

- each $\mathcal{K}$ is a polyhedron with $\mathring{\mathcal{K}} \neq \emptyset$;
- $\mathring{\mathcal{K}}_1 \bigcap \mathring{\mathcal{K}}_2 = \emptyset$ for distinct elements $\mathcal{K}_1, \mathcal{K}_2 \in \mathcal{T}_h$;
- if $F = \mathcal{K}_1 \bigcap \mathcal{K}_2 \neq \emptyset$ ($\mathcal{K}_1$ and $\mathcal{K}_2$ distinct elements of $\mathcal{T}_h$), then F is a common face, side, or vertex of $\mathcal{K}_1$ and $\mathcal{K}_2$;
- $d_{\mathcal{K}} \leq h$ for each $\mathcal{K} \in \mathcal{T}_h$, with $d_{\mathcal{K}}$ diameter of the circle inscribed in $\mathcal{K}$.

In particular, each element $\mathcal{K}$ of $\mathcal{T}_h$ can be obtained as $\mathcal{K} = T_{\mathcal{K}}(\hat{\mathcal{K}})$, where $\hat{\mathcal{K}}$ is a reference polyhedron and $T_{\mathcal{K}}$ is a suitable invertible affine map, i.e., $T_{\mathcal{K}}(X) = B_{\mathcal{K}}X + b_{\mathcal{K}}$, $B_{\mathcal{K}}$ being a non-singular matrix. In our case, we consider ***triangular elements*** $\mathcal{K}$, for which the reference polyhedron $\hat{\mathcal{K}}$ is the unit d-simplex, i.e., the triangle of vertices

(0,0), (1,0), (0,1) (for $d = 2$). The corners of the triangles are called the *nodes*, while its sides are called *edges*. The *size* of a triangle $\mathcal{K}$, i.e., $h_\mathcal{K}$ is defined as the length of its longest edge. In particular, defining the chunkiness parameter as

$$c_\mathcal{K} := h_\mathcal{K} / d_\mathcal{K} ,$$

a triangulation is called *shape regular* if there is a constant $c_0 > 0$ such that $c_\mathcal{K} \geq c_0$ $\forall\ \mathcal{K} \in \mathcal{T}_h$. This condition means that the shape of the triangles can not be too extreme, e.g. the angles of any triangle can neither be very wide nor very narrow. The global mesh size is defined as

$$h := \max_{\mathcal{K} \in \mathcal{T}_h} h_\mathcal{K}.$$

The standard way of representing a triangular mesh with n_p nodes and n_t triangular elements is to store it in the form of two matrices, the *point matrix* C and the *connectivity matrix* L. The point matrix C is of size $2 \times n_p$ and the j-th column contains the coordinates (x_j, y_j) of the node N_j. The connectivity matrix L is of size $3 \times n_t$ and the j-th column contains the numbers of the three nodes (with respect to the ordering of C matrix) constructing the triangle $\mathcal{K}_j$.

A second basic aspect of the finite element method consists in determining a finite-dimensional space X_h to use as a suitable approximation of the infinite-dimensional space X to which the solution of the PDE system belongs. In particular, for our case, we consider the subspace X_h such that every $v_h \in X_h$ is a piecewise polynomial. Precisely, defining $\mathbb{P}_k$, for $k \geq 0$ as the space of polynomials of degree less than or equal to k, we set

$$X_h^k := \{ v_h \in \mathcal{C}^0(\bar{\Omega}) \,|\, v_{h|\mathcal{K}} \in \mathbb{P}_k \ \forall \mathcal{K} \in \mathcal{T}_h \} ,$$

which is called ***space of triangular finite elements of order*** k. Here, $\mathcal{C}^0(\bar{\Omega})$ denotes the space of all continuous functions on $\bar{\Omega}$. In particular, it is worth to note that

$$X_h^k \subset H^1(\Omega) \quad \forall k \geq 1 .$$

The last step is to construct a basis for the space X_h^k. For our bidimensional case $d = 2$, we have to choose three degrees of freedom on each element $\mathcal{K}$ to identify $v_{h|\mathcal{K}}$, with the additional constraint that $v_h \in \mathcal{C}^0(\bar{\Omega})$. The simplest choice is to pick $k = 1$ and, thus, to fix the values at the vertices of each $\mathcal{K}$. If we consider $k = 2$, we might assume that the degrees of freedom of the element are given by the value at the vertices and in the middle point of each side. In particular, the validity of this choice can be proven [234] and can be also extended to the definition of the degrees of freedom for $k = 3$. These degrees of freedom are given by the values at the three vertices, two other nodes on each side (dividing it into three subintervals of equal length), and the center of gravity. The situation for the three cases $k = 1, 2, 3$ is illustrated in Figure B.1. Denoting by N_j, $j = 1, ..., n_p$, the global set of nodes in $\bar{\Omega}$, to construct a basis of X_h^k it is sufficient to choose functions $\phi_i \in X_h^k$ such that

$$\phi_i(N_j) = \delta_{ij}, \quad i, j = 1, ..., n_p ,$$

with the Kronecker symbol δ_{ij}. These basis functions ϕ_i are called ***shape functions*** and each of these functions has a "small" support. The identification of degrees of freedom and shape functions leads to the definition of the ***interpolation operator*** $\pi_h^k : \mathcal{C}^0(\bar{\Omega}) \to X_h^k$ defined on the space of continuous functions and the finite element

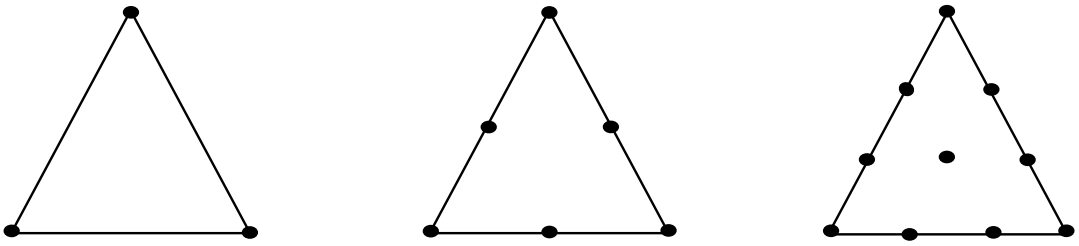

FIGURE B.1: **Degrees of freedom for triangular elements.**

space X_h^k. Precisely, for each $v \in \mathcal{C}^0(\bar{\Omega})$ the operator π_h^k is defined as

$$\pi_h^k(v) := \sum_{i=1}^{n_p} v(N_j)\phi_i \,.$$

The interpolant $\pi_h^k(v)$ is a unique function in X_h^k which assumes the same values of the given function v at all nodes N_j. Similarly, it is possible to introduce a local interpolation operator $\pi_{\mathcal{K}}^k(v)$ defined for functions restricted to $\mathcal{K}$. It can be verified that

$$\pi_h^k(v)_{|\mathcal{K}} = \pi_{\mathcal{K}}^k(v_{|\mathcal{K}}) \,.$$

The interpolation operator gives optimal error estimates in Sobolev norms whenever the function to be interpolated satisfies the minimal requirements for the continuity. Other approximation operators can also be introduced, such as the $L^2(\Omega)$ and $H^1(\Omega)$-orthogonal ***projection operators***. If H is a Hilbert space and S is a closed subspace of H, the orthogonal projection operator P_S of over S is defined as

$$P_S(v) \in S : \ (P_S(v), \phi)_H = (v, \phi)_H \quad \forall \phi \in S.$$

B.1.2 *Space-discretization: the Galerkin method*

Before referring to the specific case of parabolic initial-boundary value problems, we present a short overview of the classical ***Galerkin method*** for the discretization of a general (initial-) boundary value system. We comment on the reformulation of the problem in a weak, or variational, form and introduce the space approximation based on the Galerkin method.

Considering the bounded domain $\Omega \in \mathbb{R}^d$ and denoting its boundary with $\partial\Omega$, a boundary value problem can be written in the form

$$\begin{cases} L\,u = f & \text{in } \Omega \\ B\,u = 0 & \text{on } \partial\Omega \,, \end{cases} \tag{B.1}$$

where f is a given function, u the unknown variable, L a linear differential operator, and B an affine boundary operator. Often, L is an unbounded operator in a space H that can be either $L^2(\Omega)$ or $L^2_\omega(\Omega)$, where, the latter is a weighted Hilbert space. The objective is to find for the solution u in a space $X \subset H$, such that L and B are well defined for functions in X. System (B.1) can be reformulated in a weak form, the ***variational formulation***. Formally, this formulation can be derived after multiplication of the differential equation by a suitable set of test functions v. After performing an integration over the domain Ω and applying the Green formula of integration by parts,

the variational formulation of (B.1) reads

$$\int_\Omega \frac{\partial u}{\partial x_i} v d\mathbf{x} = -\int_\Omega u \frac{\partial v}{\partial x_i} d\mathbf{x} + \int_{\partial\Omega} u\, v\, n_i d\boldsymbol{\gamma} \qquad i = 1, ..., d$$

where $n = (n_1, ..., n_d)$ is the unit outward normal vector on $\partial\Omega$. The resulting problem reads:

$$\text{find } u \in W : \mathcal{A}(u, v) = \mathcal{F}(v) \quad \forall\, v \in V\,. \tag{B.2}$$

Here, W is the space of admissible solutions and V is the space of test functions. Both spaces can be assumed to be Hilbert spaces. $\mathcal{F}$ is a linear functional on V that accounts for the right hand side f as well as for possible non-homogeneous boundary terms and $\mathcal{A}(\cdot, \cdot)$ is a bilinear form corresponding to the differential operator L. Before considering the numerical approximations for (B.2), we recall two fundamental functional theorems about the existence and the uniqueness of the solution.

Theorem B.1. (*Lax-Milgram lemma*). Let V be a Hilbert space, equipped with the norm $||\cdot||$, $\mathcal{A}(u, v) : V \times V \to \mathbb{R}$ a bilinear form, and $\mathcal{F}(v) : V \to \mathbb{R}$ a linear continuous functional, i.e., $\mathcal{F} \in V'$, where V' denotes the dual space of V. Assume that $\mathcal{A}(\cdot, \cdot)$ is continuous, i.e.,

$$\exists \gamma > 0 : |\mathcal{A}(w, v)| \leq \gamma ||w||\, ||v|| \quad \forall w, v \in V\,,$$

and coercive, i.e.,

$$\exists \alpha > 0 : \mathcal{A}(v, v) \geq \alpha ||v||^2 \quad \forall v \in V\,.$$

Then, there exists a unique solution $u \in V$ of (B.2) that satisfies

$$||u|| \leq \frac{1}{\alpha} ||\mathcal{F}||_{V'}\,.$$

Theorem B.2. Let W and V be two Hilbert spaces, with norms $||\cdot||_W$ and $||\cdot||_V$, respectively. Assume that there exist two positive constants α and γ such that the bilinear form $\mathcal{A} : W \times V \to \mathbb{R}$ satisfies

- $|\mathcal{A}(w, v)| \leq \gamma ||w||_W ||v||_V \quad \forall w \in W,\, v \in V$
- $\sup_{v \in V,\, v \neq 0} \dfrac{\mathcal{A}(w, v)}{||v||_V} \geq \alpha ||w||_W \quad \forall w \in W$
- $\sup_{w \in W} \mathcal{A}(w, v) > 0 \quad \forall v \in V,\, v \neq 0\,.$

Then, for any $\mathcal{F} \in V'$, there exists a unique solution $u \in W$ which satisfies

$$||u||_W \leq \frac{||\mathcal{F}||_{V'}}{\alpha}\,.$$

For the proofs we direct the reader to [234].

Focusing on the particular case $W = V$, let $h > 0$ be the mesh size for the finite elements introduced above, $||\cdot||$ the norm on V, and $\{V_h \,|\, h > 0\}$ a family of finite dimensional subspaces of V (that corresponds to the generic space X_h in the previous section). We assume that

$$\forall\, v \in V\,,\ \inf_{v_h \in V_h} ||v - v_h|| \to 0 \text{ as } h \to 0\,.$$

Under this condition, the ***Galerkin approximation*** of (B.2) reads

$$\text{given } \mathcal{F} \in V' \quad \text{find } u_h \in V_h \,:\, \mathcal{A}(u_h, v_h) = \mathcal{F}(v_h) \quad \forall v_h \in V_h \,. \tag{B.3}$$

Considering $\{\phi_j \,|\, j = 1, ..., N_h\}$ a basis for the vector space V_h, the unknown $u_h \in V_h$ can be rewritten as

$$u_h(\mathbf{x}) = \sum_{j=1}^{N_h} \xi_j \phi_j(\mathbf{x})$$

with ξ_j unknown coefficients. This translates (B.3) into the following linear system of dimension N_h:

$$A\boldsymbol{\xi} = F$$

with $\boldsymbol{\xi} = (\xi_j)$, $F_i := (\mathcal{F}(\phi_i))$, $A_{ij} := \mathcal{A}(\phi_j, \phi_i)$ for $i, j = 1, ..., N_h$. Precisely, the matrix A is called *stiffness matrix* and is positive definite, i.e., for any $\boldsymbol{\eta} \in \mathbb{R}^{N_h}$, $\boldsymbol{\eta} \neq 0$, $(A\boldsymbol{\eta}, \boldsymbol{\eta}) > 0$, where $(\cdot, \cdot)$ the euclidean scalar product. Moreover, when the bilinear form $\mathcal{A}$ is symmetric, it follows immediately that A is also symmetric.

Together with the Galerkin method, there are other families of space approximations for the weak form of (B.1), such as the Petrov-Galerkin method, the collocation method and generalized Galerkin methods. In this appendix, we focus only on the Galerkin method that we use for the space discretization of our systems. However, we direct the reader to [234] for detailed descriptions of the other methods.

B.1.3 *Time-advancing methods*

After describing the setting of the space discretization with the Galerkin method, in this section we address the issue of time discretization for initial-boundary value problems. Starting from the abstract framework of the previous section, we now define the time-dependent problem

$$\begin{cases} \dfrac{\partial u}{\partial t} + L\,u = f & \text{in } (0,T) \times \Omega \\ B\,u = 0 & \text{on } (0,T) \times \partial\Omega \\ u = u_0 & \text{on } \Omega, \text{ for } t = 0\,. \end{cases} \tag{B.4}$$

Here, $T > 0$ is a fixed time-level, u and f are functions of $t \in (0,T)$ and $\mathbf{x} \in \Omega$, and $u_0 = u_0(\mathbf{x})$ is the initial value. The differential operator L and the boundary operator B can also depend on t. The weak formulation of this problem can be stated assuming that there exist three Hilbert spaces V, W, H such that W and V are contained in H with dense, continuous inclusion. The scalar product of H is denoted by $(\cdot, \cdot)$. We assume that $u_0 \in H$, $f \in L^2(0,T;H)$, and the bilinear form $\mathcal{A}(\cdot, \cdot)$ is continuous on $W \times V$. The weak formulation of (B.4) reads: find $u \in L^2(0,T;W) \cap C^0([0,T];H)$ such that

$$\frac{d}{dt}(u(t), v) + \mathcal{A}(u(t), v) = \mathcal{F}(t, v) \;\; \forall v \in V \tag{B.5}$$

with $u = u_0$ at $t = 0$. In particular, the compact notation on the right hand side stands for $(f(t), v)$ plus another possible term depending on non-homogeneous boundary conditions. The functional space $L^2(0,T;H)$ is a particular case of

$$L^q(0,T;W^{s,p}(\Omega)) := \left\{ v : (0,T) \to W^{s,p}(\Omega) \,|\, v \text{ is measurable and } \int_0^T ||v||^q_{W^{s,p}(\Omega)}\, dt < \infty \right\}$$

for $1 \leq q < \infty$ and endowed with the norm

$$||v||_{L^q(0,T;W^{s,p}(\Omega))} := \left(\int_0^T ||v||^q_{W^{s,p}(\Omega)} \, dt \right) ,$$

where $W^{s,p}(\Omega)$ describes the Sobolev space on Ω of the order $s \in \mathbb{N}$. The general problem (B.5) has to be discretized with respect to both time and space variables. For the space discretization, we rely on the Galerkin approximation described in the previous section. Thus, the resulting problem reads: for each $t \in [0,T]$ find $u_h(t,\mathbf{x}) \in V_h \subset V$ such that

$$\frac{d}{dt}(u_h(t), v_h) + \mathcal{A}(u_h(t), v_h) = \mathcal{F}(t, v_h) \quad \forall\, v_h \in V_h, \quad t \in (0,T) \tag{B.6}$$

with $u_h(0) = u_{0,h}$, a suitable element of V_h that approximates the initial value u_0. This is called *semi-discrete approximation* of (B.5). Then, considering $\{\phi_j \,|\, j = 1, ..., N_h\}$, a basis of V_h, and

$$u_h(t,\mathbf{x}) = \sum_{j=1}^{N_h} \xi_j(t)\phi_j(\mathbf{x}) \quad \text{for } t \geq 0\,, \quad u_{0,h}(\mathbf{x}) = \sum_{j=1}^{N_h} \xi_{0,j}\phi_j(\mathbf{x})\,,$$

with $\xi_{0,j} = \xi_j(0)$, the problem (B.6) can be translated into the following system of ordinary differential equations

$$\begin{cases} M\dfrac{d\boldsymbol{\xi}(t)}{dt} + A\boldsymbol{\xi}(t) = F(t) \\ \boldsymbol{\xi}(0) = \boldsymbol{\xi}_0 \end{cases} \tag{B.7}$$

where $\boldsymbol{\xi}(t) = (\xi_j(t))$, $F(t) := (\mathcal{F}(t, \phi_j))$, and $\boldsymbol{\xi}_0 = (\xi_{0,j})$, for $j = 1, ..., N_h$. The stiffness matrix A was introduces in the previous section, while $M_{ij} := (\phi_i, \phi_j)$, for $i, j = 1, ..., N_h$ is called *mass matrix*. This matrix is symmetric, positive definite, and always independent of t.

The ***time discretization*** can be achieved with several methods. We consider a partition of the time-interval $[0,T]$ into N_t subintervals $[t_n, t_{n+1}]$ of length $\Delta t = \frac{T}{N_t}$, with $t_0 = 0$ and $t_{N_t} = T$. Then, we denote by u_h^n the finite dimensional function approximating $u_h(t)$ at each time-level t_n. In particular, u_h^0 represents the approximation of u_0. First, we describe the ***θ-scheme***, a finite difference scheme according to which (B.6) is discretized as

$$\frac{1}{\Delta t}\left(u_h^{n+1} - u_h^n, v_h\right) + \mathcal{A}(\theta u_h^{n+1} + (1-\theta)u_h^n, v_h) = \theta\mathcal{F}(t_{n+1}, v_h) + (1-\theta)\mathcal{F}(t_n, v_h)$$

for all $v_h \in V_h$. In particular, $n = 0, ..., N_t - 1$ and $\theta \in [0,1]$. The extreme cases $\theta = 0$ and $\theta = 1$ define the well-known forward and backward Euler methods, respectively, while, for $\theta = \frac{1}{2}$, the scheme is known as the Crank-Nicolson (CN) method. Recalling the algebraic formulation (B.7), its time discretization reads

$$M\boldsymbol{\xi}^{n+1} + \theta\Delta t\, A\boldsymbol{\xi}^{n+1} = \boldsymbol{\eta}^{n+1} \quad n = 0, ..., N-1$$

with

$$\boldsymbol{\eta}^{n+1} := \theta\Delta t\, F(t_{n+1}) + (1-\theta)\Delta t\, F(t_n) + M\boldsymbol{\xi}^n - (1-\theta)\Delta t\, A\boldsymbol{\xi}^n$$

and $\boldsymbol{\xi}^0 = \boldsymbol{\xi}_0$. At each time step, it is necessary to solve a linear system associated with the matrix $M + \theta\Delta t\, A$. In particular, for $\theta = 1$, the backward Euler method is

first-order accurate, i.e, the norm of the truncation error $\xi(t_n) - \xi^n$ is $\mathcal{O}(\Delta t)$, and it is unconditionally stable. The forward Euler method obtained for $\theta = 0$, which is also first-order accurate, is conditionally stable. To be precise, a time-advancing method is *stable* with respect to the spatial norm $||\cdot||$ of V_h if

$$||u_h^n|| \leq C\, e^{\lambda t_n} ||u_h^0||\,, \quad n \geq 0$$

for $0 < \Delta t \leq \delta_h$, where C, λ, and δ_h are independent of Δt and both C and λ are independent of h. If δ_h is bounded from below and independently of h, the method is unconditionally stable. Otherwise, the functional dependence of δ_h from h is called the *stability limit* of the numerical method. This means that the method comes with a restriction on the time step Δt, which should be small enough compared to h, the spatial mesh size. The CN scheme is only conditionally stable, but it is second order accurate, i.e., the norm of the truncation error is $\mathcal{O}(\Delta t^2)$.

Another possibility for the time discretization of the ODE subsystem of the model described in Chapter 7 are the ***Runge-Kutta (RK) methods***. These are a family of implicit and explicit iterative methods that use the information on the 'slope' at more than one point to extrapolate the solution for future time steps. To provide a more clear introduction to RK methods, we consider the initial value problem

$$\begin{cases} \dfrac{dy}{dt}(t) = f(t, y(t)) \quad t \in (0, T) \\ y(0) = y_0 \end{cases}$$

with an unknown function y depending on time and y_0 its corresponding value at $t = 0$. Considering the time partition previously defined and let $y_n = y(t_n)$ be the approximation of $y(t)$ at time step t_n, for the family of explicit RK methods the approximation of y at t_{n+1} reads

$$y_{n+1} = y_n + \Delta t \sum_{i=1}^{s} b_i k_i \quad \text{for } n = 0, ..., N_t - 1\,,$$

where

$$\begin{aligned} k_1 &= f\left(t_n, y_n\right), \\ k_2 &= f\left(t_n + c_2 \Delta t, y_n + \Delta t\, a_{21} k_1\right), \\ k_3 &= f\left(t_n + c_3 \Delta t, y_n + \Delta t (a_{31} k_1 + a_{32} k_2)\right), \\ &\vdots \\ k_s &= f\left(t_n + c_s \Delta t, y_n + \Delta t (a_{s,1} k_1 + ... + a_{s,s-1} k_{s-1})\right). \end{aligned}$$

In particular, to choose a specific method, it is necessary to provide the integer s, which represents the number of stages, and the coefficients a_{ij}, for $1 \leq j < i \leq s$, b_i, and c_i, for $i = 1, ..., s$. The matrix $(a_{ij})_{ij}$ is called Runge-Kutta matrix, while b_i and c_i are known as the weights and nodes, respectively [158]. These data are usually arranged in the

Butcher tableau

$$\begin{array}{c|ccccc} 0 & & & & & \\ c_2 & a_{21} & & & & \\ c_3 & a_{31} & a_{32} & & & \\ \vdots & \vdots & & \ddots & & \\ c_s & a_{s1} & a_{s2} & \dots & a_{s,s-1} & \\ \hline & b_1 & b_2 & \dots & b_{s-1} & b_s \end{array}$$

The RK method is consistent if and only if $\sum_{i=1}^{s} b_i = 1$. For our discretization in Chapter 7 we use the fourth-order RK method (RK4), whose Butcher tableau reads:

$$\begin{array}{c|cccc} 0 & & & & \\ \frac{1}{2} & \frac{1}{2} & & & \\ \frac{1}{2} & 0 & \frac{1}{2} & & \\ 1 & 0 & 0 & 1 & \\ \hline & \frac{1}{6} & \frac{1}{3} & \frac{1}{3} & \frac{1}{6} \end{array}$$

Therefore, the approximation reads

$$y_{n+1} = y_n + \frac{1}{6}\Delta t \left(k_1 + 2k_2 + 2k_3 + k_4\right)$$

with

$$\begin{aligned} k_1 &= f\left(t_n, y_n\right), \\ k_2 &= f\left(t_n + \frac{\Delta t}{2}, y_n + \Delta t \frac{k_1}{2}\right), \\ k_3 &= f\left(t_n + \frac{\Delta t}{2}, y_n + \Delta t \frac{k_2}{2}\right), \\ k_4 &= f\left(t_n + \Delta t, y_n + \Delta t k_3\right). \end{aligned}$$

Here, y_{n+1} is the RK4 approximation of $y(t_{n+1})$, determined by $y(t_n)$ plus the weighted average of four increments. Each of them is the product of the size of the interval, Δt, and an estimated slope k_i depending on the function f on the right-hand side. The RK4 method is conditionally stable and fourth order accurate, meaning that the truncation error is of the order $\mathcal{O}(\Delta t^4)$. We want to remark that this is a brief presentation, with the only purpose of giving the reader an idea of some of the many possible ways to face this problem; there are many other space and time discretization that can be implemented.

B.1.4 *Discretization of an advection-diffusion-reaction PDE*

The models in Chapters 3-5 and 7 consist in systems of advection-diffusion-reaction PDEs. Their general formulation reads

$$\frac{\partial u(t,\mathbf{x})}{\partial t} - \nabla \cdot \left[A(\mathbf{x}) \nabla u(t,\mathbf{x})\right] + \nabla \cdot \left(\mathbf{b}(\mathbf{x}) u(t,\mathbf{x})\right) + a_0(\mathbf{x}) u(t,\mathbf{x}) = f(t,\mathbf{x}).$$

In this section, we first introduce a semidiscrete approximation of the PDE by discretizing with respect to the space variable $\mathbf{x}$ using the Galerkin method. Then, we

present a total discretization procedure, based on a θ-scheme, for the time derivative. We point out that the generalization to a system of PDEs is a straightforward procedure.

Starting from (B.4) and considering the bounded domain $\Omega \in \mathbb{R}^2$, with Lipschitz boundary, the differential operator L now reads

$$Lu := -\sum_{i,j=1}^{2} D_i(a_{ij}D_j u) + \sum_{i=1}^{2} D_i(b_i u) + a_0 u\,, \tag{B.8}$$

where the operator D_i denotes the partial derivative with respect to x_i, while $a_{ij} = a_{ij}(\mathbf{x})$ the components of the diffusion tensor $A(\mathbf{x})$, $b_i = b_i(\mathbf{x})$ refers to the components of the drift vector $\mathbf{b}(\mathbf{x})$, and $a_0 = a_0(\mathbf{x})$ is a given function. In particular, we observe that A and $\vec{b}$ can also depend on the unknown u. Moreover, we assume the boundary operator to be of homogenous Neumann type:

$$Bu = \frac{\partial u}{\partial \mathbf{n}} := \sum_{i,j=1}^{2} a_{ij}D_j u n_i - \sum_{i=1}^{2} b_i n_i u = 0$$

with n_i describing the components of the outward normal vector $\mathbf{n} = (n_1, n_2)$. To provide the weak formulation, let V be a closed subspace of $H^1(\Omega)$ such that $H_0^1(\Omega) \subset V \subset H^1(\Omega)$. The bilinear form associated to the operator L is given by

$$\mathcal{A}(u,v) := \int_\Omega \left[\sum_{i,j=1}^{2} a_{ij}D_i u D_j v - \sum_{i=1}^{2}(b_i u D_i v) + a_0 uv\right] \tag{B.9}$$

obtained by multiplying (B.8) by v and integrating over Ω, with the use of the Green formula and accounting for the boundary terms. The weak formulation reads as in (B.5) with the specification for the bilinear form given in (B.9). By approximating the space V with a finite dimensional space V_h, this variational formulation naturally leads to the semi-discrete problem (B.6) specified with (B.9). Defining the matrices as

$$(M_{ij}) := \int_\Omega \phi_i(\mathbf{x})\phi_j(\mathbf{x})d\mathbf{x} \quad \textit{mass matrix}\,,$$

$$(S_{ij}) := \int_\Omega A(\mathbf{x})\nabla\phi_i(\mathbf{x})\nabla\phi_j(\mathbf{x})d\mathbf{x} \quad \textit{stiffness matrix}\,,$$

$$(C_{ij}) := \int_\Omega \mathbf{b}(\mathbf{x})\phi_j(\mathbf{x})\nabla\phi_i(\mathbf{x})d\mathbf{x} \quad \textit{convection matrix}\,,$$

$$(F_i) := \int_\Omega f(\mathbf{x})\phi_i(\mathbf{x})d\mathbf{x} \quad \textit{load vector}\,,$$

$$(\bar{M}_{ij}) := \int_\Omega a_0(\mathbf{x})\,\phi_i(\mathbf{x})\phi_j(\mathbf{x})d\mathbf{x}\,,$$

the corresponding algebraic system reads

$$M\frac{d\boldsymbol{\xi}(t)}{dt} + S\boldsymbol{\xi}(t) - C\boldsymbol{\xi}(t) + \bar{M}\boldsymbol{\xi}(t) = F\,. \tag{B.10}$$

Here, the matrix $\bar{M}$ relates to the reaction term $a_0(\mathbf{x})u$, while the vector F depends on the given function f, independent of u. To provide an example of this discretization,

we recall the macroscopic equation deduced in Chapter 3:

$$\frac{\partial}{\partial t}u = \nabla \cdot (\mathbf{D}_T(\mathbf{x})\nabla u) - \nabla \cdot ((g(Q(\mathbf{x}))\mathbf{D}_T(\mathbf{x})\nabla Q - w(\mathbf{x}))u)$$
$$+ \mu(u)Q(\mathbf{x})u - L(u, R_1)u\,.$$

In this case, for the definition of the matrices, we have

$$A(\mathbf{x}) := \mathbf{D}_T(\mathbf{x})\,,$$
$$\mathbf{b}(\mathbf{x}) := g(Q(\mathbf{x}))\mathbf{D}_T(\mathbf{x})\nabla Q - w(\mathbf{x})\,,$$
$$a_0(\mathbf{x}) := \mu(u)Q(\mathbf{x}) - L(u, R_1)\,.$$

Applying the θ-scheme to the semi-discrete approximation encoded in the algebraic system (B.10) we finally get

$$\left[M + \theta\Delta t(S - C + \bar{M})\right]\boldsymbol{\xi}^{n+1} = \Delta t(\theta F(t_{n+1}) + (1-\theta)F(t_n))$$
$$+ \left[M - (1-\theta)\Delta t(S - C + \bar{M})\right]\boldsymbol{\xi}^n.$$

We apply this spatial and temporal discretization for the systems described in Chapters 3-5. In particular, we use triangular elements and linear shape functions also called *hat functions*. For the model of Chapter 7, this discretization, in its 1D formulation, is used on the subsystem of PDEs, while the subsystem of ODEs is discretized using the RK4 method introduced in the previous section. We do not refer to Chapter 6 since, in this case, we solve numerically the mesoscopic transport equation, instead of the macroscopic one. For the simulations presented therein, we use the numerical scheme proposed in [284] and described in [173] in which a kinetic model for chemotaxis is simulated in two-dimensions using a van Leer scheme for the space transport (see [173] for further details).

B.2 *Quadrature formula and numerical integration*

In this dissertation, we use different quadrature rules for the numerical approximation of the integrals involved in the finite element discretization (introduced in the previous section) as well as in the construction of the tensor $\mathbf{D}_T$ described in Chapter 2. We provide a brief introduction to some of the most commonly used methods for numerical integration. In the following, we mainly refer to [233].

Let f be a real integrable function over the interval $[a, b]$. A *quadrature formula*, also called *numerical integration formula*, is an explicit procedure that permits a suitable approximation of the integral

$$I(f) := \int_a^b f(x)dx\,.$$

The classical approach consists in replacing f with an approximation f_n, depending on the integer $n \geq 0$, in order to obtain

$$I_n(f) = \int_a^b f_n(x)dx \qquad n \geq 0 \tag{B.11}$$

as an approximation for $I(f)$. For instance, f_n can be chosen as an interpolating polynomial of degree n, i.e., $f_n \in \mathbb{P}_n$. When the function f is replaced by its interpolating polynomial, we refer to these procedures as ***interpolatory quadrature formulae***. Thus, considering a set of $n+1$ points $\{x_i\}$, with $i = 0, .., n$, (B.11) can be calculated as a weighted sum of the values of f at the points x_i, i.e.,

$$I_n(f) = \sum_{i=0}^{n} \alpha_i f(x_i) \, .$$

The points $\{x_i\}$ are called *nodes* of the quadrature formula, while the coefficients $\alpha_i \in \mathbb{R}$ are its weights. Both weights and nodes depend in general on n. For instance, a natural approach consists in the use of the interpolating Lagrange polynomial over the set of $n+1$ nodes $\{x_i\}$. In this case, the coefficients α_i are a linear combination of $\int_a^b l_i(x)dx$, with l_i characteristic Lagrange polynomial of degree n associated with the node x_i. The *degree of exactness* of a quadrature formula is defined as the maximum integer $r \geq 0$ for which

$$I_n(f) = I(f) \qquad \forall f \in \mathbb{P}_r \, .$$

Any interpolatory quadrature formula that makes use of $n+1$ distinct nodes has degree of exactness equal to n, at least. In particular, the degree of exactness is related to the quadrature error, defined as

$$E_n(f) := I(f) - I_n(f) \, .$$

In the following, we discuss the three most common quadrature formulae with $n = 0, 1, 2$, namely the midpoint formula, the trapezoidal formula, and the Cavalieri-Simpson formula. We also present the composite versions of the interpolating formulae used to improve the quadrature errors.

B.2.1 *The midpoint formula*

The most basic case is the ***midpoint formula*** with $n = 0$, obtained by replacing f over the interval $[a, b]$ with the constant function equal to the value of f at the midpoint of the integration interval, i.e., in $\frac{a+b}{2}$. This formula reads

$$I_0(f) = (b-a) f\left(\frac{a+b}{2}\right) \, . \tag{B.12}$$

In this case, the weight is chosen as $\alpha_0 = b - a$ and the node as $x_0 = \frac{a+b}{2}$. In particular, the quadrature error for the function $f \in \mathcal{C}^2([a, b])$ is given by

$$E_0(f) = \frac{(b-a)^3}{24} f''(\xi) \, , \quad \xi \in (a, b) \, .$$

Therefore, the midpoint formula (B.12) is exact for constant and affine functions and has degree of exactness equal to 1. The quadrature error, which depends on the width of the integration interval, can be improved considering the ***composite version of the interpolating formula***. The composite formula consists in using the composite interpolating polynomial of f constructed on m subintervals of $[a, b]$ of width $H = \frac{b-a}{m}$, for $m \geq 1$, and defining the quadrature nodes as $x_k = a + (2k+1)\frac{H}{2}$, for $k = 0, .., m-1$.

In this case, the *composite midpoint formula* reads

$$I_{0,m}(f) = H \sum_{k=0}^{m-1} f(x_k)\,, \qquad m \geq 1\,,$$

and the quadrature error reduces to

$$E_{0,m}(f) = \frac{b-a}{24} H^2 f''(\xi)$$

under the same assumptions on f and ξ. Algorithm 2.1 computes an approximation of the integral of the function f over the interval (a, b) via the composite midpoint formula on m equispaced subintervals.

Algorithm 2.1 Composite midpoint formula.

```
function [int] = CompMidPnt (a, b, m, f)

h = (b-a)/m;
x = [a+h/2 : h : b];
dim = length(x);
y = eval(f);
if ( size(y) == 1 ) then
    y = diag(ones(dim))*y;
end if
int = h*sum(y)

return
```

B.2.2 *The trapezoidal formula*

The ***trapezoidal formula*** is obtained by replacing f over the interval $[a, b]$ with its Lagrange interpolating polynomial of degree 1 at the nodes $x_0 = a$ and $x_1 = b$. The resulting quadrature rule has the weights $\alpha_0 = \alpha_1 = \frac{b-a}{2}$ and reads

$$I_1(f) = \frac{b-a}{2}[f(a) + f(b)]\,.$$

For $f \in \mathcal{C}^2([a, b])$, the quadrature error is given by

$$E_1(f) = -\frac{(b-a)^3}{12} f''(\xi)\,, \quad \xi \in (a, b)\,.$$

The composite counterpart of this quadrature rule is obtained, as for the case of the midpoint rule, by replacing f with its composite Lagrange polynomial of degree 1 on m subintervals ($m \geq 1$). Introducing the quadrature nodes $x_k = a + kH$, for $k = 0, .., m$ and $H = \frac{b-a}{m}$, the composite formula reads

$$I_{1,m}(f) = \frac{H}{2} \sum_{k=0}^{m-1} [f(x_k) + f(x_{k+1})]$$

with a quadrature error of

$$E_{1,m}(f) = -\frac{b-a}{12} H^2 f''(\xi) .$$

The degree of exactness of this formula, in either its normal and composite version, is again equal to 1. Algorithm 2.2 computes an approximation of the integral of the function f over the interval (a, b) via the composite trapezoidal formula on m equispaced subintervals.

Algorithm 2.2 Composite trapezoidal formula.

```
function [int] = CompTrp (a, b, m, f)

h = (b-a)/m;
x = [a : h : b];
dim = length(x);
y = eval(f);
if ( size(y) == 1 ) then
    y = diag(ones(dim))*y;
end if
int = h*(0.5*y(1) + sum(y(2 : m)) + 0.5*y(m+1));

return
```

B.2.3 *The Cavalieri-Simpson formula*

A further option of interpolatory quadrature formula, with a higher degree of exactness, is the ***Cavalieri-Simpson formula***. It is obtained by replacing f over $[a, b]$ with its interpolating polynomial of degree 2. The quadrature nodes are $x_0 = a$, $x_1 = \frac{a+b}{2}$ and $x_2 = b$, while the weights are given by $\alpha_0 = \alpha_2 = \frac{b-a}{6}$ and $\alpha_1 = 4\frac{b-a}{6}$. The resulting formula reads

$$I_2(f) = \frac{b-a}{6}\left[f(a) + 4f\left(\frac{a+b}{2}\right) + f(b)\right] . \tag{B.13}$$

The quadrature error is provided by

$$E_2(f) = -\frac{(b-a)^5}{32}\frac{1}{90} f^{(4)}(\xi) ,$$

where $f \in \mathcal{C}^4([a, b])$ and $\xi \in (a, b)$. This quadrature formula has degree of exactness equal to 3. Considering the composite polynomial of degree 2 interpolating f over $[a, b]$, the quadrature nodes $x_k = a + k\frac{H}{2}$, for $k = 0, .., 2m$, and letting $H = \frac{b-a}{m}$ ($m \geq 1$), the composite counterpart of (B.13) reads

$$I_{2,m}(f) = \frac{H}{6}\left[f(x_0) + 2\sum_{r=0}^{m-1} f(x_{2r}) + \sum_{s=0}^{m-1} f(x_{2s+1}) + f(x_{2m})\right] .$$

The associated quadrature error, for $f \in \mathcal{C}^4([a, b])$, is given by

$$E_{2,m}(f) = -\frac{b-a}{180}\frac{H^4}{16} f^{(4)}(\xi) .$$

Algorithm 2.3 computes an approximation of the integral of the function f over the interval (a, b) via the composite Cavalieri-Simpson formula on m equispaced subintervals.

Algorithm 2.3 Composite Cavalieri-Simpson formula.

```
function [int] = CompCS (a, b, m, f)

h = (b-a)/m;
x = [a : h/2 : b];
dim = length(x);
y = eval(f);
if (size(y) == 1) then
    y = diag(ones(dim))*y;
end if
int = (h/6)*(y(1) + 2*sum(y(3 : 2 : 2*m-1)) + 4*sum(y(2 : 2 : 2*m)) + y(2*m+1));

return
```

Midpoint, trapezoidal and Simpson formulae are special cases (for $n = 0, 1, 2$) of the closed ***Newton-Cotes formulae***. These are *Lagrange interpolation formulae* with equally spaced nodes in $[a, b]$, i.e., for a fixed $n \geq 0$, $x_k = x_0 + kh$, $k = 0, .., n$ and $h = b - a$. In particular, Newton-Cotes formulae are defined in a closed or opened version:

- *closed formulae* are characterized by $x_0 = a$, $x_n = b$, and $h = \frac{b-a}{n}$, $n \geq 1$;
- *open formulae* are characterized by $x_0 = a + h$, $x_n = b - h$, and $h = \frac{b-a}{n+2}$, $n \geq 0$.

The Newton-Cotes formulae can also be constructed in a composite version.

B.2.4 *The Gauss formulae*

The ***Gauss quadrature formulae*** were introduced to increase the degree of exactness of the quadrature rules. In fact, it was proven (see Theorem 10.1 and Corollary 10.2 in [233]) that a suitable choices of the nodes could provide a formula with maximum degree of exactness $r = n + m$ and $m = n + 1$. These integration methods are based on the concept of approximation of a function by orthogonal polynomials:

Definition B.1. Let $\omega = \omega(x)$ be a weight function on the interval $(-1, 1)$, i.e., a nonnegative integrable function defined on this interval. $\{p_k, k = 0, 1, ..\}$ is a system of mutually orthogonal algebraic polynomials on the interval $(-1, 1)$ with respect to ω, with p_k of degree equal to k for each $k \geq 0$, if

$$\int_{-1}^{1} p_k(x) p_m(x) \omega(x) dx = 0 \qquad \text{for } k \neq m\,.$$

There are several families of orthogonal polynomials. Two relevant examples are the *Chebyshev polynomials* and the *Legendre polynomials*. The former, denoted by $T_k(x)$, considers the weight function $\omega(x) = (1 - x^2)^{1/2}$ and is defined as

$$T_k(x) = \cos(k\theta)\,,$$

with $\theta = \arccos x$ and $k \geq 0$. In particular, for any $k \geq 0$, we notice that $T_k \in \mathbb{P}_k$, i.e., $T_k(x)$ is an algebraic polynomial of degree k with respect to x. The Legendre

polynomials, denoted by $L_k(x)$, are orthogonal polynomials over the interval $(-1,1)$ with respect to the weight function $\omega(x) = 1$. They are defined as

$$L_k(x) = \frac{1}{2^k} \sum_{l=0}^{[k/2]} (-1)^l \binom{k}{l} \binom{2k-2l}{k} x^{k-2l} \tag{B.14}$$

where $[k/2]$ is the integer part of $k/2$. For every $k \geq 0$, $L_k \in \mathbb{P}_k$.

As introduced above, these orthogonal polynomials are used for deriving quadrature formulae with maximal degrees of exactness. Denoting by $\{x_i,\, i = 0, ..., n\}$ the set of $n+1$ distinct points in the interval $[-1,1]$, we introduce the definition of a *nodal polynomial* of degree $n+1$ as

$$\omega_{n+1}(x) = \prod_{i=0}^{n} (x - x_i)\,.$$

In particular, it has been proved that

$$\int_{-1}^{1} \omega_{n+1}(x) p(x) \omega(x) dx = 0 \qquad \forall p \in \mathbb{P}_n$$

for a weighting function $\omega(x)$. Therefore, ω_{n+1} is a polynomial of degree $n+1$ orthogonal to all the polynomials of lower degree. Its roots $\{x_j\}$ are called the *Gauss nodes* associated with the weight function $\omega(x)$. Thus, the quadrature formula

$$I_{n,\omega}(f) = \sum_{i=0}^{n} \alpha_i f(x_i)$$

with nodes $\{x_j\}$ and coefficients

$$\alpha_i = \int_{-1}^{1} l_i(x) \omega(x) dx$$

has degree of exactness $2n+1$ and is called the Gauss quadrature formula. Here, $l_i(x) \in \mathbb{P}_n$ is the i-th characteristic Lagrange polynomial of f with $l_i(x_j) = \delta_{ij}$ for $i, j = 0, 1, ..., n$. If Gaussian quadratures are considered with respect to the Chebyshev weight $\omega(x) = (1-x^2)^{-1/2}$, the Gauss nodes and coefficients are given, respectively, by

$$x_j = -cos\frac{(2j+1)\pi}{2(n+1)} \quad 0 \leq j \leq n\,,$$

$$\alpha_j = \frac{\pi}{n+1} \quad 0 \leq j \leq n\,.$$

Considering the Legendre weight $\omega(x) = 1$, for $n \geq 0$, the Gauss coefficients are given by

$$\alpha_j = \frac{2}{(1-x_j^2)[L'_{n+1}(x_j)]^2} \quad 0 \leq j \leq n\,,$$

while the Gauss nodes $\{x_j\}$ are the roots of $L_{n+1}(x)$, the $(n+1)$-th Legendre polynomial defined in (B.14). Algorithm 2.4 computes the α_k (a in the algorithm) and β_k (b in the algorithm) coefficients for the Legendre polynomial of degree n, while Algorithm 2.5 computes the nodes (x in the algorithm) and the weights (w in the algorithm) of the Gauss-Legendre formula with n nodes. In particular, we use this ***Gauss-Legendre quadrature formula*** for the numerical integration of the tensor $\mathbf{D}_T$ obtained with the

orientation distribution function (see Chapter 2 for the corresponding details).

Algorithm 2.4 Coefficients of Legendre polynomials.

```
function [a, b] = coeflege(n)

if (n <= 1) then
    error('n must be > 1');
end if
a = zeros(n,1);
b = a;
b(1) = 2;
k = [2 : n];
b(k) = 1./(4 - 1./(k-1).^2);

return
```

Algorithm 2.5 Coefficients of Gauss-Legendre formula.

```
function [x, w] = zplege(n)

if (n <= 1) then
    error('n must be > 1');
end if
[a, b] = coeflege(n);
JacM = diag(a) + diag(sqrt(b(2 : n)), 1) + diag(sqrt(b(2 : n)), -1);
[w, x] = eig(JacM);
x = diag(x);
scal = 2;
w = (w(1, :)'.^2)*scal;
[x, ind] = sort(x);
w = w(ind);

return
```

Multidimensional numerical integration

All the methods proposed in this section can be extended to a multidimensional case. Considering the bidimensional case, we assume that Ω is a convex polygon on which we introduce a triangulation $\mathcal{T}_h$ of $N_{\mathcal{T}}$ triangles, or elements, with mesh size h. Similar to the one-dimensional case, the idea of the interpolatory quadrature rule consists in substituting the function $f = f(x, y)$ in the integral with its composite interpolating polynomial on the triangulation $\mathcal{T}_h$. Denoting by a_j^T, for $j = 1, 2, 3$, and a^T, the vertices and the center of gravity of the triangle $T \in \mathcal{T}_h$, respectively, and with $|T|$ the area of the triangle T, we provide here some examples of *bidimensional composite quadrature formulae*:

$$I_0^c(f) = \sum_{T \in \mathcal{T}_h} |T| \, f(a^T) \qquad \textit{composite midpoint formula},$$

$$I_1^c(f) = \frac{1}{3} \sum_{T \in \mathcal{T}_h} |T| \sum_{j=1}^{3} f(a_j^T) \qquad \textit{composite trapezoidal formula}.$$

The multidimensional counterpart of the Gaussian formula on triangles is provided by the so-called *symmetric formula*. Considering a generic triangle $T \in \mathcal{T}_h$ and denoting

by $a^T_{(j)}$, for $j = 1, 2, 3$, the midpoints of the edges of T, two examples of symmetric formulae read:

$$I_3(f) = \sum_{T \in \mathcal{T}_h} \frac{|T|}{3} \sum_{j=1}^{3} f(a^T_{(j)}),$$

$$I_7(f) = \sum_{T \in \mathcal{T}_h} \frac{|T|}{60} \left(3 \sum_{j=1}^{3} f(a^T_j) + 8 \sum_{j=1}^{3} f(a^T_{(j)}) + 27 f(a^T) \right).$$

Several other numerical methods for the approximation of integrals in higher dimensions are available in the literature. For instance, referring to the Gauss formula, choosing a different kind of interpolating polynomial (such as the *Hermite* or *Laguerre polynomials*), other Gauss quadrature formulae can be derived. Moreover, other approximation procedures, such as the *Richardson extrapolation method* can be used. However, we remark that with this appendix we just provide a brief presentation of the methods we implement in our computations, referring the reader to more detailed descriptions and other options available in the literature. In the specific, the multidimensional symmetric formula I_7 is used for the approximation of the integral involved in the stiffness and convection matrices and in the load vector of the finite element method used in Chapters 3-5 and 7. The one-dimensional Gauss-Legendre quadrature formula is implemented for the construction of the tensor $\mathbf{D}_T$ for the orientation distribution function described in Chapter 2.

C *Drosophila model and data analysis*

The biological experiments briefly introduced in Chapter 7 and used for the analysis of the protein distribution in the different tumor regions were performed in a *Drosophila* model of glioblastoma. In this appendix, we first comment in Section C.1 on the main biological features characterizing the *Drosophila* model and on the proteins involved in the study of tumor migration. Then, in Section C.2, we describe the experimental procedures and, finally, in Section C.3, we briefly introduce the main aspects related to the data analysis.

C.1 *Drosophila model and GB*

Drosophila melanogaster has been a significant model organism throughout the 20th century and into the 21st century. Many of its internal organ systems are functionally analogous to those in vertebrates, including humans. Although there are great differences in terms of gross morphological and cellular features, many of the molecular mechanisms that govern the development and drive cellular and physiological processes are conserved [282]. Therefore, the ***Drosophila model*** provides a powerful platform to perform molecular and cellular analysis of human genes and their disease variants and offers several advantages, including easy handling, rapid generation time, low cost, and a wide armamentarium of genetic techniques. In particular, concerning the study of the function of specific genes in the central nervous system, this model organism can be used to address questions related to human brain tumors.

The larval brain of a *Drosophila* is composed of two hemispheres and the ventral ganglion where the peripheral nerves originate from [299]. In its central nervous system, approximately 10% of the cells are of glial nature and are classified as either midline glia or lateral glia, the latter being positive for the glial marker reversed polarity (repo). The *Drosophila melanogaster* model of a brain tumor is based on ***genetic mutations*** in EGFR and PI3K pathways equivalent to the ones found in patients [241]. The most frequent genetic lesions in human glioblastoma include the constitutive mutation or amplification of phosphatidylinositol 3-kinase (PI3K) and Epidermal Growth Factor Receptor (EGFR) pathways. In particular, glioma-associated EGFR mutant forms show a constitutive kinase activity that chronically stimulates Ras signaling to drive cell proliferation and migration [241]. In *Drosophila*, glial cells respond to this oncogenic combination of EGFR and PI3K mutations that effectively causes a glioma-like condition. In particular, *Drosophila* glia cells show many features of human gliomas, including glia expansion, brain invasion, neuron dysfunction, synapse loss, and neurodegeneration [240]. Moreover, this model has proved to be useful in finding new kinase activities relevant to glioma progression [228].

To generate a glioma in *Drosophila melanogaster* adult flies, we use the Gal4/UAS system [32], constituted by two parts: the gene Gal4 and the sequence UAS (Upstream Activation Sequence), promoting Gal4 activation. This system is a biochemical method used to study gene expression and function in organisms such as the fruit

fly. We over-express constitutively active forms of EGFR and PI3K under the control of UAS sequences. To restrict this expression to glial cells, we use the specific enhancer repo, a paired-like homeodomain protein expressed exclusively in glial cells and required for the migration and differentiation of embryonic glial cells (genotypes: repo-Gal4>UAS-EGFRλ, UAS-dp110). In particular, this *Drosophila* model has been used for drug and genetic screenings and the results have been validated in human GB cells (see [228] and references therein).

The study of integrin and protease distribution across the tumor domain and in the healthy tissue (presented in Chapter 7) is performed using specific antibodies and immunofluorescent dyes. In the specific, the study of protease distribution is performed with a specific monoclonal antibody for the MMP1 protein. To study the integrin distribution and activity two main elements are considered: Talin and FAK. Talin is a high-molecular-weight cytoskeletal protein concentrated in regions of cell–substratum contact. It has emerged as the key cytoplasmic protein that mediates integrin adhesion to the extracellular matrix. Therefore, it is considered as a mediator of the integrin adhesivity required for integrin function. Talin co-distributes with concentrations of integrins in the plasma membrane and it links clusters of integrins bound to the ECM and the cytoskeleton. Therefore, it is essential for the formation of focal adhesion-like clusters of integrins [38]. The gene *rhea* encodes Talin in *Drosophila* [144]. FAK, focal adhesion kinase, is a cytoplasmic tyrosine kinase involved in signaling and cytoskeleton dynamics associated with integrin activity. It influences cellular adhesion and spreading processes [89, 179]. In particular, we use the gene *myospheroid (mys)* to control the adhesion/signaling process related to the β subunit of the integrin dimer. We use *Rhea* and *mys* knockdown to study the effects of integrin activity during GB expansion. It was shown in Figure 7.10 of Chapter 7, where specific RNA interferences (RNAi) tools were used to inhibit these two key players for integrin function.

C.2 *Experimental procedures*

All the experiments analyzed and used for the modeling set proposed in Chapter 7 were performed at the Instituto Cajal CSIC (Madrid, Spain) by Sergio Casas Tintó, principal investigator of the group *Glia-Neuron molecular signaling*. We provide here a brief description of the materials and the experimental procedures employed.

- The flies were raised with standard fly food at 25ºC. In particular, different ***fly stocks*** were used, i.e., from the Bloomington stock Centre: UAS-myr-RFP (BL7119), repo-Gal4 (BL7415), tub-gal80ts (BL7019), form Vienna Drosophila Resource Center (VDRC): UAS-*mys* RNAi (BL33642), UAS-*rhea* RNAi (BL28950), while UAS-dEGFRλ, UAS-PI3K92E (dp110CAAX) were kindly provided by R. Read (from the Emory University School of Medicine, USA).

- For the study of the distribution of the proteins in the tissue, we use an ***immunostaining*** procedure. As we briefly mentioned in the introduction, this technique is based on the use of antibodies to detect a specific protein in a sample and to visualize protein distribution. First, we generate *Drosophila* brain samples with a genetically induced GB (genotypes: *repo>PI3K; EGFR*). We induce the co-expression of a membrane bound version of the red fluorescent protein (*UAS-myrRFP*) in order to obtain a red marker for GB cell membranes. Then, we dissect ***third-instar larval brains*** in phosphate-buffered saline (PBS), fixed in 4% formaldehyde for 25 min, washed in PBS + 0.3% Triton X-100 (PBT), and blocked

in PBT + 5% BSA (bovine serum albumin). We use different ***antibodies*** for proteases and integrins: mouse anti-MMP1 (dilution 1:50), mouse anti-FAK (dilution 1:50), rabbit anti-Talin (dilution 1:50). The former, mouse anti-MMP1, was provided by the DSHB (Developmental Studies Hybridoma Bank), while the latter, mouse anti-FAK and rabbit anti-Talin, was kindly provided by I. Guerrero from Centro de Biología Molecular "Severo Ochoa" (Madrid, Spain). Instead, the secondary antibodies, which bind to primary antibodies (directly bound to the target antigen) and necessary for signal detection and amplification, are anti-mouse Alexa 488, 568, 647, anti-rabbit Alexa 488, 568, 647 (form Thermofisher, dilution 1:500).

- The ***imaging process*** for the visualization of the brain sample consists of mounting the *Drosophila* brain images in Vectashield mounting media with DAPI (Vector Laboratories) and analyzing by Confocal microscopy (LEICA TCS SP5) with a 63x oil immersion objective and three-fold magnification. In particular, we process the images using the Image J 1.52t[1], a Java-based image processing program. Examples of the visualization of a brain sample, marked with different antibodies, are provided in Figures C.1 and C.2.

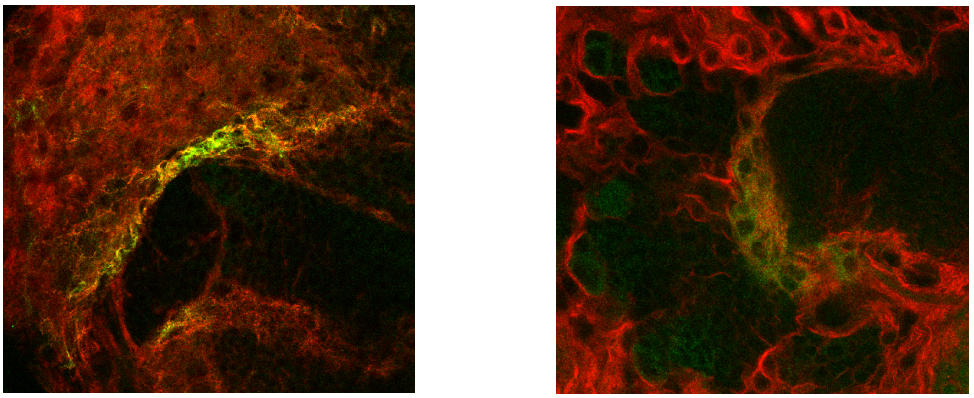

FIGURE C.1: **Examples of visualizing immunostaining images.** *Drosophila* brain samples with genetically induced GB and stained with mouse anti-MMP1 antibody (left, green) and with mouse anti-FAK antibody (right, green). Both samples are marked with a membrane bound version of the red fluorescent protein to visualize the neoplastic tissue.

- In the end, we determine the ***quantifications of the signals*** for FAK, MMP1, and Talin from images taken at the same confocal settings. In the specific, the pixel intensity is measured using the *plot profile tool* from the processing package Fiji 1.52t[2]. An example of a plot profile derived from the quantification of MMP1 and GB membrane signals is provided in Figure C.3.

- An additional step in the experiments is performed for the study of the ***animal survival*** presented in the analysis of *rhea* and *mys* knockdown (see Figure 7.10 of Chapter 7). In particular, animal survival is represented as the percentage of flies with GB induction (genotypes: repo-Gal4>UAS-EGFRλ, UAS-dp110) that reach adulthood compared to control siblings. n>100 samples analyzed per experiment.

[1] https://imagej.nih.gov/ij/index.html
[2] https://imagej.net/Fiji

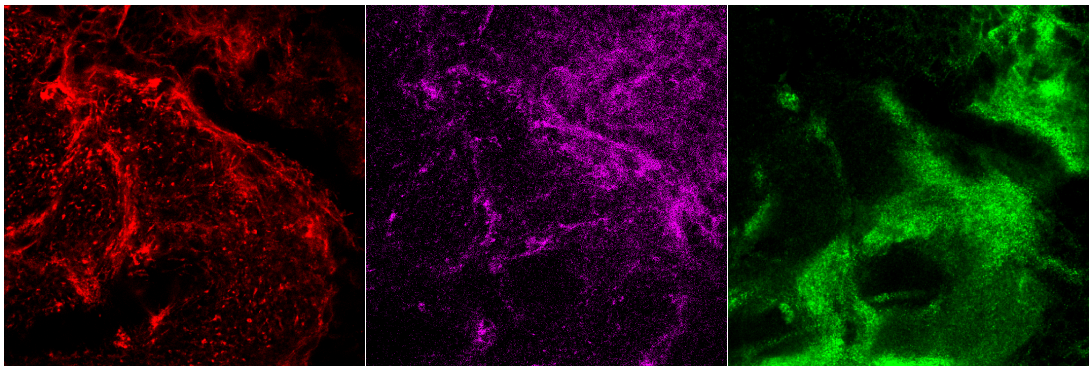

FIGURE C.2: **Examples of visualizing co-stained immunostaining images.** *Drosophila* brain sample with genetically induced GB and co-stained with mouse anti-FAK (middle, magenta) and rabbit anti-Talin (right, green) antibodies. The three images refer to the same sample where the two proteins were co-expressed together with a membrane bound version of the red fluorescent protein to visualize the neoplastic tissue.

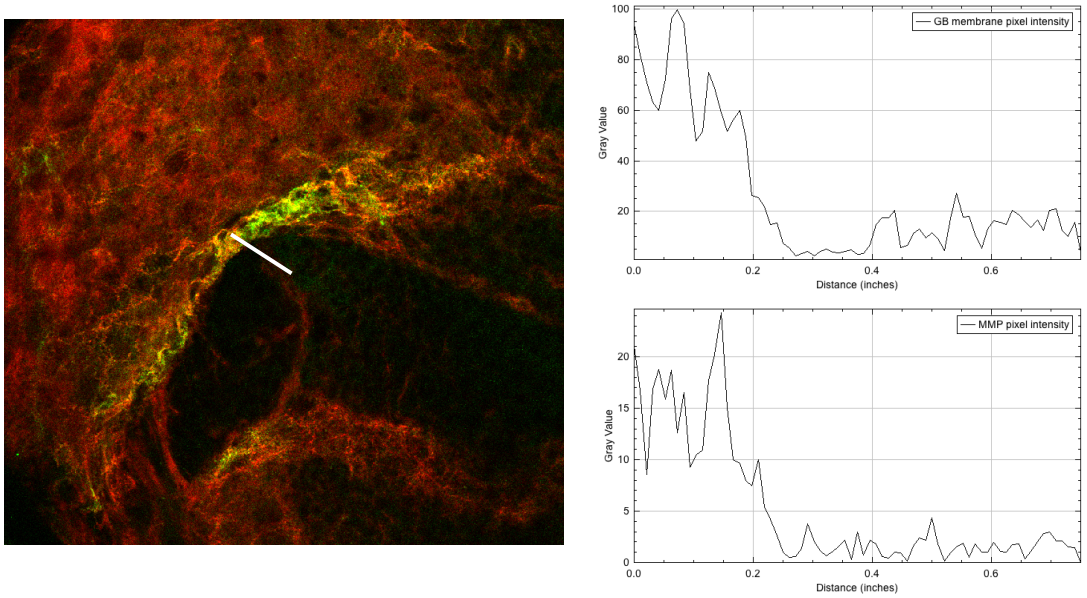

FIGURE C.3: **Example of the signal quantification.** In the brain sample on the left, where MMP (in green) and GB membrane (in red) are visualized, the pixel intensity along the white line was measured with the plot profile tool of Image J. The graphs on the right show the raw quantifications of the two signals.

C.3 *Data analysis*

For the analysis of the experimental data concerning the distributions of MMPs, active and inactive integrins, we work in the Matlab environment using the curve fitting toolbox. In particular, we start with the data obtained from the quantification of the marker signals. The plot profile tool provides the values of the pixel intensity of the signals along the chosen line. These values provide information about the position of the point along the line and the corresponding intensity of the marker. Loading this data into Matlab, we use the ***Curve Fitting Toolbox***[3] for their analysis and interpolation. In the specific, this toolbox provides several functions for fitting curves

[3] https://uk.mathworks.com/products/curvefitting.html

and surfaces to data. The toolbox permits the performance of exploratory data analysis, preprocessing and post-processing of the data, comparison of candidate models, and the removal of outliers. It uses linear and nonlinear models for regression analysis, providing optimized solver parameters and starting conditions. In particular, several fitting models are available, such as *regression models*, *interpolation methods*, including linear interpolation, cubic splines, or piecewise cubic Hermite interpolation, and *smoothing models*, including the smoothing spline method. The latter is the procedure we choose for the data at hand.

The ***smoothing spline method*** is particularly recommended for noisy data. Denoting with $\{x_i, y_i\} \in X \subseteq \mathbb{R}^2$ the set of points and the corresponding signal values, for $i = 1, ..., N_e$, this fitting model consists in the construction of a smoothing spline s for the specified *smoothing parameter* p and *weights* $\{w_i\}$. In particular, the smoothing spline minimizes

$$p \sum_{i=1}^{N_e} w_i (y_i - s(x_i))^2 + (1-p) \int_X \left(\frac{d^2 s}{dx^2} \right)^2 dx \,.$$

If the weights are not specified, they are assumed to be $w_i = 1$ for all data points. The smoothing parameter is defined in the interval $[0, 1]$. With $p = 0$ we obtain a least-squares straight-line fit to the data, while for $p = 1$ we obtain a cubic spline interpolant, i.e., a piecewise cubic polynomial fit that passes through all the data points $\{x_i, y_i\}$. When the smoothing parameter is not directly specified, the system automatically selects it, usually near the value $\frac{1}{1+h^3/6}$, being h the average spacing of the data. Smoothing splines can be considered as parametric fitting, as the smoothing parameter is associated with them. However, they belong to the class of piecewise polynomials, like cubic splines, and to the class of shape-preserving interpolants. The smoothing spline fit can be obtained interactively through the curve fitting interface or directly using the fit functions.

- Using the *curve fitting interface* form the Curve Fitting Toolbox, the user has to load the data points $\{x_i, y_i\}$, and eventually the weights $\{w_i\}$. Then, selecting *smoothing spline* from the model type list, it is possible to specify the value of the smoothing parameter, which makes the fit smoother or rougher. The toolbox attempts to select a default value appropriate for the data. Finally, it is possible to extract the plot as well as to save the output of the fitting and the goodness parameters in the workspace. The toolbox determines the goodness of fit calculating the sum of squares due to error (SSE), the R-square value, the adjusted R-square value, and the root mean squared error (RMSE)[4]. In Figure C.4, an illustrative example of the interactive window of the curve fitting interface is shown.

- Considering directly the `fit` function form the Curve Fitting Toolbox on the data point $\{x_i, y_i\}$, to use the smoothing spline model the user has to specify `'smoothingspline'` when calling the `fit` function. Moreover, it is possible to obtain several outputs for the model in order to visualize not only the fitting (`f`), but also the goodness parameters (`gof`) and other output values (`out`), like the calculated smoothing parameter (`out.p`). Defined the structure `data_point` containing the point set $\{x_i, y_i\}$, we provide the corresponding code in Algorithm 3.1.

[4]For further details about how to evaluate the goodness of the fit see https://uk.mathworks.com/help/curvefit/evaluating-goodness-of-fit.html.

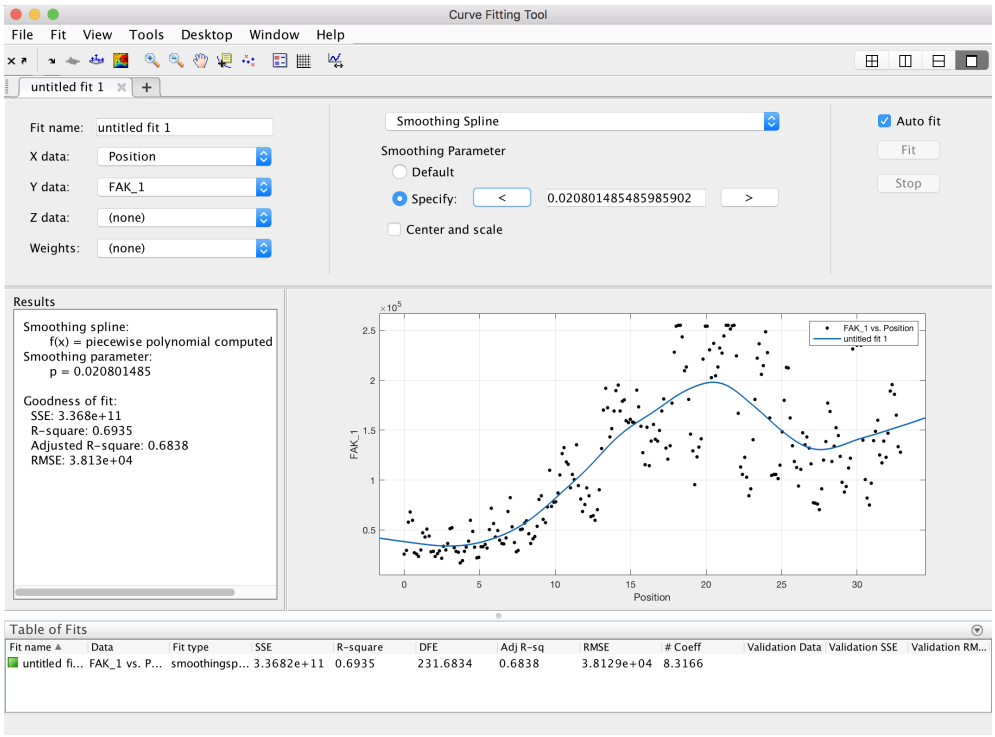

FIGURE C.4: **Interactive interface of the Curve Fitting Toolbox.**

Algorithm 3.1 Fit a smoothing spline model.

```
load data_point

[f, gof, out] = fit(x_point, y_value, 'smoothingspline');

plot(f, x_point, y_value)      ▷ Plot the data point and the model fitting them.
out.p                          ▷ Visualize the calculated smoothing parameter.
```

Alternatively, using `fitoptions` it is possible to specify the values of the smoothing parameter before the fitting, as well as many other options. In particular, some of these options are: *Method*; *SmoothingParam*; *Normalize*, centering and scaling the data; *Weights*; *Exclude*, specifying the points to exclude from the fitting; *Lower* and *Upper*, for eventually lower and upper bounds on the coefficients to be fitted; *MaxIter*, for the maximum number of iterations allowed for the fit. Many other options can be added, depending also on the chosen fitting method. In Matlab, to specification these options we have to call `fitoptions` (e.g. `options=fitoptions('Method','Smooth','SmoothingParam',0.07)`) before the `fit` function.

After creating a fit, a variety of post-processing methods for plotting, interpolation, and extrapolation can be applied, as well as for estimating confidence intervals, or calculating integrals and derivatives. In our analysis, an additional step in the processing of the data consists of the evaluation of the residual level of fluorescence in the images. In fact, during the *imaging* and *quantification* processes, we observe that a low constant level of the membrane bound red fluorescent protein, marking the GB membrane, almost everywhere in the domain. This is due to the used immunostaining and imaging technique that could not eliminate this *residual level* of the GB marker. In particular, this noise affects not only the GB marker but also all the other protein

markers. Therefore, for each image that is analyzed, we quantify both the measurements for the protein distributions in the specific regions we are interested in and the residual marker levels. This residual level is then analyzed and, thus, the calculated average estimation is subtracted from the corresponding protein quantifications.

For the study proposed in Chapter 7, we ensure the robustness of the obtained results concerning the protein distributions, i.e., we check that these results are not characteristics of a specific fly or brain sample, but are generally applicable. Therefore, for each protein distribution study, we analyzed several biological images. In total, for the study of the MMP1 distribution, we analyzed 35 measurements of this distribution taken from brain images of 11 different animals; for the distribution of Talin and FAK, we analyzed 14 measurements from brain images of 6 different animals; finally, for the combined distribution of FAK and MMP1, we analyzed 23 measurements from brain images of 13 different animals.

List of abbreviations

ADC	**A**pparent **d**iffusion **c**oefficient
ATP	**A**denosine **t**ri**p**hosphate
BBB	**B**lood-**b**rain **b**arrier
BET	**B**rain **e**xtraction **t**ool
BSA	**B**ovine **s**erum **a**lbumin
CN	**C**rank-**N**icolson method
CNR	**C**ontrast-to-**n**oise **r**atio
CNS	**C**entral **n**ervous **s**ystem
CSF	**C**erebro**s**pinal **f**luid
DICOM	**D**igital **i**maging and **co**mmunication in **m**edicine
DAI	**D**iffusion **a**nisotropy **i**ndex
DAPI	6-**di**a**m**idino-2-**p**heny**l**indole
DC	**D**endritic **c**ell
DNA	**D**eoxyribo**n**ucleic **a**cid
DSHB	**D**evelopmental **s**tudies **h**ybridoma **b**ank
DTI	**D**iffusion **t**ensor **i**maging
DWI	**D**iffusion-**w**eighted **i**maging
EC	**E**ndothelial **c**ell
ECM	Extra**c**ellular **m**atrix
EGF	**E**pidermal **g**rowth **f**actor
EGFR	**E**pidermal **g**rowth **f**actor **r**eceptor
EMT	**E**pithelial-**m**esenchymal **t**ransition
FA	**F**ractional **a**nisotropy
FAK	**F**ocal **a**dhesion **k**inase
FLIRT	**F**MRIB **l**inear **i**mage **r**egistration **t**ool
FNIRT	**F**MRIB **n**onlinear **i**mage **r**egistration **t**ool
FSL	**F**MRIB **s**oftware **l**ibrary
GAG	**G**lycos**a**mino**g**lycan
GB	**G**lio**b**lastoma
GBM	**G**lio**b**lastoma **m**ultiforme
GoG	**G**o-**o**r-**g**rowth model
GPCR	**G** **p**rotein-**c**oupled **r**eceptor
GTV	**G**ross **t**umor **v**olume
HA	**H**yaluronic **a**cid
HIF	**H**ypoxia-**i**nducible **f**actor
IDH	**I**socitrate **de**h**y**drogenase
IHC	**I**mmuno**h**isto**c**hemistry
KTAP	**K**inetic **t**heory of **a**ctive **p**article
KTE	**K**inetic **t**ransport **e**quation
IMEX	**Im**plicit **ex**plicit scheme
MD	**M**ean **d**iffusivity

mys	**mys**pheroid
MMP	**M**atrix **m**etallo**p**roteinase
MR	**M**agnetic **r**esonance
MRI	**M**agnetic **r**esonance **i**maging
MRS	**M**agnetic **r**esonance **s**pectroscopy
NIfTI	**N**euroimaging **in**formatics **t**echnology **i**nitiative
NTCP	**N**ormal **t**issue **c**omplication **p**robability
NGG	**N**o **g**o-or-**g**rowth model
ODE	**O**rdinary **d**ifferential **e**quation
ODF	**O**rientation **d**istribution **f**unction
OS	**O**veral **s**urvival
PBS	**P**hosphate-**b**uffered **s**aline
PBT	**P**oly**b**utylene **t**erephthalate
PDE	**P**artial **d**ifferential **e**quation
PDF	**P**robability **d**ensity **f**unction
PET	**P**ositron **e**mission **t**omography
PI3K	**p**hosphatidyl**i**nositol **3**-**k**inase
PME	**P**orous **m**edium **e**quation
PTV	**P**lanning **t**reatment **v**olume
RA	**R**elative **a**nisotropy
RB	**R**etino**b**lastoma protein
RFP	**R**ed **f**luorescent **p**rotein
RK	**R**unge-**K**utta method
RMSE	**R**oot **m**ean **s**quared **e**rror
RNA	**R**ibo**n**ucleic **a**cid
RNAi	**RNA i**nterferences
RT	**R**adiation **t**herapy
Shh	**S**onic **H**edge**h**og
SSE	**S**um of **s**quares of the **e**rror
TAM	**T**umor-**a**ssociated **m**acrophage
TCP	**T**umor **c**ontrol **p**robability
TM	**T**umor **m**icrotube
TME	**T**umor **m**icro**e**nvironment
TMZ	**T**e**m**o**z**olomid
UAS	**U**pstream **a**ctivation **s**equence
UTCP	**U**ncomplicated **t**umor **c**ontrol **p**robability
VEGF	**V**ascular **e**ndothelial **g**rowth **f**actor
VMF	**v**on-**M**ises-**F**isher
VR	**V**olume **r**atio
WHO	**W**orld **H**ealth **O**rganization
WM	**W**hite **m**atter

List of units

kg	kilogram	mass
m	meter	length
s	second	time
mol	mole	amount of substance
Gy	gray	absorbed dose of ionizing radiation
K	Kelvin	temperature

g	gram	10^{-3} kg
mg	milligram	10^{-6} kg
Da	dalton	$\sim 1,66054 \cdot 10^{-27}$ kg
kDa	kilodalton	$\sim 1,66054 \cdot 10^{-24}$ kg
l	liter	10^{-3} m^3
cm	centimeter	10^{-2} m
mm	millimeter	10^{-3} m
μm	micrometer	10^{-6} m
nm	nanometer	10^{-9} m
d	day	86400 s
h	hour	3600 s
min	minute	60 s
ms	millisecond	10^{-3} s
cGy	centigray	10^{-2} Gy
M	molar	mol $\cdot$ liter^{-1}

List of figures

List of tables

Bibliography

[1] N. J. Abbott. "Blood–brain barrier structure and function and the challenges for CNS drug delivery". In: *Journal of Inherited Metabolic Disease* 36.3 (2013), pp. 437–449. DOI: 10.1007/s10545-013-9608-0 (see p. 9).

[2] J. Adler. "Chemotaxis in bacteria". In: *Science* 153.3737 (1966), pp. 708–716. DOI: 10.1126/science.153.3737.708 (see p. 133).

[3] I. Aganj et al. "A Hough transform global probabilistic approach to multiple-subject diffusion MRI tractography". In: *Medical Image Analysis* 15.4 (2011), pp. 414–425. DOI: 10.1016/j.media.2011.01.003 (see pp. xv, xxii, 39).

[4] T. Alarcón et al. "Multiscale modelling of tumour growth and therapy: the influence of vessel normalisation on chemotherapy". In: *Computational and Mathematical Methods in Medicine* 7.2-3 (2006), pp. 85–119. DOI: 10.1080/10273660600968994 (see p. 124).

[5] K. M. Alblazi and C. H. Siar. "Cellular protrusions–lamellipodia, filopodia, invadopodia and podosomes–and their roles in progression of orofacial tumours: current understanding". In: *Asian Pacific Journal of Cancer Prevention* 16.6 (2015), pp. 2187–2191. DOI: 10.7314/apjcp.2015.16.6.2187 (see p. 6).

[6] A. L. Alexander et al. "Diffusion tensor imaging of the brain". In: *Neurotherapeutics* 4.3 (2007), pp. 316–329. DOI: 10.1016/j.nurt.2007.05.011 (see p. 27).

[7] K. Alhazzani et al. "Angiogenesis in Cancer Treatment: 60 Years' Swing Between Promising Trials and Disappointing Tribulations". In: *Anti-Angiogenesis Drug Discovery and Development: Volume 4* 4 (2019), p. 34. DOI: 10.2174/9781681083971170401 (see pp. 90, 91, 124).

[8] W. Alt. "Biased random walk models for chemotaxis and related diffusion approximations". In: *Journal of Mathematical Biology* 9.2 (1980), pp. 147–177. DOI: 10.1007/BF00275919 (see pp. 47, 136).

[9] A. R. A. Anderson and M. A. J. Chaplain. "Continuous and discrete mathematical models of tumor-induced angiogenesis". In: *Bulletin of Mathematical Biology* 60.5 (1998), pp. 857–899. DOI: 10.1006/bulm.1998.0042 (see p. 124).

[10] A. E. Aplin et al. "Signal transduction and signal modulation by cell adhesion receptors: the role of integrins, cadherins, immunoglobulin-cell adhesion molecules, and selectins". In: *Pharmacological Reviews* 50.2 (1998), pp. 197–264. URL: http://pharmrev.aspetjournals.org/content/50/2/197 (see p. 2).

[11] P. Baluk, H. Hashizume, and D. M. McDonald. "Cellular abnormalities of blood vessels as targets in cancer". In: *Current Opinion in Genetics & Development* 15.1 (2005), pp. 102–111. DOI: 10.1016/j.gde.2004.12.005 (see p. 2).

[12] R. Bammer, B. Acar, and M. E. Moseley. "In vivo MR tractography using diffusion imaging". In: *European Journal of Radiology* 45.3 (2003), pp. 223–234. DOI: 10.1016/S0720-048X(02)00311-X (see p. 26).

[13] L. Barazzuol et al. “A mathematical model of brain tumour response to radiotherapy and chemotherapy considering radiobiological aspects”. In: *Journal of Theoretical Biology* 262.3 (2010), pp. 553–565. DOI: 10.1016/j.jtbi.2009.10.021 (see p. 124).

[14] P. J. Basser, J. Mattiello, and D. LeBihan. “MR diffusion tensor spectroscopy and imaging”. In: *Biophysical Journal* 66.1 (1994), pp. 259–267. DOI: 10.1016/S0006-3495(94)80775-1 (see pp. 25, 28).

[15] A. M. Belkin et al. “Transglutaminase-mediated oligomerization of the fibrin (ogen) αC domains promotes integrin-dependent cell adhesion and signaling”. In: *Blood* 105.9 (2005), pp. 3561–3568. DOI: 10.1182/blood-2004-10-4089 (see p. 189).

[16] N. Bellomo and A. Bellouquid. “From a class of kinetic models to the macroscopic equations for multicellular systems in biology”. In: *Discrete & Continuous Dynamical Systems-B* 4.1 (2004), p. 59. DOI: 10.3934/dcdsb.2004.4.59 (see p. 18).

[17] N. Bellomo, D. Knopoff, and J. Soler. “On the difficult interplay between life," complexity", and mathematical sciences”. In: *Mathematical Models and Methods in Applied Sciences* 23.10 (2013), pp. 1861–1913. DOI: 10.1142/S021820251350053X (see p. 172).

[18] N. Bellomo et al. “Multicellular biological growing systems: Hyperbolic limits towards macroscopic description”. In: *Mathematical Models and Methods in Applied Sciences* 17.supp01 (2007), pp. 1675–1692. DOI: 10.1142/S0218202507002431 (see pp. 17, 18, 49).

[19] N. Bellomo et al. “Complexity and mathematical tools toward the modelling of multicellular growing systems”. In: *Mathematical and Computer Modelling* 51.5-6 (2010), pp. 441–451. DOI: 10.1016/j.mcm.2009.12.002 (see p. 47).

[20] N. Bellomo et al. “Multiscale biological tissue models and flux-limited chemotaxis for multicellular growing systems”. In: *Mathematical Models and Methods in Applied Sciences* 20.07 (2010), pp. 1179–1207. DOI: 10.1142/S0218202510004568 (see pp. 171, 174).

[21] M. E. Berens and A. Giese. ““... those left behind.” Biology and oncology of invasive glioma cells”. In: *Neoplasia* 1.3 (1999), pp. 208–219. DOI: 10.1038/sj.neo.7900034 (see p. 69).

[22] H. C. Berg. *Random walks in biology*. Princeton University Press, 1983. DOI: 10.1063/1.2819954 (see pp. 16, 136).

[23] H. C. Berg and E. M. Purcell. “Physics of chemoreception”. In: *Biophysical Journal* 20.2 (1977), pp. 193–219. DOI: 10.1016/S0006-3495(77)85544-6 (see p. 137).

[24] R. Berges et al. “End-binding 1 protein overexpression correlates with glioblastoma progression and sensitizes to Vinca-alkaloids in vitro and in vivo”. In: *Oncotarget* 5.24 (2014), p. 12769. DOI: 10.18632/oncotarget.2646 (see p. 170).

[25] R. Berges et al. “The novel tubulin-binding checkpoint activator BAL101553 inhibits EB1-dependent migration and invasion and promotes differentiation of glioblastoma stem-like cells”. In: *Molecular Cancer Therapeutics* 15.11 (2016), pp. 2740–2749. DOI: 10.1158/1535-7163.MCT-16-0252 (see p. 170).

[26] R. Berges et al. “Proscillaridin A exerts anti-tumor effects through GSK3β activation and alteration of microtubule dynamics in glioblastoma”. In: *Cell Death & Disease* 9.10 (2018), pp. 1–14. DOI: 10.1038/s41419-018-1018-7 (see p. 170).

[27] J. Besserer and U. Schneider. “Track-event theory of cell survival with second-order repair”. In: *Radiation and Environmental Biophysics* 54.2 (2015), pp. 167–174. DOI: 10.1007/s00411-015-0584-7 (see p. 61).

[28] F. Billy et al. “A pharmacologically based multiscale mathematical model of angiogenesis and its use in investigating the efficacy of a new cancer treatment strategy”. In: *Journal of Theoretical Biology* 260.4 (2009), pp. 545–562. DOI: 10.1016/j.jtbi.2009.06.026 (see pp. 89, 91).

[29] L. Bloy and R. Verma. “On computing the underlying fiber directions from the diffusion orientation distribution function”. In: *International Conference on Medical Image Computing and Computer-Assisted Intervention*. Springer. 2008, pp. 1–8. DOI: 10.1007/978-3-540-85988-8_1 (see p. 39).

[30] P.-Y. Bondiau et al. “Biocomputing: numerical simulation of glioblastoma growth using diffusion tensor imaging”. In: *Physics in Medicine & Biology* 53.4 (2008), p. 879. DOI: 10.1088/0031-9155/53/4/004 (see p. 32).

[31] L. L. Bonilla and J. Soler. “High-field limit of the Vlasov–Poisson–Fokker–Planck system: A comparison of different perturbation methods”. In: *Mathematical Models and Methods in Applied Sciences* 11.08 (2001), pp. 1457–1468. DOI: 10.1142/S0218202501001410 (see p. 17).

[32] A. H. Brand and N. Perrimon. “Targeted gene expression as a means of altering cell fates and generating dominant phenotypes”. In: *Development* 118.2 (1993), pp. 401–415. URL: https://dev.biologists.org/content/118/2/401 (see p. 241).

[33] D. J. Brat and E. G. Van Meir. “Vaso-occlusive and prothrombotic mechanisms associated with tumor hypoxia, necrosis, and accelerated growth in glioblastoma”. In: *Laboratory Investigation* 84.4 (2004), pp. 397–405. DOI: 1038/labinvest.3700070 (see p. 69).

[34] D. J. Brat et al. “Pseudopalisades in glioblastoma are hypoxic, express extracellular matrix proteases, and are formed by an actively migrating cell population”. In: *Cancer Research* 64.3 (2004), pp. 920–927. DOI: 10.1158/0008-5472.CAN-03-2073 (see pp. 4, 69).

[35] Y. Brenier. “Extended monge-kantorovich theory”. In: *Optimal Transportation and Applications*. Springer, 2003, pp. 91–121. DOI: 10.1007/978-3-540-44857-0_4 (see p. 172).

[36] D. J. Brenner. “The linear-quadratic model is an appropriate methodology for determining isoeffective doses at large doses per fraction”. In: *Seminars in Radiation Oncology*. Vol. 18. 4. Elsevier. 2008, pp. 234–239. DOI: 10.1016/j.semradonc.2008.04.004 (see p. 51).

[37] B. A. Bromberek et al. “Macrophages influence a competition of contact guidance and chemotaxis for fibroblast alignment in a fibrin gel coculture assay”. In: *Experimental Cell Research* 275.2 (2002), pp. 230–242. DOI: 10.1006/excr.2002.5481 (see p. 134).

[38] N. H. Brown et al. “Talin is essential for integrin function in Drosophila”. In: *Developmental Cell* 3.4 (2002), pp. 569–579. DOI: 10.1016/s1534-5807(02)00290-3 (see p. 242).

[39] P. K. Burgess et al. “The interaction of growth rates and diffusion coefficients in a three-dimensional mathematical model of gliomas”. In: *Journal of Neuropathology & Experimental Neurology* 56.6 (1997), pp. 704–713. DOI: 10.1097/00005072-199706000-00008 (see p. 19).

[40] J. Calvo et al. “Flux-saturated porous media equations and applications”. In: *EMS Surveys in Mathematical Sciences* 2.1 (2015), pp. 131–218. DOI: 10.4171/EMSS/11 (see pp. 20, 172).

[41] J. Calvo et al. “Pattern formation in a flux limited reaction–diffusion equation of porous media type”. In: *Inventiones Mathematicae* 206.1 (2016), pp. 57–108. DOI: 10.1007/s00222-016-0649-5 (see pp. 20, 172, 174, 178).

[42] U. Cavallaro and G. Christofori. “Cell adhesion and signalling by cadherins and Ig-CAMs in cancer”. In: *Nature Reviews Cancer* 4.2 (2004), pp. 118–132. DOI: 10.1038/nrc1276 (see p. 2).

[43] F. A .C. C. Chalub et al. “Kinetic models for chemotaxis and their drift-diffusion limits”. In: *Nonlinear Differential Equation Models*. Springer, 2004, pp. 123–141. DOI: 10.1007/978-3-7091-0609-9_10 (see pp. 17, 18, 49, 134).

[44] A. Chauviere, T. Hillen, and L. Preziosi. “Modeling cell movement in anisotropic and heterogeneous network tissues”. In: *Networks & Heterogeneous Media* 2.2 (2007), p. 333. DOI: 10.3934/nhm.2007.2.333 (see p. 55).

[45] L. Chen et al. “Mathematical models for cell migration: a nonlocal perspective”. In: *arXiv* (2019). URL: https://arxiv.org/abs/1911.05200 (see p. 137).

[46] A. E. Cherry et al. “GPR124 regulates microtubule assembly, mitotic progression, and glioblastoma cell proliferation”. In: *Glia* 67.8 (2019), pp. 1558–1570. DOI: 10.1002/glia.23628 (see p. 170).

[47] A. Chertock, A. Kurganov, and P. Rosenau. “Formation of discontinuities in flux-saturated degenerate parabolic equations”. In: *Nonlinearity* 16.6 (2003), p. 1875. DOI: 10.1088/0951-7715/16/6/301 (see p. 171).

[48] J. Chiche, M. C. Brahimi-Horn, and J. Pouysségur. “Tumour hypoxia induces a metabolic shift causing acidosis: a common feature in cancer”. In: *Journal of Cellular and Molecular Medicine* 14.4 (2010), pp. 771–794. DOI: 10.1111/j.1582-4934.2009.00994.x (see p. 85).

[49] M. R. Chicoine and D. L. Silbergeld. “Assessment of brain tumor cell motility in vivo and in vitro”. In: *Journal of Neurosurgery* 82.4 (1995), pp. 615–622. DOI: 10.3171/jns.1995.82.4.0615 (see p. 61).

[50] S. Chouaib et al. “Hypoxia promotes tumor growth in linking angiogenesis to immune escape”. In: *Frontiers in Immunology* 3 (2012), p. 21. DOI: 10.3389/fimmu.2012.00021 (see p. 75).

[51] M. M. Chowdhary, C. I. Ene, and D. L. Silbergeld. “Treatment of Gliomas: How did we get here?” In: *Surgical Neurology International* 6.Suppl 1 (2015), S85. DOI: 10.4103/2152-7806.151348 (see p. 11).

[52] M. C. Colombo et al. “Towards the personalized treatment of glioblastoma: integrating patient-specific clinical data in a continuous mechanical model”. In: *PLoS One* 10.7 (2015), e0132887. DOI: 10.1371/journal.pone.0132887 (see p. 21).

[53] M. Conte, S. Casas-Tinto, and J. Soler. “Modeling invasion patterns in the glioblastoma battlefield”. In: *bioRxiv* (2020). DOI: 10.1101/2020.06.17.156497 (see p. 169).

[54] M. Conte, L. Gerardo-Giorda, and M. Groppi. “Glioma invasion and its interplay with nervous tissue and therapy: A multiscale model”. In: *Journal of Theoretical Biology* 486 (2020), p. 110088. DOI: 10.1016/j.jtbi.2019.110088 (see pp. 47, 71).

[55] M. Conte and N. Loy. "Multi-cue kinetic model with non-local sensing for cell migration on a fibers network with chemotaxis". In: *arXiv* (2020). URL: https://arxiv.org/abs/2006.09707 (see p. 134).

[56] M. Conte and C. Surulescu. "Mathematical modeling of glioma invasion: acid- and vasculature mediated go-or-grow dichotomy and the influence of tissue anisotropy". In: *arXiv* (2020). URL: https://arxiv.org/abs/2007.12204 (see pp. 70, 124).

[57] G. Corbin et al. "Higher-order models for glioma invasion: From a two-scale description to effective equations for mass density and momentum". In: *Mathematical Models and Methods in Applied Sciences* 28.09 (2018), pp. 1771–1800. DOI: 10.1142/S0218202518400055 (see p. 18).

[58] G. Corbin et al. "Modeling glioma invasion with anisotropy- and hypoxia-triggered motility enhancement: from subcellular dynamics to macroscopic PDEs with multiple taxis". In: *arXiv* (2020). URL: https://arxiv.org/abs/2006.12322 (see p. 100).

[59] J.-F. Coulombel, F. Golse, and T. Goudon. "Diffusion approximation and entropy-based moment closure for kinetic equations". In: *Asymptotic Analysis* 45.1, 2 (2005), pp. 1–39 (see p. 171).

[60] A. Czirok. "Endothelial cell motility, coordination and pattern formation during vasculogenesis". In: *Wiley Interdisciplinary Reviews: Systems Biology and Medicine* 5.5 (2013), pp. 587–602. DOI: 10.1002/wsbm.1233 (see pp. 88, 91, 124).

[61] G. M. D'Abaco and A. H. Kaye. "Integrins: molecular determinants of glioma invasion". In: *Journal of Clinical Neuroscience* 14.11 (2007), pp. 1041–1048. DOI: 10.1016/j.jocn.2007.06.019 (see pp. 6, 47).

[62] A. Das et al. "MMP proteolytic activity regulates cancer invasiveness by modulating integrins". In: *Scientific Reports* 7.1 (2017), pp. 1–13. DOI: 10.1038/s41598-017-14340-w (see p. 186).

[63] R. J. DeBerardinis et al. "The biology of cancer: metabolic reprogramming fuels cell growth and proliferation". In: *Cell Metabolism* 7.1 (2008), pp. 11–20. DOI: 10.1016/j.cmet.2007.10.002 (see pp. 3, 69).

[64] T. Demuth and M. E. Berens. "Molecular mechanisms of glioma cell migration and invasion". In: *Journal of Neuro-oncology* 70.2 (2004), pp. 217–228. DOI: 10.1007/s11060-004-2751-6 (see pp. 6, 47).

[65] W. Diao et al. "Behaviors of glioblastoma cells in in vitro microenvironments". In: *Scientific Reports* 9.1 (2019), pp. 1–9. DOI: 10.1038/s41598-018-36347-7 (see pp. 88, 91, 124).

[66] R. B. Dickinson. "A generalized transport model for biased cell migration in an anisotropic environment". In: *Journal of Mathematical Biology* 40.2 (2000), pp. 97–135. DOI: 10.1007/s002850050006 (see p. 134).

[67] R. B. Dickinson and R. T. Tranquillo. "A stochastic model for adhesion-mediated cell random motility and haptotaxis". In: *Journal of Mathematical Biology* 31.6 (1993), pp. 563–600. DOI: 10.1007/BF00161199 (see p. 190).

[68] I. Diez et al. "A novel brain partition highlights the modular skeleton shared by structure and function". In: *Scientific Reports* 5 (2015), p. 10532. DOI: 10.1038/srep10532 (see p. 27).

[69] W. Dubitzky et al. *Encyclopedia of systems biology*. Springer Publishing Company, Incorporated, 2013. DOI: 10.1007/978-1-4419-9863-7_708 (see p. 3).

[70] J. T. Edward. "Molecular volumes and the Stokes-Einstein equation". In: *Journal of Chemical Education* 47.4 (1970), p. 261. DOI: 10.1021/ed047p261 (see p. 188).

[71] R. Eftimie. "Hyperbolic and kinetic models for self-organized biological aggregations and movement: a brief review". In: *Journal of Mathematical Biology* 65.1 (2012), pp. 35–75. DOI: 10.1007/s00285-011-0452-2 (see p. 134).

[72] M. Egeblad and Z. Werb. "New functions for the matrix metalloproteinases in cancer progression". In: *Nature Reviews Cancer* 2.3 (2002), pp. 161–174. DOI: 10.1038/nrc745 (see p. 6).

[73] A. Ellert-Miklaszewska et al. "Integrin Signaling in Glioma Pathogenesis: From Biology to Therapy". In: *International Journal of Molecular Sciences* 21.3 (2020), p. 888. DOI: 10.3390/ijms21030888 (see pp. 6, 66).

[74] C. Engwer, A. Hunt, and C. Surulescu. "Effective equations for anisotropic glioma spread with proliferation: a multiscale approach and comparisons with previous settings". In: *Mathematical Medicine and Biology: a Journal of the IMA* 33.4 (2016), pp. 435–459. DOI: 10.1093/imammb/dqv030 (see pp. xvi, xxii, 18, 50–53, 58–60, 67, 71, 86, 200).

[75] C. Engwer, M. Knappitsch, and C. Surulescu. "A multiscale model for glioma spread including cell-tissue interactions and proliferation". In: *Mathematical Biosciences & Engineering* 13.2 (2016), p. 443. DOI: 10.3934/mbe.2015011 (see pp. 18, 51, 61, 67, 70, 71, 103).

[76] C. Engwer, C. Stinner, and C. Surulescu. "On a structured multiscale model for acid-mediated tumor invasion: The effects of adhesion and proliferation". In: *Mathematical Models and Methods in Applied Sciences* 27.07 (2017), pp. 1355–1390. DOI: 10.1142/S0218202517400188 (see pp. 70, 72).

[77] C. Engwer et al. "Glioma follow white matter tracts: a multiscale DTI-based model". In: *Journal of Mathematical Biology* 71.3 (2015), pp. 551–582. DOI: 10.1007/s00285-014-0822-7 (see pp. 18, 50, 51, 53, 60, 61, 67, 88, 91, 107).

[78] R. Erban and H. G. Othmer. "From individual to collective behavior in bacterial chemotaxis". In: *SIAM Journal on Applied Mathematics* 65.2 (2004), pp. 361–391. DOI: 10.1137/S0036139903433232 (see p. 18).

[79] H. P. Erickson. "Size and shape of protein molecules at the nanometer level determined by sedimentation, gel filtration, and electron microscopy". In: *Biological Procedures Online* 11.1 (2009), p. 32. DOI: 10.1007/s12575-009-9008-x (see p. 189).

[80] M. Esteller. "Cancer epigenomics: DNA methylomes and histone-modification maps". In: *Nature Reviews Genetics* 8.4 (2007), pp. 286–298. DOI: 10.1038/nrg2005 (see p. 2).

[81] *Estimation taken from:* URL: https://bionumbers.hms.harvard.edu/bionumber.aspx{?}s=n{\&}v=0{\&}id=108941 (see pp. 61, 90, 91, 124, 188).

[82] *Estimation taken from:* URL: http://www.lab.anhb.uwa.edu.au/mb140/MoreAbout/Endothel.htm (see pp. 90, 91, 124).

[83] D. Fangliang. "Maximum Principle and Application of Parabolic Partial Differential Equations". In: *IERI Procedia* 3 (2012), pp. 198–205. DOI: 10.1016/j.ieri.2012.09.033 (see p. 59).

[84] V. P. Ferrer, V. Moura Neto, and R. Mentlein. "Glioma infiltration and extracellular matrix: key players and modulators". In: *Glia* 66.8 (2018), pp. 1542–1565. DOI: 10.1002/glia.23309 (see pp. 6, 8).

[85] A. Fick. "Ueber diffusion". In: *Annalen der Physik* 170.1 (1855), pp. 59–86. DOI: 10.1002/andp.18551700105 (see p. 19).

[86] B. Fischl. "FreeSurfer". In: *Neuroimage* 62.2 (2012), pp. 774–781. DOI: 10.1016/j.neuroimage.2012.01.021 (see pp. 61, 209).

[87] R. A. Fisher. "Dispersion on a sphere". In: *Proceedings of the Royal Society of London. Series A. Mathematical and Physical Sciences* 217.1130 (1953), pp. 295–305. DOI: 10.1098/rspa.1953.0064 (see p. 36).

[88] J. F. Fowler. "The linear-quadratic formula and progress in fractionated radiotherapy". In: *The British Journal of Radiology* 62.740 (1989), pp. 679–694. DOI: 10.1259/0007-1285-62-740-679 (see p. 51).

[89] G. L. Fox, I. Rebay, and R. O. Hynes. "Expression of DFak56, a Drosophila homolog of vertebrate focal adhesion kinase, supports a role in cell migration in vivo". In: *Proceedings of the National Academy of Sciences* 96.26 (1999), pp. 14978–14983. DOI: 0.1073/pnas.96.26.14978 (see pp. 181, 242).

[90] H. B. Frieboes et al. "Computer simulation of glioma growth and morphology". In: *Neuroimage* 37 (2007), S59–S70. DOI: 10.1016/j.neuroimage.2007.03.008 (see p. 21).

[91] P. Friedl and K. Wolf. "Plasticity of cell migration: a multiscale tuning model". In: *Journal of Cell Biology* 188.1 (2010), pp. 11–19. DOI: 10.1083/jcb.200909003 (see p. 2).

[92] H. S. Friedman et al. "Bevacizumab alone and in combination with irinotecan in recurrent glioblastoma". In: *Journal of Clinical Oncology* 27.28 (2009), pp. 4733–4740. DOI: 10.1200/JCO.2008.19.8721 (see p. 105).

[93] N. Galjart. "Plus-end-tracking proteins and their interactions at microtubule ends". In: *Current Biology* 20.12 (2010), R528–R537. DOI: 10.1016/j.cub.2010.05.022 (see p. 170).

[94] R. A. Gatenby and E. T. Gawlinski. "A reaction-diffusion model of cancer invasion". In: *Cancer Research* 56.24 (1996), pp. 5745–5753. URL: https://cancerres.aacrjournals.org/content/56/24/5745 (see pp. 70, 87, 90).

[95] R. A. Gatenby et al. "Acid-mediated tumor invasion: a multidisciplinary study". In: *Cancer Research* 66.10 (2006), pp. 5216–5223. DOI: 10.1158/0008-5472.CAN-05-4193 (see p. 87).

[96] P. Gerlee and S. Nelander. "The impact of phenotypic switching on glioblastoma growth and invasion". In: *PLoS Computational Biology* 8.6 (2012), e1002556. DOI: 10.1371/journal.pcbi.1002556 (see p. 70).

[97] J. L. Gevertz and S. Torquato. "Modeling the effects of vasculature evolution on early brain tumor growth". In: *Journal of Theoretical Biology* 243.4 (2006), pp. 517–531. DOI: 10.1016/j.jtbi.2006.07.002 (see pp. 21, 124).

[98] A. Giese et al. "Dichotomy of astrocytoma migration and proliferation". In: *International Journal of Cancer* 67.2 (1996), pp. 275–282. DOI: 10.1002/(SICI)1097-0215(19960717)67:2<275::AID-IJC20>3.0.CO;2-9 (see p. 69).

[99] A. Giese et al. "Migration of human glioma cells on myelin". In: *Neurosurgery* 38.4 (1996), pp. 755–764. DOI: 10.1227/00006123-199604000-00026 (see p. 69).

[100] A. Giese et al. “Cost of migration: invasion of malignant gliomas and implications for treatment”. In: *Journal of Clinical Oncology* 21.8 (2003), pp. 1624–1636. DOI: 10.1200/JCO.2003.05.063 (see p. 69).

[101] L. González-Méndez, A. C. Gradilla, and I. Guerrero. “The cytoneme connection: direct long-distance signal transfer during development”. In: *Development* 146.9 (2019). DOI: 10.1242/dev.174607 (see p. 170).

[102] L. González-Méndez, I. Seijo-Barandiarán, and I. Guerrero. “Cytoneme-mediated cell-cell contacts for Hedgehog reception”. In: *Elife* 6 (2017), e24045. DOI: 10.7554/eLife.24045 (see pp. 170, 179).

[103] E. Grillon et al. “The spatial organization of proton and lactate transport in a rat brain tumor”. In: *PloS One* 6.2 (2011), e17416. DOI: 10.1371/journal.pone.0017416 (see p. 69).

[104] S. I. Grivennikov, F. R. Greten, and M. Karin. “Immunity, inflammation, and cancer”. In: *Cell* 140.6 (2010), pp. 883–899. DOI: 10.1016/j.cell.2010.01.025 (see p. 3).

[105] M. Gyllenberg and G. F. Webb. “A nonlinear structured population model of tumor growth with quiescence”. In: *Journal of Mathematical Biology* 28.6 (1990), pp. 671–694. DOI: 10.1007/BF00160231 (see p. 21).

[106] T. L. Haas et al. “Integrin $\alpha 7$ is a functional marker and potential therapeutic target in glioblastoma”. In: *Cell Stem Cell* 21.1 (2017), pp. 35–50. DOI: 10.1016/j.stem.2017.04.009 (see pp. 6, 184).

[107] D. Hambardzumyan, D. H. Gutmann, and H. Kettenmann. “The role of microglia and macrophages in glioma maintenance and progression”. In: *Nature Neuroscience* 19.1 (2016), p. 20. DOI: 10.1038/nn.4185 (see p. 9).

[108] M. A. Hammoud et al. “Prognostic significance of preoperative MRI scans in glioblastoma multiforme”. In: *Journal of Neuro-Oncology* 27.1 (1996), pp. 65–73. DOI: 10.1007/BF00146086 (see pp. 100, 101).

[109] D. Hanahan and R. A. Weinberg. “The hallmarks of cancer”. In: *Cell* 100.1 (2000), pp. 57–70. DOI: 10.1016/S0092-8674(00)81683-9 (see pp. 1, 2).

[110] D. Hanahan and R. A. Weinberg. “Hallmarks of cancer: the next generation”. In: *Cell* 144.5 (2011), pp. 646–674. DOI: 10.1016/j.cell.2011.02.013 (see pp. 1–3, 11, 71, 75).

[111] R. J. Harris et al. “Simulation, phantom validation, and clinical evaluation of fast pH-weighted molecular imaging using amine chemical exchange saturation transfer echo planar imaging (CEST-EPI) in glioma at 3 T”. In: *NMR in Biomedicine* 29.11 (2016), pp. 1563–1576. DOI: 10.1002/nbm.3611 (see p. 93).

[112] K. M. Hasan, A. L Alexander, and P. A. Narayana. “Does fractional anisotropy have better noise immunity characteristics than relative anisotropy in diffusion tensor MRI? An analytical approach”. In: *Magnetic Resonance in Medicine: An Official Journal of the International Society for Magnetic Resonance in Medicine* 51.2 (2004), pp. 413–417. DOI: 10.1002/mrm.10682 (see p. 31).

[113] H. Hatzikirou et al. “‘Go or grow’: the key to the emergence of invasion in tumour progression?” In: *Mathematical Medicine and Biology: a Journal of the IMA* 29.1 (2012), pp. 49–65. DOI: 10.1093/imammb/dqq011 (see p. 21).

[114] L. Hayflick. “Mortality and immortality at the cellular level. A review”. In: *Biochemistry-New York-English Translation of Biokhimiya* 62.11 (1997), pp. 1180–1190 (see p. 2).

[115] C. Henker et al. “Volumetric quantification of glioblastoma: experiences with different measurement techniques and impact on survival”. In: *Journal of Neuro-Oncology* 135.2 (2017), pp. 391–402. DOI: 10.1007/s11060-017-2587-5 (see pp. 96, 100).

[116] T. Hillen. “M 5 mesoscopic and macroscopic models for mesenchymal motion”. In: *Journal of Mathematical Biology* 53.4 (2006), pp. 585–616. DOI: 10.1007/s00285-006-0017-y (see pp. 33, 47, 134–136, 143, 144, 164).

[117] T. Hillen and K. J. Painter. “A user’s guide to PDE models for chemotaxis”. In: *Journal of Mathematical Biology* 58.1-2 (2009), p. 183. DOI: 10.1007/s00285-008-0201-3 (see p. 134).

[118] T. Hillen et al. “Moments of von Mises and Fisher distributions and applications”. In: *Mathematical Biosciences & Engineering* 14.3 (2017), p. 673. DOI: 10.3934/mbe.2017038 (see p. 150).

[119] C. Hogea, C. Davatzikos, and G. Biros. “An image-driven parameter estimation problem for a reaction–diffusion glioma growth model with mass effects”. In: *Journal of Mathematical Biology* 56.6 (2008), pp. 793–825. DOI: 10.1007/s00285-007-0139-x (see p. 21).

[120] E. C. Holland. “Glioblastoma multiforme: the terminator”. In: *Proceedings of the National Academy of Sciences* 97.12 (2000), pp. 6242–6244. DOI: 10.1073/pnas.97.12.6242 (see p. 4).

[121] P. Holzer. “Acid-sensitive ion channels and receptors”. In: *Sensory Nerves*. Springer, 2009, pp. 283–332. DOI: 10.1007/978-3-540-79090-7_9 (see p. 71).

[122] A. Honasoge and H. Sontheimer. “Involvement of tumor acidification in brain cancer pathophysiology”. In: *Frontiers in Physiology* 4 (2013), p. 316. DOI: 10.3389/fphys.2013.00316 (see pp. 69, 71).

[123] E. Höring et al. “The “go or grow” potential of gliomas is linked to the neuropeptide processing enzyme carboxypeptidase E and mediated by metabolic stress”. In: *Acta Neuropathologica* 124.1 (2012), pp. 83–97. DOI: 10.1007/s00401-011-0940-x (see p. 69).

[124] D. A. Hsia et al. “Differential regulation of cell motility and invasion by FAK”. In: *The Journal of Cell Biology* 160.5 (2003), pp. 753–767. DOI: 10.1083/jcb.200212114 (see p. 186).

[125] H. Huang, S. Liu, and T. B. Kornberg. “Glutamate signaling at cytoneme synapses”. In: *Science* 363.6430 (2019), pp. 948–955. DOI: 10.1126/science.aat5053 (see pp. 170, 179).

[126] A. Hunt and C. Surulescu. “A multiscale modeling approach to glioma invasion with therapy”. In: *Vietnam Journal of Mathematics* 45.1-2 (2017), pp. 221–240. DOI: 10.1007/s10013-016-0223-x (see pp. xvi, xxii, 50, 51, 66, 67, 70, 103, 200).

[127] A. Huttenlocher and A. R. Horwitz. “Integrins in cell migration”. In: *Cold Spring Harbor Perspectives in Biology* 3.9 (2011), a005074. DOI: 10.1101/cshperspect.a005074 (see pp. 6, 47).

[128] G. Jacquemet, H. Hamidi, and J. Ivaska. “Filopodia in cell adhesion, 3D migration and cancer cell invasion”. In: *Current Opinion in Cell Biology* 36 (2015), pp. 23–31. DOI: 10.1016/j.ceb.2015.06.007 (see p. 170).

[129] S. Jbabdi et al. “Simulation of anisotropic growth of low-grade gliomas using diffusion tensor imaging”. In: *Magnetic Resonance in Medicine: An Official Journal of the International Society for Magnetic Resonance in Medicine* 54.3 (2005), pp. 616–624. DOI: 10.1002/mrm.20625 (see pp. 32, 60).

[130] M. Jenkinson et al. “Fsl”. In: *Neuroimage* 62.2 (2012), pp. 782–790. DOI: 10.1016/j.neuroimage.2011.09.015 (see p. 212).

[131] J. Johnson et al. “Quantitative analysis of complex glioma cell migration on electrospun polycaprolactone using time-lapse microscopy”. In: *Tissue Engineering Part C: Methods* 15.4 (2009), pp. 531–540. DOI: 10.1089/ten.TEC.2008.0486 (see p. 135).

[132] M. C. Joiner and A. Van der Kogel. *Basic clinical radiobiology (fourth edition)*. CRC press, 2009. DOI: 10.1201/b15450 (see p. 124).

[133] C. R. Justus, L. Dong, and L. V. Yang. “Acidic tumor microenvironment and pH-sensing G protein-coupled receptors”. In: *Frontiers in Physiology* 4 (2013), p. 354. DOI: 10.3389/fphys.2013.00354 (see p. 71).

[134] L. J. Kaufman et al. “Glioma expansion in collagen I matrices: analyzing collagen concentration-dependent growth and motility patterns”. In: *Biophysical Journal* 89.1 (2005), pp. 635–650. DOI: 10.1529/biophysj.105.061994 (see p. 92).

[135] L. D. Ke et al. “The relevance of cell proliferation, vascular endothelial growth factor, and basic fibroblast growth factor production to angiogenesis and tumorigenicity in human glioma cell lines”. In: *Clinical Cancer Research* 6.6 (2000), pp. 2562–2572 (see pp. 90, 91, 124).

[136] J. Kelkel and C. Surulescu. “A multiscale approach to cell migration in tissue networks”. In: *Mathematical Models and Methods in Applied Sciences* 22.03 (2012), p. 1150017. DOI: 10.1142/S0218202511500175 (see pp. 50, 107).

[137] E. F. Keller and L. A. Segel. “Initiation of slime mold aggregation viewed as an instability”. In: *Journal of Theoretical Biology* 26.3 (1970), pp. 399–415. DOI: 10.1016/0022-5193(70)90092-5 (see pp. 133, 142, 173).

[138] R. L. Kendall et al. “Vascular endothelial growth factor receptor KDR tyrosine kinase activity is increased by autophosphorylation of two activation loop tyrosine residues”. In: *Journal of Biological Chemistry* 274.10 (1999), pp. 6453–6460. DOI: 10.1074/jbc.274.10.6453 (see p. 124).

[139] Y. Kim, H. Jeon, and H. Othmer. “The role of the tumor microenvironment in glioblastoma: A mathematical model”. In: *IEEE Transactions on Biomedical Engineering* 64.3 (2016), pp. 519–527. DOI: 10.1109/TBME.2016.2637828 (see pp. 20, 190).

[140] Y. Kim and S. Roh. “A hybrid model for cell proliferation and migration in glioblastoma”. In: *Discrete & Continuous Dynamical Systems-B* 18.4 (2013), p. 969. DOI: 10.3934/dcdsb.2013.18.969 (see p. 21).

[141] Y. Kim et al. “A mathematical model for pattern formation of glioma cells outside the tumor spheroid core”. In: *Journal of Theoretical Biology* 260.3 (2009), pp. 359–371. DOI: 10.1016/j.jtbi.2009.06.025 (see pp. 19, 21).

[142] Y. Kim et al. “miR451 and AMPK mutual antagonism in glioma cell migration and proliferation: a mathematical model”. In: *PloS One* 6.12 (2011), e28293. DOI: doi.org/10.1371/journal.pone.0028293 (see pp. 19, 190).

[143] P. B. Kingsley and W. G. Monahan. "Contrast-to-noise ratios of diffusion anisotropy indices". In: *Magnetic Resonance in Medicine: An Official Journal of the International Society for Magnetic Resonance in Medicine* 53.4 (2005), pp. 911–918. DOI: 10.1002/mrm.20433 (see pp. 30, 31).

[144] B. Klapholz et al. "Alternative mechanisms for talin to mediate integrin function". In: *Current Biology* 25.7 (2015), pp. 847–857. DOI: 10.1016/j.cub.2015.01.043 (see pp. 181, 242).

[145] P. Kleihues and W. K. Cavenee. *Pathology and genetics of tumours of the nervous system*. Vol. 2. International Agency for Research on Cancer Press, 2000. DOI: 10.1002/1096-9896(200102)193:2<276::AID-PATH765>3.0.CO;2-Q (see p. 4).

[146] L. Ko, A. Koestner, and W. Wechsler. "Characterization of cell cycle and biological parameters of transplantable glioma cell lines and clones". In: *Acta Neuropathologica* 51.2 (1980), pp. 107–111. DOI: 10.1007/BF00690451 (see pp. 89, 91).

[147] M. Kohandel, S. Sivaloganathan, and A. Oza. "Mathematical modeling of ovarian cancer treatments: sequencing of surgery and chemotherapy". In: *Journal of Theoretical Biology* 242.1 (2006), pp. 62–68. DOI: 10.1016/j.jtbi.2006.02.001 (see p. 111).

[148] E. Konukoglu et al. "Extrapolating glioma invasion margin in brain magnetic resonance images: Suggesting new irradiation margins". In: *Medical Image Analysis* 14.2 (2010), pp. 111–125. DOI: 10.1016/j.media.2009.11.005 (see p. 32).

[149] T. N. Kreisl et al. "Phase II trial of single-agent bevacizumab followed by bevacizumab plus irinotecan at tumor progression in recurrent glioblastoma". In: *Journal of Clinical Oncology* 27.5 (2009), p. 740. DOI: 10.1200/JCO.2008.16.3055 (see p. 105).

[150] J. M. Kroos et al. "Patient-specific computational modeling of cortical spreading depression via diffusion tensor imaging". In: *International Journal for Numerical Methods in Biomedical Engineering* 33.11 (2017), e2874. DOI: 10.1002/cnm.2874 (see p. 27).

[151] J. M. Kroos et al. "SDE-driven modeling of phenotypically heterogeneous tumors: The influence of cancer cell stemness". In: *Discrete & Continuous Dynamical Systems-B* 24.8 (2019), p. 4629. DOI: 10.3934/dcdsb.2019157 (see p. 124).

[152] P. Kumar, J. Li, and C. Surulescu. "Multiscale modeling of glioma pseudopalisades: contributions from the tumor microenvironment". In: *arXiv* (2020). URL: https://arxiv.org/abs/2007.05297 (see pp. 70, 71, 75).

[153] S. Kumar et al. "MMP secretion rate and inter-invadopodia spacing collectively govern cancer invasiveness". In: *Biophysical Journal* 114.3 (2018), pp. 650–662. DOI: 10.1016/j.bpj.2017.11.3777 (see p. 190).

[154] A. Kurganov and P. Rosenau. "On reaction processes with saturating diffusion". In: *Nonlinearity* 19.1 (2005), p. 171. DOI: 10.1088/0951-7715/19/1/009 (see p. 171).

[155] M. Lachowicz. "Micro and meso scales of description corresponding to a model of tissue invasion by solid tumours". In: *Mathematical Models and Methods in Applied Sciences* 15.11 (2005), pp. 1667–1683. DOI: 10.1142/S0218202505000935 (see pp. 17, 18).

[156] A. Laforgia and P. Natalini. "Some inequalities for modified Bessel functions". In: *Journal of Inequalities and Applications* 2010.1 (2010), p. 253035. DOI: 10.1155/2010/253035 (see p. 155).

[157] H. Lamb. *Hydrodynamics*. University Press, 1924. URL: https://books.google.it/books?id=OztMAAAAMAAJ (see p. 188).

[158] J. D. Lambert. *Numerical methods for ordinary differential systems: the initial value problem*. John Wiley & Sons, Inc., 1991. URL: https://books.google.it/books?id=tKdUvgAACAAJ (see p. 229).

[159] K. J. Langen et al. "Advances in neuro-oncology imaging". In: *Nature Reviews Neurology* 13.5 (2017), pp. 279–289. DOI: 10.1038/nrneurol.2017.44 (see pp. 12, 13).

[160] M. G. Larson and F. Bengzon. *The finite element method: theory, implementation, and applications*. Vol. 10. Springer Science & Business Media, 2013. DOI: 10.1007/978-3-642-33287-6 (see p. 223).

[161] D. A. Lauffenburger and J. J. Linderman. *Receptors: models for binding, trafficking, and signaling*. Oxford University Press on Demand, 1996. DOI: 10.1002/aic.690400624 (see pp. 89, 91, 124, 190).

[162] D. Le Bihan. "Looking into the functional architecture of the brain with diffusion MRI". In: *Nature Reviews Neuroscience* 4.6 (2003), pp. 469–480. DOI: 10.1038/nrn1119 (see p. 27).

[163] U. Ledzewicz et al. "Realizable protocols for optimal administration of drugs in mathematical models for anti-angiogenic treatment". In: *Mathematical Medicine and Biology: a Journal of the IMA* 27.2 (2010), pp. 157–179. DOI: 10.1093/imammb/dqp012 (see p. 21).

[164] F. Lefranc, J. Brotchi, and R. Kiss. "Possible future issues in the treatment of glioblastomas: special emphasis on cell migration and the resistance of migrating glioblastoma cells to apoptosis". In: *Journal of Clinical Oncology* 23.10 (2005), pp. 2411–2422. DOI: 10.1200/JCO.2005.03.089 (see p. 51).

[165] C. D. Levermore. *Chapman–Enskog approach to flux-limited diffusion theory*. Tech. rep. California Univ., 1979. DOI: 10.1103/PhysRevE.78.061137 (see p. 171).

[166] C. D. Levermore and G. C. Pomraning. "A flux-limited diffusion theory". In: *The Astrophysical Journal* 248 (1981), pp. 321–334. DOI: 10.1086/159157 (see p. 171).

[167] H. A. Levine et al. "Mathematical modeling of capillary formation and development in tumor angiogenesis: penetration into the stroma". In: *Bulletin of Mathematical Biology* 63.5 (2001), pp. 801–863. DOI: 10.1006/bulm.2001.0240 (see p. 124).

[168] D. R. Lide. *CRC handbook of chemistry and physics*. Vol. 85. CRC press, 2004. DOI: 10.1080/08893110902764125 (see pp. 89, 91).

[169] T. Lorenz and C. Surulescu. "On a class of multiscale cancer cell migration models: Well-posedness in less regular function spaces". In: *Mathematical Models and Methods in Applied Sciences* 24.12 (2014), pp. 2383–2436. DOI: 10.1142/S0218202514500249 (see pp. 54, 71, 107).

[170] D. N. Louis. "Molecular pathology of malignant gliomas". In: *Annual Review of Pathology: Mechanisms of Disease* 1 (2006), pp. 97–117. DOI: 10.1146/annurev.pathol.1.110304.100043 (see pp. 6, 8).

[171] D. N. Louis et al. “The 2007 WHO classification of tumours of the central nervous system”. In: *Acta Neuropathologica* 114.2 (2007), pp. 97–109. DOI: 10.1007/s00401-007-0243-4 (see p. 4).

[172] S. W. Lowe, E. Cepero, and G. Evan. “Intrinsic tumour suppression”. In: *Nature* 432.7015 (2004), pp. 307–315. DOI: 10.1038/nature03098 (see p. 2).

[173] N. Loy and L. Preziosi. “Kinetic models with non-local sensing determining cell polarization and speed according to independent cues”. In: *Journal of Mathematical Biology* 80.1 (2020), pp. 373–421. DOI: 10.1007/s00285-019-01411-x (see pp. xvii, xxiv, 134, 137, 138, 149, 151, 202, 232).

[174] N. Loy and L. Preziosi. “Modelling physical limits of migration by a kinetic model with non-local sensing”. In: *Journal of Mathematical Biology* (2020), pp. 1–43. DOI: 10.1007/s00285-020-01479-w (see p. 204).

[175] P. Lu et al. “Extracellular matrix degradation and remodeling in development and disease”. In: *Cold Spring Harbor Perspectives in Biology* 3.12 (2011), a005058. DOI: 10.1101/cshperspect.a005058 (see p. 6).

[176] S. Y. Lunt and M. G. Vander Heiden. “Aerobic glycolysis: meeting the metabolic requirements of cell proliferation”. In: *Annual Review of Cell and Developmental Biology* 27 (2011), pp. 441–464. DOI: 10.1146/annurev-cellbio-092910-154237 (see p. 75).

[177] F. Mac Gabhann and A. S. Popel. “Model of competitive binding of vascular endothelial growth factor and placental growth factor to VEGF receptors on endothelial cells”. In: *American Journal of Physiology-Heart and Circulatory Physiology* 286.1 (2004), H153–H164. DOI: 10.1152/ajpheart.00254.2003 (see p. 124).

[178] F. Mac Gabhann and A. S. Popel. “Targeting neuropilin-1 to inhibit VEGF signaling in cancer: comparison of therapeutic approaches”. In: *PLoS Computational Biology* 2.12 (2006), e180. DOI: 10.1371/journal.pcbi.0020180 (see p. 124).

[179] J. P. Macagno et al. “FAK acts as a suppressor of RTK-MAP kinase signalling in Drosophila melanogaster epithelia and human cancer cells”. In: *PLoS Genetics* 10.3 (2014), e1004262. DOI: 10.1371/journal.pgen.1004262 (see pp. 181, 242).

[180] E. A. Maher et al. “Malignant glioma: genetics and biology of a grave matter”. In: *Genes & Development* 15.11 (2001), pp. 1311–1333. DOI: 10.1101/gad.891601 (see pp. 4, 10).

[181] D. G. Mallet and G. J. Pettet. “A mathematical model of integrin-mediated haptotactic cell migration”. In: *Bulletin of Mathematical Biology* 68.2 (2006), p. 231. DOI: 0.1007/s11538-005-9032-1 (see pp. 19, 178).

[182] K. V. Mardia and P. E. Jupp. *Directional statistics*. Vol. 494. John Wiley & Sons, 2009. DOI: 10.1002/9780470316979 (see p. 36).

[183] G. R. Martin and R. K. Jain. “Noninvasive measurement of interstitial pH profiles in normal and neoplastic tissue using fluorescence ratio imaging microscopy”. In: *Cancer Research* 54.21 (1994), pp. 5670–5674. URL: https://cancerres.aacrjournals.org/content/54/21/5670 (see pp. 90, 91).

[184] N. K. Martin et al. “A mathematical model of tumour and blood pHe regulation: The HCO3-/CO2 buffering system”. In: *Mathematical Biosciences* 230.1 (2011), pp. 1–11. DOI: 10.1016/j.mbs.2010.12.002 (see pp. 90, 91).

[185] A. Martínez-González et al. “Hypoxic cell waves around necrotic cores in glioblastoma: a biomathematical model and its therapeutic implications”. In: *Bulletin of Mathematical Biology* 74.12 (2012), pp. 2875–2896. DOI: 10.1007/s11538-012-9786-1 (see pp. 21, 70).

[186] R. Martínez-Zaguilán et al. “Acidic pH enhances the invasive behavior of human melanoma cells”. In: *Clinical & Experimental Metastasis* 14.2 (1996), pp. 176–186. DOI: 10.1007/BF00121214 (see p. 69).

[187] S. Matías-Román et al. “Membrane type 1–matrix metalloproteinase is involved in migration of human monocytes and is regulated through their interaction with fibronectin or endothelium”. In: *Blood* 105.10 (2005), pp. 3956–3964. DOI: 10.1182/blood-2004-06-2382 (see p. 170).

[188] R. J. McCann and M. Puel. “Constructing a relativistic heat flow by transport time steps”. In: *Annales de l'IHP Analyse Non Linéaire*. Vol. 26. 6. 2009, pp. 2539–2580. DOI: 10.1016/j.anihpc.2009.06.006 (see p. 172).

[189] J. B. McGillen et al. “A general reaction–diffusion model of acidity in cancer invasion”. In: *Journal of Mathematical Biology* 68.5 (2014), pp. 1199–1224. DOI: 10.1007/s00285-013-0665-7 (see p. 70).

[190] B. Mendoza-Juez et al. “A mathematical model for the glucose-lactate metabolism of in vitro cancer cells”. In: *Bulletin of Mathematical Biology* 74.5 (2012), pp. 1125–1142. DOI: 10.1007/s11538-011-9711-z (see p. 21).

[191] R. Mentlein, K. Hattermann, and J. Held-Feindt. “Lost in disruption: role of proteases in glioma invasion and progression”. In: *Biochimica et Biophysica Acta (BBA)-Reviews on Cancer* 1825.2 (2012), pp. 178–185. DOI: 10.1016/j.bbcan.2011.12.001 (see pp. 6, 7, 184).

[192] G. Meral, C. Stinner, and C. Surulescu. “A multiscale model for acid-mediated tumor invasion: Therapy approaches”. In: *Journal of Coupled Systems and Multiscale Dynamics* 3.2 (2015), pp. 135–142. DOI: 10.1166/jcsmd.2015.1071 (see p. 70).

[193] J. Mercapide et al. “Stromelysin-1/matrix metalloproteinase-3 (MMP-3) expression accounts for invasive properties of human astrocytoma cell lines”. In: *International Journal of Cancer* 106.5 (2003), pp. 676–682. DOI: 10.1002/ijc.11286 (see pp. 61, 189, 190).

[194] R. Milo and R. Phillips. *Cell biology by the numbers*. Garland Science, 2015. DOI: 10.1201/9780429258770 (see p. 188).

[195] R. von Mises. “Üder die “Ganzzahligkeit” der Atomgewichte und verwandte Fragen”. In: *Physikalische Zeitschrift* 19.3/4 (1918), pp. 490–500 (see p. 36).

[196] R. E. Moellering et al. “Acid treatment of melanoma cells selects for invasive phenotypes”. In: *Clinical & Experimental Metastasis* 25.4 (2008), pp. 411–425. DOI: 10.1007/s10585-008-9145-7 (see p. 69).

[197] A. R. Monteiro et al. “The role of hypoxia in glioblastoma invasion”. In: *Cells* 6.4 (2017), p. 45. DOI: 10.3390/cells6040045 (see p. 69).

[198] P. Mosayebi et al. “Tumor invasion margin on the Riemannian space of brain fibers”. In: *Medical Image Analysis* 16.2 (2012), pp. 361–373. DOI: 10.1016/j.media.2011.10.001 (see pp. 32, 33).

[199] Kolbe. N. et al. “Modeling multiple taxis: tumor invasion with phenotypic heterogeneity, haptotaxis, and unilateral interspecies repellence”. In: *arXiv* (2020). URL: https://arxiv.org/abs/2005.01444 (see p. 134).

[200] J. A. Nagy et al. “Heterogeneity of the tumor vasculature”. In: *Seminars in thrombosis and hemostasis*. Vol. 36. 03. Thieme Medical Publishers. 2010, pp. 321–331. DOI: 10.1055/s-0030-1253454 (see p. 2).

[201] M. Nakada et al. “Integrin α3 is overexpressed in glioma stem-like cells and promotes invasion”. In: *British Journal of Cancer* 108.12 (2013), pp. 2516–2524. DOI: 10.1038/bjc.2013.218 (see p. 184).

[202] Y. Niibori, H. Usui, and T. Chida. “Double porosity model to describe both permeability change and dissolution processes”. In: *Mechanical Engineering Journal* 2.5 (2015), pp. 15–00210. DOI: 10.1299/mej.15-00210 (see p. 195).

[203] K.-A. Norton and A. S. Popel. “Effects of endothelial cell proliferation and migration rates in a computational model of sprouting angiogenesis”. In: *Scientific Reports* 6 (2016), p. 36992. DOI: 10.1038/srep36992 (see pp. 90, 91, 124).

[204] C. Ogier et al. “Matrix metalloproteinase-2 (MMP-2) regulates astrocyte motility in connection with the actin cytoskeleton and integrins”. In: *Glia* 54.4 (2006), pp. 272–284. DOI: 10.1002/glia.20349 (see p. 170).

[205] B. Øksendal. “Stochastic differential equations”. In: *Stochastic Differential Equations*. Springer, 2003, pp. 65–84. DOI: 10.1007/978-3-642-14394-6 (see p. 86).

[206] M. W. Olson et al. “Kinetic analysis of the binding of human matrix metalloproteinase-2 and-9 to tissue inhibitor of metalloproteinase (TIMP)-1 and TIMP-2”. In: *Journal of Biological Chemistry* 272.47 (1997), pp. 29975–29983. DOI: 10.1074/jbc.272.47.29975 (see p. 190).

[207] M. Onishi et al. “Angiogenesis and invasion in glioma”. In: *Brain Tumor Pathology* 28.1 (2011), pp. 13–24. DOI: 0.1007/s10014-010-0007-z (see pp. 6–8, 69, 75, 105).

[208] K. E. O’Reilly et al. “mTOR inhibition induces upstream receptor tyrosine kinase signaling and activates Akt”. In: *Cancer Research* 66.3 (2006), pp. 1500–1508. DOI: 10.1158/0008-5472.CAN-05-2925 (see p. 2).

[209] M. Osswald et al. “Brain tumour cells interconnect to a functional and resistant network”. In: *Nature* 528.7580 (2015), pp. 93–98. DOI: 10.1038/nature16071 (see pp. 175, 176).

[210] Q. T. Ostrom et al. “CBTRUS statistical report: primary brain and central nervous system tumors diagnosed in the United States in 2008-2012”. In: *Neuro-Oncology* 17.suppl_4 (2015), pp. iv1–iv62. DOI: 10.1093/neuonc/nov189 (see p. 3).

[211] H. G. Othmer, S. R. Dunbar, and W. Alt. “Models of dispersal in biological systems”. In: *Journal of Mathematical Biology* 26.3 (1988), pp. 263–298. DOI: 10.1007/BF00277392 (see pp. 18, 47, 204).

[212] H. G. Othmer and T. Hillen. “The diffusion limit of transport equations derived from velocity-jump processes”. In: *SIAM Journal on Applied Mathematics* 61.3 (2000), pp. 751–775. DOI: 10.1137/S0036139999358167 (see pp. 55, 57).

[213] H. G. Othmer and T. Hillen. “The diffusion limit of transport equations II: Chemotaxis equations”. In: *SIAM Journal on Applied Mathematics* 62.4 (2002), pp. 1222–1250. DOI: 10.1137/S0036139900382772 (see pp. 17, 49, 75, 134, 137).

[214] K. J. Painter. “Modelling cell migration strategies in the extracellular matrix”. In: *Journal of Mathematical Biology* 58.4-5 (2009), p. 511. DOI: 10.1007/s00285-008-0217-8 (see p. 151).

[215] K. J. Painter. "Mathematical models for chemotaxis and their applications in self-organisation phenomena". In: *Journal of Theoretical Biology* 481 (2019), pp. 162–182. DOI: 10.1016/j.jtbi.2018.06.019 (see p. 134).

[216] K. J. Painter and T. Hillen. "Mathematical modelling of glioma growth: the use of diffusion tensor imaging (DTI) data to predict the anisotropic pathways of cancer invasion". In: *Journal of Theoretical Biology* 323 (2013), pp. 25–39. DOI: 10.1016/j.jtbi.2013.01.014 (see pp. xv, xxii, 18, 33–35, 40, 47, 53, 58).

[217] K. Palucka and J. Banchereau. "Cancer immunotherapy via dendritic cells". In: *Nature Reviews Cancer* 12.4 (2012), pp. 265–277. DOI: 10.1038/nrc3258 (see p. 9).

[218] M. Papadogiorgaki et al. "Mathematical modelling of spatio-temporal glioma evolution". In: *Theoretical Biology and Medical Modelling* 10.1 (2013), p. 47. DOI: 10.1186/1742-4682-10-47 (see p. 19).

[219] G. Pennarun et al. "Apoptosis related to telomere instability and cell cycle alterations in human glioma cells treated by new highly selective G-quadruplex ligands". In: *Oncogene* 24.18 (2005), pp. 2917–2928. DOI: 10.1038/sj.onc.1208468 (see pp. 89, 91).

[220] R. Perona. "Cell signalling: growth factors and tyrosine kinase receptors". In: *Clinical and Translational Oncology* 8.2 (2006), pp. 77–82. DOI: 10.1007/s12094-006-0162-1 (see pp. 1, 10).

[221] M. Perrin et al. "Validation of q-ball imaging with a diffusion fibre-crossing phantom on a clinical scanner". In: *Philosophical Transactions of the Royal Society B: Biological Sciences* 360.1457 (2005), pp. 881–891. DOI: 10.1098/rstb.2005.1650 (see p. 39).

[222] B. Perthame. "Mathematical tools for kinetic equations". In: *Bulletin of the American Mathematical Society* 41.2 (2004), pp. 205–244. DOI: 10.1090/S0273-0979-04-01004-3 (see pp. 17, 47).

[223] B. Perthame, M. Tang, and N. Vauchelet. "Derivation of the bacterial run-and-tumble kinetic equation from a model with biochemical pathway". In: *Journal of Mathematical Biology* 73.5 (2016), pp. 1161–1178. DOI: 10.1007/s00285-016-0985-5 (see p. 75).

[224] R. J. Petrie and K. M. Yamada. "At the leading edge of three-dimensional cell migration". In: *Journal of Cell Science* 125.24 (2012), pp. 5917–5926. DOI: 10.1242/jcs.093732 (see p. 6).

[225] K. Pham et al. "Density-dependent quiescence in glioma invasion: instability in a simple reaction–diffusion model for the migration/proliferation dichotomy". In: *Journal of Biological Dynamics* 6.sup1 (2012), pp. 54–71. DOI: 10.1080/17513758.2011.590610 (see pp. 70, 89, 91).

[226] F. Pignatti et al. "Prognostic factors for survival in adult patients with cerebral low-grade glioma". In: *Journal of Clinical Oncology* 20.8 (2002), pp. 2076–2084. DOI: 10.1200/JCO.2002.08.121 (see p. 99).

[227] K. Polyak and R. A. Weinberg. "Transitions between epithelial and mesenchymal states: acquisition of malignant and stem cell traits". In: *Nature Reviews Cancer* 9.4 (2009), pp. 265–273. DOI: 10.1038/nrc2620 (see p. 2).

[228] M. Portela et al. "Glioblastoma cells vampirize WNT from neurons and trigger a JNK/MMP signaling loop that enhances glioblastoma progression and neurodegeneration". In: *PLoS Biology* 17.12 (2019), e3000545. DOI: 10.1371/journal.pbio.3000545 (see pp. 170, 179, 241, 242).

[229] G. Powathil et al. “Mathematical modeling of brain tumors: effects of radiotherapy and chemotherapy”. In: *Physics in Medicine & Biology* 52.11 (2007), p. 3291. DOI: 10.1088/0031-9155/52/11/023 (see pp. 111, 124).

[230] S. Prag et al. “NCAM regulates cell motility”. In: *Journal of Cell Science* 115.2 (2002), pp. 283–292 (see p. 88).

[231] X. S. Qi, C. J Schultz, and X. A. Li. “An estimation of radiobiologic parameters from clinical outcomes for radiation treatment planning of brain tumor”. In: *International Journal of Radiation Oncology* Biology* Physics* 64.5 (2006), pp. 1570–1580. DOI: 10.1016/j.ijrobp.2005.12.022 (see p. 124).

[232] D. F. Quail and J. A. Joyce. “The microenvironmental landscape of brain tumors”. In: *Cancer Cell* 31.3 (2017), pp. 326–341. DOI: 10.1016/j.ccell.2017.02.009 (see p. 8).

[233] A. Quarteroni, R. Sacco, and F. Saleri. *Numerical mathematics*. Vol. 37. Springer Science & Business Media, 2010. DOI: doi.org/10.1007/b98885 (see pp. 232, 236).

[234] A. Quarteroni and A. Valli. *Numerical approximation of partial differential equations*. Vol. 23. Springer Science & Business Media, 2008. DOI: 10.1007/978-3-540-85268-1 (see pp. 223, 224, 226, 227).

[235] A. M. Rajnicek, L. E. Foubister, and C. D. McCaig. “Prioritising guidance cues: directional migration induced by substratum contours and electrical gradients is controlled by a rho/cdc42 switch”. In: *Developmental Biology* 312.1 (2007), pp. 448–460. DOI: 10.1016/j.ydbio.2007.09.051 (see p. 134).

[236] F. A. Ramírez-Weber and T. B. Kornberg. “Cytonemes: cellular processes that project to the principal signaling center in Drosophila imaginal discs”. In: *Cell* 97.5 (1999), pp. 599–607. DOI: 10.1016/s0092-8674(00)80771-0 (see p. 170).

[237] J. A. Ramos-Vara. “Technical aspects of immunohistochemistry”. In: *Veterinary Pathology* 42.4 (2005), pp. 405–426. DOI: 10.1354/vp.42-4-405 (see p. 12).

[238] J. S. Rao. “Molecular mechanisms of glioma invasiveness: the role of proteases”. In: *Nature Reviews Cancer* 3.7 (2003), pp. 489–501. DOI: 10.1038/nrc1121 (see pp. 6, 170).

[239] U. Rauch. “Brain matrix: structure, turnover and necessity”. In: *Biochemical Society Transactions* 35.4 (2007), p. 656. DOI: 10.1042/BST0350656 (see p. 5).

[240] R. D. Read. “Drosophila melanogaster as a model system for human brain cancers”. In: *Glia* 59.9 (2011), pp. 1364–1376. DOI: 10.1002/glia.21148 (see p. 241).

[241] R. D. Read et al. “A drosophila model for EGFR-Ras and PI3K-dependent human glioma”. In: *PLoS Genetics* 5.2 (2009), e1000374. DOI: 10.1371/journal.pgen.1000374 (see p. 241).

[242] D. A. Reardon et al. “A review of VEGF/VEGFR-targeted therapeutics for recurrent glioblastoma”. In: *Journal of the National Comprehensive Cancer Network* 9.4 (2011), pp. 414–427. DOI: 10.6004/jnccn.2011.0038 (see pp. 11, 105).

[243] M. Reed. *Methods of modern mathematical physics: Functional analysis*. Elsevier, 2012. DOI: 10.1016/B978-0-12-585001-8.X5001-6 (see p. 57).

[244] S. W. Rhee et al. “Patterned cell culture inside microfluidic devices”. In: *Lab on a Chip* 5.1 (2005), pp. 102–107. DOI: 10.1039/b403091e (see p. 135).

[245] B. Ribba et al. “A tumor growth inhibition model for low-grade glioma treated with chemotherapy or radiotherapy”. In: *Clinical Cancer Research* 18.18 (2012), pp. 5071–5080. DOI: 10.1158/1078-0432.CCR-12-0084 (see p. 21).

[246] A. J. Ridley. “Life at the leading edge”. In: *Cell* 145.7 (2011), pp. 1012–1022. DOI: 10.1016/j.cell.2011.06.010 (see p. 6).

[247] L. L. Rodriguez and I. C. Schneider. “Directed cell migration in multi-cue environments”. In: *Integrative Biology* 5.11 (2013), pp. 1306–1323. DOI: 10.1039/c3ib40137e (see p. 135).

[248] A. M. Rojiani and K. Dorovini-Zis. “Glomeruloid vascular structures in glioblastoma multiforme: an immunohistochemical and ultrastructural study”. In: *Journal of Neurosurgery* 85.6 (1996), pp. 1078–1084. DOI: 10.3171/jns.1996.85.6.1078 (see p. 95).

[249] Y. Rong et al. “‘Pseudopalisading’necrosis in glioblastoma: a familiar morphologic feature that links vascular pathology, hypoxia, and angiogenesis”. In: *Journal of Neuropathology & Experimental Neurology* 65.6 (2006), pp. 529–539. DOI: 10.1097/00005072-200606000-00001 (see pp. 8, 9, 105).

[250] P. Rosenau. “Tempered diffusion: A transport process with propagating fronts and inertial delay”. In: *Physical Review A* 46.12 (1992), R7371. DOI: 10.1103/PhysRevA.46.R7371 (see p. 171).

[251] M. Ruzicka. *Nichtlineare Funktionalanalysis: Eine Einführung*. Springer-Verlag, 2006. DOI: 10.1007/3-540-35022-5 (see p. 58).

[252] T. Saitou et al. “Mathematical modeling of invadopodia formation”. In: *Journal of Theoretical Biology* 298 (2012), pp. 138–146. DOI: 10.1016/j.jtbi.2011.12.018 (see p. 190).

[253] S. Sathornsumetee et al. “Molecularly targeted therapy for malignant glioma”. In: *Cancer* 110.1 (2007), pp. 13–24. DOI: 10.1002/cncr.22741 (see p. 11).

[254] H. J. Scherer. “Structural development in gliomas”. In: *The American Journal of Cancer* 34.3 (1938), pp. 333–351. DOI: 10.1158/ajc.1938.333 (see p. 6).

[255] J. D. Schmahmann et al. “Association fibre pathways of the brain: parallel observations from diffusion spectrum imaging and autoradiography”. In: *Brain* 130.3 (2007), pp. 630–653. DOI: 10.1093/brain/awl359 (see p. 26).

[256] G. L. Semenza. “Tumor metabolism: cancer cells give and take lactate”. In: *The Journal of Clinical Investigation* 118.12 (2008), pp. 3835–3837. DOI: 10.1172/JCI37373 (see p. 3).

[257] C. J. Sherr and F. McCormick. “The RB and p53 pathways in cancer”. In: *Cancer Cell* 2.2 (2002), pp. 103–112. DOI: 10.1016/S1535-6108(02)00102-2 (see p. 2).

[258] R. E. Showalter. *Monotone operators in Banach space and nonlinear partial differential equations*. Vol. 49. American Mathematical Soc., 2013. DOI: 10.1090/surv/049 (see pp. 58, 59).

[259] M. Sidani et al. “Cofilin determines the migration behavior and turning frequency of metastatic cancer cells”. In: *The Journal of Cell Biology* 179.4 (2007), pp. 777–791. DOI: 10.1083/jcb.200707009 (see pp. 61, 88, 91, 124).

[260] H. E. Skipper. “Experimental evaluation of potential anticancer agents XIII, on the criteria and kinetics associated with" curability" of experimental leukemria”. In: *Cancer Chemotherapy Report* 35 (1964), pp. 3–111 (see p. 111).

[261] K. Smallbone, R. A. Gatenby, and P. K. Maini. “Mathematical modelling of tumour acidity”. In: *Journal of Theoretical Biology* 255.1 (2008), pp. 106–112. DOI: 10.1016/j.jtbi.2008.08.002 (see p. 70).

[262] S. M. Smith et al. “Advances in functional and structural MR image analysis and implementation as FSL”. In: *Neuroimage* 23 (2004), S208–S219. DOI: 10.1016/j.neuroimage.2004.07.051 (see pp. 212, 213).

[263] S. Standring. *Gray's anatomy: the anatomical basis of clinical practice*. Elsevier Health Sciences, 2015 (see pp. 4, 25).

[264] C. Stinner, C: Surulescu, and G. Meral. “A multiscale model for pH-tactic invasion with time-varying carrying capacities”. In: *IMA Journal of Applied Mathematics* 80.5 (2015), pp. 1300–1321. DOI: 10.1093/imamat/hxu055 (see p. 70).

[265] C. Stinner, C. Surulescu, and A. Uatay. “Global existence for a go-or-grow multiscale model for tumor invasion with therapy”. In: *Mathematical Models and Methods in Applied Sciences* 26.11 (2016), pp. 2163–2201. DOI: 10.1142/S021820251640011X (see p. 70).

[266] C. L. Stokes and D. A. Lauffenburger. “Analysis of the roles of microvessel endothelial cell random motility and chemotaxis in angiogenesis”. In: *Journal of Theoretical Biology* 152.3 (1991), pp. 377–403. DOI: 10.1016/s0022-5193(05)80201-2 (see pp. 89–91).

[267] C. L. Stokes et al. “Chemotaxis of human microvessel endothelial cells in response to acidic fibroblast growth factor.” In: *Laboratory Investigation; a Journal of Technical Methods and Pathology* 63.5 (1990), p. 657 (see pp. 89, 91).

[268] O. Straume et al. “Prognostic importance of glomeruloid microvascular proliferation indicates an aggressive angiogenic phenotype in human cancers”. In: *Cancer Research* 62.23 (2002), pp. 6808–6811 (see pp. 8, 95).

[269] D. W. Stroock. “Some stochastic processes which arise from a model of the motion of a bacterium”. In: *Zeitschrift für Wahrscheinlichkeitstheorie und verwandte Gebiete* 28.4 (1974), pp. 305–315. DOI: 10.1007/BF00532948 (see p. 136).

[270] W. Stummer et al. “Extent of resection and survival in glioblastoma multiforme: identification of and adjustment for bias”. In: *Neurosurgery* 62.3 (2008), pp. 564–576. DOI: 10.1227/01.neu.0000317304.31579.17 (see p. 10).

[271] R. Stupp and C. Ruegg. *Integrin inhibitors reaching the clinic*. 2007. DOI: 10.1200/JCO.2006.09.8376 (see p. 66).

[272] S. Sun, I. Titushkin, and M. Cho. “Regulation of mesenchymal stem cell adhesion and orientation in 3D collagen scaffold by electrical stimulus”. In: *Bioelectrochemistry* 69.2 (2006), pp. 133–141. DOI: 10.1016/j.bioelechem.2005.11.007 (see p. 53).

[273] H. G. Sundararaghavan et al. “Fiber alignment directs cell motility over chemotactic gradients”. In: *Biotechnology and Bioengineering* 110.4 (2013), pp. 1249–1254. DOI: 10.1002/bit.24788 (see p. 134).

[274] A. Swan et al. “A patient-specific anisotropic diffusion model for brain tumour spread”. In: *Bulletin of Mathematical Biology* 80.5 (2018), pp. 1259–1291. DOI: 10.1007/s11538-017-0271-8 (see pp. 58, 63).

[275] K. R. Swanson, E. C. Alvord Jr, and J. D. Murray. “A quantitative model for differential motility of gliomas in grey and white matter”. In: *Cell Proliferation* 33.5 (2000), pp. 317–329. DOI: 10.1046/j.1365-2184.2000.00177.x (see pp. 19, 32).

[276] K. R. Swanson et al. “Quantifying the role of angiogenesis in malignant progression of gliomas: in silico modeling integrates imaging and histology”. In: *Cancer Research* 71.24 (2011), pp. 7366–7375. DOI: 10.1158/0008-5472.CAN-11-1399 (see pp. 19, 21, 70, 89–91, 101, 124).

[277] A. Szabó et al. “Collective cell motion in endothelial monolayers”. In: *Physical Biology* 7.4 (2010), p. 046007. DOI: 10.1088/1478-3975/7/4/046007 (see pp. 88, 91, 124).

[278] S. Takano et al. “Concentration of vascular endothelial growth factor in the serum and tumor tissue of brain tumor patients”. In: *Cancer Research* 56.9 (1996), pp. 2185–2190. URL: https://cancerres.aacrjournals.org/content/56/9/2185 (see pp. 124, 125).

[279] J. W. Tamkun et al. “Structure of integrin, a glycoprotein involved in the transmembrane linkage between fibronectin and actin”. In: *Cell* 46.2 (1986), pp. 271–282. DOI: 10.1016/0092-8674(86)90744-0 (see p. 6).

[280] P. Tracqui et al. “A mathematical model of glioma growth: the effect of chemotherapy on spatio-temporal growth”. In: *Cell Proliferation* 28.1 (1995), pp. 17–31. DOI: 10.1111/j.1365-2184.1995.tb00036.x (see p. 19).

[281] D. S. Tuch et al. “Diffusion MRI of complex neural architecture”. In: *Neuron* 40.5 (2003), pp. 885–895. DOI: 10.1016/S0896-6273(03)00758-X (see p. 47).

[282] B. Ugur, K. Chen, and H. J. Bellen. “Drosophila tools and assays for the study of human diseases”. In: *Disease models & mechanisms* 9.3 (2016), pp. 235–244. DOI: 10.1242/dmm.023762 (see p. 241).

[283] N. Upadhyay and A. D. Waldman. “Conventional MRI evaluation of gliomas”. In: *The British Journal of Radiology* 84.special_issue_2 (2011), S107–S111. DOI: 10.1259/bjr/65711810 (see p. 12).

[284] N. Vauchelet. “Numerical simulation of a kinetic model for chemotaxis”. In: *Kinetic & Related Models* 3.3 (2010), pp. 501–528. DOI: 10.3934/krm.2010.3.501 (see p. 232).

[285] P. Vaupel, F. Kallinowski, and P. Okunieff. “Blood flow, oxygen and nutrient supply, and metabolic microenvironment of human tumors: a review”. In: *Cancer Research* 49.23 (1989), pp. 6449–6465 (see pp. 89–92).

[286] J. L. Vázquez. *The porous medium equation: mathematical theory*. Oxford University Press, 2007. DOI: 10.1093/acprof:oso/9780198569039.001.0001 (see p. 19).

[287] M. Verbeni et al. “Morphogenetic action through flux-limited spreading”. In: *Physics of Life Reviews* 10.4 (2013), pp. 457–475. DOI: 10.1016/j.plrev.2013.06.004 (see pp. 170, 172, 179, 188).

[288] A. Vollmann-Zwerenz et al. “Tumor Cell Invasion in Glioblastoma”. In: *International Journal of Molecular Sciences* 21.6 (2020), p. 1932. DOI: 10.3390/ijms21061932 (see p. 7).

[289] M. A. Wagle and R. T. Tranquillo. “A self-consistent cell flux expression for simultaneous chemotaxis and contact guidance in tissues”. In: *Journal of Mathematical Biology* 41.4 (2000), pp. 315–330. DOI: 10.1007/s002850000040 (see pp. 134, 164).

[290] Y. L. Wang et al. “Association between tumor acidity and hypervascularity in human gliomas using pH-weighted amine chemical exchange saturation transfer echo-planar imaging and dynamic susceptibility contrast perfusion MRI at 3T”. In: *American Journal of Neuroradiology* 40.6 (2019), pp. 979–986. DOI: 10.3174/ajnr.A6063 (see pp. 69, 71).

[291] O. Warburg. “On the origin of cancer cells”. In: *Science* 123.3191 (1956), pp. 309–314. DOI: 10.1126/science.123.3191.309 (see p. 3).

[292] G. S. Watson and E. J. Williams. “On the construction of significance tests on the circle and the sphere”. In: *Biometrika* 43.3/4 (1956), pp. 344–352. DOI: 10.1093/biomet/43.3-4.344 (see p. 36).

[293] B. A. Webb et al. “Dysregulated pH: a perfect storm for cancer progression”. In: *Nature Reviews Cancer* 11.9 (2011), pp. 671–677. DOI: 10.1038/nrc3110 (see pp. 8, 69, 87, 89, 91).

[294] K. T. Weiß et al. “Proton-sensing G protein-coupled receptors as regulators of cell proliferation and migration during tumor growth and wound healing”. In: *Experimental Dermatology* 26.2 (2017), pp. 127–132. DOI: 10.1111/exd.13209 (see p. 71).

[295] P. C. Wilkinson and J. M. Lackie. “The influence of contact guidance on chemotaxis of human neutrophil leukocytes”. In: *Experimental Cell Research* 145.2 (1983), pp. 255–264. DOI: 10.1016/0014-4827(83)90004-6 (see p. 135).

[296] F. Winkler et al. “Imaging glioma cell invasion in vivo reveals mechanisms of dissemination and peritumoral angiogenesis”. In: *Glia* 57.12 (2009), pp. 1306–1315. DOI: 10.1002/glia.20850 (see p. 6).

[297] F. J. Wippold et al. “Neuropathology for the neuroradiologist: palisades and pseudopalisades”. In: *American Journal of Neuroradiology* 27.10 (2006), pp. 2037–2041. DOI: 10.3174/ajnr.A0682 (see pp. 69, 99).

[298] E. Witsch, M. Sela, and Y. Yarden. “Roles for growth factors in cancer progression”. In: *Physiology* 25.2 (2010), pp. 85–101. DOI: 10.1152/physiol.00045.2009 (see p. 1).

[299] H. T. Witte et al. “Modeling glioma growth and invasion in Drosophila melanogaster”. In: *Neoplasia* 11.9 (2009), pp. 882–888. DOI: 10.1593/neo.09576 (see p. 241).

[300] K. Wolf et al. “Compensation mechanism in tumor cell migration: mesenchymal–amoeboid transition after blocking of pericellular proteolysis”. In: *The Journal of Cell Biology* 160.2 (2003), pp. 267–277. DOI: 10.1083/jcb.200209006 (see p. 135).

[301] K. Wolf et al. “Physical limits of cell migration: control by ECM space and nuclear deformation and tuning by proteolysis and traction force”. In: *Journal of Cell Biology* 201.7 (2013), pp. 1069–1084. DOI: 10.1083/jcb.201210152 (see p. 195).

[302] M. W. Woolrich et al. “Bayesian analysis of neuroimaging data in FSL”. In: *Neuroimage* 45.1 (2009), S173–S186. DOI: 10.1016/j.neuroimage.2008.10.055 (see p. 212).

[303] Q. Xie, S. Mittal, and M. E. Berens. “Targeting adaptive glioblastoma: an overview of proliferation and invasion”. In: *Neuro-Oncology* 16.12 (2014), pp. 1575–1584. DOI: 10.1093/neuonc/nou147 (see p. 69).

[304] L. Xu, D. Fukumura, and R. K. Jain. "Acidic extracellular pH induces vascular endothelial growth factor (VEGF) in human glioblastoma cells via ERK1/2 MAPK signaling pathway Mechanism of low pH-induced VEGF". In: *Journal of Biological Chemistry* 277.13 (2002), pp. 11368–11374. DOI: 10.1074/jbc.M108347200 (see p. 75).

[305] Q. Yu and I. Stamenkovic. "Cell surface-localized matrix metalloproteinase-9 proteolytically activates TGF-β and promotes tumor invasion and angiogenesis". In: *Genes & Development* 14.2 (2000), pp. 163–176. DOI: 10.1101/gad.14.2.163 (see p. 170).

[306] T. L. Yuan and L. C. Cantley. "PI3K pathway alterations in cancer: variations on a theme". In: *Oncogene* 27.41 (2008), pp. 5497–5510. DOI: 10.1038/onc.2008.245 (see p. 2).

[307] P. D. Yurchenco. "Basement membranes: cell scaffoldings and signaling platforms". In: *Cold Spring Harbor Perspectives in Biology* 3.2 (2011), a004911. DOI: 10.1101/cshperspect.a004911 (see p. 6).

[308] M. H. Zaman et al. "Migration of tumor cells in 3D matrices is governed by matrix stiffness along with cell-matrix adhesion and proteolysis". In: *Proceedings of the National Academy of Sciences* 103.29 (2006), pp. 10889–10894. DOI: 10.1073/pnas.0604460103 (see p. 195).

[309] Z. Zhao et al. "A comprehensive review of available omics data resources and molecular profiling for precision glioma studies". In: *Biomedical Reports* 10.1 (2019), pp. 3–9. DOI: 10.3892/br.2018.1168 (see p. 14).

[310] A. Zhigun, C. Surulescu, and A. Hunt. "A strongly degenerate diffusion-haptotaxis model of tumour invasion under the go-or-grow dichotomy hypothesis". In: *Mathematical Methods in the Applied Sciences* 41.6 (2018), pp. 2403–2428. DOI: 10.1002/mma.4749 (see p. 70).

[311] P. Zhou et al. "CD151-α3β1 integrin complexes are prognostic markers of glioblastoma and cooperate with EGFR to drive tumor cell motility and invasion". In: *Oncotarget* 6.30 (2015), p. 29675. DOI: 10.18632/oncotarget.4896 (see p. 6).

[312] P. O. Zinn et al. "Radiogenomic mapping of edema/cellular invasion MRI-phenotypes in glioblastoma multiforme". In: *PloS One* 6.10 (2011), e25451. DOI: 10.1371/journal.pone.0025451 (see p. 63).